



JAEA-Review
2012-046

JAEA Takasaki Annual Report 2011

(Ed.) Takuji KOJIMA

Takasaki Advanced Radiation Research Institute

JAEA-Review

January 2013

Japan Atomic Energy Agency

日本原子力研究開発機構

本レポートは独立行政法人日本原子力研究開発機構が不定期に発行する成果報告書です。
本レポートの入手並びに著作権利用に関するお問い合わせは、下記あてにお問い合わせ下さい。
なお、本レポートの全文は日本原子力研究開発機構ホームページ (<http://www.jaea.go.jp>)
より発信されています。

独立行政法人日本原子力研究開発機構 研究技術情報部 研究技術情報課
〒319-1195 茨城県那珂郡東海村白方白根2番地4
電話 029-282-6387, Fax 029-282-5920, E-mail:ird-support@jaea.go.jp

This report is issued irregularly by Japan Atomic Energy Agency
Inquiries about availability and/or copyright of this report should be addressed to
Intellectual Resources Section, Intellectual Resources Department,
Japan Atomic Energy Agency
2-4 Shirakata Shirane, Tokai-mura, Naka-gun, Ibaraki-ken 319-1195 Japan
Tel +81-29-282-6387, Fax +81-29-282-5920, E-mail:ird-support@jaea.go.jp

© Japan Atomic Energy Agency, 2013

JAEA Takasaki Annual Report 2011

(Ed.) Takuji KOJIMA

Takasaki Advanced Radiation Research Institute

Japan Atomic Energy Agency

Watanuki-machi, Takasaki-shi, Gunma-ken

(Received November 22, 2012)

JAEA Takasaki annual report 2011 describes research and development activities performed from April 1, 2011 to March 31, 2012 with Takasaki Ion Accelerators for Advanced Radiation Application (TIARA, four ion accelerators), and electron/gamma-ray irradiation facilities (an electron accelerator and three ^{60}Co gamma-ray irradiation facilities) at Takasaki Advanced Radiation Research Institute, Japan Atomic Energy Agency (JAEA Takasaki). These activities are classified into four research fields: 1) Space, Nuclear and Energy Engineering, 2) Environmental Conservation and Resource Exploitation, 3) Medical and Biotechnological Application, and 4) Advanced Materials, Analysis and Novel Technology for Facilities.

This annual report contains 158 reports consisting of 150 research papers and 8 status reports on operation/maintenance of the irradiation facilities described above, and a list of publications, patents, related press-releases, television broadcasting, and the type of research collaborations as appendices.

Keywords: TIARA, Ion Accelerators, Electron Accelerator, Gamma-ray Facilities, Nuclear and Energy Engineering, Environmental Conservation, Resource Exploitation, Medical Application, Biotechnological Application, Advanced Materials, Analysis, Novel Technology, Materials for Space, Semiconductors, Inorganic Materials, Organic Materials, Functional Materials, Radiation Chemistry, Radiation Biology, Radioisotope Production, Nuclear Chemistry, Material Analyses, Solid State Physics, Beam Technology, Accelerator Technology, Facility Operation, Safety Control

(Editorial committee) Takuji KOJIMA, Hisayoshi ITOH, Atsushi TANAKA,
Watalu YOKOTA, Shimpei MATSUHASHI, Kiyoshi MIZUHASHI,
Hiroshi YOSHIDA and Yoshiteru NAKAMURA

高崎量子応用研究所研究年報 2011

日本原子力研究開発機構 高崎量子応用研究所
(編) 小嶋 拓治

(2012年11月22日受理)

高崎量子応用研究所研究年報 2011 は、同研究所にある TIARA 施設(イオン加速器 4 基)及び電子・ガンマ線照射施設(電子加速器 1 基、 ^{60}Co ガンマ線照射施設 3 棟)を利用して 2011 年 4 月 1 日から 2012 年 3 月 31 日までの間に行われた研究・技術開発成果をまとめたものである。この研究年報には、1) 宇宙・原子力・エネルギー、2) 環境保全・資源利用、3) 医療・バイオ技術応用、4) 先端材料・分析・基盤技術の 4 分野に分類した 150 編の論文及び 8 編の施設の運転・管理状況報告からなる合計 158 編を収録する。また、論文リスト、出願特許、新聞発表、テレビ放映及び研究実施形態・利用施設の一覧表を付録として含む。

高崎量子応用研究所：〒370-1292 群馬県高崎市綿貫町 1233

編集委員：(著者代表) 小嶋 拓治、伊藤 久義、田中 淳、横田 渉、
松橋 信平、水橋 清、吉田 宏、中村 義輝

PREFACE

This report covers activities of research and development conducted with TIARA (Takasaki Ion Accelerators for Advanced Radiation Application), electron beam and Co-60 gamma-ray irradiation facilities in Takasaki Advanced Radiation Research Institute, JAEA, from April 2011 to March 2012.

This annual report contains 158 papers in the fields of

- 1) Space, Nuclear and Energy Engineering,
- 2) Environmental Conservation and Resource Exploitation,
- 3) Medical and Biotechnological Application,
- 4) Advanced Materials, Analysis and Novel Technology for Facilities,
- 5) Status of Irradiation Facilities.

In the field of Space Engineering, radiation induced degradation and malfunction of semiconductor devices have been investigated to develop next generation electronic system equipped for artificial satellites. R&Ds of radiation resistant and new functional devices based on wide bandgap semiconductors like SiC, GaN and diamond have also been performed. For Nuclear and Energy Engineering, the practically available results were obtained for durability of polymeric insulators used in nuclear facilities, radiation stabilities of organic extractants, and hydrogen gas generation from cements, zeolites and metal ferrocyanide compounds used for radioactive waste treatment. As for structural materials used in light water, fast and fusion reactors, microstructural change in pressure vessel steels, fuel claddings and blanket materials has been intensively studied using TIARA. Polymer electrolyte membranes exhibiting high performance suitable for fuel cell application have been developed by radiation grafting and cross-linking technique.

In the field of Environmental Conservation and Resource Exploitation, metal ion adsorbents have been developed with radiation grafting technique and applied for removing toxic elements like Pb, B, As and Cs in waste water. Radiation grafting technique was also adopted for surface modification of industrial materials, leading to success in improving vulcanized rubber for car wiper. Radiation crosslinking technique was used for developing micro-fabrication technology of biodegradable polymers like polylactic acid in connection with their application to bio-micro/nano electro mechanical systems. Hydro-gels produced by crosslinking of hydroxypropyl cellulose were investigated for realizing three dimensional polymer gel dosimeter. R&Ds of the decomposition and removal of persistent antibiotics in waste water using electron beams and gamma-rays have been performed to develop new process technologies for environmental conservation.

In the field of Medical and Biotechnological Application, localization of apurinic lesions on DNA (AP-sites) induced by ionizing radiation was estimated by the Förster resonance energy transfer (FRET) method. Interestingly, not only He ions but also γ -rays seem to produce more localized AP-sites than randomly-distributed case. Bystander cell-killing effects were investigated. Survival of the cell population, in which about 0.02% of cells were irradiated with heavy ion microbeams, decreased at 24 hours. In contrast, survival of bystander cells co-cultured with cells irradiated with carbon ion broad-beams and γ -rays decreased at 6 hours or later suggesting that an increase in the number of irradiated cells in a cell population leads to an earlier emergence of the bystander cell-killing effect. The in-air micro particle-induced X-ray/Gamma-ray emission (micro-PIXE/PIGE) system has been utilized to obtain distribution of trace-elements in the micron-sized samples for bio-medical applications analyzing of asbestos in lung tissues, histamine in brain tissues, fluorine uptakes in carious enamel, erythrocyte elements in hepatitis C patients and so on. Radionuclides, which are produced with AVF cyclotron, have been used for cancer therapy and diagnosis. Radiopharmaceutical for diagnosis of malignant tumors which is ^{76}Br -labeled amino acid derivative ($[^{76}\text{Br}]$ bromo- α -methyl phenylalanine) was successfully prepared and evaluated as a potential PET tracer. The radionuclides are also applied to the plant studies on plant functions, absorption of various nutrients and pollutants from the environment, which is crucial for the human society. New experimental methods with the positron-emitting tracer imaging system (PETIS) have been developed for visualization and quantitative analyses of assimilation of carbon and nitrogen from the air, and uptake of cadmium and radiocesium from the soil. The ion beam breeding has been applied for many kinds of plants and microorganisms such as chrysanthemum, dahlia, rice, poplar, yeast and endophyte to obtain new useful varieties. By ion-beam irradiation, high temperature tolerant mutants of *Bradyrhizobium japonicum* were obtained. Study on lethal effect of ion beams in Arabidopsis seeds suggested that carbon ions near range end induce irreparable DNA lesions.

In the field of Advanced Materials and Analysis, various materials were developed by applying ion- or electron-irradiation effect: gasochromic metal oxide film, epoxy or fluoropolymer with nano/micro structures, nanowire/fiber, platinum nanoparticles, FeSi_2 nanocrystals, SiC membranes, charge stripper-foil, Mach-Zehnder polymer waveguides, hydrogen-storage alloys, ZnTeO alloys. Analyses of characteristics of various materials with and without irradiation were performed using conventional methods (e.g. photospectrometry, microscopy (TEM, AFM, MFM), and ESR) and radiation-applied analysis (e.g. activation, RBS, ISA, positron annihilation life time spectroscopy, and RHEPD). As for the Novel Technology, radiation chemistry studies on radiolysis of water or organics were carried out

using MeV-electron beams and pulsed heavy ion beams involving the development of time-resolved radiolysis techniques. Different kinds of measurements, CR-39 detector, TOF, and activation were studied for low-energy neutrons with improvements. Characteristics of alanine, rock-salt, diamond, and $\text{Al}_2\text{O}_3:\text{Eu}$, and polymer/cross-linker film were examined for new applications. The fundamental studies on the interaction between MeV/atom cluster ions and target materials for $\text{C}_2\text{-C}_{60}$ were performed on the basis of the measurement of secondary ions/electrons or luminescence emitted from materials, and theoretical estimation of energy deposition/loss. Technical developments at AVF cyclotron for single-ion-hit irradiation and wide uniform irradiation were in progress besides quick beam change for microbeams and emittance/acceptance measurement for higher available beam intensity. New beam line for cluster ion irradiation was settled at the single-ended accelerator.

About the Status of Irradiation Facilities, all the accelerators in TIARA, the AVF cyclotron, the 3-MV tandem accelerator, the 3-MV single ended accelerator and the 400-kV ion implanter, were stopped till the middle of May due to the influence of the Fukushima nuclear accident, though the immediate damage by the Great East Japan Earthquake was small. They were operated steadily and safely after resumption as well as MeV-electron and Co-60 gamma-ray irradiation facilities. Their operation on Saturday was carried out twelve times to make up for the lost beam time, and the yearly operation time of each accelerator was as long as in the normal year in consequence. The AVF cyclotron accelerated low-energy light ions during daytime in July, August and September in order to lower the peak electric power consumption according to the decision of the Japanese Government. Total operation times of the tandem accelerator, the single-ended accelerator and the ion implanter were 36,598, 41,674 and 32,457 hours, respectively, since the beginning of their operation. The total number of experiments made by various users using the AVF cyclotron was 9,241 from the first beam extraction in 1991 to March 2012, as a result of continuous efforts such as regular maintenance and trouble shooting.



Masao Tamada,
Director General
Takasaki Advanced Radiation Research Institute
Japan Atomic Energy Agency

This is a blank page.

Contents

1. Space, Nuclear and Energy Engineering	1
1-01 Estimation of Current-Voltage Characteristics of Subcells in a Multi-junction Solar Cell	5
1-02 Seebeck Coefficient of Hydrogenated Amorphous Silicon Semiconductors Irradiated with Protons	6
1-03 Improved Radiation Hardness of Phase-Locked Loop Circuits with Redundant Pairs of SOI Transistors for Analog Circuits	7
1-04 Research of Radiation Tolerance for Application of General Electronic Devices to Space Environment	8
1-05 Heavy Ion Induced Current Pulse Cross-Section Measurement on an Advanced MOSFET	9
1-06 Heavy-ion Induced Current in SOI pn Junction Diode	10
1-07 Peak Degradation of Heavy-Ion Induced Transient Currents in 6H-SiC MOS Capacitors	11
1-08 The Atomic Networks at the Amorphous SiO ₂ /SiC Interface of the Slab Model Generated with First-principles Molecular Dynamics Simulation	12
1-09 Single Ion Beam Induced Luminescence from Diamond Containing NV Centers	13
1-10 Isotopic Identification of Nitrogen-Vacancy Centers in Diamond Created by MeV Range ¹⁵ N Ion Implantation	14
1-11 Experimental Study on Radiation Effects on Magnetic Tunnel Junctions	15
1-12 Investigation of Europium Ion-implantation into Single-and Double-hetero AlGaN/GaN for Light Emitting Transistor	16
1-13 Study on Accelerated Ageing Tests of Ultra High Molecular Weight Polyethylene by Thermogravimetry	17
1-14 Radiation Effect on Solvent Extraction of Minor Actinide	18
1-15 Effect of Gamma Ray Irradiation on Hydrogen Absorption of Titanium in Nitric Acid Solution	19
1-16 Evaluation of Hydrogen Gas Generation from Cement Solidification Form by Gamma-ray Irradiation	20
1-17 Experimental Studies of Irradiation Effects on Zeolite Wastes after Decontamination of Radioactive Water	21
1-18 Behavior of Irradiated Nickel Ferrocyanide as Cesium Adsorbent with Gamma Ray	22
1-19 Study on Durability of Insoluble Ferrocyanides Adsorbents Incorporated into the Mordenites against Gamma Irradiation	23
1-20 Multi-Scale Models to Estimate Mechanical Response of Neutron-Irradiated Austenitic Steel Reactor Components	24
1-21 Radiation-Induced Hardening for Stainless Steel SUS316L with Bending Deformation	25

1-22	Irradiation Hardening in Extra High Purity Ni-base Superalloy under External Stress	26
1-23	Precipitate Stability in G-Phase Strengthened Ni-base Alloy under Multi-ion Irradiation	27
1-24	Effects of Displacement Damage and Gas Atoms on Radiation Hardening and Microstructure in F82H Weldment	28
1-25	Ionizing Dose Dependences of Radiation-induced Conductivity and Radiation-induced Electrical Degradation of Chemical Vapor Deposited Silicon Carbides under Gamma-ray Irradiation	29
1-26	Synthesis of Novel Anion Conductive Membranes Consisting of Iminium Cation by Radiation Grafting	30
1-27	Preparation of Anion-Exchange Membranes for Fuel Cell Applications by γ -ray Pre-Irradiation Grafting: Effect of the Structure of Quaternary Ammonium Ions	31
1-28	Wide- q Observation in Small Angle X-ray Scattering of ETFE-Based Graft-Type Polymer Electrolyte Membranes	32
1-29	Development of Grafted Type Poly(ether ether ketone) Electrolyte Membranes	33
1-30	Preparation of Novel Polymer Electrolyte Membranes by Combination of Radiation Induced Grafting and Atom Transfer Radical Polymerization	34
1-31	Ion-track Membranes of Poly(vinylidene fluoride): Etching Characteristics during Conductometric Analysis	35
1-32	Effect of Temperature on Conductivity of Ion Exchange Membrane in HCl Solution	36
1-33	Nanoparticle Formation by Tungsten Ion Implantation in Glassy Carbon	37
2.	Environmental Conservation and Resource Exploitation	39
2-01	Pb(II) Adsorption Performance of Fibrous Graft Adsorbent Having Phosphate Groups	41
2-02	Removal of Radioactive Cesium from Contaminated Environmental Water by Graft Adsorbent	42
2-03	Boron Removal and Recovery Using Adsorbent Prepared by Radiation Grafting	43
2-04	Arsenic Removal from Streaming Water by Graft Adsorbent Synthesized with Cellulose Nonwoven Fabric	44
2-05	Surface Modification of Vulcanized Rubber by Radiation Grafting	45
2-06	Micro-fabrication of Biodegradable Polymers by Focused Ion Beam Direct Etching	46
2-07	Preparation of Polymer Gel Dosimeters Based on Radiation-crosslinked Hydroxypropyl Cellulose Gels	47
2-08	Improvement of Mechanical Properties of Poly (L -Lactic Acid) by Blending with Polyamide 11 and Radiation-induced Crosslinking	48

2-09	Radiation Preparation of P(NIPAM-co-HEMA) and Micelles from PLLA-g-P(NIPAM-co-HEMA)	49
2-10	Reactivity of Oxidative/Reductive Species toward Persistent Antibiotics under Ionizing Radiation	50
2-11	Solution Properties of Seaweed Polysaccharide Funoran	51
2-12	Immobilization of Nitrifying Bacteria to the HPC Gel Medium Synthesized by Electron Beam Irradiation	52
2-13	Interaction between <i>Paramecium bursaria</i> and Heavy Elements	53
2-14	Measurement of Trace Elements in Natural Water in Iwaki City after Earthquake by In - Air Micro-PIXE	54
3.	Medical and Biotechnological Application	55
3-01	Development of a Method for Estimating Localization of Lesions on DNA by Ionizing Radiations	61
3-02	Mutagenic Effects of He Ion Particles in DNA Repair Mutants of <i>Escherichia coli</i>	62
3-03	Target Irradiation of Individual Cells Using Focusing Heavy-Ion Microbeam of JAEA-Takasaki (III): A Development of Rapid Cell-Targeting System Using Beam Scanner	63
3-04	Responsible Site for the Radiation Response of the Salt Chemotaxis Learning in <i>C. elegans</i> Using Heavy-ion Microbeam	64
3-05	Time-course Analysis of Radiation-induced Bystander Cell-killing Effect Using Heavy-ion Beams and γ -rays	65
3-06	Interaction of Etoposide with High LET Irradiation in Lung Cancer Cells Compared to X-Ray Irradiation	66
3-07	Mechanisms for the Induction of Radioadaptive Response by Radiation-Induced Bystander Response	67
3-08	Analysis of Bystander Cell Signaling Pathway Activated by Heavy Ion-Microbeam III	68
3-09	Chromosomal Aberrations Induced by Intercellular Communication Mediated Bystander Effect in Normal Human Fibroblasts Induced by C-, Ne- and Ar-ion Microbeams	69
3-10	Analysis of Bystander Effect Induced by Cell Membrane Response in Glioma Cells	70
3-11	Ion Beam Irradiation Has Different Influences on the Expression of Bcl-2 in Cultured Human Retinal Vascular Endothelial Cells Exposed to L-dopa among ^{20}Ne , ^{12}C , and ^4He	71
3-12	Ionizing Radiation Alters the Dynamics of Human Long Interspersed Nuclear Elements 1 (LINE1) Retrotransposon	72
3-13	Degradation of Nucleus in the Heavy-ion Irradiated Silkworm Egg just after Having Reached the Peripheral Region of the Egg	73

3-14	Neurocytotoxic Effects of Micro-beam Irradiation of Heavy Carbon-ions on the Developing Medaka Brain Measured in vivo	74
3-15	Wide Overlap in Gene Expression Response to Desiccation and Ionizing Radiation in the Sleeping Chironomid Larvae	75
3-16	The Effects of THP-1 Macrophages on the Migration of Heavy-ion Irradiated Human Lung Cancer Cells	76
3-17	Effects of Carbon-ion Microbeam Irradiation on Locomotion in <i>Caenorhabditis elegans</i>	77
3-18	Rapid ESR Measurement of Irradiated Fresh Papaya	78
3-19	ESR Studies on Decay of Radicals Induced in Irradiated Foods	79
3-20	Improvement of Spatial Resolution of PIXE-CT Using ML-EM Algorithm in TIARA	80
3-21	Measurement of Trace Elements in Histamine Receptor Deficient Mice Brain Slices by In - Air Micro-PIXE	81
3-22	Comparison of Two Fluoride Regimens on Fluorine Uptake in Carious Enamel during pH-cycling	82
3-23	Imaging of Metallofullerene Distribution Using Micro-particle Induced X-ray Emission for Gadolinium Neutron Capture Therapy	83
3-24	Analysis of Particles in Interstitial Pneumonia Lung Tissue Obtained by Transbronchial Biopsy	84
3-25	Analysis of Erythrocyte Elements in Hepatitis C Patients Treated with Peginterferon-alfa and Ribavirin	85
3-26	Decreasing Size of Microcapsules and Increased Radiation-induced Release of Antitumor Drugs	86
3-27	Cultivation of Marine Planktons by the Artificial Seawater and Elemental Mapping by Micro Beam PIXE System of TIARA	87
3-28	Synthesis of Radioiodinated Antitumor Cyclic Peptide, [¹²⁵ I]-Sansalvamide A Derivative	88
3-29	Development of a ⁷⁶ Br-labeled Amino Acid Derivative for PET Imaging of Tumor	89
3-30	The Process to Improve the Production of ¹³ N-labeled Nitrogen Gas Tracer for the Imaging of Nitrogen Fixation in Soybean Nodules	90
3-31	Real-Time Imaging and Analysis of Differences in Cadmium Dynamics in Rice Cultivars (<i>Oryza sativa</i>) Using Positron-Emitting ¹⁰⁷ Cd Tracer	91
3-32	Imaging of Root Exudates Secreted from Soybean Root to Soil by Using Carbon-11-Labeled Carbon Dioxide and PETIS	92
3-33	A New Method to Analyze Individual Photosynthetic Abilities of Young Plant Seedlings Using Positron-Emitting Tracer Imaging System (PETIS)	93
3-34	Production of Cs-129 Tracer by Using Ion Beam Bombardment for Positron Imaging Applications	94
3-35	Development of Ion Beam Breeding Technology in Plants and Creation of Useful Plant Resources	95

3-36	Ion Beam Irradiation on Rice Seeds for the Mutation Breeding Project of the Forum for Nuclear Cooperation in Asia (FNCA)	96
3-37	Generating New Ornamental Plant Varieties Using Ion Beams	97
3-38	Mutational Effects of Carbon Ions near the Range End and Development of an Efficient Mutagenesis Technique Using Ion Beams	98
3-39	Effect of Carbon Ion Beam Irradiation on Callus Growth in Arabidopsis and Rice	99
3-40	Developing Protocol for Screening of Drought/Salt Tolerant Mutants with Ion Beam Mutagenesis in <i>Populus</i> sp.	100
3-41	Effects of Gamma Ray Irradiation on <i>Rumex obtusifolius</i> L.	101
3-42	Production of Mutants by Ion Beam Irradiation in <i>Dahlia</i> spp.	102
3-43	Analysis of Mutant Frequencies for Different LET Radiations in <i>Deinococcus radiodurans</i>	103
3-44	Functional analysis of Universally Conserved Genes, <i>ygiD</i> and <i>yeaZ</i> Orthologs, in DNA Repair of <i>Deinococcus radiodurans</i>	104
3-45	DNA Damage Evaluation System of the High-LET Ion Beam Using the Polymerase Chain Reaction	105
3-46	Application of Bio-pesticide with Plant Growth Promoter Made from Oligo-chitosan	106
3-47	Phenotypic Characterization of High Temperature Tolerant Mutants of <i>Bradyrhizobium japonicum</i> USDA110 Generated by Ion-beam Irradiation	107
3-48	FACS-based Screening for Yeast Clone Highly Expressing Cellulase	108
3-49	Benomyl-tolerant Mutation of Entomopathogenic Fungi Induced by Carbon Ion Beams	109
3-50	Identification of Mutation Sites in High Ethyl Caproate Producing Sake Yeasts Generated by Ion Beam Breeding	110
3-51	Effects of Ion Beam Radiation on Genome Integrity in <i>Saccharomyces cerevisiae</i>	111
3-52	The Effect of γ -sterilization of Biofertilizer's Carrier on Bacterial Inoculants Survival	112
4. Advanced Materials, Analysis and Novel Technology for Facilities ..		113
4-01	Preparation of Gasochromic Transition Metal Oxide Thin Films by Pulsed Laser Deposition	117
4-02	Three-dimensional Micro-assembly on the Single Particle Nano-fabrication Technique	118
4-03	Fabrication of Poly(vinylphenol)/Ti-O Hybrids Nanowires by High Energy Ion Beam	119
4-04	Formation of Nano Fiber Including Au Particles by Ion Beam Irradiation	120
4-05	Production of Platinum Nanoparticles Using a Few Tens keV Electron Beams	121

4-06	Stability of Silicon Carbide Membrane Prepared from Polymer Precursor in Steam	122
4-07	Ion Beam Synthesis of Carbon Doped β -FeSi ₂ Nanocrystals Embedded in Si and Their Photoluminescence Enhancement	123
4-08	Synthesis of Highly-mismatched ZnTeO Alloys with Multiple Band Gaps by Oxygen Ion Implantation	124
4-09	Microscopic Observation for Damage of Hybrid Type Boron-Doped Carbon Stripper Foil by Ion Beam	125
4-10	Mach-Zehnder Polymer Waveguides Fabricated Using Proton Beam Writing ..	126
4-11	Multiplex Energy Proton Irradiation Effects on Hydriding Property of a Hydrogen Storage Alloy	127
4-12	Fabrication of Microstructure at a Fluoropolymer Surface by Ion Microbeam ..	128
4-13	Electroplating of Ni Microstructures on the Cross Section of Cu Wire Using PMMA Mother Fabricated by Proton Beam Writing	129
4-14	Epitaxial Transformation of Evaporated-Ti Thin Films during Nitriding Processes due to Ion-Implantation	130
4-15	Gamma-ray Induced Defect Formation in High-purity α -Quartz	131
4-16	Thermal Stability of Fe ₂ MnSi/Ge(111) Heteroepitaxial Interfaces	132
4-17	MFM Observation of Micrometer-sized Magnetic Patterns Produced by Heavy Ion Microbeam Irradiation in FeRh Films	133
4-18	Nuclear Reaction Imaging of Boron Doped Iron	134
4-19	Ion Scattering Spectroscopy of Polarity-controlled ZnO Surfaces by 1 - 2 MeV C ⁺ Ions	135
4-20	He ⁺ Ion Implantation Effect on Cathodoluminescence of Plagioclase	136
4-21	Reconstruction of the Tectonic Activity in the Southwestern Tarim Basin	137
4-22	Development of Spin-Polarized Positron Beam and Its Application to Spintronics Study	138
4-23	Thermal Stability of Vacancies in Zr-Doped Stainless Steels	139
4-24	Observation of Spatial Distribution of Vacancy Defects in Semiconductor by Positron Microbeam and Electron Beam Induced Current Measurement	140
4-25	Atomic Displacement of Pb/Ag(111) Surface Studied by Reflection High-energy Positron Diffraction	141
4-26	Phase Transition of Quasi One-dimensional Nanowire on Pt/Ge(001) Surface Studied by Reflection High-energy Positron Diffraction	142
4-27	Pulse Radiolysis of Water by Energetic Heavy Ion	143
4-28	Transient Absorption of Pyrene-Dodecane Solution Measured by Microsecond Ion Beam Pulse Radiolysis	144
4-29	Solvent Effect on the Radiation Induced Copolymerization of Maleimide with Styrene	145
4-30	Improvement of Source Neutron Spectrum Measurement Down to a Few MeV	146

4-31	Measurements of Low Energy Neutron Spectra of Quasi-Monoenergetic Neutron Fields by the TOF Method at TIARA	147
4-32	Measurements of Neutron and Charged Particle Production Cross Sections on Be and Fe Bombarded with 13 MeV/nucleon ^{20}Ne Beam	148
4-33	Measurement of Thick Target Neutron Yields by 10 MeV Deuteron Incidence on Tungsten	149
4-34	Development of Spatial Resolution Test-chart and Novel Fluorescent Converter Plates for Neutron Radiography	150
4-35	Response Studies of CR-39 Track Detectors Irradiated Heavy Ions under Vacuum	151
4-36	Measurement of Radio Wave Reflection Due to Rock Salt and Ice Irradiated by an Electron Beam for an Ultra-high-energy Neutrino Detector	152
4-37	Effect of Temperature on the Response of Alanine Dosimeters under Low Dose and Long Time Irradiation	153
4-38	Status Report on Technical Developments of the JAEA AVF Cyclotron	154
4-39	Development of Beam Generation and Irradiation Technology for Electrostatic Accelerators	155
4-40	Fast Single-Ion Hit System for Heavy-Ion Microbeam at TIARA Cyclotron (V)	156
4-41	Use of Gafchromic Dosimetry Films to Measure a Large-Area Ion-Beam Distribution	157
4-42	Detection Method for Dose Distribution of Focused Proton Beam by Using Common Polymer Film	158
4-43	Development of Visible Light Measurement Techniques for Detention of Single-ion Hit	159
4-44	Development of Transmission Thin Diamond Sensors for the Single Hit Detection of High-energy Ions	160
4-45	Quantitative Evaluation of Charge State for Internuclear Distance of Constituent Ions Dissociated from C_2^+ Ion Moving in a Solid	161
4-46	Ion Induced Luminescence from Sapphire Irradiated with Swift Cluster Ion Beams - Cluster Ion Size and Energy Dependences -	162
4-47	Visualization of a Single Cluster Particle Track in Polystyrene Films	163
4-48	Electronic Stopping Power Connected with Average Charge Reduction for Swift Carbon Cluster Ions in Carbon	164
4-49	Reduction of Charging Effects on Negative Secondary Ion TOF Mass Spectra of PMMA Using Cluster Ion Impacts	165
4-50	Cluster Effect on Damage Accumulation in a Si Crystal Bombarded with 10-540-keV C_{60} Ions	166
4-51	Cluster Effect on Projected Range of 30-keV C_{60}^+ in Silicon	167

5. Present Status of Irradiation Facilities 2011	169
5-01 Feature in FY2011, Utilization Status and Beam Time Proportion at TIARA Facility	171
5-02 Operation of the AVF Cyclotron	172
5-03 Operation of Electrostatic Accelerators	173
5-04 Operation of the Electron Accelerator and the Gamma-ray Irradiation Facilities	174
5-05 Utilization of the Electron Accelerator and the Gamma-ray Irradiation Facilities	175
5-06 Radiation Control in TIARA	176
5-07 Radioactive Waste Management in TIARA	177
5-08 FACILITY USE PROGRAM in Takasaki Advanced Radiation Research Institute	178
 Appendix	 179
 Appendix 1 List of Publication	 181
Appendix 2 List of Related Patents	202
Appendix 3 List of Related Press-Release and Television Broadcasting	204
Appendix 4 Type of Research Collaboration and Facilities Used for Research	206
Appendix 5 Examples of Typical Abbreviation Name for Organizations in Japan Atomic Energy Agency (JAEA)	208

1. Space, Nuclear and Energy Engineering

1-01	Estimation of Current-Voltage Characteristics of Subcells in a Multi-junction Solar Cell	5
	T. Nakamura, M. Imaizumi, S. Sato and T. Ohshima	
1-02	Seebeck Coefficient of Hydrogenated Amorphous Silicon Semiconductors Irradiated with Protons	6
	S. Sato and T. Ohshima	
1-03	Improved Radiation Hardness of Phase-Locked Loop Circuits with Redundant Pairs of SOI Transistors for Analog Circuits	7
	S. Kuboyama, A. Maru, H. Shindou, H. Abe, T. Hirao and T. Ohshima	
1-04	Research of Radiation Tolerance for Application of General Electronic Devices to Space Environment	8
	T. Maeda, Y. Kakimi, N. Sasaki, H. Kumagai, H. Miyata T. Ohshima, T. Hirao and S. Onoda	
1-05	Heavy Ion Induced Current Pulse Cross-Section Measurement on an Advanced MOSFET	9
	T. Makino, S. Onoda, T. Hirao, T. Ohshima, D. Kobayashi, H. Ikeda and K. Hirose	
1-06	Heavy-ion Induced Current in SOI pn Junction Diode	10
	Y. Takahashi, Y. Okazaki, S. Ogura T. Hirao, S. Onoda and T. Ohshima	
1-07	Peak Degradation of Heavy-Ion Induced Transient Currents in 6H-SiC MOS Capacitors	11
	T. Makino, N. Iwamoto, S. Onoda, T. Ohshima, K. Kojima and S. Nozaki	
1-08	The Atomic Networks at the Amorphous SiO ₂ /SiC Interface of the Slab Model Generated with First-principles Molecular Dynamics Simulation ..	12
	A. Miyashita and M. Yoshikawa	
1-09	Single Ion Beam Induced Luminescence from Diamond Containing NV Centers	13
	S. Onoda, T. Makino and T. Ohshima	
1-10	Isotopic Identification of Nitrogen-Vacancy Centers in Diamond Created by MeV Range ¹⁵ N Ion Implantation	14
	T. Yamamoto, S. Onoda, T. Ohshima, K. Jahnke, P. Heller, A. Gerstmayr, A. Häußler, B. Naydenov, F. Jelezko, F. Dolde, H. Fedder, J. Honert, J. Wrachtrup, K. Watanabe, T. Teraji, T. Taniguchi, S. Koizumi, M. L. Markham, D. J. Twitchen, T. Umeda and J. Isoya	
1-11	Experimental Study on Radiation Effects on Magnetic Tunnel Junctions	15
	D. Kobayashi, Y. Takehashi, K. Hirose, S. Ikeda, T. Endoh, H. Ohno, S. Onoda and T. Makino	
1-12	Investigation of Europium Ion-implantation into Single-and Double-hetero AlGaIn/GaN for Light Emitting Transistor	16
	H. Okada, M. Kondo, A. Wakahara, S. Sato and T. Ohshima	

1-13	Study on Accelerated Ageing Tests of Ultra High Molecular Weight Polyethylene by Thermogravimetry	17
	A. Shimada, M. Arai, M. Sugimoto, M. Yoshikawa and H. Kudo	
1-14	Radiation Effect on Solvent Extraction of Minor Actinide	18
	Y. Sugo, M. Taguchi, Y. Sasaki, Y. Morita and N. S. Ishioka	
1-15	Effect of Gamma Ray Irradiation on Hydrogen Absorption of Titanium in Nitric Acid Solution	19
	T. Motooka, Y. Ishijima, F. Ueno and M. Yamamoto	
1-16	Evaluation of Hydrogen Gas Generation from Cement Solidification Form by Gamma-ray Irradiation	20
	T. Nakayama, Y. Kawato and Y. Meguro	
1-17	Experimental Studies of Irradiation Effects on Zeolite Wastes after Decontamination of Radioactive Water	21
	R. Nagaishi, Y. Kumagai, N. Aoyagi, I. Yamagishi and K. Nishihara	
1-18	Behavior of Irradiated Nickel Ferrocyanide as Cesium Adsorbent with Gamma Ray	22
	Y. Koma, Y. Arai, Y. Takahatake, S. Watanabe, K. Nomura and Y. Nakajima	
1-19	Study on Durability of Insoluble Ferrocyanides Adsorbents Incorporated into the Mordenites against Gamma Irradiation	23
	Y. Itoh, Y. Saitoh and T. Hirata	
1-20	Multi-Scale Models to Estimate Mechanical Response of Neutron-Irradiated Austenitic Steel Reactor Components	24
	S. Jitsukawa, Y. Abe, M. Ando, N. Ishikawa, N. Okubo, K. Suzuki and S. Ohnuki	
1-21	Radiation-Induced Hardening for Stainless Steel SUS316L with Bending Deformation	25
	N. Ishikawa, N. Okubo and K. Kondo	
1-22	Irradiation Hardening in Extra High Purity Ni-base Superalloy under External Stress	26
	I. Ioka, G. H. Kim and K. Shiba	
1-23	Precipitate Stability in G-Phase Strengthened Ni-base Alloy under Multi-ion Irradiation	27
	G. H. Kim, I. Ioka, T. Sawai and S. Yamashita	
1-24	Effects of Displacement Damage and Gas Atoms on Radiation Hardening and Microstructure in F82H Weldment	28
	M. Ando and H. Tanigawa	
1-25	Ionizing Dose Dependences of Radiation-induced Conductivity and Radiation-induced Electrical Degradation of Chemical Vapor Deposited Silicon Carbides under Gamma-ray Irradiation	29
	B. Tsuchiya, T. Shikama, S. Nagata, K. Saito and S. Yamamoto	

1-26	Synthesis of Novel Anion Conductive Membranes Consisting of Iminium Cation by Radiation Grafting	30
	K. Yoshimura W. Sinananwanich, H. Koshikawa, M. Asano, T. Yamaki, K. Yamamoto, H. Shishitani, K. Asazawa, S. Yamaguchi, H. Tanaka and Y. Maekawa	
1-27	Preparation of Anion-Exchange Membranes for Fuel Cell Applications by γ -ray Pre-Irradiation Grafting: Effect of the Structure of Quaternary Ammonium Ions	31
	H. Koshikawa, K. Yoshimura, T. Yamaki, M. Asano and Y. Maekawa	
1-28	Wide- q Observation in Small Angle X-ray Scattering of ETFE-Based Graft-Type Polymer Electrolyte Membranes	32
	T. D. Tran, S. Sawada, S. Hasegawa, K. Yoshimura, Y. Oba, M. Ohnuma, Y. Katsumura and Y. Maekawa	
1-29	Development of Grafted Type Poly(ether ether ketone) Electrolyte Membranes	33
	S. Hasegawa, H. Iwase, S. Koizumi, Y. Oba, M. Ohnuma and Y. Maekawa	
1-30	Preparation of Novel Polymer Electrolyte Membranes by Combination of Radiation Induced Grafting and Atom Transfer Radical Polymerization	34
	S. Sawada, S. Hasegawa and Y. Maekawa	
1-31	Ion-track Membranes of Poly(vinylidene fluoride): Etching Characteristics during Conductometric Analysis	35
	N. Nuryanthi, T. Yamaki, H. Koshikawa, M. Asano, S. Sawada, S. Hasegawa, Y. Katsumura and Y. Maekawa	
1-32	Effect of Temperature on Conductivity of Ion Exchange Membrane in HIX Solution	36
	N. Tanaka, T. Yamaki, M. Asano, T. Terai and K. Onuki	
1-33	Nanoparticle Formation by Tungsten Ion Implantation in Glassy Carbon	37
	S. Kato, T. Yamaki, S. Yamamoto, T. Hakoda, K. Kawaguchi, T. Kobayashi, Y. Maekawa, A. Suzuki and T. Terai	

This is a blank page.

1 - 01 Estimation of Current-Voltage Characteristics of Subcells in a Multi-junction Solar Cell

T. Nakamura ^{a)}, M. Imaizumi ^{a)}, S. Sato ^{b)} and T. Ohshima ^{b)}

^{a)} Aerospace Research and Development Directorate, JAXA,

^{b)} Environment and Industrial Materials Research Division, QuBS, JAEA

Multi-junction (MJ) solar cells are currently used for space since they have high conversion efficiency. In order to utilize such solar cells in space environment, we need to experimentally clarify the radiation resistance of their output performance, because the performance degrades by radiation. However, multi-junction solar cells are composed of a number of subcells which are electrically connected in series. Their degradation behavior is, therefore, complicated and difficult to understand.

It is possible to obtain the value of I_{sc} of each subcell by changing the current-limiting subcell using color bias lights. On the other hand, the technique to estimate dark current-voltage (DIV) in MJ cells, their shortcircuit current (I_{sc}) is determined by a subcell that generates the smallest I_{sc} , while their open-circuit voltage (V_{oc}) is the sum of $V_{oc,s}$ of all subcells. DIV characteristics of subcells in a MJ cell using electroluminescence (EL) intensity has been proposed¹⁾. The combination of the above two method enables us to deduce IV characteristics under light illumination (LIV) of each subcell²⁾.

In this work, we applied the methods to obtain LIV characteristics including values of I_{sc} and V_{oc} of each subcell in a MJ cell before and after proton and electron irradiations. In addition, change in series (R_s) and shunt (R_{sh}) resistances of the subcells were also analyzed.

InGaP/GaAs dual-junction (2J) solar cells (bare type, 2 cm × 2 cm in size) were prepared for this study. They were irradiated with 3 MeV, 120 keV, and 60 keV protons and 1 MeV electrons. According to simulation results of The Stopping and Range of Ions in Matter (SRIM), 3 MeV protons penetrate the whole 2J layers, while 120 keV and 60 keV protons stop at p/n junction of the GaAs bottom-subcell and InGaP top-subcell, respectively. Before and after the irradiations, DIV of the subcells were characterized using the EL method. Also, LIV of the 2J cell was measured under illumination of an air mass zero solar simulator. The DIV curves obtained by the EL method were compensated by adding R_{sh} and R_s factors; both of the values were estimated by numerical fitting to the measured IV curves using the Simulation Program with Integrated Circuit Emphasis (SPICE). The LIV of each subcell was estimated by adding I_{sc} from the bias light method to its DIV from the EL method. Then the LIV of the 2J cell was composed from the estimated subcell LIV characteristics.

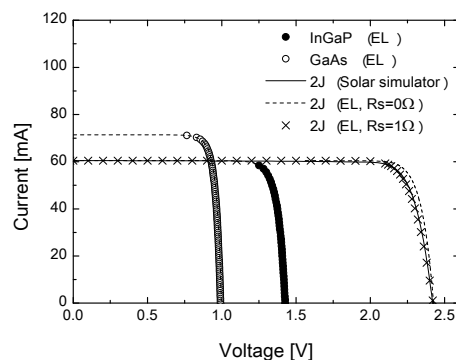
Figure 1 indicates the comparison of the measured LIV of the 2J cell under the solar simulator and the composed LIV of one from the estimated subcell LIVs. Both the

cases of (a) before and (b) after the 3 MeV proton irradiation (fluence = $3 \times 10^{12} \text{ p}^+/\text{cm}^2$) are shown. For the fitting LIV curves of the subcells, the two-diode model was used. By adding the consideration of change in R_s and R_{sh} , the measured and simulated LIV characteristics of the 2J cell agrees sufficiently.

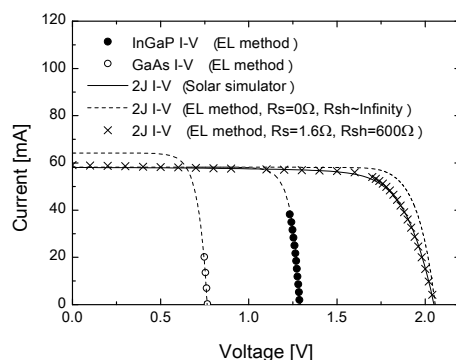
These results promise us to enable more precise analysis of radiation degradation behavior of MJ cells. This leads to establish a degradation model and consequently an accurate degradation prediction methodology for MJ cells. Studies on other types of MJ cells irradiated with various energies of protons and electrons are underway.

References

- 1) T. Kirchartz et al., Appl. Phys. Lett. **92** (2008) 123502.
- 2) S. Roensch et al., Appl. Phys. Lett. **98** (2011) 251113.



(a) Before irradiation



(b) After irradiation

Fig. 1 Composed LIV characteristic of InGaP and GaAs subcells, and measured and simulated LIVs of 2J cell; (a) before irradiation and (b) after 3 MeV proton irradiation with the fluence of $3 \times 10^{12} \text{ p}^+/\text{cm}^2$.

1 - 02 Seebeck Coefficient of Hydrogenated Amorphous Silicon Semiconductors Irradiated with Protons

S. Sato and T. Ohshima

Environment and Industrial Materials Research Division, QuBS, JAEA

I. Introduction

Hydrogenated amorphous silicon (a-Si:H) semiconductor devices have high radiation tolerance and are expected to be utilized in radiation environments¹⁾ (e.g. space solar cells and photo-detectors in nuclear reactors or accelerator facilities). In order to make the radiation hardened a-Si:H device design, variations of the electrical properties due to radiation exposure should be clarified. In this context, we have studied variations of the electrical properties due to radiation exposure²⁻⁵⁾.

II. Experimental

The samples were device-grade undoped a-Si:H thin films fabricated on glass substrates by Plasma Enhanced Chemical Vapor Deposition (PECVD). The film thickness was 0.30 μm and coplanar-type aluminum Ohmic electrodes were formed on the film.

The samples were irradiated with 0.10 and 3.0 MeV protons, and subsequently the Seebeck coefficient variations of the irradiated samples were investigated by the *in-situ* thermoelectric power measurement system shown in Fig. 1⁴⁾. Since the Seebeck coefficient of an n-type semiconductor is negative and that of a p-type is positive, the conduction type of the irradiated samples can be clarified from the analysis of the Seebeck effect. The temperature difference was produced between the upper and lower parts of the sample, and the electric potential difference (thermoelectric power) between the electrodes was measured. The proton irradiation and the thermoelectric power measurement were performed alternately in the irradiation chamber. The proton beams were stopped by a shutter during measurements.

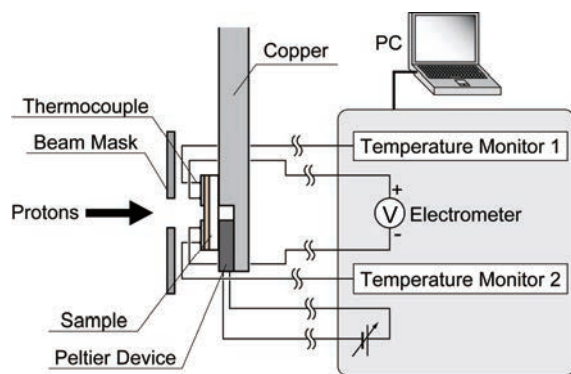


Fig. 1 A schematic drawing of experimental setup.

III. Results and Discussion

Seebeck coefficient variations of the undoped a-Si:H irradiated with 0.10 MeV and 3.0 MeV protons are shown in Fig. 2. The negative Seebeck effect was observed in the undoped a-Si:H irradiated with 3.0 MeV protons at the fluence above $3.0 \times 10^{11} / \text{cm}^2$, although no Seebeck effect was observed before irradiation. Slightly increasing up to the fluence of around $10^{13} / \text{cm}^2$, the Seebeck coefficient decreased at above $2.0 \times 10^{13} / \text{cm}^2$, and eventually could not be measured again at above $4.0 \times 10^{14} / \text{cm}^2$. The negative Seebeck effect was also observed between $1.0 \times 10^{11} / \text{cm}^2$ and $3.0 \times 10^{12} / \text{cm}^2$ in the case of 0.10 MeV proton irradiation. The Seebeck effect could not be measured again at the fluences above $1.0 \times 10^{13} / \text{cm}^2$. These results indicate that the conduction type of undoped a-Si:H was n-type in that fluence regime and donor-centers were generated due to proton irradiation. Therefore, it is concluded that the increase in dark conductivity and photoconductivity due to proton irradiation, which we have reported previously^{2,3,5)}, is attributed to the donor-center generation.

We would like to thank Dr. Hitoshi Sai of National Institute of Advanced Industrial Science and Technology (AIST) for fabricating the a-Si:H samples.

References

- 1) P. J. Sellin et al., Nucl. Instrum. Meth. Phys. Res. A **557** (2006) 479-89.
- 2) S. Sato et al., Proc. 35th IEEE PVSC (2010) 2620-24.
- 3) S. Sato et al., J. Non-Cryst. Sol. **356** (2010) 2114-19.
- 4) S. Sato et al., Appl. Phys. Express **4** (2011) 061401.
- 5) S. Sato et al., J. Non-Cryst. Sol. (2012) *in Press*.

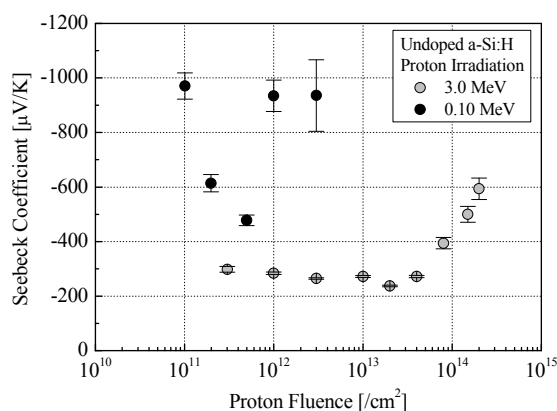


Fig. 2 Seebeck coefficient variations of undoped a-Si:H thin films irradiated with 0.10 MeV and 3.0 MeV protons.

1 - 03 Improved Radiation Hardness of Phase-Locked Loop Circuits with Redundant Pairs of SOI Transistors for Analog Circuits

S. Kuboyama ^{a)}, A. Maru ^{a)}, H. Shindou ^{a)}, H. Abe ^{b)}, T. Hirao ^{b)} and T. Ohshima ^{b)}

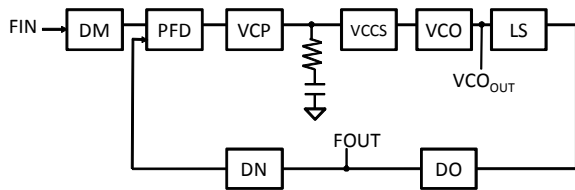
^{a)} Aerospace Research and Development Directorate, Japan Aerospace Exploration Agency (JAXA),
^{b)} Environment and Industrial Materials Research Division, QuBS, JAEA

Single-event transient (SET) pulse in nano-meter scale integrated circuits caused by high energy heavy ions and protons in space radiation is serious problem for electronic equipments intended to be operated in the space environments. Many mitigation techniques such as triple modular redundancy (TMR)¹⁾ have been studied extensively for a long time. SET free inverter (SFI) circuit²⁾ is one of the mitigation techniques. The SFI circuit is only applicable to SOI process technology. However it has a unique feature that SET pulse generation is essentially prevented by the circuit itself. All other techniques cannot prevent the generation of pulses and only reject them with voting or filtering circuits with additional timing penalty.

The principle of SFI circuit is easily extended to all other combinational and sequential logic circuits and successfully applied to application specific integrated circuits (ASICs)³⁾ including micro-processor unit (MPU) for space applications.

In this study, the principle of SFI operation is extended to analog circuits such as current mirror circuits. It has been demonstrated with a phase-locked loop circuits intended to be utilized in ASICs, which includes some analog circuit blocks, such as the current mirror, differential amplifiers and so on.

The Phase-locked Loop (PLL) circuits are composed of several functional circuit blocks as shown in Fig. 1. The programmable divider (DM/DN/DO) and phase detector (PFD) are digital circuits, which can be hardened by using SFI and derivative basic logic circuits. Remaining analog circuit blocks are voltage-switching charge pump (V-CP), voltage controlled current source (VCCS), and voltage controlled oscillator (VCO). In this study, all these circuits were hardened utilizing the redundant pair transistors.



DM/DN/DO: Programmable Divider circuits
 PFD: Phase Detector
 VCP: Voltage Charge Pump
 VCCS: Voltage Controlled Current Source
 VCO: Voltage Controlled Oscillator
 LS: Level Shifter

Fig. 1 Block diagram of PLL designed.

VCCS is the most complicate analog circuit block in our PLL, the circuit was also hardened by using the redundant pair transistors as shown in Fig. 2. Its SET immunity was confirmed in detail with Simulation Program with Integrated Circuit Emphasis (SPICE) and Hyper Device-Level Electrical Operation Simulator (HyDeLEOS)⁴⁾ and obtained a good result.

The PLL was fabricated and evaluated for SET immunity by using heavy ions with LET of 3.4 ~ 68.8 MeV/(mg/cm²). The input frequency was 10 MHz, VCO was oscillating at 600 MHz, and the output frequency of PLL was set to 100 MHz for the experiments. No burst mode error was observed up to LET of 68.8 MeV/(mg/cm²). The observed error mode was only single prolonged period. For the clock source, the incidence of the single prolonged period is not critical. This error mode was caused by the event in the level converter which was not hardened utilizing the redundant pair transistors. The level converter will be hardened utilizing the redundant pair transistors in the second sample, we will continue to evaluate its radiation tolerance.

References

- 1) F. L. Kastensmidt, IEEE NSREC Short Course Notebook, 2007.
- 2) A. Makihara, IEEE Trans. Nucl. Sci. 53 (6) (2006) 3422-27.
- 3) A. Makihara, Proc. IEEE RADECS 2010.
- 4) HyDeLEOS : 3 dimensional device simulator (Hyper Device-Level Electrical Operation Simulator) ver.5.5, Users Manual from Semiconductor Leading Edge Technologies Inc., 2011.

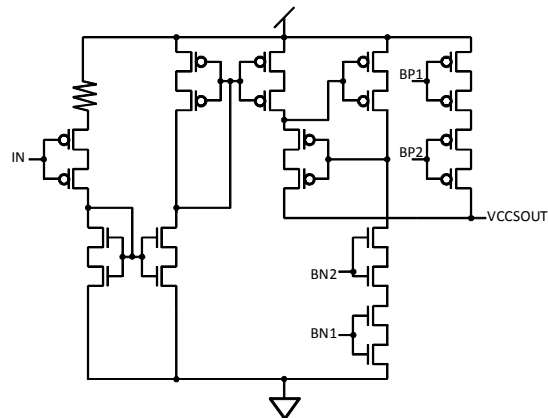


Fig. 2 VCCS utilizing redundant transistor pairs.

1 - 04 Research of Radiation Tolerance for Application of General Electronic Devices to Space Environment

T. Maeda ^{a)}, Y. Kakimi ^{a)}, N. Sasaki ^{a)}, H. Kumagai ^{a)}, H. Miyata ^{a)},
T. Ohshima ^{b)}, T. Hirao ^{b)} and S. Onoda ^{b)}

^{a)} Advanced Engineering Services Co., Ltd.,
^{b)} Environment and Industrial Materials Research Division, QuBS, JAEA

We have tested general electronic devices about radiation tolerance since 2008. This study aims to apply these electronic devices to Small-Satellite design. This time, we tested two memories, which have different architecture each other and a FET (Field Effect Transistor) by heavy-ion beam irradiation. As a result, both memories have strong tolerance for SEE (Single Event Effect). Probability of SEE occurrence which estimated from irradiation results is less than once in the Small-Satellite's operation life on orbit (about 1 year). The FET has strong tolerance for SEGR similarly. Especially, it turned out that probability of SEGR occurrence will be suppressed by $1/10^7$ compared with the case where the FET is used on maximum rating voltage when the FET is used by below 63% of maximum rating voltage. Also, if SEGR occurred, the circuit between gate and source in the FET was in the short circuit state. Therefore, since large current may flow between gate and source, it is necessary to put protecting resistance into the gate line to protect circumference circuit.

小型衛星 (質量 100 kg 以下) の現場では、大型衛星に比べ、短期間開発という利点を最大限に活かすため、民生電子部品の使用が望まれている。しかし、民生電子部品を使用するためには、宇宙環境での動作状況、劣化状況を把握し、宇宙環境への適合性を探る必要がある。そこで我々は、宇宙環境への適合性を把握するため、平成 21 年度より小型衛星 (軌道高度 1,000 km 以下、運用期間 1 年程度) での使用を想定した民生電子部品に対し重粒子線照射試験を実施し、特にシングルイベントについて宇宙環境への適合性評価を行ってきた。本稿では平成 23 年度に実施した 2 種類のメモリ及び FET の試験結果について報告する。

重粒子線照射試験は、AVF サイクロトロン No.12 散乱ビーム照射試験装置 (第 4 重イオン室設置) にて、 $^{15}\text{N}^{3+}$ 、 $^{20}\text{Ne}^{4+}$ 、 $^{40}\text{Ar}^{8+}$ 、 $^{84}\text{Kr}^{17+}$ の 4 線種で照射を行った。

メモリの重粒子線照射試験は、A 社メモリ A (シリアル強誘電体メモリ) と B 社メモリ B (シリアルフラッシュメモリ) について行った。メモリ A、B とも評価項目は、SEL (Single Event Latch-up)、SEU (Single Event Upset) について行った。SEL は照射中に消費電流のモニタを行い検出し、SEU は外部 PC から内部データを読み出し検出した。算出結果を Table 1 に示す。宇宙環境への適合性は、Weibull 関数を用いて反転断面積と LET の関係を推定し、CREME2009 より導出した軌道上での放射線環境から各イベントの発生確率を算出し評価した。CREME2009 では軌道条件として高度 700 km、衛星構体 2 mm 厚アルミニウム、運用期間 1 年とした。算出結果より、SEL の発生確率は、メモリ A は 2.57×10^{-5} (event/year)、メモリ B は 1.72×10^{-2} (event/year) であった。また、メモリ A、B ともに SEU は観測されなかった。

以上より、重粒子線照射試験を実施したメモリ A、B

Table 1 Result of Memories evaluation.

		LET threshold [MeV/mg/cm ²]	Saturated cross section[cm ²]	Probability [event/year]
SEL	Memory A	5.9	7.7×10^{-7}	2.6×10^{-5}
	Memory B	5.9	5.2×10^{-4}	1.7×10^{-2}
SEU	Memory A	>34.0	8.4×10^{-7}	$<3.0 \times 10^{-11}$
	Memory B	>34.0	1.4×10^{-5}	$<4.8 \times 10^{-7}$

のシングルイベント発生確率は、1 年に 1 回未満であるということが分かった。また、メモリ A、B は照射中に SEL の発生による消費電流増加が確認されたが、電源をリセットすることによりメモリ A、B の動作が復帰することを試験にて確認した。よって、メモリ A、B は、小型衛星での使用を想定した場合、シングルイベントに対して耐性があると判断した。

FET(P-ch)の重粒子線照射試験は、SEGR (Single Event Gate Rupture) について評価を行った。試験方法は Vds (ソースドレイン間電圧) と Vg (ゲート電圧) を印加した状態で照射を行い、ゲート電流をモニタし、さらに照射後ゲート電流が増加した FET の抵抗値測定を行い、SEGR の発生を確認した。評価は、メモリと同様の方法で軌道上での発生確率を算出し評価を行った。算出結果を Table 2 に示す。これより、Vds が最大定格である 55 V、Vg が 16~20 V での SEGR の発生確率は 0.16~0.19 (event/year) であった。一方、Vds を 55 V から 35 V に下げ、Vg を 12~20 V とした場合の SEGR の発生確率は 3.70×10^{-8} (event/year) であった。

以上より、重粒子線照射試験を実施した FET は、小型衛星での使用を想定した場合、最大定格電圧の 63% 以下で使用することで、最大定格電圧で使用した場合に比べ SEGR の発生を 10^7 分の 1 程度に抑えられることがわかった。また SEGR が発生した場合、ゲートソース間に大電流が流れるため、周辺回路保護対策としてゲートに保護抵抗を入れる必要があると考えられる。

最後に、使用した民生部品は、宇宙環境での使用を想定して作られたものではないため、この結果が部品の優劣を表すものではないということを付記しておく。

Table 2 Result of FET evaluation.

applied voltage [V] ※	LET threshold [MeV/mg/cm ²]	Saturated cross section[cm ²]	SEGR Probability [event/year]
Vds : 55	Vg: 20	14.0	4.9×10^{-3}
	Vg: 16	14.0	6.1×10^{-3}
	Vg: 14	14.0	4.1×10^{-4}
	Vg: 12	14.0	7.9×10^{-4}
Vds : 35	Vg: 20	>34.0	$<5.1 \times 10^{-6}$
	Vg: 12	>34.0	$<5.1 \times 10^{-6}$

※Maximum applied voltage Vds:55[V], Vg:20[V].

1 - 05 Heavy Ion Induced Current Pulse Cross-Section Measurement on an Advanced MOSFET

T. Makino^{a)}, S. Onoda^{a)}, T. Hirao^{a)}, T. Ohshima^{a)},
D. Kobayashi^{b)}, H. Ikeda^{b)} and K. Hirose^{b)}

^{a)} Environment and Industrial Materials Research Division, QuBS, JAEA,
^{b)} Institute of Space and Astronautical Science, JAXA

Transient errors in logic LSI systems mounted on satellites are caused by high energy cosmic rays. These transient errors are called soft errors. A single event transient (SET) has emerged as a new factor that causes soft errors. The SET is momentary voltage noise due to an ion hit in the logic cell that configures logic LSI systems. Therefore, previously, pulse-widths and generation cross-section of the SETs from a logic cell have been measured by using specially built self-triggering latches/flip-flops¹⁾ to gather knowledge on the SET. The logic of NOT cell consists of two transistors (an n-type and a p-type MOSFET: pMOSFET and nMOSFET). A source of the SET is heavy ion induced current pulse on the transistors. However, an impact of the cross-section on the transistors for the SET cross-section on the logic cell is not known. In this study, we measured heavy ion induced current pulse cross-section on the p-type MOSFET used in the logic cell, to investigate an impact of the cross-section for the SET cross-section on the logic cell.

Figure 1 shows the schematic view of an experimental setup used in this study. The p-type MOSFET was fabricated using a 0.2- μm Full Depleted SOI (FD-SOI) process²⁾ that was mounted on a chip carrier with four strip-lines with short bonding wires from pads to strip-lines. The heavy-ion irradiation induced transient drain currents in the single p-type MOSFET were measured under 1.8 V drain biases. The pMOSFET is in an off-state. We used the 15 GHz of a high-bandwidth single-shot digital

oscilloscope to measure the transient drain currents. The oscilloscope limits the bandwidth of the measurement system to 15 GHz. The drain currents were amplified by a charge pre-amplifier with 21.5 dB before input to the oscilloscope. All waveform were stored to the oscilloscope.

The heavy-ion irradiation tests were performed using the cyclotron at the Takasaki Ion Accelerators for Advanced Radiation Application (TIARA), Japan Atomic Energy Agency (JAEA), Takasaki. The test transistor was irradiated in a vacuum chamber with a broad beam of 322 MeV Krypton (Kr) at an irradiation angle of 0 degree to achieve an LET of 40 MeV-cm²/mg.

Table 1 shows the ion induced current pulse cross-section on the pMOSFET and the SET pulse cross-section on the NOT cell. The SET pulse cross-section on the NOT cell was measured by using the self-triggering latches/flip-flops previously. From the results, we assume that current pulses from pMOSFET induce 25% of SET pulses. To discuss the detail of the impact of the cross-section for the SET cross-section on the logic cell, we have to improve the accuracy of beam flux monitoring.

References

- 1) T. Makino et al., IEEE Trans. Nucl. Sci. 56 (6) (2009) 3180.
- 2) K. Hirose et al., IEEE Trans. Nucl. Sci. 49 (6) (2002) 2965.

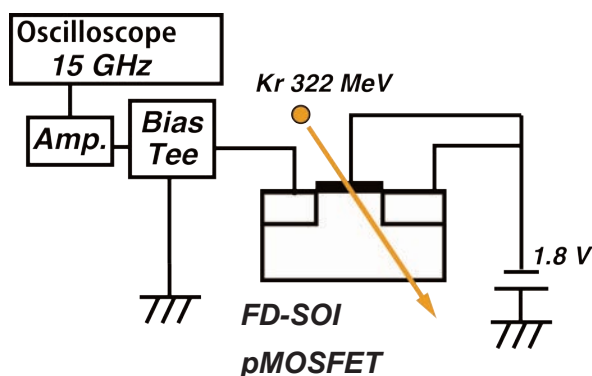


Fig. 1 Experimental setup.

Table 1 Transient event generation cross-sections.

	Cross-Section (cm ²)
pMOSFET	2.5×10^{-9}
NOT	1.1×10^{-8}

1 - 06 Heavy-ion Induced Current in SOI pn Junction Diode

Y. Takahashi^{a)}, Y. Okazaki^{a)}, S. Ogura^{a)},
T. Hirao^{b)}, S. Onoda^{b)} and T. Ohshima^{b)}

^{a)} College of Science and Technology, Nihon University,
^{b)} Environment and Industrial Materials Research Division, QuBS, JAEA

One of the most detrimental effects on semiconductor devices in radiation environments is the single-event effect (SEE). Recently, silicon-on-insulator (SOI) technology has been developed to reduce SEE, because it was believed that the charge collection is suppressed by the existence of a buried oxide (BOX) layer¹⁾. However, anomalous charge collection through the BOX layer was also reported²⁾. In the present work, we concluded that the charge collection through the oxide layer is dominated by a displacement current³⁾. In this work, we discuss the suppression of the displacement current in SOI pn junction diode to improve radiation immunity of SOI devices.

Two types of SOI-pn junction diodes, n/n device and p/n device, with the junction area of 100 μm in diameter were used in this study as shown in Fig. 1. The n/n device is p⁺n diode fabricated on SOI wafer with n-type active layer and n-type handle substrate. The p/n device is n⁺p diode fabricated on SOI wafer with p-type active layer and n-type handle substrate. In both wafers, the impurity concentration of each layer is about 10¹⁵ cm⁻³ and the thicknesses of active layer and BOX layer are 1.5 μm and 0.3 μm, respectively. The transient currents and the collected charges, the integration value along a time after irradiation, in these diodes induced by 15 MeV Oxygen ions were measured. The value of LETs and project range of the ions are 6.5 MeV/(mg/cm²) and 12.3 μm, respectively. Heavy-ion irradiation tests were carried out using the Single Ion hit (SIH) system in JAEA and the transient current caused by the single ion was measured by Transient Ion Beam Induced Current (TIBIC) measurement system.

Figure 2 shows the collected charge in these devices as a function of the heavy-ion hit location, in which the reverse bias of 10 V is applied during irradiation test. Dashed line shows the collected charge of anode electrode of n/n device when $V = -10$ V. In this case, the collected charge is about 300 fC when the ion hit to the whole of p⁺ diffusion region. However, the charge generated in active layer due to irradiation is 100 fC and the measured charge is about 3 times as much as the generated charge. This phenomenon indicates that the some of charges generated in handle substrate due to irradiation is collected by anode electrode through the BOX layer as displacement current. The displacement current is caused by the charges accumulated at the surface of substrate due to an electric field in depletion layer. So it is considered that the current can be suppressed by reducing of the width of depletion layer. In p/n device, when the reverse bias is applied to cathode electrode ($V > 0$), the surface of handle substrate under n⁺

diffusion region is in accumulation condition and the width of depletion layer can be reduced. Solid line in Fig. 2 shows the collected charge of cathode electrode of p/n device when $V = +10$ V. It was found that the collected charge when the ion hit to the center area of n⁺ region could be suppressed to almost 0. When the ion hit to the edge of n⁺ region, the collected charge is about 100 fC. It is considered that the charges are generated in active layer and collected by lateral electric field at the edge.

From these results, it was confirmed that the collected charge in SOI device could be reduced by decreasing of the width of depletion layer at the surface of handle substrate.

References

- 1) O. Musseau, IEEE Trans. Nucl. Sci. NS-43 2 (1996) 603-13.
- 2) T. Hirao et al., Nucl. Instrum. Meth. Phys. Res. B-206 (2003) 457-61.
- 3) Y. Takahashi et al., Nucl. Instrum. Meth. Phys. Res. B-260 (2007) 309-13.

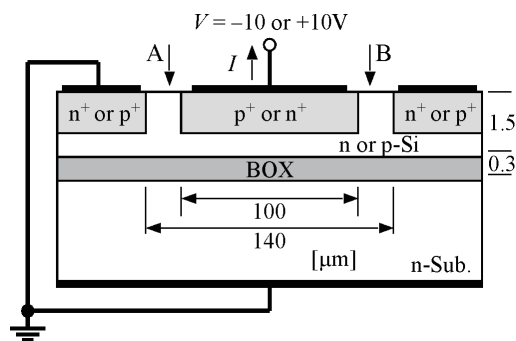


Fig. 1 Device structure of SOI-pn junction diode.

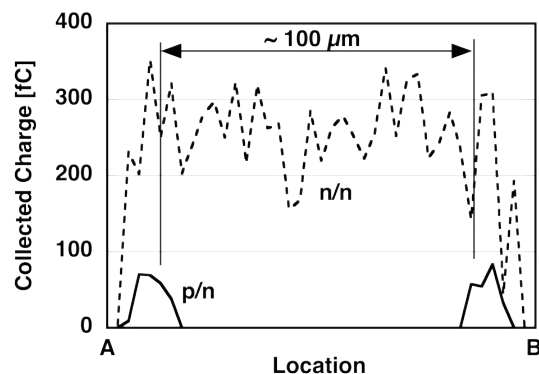


Fig. 2 Collected charge of two types of SOI-pn junction diode, n/n and p/n devices, induced by oxygen ion irradiation as a function of ion hit location.

1 - 07 Peak Degradation of Heavy-Ion Induced Transient Currents in 6H-SiC MOS Capacitors

T. Makino^{a)}, N. Iwamoto^{a, b)}, S. Onoda^{a)}, T. Ohshima^{a)},
K. Kojima^{c)} and S. Nozaki^{b)}

^{a)}Environment and Industrial Materials Research Division, QuBS, JAEA,
^{b)}Department of Electronic Engineering, The University of Electro-Communications,
^{c)}National Institute of Advanced Industrial Science and Technology (AIST)

Silicon carbide (SiC) is regarded as a promising candidate for electronic devices with high radiation tolerance. Ohshima et al.¹⁾ reported that SiC Metal-Oxide-Semiconductor (MOS) Field Effect Transistors (FETs) showed higher radiation resistance than Si MOSFETs. It was also reported that Metal-Semiconductor FETs (MESFETs)³⁾ were operated up to 10 MGy without significant degradation. These results indicate that SiC has superior radiation tolerance from the point of view of Total Ionizing Dose effects (TIDs). As for Single Event Effects (SEEs), charge generated in SiC diodes by ion incidence was reported⁴⁾. In the case of MOS devices, Iwamoto et al.⁵⁾ reported that ion induced charge in SiC MOS capacitors did not depend on the change in their electrical characteristics due to gamma-ray irradiation. It was also reported by Ohshima et al.⁶⁾ that the peak amplitude of ion induced transient current in n-type 6H-SiC MOS capacitors decreased as the number of incident ions increased and the decrease was recovered to the initial value by applying a positive bias at +1 V. Although such a unique behavior in n-type SiC MOS capacitors was experimentally observed, the behavior has not yet been fully understood. In this study, we detect transient current induced in n-type 6H-SiC MOS capacitors by 18 MeV-oxygen ions. In addition, newly we monitor a change in the capacitance for the MOS capacitors during ion irradiation to reveal the effect of heavy ion induced charge for this peak degradation in the MOS capacitors.

The samples used in this study were MOS capacitors (200 mm in diameter) fabricated on a 4.9 μm n-type 6H-SiC epitaxial layer on n-type 6H-SiC substrates. The dopant concentration of the n-type epitaxial layer is $3.9 \times 10^{15} / \text{cm}^3$. Transient currents induced by 18 MeV oxygen ions were measured using a Transient Ion Beam Induced Current (TIBIC) system in conjunction with a 3 MV tandem accelerator at JAEA, Takasaki. In this study, a single ion hitting system was applied to minimize the damage creation. During the TIBIC measurements, a negative bias of -15 V was applied to the gate oxide of the n-type MOS capacitor. In addition, the capacitance of the MOS capacitors was also measured during ion irradiation.

Figure 1 shows the TIBIC peak current in the negatively biased n-type MOS capacitor as a function of the number of incident ions. As reported in reference 6), the peak current of the negatively biased n-type MOS capacitor decreases as the number of incident ions increases up to 700 ions, where it saturates. The collected charge also decreased as the number of incident ions increased up to 700 ions, after which it saturated (not shown). The collected charge value was also refreshed by the application of a positive bias.

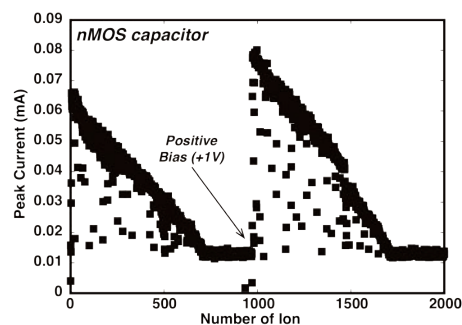


Fig. 1 TIBIC signal peak as a function of number of incident ions.

Figure 2 shows the variation in capacitance of n-type MOS capacitors during ion irradiation when biased into depletion at -15 V. The TIBIC peak current degradation shown in Fig. 1 is superimposed in Fig. 2. The capacitances of MOS capacitors increase as the number of incident ion increase. Thus, the result obtained in this study indicates that the depletion layer decreased as the increasing number of incident ions and saturated. Since the number of incident ions at the peak current saturation corresponds to the saturation of the capacitance, we can conclude that the decrease in peak current comes from the decrease in the depletion layer. In addition, the generation of electron-hole pairs by incident ion may result in the formation of an inversion layer.

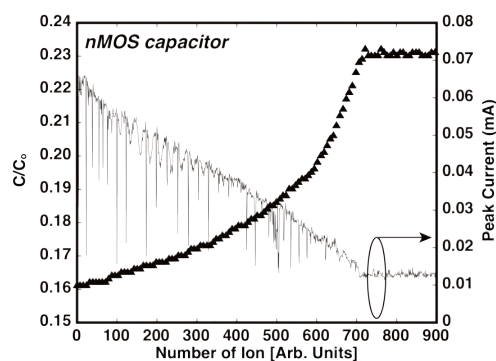


Fig. 2 Capacitances of n-type MOS capacitors during ion irradiation.

References

- 1) T. Ohshima et al., J. Appl. Phys. 90 (2001) 3038.
- 2) Y. Tanaka et al., Mater. Sci. Forum 645-648 (2010) 941.
- 3) S. Onoda et al., IEEE Trans. Nucl. Sci. 56 (2009) 3218.
- 4) S. Onoda et al., Mater. Sci. Forum 615-617 (2009) 861.
- 5) N. Iwamoto et al., Mater. Sci. Forum 615-617 (2009) 517.
- 6) T. Ohshima et al., Mater. Sci. Forum 679-680 (2011) 362.

1 - 08 The Atomic Networks at the Amorphous SiO₂/SiC Interface of the Slab Model Generated with First-principles Molecular Dynamics Simulation

A. Miyashita and M. Yoshikawa

Environment and Industrial Materials Research Division, QuBS, JAEA

Silicon carbide (SiC) semiconductor devices are expected to be used in severe environments such as outer space and/or nuclear power plants. However, the electrical performance of SiC metal-oxide-semiconductor (MOS) devices to date is low as compared with the ideal performance. This performance degradation is considered to be attributed to defects generated at the interface between amorphous SiO₂ layers and 4H-SiC substrates (*a*-SiO₂/4H-SiC interface) of MOS devices. At present, the defects that affect the degradation of the electrical performance are not clear. We have developed large-scale simulation techniques of *a*-SiO₂/4H-SiC interface in actual MOS devices and successfully obtained the theoretical *a*-SiO₂/4H-SiC interface involving the various types of defects¹⁾. Figure 1 shows the side view of the theoretical *a*-SiO₂/4H-SiC interface we obtained. In this work, characteristics of the atomic networks at the theoretical *a*-SiO₂/4H-SiC interface generated by an *ab initio* calculation based on the first principles molecular dynamics method are discussed.

In the generated theoretical *a*-SiO₂/4H-SiC interface, topmost Si atoms of 4H-SiC substrate (t-Si atoms) connect to Si atoms in the SiO₂ layers (central Si atom) directly or via O atoms. Two top layers of 4H-SiC substrate and oxides composed of central Si atoms and nearest neighbor O atoms of central Si atoms were extracted from the generated theoretical *a*-SiO₂/4H-SiC interface as an interfacial atomic network (IAN). Figure 2 shows the plane figure of the extracted IAN. Our IAN can be divided into microstructures composed of the oxide of specified central Si atom and atoms in the 4H-SiC layer connected to the oxide as shown in the dotted circle of Fig. 2. Figure 3 shows the atomic networks of the six different types of microstructures. The microstructures labeled type- α , type- β and type- γ have no defect at the interface and involve three t-Si atoms, two t-Si atoms and an t-Si atom respectively; therefore the number of bonds exposed from central Si atom toward the SiO₂ layers is one, two and three respectively. The microstructure labeled type- σ contains a defect called Si-Si

bond which joins t-Si atom with central Si atom and involves three t-Si atoms; therefore one bond is exposed from central Si atom. The microstructure labeled type- $\sigma 5$ also contains the Si-Si bond and involves three t-Si atoms, in addition, the central Si atom is in 5-coordination; therefore two bonds are exposed from central Si atom. In our IAN, the total number of bonds exposed from t-Si atoms toward the SiO₂ layers is 27. The total number of bonds exposed from central Si atoms was reduced to 19 via the microstructures mentioned above. Although the number of bonds exposed from the surface of *a*-SiO₂ with a regular density in the corresponding area of our IAN is 18 on an average²⁾, all bonds exposed from central Si atoms were able to be saturated with O atoms of *a*-SiO₂ because of the flexibility of the bond angle, especially Si-O-Si bond angle, in the *a*-SiO₂ layers. In the model of the interfacial structure reported previously in the reference³⁾, the number of bonds exposed from t-Si atoms was reduced via IAN artificially composed only of the microstructures labeled type- α and type- β in our work. On the other hand, we obtained the model that has an abrupt interface between *a*-SiO₂ layers and 4H-SiC substrates by using only an *ab initio* calculation based on the first principles molecular dynamics method. In our IAN, not only the microstructures of type- α and type- β assumed by the previous work, but also the microstructures of other types are included. It is considered that the abrupt interfacial model, in which the number of excess O atoms at the interface decreased, was obtained because of existence of microstructures that contain the defects such as Si-Si bond and Si dangling-bond at the interface.

References

- 1) A. Miyashita et al., JAEA Takasaki Annu. Rep. 2006 (2008) 13.
- 2) A. Pasquarello et al., Phys. Rev. B53 (1996) 10942.
- 3) F. Devynck et al., Phys. Rev. B76 (2007) 075351.

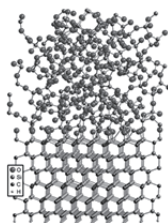


Fig. 1 Side view of the theoretical interface with the number of 1,017 atoms.

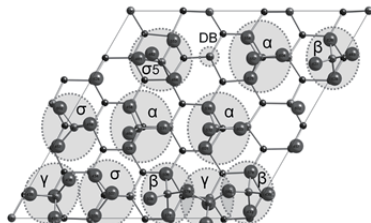


Fig. 2 Plane figure of the interfacial atomic network and arrangement of the microstructures.

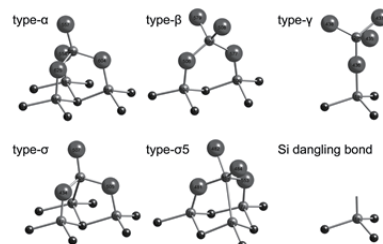


Fig. 3 Atomic networks of the six different types of microstructures.

1 - 09 Single Ion Beam Induced Luminescence from Diamond Containing NV Centers

S. Onoda, T. Makino and T. Ohshima

Environment and Industrial Materials Research Division, QuBS, JAEA

In order to measure the Single Event Effect (SEE) mapping on a semiconductor device, we are developing the Ion Photon Emission Microscopy (IPEM). By using this system, the position where an ion strikes a scintillator placed over a semiconductor device is recorded together with the ion induced event detected by a semiconductor device. Since the spatial resolution is determined by the spot size of the Ion Beam-Induced Luminescence (IBIL), the scintillator is one of the most important parts of the IPEM. In this report, we have evaluated the spot size of IBIL from various scintillators.

IBIL from the scintillators are detected by the GaAsP Image Intensifier (I.I.) (Hamamatsu, C8600) and the cooled Charge Coupled Device (CCD) camera (Hamamatsu, C4880-50-26A). The Quantum Efficiencies (QEs) of these detectors (the sensitive wavelength is ranging from 350 to 750 nm) have to match the emission spectrum from scintillators. Three different varieties of scintillators are studied; An inorganic scintillator, ZnS:Ag is used. The emission maximum is at 450 nm. The ZnS:Ag particles are adhered to a plastic sheet by using an organic resin adhesive. The thicknesses of the ZnS:Ag and plastic layers are 20 and 15 μm , respectively. A YAG:Ce is used. The previous studies suggested that YAG:Ce is the most promising scintillator for IPEM¹⁾. The thickness of YAG:Ce is 0.2 mm. The emission maximum is at 550 nm and the Photo Luminescence (PL) spectrum completely matches the QEs of the detectors. A non-commercial HPHT (High Pressure High Temperature) single crystal diamond containing Nitrogen-Vacancy (NV) centers is studied. The NV centers are created by high energy electron irradiation and annealing. The distribution of NV centers is uniform and its concentration is about 0.14 ppm ($2.5 \times 10^{16} \text{ cm}^{-3}$). The emission maximum is at about 700 nm. The value of QEs decrease at the emission maximum of NV centers. However there is partial overlap between them, the portion of the emitted photons from NV centers in the diamond can be detected.

Figure 1 (a) shows the averaged spot distribution observed from ZnS:Ag, YAG:Ce and diamond when 150 MeV Ar passes through them. The dashed line shows the noise level. As shown, the spot sizes in YAG:Ce and diamond are much smaller than that of ZnS:Ag. It was found that the spot size of ZnS:Ag corresponds to the diameter of ZnS:Ag powders. The Full Width at Half Maximums (FWHMs) of each spot are evaluated to be 16, 2.9 and 3.8 μm , respectively. The Signal to Noise (S/N) ratios of each scintillator are 7.7, 3.4 and 4.6, respectively. Figure 1 (b) shows the IBIL intensity normalized by the

peak value. The spot distribution of YAG:Ce agrees well with that of the diamond. In contrast with our data, it was reported that the spatial resolution of about 5 μm has been achieved by using YAG:Ce¹⁾. In the case of n-type Gallium Nitride (n-GaN), the spatial resolution of about 2.5 μm has been demonstrated²⁾. According to these facts, we suggest that a diamond containing NV centers is a rival candidate of YAG:Ce and n-GaN from the point of view of spatial resolution and IBIL intensity.

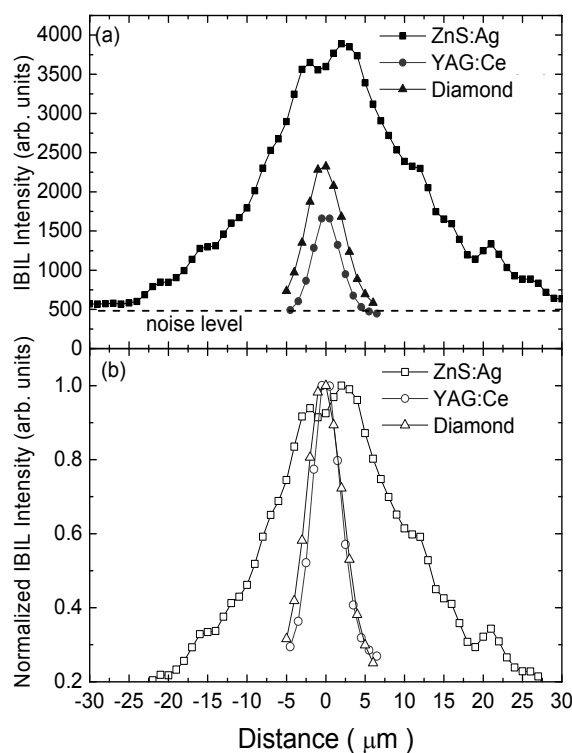


Fig. 1 Averaged IBIL intensity as a function of distance across each spot is shown in (a). The normalized IBIL is represented in (b). IBIL is observed after the 150 MeV Ar ion strikes.

References

- 1) J. V. Branson et al., Nucl. Instrum. Meth. B 269 (2011) 2326-29.
- 2) J. V. Branson et al., Nucl. Instrum. Meth. B 267 (2009) 2085-89.

Acknowledgments

YAG:Ce was provided by Mr. A. Yokoyama of the Department of Advanced Radiation Technology, TARRI, JAEA. Diamond was provided by Prof. Isoya of Tsukuba University.

1 - 10 Isotopic Identification of Nitrogen-Vacancy Centers in Diamond Created by MeV Range ^{15}N Ion Implantation

T. Yamamoto^{a)}, S. Onoda^{a)}, T. Ohshima^{a)}, K. Jahnke^{b)}, P. Heller^{b)}, A. Gerstmayr^{b)},
 A. Häubler^{b)}, B. Naydenov^{b)}, F. Jelezko^{b)}, F. Dolde^{c)}, H. Fedder^{c)}, J. Honert^{c)},
 J. Wrachtrup^{c)}, K. Watanabe^{d)}, T. Teraji^{d)}, T. Taniguchi^{d)}, S. Koizumi^{d)}, M. L. Markham^{e)},
 D. J. Twitchen^{e)}, T. Umeda^{f)} and J. Isoya^{g)}

^{a)} Environment and Industrial Materials Research Division, QuBS, JAEA,

^{b)} Institute for Quantum Optics, University of Ulm,

^{c)} 3rd Physical Institute, University of Stuttgart,

^{d)} Environment and Energy Materials Division, Optical and Electronic Materials, NIMS,

^{e)} Element Six,

^{f)} Graduate School of Pure and Applied Science, Applied Physics, University of Tsukuba,

^{g)} Graduate School of Library, Information and Media Studies, University of Tsukuba

The utilization of negatively charged nitrogen-vacancy (NV) fluorescent centers in diamond — the crystal structure is shown in Fig. 1 (a) — show significant promise as a biomarker, an ultra-sensitive magnetic sensor, and quantum bits in a quantum computer operating at room temperature. The top-down method using nitrogen implantation and subsequent annealing is preferable to form NV centers artificially. However, the formation route subject to the vacancy diffusion — whether the NV centers are formed from implanted N atoms and/or native N ones in substrate as shown in Fig. 1 (b) — has not been clarified yet.

The confocal microscopy with an optically detected magnetic resonance (ODMR) enables us to distinguish ^{14}NV ($I = 1$) from ^{15}NV ($I = 1/2$)¹⁾. This technique with combination of ^{15}N implantation can be a powerful tool to investigate the dynamics of vacancy diffusion which governs the NV formation. In this paper, we estimate the conversion ratio between ^{14}NV from native N atoms in substrate and ^{15}NV from implanted ^{15}N ions.

The sample used in this study was a high-purity Type-IIa diamond (Element Six Ltd.) implanted by $^{15}\text{N}^{3+}$ microbeam at an energy of 10 MeV at TIARA, JAEA. The number of incident ions into each spot was measured to be 2.8 ions/spot. The implanted sample was annealed at 1000 °C for 2 h in vacuum. The annealing condition was identified as a highly productive method for NV formation in our previous work²⁾.

Figure 1 (c) shows the ODMR spectrum of a pair consisting of ^{14}NV and ^{15}NV . The triplet and doublet transitions represent ^{14}NV center with the hyperfine constant $A = 2.2$ MHz and ^{15}NV center with $A = 3.1$ MHz, respectively. As can be seen in Fig. 1 (d), the ODMR measurements for individual centers in each implanted spot (9 spots labeled as S_0 – S_8) revealed that half numbers of NV centers were created from implanted ^{15}N ions, while the remaining NV centers from native ^{14}N atoms in the substrate.

In future, the detailed analyses of spatial distribution of the isotopically-labeled NV centers would lead to the understanding of the behavior of vacancy diffusion.

References

- 1) J. R. Rabeau et al., Appl. Phys. Lett. **88** (2006) 023113.
- 2) J. Isoya et al., JAEA Takasaki Annu. Rep. 2010 (2012) 14.

Acknowledgements

This work is partially supported by the Strategic Japanese-German Joint Research Project (JST).

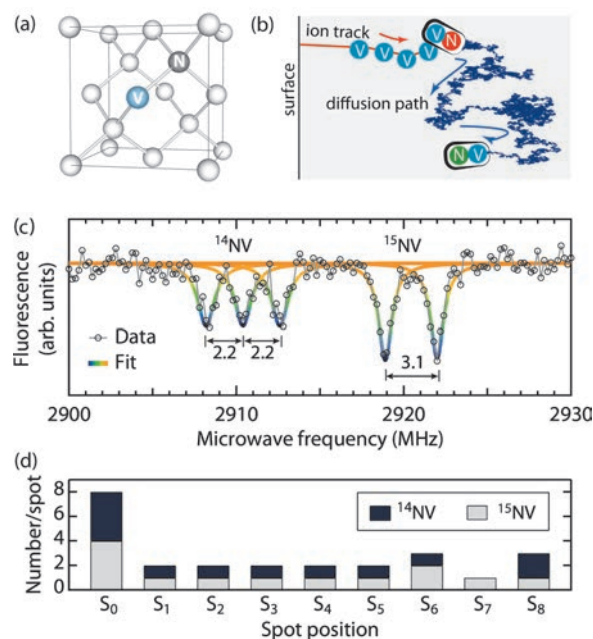


Fig. 1 (a) The crystal structure of NV center; nitrogen (N) and vacancy (V). (b) The schematic of a possible formation route of NV centers; an implanted N atom (red), the created vacancies (aqua) along the ion trajectory (red line), a random walking path of one of the created vacancies (dark blue line), and a native N atom in substrate (green). (c) The ODMR spectrum of a pair consisting of ^{14}NV and ^{15}NV . (d) The number of ^{14}NV center (dark blue) and ^{15}NV center (gray) in each spot when the number of incident N ions was 2.8 ions/spot.

1 - 11 Experimental Study on Radiation Effects on Magnetic Tunnel Junctions

D. Kobayashi^{a)}, Y. Kakehashi^{a)}, K. Hirose^{a)}, S. Ikeda^{b)}, T. Endoh^{b)}, H. Ohno^{b)}, S. Onoda^{c)} and T. Makino^{c)}

^{a)} Institute of Space and Astronautical Science, JAXA,

^{b)} Center for Spintronics Integrated Systems, Tohoku University,

^{c)} Environment and Industrial Materials Research Division, QuBS, JAEA

Magnetic tunnel junctions or MTJs, which are the key device of spintronics, i.e., an emerging semiconductor device technology that utilizes the spin of the electron, are investigated in terms of their tolerance to radiation. Tested structure is a perpendicular-anisotropy MTJ that consists of CoFeB ferromagnetic metals and an ultra-thin MgO insulator, monolithically combined with additional metal structures such as interconnects and electrodes designed for measurement. While no clear deterioration in DC characteristics is observed after 540-kGy gamma-ray exposure, significant increases in electrical resistance, i.e., open-circuit failures, are exhibited in several samples exposed to 1-h irradiation of 3-MeV protons at a flux of 150 pA. An analysis of the test results based on microscopic observations by transmission electron microscopy shows that the measured failures are caused by broken MTJ structures attributed to extrinsic electric impacts from the additional metal structures, which are charged up by irradiation; not caused by intrinsic, direct interactions of the ions with the MTJ structure itself.

プロセッサに代表される半導体集積回路は情報エレクトロニクス機器の心臓部である。計算速度を上げるために回路素子の微細化が進められてきたが、その弊害として消費電力の増大と放射線耐性の低下が深刻になっており、それらをいかに克服するかが課題となっている。この課題を解決する技術として、電子が持つ磁石としての性質であるスピンを活用した新しい半導体集積回路技術「スピントロニクス」が注目されている。磁気トンネル接合「MTJ (Magnetic Tunnel Junction)」はこの技術の基本素子である。原理的に放射線に耐性があると言われており、いくつかの論文でそれを支持する実験結果も報告されているが、近年のMTJにはそれらで調べられているものに比べてより小さい素子サイズが採用されている上に、新しい制御方式も導入されているため、これまで通り放射線耐性があるかどうか確認する必要がある。そこで、この素子に対する放射線照射効果を日本原子力研究開発機構の施設供用制度を利用して追求した。

評価した素子は CoFeB/MgO 垂直磁気異方性 MTJ である¹⁾。シリコンウエハ上に 40、70、100 nm 径の接合サイズを有する MTJ を作製した。Figure 1 は 40 nm 径の MTJ のスピン注入磁化反転特性の一例である。MTJ は挿入図の通り A と B の二端子からなる抵抗素子であり、極薄い絶縁体（本素子では MgO）を金属強磁性体（CoFeB）で挟んだ構造からなる。素子に流れる電流があまり大きくない範囲で低抵抗状態または高抵抗状態のいずれかを安定的に取り得ることができ、両者の切り替えはスイッチング電流を越える大きさの電流を流すことで実現できる。この図の場合では、負性電流を流すと低抵抗状態、逆の場合高抵抗状態となる。この素子では、零電流での抵抗比 $(R_H - R_L)/R_L = 109\%$ 、平均スイッチング電流 $(I_{Cp} + I_{Cn})/2 = 43 \mu\text{A}$ を示した。作製したウエハを切り出して以下のような照射試験を行なった。

照射試験で用いた線種は 5 kGy/h ガンマ線（コバルト 60・第 6 照射室）、150 pA・3 MeV プロトン線、（タンデム加速器・TA1 照射ポート）、4.5 nA・3 MeV シリコ

ン線（同 TA1）である。総線量はガンマ線照射では 540 kGy、プロトン線照射では $8.4 \times 10^{11} \text{ cm}^{-2}$ または $8.4 \times 10^{10} \text{ cm}^{-2}$ 、シリコン線照射では $1.3 \times 10^{12} \text{ cm}^{-2}$ とした。照射時、素子は端子 A、B を開放回路状態とした。本素子は実利用の際、開放回路状態で放射線を浴びる可能性があるためである。放射線照射前後でスピン注入磁化反転特性を測定し比較した。

コバルト照射の結果、抵抗比の明確な変化を示したものはなかった。プロトン線照射の結果では抵抗が増加し導通が取れない開放回路故障が一部の試料で確認されたが、TEM による構造解析や組成分析の結果、ならびに、素子本体に当たる放射線は数個でしかないことから、測定用に引き出した配線と電極が帯電して生じた電氣的衝撃によると考えるのが妥当であり、素子そのものと放射線の相互作用によるものではないと考えられる。素子そのものの放射線耐性について結論するには、測定用配線と電極形状の改良や、照射時の回路状態を閉回路にするなどした上での更なる試験が必要である。

Reference

- 1) S. Ikeda et al., Nature Materials **9** (2010) 721.

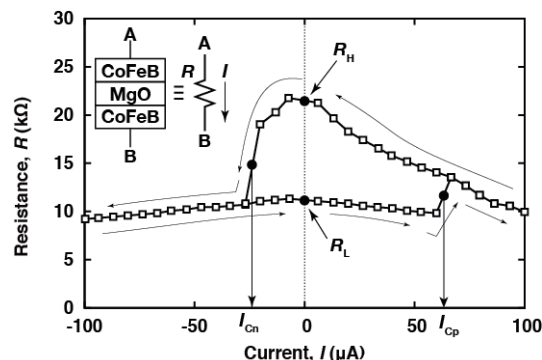


Fig. 1 DC switching characteristics of one of the 40-nm MTJs before irradiation.

1 - 12 Investigation of Europium Ion-implantation into Single- and Double-hetero AlGaIn/GaN for Light Emitting Transistor

H. Okada ^{a)}, M. Kondo ^{a)}, A. Wakahara ^{a)}, S. Sato ^{b)} and T. Ohshima ^{b)}

^{a)} Department of Electrical and Electronic Information Engineering, Toyohashi University of Technology, ^{b)} Environment and Industrial Materials Research Division, QuBS, JAEA

Europium ion implantation effects on the channel conductance of AlGaIn/GaN single heterostructure and AlGaIn/GaN/AlGaIn double heterostructure were investigated for realization of high efficiency light emitting transistor. After Eu ion-implantation, decrease in channel conductance was marked in double-heterostructure as compared with the single-heterostructure, suggesting current confinement by heterointerface was effective to control the current path in novel light-emitting device having selective ion-implantation in the channel.

窒化物半導体などの広いバンドギャップを有する半導体に添加した希土類元素は、内殻準位の遷移に基づいた鋭い発光スペクトルや、発光波長や強度が安定した温度特性を有するといった特徴をもつことから、従来にはない極微細発光素子の実現が期待される。本研究グループは、チャンネル部分に選択的に希土類元素 (Eu) をイオン注入した AlGaIn/GaN の高電子移動度トランジスタ (HEMT) 構造における Eu からの電流注入発光を報告している ¹⁾。このデバイスの発光のメカニズムは、HEMT 構造の 2 次元電子ガス (2DEG) 層を走行する電子による希土類元素の衝突励起によるものと考えており、2DEG のエネルギーをドレイン端に選択的に添加した希土類元素を効率的に励起できれば、高効率な発光に繋がると考えられる。これまでの研究では電子デバイスとして一般的な AlGaIn/GaN のシングルヘテロ HEMT 構造を母材として用いてきたが、今回は新たな試みとして AlGaIn/GaN/AlGaIn のダブルヘテロ構造を母材とした素子を作製し、その電気的特性を評価した。

本実験では有機金属気相成長法により Si 基板上に形成されたシングルヘテロおよびダブルヘテロ HEMT 構造を使用した。Eu 注入前のドレイン電流-電圧特性から得たシングルヘテロ構造およびダブルヘテロ構造のコンダクタンスは、それぞれ 4.5 mS および 1.9 mS と同程度であった。

次に Eu 注入を行ったトランジスタ構造の電気的特性評価を行った。イオン注入後の結晶性の回復のために N₂ と NH₃ の混合雰囲気中で 1,100 °C、120 s の高速熱処理 (RTA) を行い、ソース・ドレイン電極およびゲート電極を形成した。種々のイオン注入条件で Eu を添加したチャンネルの電気的特性について評価し、チャンネルコンダクタンスをまとめたものを Fig. 1 および Fig. 2 に示す。シングルヘテロ構造では注入前に比べて 1 桁以上、ダブルヘテロ構造では 4~5 桁以上コンダクタンスが低下した。シングルヘテロにおいて 1 × 10¹⁶ cm⁻² 以上の Eu 注入に対してコンダクタンスが増加したがその理由は不明である。

両構造におけるドーズ量依存性の違いは次のように考えられる。シングルヘテロの場合、Eu 注入により高抵抗化した 2DEG 層の下を迂回するような電流経路が存在するが、ダブルヘテロではこうした迂回路が下側の AlGaIn 層で閉ざされるため、同程度の Eu ドーズ量に対して顕著なチャンネルの高抵抗化が観測されたと考

えられる。以上の結果から、効率的な発光デバイスを実現するためには、欠陥の導入をもたらす高濃度の Eu 注入を避け、ダブルヘテロ構造の採用が有用であることが示された。また、窒化物半導体の HEMT 構造プロトン照射実験から、AlGaIn/GaN の 2DEG 構造は、イオン注入に対して高い耐性を示す一方、チャンネルの高抵抗化はシートキャリアの減少よりも電子移動度の減少によるものが主であることが示された ²⁾。従って、効率の良い発光素子の実現には、Eu イオン注入ダメージの導入を抑えた注入条件およびプロセス条件の選択が重要である。

References

- 1) H. Okada et al., Phys. Stat. Solidi (c) 6 (2009) S631.
- 2) H. Okada et al., J. Phys.: Conf. Ser. 352 (2011) 012010.

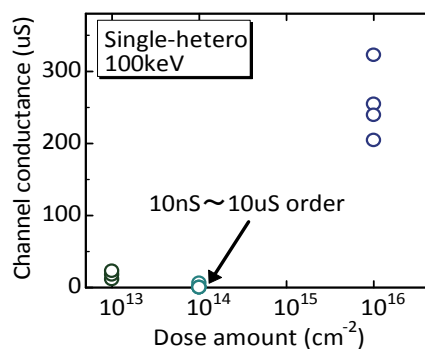


Fig. 1 Channel conductance variations of single-hetero AlGaIn/GaN HEMT due to Eu ion-implantation.

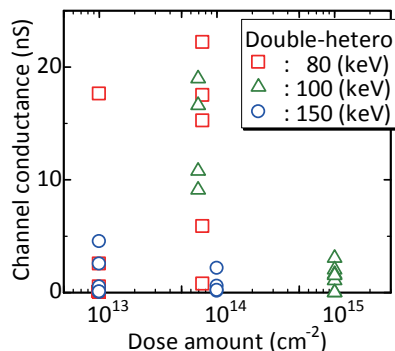


Fig. 2 Channel conductance variations of double-hetero AlGaIn/GaN HEMT due to Eu ion-implantation.

1 - 13 Study on Accelerated Ageing Tests of Ultra High Molecular Weight Polyethylene by Thermogravimetry

A. Shimada ^{a)}, M. Arai ^{a, b)}, M. Sugimoto ^{a)}, M. Yoshikawa ^{a)} and H. Kudo ^{b)}

^{a)} Environment and Industrial Materials Research Division, QuBS, JAEA,

^{b)} Graduate School of Engineering, The University of Tokyo

Some of nuclear power plants (NPPs) in Japan have been working for more than 30 years, therefore, it is essential to evaluate integrity of the NPPs for safe operation. Many instruments and equipment are used in the NPPs; one of the most important items is cables. Cables are used for various instruments as power cables, signal cables, and so on, and they are expected to be utilized for 40-60 years. Cables are composed of conductors, insulation and so on. Insulation, which is made of polymers (e.g. crosslinked polyethylene (XLPE)), is degraded by thermal ageing and radiation ageing. The durability tests of cable insulation have been conducted at various institutes around the world^{1,2)}. In many cases, accelerated ageing tests at high temperature with short period are conducted to evaluate the durability and life time of the cables. While the life time of cables is estimated by activation energy, it has been found that the activation energy changes above/below 100 °C. Above 100 °C, obtained activation energy is higher than that below 100 °C. High activation energy means high durability of the materials, however, it may lead overestimation of their lifetime. Therefore, it is required to develop an accelerated ageing test for estimation of accurate lifetime at high temperature with short period. In this work, ultra high molecular weight polyethylene (UHMWPE) was selected as the experimental sample, which has similar structure to XLPE and contains lower amount of additives than XLPE. The thermogravimetric analysis of UHMWPE was examined.

0.2 phr (part per hundred resin) of Irganox1010TM, a kind of antioxidant, were used for the experiment. The sheets were thermally aged at 80, 100, 135, 165 and 175 °C for 100-400 h in air. And then, thermogravimetric analysis under helium atmosphere from room temperature to 500 °C with several heating rates was conducted. The temperature where the weight of UHMWPE decreases by 5% was measured, and activation energy was calculated. Figure 1 shows the relationship between ageing time and activation energy for UHMWPE thermally aged at various temperatures. It was found that the activation energy decreased as the ageing time and temperature increased. Figure 2 shows relationship between reciprocal of the ageing temperature and the value which is obtained by taking the logarithm of the slope of the activation energy for each ageing temperature shown in Fig. 1. The plots showed good linear relationship in the temperature range from 80 to 175 °C (353-448 K). This suggests that accelerated ageing test at high temperature with short period can simulate the test under practical conditions. As a conclusion, the thermogravimetric analysis is expected to be a good tool for estimation of life time of cable materials.

Sheets of UHMWPE with thickness of 1 mm containing

References

- 1) T. Yamamoto, T. Minakawa., Jpn. Nucl. Ener. Safety Organi. Rep. JNES-SS-0903 (2009).
- 2) T. Seguchi et al., Radiat. Phys. Chem. 80 (2011) 268-73.

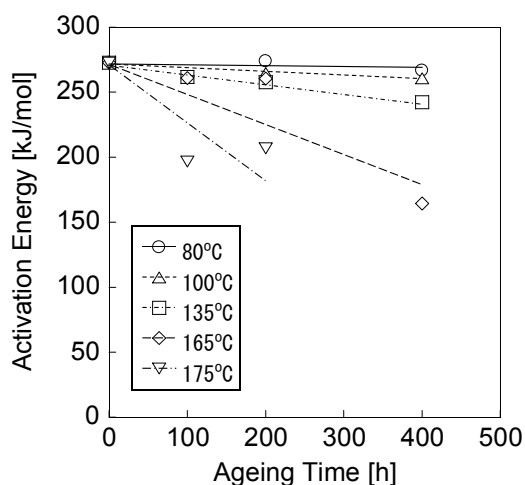


Fig. 1 Activation energy of 5% weight loss of UHMWPE of thermogravimetry vs. thermal ageing time of UHMWPE.

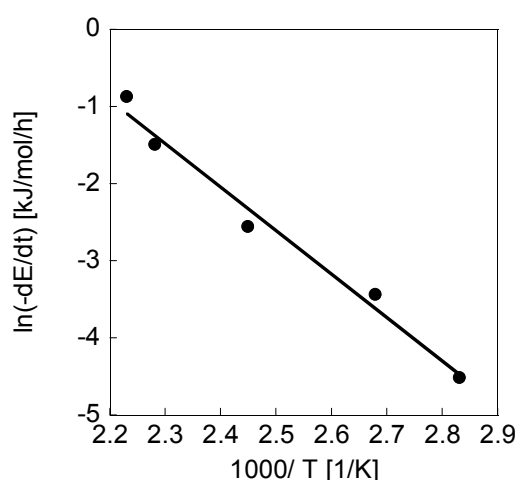


Fig. 2 Natural logarithm of the slope of Fig. 1 vs. the reciprocal of thermal ageing temperature.

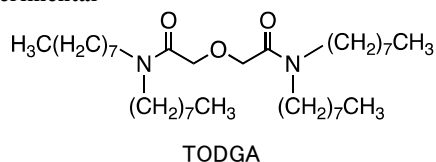
1 - 14

Radiation Effect on Solvent Extraction
of Minor ActinideY. Sugo ^{a, c)}, M. Taguchi ^{b)}, Y. Sasaki ^{c)}, Y. Morita ^{c)} and N. S. Ishioka ^{a)}^{a)} Medical and Biotechnological Application Division, QuBS, JAEA,^{b)} Environment and Industrial Materials Research Division, QuBS, JAEA,^{c)} Division of Fuels and Materials Engineering, NSED, JAEA

1. Introduction

For the purpose of reduction in the long-term environmental burden of high-level radioactive waste (HLW), the partitioning and transmutation (P&T) technologies have been developed and studied in several countries. In the concept of P&T, long-lived minor actinides such as americium (Am) and curium (Cm) are partitioned and transmuted to short-lived or stable nuclides by nuclear reaction. We have developed a tridentate diamide, *N,N,N',N'*-tetraoctyldiglycolamide (TODGA) as one of the most promising extractants for the partitioning of minor actinides from HLW. In order to evaluate the applicability of TODGA to the partitioning process in high radiation fields, it is an important task to investigate the radiolysis of TODGA and its effect on the extraction of minor actinides. In the previous work, the radiolytic mechanism of TODGA dissolved in *n*-dodecane and the effect of linear energy transfer on the radiolysis have been clarified^{1,2)}. In this study, radiation effect on the extraction of Am was investigated using the solution of TODGA pre-irradiated with α -particles and γ -rays.

2. Experimental



The organic solution of 0.1 M TODGA in *n*-dodecane pre-equilibrated with nitric acid was irradiated with helium ions provided by a tandem accelerator according to the previous report¹⁾. Incident energy of the ions was adjusted to 5 MeV corresponding to the typical energies of the α -rays emitted from actinide radionuclides. The absorbed dose rate was approximately 1-3 kGy min⁻¹. The sample was also irradiated with ⁶⁰Co γ -rays at an absorbed dose rate of 5 kGy h⁻¹.

The pre-irradiated solution was taken in an extraction tube with an equal volume of an aqueous 3.0 M nitric acid solution spiked with the radioactive tracer of ²⁴¹Am. The extraction tube was shaken mechanically for 30 min at 25 ± 0.1 °C. After centrifugation, the aliquots of both phases were taken and their alpha activities were measured by liquid scintillation counter.

3. Results and Discussion

The aqueous solutions containing ²⁴¹Am at radioactive concentration of 1.3 and 0.2 kBq mL⁻¹ were used for the extraction using the organic solutions pre-irradiated with α - and γ -rays, respectively. After extraction, ²⁴¹Am concentration in the aqueous phase was less than 1 Bq mL⁻¹. This indicates that ²⁴¹Am is extracted almost quantitatively from the aqueous phase into the organic one. Figure 1 shows ²⁴¹Am concentration in the organic phase as a function of dose absorbed by the organic solution. The concentration in the organic phase nearly kept constant even after irradiation with both α - and γ -rays. The absorbed dose had been estimated to be approximately 5 kGy per cycle in the actual process³⁾. Consequently, it is suggested that the extractability of TODGA for minor actinides can be maintained after recycling on the order of dozens of cycles in the process.

References

- 1) Y. Sugo et al., Radiat. Phys. Chem. 78(12) (2009) 1140.
- 2) Y. Sugo et al., JAEA Takasaki Annu. Rep. 2010 (2012) 18.
- 3) G. M. Gasparini et al., Solv. Extr. Ion Exch. 4 (6) (1986) 1233.

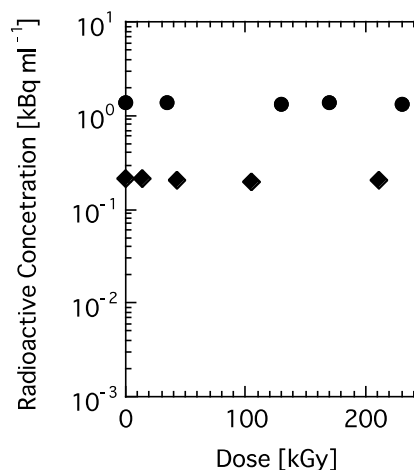


Fig. 1 ²⁴¹Am Concentration in the organic phase as a function of dose, obtained in the extraction using the solution of 0.1 M TODGA in *n*-dodecane pre-irradiated with α -particles (●) and γ -rays (◆).

1 - 15 Effect of Gamma Ray Irradiation on Hydrogen Adsorption of Titanium in Nitric Acid Solution

T. Motooka, Y. Ishijima, F. Ueno and M. Yamamoto

Division of Fuels and Materials Engineering, NSED, JAEA

The effect of gamma ray irradiation on hydrogen adsorption of titanium in nitric acid solution was investigated. The amount of hydrogen gas released from nitric acid solution under gamma ray irradiation was analyzed and titanium was immersed in nitric acid solutions for several months in the presence of gamma ray radiation. The relation between the nitric acid concentration and the amount of the hydrogen gas was summarized and the amount of absorbed hydrogen in titanium under gamma ray irradiation was evaluated in terms of absorbed dose.

Test solution was nitric acid solutions made from an analytical grade reagent and distilled water. Five mL of solution was put in the vial container of 22 mL in capacity. The solution was irradiated with Co-60 gamma ray at a dose rate of 7.5 kGy/h. After the irradiation, the amount of the hydrogen gas released from nitric acid solution with gamma ray irradiation was analyzed by gas chromatography. The titanium wire with 0.5 mm diameter and 20 mm length was immersed in the vial container with 10 mL of test solution at a dose rate of 7.5 kGy/h for 1, 3 and 5 months (approx. 720, 2,160 and 3,600 h). After the irradiation the absorbed hydrogen in the wire was measured with a thermal desorption mass analyzer.

Figure 1 shows the relation between the concentration of nitric solution and hydrogen gas released from nitric acid solution. The amount of the hydrogen gas was decreased with increase of nitric acid concentration. It was suggested that nitrate anion inhibits the hydrogen formation. Figure 2 shows hydrogen desorption rate of titanium wires with and without irradiation. The wires were immersed in 0.1 mol/L HNO₃. The peak around 400 to 600 °C

indicating hydrogen release was observed. The peak was higher after 3 months than 1 month. Figure 3 shows dependence of absorbed hydrogen on absorbed dose. Absorbed hydrogen was increased with irradiation time according to parabolic rule. This indicates hydrogen gas in the solution was absorbed into titanium according to parabolic. In order to confirm hydrogen absorption into titanium cross sectional observation of titanium was conducted. Figure 4 shows a SEM image of titanium irradiated for 5 months in 0.1 mol/L HNO₃. The hydride layer was observed on the outer surface. The thickness was about 10 μm. The layer acted as a barrier for diffusive intrusion of hydrogen into titanium matrix. It was expected that thicker nitric acid solution with lower hydrogen gas evolution forms thinner hydride layer than weaker nitric acid.

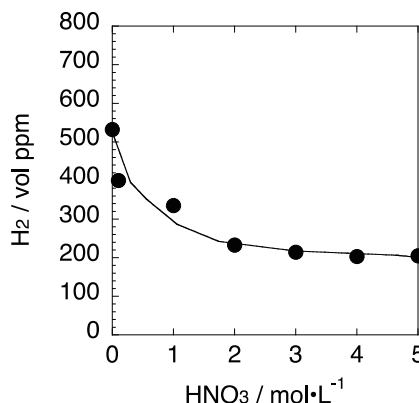


Fig. 1 Dependence of hydrogen by gamma ray irradiation on nitric acid concentration.

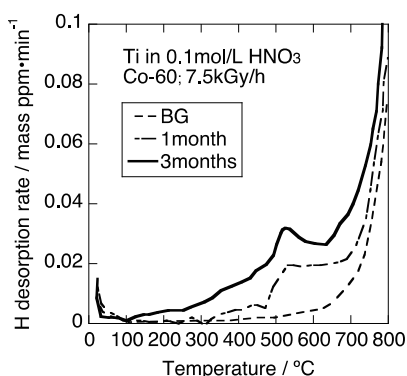


Fig. 2 Curves of hydrogen desorption rate for titanium irradiated in 0.1 mol nitric acid solution for 1 and 3 months.

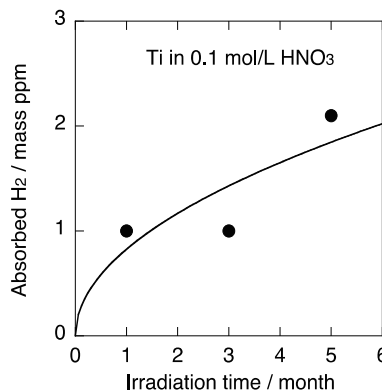


Fig. 3 Adsorbed H₂ dependence on irradiation time. Dose rate is 7.5 kGy/h.

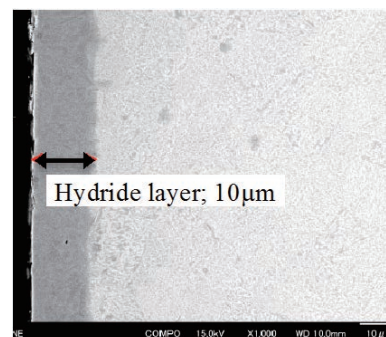


Fig. 4 Cross sectional view of titanium after 5 months gamma ray irradiation. Dose rate is 7.5 kGy/h.

1 - 16 Evaluation of Hydrogen Gas Generation from Cement Solidification Form by Gamma-ray Irradiation

T. Nakayama, Y. Kawato and Y. Meguro

Nuclear Cycle Backend Technology Development Unit, NCBD, JAEA

Radioactive combustible wastes generated in Japan Atomic Energy Agency (JAEA) are incinerated and the ash obtained by incineration will be solidified with cement. After conditioning, the cement solidification forms will continuously generate hydrogen gas by radiolysis. Therefore amount of hydrogen gas generated from the cement solidification form of incinerated ash should be understood in order to evaluate the soundness of form during their storage. In this study a G-value of hydrogen gas generated from the cement solidification form of incinerated ash was determined by means of irradiation test of a cement solidification form using incinerated ash of municipal wastes.

From a fabrication specification for waste package of incinerated ash generated in Fugen Decommissioning Engineering Center, JAEA, the ⁶⁰Co radioactivity of a cement solidification form in 200 L drum was estimated to be 16 GBq. Absorbed dose of 200 L drum was calculated to be 2.8 kGy using the ORNL Isotope Generation and Depletion Code (ORIGEN2.1) and the Electron Beam Irradiation using a Monte Carlo Code (EGS4-SPG) for 50 years of the temporary storage. In the calculation, a tentative cement solidification form, consisting of an incinerated ash of municipal wastes¹⁾ and Ordinary Portland Cement, having a composition as shown in Table 1 was supposed.

Incinerated ash of nonradioactive wastes generated in Nuclear Science Research Institute, JAEA and Ordinary Portland Cement were employed to prepare several test cement solidification forms. In addition, a water-reducing admixture and a silica fume admixture were added. The cement solidification forms were formed with composition as shown in Table 2. The solidified sample was cut to a piece that was able to be placed in a 50 mL vial container as shown in Fig. 1. Three samples were prepared and each weight was 4.85, 4.00 and 4.35 g. Amount of hydrogen gas generated from each sample was estimated using G-value of pure cement, 0.21²⁾, and the absorbed dose of 2.8 kGy estimated by EGS4-SPG. Amount of hydrogen gas generated from each sample was calculated as 9.2, 7.5 and 8.6 μL.

The solidified sample in the 50 mL vial container was irradiated for 1 hour with gamma-ray, whose dose rate was 2.7 kGy/h, from ⁶⁰Co source. Cerium dosimeters were used to evaluate the actual absorbed doses. After irradiation, amount of hydrogen gas generated in the vial was determined by gas chromatography. The results were summarized in Table 3. Amount of hydrogen gas generated from each sample was 45.8, 38.2 and 31.1 μL, and

G-value was calculated to be 1.22±0.18. This value was about 6 times higher than that of pure cement G-value 0.21.

The irradiation dose rate 2.7 kGy/h of this experiment was much higher than 6.4 μGy/h of Fugen's incinerated ash. In future, some experiments by lower dose rate will be carried out to understand amount of hydrogen gas generated from cement solidification forms of Fugen's incinerated ash.

References

- 1) Y. Kawato et al., JAEA-Technol. (2010) 013.
- 2) R. E. Barletta et al., NUREG CR 2969. (1982).

Table 1 Composition of cement solidification form of incinerated ash for absorbed dose calculation.

Incinerated Ash	30%
Cement	35%
Water	35%

Table 2 Composition of cement solidification form of incinerated ash for irradiation test.

Incinerated Ash	34.9%
Cement	25.2%
Silica fume	10.8%
Water	28.7%
Water-reducing admixture	0.4%

Table 3 Hydrogen gas generation.

Sample	H ₂ gas generation (μL)	G-value (molecule/100eV)
A	45.8	1.39
B	38.2	1.40
C	31.1	1.05

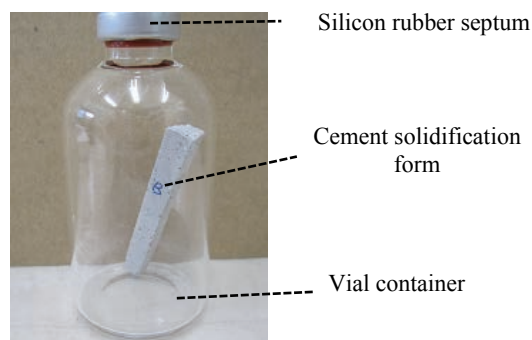


Fig. 1 Photograph of irradiation sample.

1 - 17 Experimental Studies of Irradiation Effects on Zeolite Wastes after Decontamination of Radioactive Water

R. Nagaishi^{a)}, Y. Kumagai^{a)}, N. Aoyagi^{a)}, I. Yamagishi^{b)} and K. Nishihara^{c)}

^{a)} Division of Environment and Radiation Sciences, NSED, JAEA,

^{b)} Division of Fuels and Materials Engineering, NSED, JAEA,

^{c)} Division of Nuclear Data and Reactor Engineering, NSED, JAEA

Radioactive water has been emitted in the Fukushima Dai-ichi Nuclear Power Station (NPS) accident, and needed to be quickly decontaminated by the adsorption and/or the coagulation sedimentation of radioactive nuclides, where hydrogen gas (H₂) is generated by water radiolysis. We have measured observed yields, $G(H_2)$, of H₂ as a final product in Co-60 γ -radiolysis of mixture of zeolites and seawater, and estimated the generation rate of H₂ in the decontamination by using several zeolites as adsorbents of radioactive Cs before the operation at the NPS started¹⁻²⁾. On the other hand, the radioactive wastes of zeolites and sludge have been accumulating since the operation started. Total dose absorbed in their wastes has increased with the passage of time, leading to the degradation of zeolites and sludge, which would affect the H₂ generation, retention state of Cs and thermal conduction inside the vessel. Thus we conducted the irradiation of zeolites by electron beams to study the degradation and its successive effects.

Two types of zeolites, which were examined to remove Cs from radioactive water³⁾, were used: one mordenite (MOR) and two chabazite (CHA-1, CHA-2). The dried zeolites and wet ones immersed in pure water or seawater were prepared as irradiation samples. Each sample was put into a Ti-petri dish, covered with a Kapton film, and then irradiated vertically on water-cooling SUS plate, where the sample height was almost same as extrapolated range of electron beams in the sample. The incident energy of electron beams was set as 1.0 MeV, which is comparable to averaged energy of β -ray from Y-90, and the current was 1.0 mA (0.76 kGy/s). Temperature change in the sample during the irradiation was measured within 1.0 degree. After irradiated, the sample was separated into aqueous solution and zeolites. The irradiated zeolites were washed with pure water, dried, and then applied to the surface analysis by gas adsorption and also to the experiments of H₂ generation by Co-60 γ -radiolysis.

The sample was irradiated at absorbed dose of 10 MGy. It means that the damp zeolite wastes have been kept in the

adsorption vessel for one year. Table 1 shows the specific surface area of zeolites before and after the irradiation. The surface area of zeolites decreased by the irradiation, while that of asbestos as an oxide fiber, in which scission of its needle structure takes place at the initial stage, increased⁴⁾. Since the surface area of zeolites was determined mainly by that of micropore inside zeolite particles, these suggest that the destruction of micropore took place, and consequently that finely divided powder was generated from the particles.

The degradation of zeolites affected the H₂ generation by water radiolysis. Figure 1 shows the observed yields, $G(H_2)$ in the mixture of seawater and zeolites without and with the irradiation by electron beams. Depending on the species of zeolites, the $G(H_2)$ for MOR decreased by the irradiation, and those for CHA increased, although under the present condition, *ca.* 70 % of $G(H_2)$ was due to water radiolysis originated from the energy dissipation of radiation to water but not to zeolites¹⁾. Further analysis and experiments are in progress.

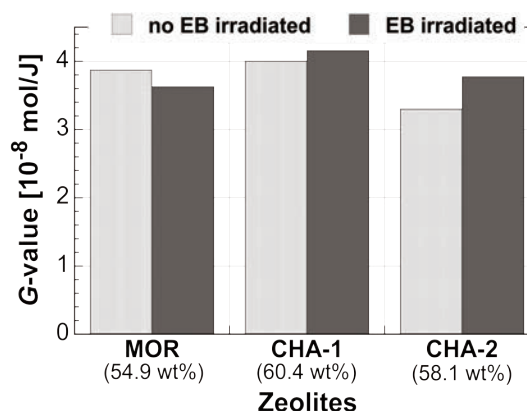


Fig. 1 Observed yields of H₂ generation in mixture of seawater and zeolites without and with irradiation by electron beams (EB). Parenthesis indicates weight fraction of water in the mixture. Co-60 γ -radiolysis was made at aerated condition and room temperature.

Table 1 Specific surface area of zeolites before and after the irradiation with immersing in seawater. Adsorbate gas: N₂, Temperature: 77 K (liq. nitrogen), Measured range of relative pressure (p/p_0): 0.1-0.2.

	Specific surface area [m ² /g]		
	MOR	CHA-1	CHA-2
Non-irradiated	180	379	349
Irradiated	163	357	293

References

- 1) Y. Kumagai et al., Trans. Atom. Ener. Soc. Jpn. 10(4) (2011) 235.
- 2) R. Nagaishi, Biannu. J. Jpn. Soc. Radiat. Chem. No. 92 (2011) 15.
- 3) "Contaminated liquid water treatment for Fukushima Dai-ichi NPS", Atom. Ener. Soc. Jpn. (2011).
- 4) N. Aoyagi et al., Chem. Lett. 36(7) (2007) 890.

1 - 18 Behavior of Irradiated Nickel Ferrocyanide as Cesium Adsorbent with Gamma Ray

Y. Koma, Y. Arai, Y. Takahatake, S. Watanabe, K. Nomura and Y. Nakajima

Nuclear Cycle Engineering Department, NFCEL, JAEA

Due to the accident of the Fukushima Dai-ichi Nuclear Power Plant of Tokyo Electric Power Company in 2011, radioactive cesium was released and widely dispersed in the environment besides the plant site. Transition metal ferrocyanides are useful to decontaminate water containing ionic cesium since it is highly selective to the element. The resulted ferrocyanide for disposal will be stored for quite a while. Metal ferrocyanide compounds are known to be chemically stable, however, safety on cyanide and hydrogen generation should be ascertained. Report on degradation of ferrocyanides in a solution is limited to that of alkaline¹⁾. Use of ferrocyanides for a contaminated neutral water is important for restoring from the accident and alkaline media may accelerate to decompose the compound, therefore, the irradiation of nickel ferrocyanide as a cesium adsorbent was carried out with simulating the conditions for decontaminating Cs and for storage after use.

Potassium nickel ferrocyanide was prepared with the method which Mimura et al. described²⁾ by adding a potassium ferrocyanide solution with a nickel nitrate solution to obtain the Ni/Fe molar ratio of 4.0. The fine and greenish compounds were obtained as shown in Fig. 1. According to the paper¹⁾, its composition was $K_{1.15}Ni_{1.43}[Fe(CN)_6]$. A portion of the compound was immersed in the $CsNO_3$ solution to adsorb Cs and turned to brown. Ten grams of water with 10 mg of the compound was sealed in a glass vial and irradiated with gamma ray from ^{60}Co source at room temperature with the dose rate of 13.6 kGy/h up to 1.3 MGy. The absorbed dose was measured by the alanine-ESR method. After irradiation, the water was filtrated with a syringe filter of 0.45 μm in pore size to provide for analysis. Cyanide concentration was determined by colorimetry with pyridine-pyrazolone. Concentrations of Cs and Fe were analyzed by atomic absorption spectrometry, and hydrogen by gas chromatography.

A correlation between the cyanide concentration after irradiation and dose or Cs adsorption was not observed as shown in Table 1. Hydrogen cyanide which is soluble in water should have been evaporated, although its concentration in the air was estimated to be lower than the administrative level of working environment (3 ppm). Cs and Fe were not detected in the water.

Concerning hydrogen generation, adding metal

ferrocyanide to water promoted it. Besides, it seems that G-value for H_2 increases with adsorption of cesium and dose as shown in Table 2 of the H_2 concentrations in the air and calculated G-values. Reproducibility of the data should be verified by another experiment, furthermore, in order to obtain radiation chemical yields concerning ferrocyanides, further investigation is required.

References

- 1) W. E. Prout et al., J. Inorg. Nucl. Chem. 27 (1965) 473-79.
- 2) H. Mimura et al., Solvent Extraction and Ion Exchange, 16(4) (1998) 1013-31.



Fig. 1 Nickel ferrocyanide prepared (right; after Cs adsorption).

Table 1 The cyanide concentrations in the water containing nickel ferrocyanide (NiFC) after irradiation.

Sample	Dose (MGy)	[CN] (mg/L)
NiFC	1.3	0.2
	0.52	0.2
Cs-NiFC	1.3	<0.1
	0.52	2.1

Table 2 The hydrogen concentrations in the air after irradiation and G-values from the water containing nickel ferrocyanide (NiFC).

Sample	Dose (MGy)	[H_2] (%)	G value (arb.)
NiFC	1.3	5.6	1.1
	0.52	1.6	1.0 *
Cs-NiFC	1.3	8.1	1.7
	0.52	3.0	1.9 *

* Not corrected for "blank."

1 - 19 Study on Durability of Insoluble Ferrocyanides Adsorbents Incorporated into the Mordenites against Gamma Irradiation

Y. Itoh, Y. Saitoh and T. Hirata

Tokai Reprocessing Technology Development Center, NFCEL, JAEA

Low-level radioactive liquid wastes (LLW) from Tokai reprocessing plant is transferred to the low-level radioactive waste treatment facility (LWTF). In the LWTF, the LLW will be treated by a radio-nuclides removal process and subsequently solidified in cement.

The T-KCFC adsorbents are used by the radio-nuclides removal process, which made from potassium cobalt hexacyanoferrates (KCoFC) with polyacrylonitrile. However, the adsorption capacity of the T-KCFC adsorbent is small and decrease with irradiated dose.

In our previous study, insoluble ferrocyanides adsorbents were incorporated into the mordenites. These adsorbents (namely KCoFC-NM) were prepared by incorporating KCoFC into the porous matrix of natural mordenites (NM) by successive impregnation with $\text{Co}(\text{NO}_3)_2$ and $\text{K}_4\text{Fe}(\text{CN})_6$ solutions¹⁾. It was confirmed that the KCoFC-NM adsorbents have large adsorption capacity comparing the T-KCFC adsorbents.

In this study, durability of the KCoFC-NM adsorbents against gamma-ray irradiation were investigated and compared to the T-KCFC adsorbents. Each KCoFC-NM and T-KCFC adsorbents were contacting with simulated LLW (5 M NaNO_3 solution) in a vial, and they were irradiated at room temperature with Co-60 gamma-rays at a dose rate of around 3 kGy/h. The maximum accumulated doses of both adsorbents were 2.6 and 2.7 MGy. After the gamma irradiation, the adsorbents separated from the sodium nitrate solution and the supernatant were analyzed by ICP-AES. The distribution coefficients and adsorption capacity of the irradiated adsorbents were also examined by the batch adsorption experiments after washing and drying of the adsorbents.

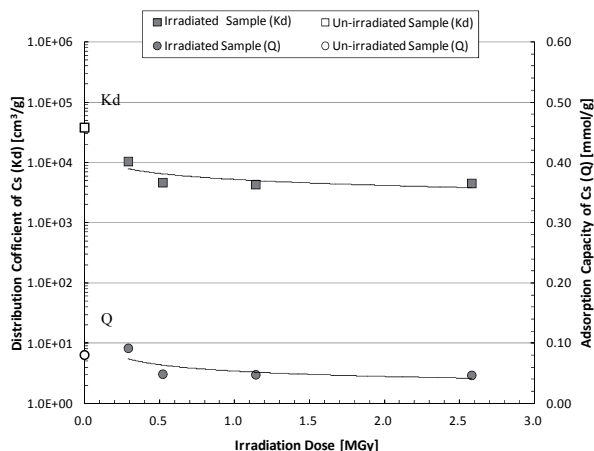


Fig. 1 Distribution coefficient and Adsorption capacity of Cs onto T-KCFC adsorbents from 5 M NaNO_3 solution.

Figure 1 shows the distribution coefficient and the adsorption capacity of Cs onto the T-KCFC adsorbents in the sodium nitrate solution. The distribution coefficient and the adsorption capacity onto the T-KCFC adsorbents decreased with absorbed dose. After an irradiation of 2.6 MGy, the adsorption capacity of Cs to that of un-irradiated one was decreased to be around 1/2, and degradation by irradiation was apparently observed through the change of appearance of the adsorbent. It is considered that decrease of adsorption capability is due to generate nitrous acid and degrade polyacrylonitrile in the adsorbents by gamma radiation.

Figure 2 shows the distribution coefficient and the adsorption capacity of Cs onto the KCoFC-NM adsorbents in the sodium nitrate solution. The distribution coefficient onto the irradiated adsorbent decreased a little comparing un-irradiated one, although the adsorption capacity onto the irradiated adsorbent was at the same level as un-irradiated one. And also the adsorption capacity was 0.7 mmol/g, the KCoFC-NM indicated large adsorption capacity comparing the T-KCFC.

Therefore, it was confirmed that the KCoFC-NM adsorbents had durability against gamma irradiation comparing the T-KCFC adsorbents.

Acknowledgements

We would like to thank Professor Dr. Hitoshi Mimura, Mr. Shunsuke Susa of Tohoku University and Mr. R. Yamagata at Irradiation Service Section in TARRI for their advice and assistance on the experiment.

Reference

- 1) H. Mimura et al., WM'99 Conference (1999).

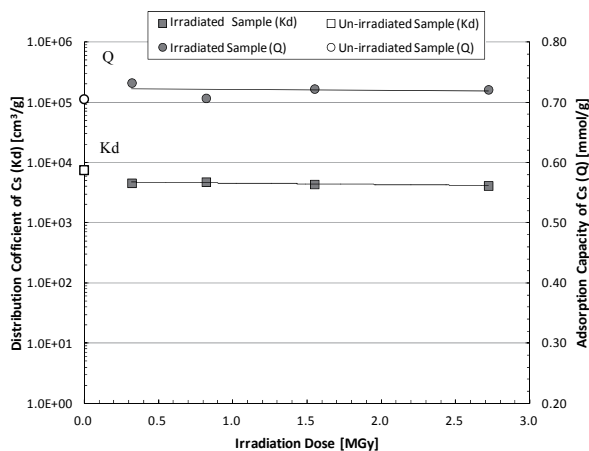


Fig. 2 Distribution coefficient and Adsorption capacity of Cs onto KCoFC-NM adsorbents from 5 M NaNO_3 solution.

1 - 20 Multi-Scale Models to Estimate Mechanical Response of Neutron-Irradiated Austenitic Steel Reactor Components

S. Jitsukawa^{a)}, Y. Abe^{a)}, M. Ando^{b)}, N. Ishikawa^{a)}, N. Okubo^{a)}, K. Suzuki^{a)} and S. Ohnuki^{c)}

^{a)} Division of Fuels and Materials Engineering, NSED, JAEA, ^{b)} Division of Fusion Reactor Engineering, FRDD, JAEA, ^{c)} Faculty of Engineering, Hokkaido University

One of the main objectives of our research program for last three years in the frame work of the JAEA-Universities “Renkei Jyuten Kenkyu” project is to develop the multi-scale models to describe the irradiation effects on mechanical properties of the reactor structural materials. We have developed a series of the models to describe damage production and microstructural change during irradiation in structural alloys, including those of the deformation of irradiation produced microstructures, constitutive equation of the irradiated materials and failure condition of irradiated structures^{1,2)}. The models, equations and computer codes have been prepared by theoretical analyses and by the materials parameters obtained experimentally. They are briefly introduced in the following.

Figure 1 shows the outline from atomistic collisions to the constitutive equation as functions of damage level, damage rate and temperature for austenitic alloys. Displacement damage production is estimated by a Molecular Dynamics (MD) method using the inter atomic potential of Cu¹⁾; there are no reliable potential for γ -Fe, but the difference may not introduce large errors because of the high energy processes of atomistic collisions. Results on the displacement damage production including that of the cascade produced point defect clusters are used for the input of the rate equation (RE) method to obtain microstructural change. The RE method is prepared taking cares to simulate the number density of the self interstitial atom (SIA) clusters. The number density and the size of the SIA clusters dominate irradiation hardening at temperatures below 400 °C. An experimentally obtained parameter of the capture radius of SIA clusters has introduced. Within the capture radius, SIAs and SIA clusters tend to react with each other. To estimate the capture radius, in situ ion-irradiation experiments were conducted at TIARA facility (IX chamber). Also, it is supposed that all the SIA-clusters are mobile depending on their size. An example of the calculated size distribution of SIA clusters is

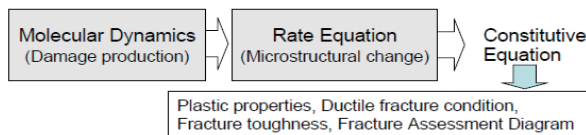


Fig. 1 Outline of the Multi-Scale Models.

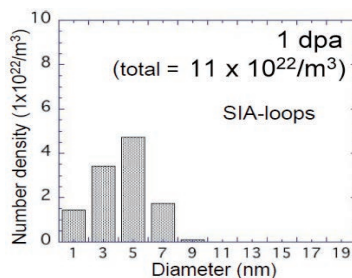


Fig. 2 Calculated size distribution of SIA clusters at 1 dpa. The total number density of calculated SIA clusters was of 11E22/m³.

shown in Fig. 2.

The dispersed barrier hardening model was used to obtain yield stress (YS) from calculated microstructure. Figure 3 is the damage level dependence of calculated YS with the results obtained by the experiments. True stress-strain (Ts-s) relation is obtained from YS and a constitutive equation of $\sigma = A(\epsilon_0 + \epsilon_p)^n$, where the constants A and n are strength coefficient and work hardening exponent. By substituting the equivalent plastic strain for irradiation hardening calculated from YS value into ϵ_0 , Ts-s relation of irradiation hardened austenitic alloys is determined as shown in Fig. 4. Fracture Assessment Diagram (FAD) of the R6 method may be obtained from the Ts-s relation to evaluate the fracture condition of the structure after irradiation. Figure 5 shows an example of FAD.

References

- 1) Y. Abe, S. Jitsukawa, in press, ASTM STP.
- 2) S. Jitsukawa et al., in press, ASTM STP.

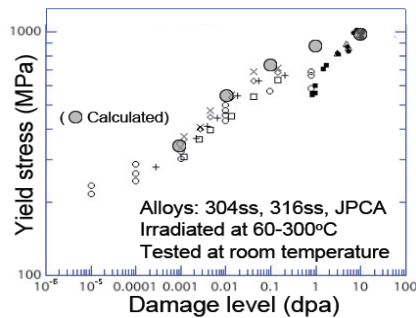


Fig. 3 Damage level dependence of the irradiation hardening.

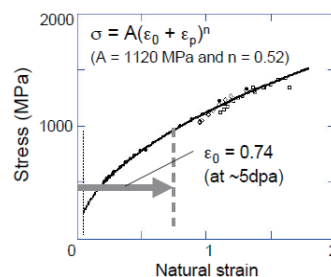


Fig. 4 Constitutive equation and true stress-strain relations before and after irradiation.

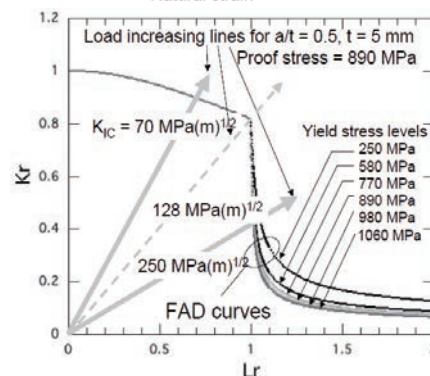


Fig. 5 Estimated fracture condition of a flawed structure and the Fracture Assessment Diagram.

1 - 21 Radiation-Induced Hardening for Stainless Steel SUS316L with Bending Deformation

N. Ishikawa, N. Okubo and K. Kondo

Division of Fuels and Materials Engineering, NSED, JAEA

Irradiation assisted stress corrosion cracking (IASCC) is one of the important phenomena that appear in in-core components in light water reactors. In spite of extensive studies over a long period of time it is not yet fully understood. Since IASCC is a complicated phenomenon, it is important to elucidate the mechanism by understanding each of the elementary processes that compose the phenomenon. One of the keys to unlock the problem, we believe, is to understand the effect of welding. It should be noted that the phenomenon is often found at welded zones, where irradiation hardening, irradiation induced stress relaxation, radiation induced segregation and swelling may be affected by a presence of strong stress. Based on this recognition, the effect of stress on irradiation-induced hardening is investigated in the present study.

Specimens used in this study were austenitic stainless steel (SUS316L). The specimens were solution annealed at 1,030 °C and then water quenched. The specimen size was prepared to be about 20 mm long, 5 mm wide and 0.3 - 0.4 mm thick by mechanical and electrochemical polishing. As illustrated in Fig. 1, both specimen bended and that without bended were irradiated simultaneously. Specimen holder for the specimen with bending deformation is such that the curvature radius is 12.5 mm to give about 2% plastic strain into a 0.5 mm thick specimen. Half of the specimen was masked with aluminum foils during the irradiation, so that hardness for unirradiated area and that for irradiated area can be easily compared without influenced by a possible difference of specimen conditions. Both specimens were heated at 330 °C and were irradiated with 12 MeV Ni³⁺ ions provided by the tandem accelerator in TIARA facility of JAEA. The displacement level was varied from 2.1 to 15 dpa. The surface temperature of both specimens was measured by two-dimensional infrared pyrometer.

After the irradiation, the micro-hardness was measured by using nanoindenter (ENT-1100a, ELIONIX) for both irradiated area and unirradiated area of the specimen. The change in micro-hardness was estimated by subtracting the micro-hardness of the irradiated area from that of the unirradiated area. The micro-hardness was measured by fixing the indentation depth of 0.3 μm, which is much smaller than the projected range of the ion (3.2 μm).

Figure 2 shows the dependence of irradiation-induced hardening on displacement damage for SUS316L specimens with and without bending deformation. In both cases, the micro-hardness monotonically increases as a function of displacement. The different behaviour of irradiation-induced micro-hardness is found for different stress which

depends on whether the specimen is bended or not. At this moment, the origin of the larger change in irradiation-induced hardness for bended specimen is not clear, but it is suspected that survival rate of displaced atoms may be higher for bended specimen. For example, larger fraction of the displaced atoms can survive, if diffusivity of the displaced atoms is lower for bended specimen. Such hypothesis should be tested by examination of diffusing atoms under irradiation. Since the present result may be related to the high IASCC susceptibility of welded zone, it encourages revisiting IASCC mechanism from the viewpoint of effect of stress.

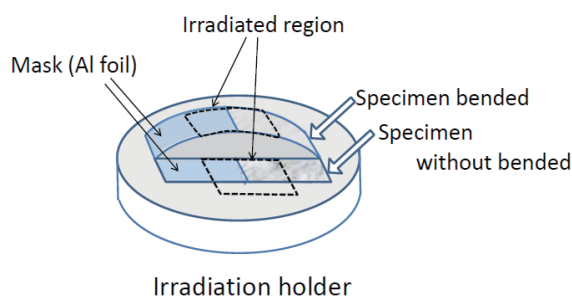


Fig. 1 Schematic illustration of the irradiation holder.

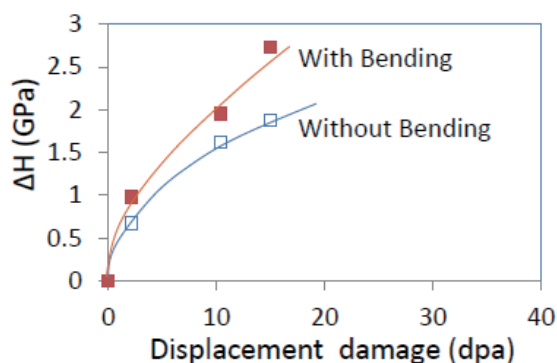


Fig. 2 Dependences of change in micro-hardness, ΔH, on displacement damage for the specimens with bending deformation and without bending deformation. The solid curves are just guides for the eyes.

1 - 22 Irradiation Hardening in Extra High Purity Ni-base Superalloy under External Stress

I. Ioka, G. H. Kim and K. Shiba

Nuclear Engineering Research Collaboration Center, JAEA

An extra high purity (EHP) Ni-base superalloy has been developed as MA doped MOX fuel claddings for sodium cooled fast reactors. In EHP alloys, impurities, such as C, O, N, P, S were reduced to less than 100 ppm in total to improve workability, irradiation embrittlement, intergranular corrosion resistance. The cladding materials suffer from stress (external pressure, thermal stress) under the operation. There have been many irradiation experiments done under external stress to investigate stress effects on microstructural evolution of 300 series austenitic stainless steels. It is reported that the total nucleation rate of Frank loops increased with increasing external stress¹⁾. However, there are few studies on the effect of external stress on microstructural evolution of Ni-base superalloy under irradiation. The purpose of this study is to evaluate the effect of external stress on irradiation hardening of EHP Ni-base superalloy.

The material used in this study was W-rich silicide phase strengthened EHP Ni-base alloy, so called EHP(WSi) alloy. The EHP(WSi) alloy was manufactured by the multiple refined melting process. The ingot was solution-treated at 1,498 K for 1 h and then aged at 1,123 K for 24 h. The chemical composition of the alloy is given in Table 1. The materials were cut to small coupon type specimens (20 × 5 × 0.5 mm³). Specimens were plastically deformed by means of a special bending holder during the irradiation as shown in Fig. 1. Tensile strain on the surface of bent specimens was calculated to be about 2%, so that the initial stress was in 0.2% offset stress level. Both deformed and undeformed specimens were simultaneously irradiated using the holder. Irradiation was performed under triple (Ni³⁺+He⁺+H⁺) ion beams at 673 K in the TIARA facility at JAEA. Ions of 12 MeV Ni³⁺, 1.05 MeV He²⁺ and 380 keV H⁺ were injected to simulate a FaCT core irradiation environment. The peak depth of displacement damage was calculated to be 2 μm by SRIM-2000. The mean displacement damage, of which value was selected at depth of 1.5 μm, was changed from 1 to 35 dpa. The injection rates for He and H were 1 appmHe/dpa and 15 appmH/dpa, respectively. The surface temperature of the both specimens was measured by two-dimensional infrared pyrometer and kept to be constant under irradiation. The micro-hardness was measured by using a nanoindenter. The hardening behaviour of the irradiated specimens was evaluated by indentation depth of 500 nm in consideration of the damage depth. The

micro-hardness was calculated from mean values of 10 points per each specimen.

The dependence of micro-hardness on the irradiation damage was evaluated for EHP(WSi) alloy with and without bending deformation. Figure 2 shows the behavior of irradiation hardening at 673 K. In both of deformed and undeformed specimens, the micro-hardness increased immediately up to 5 dpa and saturated around 10 dpa. The micro-hardness of deformed specimens, however, was slightly higher than that of undeformed ones from initial condition. There is no effect of irradiation on micro-hardness of EHP(WSi) alloy in this study. However, Okubo et al.²⁾ reported that irradiation hardening of SUS316L bent specimen was suppressed at about 10 dpa in comparing with that of un-bent specimen for the irradiation at 673 K. The difference in the irradiation hardening between EHP(WSi) and SUS316L was not clear, so the microstructural evaluation by TEM is essential issue for interpreting the difference.

References

- 1) H. Tanigawa et al., Nucl. Instrum. Meth. Phys. Res. B 102 (1995) 151.
- 2) N. Okubo et al., J. Nucl. Mater. 386-388 (2009) 290.

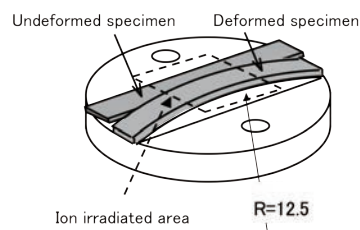


Fig. 1 Schematic illustration of special bending holder for ion irradiation.

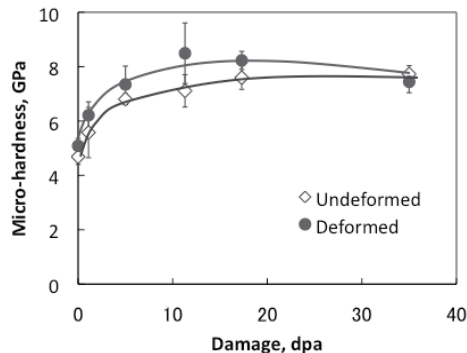


Fig. 2 Dependence of micro-hardness on irradiation damage at 673 K for EHP(WSi).

Table 1 Chemical composition of EHP(WSi) alloy (wt%).

Fe	Ni	Cr	W	Si	C	P	S	O	N
bal.	42.8	25.35	10.24	2.75	0.004	0.0005	<0.0005	<0.0005	0.0006

1 - 23 Precipitate Stability in G-Phase Strengthened Ni-base Alloy under Multi-ion Irradiation

G. H. Kim^{a)}, I. Ioka^{a)}, T. Sawai^{b)} and S. Yamashita^{c)}

^{a)}Nuclear Engineering Research Collaboration Center, JAEA, ^{b)}Advanced Science Research Center, JAEA, ^{c)}Division of Fuels and Materials Engineering, NSED, JAEA

1. Introduction

Precipitation-strengthened Ni-base alloys have been considered for fuel cladding in advanced reactors. Because these alloys have not only excellent properties at high temperature, but also very good performance with respect to swelling and creep resistance during irradiation. The main factor of high temperature strength in these alloys is the formation of ordered phase γ' [$\text{Ni}_3(\text{Ti, Al})$] or γ'/γ'' [Ni_3Nb] in the matrix¹⁾. However, many studies reported that these alloys exhibited the significant ductility loss due to irradiation at high temperature¹⁻³⁾. The reasons of poor ductility were believed to be the re-distribution of ordered phase γ' and solute segregation during irradiation at defect sink sites, such as grain boundary, void surface and dislocation.

From this view point, we have developed an alternative Ni-base alloy strengthened by W-rich silicide (G phase), which has a good stability at high temperature. The aim of this work was to evaluate the stability of G phase for the G-strengthened Ni-base alloy irradiated over 100 dpa at high temperatures. The stability of G phase was compared with those of ordered phase γ' in Nimonic PE16, which is a representative commercial alloy of precipitation-strengthened Ni-base alloys.

2. Experimental

G-strengthened Ni-base alloy (Fe-43Ni-25Cr-10W-2.7Si) under extra high purity grade so-called EHP(WSi) alloy was used for the ion-beam irradiation experiments. To estimate precipitate stability, ion-irradiation were performed under both triple ($\text{Ni}^{3+} + \text{He}^+ + \text{H}^+$) ion beams at 873 K to 100 dpa and dual ($\text{Ni}^{3+} + \text{He}^+$) beams at 973 K to 250 dpa, which is maximum operation temperature and target dose for cladding material of JSFR. Twelve MeV Ni^{3+} was injected to produce radiation damage and ions of 1.05 MeV He^{2+} and 380 keV H^+ were implanted through Al degrader foils to simulate a FaCT core irradiation environment. The injection rates for He and H are 1 appm/dpa and 15 appm/dpa, respectively.

Thin foils for transmission electron microscopy (TEM) were fabricated using a focused ion beam (FIB) instrument FB-2000A (Hitachi, Japan) with micro-sampling system. In order to understand precipitates stability for Nimonic PE16 and EHP(WSi) alloy, TEM observations were carried out with a JEM-2100F (JEOL, Japan) operated at 200 kV.

3. Results and discussion

Figure 1 (a) shows the microstructure evolution of γ' as

functions of irradiation temperature and fluence for Nimonic PE16. As can be seen, a low swelling response is obvious, and the general features of microstructure are γ' coarsening and γ' precipitation on dislocations, void surfaces and grain boundaries. These evolutions increased with increasing irradiation temperature and fluence. Generally dislocations, void surfaces and grain boundaries are highly effective sinks for point defects^{2,3)}.

Whereas, the microstructure evolution of G-phase in EHP(WSi) alloy are illustrated in Fig. 1 (b). In spite of irradiation at maximum operation temperature to target dose, no change was observed. There was much evidence for stability of G-phase during irradiation at high temperature region. In previous study, the EHP(WSi) alloy showed excellent swelling resistance. Therefore, it is considered that the EHP(WSi) alloy probably deserve an advanced material for FaCT core.

In future, void swelling of EHP(WSi) alloy to target dose (250 dpa) will be evaluated.

References

- 1) W. J. S. Yang et al., J. Nucl. Mater. 132 (1985) 249.
- 2) W. J. S. Yang, J. Nucl. Mater. 108&109 (1982) 339.
- 3) D. J. Mazey et al., J. Nucl. Mater. 160 (1988) 153.

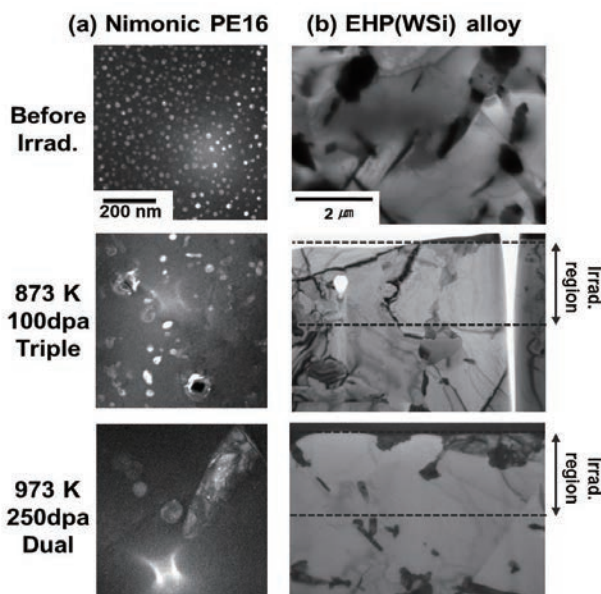


Fig. 1 Microstructure evolution of precipitates by ion-irradiation: (a) Dark field TEM images of ordered phase γ' in Nimonic PE16, (b) Bright field TEM images of G phase in EHP(WSi) alloy.

1 - 24 Effects of Displacement Damage and Gas Atoms on Radiation Hardening and Microstructure in F82H Weldment

M. Ando and H. Tanigawa

Division of Fusion Energy Technology, FRDD, JAEA

Introduction

Reduced activation ferritic/martensitic steel (RAFs) is the most promising candidate for the blanket structural material in fusion reactor. This blanket contains many joints of F82H plates using tungsten inert gas (TIG) welding, electron beam (EB) welding, hot isostatic pressing (HIP) and so on. These joints are also exposed to high neutron flux irradiation in fusion reactor. Neutron irradiation experiments are being performed at HFIR, JMTR and so on. Some data of modified F82H and welded F82H are also obtained from post irradiation experiment. On the other hand, the effect of transmutation helium on mechanical properties and void swelling in RAFs is also an important subject. Multi ion irradiation method contributed to this subject in F82H base metal because this method can easily simulate the ratio of displacement damage and helium/hydrogen production. However study of helium/hydrogen gas effect with F82H welded joints is not enough.

The objective of this study is to evaluate radiation hardening and void swelling on multi-ion irradiated F82H weldments up to 20 dpa.

Experimental procedure

The material used in this study was reduced activation ferritic/martensitic steel (F82H IEA; Fe-8Cr-2W-0.2V-0.04Ta-0.1C). The heat treatment was normalized at 1,040 °C for 0.63 h and tempered at temperatures of 750 °C for 1 h. TIG and EB weldments were annealed at 720 °C for 1 h (PWHT; post weld heat treatment). More details are reported elsewhere¹⁾. Small coupons specimens (6×3×0.8 mm) were irradiated in the TIARA facility by 10.5 MeV Fe³⁺ ions with/without 1.05 MeV He⁺ ions and

0.38 MeV H⁺ ions. He⁺ and H⁺ ions implantation were performed using aluminum foil energy degraders. The irradiation was performed to 20 dpa at the depth of 1.0 μm and the damage rate was about 1.0×10⁻³ dpa/s at this depth.

Micro-indentation tests were performed at loads to penetrate about 0.30 μm in the irradiated specimens using an ENT-1100a (Elionix INC). The micro-hardness showed the average of 35 measurements per irradiated specimen. The direction of indentation was chosen to be parallel to the ion beam axis.

Results and discussion

Figure 1 a) and 1 b) show the relationship between micro-hardness and distance from EB Weld Metal (WM) area. Figure 1 a) is the result of micro-hardness from an unirradiated specimen. The micro-hardness around WM area tends to be higher than that of Base Metal (BM) area. This trend is similar to the result of a Vickers hardness testing. On the other hand, Figure 1 b) is the result from a triple ion beam irradiated specimen at 470 °C up to 20 dpa. Micro-hardness is almost constant (~3 GPa) from WM to BM area. It is considered that some recovery at WM occurred during ion-irradiation and then micro-hardness decreased around WM area.

Detailed investigation of these microstructures after dual/triple irradiated specimens will be performed in future studies.

Reference

- 1) K. Shiba, Proc. IEA Work. Group Meet. Ferritic/Martensitic Steels, Switzerland, ORNUM-4939 (1995).

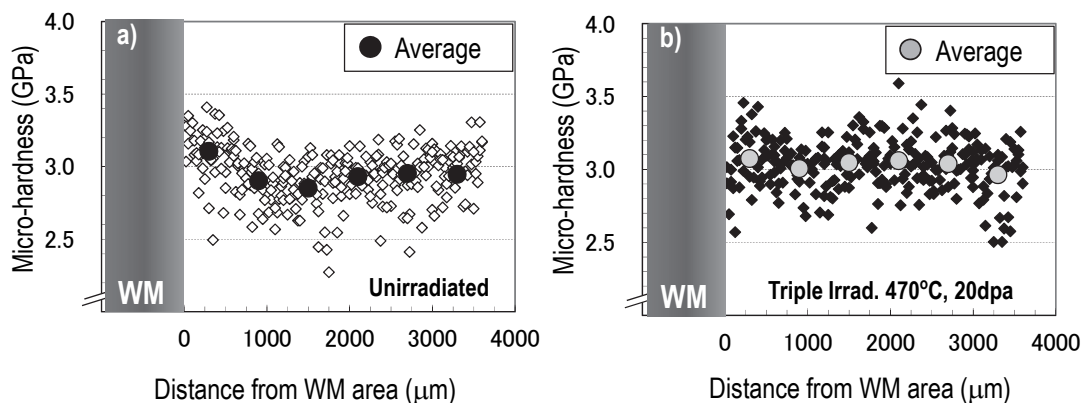


Fig. 1 The result of micro-hardness for F82H with EB weldment, a) Unirradiated specimen, b) Triple irradiation at 470 °C, 20 dpa.

1 - 25 Ionizing Dose Dependences of Radiation-induced Conductivity and Radiation-induced Electrical Degradation of Chemical Vapor Deposited Silicon Carbides under Gamma-ray Irradiation

B. Tsuchiya ^{a)}, T. Shikama ^{b)}, S. Nagata ^{b)}, K. Saito ^{b)} and S. Yamamoto ^{c)}

^{a)} Department of General Education, Faculty of Science and Technology, Meijo University,

^{b)} Institute for Materials Research, Tohoku University,

^{c)} Environment and Industrial Materials Research Division, QuBS, JAEA

Silicon carbides (SiCs) are potential candidates as insulating materials in nuclear fusion systems such as separators or insulating flow channel inserts, between tritium breeding and neutron multiplier materials composing Li-Pb blanket modules. So far, it has been reported that the electrical properties of insulating ceramics are dynamically modified by electrons that are excited from valence bands to conduction bands by the so-called dynamic radiation effects^{1,2)}. In fact, for CVD-SiC materials with high purity and density, synthesized by the chemical vapor deposition technique, the radiation enhanced phenomena such as radiation induced conductivity (RIC) and radiation induced electrical conductivity (RIED)-like behavior have been observed by in situ radiation experiments under gamma-ray and fast neutron irradiations³⁾. The RIC and RIED-like behavior according to radiation-induced modification of the electrical property occurred with essentially no displacement damage, but ionizing effects (radiolysis). However, it has not been clarified fully, yet. It is significant important to investigate the radiation damage process and physical mechanism on the degradation of the electrical property by radiation in more detail by combining in situ radiation experiments with post-irradiation examinations.

Figures 1(a) and (b) show effects of dose on RIC, σ_{RIC} , under gamma-ray irradiation (beam-on) and on the base conductivity, σ_{BC} , in the absence of radiation (beam-off) for the irradiated CVD-SiC samples at 0.52, 1.2, 4.8, 5.2, and 5.9 Gy/s, respectively, and room temperature in air. These relationships were determined from the Ohm's law using the increase in the currents when applied from 0 to +3 V and the volume of the samples. The radiation-induced current was also proportional to the applied voltage under a constant irradiation intensity. A rapid increase in the electrical conductivities of the irradiated samples at several dose rates; this is indicative of RIC, was observed at the beginning of the irradiation. The σ_{RIC} values gradually increased with an increase in the dose and subsequently became almost constant. Similarly, the σ_{BC} values also changed with rapid increases at initial doses below approximately 10 kGy, as compared with those that before irradiation, and hereafter with gradual increases at doses above approximately 10 kGy. These two kinds of rapid and gradual degradations in the insulating characteristics indicate the occurrence of RIED-like behavior²⁾.

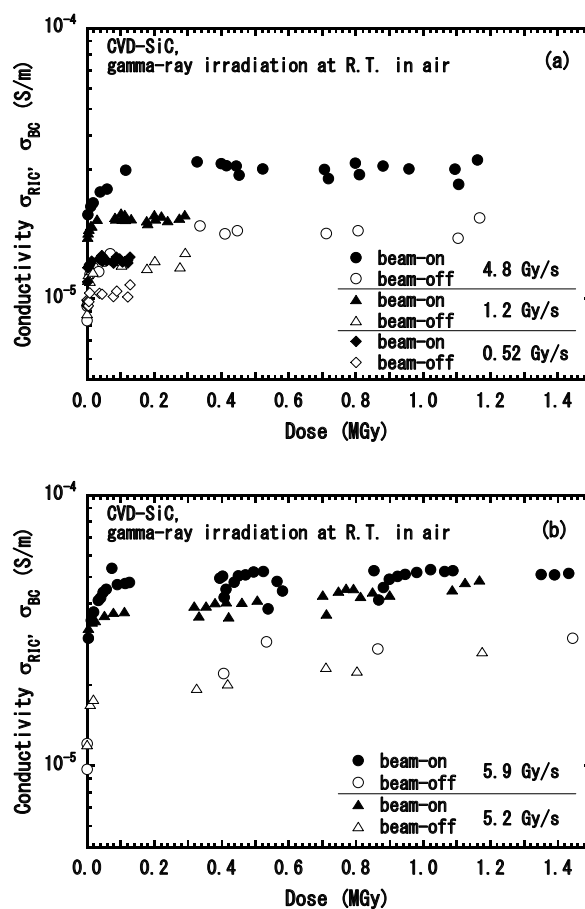


Fig. 1 Dose dependence of RIC, σ_{RIC} , and base conductivity, σ_{BC} , of CVD-SiC samples, during 1.17 and 1.33-MeV gamma-ray beam-on at approximately (a) 0.52, 1.2, 4.8 Gy/s, and (b) 5.2, 5.9 Gy/s, and room temperature in air, and after beam-off.

References

- 1) E. R. Hodgson, Nucl. Instrum. Meth. Phys. Res. B 191 (2002) 744.
- 2) S. J. Zinkle, E. R. Hodgson, J. Nucl. Mater. 191-194 (1992) 58.
- 3) B. Tsuchiya et al., Fusion Eng. Des. 86 (2011) 2487.

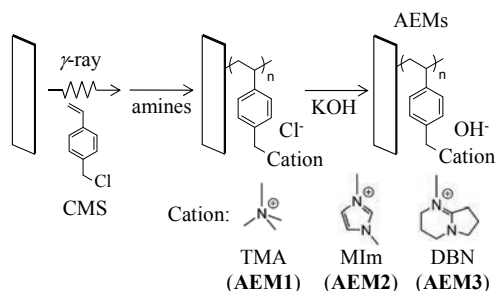
1 - 26 Synthesis of Novel Anion Conductive Membranes Consisting of Iminium Cation by Radiation Grafting

K. Yoshimura^{a)}, W. Sinananwanich^{a)}, H. Koshikawa^{a)}, M. Asano^{a)}, T. Yamaki^{a)},
K. Yamamoto^{b)}, H. Shishitani^{b)}, K. Asazawa^{b)}, S. Yamaguchi^{b)},
H. Tanaka^{b)} and Y. Maekawa^{a)}

^{a)} Environment and Industrial Materials Research Division, QuBS, JAEA, ^{b)} Daihatsu Motor Co., Ltd.

There has been a growing interest in anion exchange membrane fuel cell (AEMFCs) because of the non-precious metals such as nickel, cobalt and silver can be used as the catalyst¹⁾. An anion exchange membrane (AEM) is one of the key materials for AEMFC. Since the anion conducting groups, for which quaternary alkylammonium hydroxides are mainly used, are subject to degradation in operating conditions probably due to its high water uptake. Thus we have applied a radiation-induced grafting method to the preparation of a series of AEM having various cation groups to control the properties of AEMs. In this work, we prepare AEMs with iminium cation groups by radiation-induced grafting and investigate their properties.

The poly(ethylene-co-tetrafluoroethylene) (ETFE) films were irradiated with a ⁶⁰Co γ -ray source to a total dose of 50 kGy. The pre-irradiated ETFE films were immersed into the argon-purged monomer solution consisting of 50 wt% chloromethylstyrene (CMS) in xylene at 60 °C for 2 h. The chloromethyl groups in the grafted ETFE were quaternarized with alkylamine or imines and the resultant AEMs were immersed in 1 M KOH solution to convert into the hydroxide form (Scheme. 1).



Scheme. 1 Preparation of AEMs by radiation grafting.

The CMS-grafted ETFE films were prepared with grafting degrees of 70% and the quaternization reaction for chloromethyl group proceeds quantitatively. The values of ion-exchange capacity (IEC), water uptake(WU), and conductivity at 60 °C (σ) of the prepared AEMs are summarized in Table 1. The theoretical IEC values were calculated based on the weight gain after quaternization of each membrane. As listed in Table 1, the experimental values of IEC from titration corresponded to the theoretical values, and these AEMs take almost same IEC value.

The water uptake values of AEM are drastically changed by the structure of cation groups. The water uptake of **AEM2** shows about half of **AEM1** and the **AEM3** shows the water uptake of 18%. The conductivity values are also

Table 1 Properties of the AEMs.

Membrane	IEC (meq/g)		WU (%)	σ (mS/cm)
	theor	exp		
AEM1	2.08	1.81	111	144
AEM2	2.03	1.77	68	127
AEM3	1.90	1.69	18	0.40

affected by the cation structure. The conductivity of **AEM2** is 127 mS/cm which is nearly identical to **AEM1**. On the other hand, **AEM3** shows almost no conductivity. These results might be explained by the basicity of hydroxide salt of iminium cation. The more basic imine brings less basic iminium cation, and also, the cation center of iminium cation is stabilized by the resonance structure. These two effect decrease hydrophilicity of the cation groups and the AEMs show lower water uptake. However, It was founded that the too much loss of water causes disappearance of conductivity.

The thermal stability of AEMs is always a concern for AEMFCs because of its high operating temperature (80 °C). Figure 1 shows the derivative TGA curves of the prepared AEMs. The weight loss between 150 - 300 °C was associated with the degradation of the cation groups. The further weight loss of the AEMs occurring from 400 °C was related to the degradation of graft chain. As can be seen, the thermal stability of **AEM2** and **AEM3** is better than **AEM1**. This result might be due to the thermally stable imine structure.

These results demonstrate the great prospect of prepared AEM consisting of imidazolium cation for direct hydrazine fuel cells.

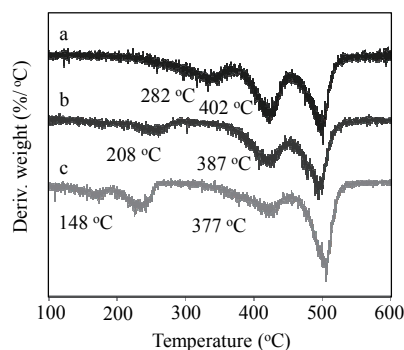


Fig. 1 Comparison of the TGA derivative curves of (a) **AEM3**, (b) **AEM2**, and (c) **AEM1**.

Reference

- 1) K. Asazawa et al., *Angew. Chem. Int. Ed.* 46 (2007) 8024.

1 - 27 Preparation of Anion-Exchange Membranes for Fuel Cell Applications by γ -ray Pre-Irradiation Grafting: Effect of the Structure of Quaternary Ammonium Ions

H. Koshikawa, K. Yoshimura, T. Yamaki, M. Asano and Y. Maekawa

Environment and Industrial Materials Research Division, QuBS, JAEA

Widespread commercialization of fuel cells has been hindered by economic problems associated with the extensive use of platinum as well as by many restrictions due to much additional infrastructure and insufficient hydrogen storage capacity. In order to overcome such difficulties, researchers have so far developed anion-exchange membrane fuel cells (AEMFCs), which do not need expensive platinum catalysts in the electrodes. Our recent focus has been the preparation of new membranes for applications to “hydrazine-fueled” AEMFCs¹⁾ by the γ -ray pre-irradiation grafting method^{2,3)}. We investigated here the effect of the structure of quaternary ammonium ions ($-N^+R_2R'$ where $R=CH_3$ and $R'=C_nH_{2n+1}$), *i.e.*, the length of the linear R' chain on them (n), on the membrane properties such as durability of ion conductivity.

Our membrane preparation involved the grafting of chloromethylstyrene (CMS) into poly(ethylene-co-tetrafluoroethylene) (ETFE) films and subsequent quaternization (Fig. 1)^{2,3)}. A 50 μ m-thick ETFE film was pre-irradiated at room temperature in an Ar atmosphere with a ⁶⁰Co γ -ray at a dose of 30 kGy. Graft polymerization was performed by immersing the irradiated ETFE film in the CMS /xylene 33 /67 vol% solution in an Ar atmosphere at 60 °C for 4 h. The ETFE-g-CMS film was then quaternized in four different tertiary amines, that is, trimethylamine ($n = 1$), dimethylethylamine ($n = 2$),

n -butyldimethylamine ($n = 4$) and n -hexyldimethylamine ($n = 6$) solutions at room temperature for 24 h. After the membrane was washed several times in water and in a 1 mol/dm³ HCl solution for 24 h (to remove residual amine), the chloride (Cl⁻) form of the membrane was converted to the alkaline (OH⁻) form in a 1 mol/dm³ aqueous KOH solution for 12 h.

Figure 2 shows the n dependence of the OH⁻ conductivity and chemical durability, which was represented by a residual percentage of the conductivity after treatment with a Fenton solution (3% H₂O₂+4 ppm FeSO₄) at 80 °C for 2 h. When n increased from 1 to 6, the OH⁻ conductivity decreased slightly, but it still stayed 20 mS/cm for $n = 6$. Interestingly, the chemical durability seemed to increase eight-fold at the same time. The chemical attack by hydroxyl radicals (from H₂O₂) on the quaternary ammonium ions would be controlled by hydrophobicity and steric hindrance of the alkyl group.

References

- 1) K. Asazawa et al., J. Electrochem. Soc. 156 (2009) B509.
- 2) H. Koshikawa et al., Proc. RadTech Asia 2011 (2011) 240.
- 3) T. Yamaki, Maku (Membrane) 36 (2011) 240.

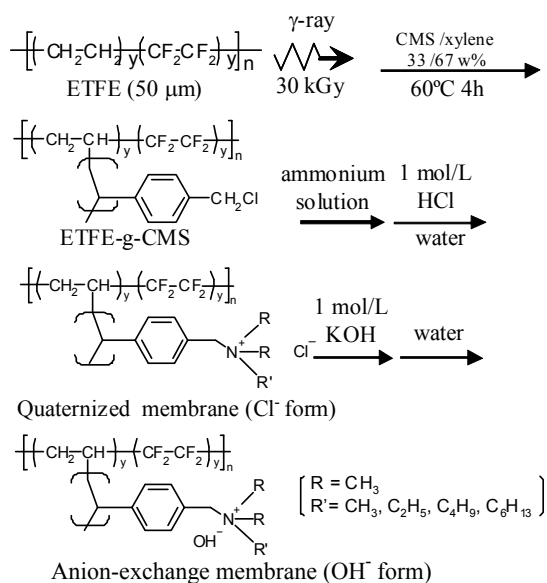


Fig. 1 Scheme for the preparation of anion-exchange membranes.

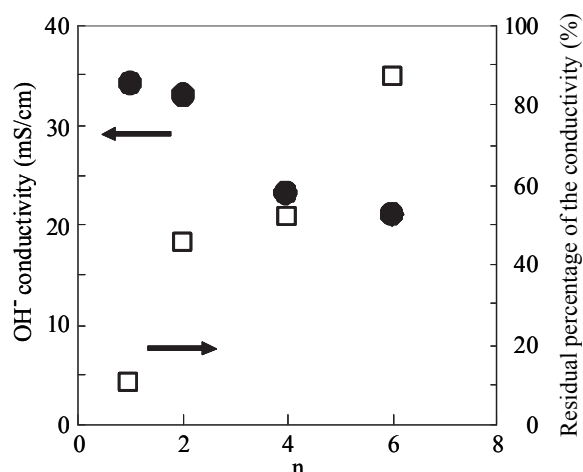


Fig. 2 n dependence of the OH⁻ conductivity and its residual percentage after treatment with a Fenton solution at 80 °C for 2 h.

1 - 28 Wide- q Observation in Small Angle X-ray Scattering of ETFE-Based Graft-Type Polymer Electrolyte Membranes

T. D. Tran^{a, b)}, S. Sawada^{a)}, S. Hasegawa^{a)}, K. Yoshimura^{a)}, Y. Oba^{c)},
M. Ohnuma^{c)}, Y. Katsumura^{b)} and Y. Maekawa^{a)}

^{a)} Environment and Industrial Materials Research Division, QuBS, JAEA,

^{b)} The University of Tokyo, ^{c)} Quantum Beam Center, National Institute for Materials Science

Fundamental understanding of the structure-property relationship of polymer electrolyte membrane (PEM) is prerequisite for proper material design to improve PEM performance. For this purpose, we have studied hierarchical structures of poly(ethylene-*co*-tetrafluoroethylene) (ETFE)-based graft-type polymer electrolyte membranes (ETFE-PEMs) by comparing the SAXS profiles with those of precursor original ETFE and polystyrene-grafted film (grafted ETFE) using small-angle X-ray scattering (SAXS).

ETFE-PEMs were prepared by a pre-irradiation grafting of styrene to obtain polystyrene grafted ETFE, followed by subsequent sulfonation reactions of the polystyrene grafts. SAXS measurements were performed at the National Institute of Material Science (NIMS), Tsukuba, and at SPring-8, Japan. Both pinhole SAXS were carried out to cover a wide q range observation ($0.0038 \text{ nm}^{-1} < q < 10.5 \text{ nm}^{-1}$) corresponding to a large Bragg spacing (d -spacing) scale ($0.6 \text{ nm} < d < 1,652 \text{ nm}$). The ion exchange capacity (IEC) of the samples was determined by titration analysis.

Figure 1 shows SAXS profiles of the original ETFE, grafted ETFE with a grafting degree of 59%, and ETFE-PEM (sulfonated form of the grafted ETFE) with IEC of 2.4 mmol/g. At low q range ($0.0038 \text{ nm}^{-1} \leq q \leq 0.1 \text{ nm}^{-1}$), the original ETFE exhibited no appreciable scattering, while the grafted ETFE and ETFE-PEM showed discernible shoulder-like peaks at q values of 0.0174 and 0.0162 nm^{-1} , corresponding the d -spacing of 361 and 387 nm, respectively. The newly appeared peaks were assigned to originate from graft polymer domains, which should act as ion conducting layer in ETFE-PEM.

At intermediate q range ($0.1 \text{ nm}^{-1} \leq q \leq 2.0 \text{ nm}^{-1}$), the original ETFE possesses a peak at q -position of 0.328 nm^{-1} with d -spacing of 19.0 nm. The maximum peak of the original ETFE was assigned as the scattering from lamellar stacks, in which SAXS profile is originated from the electron density difference between the crystalline and amorphous domains, as previously reported¹⁾. The grafted ETFE and ETFE-PEM showed shoulder-like peaks at q -positions of 0.219 and 0.216 nm^{-1} , respectively. The Bragg peaks at similar q -position to that in the original ETFE film indicate that new phases consisting of polystyrene grafts and poly(styrene sulfonic acid) grafts generated under the influences of the lamellar structure of the original ETFE film. The accurate values of d -spacing at intermediate q range were evaluated by Lorentz correction of the original SAXS profiles because of the randomly

oriented lamellar bundles (crystallites) in the samples²⁾. Based on Lorentz correction, the lamellar spacing of the grafted ETFE and ETFE-PEM were determined to be 28.7 and 29.1 nm, respectively. These values of grafted ETFE and ETFE-PEM are about 12% and 17 % lower than those estimated from the shoulder-like peaks in the SAXS profiles in Fig. 1. The d -spacing of grafted ETFE is 9.7 nm larger than that of the original ETFE. This expansion indicated that some portions of polystyrene graft-polymers were introduced in the amorphous regions in the lamellar stacks. On the other hand, the expansion of the d -spacing by the sulfonation of grafted ETFE (i.e., the difference of the d -spacing in grafted ETFE and ETFE-PEM) is very small (only 0.4 nm), indicating that the introduction of sulfonic acid groups in the graft domains did not enlarge the total lamellar spacing.

At high q range ($2.0 \text{ nm}^{-1} \leq q \leq 10.5 \text{ nm}^{-1}$), the grafted ETFE and ETFE-PEM showed new peaks with d -spacing of 0.94 nm and 1.48 nm, respectively while the original ETFE film did not. Thus, the peak at 0.94 and 1.48 nm should be originated from correlation distances of the monomer units of polystyrene monomer and poly(styrene sulfonic acid). The d -spacing of ETFE-PEM at larger q range is 0.54 nm larger than that of grafted ETFE. This could be also owing to the increases of sulfonic acid group content in the graft domains.

References

- 1) K. Jokela et al., J. Polym. Sci. Polym. Phys. Ed., 40, (2002) 1539.
- 2) B. Crist et al., J. Polym. Sci. Polym. Phys. Ed., 11, (1973) 1023.

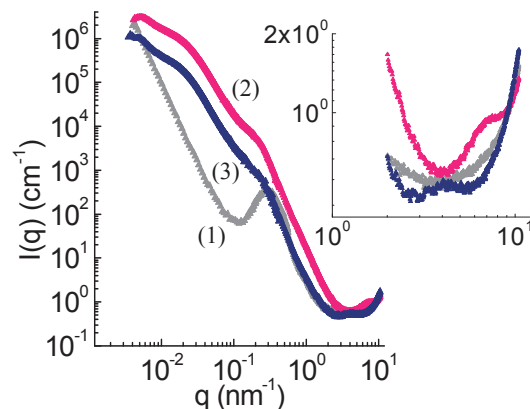


Fig. 1 SAXS profiles of (1) original ETFE, (2) grafted ETFE, and (3) ETFE PEM with grafting degree of 59%.

1 - 29 Development of Grafted Type Poly(ether ether ketone) Electrolyte Membranes

S. Hasegawa^{a)}, H. Iwase^{b)}, S. Koizumi^{b)}, Y. Oba^{c)}, M. Ohnuma^{c)} and Y. Maekawa^{a)}

^{a)} Environment and Industrial Materials Research Division, QuBS, JAEA,

^{b)} Materials Science Research Division, QuBS, JAEA,

^{c)} Quantum Beam Center, National Institute for Materials Science (NIMS)

A pre-irradiation grafting method is a fascinating technique for direct introduction of a new functional polymer phase as a grafting chain (grafts) into polymer films serving as a substrate without any damage of those films. The radiation technique has been widely applied to the preparation of high performance fuel cell polymer electrolyte membranes (PEMs) for mobile electricities, vehicles, and domestic co-generation systems.

The PEMs of aromatic hydrocarbon polymers, so-called “super engineering plastics” including poly(ether ether ketone) (PEEK), have useful characteristics such as high mechanical strength, gas barrier property, and radiation resistance¹⁾.

In this work, we investigated the mechanism of graft polymerization of PEEK from the view point of morphology of PEEK films using small angle X-ray scattering experiments (SAXS).

Graft polymerization of ethyl 4-styrenesulfonate (E4S) into a high crystalline PEEK film (crystallinity: 32%) hardly progressed, whereas graft polymerization gradually progressed into a low crystalline PEEK film (crystallinity: 11%), achieving a grafting degree (*GD*) of 52% after 72 h (Fig.1, Table 1)¹⁾. Accordingly, in order to investigate the effect of crystallinity of PEEK films on grafting of E4S, PEEK films having various crystallinity from 11 to 32% were prepared by annealing at 160 °C for 0.25 to 21 hours. The *GD* was calculated from the following equation, $GD = 100 \times (W_g - W_0) / W_0$, where W_0 and W_g are the film weights before and after the grafting, respectively. The PEEK films with various crystallinity were irradiated at 60 kGy and grafting was conducted at 80 °C for 72 h.

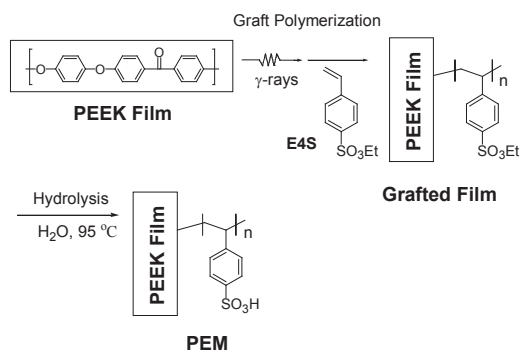


Fig. 1 Radiation induced-graft polymerization of E4S into PEEK films and subsequent hydrolysis of poly (E4S) grafts.

Table 1 *GD* of E4S into PEEK films.

Crystallinity (%)	<i>GD</i> (%)
11	52
32	3

Irradiation dose, 60 kGy; grafting temperature, 80 °C; grafting solution, 50 wt% E4S in dioxane.

The *GD* was found to be constant (70%) in the range of crystallinity up to 26%. However, the *GD* suddenly decreased with increasing crystallinity above 26% (Fig. 2(a)). When the morphological change in these films was measured by SAXS, the PEEK films with crystallinity larger than 26% showed a new peak at a correlation distance $d = 14$ nm, corresponding to the formation of lamella structure (Fig. 2(b)). Thus, we concluded that the suppression of graft polymerization of PEEK films with crystallinity above 26% was due to obstruct of monomer diffusion by the formation of the oriented lamella structure.

Reference

- 1) S. Hasegawa et al., Polymer 52 (2011) 98-106.

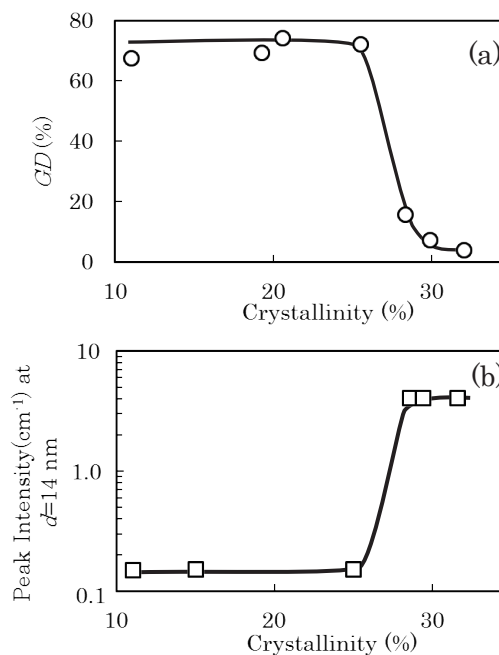


Fig. 2 Changes in *GD* of E4S (a) and the peak intensity obtained at $d = 14$ nm by SAXS (b) as a function of crystallinity for PEEK films.

1 - 30 Preparation of Novel Polymer Electrolyte Membranes by Combination of Radiation Induced Grafting and Atom Transfer Radical Polymerization

S. Sawada, S. Hasegawa and Y. Maekawa

Environment and Industrial Materials Research Division, QuBS, JAEA

The most vital components in polymer electrolyte membrane (PEM) fuel cells are PEM materials. In the case of Nafion (DuPont Co.), the most widely used PEMs, the proton conductivity markedly decreases at high temperature (> 80 °C) and low relative humidity (RH) (< 30%). This drawback limits the use of Nafion in practical and commercial applications.

Our research group is developing the Nafion-alternative PEMs by using a radiation-induced grafting method¹⁾. In these PEMs, the graft chain structures should significantly affect the proton conduction properties. Then, in this study, by combination of radiation grafting and atom transfer radical polymerization (ATRP), we designed the novel PEMs possessing both the hydrophobic and hydrophilic graft chains.

The two-types of PEMs (type A and B) were prepared as shown in Fig. 1. At first, the base poly(vinylidene fluoride) (PVDF) films were irradiated with 15-kGy γ -ray in an Ar atmosphere. For preparation of type-A PEMs, the irradiated films were immersed in ethylstyrenesulfonate (ETSS) / chloromethylstyrene (CMS) mixtures for the grafting. Next, for the ATRP, the films were immersed in styrene (St) solutions, which contained CuBr and N,N,N',N'',N''- Pentamethyldiethylenetriamine (PMDETA) as catalyst and ligand, respectively. The St graft chains were elongated from the Cl atoms in CMS units (see Fig. 1). On the other hand, for type-B PEM preparation, the irradiated PVDF films were immersed in St/CMS mixtures for the grafting, and then immersed in ETSS solutions containing CuBr and PMDETA for the ATRP. The films after the ATRP were hydrolyzed in pure water to change from ETSS units to proton conductive poly(styrene sulfonic acid) (PSSA) units.

In both the type-A and type-B PEM preparation, the contents of CMS, St, ETSS were widely controlled by changing the reaction time of the radiation grafting and ATRP. Table 1 shows the representative result for the prepared PEMs. The weight percentage of the hydrophobic parts (CMS and St units), R_1 , and hydrophilic parts (PSSA units), R_2 , are shown in this Table. It is noteworthy that these PEMs have quite different R_1 and R_2 values in spite of the similar ion exchange capacity (IEC) of around 2.0 meq/g.

Figure 2 shows the proton conductivity of the PEMs at 80 °C and RH of 30% as a function of R_1 . The plot at R_1 of 0% is the data for the conventional PEM, which was prepared by only radiation grafting of styrene into the PVDF film and subsequent sulfonation. The proton conductivity

of the type-A PEMs did not depend on the R_1 . In contrast, for the type-B PEMs, the conductivity increased as the R_1 became larger. When the hydrophobic grafts are introduced near the base PVDF film, the peculiar hydrophilic / hydrophobic phase-separation morphology is possibly formed. This might be the reason for the higher proton conductivity of the type-B PEMs.

Reference

- 1) S. Sawada et al., ECS Trans. 41 (2011) 2125.

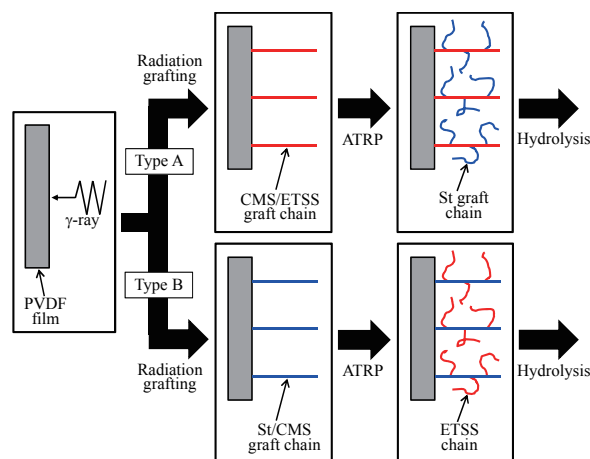


Fig. 1 Scheme of preparation of type-A and type-B PEMs.

Table 1 The R_1 , R_2 , and IEC of the prepared PEMs.

Type	R_1 (%)	R_2 (%)	IEC (meq.g)
A	12	88	1.9
A	20	80	2.1
A	31	69	2.0
B	12	88	2.0
B	27	73	2.2

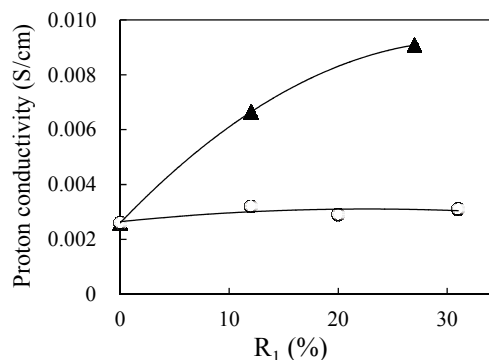


Fig. 2 Proton conductivity of the (○) type-A and (▲) type-B PEMs as a function of R_1 .

1 - 31 Ion-track Membranes of Poly(vinylidene fluoride): Etching Characteristics during Conductometric Analysis

N. Nuryanthi^{a, b)}, T. Yamaki^{a)}, H. Koshikawa^{a)}, M. Asano^{a)}, S. Sawada^{a)}, S. Hasegawa^{a)},
Y. Katsumura^{b)} and Y. Maekawa^{a)}

^{a)}Environment and Industrial Materials Research Division, QuBS, JAEA,

^{b)}Department of Nuclear Engineering and Management, The University of Tokyo

Ion tracks in an organic polymer can sometimes be etched out with a suitable solution to give nanopores. The resulting ion-track membrane has been used for many applications in industry and research. Although the ion-track technique has mainly been studied for a series of hydrocarbon polymers, our focus has been placed on the ion-track membrane of poly(vinylidene fluoride) (PVDF), a type of fluoropolymer, because of its superior chemical, mechanical and ferro-electric properties¹⁻⁴⁾. We previously performed conductometric etching, which allows monitoring pore evolution versus etching time by recording the electrical conductance through the membrane⁵⁾. There was a main conclusion: the track etching before breakthrough was accelerated at higher applied voltages up to 2.0 V^{1,2)}. Therefore, there has been a strong motivation to investigate how conditions of the conductometric analysis affect the etching characteristics. We report here the results in this regard obtained by scanning electron microscopy (SEM) as well as by conductometry.

A 25 μm -thick PVDF film was irradiated with 450 MeV ¹²⁹Xe ions at a fixed fluence of 3×10^7 ions/cm². The irradiation was performed in a vacuum chamber of the LD beamline at the TIARA cyclotron. The tracks were then etched in a 9 mol/dm³ aqueous KOH solution at 80 °C in a conductometric cell⁵⁾. An AC voltage of different amplitudes and frequencies (typically 0.3-2.0 V and 1 kHz, respectively) was applied during this conductometric etching. For comparison, the etching was carried out in the same solution, but in a teflon vessel without applying the voltage. SEM observations were performed to determine the final diameter of the etched pores.

Figure 1 shows SEM photographs of the ion-track membranes obtained by the etching for 30 h (a) without and (b) with an applied voltage of 1.0 V. We first compare the results of the etching in the conductometric cell; the surface pore diameter was 168 ± 20 nm at 1.0 V (shown in (b)), while it was 178 ± 7 nm at 0.3 V (the result not shown). Considering a large relative error in the pore-size evaluation, we can say that the finally-obtained pores were similar to each other. This result seems reasonable because we did not previously see any significant change in the conductometry results, when the applied voltage was increased from 0.3 to 1.0 V²⁾.

On the other hand, as shown in Fig. 1 (a), the etching without an applied voltage gave the ion-track membrane with a diameter of 113 ± 11 nm, which is approximately two-thirds smaller than that for the conductometrically-etched membranes. A few research groups including Cornelius *et al.*⁶⁾ and us^{1,2)} previously made similar findings and then, as a probable cause, took into account the electrophoretic migration of ionic or polar dissolved products occurring out of each pore. The details were discussed elsewhere^{1, 2, 6)}. Finally, the conductometric etching would provide a higher degree of freedom for controlling the pore diameter.

References

- 1) N. Nuryanthi et al., *Electrochemistry* 78 (2010) 146.
- 2) T. Yamaki et al., *ECS Trans.* 35 (2011) 1.
- 3) T. Yamaki et al., *JAEA Takasaki Annu. Rep.* 2010 (2012) 35.
- 4) T. Yamaki et al., *GSI Sci. Rep.*, in press.
- 5) T. Yamaki et al., *Trans. Mater. Res. Soc. Jpn.*, in press.
- 6) T.W Cornelius et al., *Nucl. Instrum. Meth. Phys. Res. B* 265 (2007) 553.

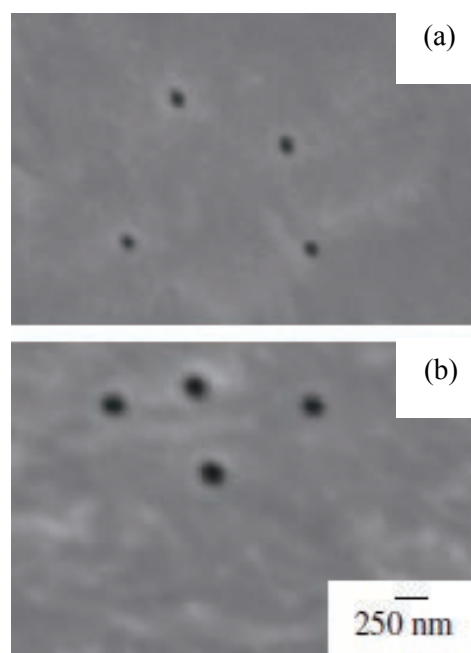


Fig. 1 SEM photographs of the ion-track membranes obtained by the etching (a) without and (b) with an applied voltage.

1 - 32 Effect of Temperature on Conductivity of Ion Exchange Membrane in HIx Solution

N. Tanaka ^{a, b)}, T. Yamaki ^{c)}, M. Asano ^{c)}, T. Terai ^{b)} and K. Onuki ^{a)}

^{a)} Nuclear Hydrogen and Heat Application Research Center, JAEA,

^{b)} Department of Nuclear Engineering and Management, The University of Tokyo,

^{c)} Environment and Industrial Materials Research Division, QuBS, JAEA

JAEA has been conducting R&D on a hydrogen production thermochemical water-splitting Iodine-Sulfur (IS) process as a heat utilization system using HTGR¹⁾. In hydrogen iodide (HI) decomposition section of the IS process, an electro-electrodialysis (EED) using ion exchange membrane has been used in order to concentrate a HI in HI-I₂-H₂O mixture (HIx solution) over quasi-azeotropic point²⁾. The EED operation should preferably be performed at high temperatures because it is then energetically favored and no preheating devices are required. In addition, the EED performance strongly depends on the conductivity that also increases with temperature. Thus, we investigated the temperature dependence of the conductivity in order to optimize the operating condition. In this study, we derive a theoretical formula on the basis of Nernst-Planck equation, and demonstrate its validity using experimental data of commercial and test-fabricated membranes.

Transport phenomena of protons (H⁺) in ion exchange membranes can be described by Nernst-Planck equation. Assuming that the diffusion coefficient of H⁺ was expressed by Arrhenius type, the conductivity, σ [S/m] was given by

$$\sigma = \frac{id}{E} = \frac{Y}{t_+ T} \exp\left(-\frac{\Delta U_{H^+}}{RT}\right), Y \equiv \frac{F^2 D_{H^+}^{m_0} n_{H^+}^m}{RV_g} \quad (1)$$

where i [A/m²], d [m], E [V], t_+ [-], T [K], R [J/mol·K], F [C/mol], V_g [m³/kg], $n_{H^+}^m$ [mol/kg], $D_{H^+}^{m_0}$ [m²/s] and ΔU_{H^+} [J/mol] denote current density, thickness, cell voltage, transport number, temperature, gas constant, Faraday constant, volume per dry membrane weight, H⁺ content per dry membrane weight, pre-exponential factor of H⁺ diffusion coefficient and activation energy of it, respectively.

The membrane was prepared by γ -ray pre-irradiation of ETFE base film, graft polymerization of monomer, and sulfonation³⁾. Styrene (St) was used as the grafting agent. The ion exchange capacity (IEC) was 1.1 mmol/g. Nafion212 (E.I. Du Pont, IEC: 0.89 mmol/g) was used as reference. In the following, the membranes are denoted as ETFE-g-St and Nafion 212, respectively. The measurement of conductivity was carried out using a filter-press type EED cell. The effective membrane area was 5 cm². The HIx solution of [HI]=[I₂]=10 mol/kg was used as the test solution. The cell voltage was measured by supplying direct current to the cell at a current density of 200 mA/cm² at different temperatures (i.e., 313, 343, and 373 K). The measured cell voltage was directly used to calculate σ by using eq. (1), because it was dominated by the

applied voltage between only both sides of membrane⁴⁾. For the following discussion, the transport number was measured by the experimental procedure described elsewhere²⁾.

Figure 1 (A) shows the obtained values of σ of the tested membranes and the regression analysis results of eq. (1) performed with the least square method. The regression analysis results appeared to be in good agreement, showing the temperature dependence of σ can be described by eq. (1). Here, Y and ΔU_{H^+} are temperature independent and the values were determined by the regression analysis. Figure 1 (B) shows the temperature dependence of the H⁺ diffusion coefficient obtained by the regression analysis. It was suggested that the temperature dependence of σ was determined by that of H⁺ diffusion.

References

- 1) S. Kubo et al., Nucl. Eng. Des. 233 (2004) 355.
- 2) N. Tanaka et al., J. Membr. Sci. 346 (2010) 136.
- 3) T. Yamaki et al., Maku (Membrane) 36 (2011) 240.
- 4) M. Yoshida et al., Int. J. Hydrogen Energy 33 (2006) 166.

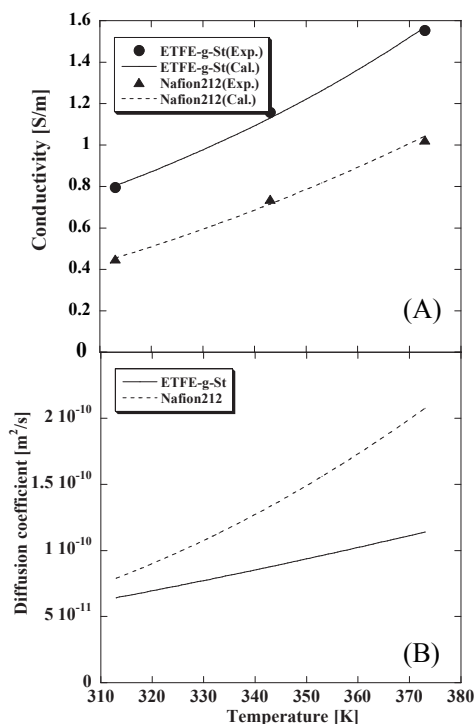


Fig. 1 Temperature dependence of (A) σ and (B) H⁺ diffusion coefficient in the tested membranes.

1 - 33 Nanoparticle Formation by Tungsten Ion Implantation in Glassy Carbon

S. Kato ^{a, b)}, T. Yamaki ^{b)}, S. Yamamoto ^{b)}, T. Hakoda ^{b)}, K. Kawaguchi ^{b, c)},
T. Kobayashi ^{d)}, Y. Maekawa ^{b)}, A. Suzuki ^{a)} and T. Terai ^{a)}

^{a)} Department of Nuclear Engineering and Management, The University of Tokyo,
^{b)} Environment and Industrial Materials Research Division, QuBS, JAEA,
^{c)} Department of Chemistry and Materials Technology, Kyoto Institute of Technology,
^{d)} Atomic Physics Laboratory, Advanced Science Institute, RIKEN

Nanoparticles prepared by implantation of metal ions have been intensively studied in terms of their size, shape or composition, high surface area, and reactivity with a substrate for electronic and optical applications. In this research, we investigated nanoparticle formation in a glassy carbon (GC) substrate implanted with tungsten (W) ions. Tungsten-ion implantation in silica caused the formation of metallic-W precipitates with a small amount of W oxides¹⁾; on the other hand, the implantation in GC is expected to generate carbides²⁾. In addition to implantation effects, the electrochemical and morphological properties of the obtained nanoparticles were discussed here for the first time.

Our implantation experiments were performed in an IAI chamber at the TIARA 400-kV ion implanter³⁻⁵⁾. We implanted 100 keV W⁺ in an unpolished GC substrate at nominal fluences up to 1.8×10^{17} ions/cm². The implanted samples were analyzed by Rutherford backscattering spectrometry (RBS), X-ray photoelectron spectroscopy (XPS), hydrodynamic voltammetry using a rotating disk electrode, and transmission electron microscopy (TEM).

According to the RBS results, a significant sputtering effect limited the maximum retained fluence to approximately 6×10^{16} W/cm². Figure 1 shows XPS W 4f spectra of the implanted GC substrate before and after an Ar⁺-beam sputtering for different times. The concentration of W increased during the course of sputtering and peaked at 180 s. A peak of the W 4f_{7/2} state at 32.1 eV (0.6 eV higher than that of metallic W) can be ascribed to carbides, WC⁶⁾. A current density in the voltammogram^{7, 8)}, representing the electrochemical activity of a surface, seemed lower for the W-implanted sample than for the

unimplanted one. This is probably due to a decrease in the surface area by the observed sputtering effect.

The subsequent electrochemical etching in a 0.1 M NaOH aqueous solution⁹⁾ achieved the maximum area density of the nanoparticles on the surface. Figure 2 shows a cross-sectional TEM micrograph of the resulting sample, in which the implanted layer is situated between the GC substrate and a carbon (C) layer deposited during specimen preparation. Particulate aggregates near the surface were found to contain spherical nanoparticles with a diameter of < 10 nm.

References

- 1) R. Bertone et al., *J. Non-Cryst. Solids* 162 (1993) 205.
- 2) A. Hoffman et al., *J. Appl. Phys.* 72 (1992) 5687.
- 3) T. Umebayashi et al., *J. Appl. Phys.* 93 (2003) 5156.
- 4) T. Yamaki et al., *Nucl. Instrum. Meth. Phys. Res. B* 206 (2003) 254.
- 5) T. Yamaki et al., *J. Mater. Sci. Lett.* 21 (2002) 33.
- 6) G. E. McGuire et al., *Inorg. Chem.*, 12 (1973) 2450.
- 7) T. Hakoda et al., *Appl. Surf. Sci.* 257 (2010) 1556.
- 8) T. Yamaki et al., *Mater. Res. Soc. Symp. Proc.* 1217 (2010) 151.
- 9) G. K. Kiem et al., *J. Electrochem. Soc.* 151 (2004) C142.

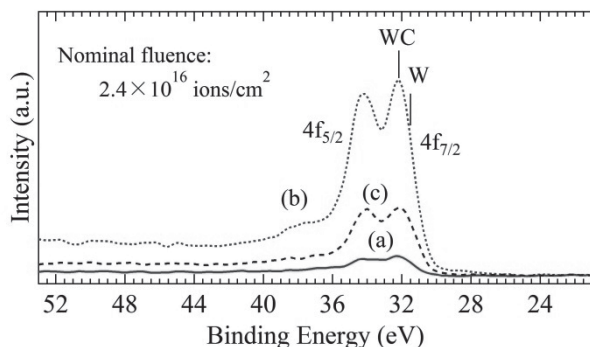


Fig. 1 XPS W 4f spectra of the implanted GC substrate (a) before and after the Ar⁺ sputtering for (b) 180 or (c) 300 s.

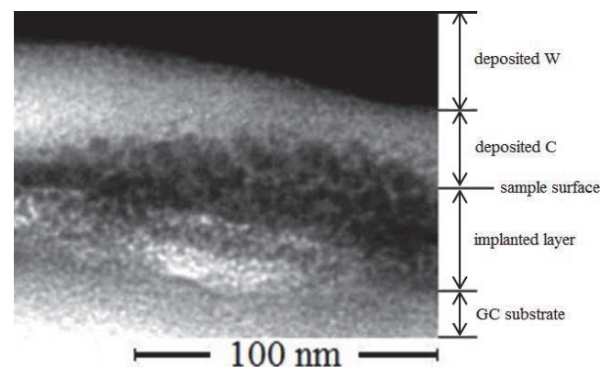


Fig. 2 TEM micrograph of the GC substrate implanted with 2.4×10^{16} W/cm² and then etched electrochemically in an alkaline aqueous solution. During specimen preparation in a cross-sectional geometry, C and W layers were deposited on the surface.

This is a blank page.

2. Environmental Conservation and Resource Exploitation

2-01	Pb(II) Adsorption Performance of Fibrous Graft Adsorbent Having Phosphate Groups	41
	Y. Ueki, N. C. Dafader, N. Seko and M. Tamada	
2-02	Removal of Radioactive Cesium from Contaminated Environmental Water by Graft Adsorbent	42
	S. Saiki, A. Iwanade, N. Kasai, H. Hoshina, Y. Ueki and N. Seko	
2-03	Boron Removal and Recovery Using Adsorbent Prepared by Radiation Grafting	43
	A. Katakai, T. Yotsumoto, A. Takahashi, Y. Ueki and N. Seko	
2-04	Arsenic Removal from Streaming Water by Graft Adsorbent Synthesized with Cellulose Nonwoven Fabric	44
	H. Hoshina, N. Kasai, T. Shibata, M. Takahashi, A. Yoshii, Y. Tsunoda, Y. Aketagawa and N. Seko	
2-05	Surface Modification of Vulcanized Rubber by Radiation Grafting	45
	H. Saito, N. Mizote, Y. Ueki and N. Seko	
2-06	Micro-fabrication of Biodegradable Polymers by Focused Ion Beam Direct Etching	46
	A. Oshima, S. Okubo, N. Nagasawa, T. G. Oyama, M. Taguchi, M. Washio and S. Tagawa	
2-07	Preparation of Polymer Gel Dosimeters Based on Radiation-crosslinked Hydroxypropyl Cellulose Gels	47
	A. Hiroki, S. Yamashita, N. Nagasawa and M. Taguchi	
2-08	Improvement of Mechanical Properties of Poly (L -Lactic Acid) by Blending with Polyamide 11 and Radiation-induced Crosslinking	48
	T. Tago, N. Nagasawa, H. Kudo, Y. Katsumura and M. Taguchi	
2-09	Radiation Preparation of P(NIPAM- <i>co</i> -HEMA) and Micelles from PLLA- <i>g</i> -P(NIPAM- <i>co</i> -HEMA)	49
	TM. Quynh, Y. Maki, N. Nagasawa and T. Dobashi	
2-10	Reactivity of Oxidative/Reductive Species toward Persistent Antibiotics under Ionizing Radiation	50
	A. Kimura and M. Taguchi	
2-11	Solution Properties of Seaweed Polysaccharide Funoran	51
	S. Takigami, H. Yamaguchi, R. Takahasi and N. Nagasawa	
2-12	Immobilization of Nitrifying Bacteria to the HPC Gel Medium Synthesized by Electron Beam Irradiation	52
	T. Yanagisawa, T. Kojima, N. Nagasawa, M. Taguchi and T. Tanaka	
2-13	Interaction between <i>Paramecium bursaria</i> and Heavy Elements	53
	N. Kozai, T. Ohnuki, T. Satoh, M. Koka and T. Kamiya	
2-14	Measurement of Trace Elements in Natural Water in Iwaki City after Earthquake by In - Air Micro-PIXE	54
	E. Sakurai, K. Ishii, S. Yamauchi, H. Yamazaki, A. Yamazaki, W. Kada, M. Koka, T. Satoh and T. Kamiya	

This is a blank page.

2 - 01 Pb(II) Adsorption Performance of Fibrous Graft Adsorbent Having Phosphate Groups

Y. Ueki^{a)}, N. C. Dafader^{b)}, N. Seko^{a)} and M. Tamada^{a)}

^{a)} Environment and Industrial Materials Research Division, QuBS, JAEA,

^{b)} Nuclear and Radiation Chemistry Division, Institute of Nuclear Science and Technology, Bangladesh Atomic Energy Commission

Radiation-induced graft polymerization, one of the surface modification techniques of polymer materials, has recently been attracting attention as a refined artifice because the adsorption rate of a grafted polymer is 10-100 times higher than that of a commercial granular resin. We reported the simple and easy grafting methodology that could be performed using not unique but general apparatus in the previous study¹⁾. The objective of this study is to evaluate a metal adsorption performance of fibrous graft adsorbent having phosphate groups.

The graft polymerization was carried out by contacting the nonwoven polyethylene fabric irradiated by 100 kGy electron beam with de-aerated monomer emulsion, which was composed of 5 wt% glycidyl methacrylate (GMA), 0.5 wt% Tween 20 and 94.5 wt% water, in a polyethylene bottle for 4 h at 40 °C. After grafting, the grafted fabric was treated with 98 wt% phosphoric acid at 120 °C for 6 h to introduce phosphate groups. The metal adsorption performance of the fibrous graft adsorbent having phosphate groups was evaluated through column-mode adsorption and elution tests of Pb(II). Sixty mg of fibrous graft adsorbent having 2.65 mmol-H₂PO₄/g-adsorbent was packed into a column (7 mm i.d. × 2.9 mm long). In the adsorption test, 300 ppm of Pb(II) solution was supplied to the column at different flow rates such as 200, 500, and 1,000 h⁻¹ in space velocity (SV), and the adsorbed Pb(II) on the fibrous graft adsorbent was eluted with 1 M HNO₃ solution.

Figure 1 and Table 1 show the results of absorption and elution tests. For comparison, the results for granular methylenephosphonic acid resin (RCSP), published by Jyo et al.²⁾, are listed in Table 1. In the case of the fibrous graft adsorbent, although the breakthrough points (BP) and saturation points (SP) were slightly changed at an extremely high flow rate, the shapes of the breakthrough curves were

not essentially dependent on the flow rates of the each feed. In the case of RCSP, the BP significantly decreased with an increase in flow rates, and the RCSP could not effectively adsorb Pb(II) at flow rates higher than 50 h⁻¹. Furthermore, the breakthrough capacity (C_{BP}) is more important than the total metal adsorption capacity (denoted as saturation capacity; C_{SP}) in terms of the elimination of a toxic substance. The C_{BP} of the fibrous graft adsorbent were little affected by the flow rate, and the utilization ratios of phosphate groups at breakthrough point (C_{BP}/C_{SP}) were about 57% of the C_{SP} at any flow rate. However, that of RCSP markedly decreased with an increase in flow rates, indicating that the phosphate groups in RCSP cannot efficiently capture Pb(II) at flow rates higher than 50 h⁻¹, due to slow diffusion of ionic species into the cross-linked network structures. In the case of RCSP, the utilization ratios of phosphate groups at breakthrough point (C_{BP}/C_{SP}) were 53.3, 44.4, 21.7, 16.4 and 9.1% for flow rates of 10, 50, 100, 200 and 500 h⁻¹ in SV, respectively. As can be seen in Fig. 1, the elution curves of eluted Pb(II) were very narrow and sharp, and all the adsorbed Pb(II) could only be eluted by 1 M HNO₃ solution of less than 46 bed volume (BV) at any flow rate. Thus, the Pb(II) could be concentrated about 91 times of initial concentration (300 ppm) by the fibrous graft adsorbent. Besides, even after 10 adsorption-elution cycles were repeated, the fibrous graft adsorbent did not suffer serious physical or chemical damage, and the metal adsorption capacity still maintained its initial adsorptivity. Consequently, it was found that the fibrous graft adsorbent had good durability for long-term use.

References

- 1) Y. Ueki et al., JAEA Takasaki Annu. Rep. **2010** (2012) 43.
- 2) A. Jyo et al., Anal. Sci., **17 Suppl.** (2001) i201-04.

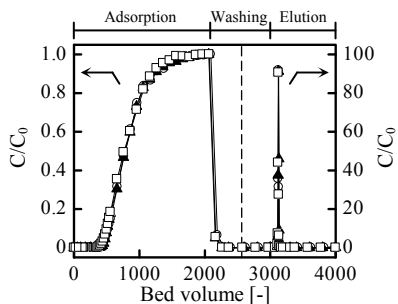


Fig. 1 Breakthrough and elution curves of Pb(II) through the fibrous graft adsorbent at different flow rates.

SV: ○ 200 h⁻¹; ▲ 500 h⁻¹; □ 1,000 h⁻¹.

Table 1 Summary of adsorption and elution of Pb(II) by the fibrous graft adsorbent and RCSP.

SV ^{a)} [h ⁻¹]	Adsorption test					Elution test		
	BP ^{b)} [BV ^{c)}]	C _{BP} ^{d)} [mmol/g]	SP ^{e)} [BV ^{c)}]	C _{SP} ^{f)} [mmol/g]	C _{BP} /C _{SP} ^{g)} [%]	V _E ^{h)} [BV ^{c)}]	C _E ⁱ⁾ [mmol/g]	Recovery [%]
Fibrous graft adsorbent								
200	483	1.16	1683	2.04	57.2	45.3	1.98	97.5
500	477	1.15	1658	2.01	57.0	44.9	2.07	102.5
1000	462	1.16	1665	1.98	58.4	45.1	1.94	98.0
Granular methylenephosphonic acid resin (RCSP) ²⁾								
10	47	1.6	-	3.0	53.3	-	-	-
50	39	1.2	-	2.7	44.4	-	-	-
100	21	0.63	-	2.9	21.7	-	-	-
200	13	0.41	-	2.5	16.4	-	-	-
500	7	0.20	-	2.2	9.1	-	-	-

a) Space velocity, b) breakthrough point, c) bed volume, d) breakthrough capacity, e) saturation point, f) saturation capacity, g) utilization ratio of functional group at breakthrough point, h) supplied volume for metal elution, i) amount of eluted Pb(II).

2 - 02 Removal of Radioactive Cesium from Contaminated Environmental Water by Graft Adsorbent

S. Saiki^{a)}, A. Iwanade^{a, b)}, N. Kasai^{a)}, H. Hoshina^{a)}, Y. Ueki^{a)} and N. Seko^{a)}

^{a)} Environment and Industrial Materials Research Division, QuBS, JAEA,

^{b)} Department of Advanced Radiation Technology, TARRI, JAEA

On 11th March 2011, the Fukushima Daiichi Nuclear Power Plant operated by Tokyo Electric Power Co., Inc., was severely damaged by the Great East Japan Earthquake and the ensuing tsunami, resulting in the leakage and spread of radioisotopes such as ¹³¹I, ¹³⁴Cs and ¹³⁷Cs etc. Therefore, an adsorbent with high capacity and selectivity for Cs removal must be developed with the additional requirement of total volume reduction of the pollutant.

In this study, we propose a novel fabric-loaded ammonium 12-molybdophosphate (AMP) adsorbent for Cs prepared by radiation-induced graft polymerization. AMP is embedded during the graft polymerization in a mix solution of a monomer and an inorganic ion exchanger (AMP). The adsorption performance of the fabric-loaded adsorbent containing AMP with regard to Cs was evaluated by a batch experiment as well as by a column experiment using a solution containing nonradioactive Cs. Finally, we demonstrated that the proposed fabric-loaded adsorbent can decontaminate environmental water containing radioactive Cs, which can be used to reduce the radiation level in Fukushima Prefecture and other contaminated areas.

The scheme for impregnation of AMP on nonwoven fabric (NF) is as follows. A few pieces of NF were irradiated with an electron beam of 200 kGy in an atmosphere of nitrogen gas, and the irradiated NF was grafted in a monomer solution prepared by mixing acrylonitrile (AN), dimethyl sulfoxide (DMSO), AMP and Tween 80. Grafting and impregnation of AMP on NF were carried out at 323 K for 24 h by immersing into a water bath. The resulting sample was dried under reduced pressure. As a result, the degree of grafting of these samples reached 450 - 800%.

The Cs adsorption performance of the AMP-AN fabric was first evaluated in a batch adsorption experiment. The fabric cut into 1 cm square was immersed in 50 mL of 1 ppm Cs solution and stirred for 24 h. Subsequently, the Cs concentration was measured by inductively coupled plasma mass spectroscopy (ICP-MS). The result showed that AMP-AN fabric was able to remove a large portion of Cs from pure and acidic water (90 and 87%, respectively), although its performance with respect to seawater was lower (64%).

In column adsorption, the circular pieces of AMP-AN fabric were packed into the column (diameter 7 mm) to a height of 5 cm, and a solution containing Cs with a concentration of 1 ppm at pH 7 was pumped through the column. The flow rate of the Cs solution was 300 h⁻¹ in terms of space velocity (SV). The outlet solution was

fractionally collected and the concentration of Cs was quantitatively analyzed with ICP-MS. The breakthrough point (BP) was defined as the point at which the Cs concentration in the outlet reached 1% of that in the supplied Cs solution. The breakthrough capacity of the AMP-AN fabric for Cs was calculated as

$$\text{Breakthrough capacity} = \int_0^{V_{0.01}} (C_0 - C) dV / W$$

Here, C₀, C, V and V_{0.01} are the Cs concentrations of the feed and the effluent volume and the effluent volume when C/C₀ reaches 0.01, respectively. W is the weight of the AMP-AN fabric. The breakthrough capacity of the AMP-AN fabric was 54 g-Cs/kg-adsorbent, indicating that a column charged with AMP-AN fabric can process about 3,000 times its packed volume of 1 ppm Cs solution to remove between 99 and 100% of the dissolved Cs.

In an experiment involving the decontamination of actual environmental water (Iitate-mura in Fukushima Prefecture), radioactive Cs was removed with a column (diameter 40 mm) charged with AMP-AN fabric (height 3.8 cm) after permeating two pre-columns with respective pore sizes of 25 and 10 μm. The radioactivity of ¹³⁴Cs and ¹³⁷Cs was measured with a germanium semiconductor detector (SEIKO EG&G). As a result, the radiation level of the contaminated water was reduced to one-third of its original level (Fig. 1). AMP-AN fabric is expected to find application in the decontamination of water from nuclear power plants.

Reference

- 1) A. Iwanade et al., J. Radioanal. Nucl. Chem. 293 (2012) 703-9.

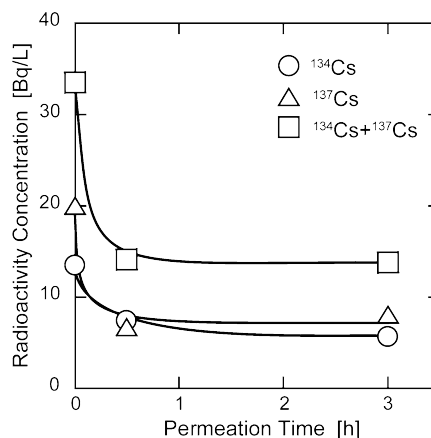


Fig. 1 The removal of radioactive Cs from environmental water by the AMP-AN fabric.

2 - 03 Boron Removal and Recovery Using Adsorbent Prepared by Radiation Grafting

A. Katakai^{a)}, T. Yotsumoto^{a)}, A. Takahashi^{a)}, Y. Ueki^{b)} and N. Seko^{b)}

^{a)}CLEANTECH Inc.,

^{b)}Environment and Industrial Materials Research Division, QuBS, JAEA

Fibrous graft adsorbent for boron was prepared by economical radiation grafting of glycidyl methacrylate (GMA) onto nonwoven fabric, followed by chemical modification with N-methyl-D-glucamine (NMG). In cases where 1-butanol was used as solvent for grafting, it was found that the degree of grafting reached over 150% even if the pre-irradiation dose was only 20 kGy, at which dose was one-tenth of conventional methods. The performance of the fibrous graft adsorbent with 2 mmol-NMG/g-adsorbent was evaluated through column-mode adsorption with the industrial effluent, and consequently the breakthrough capacity of 5.5 h⁻¹ in space velocity was 11.5 g-B/kg-adsorbent. Adsorbed boron on the graft adsorbent was easily recovered by the cooling crystallization using 1 N HCl at 30-40 °C.

平成 13 年に水質汚濁防止法が改正され、ホウ素に対する排水基準が 10 mg/L と設定された。その際、10 業種については、安価で効果的な処理方法がなく、この基準に直ちに対応することが困難であるとして、3 年間の期限で暫定排水基準が設定された。その後、3 年ごとに見直しが行われ、平成 22 年度の見直し（期限：平成 25 年 6 月末日）でも依然として 9 業種において暫定排水基準（50~500 mg/L）が設定され、永年にわたり規制が先送りされている。今後、規制が強化され暫定排水基準が撤廃される可能性もあることから、安価で効果的なホウ素処理システムの開発が必須である。これまでに我々は、放射線グラフト重合技術により高いハンドリング特性と高い選択的ホウ素吸着特性とを併せ持つ繊維状ホウ素捕集材の開発に成功してきたものの、捕集材の製造コスト高が実用化への課題であることが分かった。そこで本研究では、低コスト化を目指したより経済的な捕集材合成方法の検討を行うとともに得られた捕集材の水処理システムへの適応性について検討した結果を報告する。

ポリプロピレン (PP) 被覆ポリエチレン (PE) 繊維から成る不織布を窒素雰囲気下において電子線照射（線量：10~200 kGy）した後、予め窒素置換により脱酸素処理した 40 wt%メタクリル酸グリシジル (GMA) 溶液（溶媒：1-ブタノール）中に浸漬した。所定時間経過後、不織布重量に対する GMA 溶液の含浸率を 500%に調整した後、減圧容器内にて反応温度 40 °C で 3 時間グラフト重合を行った。次に、得られたグラフト繊維をホウ素に対して高い親和性を有する N-メチルグルカミン (NMG) を含む反応溶液（NMG 濃度：150 g/L、溶媒：

N-イソプロピルアルコール/水（比率：6/4）、反応温度：70 °C、反応時間：1 時間）中に浸漬し、目的とする繊維状ホウ素捕集材（NMG 密度：2 mmol/g）を合成した。

放射線グラフト重合において、捕集材を経済的に合成するためには、照射線量の低減化が重要な要素である。そこで、グラフト率に及ぼす照射線量の影響について検討した結果を Fig. 1 に示す。本研究で提案するグラフト重合により、従来法と比較して 1/10 の照射線量である 20 kGy でも実用的に十分なグラフト率 150%を得られ、実用化に向けた捕集材製造コストを低減化することが出来た。

次に、捕集材の性能評価を廃水処理プラント中間槽内の工程水（ホウ素濃度：17.2 mg/L、pH 6.6）を用いて実施した結果（空間速度 (SV)：10 h⁻¹、通水量：2 L）、ホウ素除去率は 98%を示し、夾雑物質存在下でも高いホウ素選択性を有することが分かった。また、その際の吸着容量は 10 mg-B/g-捕集材であった。

実工場廃水中に含まれるホウ素の除去/回収を目的として、ホウ素捕集材 3.5 kg を高さ 240 cm の吸着塔（内径：10 cm、長さ：240 cm）に充填し、SV 5.5 h⁻¹ でホウ素含有廃水を通液した結果、11.5 g-B/kg-捕集材の破過容量を示した。また、ホウ素溶離試験を 30~40 °C に加温した鉍酸（1 N HCl）を用いて行ったところ、捕集材体積の 1.5 倍の鉍酸体積 (BV: 1.5) でほぼ 100%のホウ素を溶離することが出来た (Fig. 2)。さらに、ここで得られた溶離液を 5 °C 以下に冷却すると、白色透明の板状ホウ酸結晶が生成した。この結果から、捕集したホウ素を資源として転用出来る可能性を示すことができた。

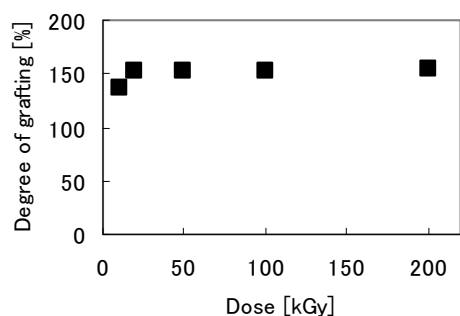


Fig. 1 Effect of irradiation dose on degree of grafting.

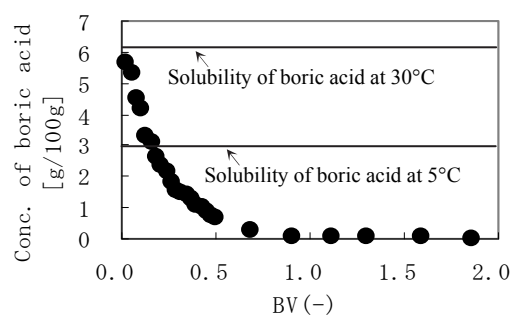


Fig. 2 Elution curve of boron from adsorbent.

Arsenic Removal from Streaming Water by Graft Adsorbent Synthesized with Cellulose Nonwoven Fabric

H. Hoshina^{a)}, N. Kasai^{a)}, T. Shibata^{a)}, M. Takahashi^{b)}, A. Yoshii^{c)},
Y. Tsunoda^{c)}, Y. Aketagawa^{d)} and N. Seko^{a)}

^{a)} Environment and Industrial Materials Research Division, QuBS, JAEA,
^{b)} ERH Techno Research Co. Ltd., ^{c)} Daiichi Techno Co. Ltd., ^{d)} WeeGI Co. Ltd.

Since waste water treatment is important issue from the viewpoint of environmental preservation, an environmental functional material is demand for contributing to the purpose. Graft polymerization is useful technique for modification of the conventional polymer to highly efficient adsorbents which could keep the original properties having trunk materials. In the case of fibrous adsorbents, these superior characteristics depend on the high diffusion rate of dissolved ions in the fibrous adsorbent, in which the fiber diameters of around 10 μm are ten times smaller than that of a spherical resin type adsorbent. In general, synthetic polymers such as polyethylene and polypropylene have been used as these trunk materials due to their reactivity in the grafting process and high mechanical strength¹⁾. However, these trunk polymers are derived from petroleum resources. If a natural polymer such as cellulose is used as the trunk polymer for graft polymerization, the dependence on petroleum resources would decrease. Furthermore, it is natural polymer and is biologically degradable.

In this study, a fibrous adsorbent, by which arsenic could be removed, was synthesized by radiation-induced emulsion graft polymerization of phosphoric acid monomer (PA), which is composed of phosphoric acid mono- and di-ethyl methacrylate ester, onto nonwoven cellulose fabric, and subsequent chemical modification by zirconium loading. The optimal pre-irradiation dose for initiation of graft

polymerization of PA, which minimized the effects of radiation damage on the mechanical strength of the nonwoven cellulose fabric, was found to be 20 kGy²⁾. To evaluate the adsorption performance the synthesized fibrous adsorbents for arsenic were demonstrated with a real streaming water. The adsorption system for arsenic removal in a 10 m³ scale equipment (Fig. 1) was assembled by stack of graft adsorbents. The waste water pumped up from streaming river which the arsenic concentration was 360 μg/L, pass through at space velocity of 150 h⁻¹ into these stacks consisting of two columns, 10 cm in internal diameter. The volume of adsorbents in the column was 1,700 cm³. After waste water treatment, the concentration of arsenic could decreased to 10 μg/L (Fig. 2).

References

- 1) H. Hoshina et al., JAEA Takasaki Annu. Rep. 2007 (2008) 40.
- 2) N. Kasai et al., JAEA Takasaki Annu. Rep. 2010 (2012) 46.

Acknowledgments

This research was supported by the Adaptable and Seamless Technology Transfer Program of Japan Science and Technology Agency.

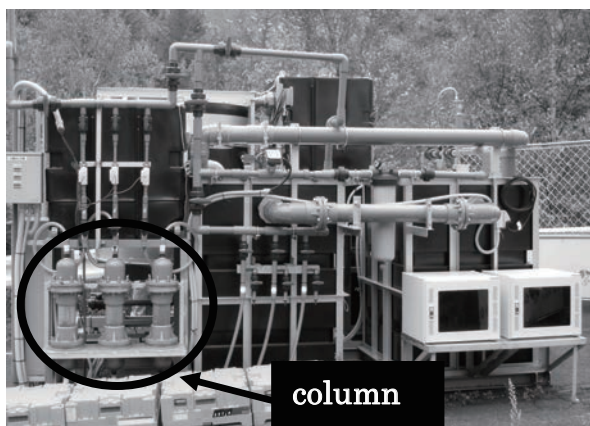


Fig. 1 The purification system for 10 m³ streaming water.

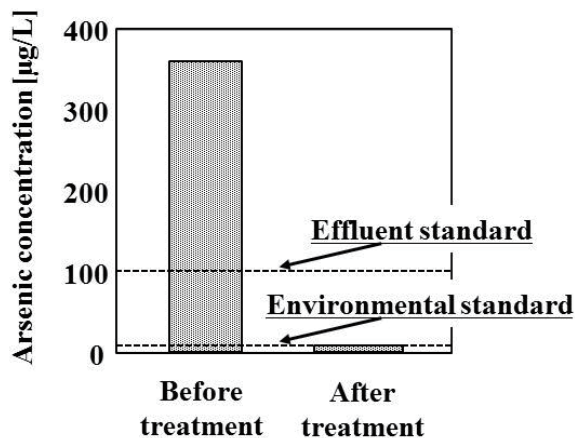


Fig. 2 Concentration of arsenic in water before and after treatment with graft adsorbent.

2 - 05 Surface Modification of Vulcanized Rubber by Radiation Grafting

H. Saito^{a)}, N. Mizote^{a)}, Y. Ueki^{b)} and N. Seko^{b)}

^{a)} Mitsuba Corporation,

^{b)} Environment and Industrial Materials Research Division, QuBS, JAEA

In this study, a hydrophilic monomer, namely, methacrylic acid (MAA) was grafted on vulcanized rubber surface by simultaneous electron beam irradiation followed by alkali treatment for the rubber. With that surface-modified rubber, we measured the frictional property, hardness and abrasive wear resistance, and found that the coefficient of friction decreased significantly compared to the initial rubber. Furthermore, when the initial and grafted rubbers were compared in wet condition, the wear resistance of the grafted rubber was improved although it became softer.

我々はこれまでに、放射線グラフト重合法を用いて、ゴムの表面改質に関する研究に精力的に取り組み、摩擦変動が少なく、かつ、耐摩耗性に優れた新規表面改質ゴムの開発に成功するとともに、ある条件下において表面改質ゴムが特異的な水潤滑特性を示すことを見出した。そこで本研究では、放射線グラフト重合法によりゴム表面を親水化し、水を潤滑剤として活用することのできる新規水潤滑材料の開発を試みた。

ゴム基材には、カーボンブラックを配合したNBR（アクリロニトリル-ブタジエンゴム）シートを用いた。そのシートにメタクリル酸（MAA）を接触させた後、加速電圧 2 MeV、電流値 1 mA、照射線量 5~9 kGy の条件で電子線同時照射グラフト重合を行った。さらに水酸化カリウムでアルカリ処理を行い、MAA グラフト鎖中に含まれるカルボキシル基末端の水素イオンをカリウムイオンに置換することにより、目的とする表面改質型親水性ゴムシートを得た。得られたゴムシートの水存在下での摩擦係数、及び、ドライ/ウェット状況下での耐摩耗性は、ピンオンディスク型摩擦試験機により評価し、また、ドライ/ウェット状況下での表面硬度は、マイクロゴム硬度計により評価した。

Figure 1 は未処理、グラフト重合後、及び、アルカリ処理後のゴムシートの表面摩擦係数変化を示したものである。本試験では 10 wt% MAA 溶液を用いて照射線量 7 kGy で作製したものを使用した。Figure 1 に示されるようにグラフト重合後のゴムシートの摩擦係数は、未処理の 1/6 に低下し、さらにアルカリ処理することにより未処理の 1/30 にまで低下した。以上の結果より、MAA のグラフト重合がゴムシートの表面改質に有効

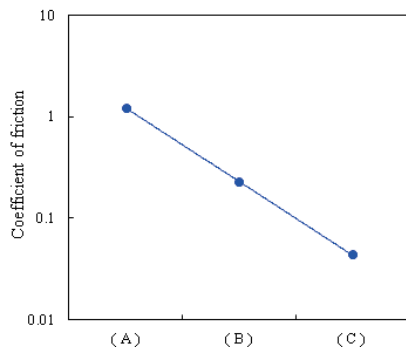


Fig. 1 Coefficient of friction of rubber, A; initial rubber, B; grafted rubber, C; ion exchanged rubber.

な手法であるとともに、グラフト重合後のアルカリ処理が極めて効果的であることが分かった。

Figure 2 にドライ/ウェット状況下での表面硬度とグラフト率との関係を示す。本研究で作製した表面改質型親水性ゴムシートは、グラフト率が高くなるほどドライ状況下において硬化傾向を示し、逆にウェット状況下においては、高グラフト率のものほど軟化傾向を示すといった特異的な硬化特性を有することが分かった。

さらに、ピンオンディスク型摩耗試験機により、ドライ、もしくは、ウェット状況下において表面改質ゴムシートを摩耗させた時の結果を Fig. 3 に示す。ドライではグラフト率の増加と共に硬度も高くなるので摩耗深さも小さくなるが、ウェットでもグラフト率の増加と共に小さくなっている。これは硬度低下よりも摩擦低下の方がより大きく影響している為だと思われる。

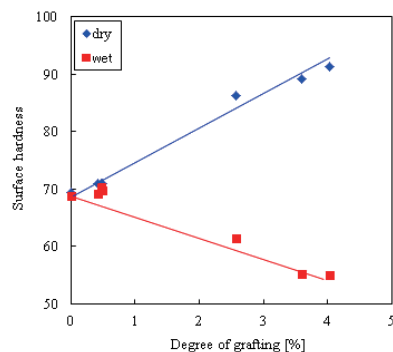


Fig. 2 Relationship between the degree of grafting and the surface hardness.

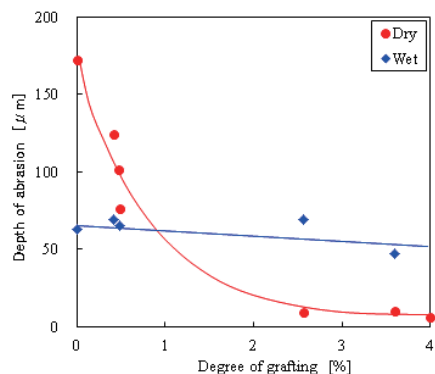


Fig. 3 Relationship between the degree of grafting and the abrasive wear resistance.

2 - 06 Micro-fabrication of Biodegradable Polymers by Focused Ion Beam Direct Etching

A. Oshima^{a)}, S. Okubo^{b)}, N. Nagasawa^{c)}, T. G. Oyama^{d)}, M. Taguchi^{c)},
M. Washio^{b)} and S. Tagawa^{a, b)}

^{a)}The Institute of Scientific and Industrial Research (ISIR), Osaka University, ^{b)}Research Institute for Science and Engineering, Waseda University, ^{c)}Environment and Industrial Materials Research Division, QuBS, JAEA, ^{d)}JSPS Post-Doctoral Research Fellow (QuBS, JAEA)

Biodegradable polymers are expected to be next-generation polymeric materials for a recycling-oriented society, because they are decomposed into water and carbon dioxide by the microbial cleavage. In addition, with their biocompatibility, biodegradable polymers can be applied to bio-micro/nano electro mechanical systems (MEMS/NEMS) and self-contained mechanical micro-machines. In order to establish the micro/nano-fabrication methods, we evaluated maskless direct etching of several kinds of biodegradable polymers using a focused ion beam (FIB).

Poly(butylenes succinate-co-adipate) (PBSA; Bionolle 3001, Showa Highpolymer), poly(ϵ -caprolactone) (PCL; CELLGREEN PH, Daicel Chemical Industries), and poly(L-lactic acid) (PLLA; Eco-Plastic U'z S-12, TOYOTA MOTOR CORPORATION) were used for the experiments. The film samples were prepared by hot-pressing, and the thicknesses of the PBSA, PCL, and PLLA films were about 180, 100, and 280 μm , respectively. Micro-fabrication experiment was carried out with FIB irradiation (SMI 2050 SII-NanoTechnology, installed at ISIR, Osaka University, source: 30 keV Ga^+ , beam current: 188 pA/1.3 nA, ion fluence: $0.2 - 1.5 \times 10^{18}$ ions/ cm^2) under the vacuum ($< 1.0 \times 10^{-4}$ Pa) at room temperature. The fabricated structures were observed by a scanning electron microscope (SEM, S-4500 HITACHI).

With the beam current of 1.3 nA, micro-patters were successfully fabricated on PCL and PBSA (Figs. 1(a) and (b)). On the other hand, the fabricated surfaces of PLLA were disordered and the etching depth could not be evaluated (Fig. 1(c)). It is known that PLLA has poor heat

stability above its T_g (~ 57 $^\circ\text{C}$). High current ion beam would induce the beam-heating at localized areas; therefore, PLLA was fabricated with the lower beam current of 188 pA. As shown in Fig. 1(d), relatively smooth micro-pattern was obtained compared with Fig. 1(c).

The etching depths were summarized in Fig. 2. The etching rate (the etching depth per ion fluence) for PBSA, PCL, and PLLA films were about 1.3, 1.2, and 1.8×10^{-18} $\mu\text{m}/(\text{ions}/\text{cm}^2)$, respectively. These obtained etching rates of biodegradable polymers were about two orders lower than those for perfluorinated polymers (about 5×10^{-16} $\mu\text{m}/(\text{ions}/\text{cm}^2)$)¹⁾ and about 2.5 times higher than polystyrene (6.9×10^{-19} $\mu\text{m}/(\text{ions}/\text{cm}^2)$)²⁾. It is considered that G -value of chain scission (scission per 100 eV) would be one of the important factors of the etching rate. In order to analyze the ion beam induced etching mechanisms, systemic discussion is necessary including morphology, molecular chain mobility, and intermediate species induced by ion irradiation.

It has been reported that the fabrication accuracy is influenced by sample thickness, due to the effects of beam-heating and charge-up. Sub-micrometer patterns have been obtained on spin-coated PBSA and PCL samples³⁾. By choosing appropriate sample thickness and irradiation conditions, arbitrary-shaped micro/nano-structures of biodegradable polymers will be fabricated with the FIB direct etching.

References

- 1) N. Miyoshi, et al., Radiat. Phys. Chem. 80 (2011) 230.
- 2) A. Oshima et al., Radiat. Phys. Chem. 81 (2012) 584.
- 3) S. Okubo et al., J. Photopolym. Sci. Technol. 23 (2010) 393.

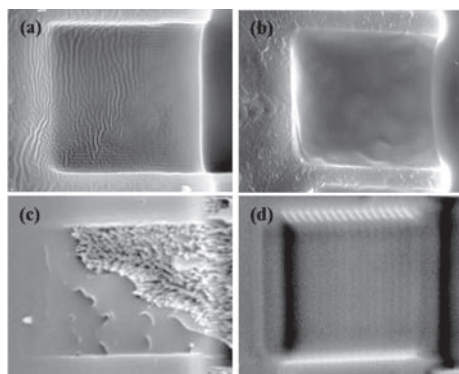


Fig. 1 SEM images of the fabricated areas ($30 \times 50 \mu\text{m}^2$). (a) PBSA (1.3 nA, 4.0×10^{18} ions/ cm^2), (b) PCL (1.3 nA, 4.0×10^{18} ions/ cm^2), (c) PLLA (1.3 nA, 1.5×10^{18} ions/ cm^2), and (d) PLLA (188 pA, 1.5×10^{18} ions/ cm^2).

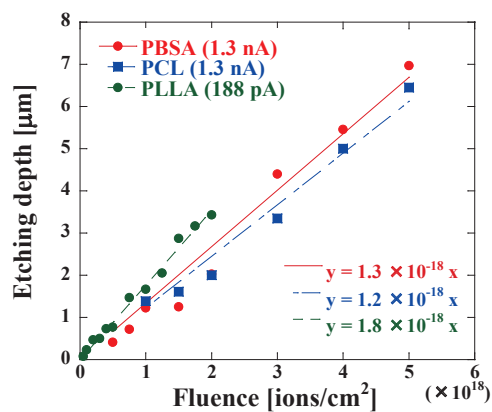


Fig. 2 Etching depth of PBSA, PCL, and PLLA.

2 - 07 Preparation of Polymer Gel Dosimeters Based on Radiation-crosslinked Hydroxypropyl Cellulose Gels

A. Hiroki, S. Yamashita, N. Nagasawa and M. Taguchi

Environmental and Industrial Materials Research Division, QuBS, JAEA

Polymer gel dosimeters consisting of monomers with a gel matrix are drawing attention as a tool of the three-dimensional dose distribution measurement in the radiation therapy. In the gel matrix, monomers are polymerized by irradiation, and then the polymers aggregate, resulting in an increase in optical density with dose. The conventional polymer gel dosimeters comprise of harmful monomers such as acrylamide and methacrylic acid and gelatin which is re-melted at temperatures over 35 °C¹⁾. Therefore, we propose new polymer gel dosimeters comprising less toxic monomers with thermo-stable gels. In this work, we used hydroxypropyl cellulose (HPC) gels as the gel matrix and 14 kinds of monomers. It is known that the HPC gels prepared by electron beam (EB) irradiation to the highly concentrated aqueous solution are thermo-stable as well as transparent materials²⁾. The effects of the types of monomers and the composition ratio on the dose response of the polymer gel dosimeters were investigated.

HPC, which is the grade of 1,000-5,000 cP, was purchased from Wako Pure Chemical Industries, Ltd., Japan. Twenty wt% of HPC aqueous solution as a paste-state was formed to 1.0 mm thickness by pressing, and was irradiated with EB to obtain gel membranes. The HPC gel membranes after washing and drying were immersed into aqueous monomer solutions, and then vacuum-packed to obtain polymer gel dosimeters. Thirty three monomer solutions with various compositions were prepared by using one or two selected from 14 kinds of monomers such as methacrylate- or acrylamide-type. The dose response of the samples was evaluated from a degree of cloudiness by γ -irradiation. EB- and γ -irradiations were carried out using Cockcroft Walton electron accelerator and ⁶⁰Co sources at Takasaki Advanced Radiation Research Institute, JAEA, respectively.

The gel fraction of the HPC gels increased sharply up to 10 kGy to be about 75%, and then reached about 90% at 50 kGy. The degree of swelling (Sw) of the HPC gel

swollen in pure water decreased from 26 to 8 with increasing the dose of 10 to 50 kGy, as shown in Fig. 1. The HPC gel obtained at 10 kGy showed the Sw between 25 and 27 in each aqueous monomer solutions, which was independent of the type of monomers and their composition ratio. The HPC gel at 10 kGy, therefore, was deduced to be suitable as gel matrix for dosimeters. All of the swollen HPC gels were transparent.

Seventeen of thirty three polymer gel dosimeters became cloudy by γ -irradiation at 10 Gy. It was found that 9 kinds of monomers can be utilized in the polymer gel dosimeters. Especially methacrylate monomers such as 2-hydroxyethyl methacrylate (HEMA) and 2-hydroxypropyl methacrylate were useful to induce the cloudiness of polymer gel dosimeter in comparison with acrylamide-type monomers. The polymer gel dosimeters consisting of HEMA and polyethylene glycol 400 dimethacrylate (9G) became cloudy at only 2 Gy, and the degree of the cloudiness increased obviously with increasing dose. The polymer gel dosimeter containing HEMA and 9G at 2 and 3 wt%, respectively, showed higher cloudiness than that at 3 and 2 wt%, as shown in Fig. 2. The irradiated polymer gel dosimeters were optically analyzed by using an UV-Vis spectrophotometer. The absorbance of the polymer gel dosimeters increased approximately linearly with an increase in the dose up to 10 Gy. It was found that the dose response can be adjusted by changing the composition ratio. In future, more sensitive polymer gel dosimeters will be developed by optimizing the kinds of monomers and the composition ratio.

References

- 1) M. J. Maryanski, et al., *Phys. Med. Biol.* **39** (1994) 1437-55.
- 2) A. Hiroki et al., *JAEA Takasaki Annu. Rep.* 2010 (2012) 50.

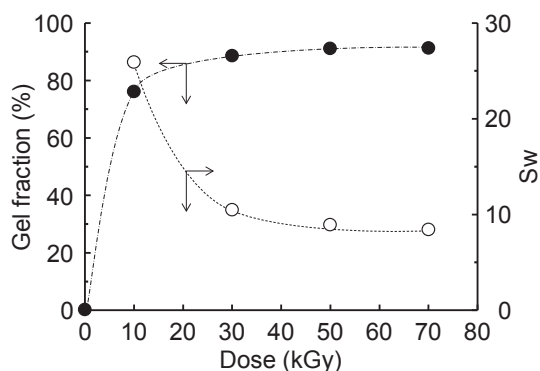


Fig. 1 Gel fraction and degree of swelling (Sw) of the HPC hydrogels as a function of γ -ray dose.

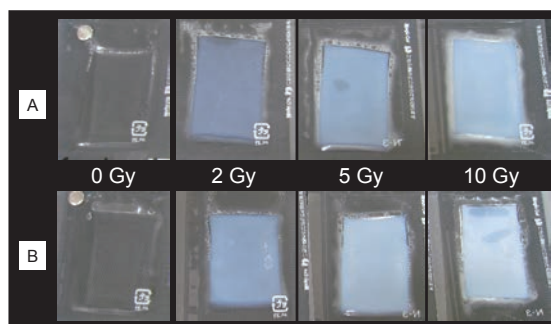


Fig. 2 Photographs of the non-irradiated and irradiated polymer gel dosimeters consisting of HEMA and 9G. The concentrations of HEMA/9G are 3/2 wt% (A) and 2/3 wt% (B).

2 - 08

Improvement of Mechanical Properties of Poly (*L*-Lactic Acid) by Blending with Polyamide 11 and Radiation-induced Crosslinking

T. Tago^{a, b)}, N. Nagasawa^{a)}, H. Kudo^{b)}, Y. Katsumura^{b)} and M. Taguchi^{a)}

^{a)} Environment and Industrial Materials Research Division, QuBS, JAEA,
^{b)} Graduate School of Engineering, The University of Tokyo

Poly (*L*-lactic acid) (PLA) derived from corn starch is a hard and transparent bioplastic, and now one of the most widespread materials with a potential to replace the conventional petroleum-derived plastics. However, PLA has a poor impact resistance and thermal stability comparing the conventional plastics above its glass transition temperature of 60 °C. Radiation-induced crosslinking is an effective method to improve the thermal stability of polymers. It has been already reported that PLA is a radiation-degradable type polymer but its thermal property is improved by crosslinking by radiation with crosslinking agent, triallyl isocyanurate (TAIC)¹⁾. Improvement of the impact resistance is of critical issue for expanding applications. In this study, to improve the above-mentioned two properties of PLA, we investigated new combination methods by blending of polyamide11 (PA11) having high impact resistance and radiation-crosslinking with TAIC by electron beams (EB)-irradiation.

PLA (trade name: Ecoplastics U'z S-12) was purchased from Toyota Motor, Co., Ltd, Japan. PA11 (trade name: Rilsan® B) and TAIC were contributed from Arkema, Co. Ltd, France and Nippon Kasei Chemical Co., Ltd, Japan, respectively. PLA and PA11 pellets were dried in a vacuum oven at 90 °C. Films, 0.5 mm thickness, of blends with PLA/PA11 weight ratio of 25/75, 50/50, 75/25 including 3.0 phr (per hundred resin) TAIC were prepared by using a twin screw extruder (Labo Plastomill Model 50C150, Toyoseiki, Japan) at mixing speed of 20 rpm at 210 °C for 10 min and hot-pressed at 210 °C for 5 min. The crosslinking was induced by EB irradiation in the dose range of 10-200 kGy. The gel fraction was determined by weighing insoluble parts of the crosslinked PLA/PA11 blend films after immersion in mixed solvent of chloroform and formic acid for 48 h at room temperature.

Figure 1 shows that the gel contents of the PLA/PA11 blends increased with increasing mixing ratio of PA11 and absorbed dose, and reached about 80% at the dose of 100 kGy and above. The thermal properties of the blends were evaluated from the deformation by the thermo-mechanical analysis. The blends with high gel contents (>80%) exhibited very little deformation even at above the melting temperature (around 185 °C) of PA11. The crosslinked PLA/PA11 (50/50 wt%) blend showed

about 2.5 times higher impact resistance than original PLA by the Charpy impact test, as shown in Fig. 2. The applications of bioplastics, therefore, will be expanded by the combination method of blending and radiation-induced crosslinking.

Reference

- 1) N. Nagasawa et al., Nucl. Instrum. Meth. Phys. Res. B 236 (2005) 611.

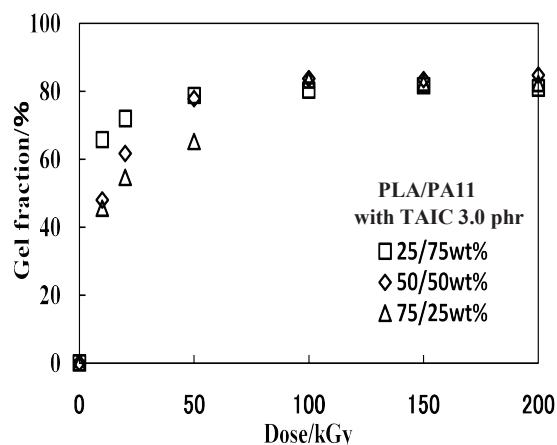


Fig. 1 Gel fraction of Crosslinked PLA/PA11 blends.

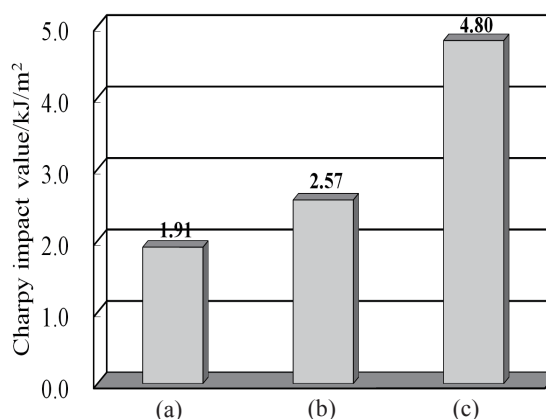


Fig. 2 Impact resistance of PLA/PA11 blend with TAIC 3 phr by EB-irradiation at the dose of 100 kGy. (a) Original PLA, (b) Crosslinked PLA, (c) Crosslinked PLA/PA11 (50/50 wt%) blend.

2 - 09 Radiation Preparation of P(NIPAM-*co*-HEMA) and Micelles from PLLA-*g*-P(NIPAM-*co*-HEMA)

TM. Quynh^{a, d)}, Y. Maki^{b)}, N. Nagasawa^{c)} and T. Dobashi^{b)}

^{a)} Advanced Technology Research Center, Gunma University, ^{b)} Department of Biological and Chemical Engineering, Graduate School Engineering, Gunma University, ^{c)} Environment and Industrial Materials Research Division, QuBS, JAEA, ^{d)} Vietnam Atomic Energy Institute

Radiation-induced polymerization has been studied and applied as an effective method for preparation of polymers recently. By means of this method, poly(*N*-isopropyl acrylamide), PNIPAM and some copolymers without chemical residues were prepared from NIPAM monomers for biomedicine¹⁻³⁾. In our present study, some poly(*N*-isopropyl acrylamide -*co*-hydroxyethylmethacrylate), P(NIPAM-*co*-HEMA) copolymers were prepared by radiation for synthesis of poly(L-lactide)-*g*-P(NIPAM-*co*-HEMA) graft copolymers and some their characteristics were studied.

Admixture solutions composed of NIPAM and HEMA in *N,N*-dimethylformamide (DMF) were purged with nitrogen gas for 20 minutes, and then irradiated with gamma rays from ⁶⁰Co source at the same dose rate of 10 kGy/h to obtain P(NIPAM-*co*-HEMA) copolymers. The molecular properties of the obtained materials were presented in Table 1.

Different PLLA-*g*-P(NIPAM-*co*-HEMA) copolymers were synthesized by ring-opening polymerization of L-lactide in the presence of P(NIPAM-*co*-HEMA), and the

solution of these graft copolymers in DMF was dialyzed against distilled water for micelle formation. The structure and morphology of the obtained nano-sized micelles were studied using nuclear magnetic resonance (NMR) and AFM.

Figure 1 shows the NMR spectra of typical copolymers. There are peaks corresponding to the methyl (CH₃), methylene (CH₂) and methine (CH) protons of PNIPAM, HEMA and PLLA segments in the spectrum of PLLA-*g*-P(NIPAM-*co*-HEMA)⁴⁾, whereas no specific peaks of PLLA could be observed in NMR spectrum of the graft copolymers after dialysis process. It can be explained by self-assembles of PLLA-*g*-P(NIPAM-*co*-HEMA) to form micelles in aqueous solution. Morphology of these micelles was observed by AFM after a drop of them on a mica sheet as presented in Fig. 2. The micelles have spherical structures, though some micelles are contact with each other into aggregates.

In summary, different P(NIPAM-*co*-HEMA) copolymers were obtained by radiation polymerization, and then micelles of PLLA-*g*-P(NIPAM-*co*-HEMA) were prepared.

Table 1 Radiation preparation of P(NIPAM-*co*-HEMA).

Monomer ratio in P(NIPAM- <i>co</i> -HEMA)	Dose (kGy)	<i>M_w/M_n</i>	<i>M_w</i> (kDa)	<i>T_p</i> (°C)
80:20	10	2.37	14.0	38.7
80:20	20	2.14	13.7	40.1
80:20	30	1.91	12.6	40.4
90:10	10	2.13	11.3	37.2
90:10	20	2.07	11.4	37.6
90:10	30	1.86	10.8	38.0

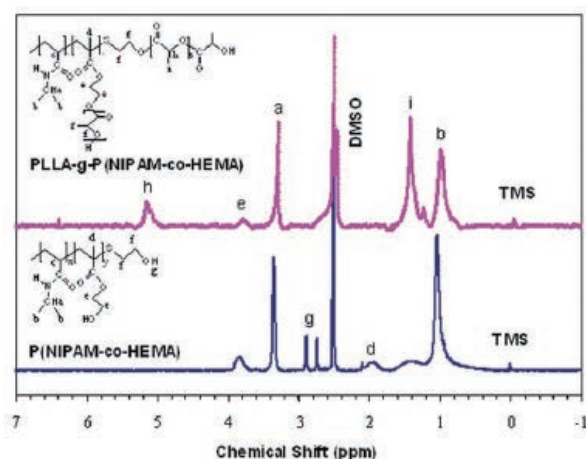


Fig. 1 ¹H-NMR spectra of different copolymers in dimethyl sulfoxide.

References

- 1) V. Y. Kabanov, Radiat. High Energ. Chem. 34 (2000) 203.
- 2) N. Nagaoka et al., Macromolecules 26 (1993) 7386.
- 3) A. Ortega et al., Polymer Bulletin 58 (2007) 565.
- 4) I. S. Kim et al., Int. J. Pharm. 211 (2000) 1.

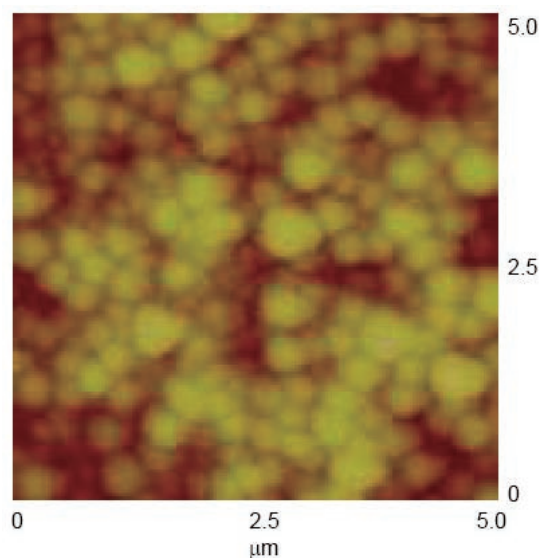


Fig. 2 The AFM image of spherical micelles formed from PLLA-*g*-P(NIPAM-*co*-HEMA) copolymers.

2 - 10 Reactivity of Oxidative/Reductive Species toward Persistent Antibiotics under Ionizing Radiation

A. Kimura and M. Taguchi

Environment and Industrial Materials Research Division, QuBS, JAEA

Pharmaceuticals and antibiotics have great benefits for human health and protection against infectious diseases to domestic animals. The consumption and environmental concentration of them has increased remarkably because of the population growth and diversification of advanced medical worldwide, and it feels uneasy about generation of the drug resistance bacteria. These bacteria would induce obstinate infectious diseases, which give hazardous effect to human, domestic animals, and aquatic animals¹⁾. The antibiotics also have been detected at the downstream of water treatment facilities, indicating that the physical-chemical treatment and activated sludge system could not remove them completely. These persistent organic pollutants in wastewater could be effectively decomposed by ionizing radiation method, which produces oxidative and reductive species homogeneously in water. We investigated treatment of the antibiotics in wastewater by use of the ionizing radiation method. Decomposition of some antibiotics in wastewater by the combination method was investigated in the previous works²⁾. The amounts of total organic carbons (TOCs) in real wastewater, however, strongly effect required for treatment but change every moment. It is necessary to construct simulation code to estimate the required dose for treatment of the antibiotics by the combination method. In this work, rate constants of some antibiotics with radiation-induced reactive species were estimated by a competition reaction method and pulse radiolysis method for the simulation code.

Sulfa drugs (sulfamerazine, sulfapyridine, sulfamethazine, sulfamethoxazole) and chloramphenicol were selected as experimental samples because they were reported to be consumed a lot on the domestic animals and medical treatment site, and detected in the water environment. Phenol was used without further purification as a reference material to evaluate the rate constant of the reaction of Sulfa drugs with hydroxyl radicals. Sulfa drugs and phenol at 5 $\mu\text{mol dm}^{-3}$ each were dissolved in pure water under aerated condition. The γ -ray irradiations were carried out at 293 K at Japan Atomic Energy Agency (JAEA), Takasaki to the doses in the range from 1 to 10 Gy. Pulse radiolysis was performed with photocathode LINAC system at University of Tokyo. The absorbed dose was estimated to be 25 Gy/pulse by using the extinction coefficient of $(\text{SCN})_2^-$ ($\epsilon = 7,600 \text{ dm}^3 \text{ mol}^{-1} \text{ cm}^{-1}$ at 472 nm) in aqueous KSCN solution and the G -value of 2.7 for hydroxyl radicals.

Both sulfa drugs and phenol have a phenyl ring, and radiation-induced hydroxyl radicals would attack mainly the phenyl ring because hydrated electrons and hydrogen atoms are converted into superoxide radical anions immediately, which are very less reactive compared with hydroxyl

radicals in the presence of oxygen. Thus phenol can be regarded as a standard to estimate the relative rate constant of sulfa drugs with hydroxyl radicals. The concentrations of both solutes were 5 $\mu\text{mol dm}^{-3}$, and the decomposition ratio of Sulfa drugs to phenol is the ratio of the rate constants under the same dose rate irradiation:

$$-\frac{d[S]}{dD} / -\frac{d[\text{Phenol}]}{dD} = k_S / k_{\text{Phenol}} \quad (1)$$

D , k_S and k_{Phenol} are the absorbed dose, the reaction rate constants of hydroxyl radicals with sulfa drug and phenol, respectively. Mixed aqueous solution of sulfamerazine and phenol at the 5- $\mu\text{mol dm}^{-3}$ initial concentration was investigated with γ -ray irradiation, and the ratio of the decomposition yield of sulfamerazine to that of phenol was determined to be 0.97. The reaction rate constant of sulfamerazine with hydroxyl radicals was estimated to be $6.4 \times 10^9 \text{ mol}^{-1} \text{ dm}^3 \text{ s}^{-1}$ since k_{Phenol} is $6.6 \times 10^9 \text{ mol}^{-1} \text{ dm}^3 \text{ s}^{-1}$ ²⁾. The rate constants of the other sulfa drugs with hydroxyl radicals were also estimated by the competition reaction method and listed in Table 1. The rate constant of sulfa drugs with hydroxyl radicals were almost the same because they do not have electrophilic substituents other than the phenyl rings. Halogenated organic compounds in water are decomposed by not only radiation-induced hydroxyl radicals but also hydrated electrons. The rate constants of hydrated electron with chloramphenicol was estimated by pulse radiolysis experiment, and was higher than that with oxygen as listed in Table 1³⁾. Reaction simulation for treatment of these antibiotics in real wastewater will be constructed by use of the estimated rate constants.

The authors thank Mr. Kazuhiro Iwamatsu, Dr. Kuniki Hata, and Dr. Yusa Muroya for help in a part of the experiment.

Table 1 Rate constant of antibiotics with reactive species.

Antibiotics	$k(\text{OH})$ / $\text{mol}^{-1} \text{ L s}^{-1}$	$k(e_{\text{aq}}^-)$ / $\text{mol}^{-1} \text{ L s}^{-1}$
Sulfapyridine	6.0×10^9	
Sulfamerazine	6.4×10^9	
Sulfamethazine	5.4×10^9	
Sulfamethoxazole	5.4×10^9	
Phenol	6.6×10^9	
Chloramphenicol	1.9×10^{10}	3.6×10^{10}

References

- 1) M. Sasaki et al., Miyagi Pref. Inst. Pub. Heal. Environ. Annu. Rep. 26 (2008) 31-34.
- 2) A. Kimura et al., JAEA Takasaki Annu. Rep. 2010 (2012) 53.
- 3) G. V. Buxton et al., J. Phys. Chem. Ref. Data 17 (1988) 513.

2 - 11 Solution Properties of Seaweed Polysaccharide Funoran

S. Takigami ^{a)}, H. Yamaguchi ^{b)}, R. Takahasi ^{b)} and N. Nagasawa ^{c)}

^{a)} Center for Material Research by Instrumental Analysis, Gunma University,

^{b)} Graduate School of Engineering, Gunma University,

^{c)} Environment and Industrial Materials Research Division, QuBS, JAEA

Funoran is a main component of funori, which is a seaweed of the *Rhodophyceae* and is used as food products and a sizing agent. Funoran is one of sulphated polysaccharides and its main chain is consisted of a common backbone with repeat units of (1→3) -linked β- and (1→4)-linked α-Galactose (or its 3,6-anhydride) residues¹⁾.

In this study, γ-irradiation and acid hydrolysis were used to prepare low molar mass funoran and characterization of the treated funoran was investigated.

Funoran was obtained from commercial funori aqueous solution by precipitation using methanol. The γ-irradiation was carried out under reduced pressure. The absorbed dose was varied from 1 to 30 kGy and the dose rate was 1 kGy/h. Acid hydrolysis of funoran was performed at 80 °C for 30 min using hydrochloric acid solution with the pH of 1 to 4.

Molar mass of funoran was determined by a multiangle laser light scattering (MALS) method. SEC MALS chromatograms of the irradiated funoran are shown in Fig. 1. The chromatogram shifted to lower molar mass side and the width of peak enlarged with absorbed dose. The weight average molar mass (Mw) was changed from 799 × 10³ g/mol to 155 × 10³ g/mol by the irradiation.

Funoran was dissolved in 500 mM sodium nitrate aqueous solution and intrinsic viscosity ([η]) was measured using an Ubbelohde viscometer at 25.00 °C. Figure 2 shows the log-log plot of [η] vs. Mw for irradiated funoran. The log [η] increased linearly with log Mw. The linear relationship gave the following Mark - Houwink - Sakurada equation:

$$[\eta] = 1.52 \times 10^{-5} Mw^{1.01} \quad (\text{dL/g})$$

The α value (exponent value) is related to the shape of

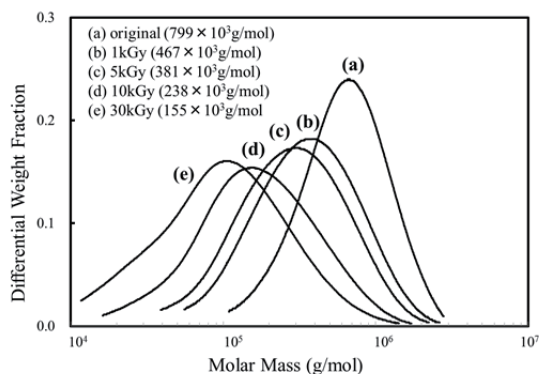


Fig. 1 Molar mass distribution of irradiated funoran; (a) 0 kGy, (b) 1 kGy, (c) 5 kGy, (d) 10 kGy, (e) 30 kGy.

polymer in solution and the value of funoran was 1.01. Accordingly, it was deduced that funoran is a semi-flexible polysaccharide and has rigid and rod-like shape in aqueous solution.

Figure 3 shows temperature dependence of the [η] of funoran with different molar mass. The [η] of original funoran kept constant value until 40 °C and then increased with decrease of temperature, especially remarkable change was observed from 30 to 20 °C. It is inferred that the increment of the value of [η] was due to formation of double helical structure of funoran chains. Transition temperature of double helical structure shifted to higher temperature for low molar mass funoran.

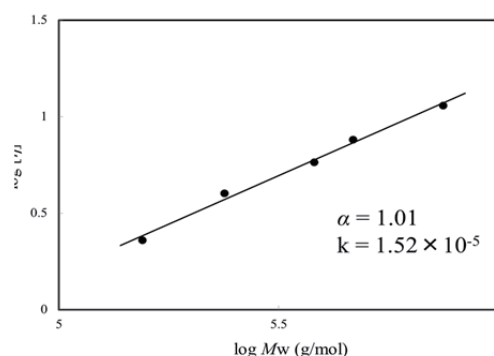


Fig. 2 Relationship between intrinsic viscosity and molar mass of irradiated funoran.

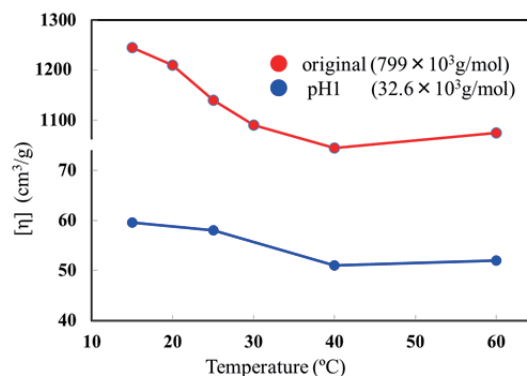


Fig. 3 Temperature dependence of intrinsic viscosity of funoran with different molar mass.

Reference

- 1) R. Takano et al., Carbohydr. Polym. 27 (1995) 305-11.

2 - 12 Immobilization of Nitrifying Bacteria to the HPC Gel Medium Synthesized by Electron Beam Irradiation

T. Yanagisawa^{a)}, T. Kojima^{a)}, N. Nagasawa^{b)}, M. Taguchi^{b)} and T. Tanaka^{a)}

^{a)} Department of Civil and Environmental Engineering, Maebashi Institute of Technology,

^{b)} Environment and Industrial Materials Research Division, QuBS, JAEA

A novel porosity medium for nitrifying bacteria was developed using a radiation-induced crosslinking technology of polysaccharide. The porosity medium consisted of a nitrifying culture solution and hydroxypropylcellulose (HPC). The medium was readily insolubilized by the electron beam irradiation. The nitrification experiments were carried out using the HPC medium. The experimental results showed that nitrifying bacteria was selectively immobilized to the HPC medium.

生活系排水等の処理においては、その安定性や簡便性などから活性汚泥法が主に用いられている。しかしながら、活性汚泥法による排水処理に関して、余剰汚泥が大量に発生すること、栄養塩類の除去能が有機物のそれに比較して低いこと、またランニングコストが比較的高いことなどの問題が以前より指摘されている。余剰汚泥発生量の低減化や窒素除去能の改善等に対しては、活性汚泥反応槽における微生物量を増加させることが有効であり、これまで微生物担体を反応槽に直接投入する担体投入型活性汚泥法などの高度化プロセスが提案されている。担体の材質としては、プラスチック、塩ビ、炭素材、ポリエチレン等が一般に知られている。本研究では、放射線加工で作製した HPC ゲルを微生物担体として用いることを提案し、その特性について実験的に検討した。HPC ゲルの電子顕微鏡による観察¹⁾、およびゲル分率や膨潤率の測定^{2,3)}などより、放射線加工 HPC ゲルは担体として利用可能と考えられた。ここでは、HPC 担体への微生物、特に硝化細菌の選択的固定化の可能性について検討した。

HPC と硝化細菌用培地を練り混ぜて、放射線を照射して HPC ゲル担体を作製した。HPC 濃度は 30%、線量は電子線で 20 kGy とした。電子線架橋により、水溶性の HPC が不溶性のゲル様物質へと変化するとともに、微生物が固定化されやすい細やかな網目状の構造が形成された。上記の照射条件において、ゲル分率：81～94%、膨潤率：6～13%であった²⁾。また、ポアサイズは 50～80 nm であった³⁾。

硝化細菌の選択的固定化試験では、縦 0.5 cm 横 0.5 cm 長さ 10 cm の大きさに成形したものを担体として用い、形状が崩れないように、直径約 1 cm のメッシュ状のプラスチック筒に挿入してから反応器に充填した。反応器の有効容量は約 1 リットルで、その中に比表面積（反応器の有効容量に対する担体ゲルの総表面積）が約 70 m²/m³ となるように HPC ゲル担体ユニットを 36 セット充填した。

HPC ゲル担体への微生物の固定化は、上記の反応器（担体充填後）を約 500 mL の下水二次処理水で満たし、連続曝気方式で行った。このとき、反応器内の溶存酸素濃度は 2 mg/L 以上、酸化還元電位は +50 mV 以上となるように制御した。固定化の期間は 26 日とした。その後、反応器内の溶液を下水二次処理水からアンモニア溶液へと交換し、同様に連続曝気・回分方式で硝化実験を行った。硝化実験は、水温 25 °C の常温条件と

10 °C の低温条件の双方で行った。曝気条件は、微生物固定化におけるそれと同様とした。サンプリングは実験開始から 0、1、3、7、14、21 日後に反応器より行った。サンプリング試料について、イオンクロマトグラフィを用いて陽イオン（アンモニウムイオン：NH₄⁺）および陰イオン（亜硝酸イオン：NO₂⁻と硝酸イオン：NO₃⁻）の濃度を測定した。

硝化実験の結果（NH₄⁺、NO₃⁻、NO₂⁻濃度の経時変化）を Fig. 1 に示す。常温実験と低温実験の双方において、反応器内の NO₃⁻濃度は時間の経過とともに上昇した。常温実験において NO₃⁻生成速度は高かったが、低温実験においても一定の速度で NO₃⁻が生成された。これは、担体に選択的に硝化細菌が固定化された結果と考えられる。しかしながら、反応器内の NH₄⁺濃度も時間の経過とともに上昇することが確認できた。これは、硝化細菌用培地の成分である NH₄⁺が担体より溶出した結果と考えられる。本実験より硝化細菌の HPC ゲル担体への固定化の可能性は示されたが、今後は、NH₄⁺溶出を制御・抑制する方法を検討する必要がある。

References

- 1) 杉山拓也、田中恒夫：放射線加工による微生物担体の創製、前橋工科大学卒業論文、(2009.3) 1-6.
- 2) 吉池友則、田中恒夫：放射線による微生物担体の加工、前橋工科大学卒業論文、(2010.3) 1-6.
- 3) 池上直斗、田中恒夫：HPC 担体による選択培養の可能性、前橋工科大学卒業論文、(2011.3) 1-8.

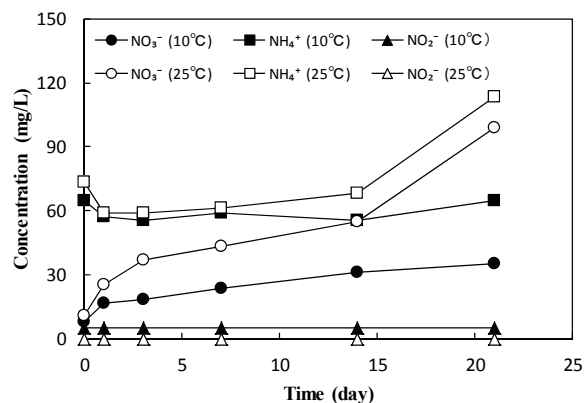


Fig. 1 Changes in the NH₄⁺, NO₃⁻, NO₂⁻ concentrations at 25 °C and 10 °C.

2 - 13 Interaction between *Paramecium bursaria* and Heavy Elements

N. Kozai^{a)}, T. Ohnuki^{a)}, T. Satoh^{b)}, M. Koka^{b)} and T. Kamiya^{b)}

^{a)} Advanced Science Research Center, JAEA,

^{b)} Department of Advanced Radiation Technology, TARRI, JAEA

It is known that activity of microorganisms such as bacteria, algae, and yeasts has a great impact on the geological migration of the radionuclides leached from the radioactive waste forms buried underground. Retardation of the radionuclides migration by adsorption on the cells is the most desirable function of those microorganisms. It is also known that protozoa, who prey those microorganisms, are found not only in surface water and soil but also in deep ground water. Protozoa are defined as one-celled (unicellular) organisms and control the number of those bait-microorganisms. However, no knowledge on the role of protozoa on the radionuclide migration is available. The chemical forms of the radionuclides sorbed on or taken up by those bait-microorganisms may change during the process of digestion and absorption by protozoa. Protozoa may take up radionuclides directly from water. The objective of this study is therefore to elucidate the role of protozoa in the migration of radionuclides. In the present report, uptake or sorption of metals in aqueous solutions by paramecia was investigated. Paramecia are the most common species of protozoa in fresh waters and most extensively used in research. Depending on the species, paramecia are 70-350 μm length and several tens of μm wide. This size is suitable for micro particle-induced X-ray emission (micro-PIXE) analysis considering the special resolution, less than 1 μm , of the micro-PIXE analyzing system in the TIARA facility.

In the first year of this study, the uptake (or sorption) of metals in aqueous solutions at pH 7 by *Paramecium bursaria* was investigated¹⁾. It was found that Sr, Eu, and Pb were hardly adsorbed on living cells of *P. bursaria*. It is very interesting why Eu and Pb, which are very adsorptive to bacterial cell surfaces, are not adsorbed on *P. bursaria* cells. No evidences for mineralization of those metals on cell surfaces of *P. bursaria* were also obtained. In the second year, the uptake of Eu by the cells was investigated during the culture of *P. bursaria* cells by feeding the yeast cells on which Eu was adsorbed beforehand²⁾. We found that the uptake behavior of Eu by cells differed depending on stage of the growth. That is, only the cell at inductive phase accumulated Eu and the cells at any other growth phase did not. Here the question arose about this result. Where was the Eu detected, inside or outside the cells? The location of the Eu reflects the reaction mechanism of the cells towards Eu. However, the conventional two-dimensional micro-PIXE analysis is not capable of locating the elements in the conformation of cells. The present study investigated the uptake of Eu by the cells of *P.*

bursaria at inductive phase by introducing the cells to an aqueous solution containing Eu. The elemental distribution of the cells was analyzed first by the conventional micro-PIXE method and then by the recently developed PIXE-CT method to determine three-dimensional distribution of Eu.

An inorganic medium containing 200 mg/L $\text{Ca}(\text{NO}_3)_2 \cdot 4\text{H}_2\text{O}$, 20 mg/L $\text{MgSO}_4 \cdot 7\text{H}_2\text{O}$, 0.8 mg/L $\text{Fe}_2(\text{SO}_4)_3 \cdot n\text{H}_2\text{O}$, and 590 mg/L NaCl was prepared by dissolving these salts in purified water. A Eu solution was prepared by dissolving $\text{Eu}(\text{OCOCH}_3)_3 \cdot n\text{H}_2\text{O}$ in the inorganic medium to have Eu at 0.05 mM. The initial pH of the Eu solution was adjusted to 7.0. The cells of *P. bursaria* were cultured with yeast cells for two days. After the culture, the cells were separated from the yeast cells, washed with the inorganic medium at pH 7.0, and finally transferred in a beaker with the same medium. All of the *P. bursaria* cells in the suspended medium thus prepared were alive. A portion (1 mL) of the cell suspension was introduced to 9 mL of the Eu solution in a glass beaker. The beaker was sealed and kept at 25 °C. After 24 h, the cells were collected on a membrane filter and washed with purified water three times. The cells moving around were sampled, then fixed with a fixative, and washed with purified water. The cells thus prepared were analyzed by the conventional micro-PIXE and PIXE computed tomography (PIXE-CT) methods.

The size, shape, and location of cells are easily and clearly determined by mapping of phosphate abundantly contained in the cells as essential element. The conventional micro-PIXE analysis of the cells detected Eu. The Eu was distributed inside the two-dimensional distribution range of P. PIXE-CT analysis of one of the cells revealed that the Eu was located inside the three-dimensional distribution range of P. This finding indicates that the Eu was not adsorbed on the cell membranes but taken up inside the cells. The cells tested in our first study¹⁾ were collected between the late log growth phase and the stationary phase. In our second study²⁾, Eu was detected only for the cells at inductive phase. These results strongly suggest that the uptake of Eu inside the cells is characteristic of the cells at inductive phase.

References

- 1) N. Kozai et al., JAEA Takasaki Annu. Rep. 2008 (2009) 31.
- 2) N. Kozai et al., JAEA Takasaki Annu. Rep. 2009 (2011) 28.

2 - 14 Measurement of Trace Elements in Natural Water in Iwaki City after Earthquake by In - Air Micro-PIXE

E. Sakurai ^{a)}, K. Ishii ^{b)}, S. Yamauchi ^{b)}, H. Yamazaki ^{b)}, A. Yamazaki ^{c)}, W. Kada ^{c)}, M. Koka ^{c)}, T. Satoh ^{c)} and T. Kamiya ^{c)}

^{a)} Faculty of Pharmacy, Iwaki Meisei University,

^{b)} Department of Quantum Science and Energy Engineering, Tohoku University,

^{c)} Department of Advanced Radiation Technology, TARRI, JAEA

East Japan was struck by a huge earthquake on March 11, 2011. Iwaki City also suffers from serious damage. A part of this area locates within the range of 25-60 kilometers from Fukushima Daiichi Nuclear Power Plant. Then an aftershock measuring a lower 6 on the Japanese scale of 7 struck the area a month later and caused groundwater depletion. People, who have been living in Kawamae, Tabito, Miwa, Tohno, Hisanohama-Ohhisa or Ogawa district in Iwaki City, usually use spring water, well water or the surface water of the river nearby. So that, it was required to immediately assess of safety on the water. Particle Induced X-ray Emission (PIXE) is a powerful method for the analysis of trace elements ¹⁾. In-air micro-PIXE was developed at the Takasaki Ion Accelerators for Advanced Radiation Application (TIARA) ²⁾, JAEA. Micro-PIXE allows analyzing the spatial distribution of the elements quantitatively.

Water samples were collected in Kawamae, Tabito, Miwa, Tohno, Hisanohama-Ohhisa and Ogawa districts. The waters were usually used by peoples in these areas, which were spring water and well water. These liquid samples were collected in plastic bottles after flowing 3 minutes from a tap. Water sample of 1 mL was put on a polycarbonate film of 2 μm-thickness and dried at room temperature overnight. The water samples were examined with 3 MeV proton microbeams. Typical beam current is 100 pA. Data analysis was made by micro-PIXE analysis software developed at TIARA ¹⁾.

Figure 1 shows two sample photographs of water-source in Iwaki City.

Figure 2 shows PIXE spectra for various water samples. Hisanohama 1, 2 and kawamae samples are well waters. Tabito SP and Tohno SP are spring waters.

The average amount of elements in the area is shown in Fig. 3.



Fig. 1 Photograph A shows a source of surface water of the river nearby and photograph B is spring water.

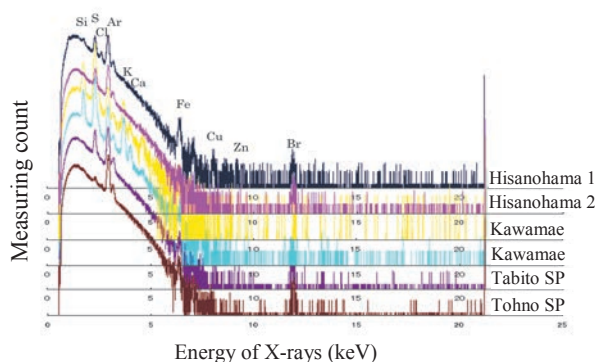


Fig. 2 PIXE spectra in water samples.

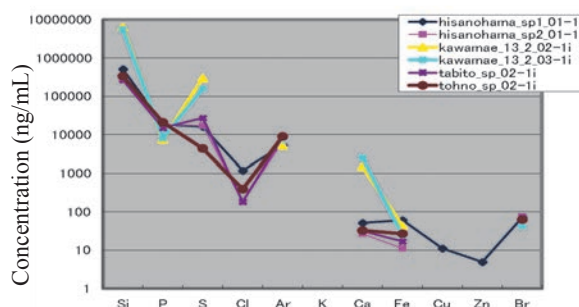


Fig. 3 Concentration of elements level in each sample waters.

Interestingly, the highest concentration of element is silicon in all of water samples. Radiological material I-131, Cs-134 and Cs-137 were not detected in the sample waters in the sample waters. On the other hand, the Kawamae sample water is involving coli form bacteria which were detected by simple test method. From these results suggested that high level of sulfur and calcium bear testimony to the bacteria in the water.

The micro-PIXE method is useful to determine the elemental distribution in natural water, water system analysis and estimate of drainage network.

References

- 1) T. Kamiya et al., Nucl. Instrum. Meth. Phys. Res. B 118 (2006) 447-50.
- 2) A. Tanaka et al., Int. J. PIXE 12(3&4) (2002) 79-83.

3. Medical and Biotechnological Application

3-01	Development of a Method for Estimating Localization of Lesions on DNA by Ionizing Radiations	61
	K. Akamatsu and N. Shikazono	
3-02	Mutagenic Effects of He Ion Particles in DNA Repair Mutants of <i>Escherichia coli</i>	62
	M. Sakai, M. Takahashi, N. Shikazono and K. Awazu	
3-03	Target Irradiation of Individual Cells Using Focusing Heavy-Ion Microbeam of JAEA-Takasaki (III): A Development of Rapid Cell-Targeting System Using Beam Scanner	63
	T. Funayama, Y. Yokota, T. Sakashita and Y. Kobayashi	
3-04	Responsible Site for the Radiation Response of the Salt Chemotaxis Learning in <i>C. elegans</i> Using Heavy-ion Microbeam	64
	T. Sakashita, M. Suzuki, Y. Hattori, H. Ikeda, Y. Mutou, Y. Yokota, T. Funayama, N. Hamada, K. Fukamoto and Y. Kobayashi	
3-05	Time-course Analysis of Radiation-induced Bystander Cell-killing Effect Using Heavy-ion Beams and γ -rays	65
	Y. Yokota, T. Funayama, Y. Mutou-Yoshihara, H. Ikeda and Y. Kobayashi	
3-06	Interaction of Etoposide with High LET Irradiation in Lung Cancer Cells Compared to X-Ray Irradiation	66
	K. S. Subedi, T. Takahashi, Y. Yoshida, K. Ando, T. Funayama and T. Nakano	
3-07	Mechanisms for the Induction of Radioadaptive Response by Radiation-Induced Bystander Response	67
	H. Matsumoto, M. Hatashita, M. Tomita, K. Otsuka, M. Maeda, T. Funayama, Y. Yokota, Y. Mutou, M. Suzuki, T. Sakashita and Y. Kobayashi	
3-08	Analysis of Bystander Cell Signaling Pathway Activated by Heavy Ion-Microbeam III	68
	M. Tomita, H. Matsumoto, K. Otsuka, M. Maeda, T. Funayama, Y. Yokota, Y. Mutou, M. Suzuki, T. Sakashita and Y. Kobayashi	
3-09	Chromosomal Aberrations Induced by Intercellular Communication Mediated Bystander Effect in Normal Human Fibroblasts Induced by C-, Ne- and Ar-ion Microbeams	69
	M. Suzuki, N. Autsavapromporn, T. Funayama, Y. Yokota, Y. Mutou, H. Ikeda, Y. Kobayashi and T. Murakami	
3-10	Analysis of Bystander Effect Induced by Cell Membrane Response in Glioma Cells	70
	S. Wada, M. Yamamoto, A. Yoshikubo, T. Kakizaki, T. Funayama, T. Sakashita, Y. Yokota, Y. Kobayashi and N. Ito	
3-11	Ion Beam Irradiation Has Different Influences on the Expression of Bcl-2 in Cultured Human Retinal Vascular Endothelial Cells Exposed to L-dopa among ^{20}Ne , ^{12}C , and ^4He	71
	K. Akeo, T. Funayama, Y. Kobayashi and Y. Akeo	

3-12	Ionizing Radiation Alters the Dynamics of Human Long Interspersed Nuclear Elements 1 (LINE1) Retrotransposon	72
	A. Tanaka, Y. Nakatani, N. Hamada, A. Jinno-Oue, N. Shimizu, S. Wada, T. Funayama, T. Mori, S. Islam, S. A. Hoque, M. Shinagawa, T. Ohtsuki, Y. Kobayashi and H. Hoshino	
3-13	Degradation of Nucleus in the Heavy-ion Irradiated Silkworm Egg just after Having Reached the Peripheral Region of the Egg	73
	K. Shirai, C. Xu, T. Funayama, T. Sakashita, Y. Yokota, Y. Kobayashi and K. Kiguchi	
3-14	Neurocytotoxic Effects of Micro-beam Irradiation of Heavy Carbon-ions on the Developing Medaka Brain Measured in vivo	74
	T. Yasuda, Y. Hibi, T. Funayama, Y. Yokota, Y. Mutou, H. Ikeda, Y. Kobayashi, S. Oda and H. Mitani	
3-15	Wide Overlap in Gene Expression Response to Desiccation and Ionizing Radiation in the Sleeping Chironomid Larvae	75
	O. Gusev, K. Mukae, T. Kikawada, T. Sakashita, T. Funayama, Y. Kobayashi and T. Okuda	
3-16	The Effects of THP-1 Macrophages on the Migration of Heavy-ion Irradiated Human Lung Cancer Cells	76
	Y. Mutou-Yoshihara, T. Funayama, Y. Yokota, T. Sakashita, M. Suzuki, H. Ikeda and Y. Kobayashi	
3-17	Effects of Carbon-ion Microbeam Irradiation on Locomotion in <i>Caenorhabditis elegans</i>	77
	M. Suzuki, Y. Hattori, T. Sakashita, T. Funayama, Y. Yokota, Y. Mutou-Yoshihara, H. Ikeda and Y. Kobayashi	
3-18	Rapid ESR Measurement of Irradiated Fresh Papaya	78
	M. Kikuchi, Y. Shimoyama, M. Ukai and Y. Kobayashi	
3-19	ESR Studies on Decay of Radicals Induced in Irradiated Foods	79
	Y. Kaimori, Y. Sakamoto, S. Kawamura, K. Kishita, M. Kikuchi, H. Nakamura, Y. Kobayashi and M. Ukai	
3-20	Improvement of Spatial Resolution of PIXE-CT Using ML-EM Algorithm in TIARA	80
	T. Satoh, M. Koka, W. Kada, A. Yokoyama, T. Ohkubo, A. Yamazaki, Y. Ishii and T. Kamiya	
3-21	Measurement of Trace Elements in Histamine Receptor Deficient Mice Brain Slices by In - Air Micro-PIXE	81
	E. Sakurai, K. Yanai, K. Ishii, S. Hiraishi, S. Yamauchi, H. Yamazaki, S. Matsuyama, N. Okamura, A. Yokoyama, W. Kada, M. Koka, T. Satoh and T. Kamiya	
3-22	Comparison of Two Fluoride Regimens on Fluorine Uptake in Carious Enamel during pH-cycling	82
	H. Komatsu, Y. Matsuda, S. Ooki, N. Hashimoto, K. Okuyama, H. Yamamoto, Y. Iwami, S. Ebisu, M. Nomachi, K. Yasuda, T. Satoh and M. Koka	

3-23	Imaging of Metallofullerene Distribution Using Micro-particle Induced X-ray Emission for Gadolinium Neutron Capture Therapy	83
	Y. Yamamoto, K. Nakai, F. Yoshida, M. Shirakawa, K. Endo, Y. Horiguchi, Y. Nagasaki and A. Matsumura	
3-24	Analysis of Particles in Interstitial Pneumonia Lung Tissue Obtained by Transbronchial Biopsy	84
	K. Dobashi, Y. Shimizu, S. Matsuzaki, T. Satoh, M. Koka, A. Yokoyama, T. Ohkubo, Y. Ishii, T. Kamiya and M. Mori	
3-25	Analysis of Erythrocyte Elements in Hepatitis C Patients Treated with Peginterferon-alfa and Ribavirin	85
	T. Nagamine, T. Akutsu, M. Koka T. Satoh and T. Kamiya	
3-26	Decreasing Size of Microcapsules and Increased Radiation-induced Release of Antitumor Drugs	86
	S. Harada, S. Ehara, K. Ishii, T. Satoh, T. Kamiya and N. Matsuyama	
3-27	Cultivation of Marine Planktons by the Artificial Seawater and Elemental Mapping by Micro Beam PIXE System of TIARA	87
	Y. Iwata, S. Takahashi, K. Ishii, T. Kamiya and T. Satoh	
3-28	Synthesis of Radioiodinated Antitumor Cyclic Peptide, [¹²⁵ I]-Sansalvamide A Derivative	88
	Sh. Watanabe, K. Yamada, N. Tsukui, H. Hanaoka, Y. Ohshima, A. Yamaguchi, H. Oku and N. S. Ishioka	
3-29	Development of a ⁷⁶ Br-labeled Amino Acid Derivative for PET Imaging of Tumor	89
	H. Hanaoka, Sh. Watanabe, H. Tominaga, Y. Ohshima, Sa. Watanabe, K. Yamada, Y. Iida, N. S. Ishioka and K. Endo	
3-30	The Process to Improve the Production of ¹³ N-labeled Nitrogen Gas Tracer for the Imaging of Nitrogen Fixation in Soybean Nodules	90
	S. Ishii, N. Suzui, Yong-Gen Yin, N. Kawachi, H. Yamazaki, A. Koyanagi, N. Ohtake, T. Ohyama and S. Fujimaki	
3-31	Real-Time Imaging and Analysis of Differences in Cadmium Dynamics in Rice Cultivars (<i>Oryza sativa</i>) Using Positron-Emitting ¹⁰⁷ Cd Tracer	91
	S. Ishikawa, N. Suzui, S. Ito-Tanabata, S. Ishii, M. Igura, Tadashi Abe, M. Kuramata, N. Kawachi and S. Fujimaki	
3-32	Imaging of Root Exudates Secreted from Soybean Root to Soil by Using Carbon-11-Labeled Carbon Dioxide and PETIS	92
	Y-G. Yin, N. Suzui, N. Kawachi, S. Ishii, H. Yamazaki, A. Koyanagi and S. Fujimaki	
3-33	A New Method to Analyze Individual Photosynthetic Abilities of Young Plant Seedlings Using Positron-Emitting Tracer Imaging System (PETIS)	93
	N. Kawachi, A. Koyanagi, N. Suzui, S. Ishii, Yong-Gen Yin, H. Yamazaki, A. Iwasaki, K. Ogawa and S. Fujimaki	
3-34	Production of Cs-129 Tracer by Using Ion Beam Bombardment for Positron Imaging Applications	94
	N. Suzui, Y.-G. Yin, N. Kawachi and S. Fujimaki	

3-35	Development of Ion Beam Breeding Technology in Plants and Creation of Useful Plant Resources	95
	Y. Hase, S. Nozawa, T. Okada, I. Asami, T. Nagatani, Y. Matsuo, A. Kanazawa, K. Honda and I. Narumi	
3-36	Ion Beam Irradiation on Rice Seeds for the Mutation Breeding Project of the Forum for Nuclear Cooperation in Asia (FNCA)	96
	A. Tanaka, S. Nozawa, Y. Hase, I. Narumi, H. Ishikawa and A. Koike	
3-37	Generating New Ornamental Plant Varieties Using Ion Beams	97
	A. Zaiton, A. H. Affrida, S. Shakinah, S. Nozawa, I. Narumi, Y. Hase and Y. Oono	
3-38	Mutational Effects of Carbon Ions near the Range End and Development of an Efficient Mutagenesis Technique Using Ion Beams	98
	Y. Hase, R. Yoshihara, S. Nozawa and I. Narumi	
3-39	Effect of Carbon Ion Beam Irradiation on Callus Growth in Arabidopsis and Rice	99
	H. Saika, R. Yoshihara, A. N. Sakamoto and S. Toki	
3-40	Developing Protocol for Screening of Drought/Salt Tolerant Mutants with Ion Beam Mutagenesis in <i>Populus</i> sp.	100
	K. K. Biswas, T. Mohri, S. Kogawara, I. Narumi and Y. Oono	
3-41	Effects of Gamma Ray Irradiation on <i>Rumex obtusifolius</i> L.	101
	S. Kitano, A. Miyagi, Y. Oono, Y. Hase, I. Narumi, H. Uchimiya and M. Kawai-Yamada	
3-42	Production of Mutants by Ion Beam Irradiation in <i>Dahlia</i> spp.	102
	Y. Uyama, H. Ohya, Y. Amano, K. Kashimoto, S. Hatano, S. Nozawa, R. Yoshihara, Y. Hase and I. Narumi	
3-43	Analysis of Mutant Frequencies for Different LET Radiations in <i>Deinococcus radiodurans</i>	103
	K. Satoh, K. Tejima, T. Onodera and I. Narumi	
3-44	Functional analysis of Universally Conserved Genes, <i>ygjD</i> and <i>yeaZ</i> Orthologs, in DNA Repair of <i>Deinococcus radiodurans</i>	104
	T. Onodera, K. Satoh, T. Ohta and I. Narumi	
3-45	DNA Damage Evaluation System of the High-LET Ion Beam Using the Polymerase Chain Reaction	105
	Y. Matuo, Y. Izumi, Y. Hase, A. Sakamoto, S. Nozawa, I. Narumi and K. Shimizu	
3-46	Application of Bio-pesticide with Plant Growth Promoter Made from Oligo-chitosan	106
	M. Aino, K. Matsuura, N. Nagasawa, F. Yoshii, M. Taguchi, K. Satoh and I. Narumi	
3-47	Phenotypic Characterization of High Temperature Tolerant Mutants of <i>Bradyrhizobium japonicum</i> USDA110 Generated by Ion-beam Irradiation	107
	K. Takeda, K. Tejima, K. Satoh, I. Narumi and T. Yokoyama	
3-48	FACS-based Screening for Yeast Clone Highly Expressing Cellulase	108
	K. Ninomiya, T. Nomura, K. Satoh, I. Narumi and N. Shimizu	

3-49	Benomyl-tolerant Mutation of Entomopathogenic Fungi Induced by Carbon Ion Beams	109
	T. Saito, S. Shinohara, K. Satoh and I. Narumi	
3-50	Identification of Mutation Sites in High Ethyl Caproate Producing Sake Yeasts Generated by Ion Beam Breeding	110
	T. Masubuchi, C. Takashima, O. Kamiyama, H. Ikenaga,	
3-51	Effects of Ion Beam Radiation on Genome Integrity in <i>Saccharomyces cerevisiae</i>	111
	T. Nunoshiba, Y. Hirasawa, A. Yamauchi, K. Satoh, K. Tejima, T. Onodera and I. Narumi	
3-52	The Effect of γ -sterilization of Biofertilizer's Carrier on Bacterial Inoculants Survival	112
	K. Tejima, T. Yokoyama, K. Satoh, K. Takeda and I. Narumi	

This is a blank page.

3 - 01 Development of a Method for Estimating Localization of Lesions on DNA by Ionizing Radiations

K. Akamatsu and N. Shikazono

Medical and Biotechnological Application Division, QuBS, JAEA

1. Introduction

It is known that DNA lesions induced by ionizing radiation and chemicals can cause mutation and carcinogenesis. In particular, ‘clustered damage’ site, that is a DNA region with multiple lesions within one or two helical turns, is believed to be hardly repaired. This damage is considered to be induced, e.g., around high-LET ionizing radiation tracks. However, detail of the damage is not known. So, we have developed a method for estimating degree of localization of apurinic(AP)- sites on DNA using Förster resonance energy transfer (FRET). First, we prepared plasmid DNA with AP-sites (AP-DNA) by heating in acidic buffer as a randomly-distributed AP-DNA model. The AP-DNA was labeled both with AlexaFluor® 350 (AF350) and 488 (AF488) fluorescent dyes with an alchoxyamino group (donor and acceptor probes, respectively). The FRET efficiency (E) was calculated using the donor fluorescence intensities before/after enzymatic digestion of the labeled AP-DNA. Moreover, we have constructed a theoretical equation to obtain E as the functions both of AP-site density (λ_{AP}) and of labeling ratio of acceptor to total AP-sites (r_A). As a result, we found that experimentally-obtained E values for the heat-treated AP-DNA correspond to theoretical ones calculated on the basis of exponential distribution. Now we have tried to apply the method to $^4\text{He}^{2+}$ - and ^{60}Co γ -irradiated DNA.

2. Experiments

•Sample preparation and He beam irradiation

Plasmid DNA digested by Sma I was used (linear formed). The DNA aq. was mounted on a glass plate and dried in vacuum. The plate was irradiated with linear energy transfer (LET) of ~ 70 keV/ μm (< 400 kGy) of $^4\text{He}^{2+}$ beam (TC), which was controlled by a depth-tunable cell irradiation equipment¹⁾ at r.t.. Moreover, ^{60}Co γ -rays were also used as a standard radiation source (6th ^{60}Co - γ cell).

•Preparation of fluorophore-labeled irradiated DNA and the fluorescence spectroscopy for FRET observation

The irradiated DNA (10 μL in water) and 10 μL of 100 mM Tris-HCl (pH 7.5) were mixed in a microtube. Two microliters of a mixture containing AF350 and AF488 with a given molar ratio was added to the DNA solution and was incubated overnight at 37 °C. The fluorophore-labeled DNA was purified by ethanol precipitation. Twenty microliters of water was added to the residue immediately after removal of the supernatant. Two hundreds microliters of 100 mM TrisHCl with 10 mM MgCl_2 (pH 8) was added to the purified labeled DNA sample. The fluorescence

intensities were measured both at 449 (ex. 347) nm for AF350 and at 520 (ex. 460) nm for AF488. After the measurement, the enzyme cocktail containing DNase I and phospho- diesterase I was added to the solution, and it was incubated for 2 h at 37 °C. E values were calculated from the donor intensity before/after the digestion.

3. Results and Discussion

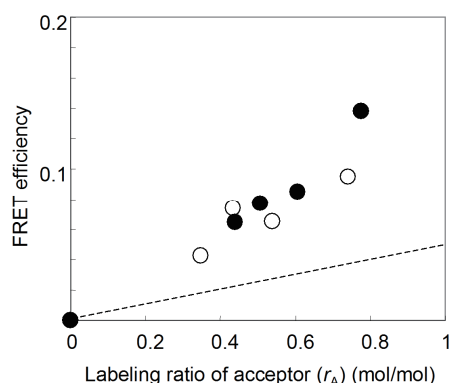


Fig. 1 FRET efficiencies for $^4\text{He}^{2+}$ beam and ^{60}Co γ -rays as a function of labeling ratio of acceptor (\bullet : He (100 kGy, λ_{AP} : 0.0021/base pair); \circ : ^{60}Co γ -rays (200 kGy, λ_{AP} : 0.0020). The dotted line indicates a theoretical one for random distribution at λ_{AP} : 0.0020.

Figure 1 shows characteristics of FRET efficiency (E) for $^4\text{He}^{2+}$ and ^{60}Co γ -rays. Interestingly, not only He ions but also the γ -rays seem to produce more localized AP-sites than randomly-distributed case as seen in heat-treated DNA. On the other hand, the radiation chemical yield for He is larger than that for the γ -rays. As far as the direct radiation effects on DNA, differences in LET are one of the important factors to elucidate the fundamental nature of ionizing radiations. Though the FRET method is unique for estimating localization of the lesions, no significant differences in E were seen between these radiations. It is noted that reliability of the data would decrease with decreasing E and with deviating from $r_A = 0.5$. More studies are needed to clarify the difference not only in LET, but also in Z of the ion and in surrounded water on DNA.

4. Acknowledgments

We would like to gratefully thank Dr. Y. Sugo for operating the TC line, and also thank Drs. M. Kikuchi and Y. Kobayashi for ^{60}Co γ -ray irradiation experiments.

Reference

- 1) A. Tanaka et al., Nucl. Instrum. Meth. Phys. Res. **B 129** (1997) 42.

3 - 02 Mutagenic Effects of He Ion Particles in DNA Repair Mutants of *Escherichia coli*

M. Sakai^{a, b)}, M. Takahashi^{b)}, N. Shikazono^{b)} and K. Awazu^{a)}

^{a)} Division of Sustainable Energy and Environmental Engineering, Graduate School of Engineering, Osaka University, ^{b)} Medical and Biotechnological Application Division, QuBS, JAEA

Non-DSB type of clustered damage is induced by ionizing radiation and is proposed to cause deleterious effects to cells¹⁾. Their yields and configurations likely depend on the radiation qualities, which is defined by the ionization density along the particle track, in most cases characterized by LET (linear energy transfer)^{1,2)}. To date, the biological consequences of radiation of both low and high LETs have been extensively studied in various organisms, including bacteria, yeasts, higher plants, and mammalian cells. It is, however, still not clear how and to what extent the damage is induced, processed in the cell, and thus related to biological consequences especially to mutations. In this project, we aim to find out the significance of clustering of DNA damage in mutagenesis. Here, we present the results of *lacI* mutation assay of wild-type and DNA repair deficient cells after irradiation of He ion particles comparing with X-rays.

The cells of CSH100 (wild type *E. coli*) and CSH100*lexA3*, and CSH100*uvrA* were incubated in 0.2% glucose minimal medium at 37 °C unless otherwise stated. LexA is the repressor of SOS response, RecA plays a central role in both homologous recombination as well as activating the SOS response, and UvrA is required for nucleotide excision repair. Cells ($2-3 \times 10^8$) were filtered through a nitrocellulose membrane of a diameter of 1.3 cm. To prevent cells from drying, the membrane was placed on a filter paper pre-wetted with 300 μ L of 0.15 M NaCl solution with 20% glycerol. Subsequently, the membrane was placed on 0.15 M NaCl agar in a Petri dish, and then the dish was covered with a polyimide film (Kapton film, 7.5 μ m thickness). Cells were irradiated with He ions (at dose rates of 1~4 Gy/s) or with X-rays (at a dose rate of 0.47 Gy/s). The LET of He ions was altered by placing a Ni foil in front of the samples, and the LET of the sample was estimated to be 89 keV/ μ m by the ELOSS code. After irradiation, cells were plated and incubated overnight to determine the fraction of survived cells and the mutation frequency. In this study, the mutation frequency of *lacI* gene was measured. Mutations in the *lacI* gene enable the cells to grow on a medium with phenyl- β -D-galactopyranoside (P-gal) as the only carbon source³⁾. In determining the mutation frequency, irradiated cells were plated on a 0.2% P-gal minimal medium, and were incubated at 37 °C for 40 hours to score the number of *lacI* mutants.

Mutagenic effects of radiations with different qualities were assessed from dose response curves. In wild type, the mutation frequencies after He ions were significantly lower

than those after X-rays, especially at higher doses (Fig. 1). In contrast, no significant difference between the mutation frequencies with X-rays and He-ions was observed in CSH100*lexA3*, as mutation frequencies hardly increased after exposure to both types of radiation. The mutation frequency with He ion was also comparable to that with X-rays in CSH100*uvrA*. Thus, UvrA seems to specifically reduce the frequencies of He ion-induced mutations. These results suggest that (1) the types of DNA damage induced by X-rays and He ions are different, (2) LexA, and therefore the SOS response, may play an important role for mutation induction in *E. coli* after X-irradiation and (3) mutagenic lesions that are processed by nucleotide excision repair is predominantly generated after He-irradiation. Studies on mutation induction in other DNA repair mutants (*recQ* and *mutS*) are now underway.

References

- 1) N. Shikazono et al., J. Radiat. Res. 50 (2009) 27.
- 2) H. Nikjoo et al., Radiat. Res. 156 (2001) 577.
- 3) J. H. Miller, A Short Course in Bacterial Genetics, Cold Spring Harbor Laboratory Press, (1992) 131.

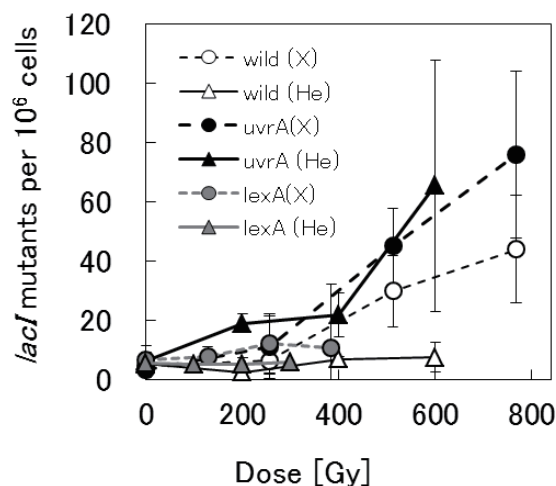


Fig. 1 Mutation frequencies of the *lacI* gene in wild type *E. coli* (CSH100) and mutants. Wild type CSH100 were exposed to X-rays (○) or He ions (△), CSH100*uvrA* were exposed to X-rays (●) or He ions (▲) and CSH100*lexA3* were exposed to X-rays (●) or He ions (▲).

3 - 03 Target Irradiation of Individual Cells Using Focusing Heavy-Ion Microbeam of JAEA-Takasaki (III): A Development of Rapid Cell-Targeting System Using Beam Scanner

T. Funayama, Y. Yokota, T. Sakashita and Y. Kobayashi

Medical and Biotechnological Application Division, QuBS, JAEA

Target irradiation of individual cells using heavy-ion microbeam is a useful means for measuring exact hit effect of heavy-ion on cell. Moreover, heavy-ion microbeam is a powerful tool for analyzing mechanisms underlying radiation-induced bystander effect, which is induced on a cell population exposed to low fluence, low dose radiation¹⁾. Thus we installed a focusing heavy-ion microbeam system under a vertical beam line of an AVF cyclotron of JAEA-Takasaki, and developed a method to irradiate individual cells using focusing heavy-ion microbeam.

Using the system, we established a method to irradiate finer heavy-ion microbeam on individual HeLa cells¹⁾. However an irradiation speed could not be faster than 1 cells/sec. A limitation factor of the speed was a movement speed of the automatic mechanical stage, which was used to move each targeted cell to the position of the focusing microbeam spot. Thus, to improve a throughput of the cell irradiation using focusing microbeam, we developed a method to use a beam scanner, which is able to move a beam spot rapidly to the position of individual targeted cells.

To develop the method, first we developed a code that calculates the voltages from the cell positions, which will be applied to a beam scanner for moving a beam spot rapidly to the target positions. Using a developed code, a set of voltages was calculated from a set of cell positions, which was extracted from a pre-obtained cell image using cell detection code (Fig. 1a, green cross mark indicates extracted positions). Thereafter, a film of CR-39 was irradiated by a scanned beam according to the calculated voltages. After irradiation, hit positions of the ion were visualized as etch pits, and the spatial distribution of them was observed (Fig 1b). Figure 1c exhibits a merged image of the cells and the etch pits. A distribution pattern of the etch pits on CR-39 film (converted to green color) well correlated to a distribution pattern of the source cell image. The result suggested that the developed code can finely convert detected cell positions to corresponding scanner voltages. Thus we concluded that using the developed code we will become able to irradiate cell rapidly with scanned heavy-ion microbeam.

References

- 1) T. Funayama et al., IEEE Trans. Plasma Sci. 36 (2008) 1432-40.
- 2) T. Funayama et al., JAEA Takasaki Annu. Rep. 2010 (2012) 65.

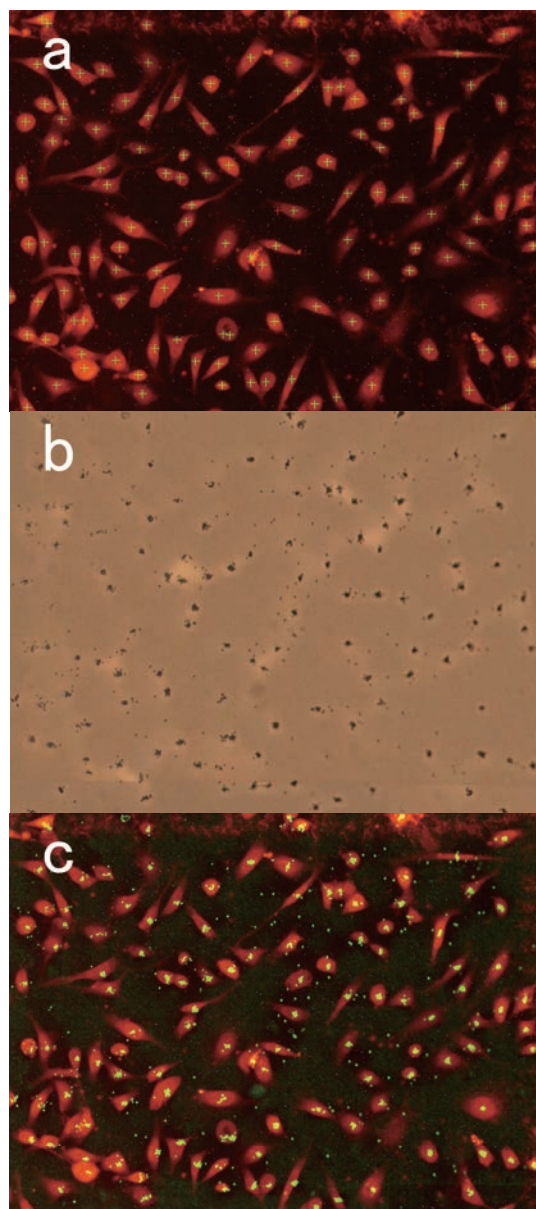


Fig 1. Irradiation of cell distribution pattern using scanning heavy-ion microbeam. (a) Detection of cell position from an image. Green cross mark indicates extracted positions. (b) Irradiation of CR-39 film with scanned beam. (c) Merged image of cells and etch pits. Etch pit image was converted to green color and overlaid.

3 - 04 Responsible Site for the Radiation Response of the Salt Chemotaxis Learning in *C. elegans* Using Heavy-ion Microbeam

T. Sakashita^{a)}, M. Suzuki^{a)}, Y. Hattori^{a)}, H. Ikeda^{a)}, Y. Mutou^{a)}, Y. Yokota^{a)},
T. Funayama^{a)}, N. Hamada^{b)}, K. Fukamoto^{c)} and Y. Kobayashi^{a)}

^{a)} Medical and Biotechnological Application Division, QuBS, JAEA,

^{b)} Radiation Safety Research Center, Central Research Institute of Electric Power Industry,

^{c)} Faculty of Textile Science and Technology, Shinshu University

An increasing body of data indicates that ionizing radiation affects the nervous system and alters its function¹⁾. Chemotaxis of *C. elegans* during the salt chemotaxis learning was modulated by gamma irradiation²⁾. Our preliminary results showed the similar response of the salt chemotaxis learning to whole-body carbon-ion irradiation. However, we have no direct evidence for the interaction of ionizing radiation with the central neuronal tissue (nerve ring) in *C. elegans*. Microbeam irradiation is useful to analyze direct radiation effects at a cellular or tissue level. Thus, we applied the microbeam irradiation (¹²C, 18.3 MeV/u, LET = 119 keV/μm) to the *C. elegans* nerve ring and examined the effect on the salt chemotaxis learning.

Well-fed adults of *C. elegans* grown at 20 °C on the plate spread with *E. coli* OP50 were used in all experiments. The area of nerve ring (Head) of *C. elegans* in a ditch filled with the S-basal of the micro total analysis systems (μTAS)³⁾ were irradiated with 12,000 carbon ions corresponding to 500 Gy at 20 μmφ micro-aperture area (Fig. 1). Also, a counter part (Tail) of *C. elegans* was irradiated with carbon ion microbeam according to the previous report⁴⁾. On the other hand, whole-body carbon ion irradiation by the broad beam irradiation facility was carried out as a positive control. Immediately after irradiation, chemotaxis to NaCl during learning was measured. Using the assay plate with a gradient of NaCl concentration, we evaluated chemotaxis based on the chemotaxis index (CI) that was calculated as {(number of animals at the high-concentration spot) – (number of animals at the control spot)} / (total number of animals in the assay plate)⁵⁾. The positive CI indicates moving towards higher concentration of chemical compounds. The results of CI were evaluated as mean ± 95% confidential interval. Statistical test was carried out by the chi-square test with a Yates' correction.

As shown in Fig. 2, we demonstrate the modulation of the chemotaxis to NaCl during learning as well as those of broad beam irradiation (CI: 0.06 ± 0.04 in broad beam irradiated animals, 0.01 ± 0.02 in the Head locally irradiated animals). Intriguingly, the counter part (Tail) irradiation of *C. elegans* also demonstrated the modulation effect of chemotaxis like a result of the Head microbeam irradiation experiment (Fig. 2; CI: -0.02 ± 0.04 in the Tail locally irradiated animals). The modulatory response of

chemotaxis by the Tail irradiation might be caused by the *gpc-1* gene, which codes for the γ subunits of the heterotrimeric G-protein, expressed in not only the Head area but also the Tail area, related to the γ ray induced modulatory effect of chemotaxis²⁾. To understand the detail of direct radiation effects, we are planning the further microbeam irradiation to the other part of *C. elegans* in the near future.

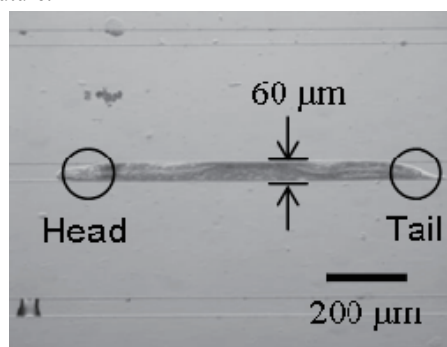


Fig. 1 *C. elegans* in a ditch of the micro total analysis systems. Circles show the areas of nerve ring (Head) and Tail.

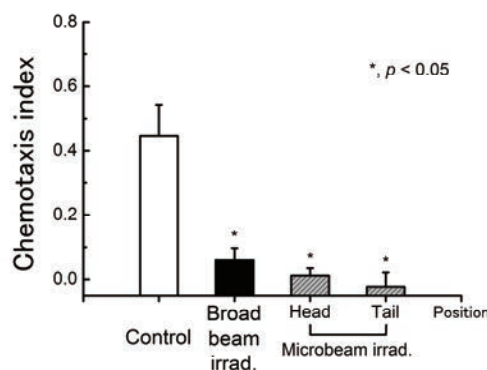


Fig. 2 Carbon ion broad and microbeam induced modulatory effects on chemotaxis of *C. elegans*. Error bars show the 95% confidential interval, and asterisks indicate the significant differences in CI.

References

- 1) T. Sakashita et al., J. Radiat. Res. 51 (2010) 107-21.
- 2) T. Sakashita et al., FASEB J. 22 (2008) 713-20.
- 3) S. R. Lockery et al., J. Neurophysiol. 99 (2008) 3136-43.
- 4) T. Sugimoto et al., Int. J. Radiat. Biol. 82 (2006) 31-38.
- 5) S. Saeki et al., J. Exp. Biol., 204 (2001) 1757-64.

3 - 05 Time-course Analysis of Radiation-induced Bystander Cell-killing Effect Using Heavy-ion Beams and γ -rays

Y. Yokota^{a)}, T. Funayama^{a)}, Y. Mutou-Yoshihara^{a)}, H. Ikeda^{a, b)} and Y. Kobayashi^{a)}

^{a)} Medical and Biotechnological Application Division, QuBS, JAEA,

^{b)} Graduate School of Medicine, Gunma University

Radiation-induced bystander effect manifests cell killing, induction of chromosomal aberration and mutation in cells that are not irradiated but are close to irradiated cells via intercellular communication. The mechanism of bystander effect is left to be cleared perfectly, although it is necessary to estimate the potential risks of low-dose or low-dose-rate radiation accurately. In the present study, we thus investigate the time dependency of bystander cell-killing effect using heavy ion beams and γ -rays to shed light on the mechanism of bystander effect and update the data previously reported¹⁾.

Normal human lung fibroblasts WI-38 cell line was cultured with MEM medium supplemented with 10% fetal bovine serum. Cells were inoculated into irradiation vessel 7 days prior to irradiation and medium was exchanged 3 or 4 days following inoculation. Twenty-five lattice points of cells inoculated in coverslip-based dishes were irradiated with 10 particles each of carbon (LET=103 keV/ μ m) or neon (380 keV/ μ m) ion microbeams as previously reported²⁾, and the cell population including hit cells and bystander cells was incubated up to 24 h following irradiation. The percentage of cells hit in a cell population was estimated to be about 0.02% since 25 cells were targeted and 75-100 non-targeted cells were also hit by scattered ions in a population comprising about 6×10^5 cells. This means almost all of the cell population comprised bystander cells. Given the presence of ion scattering, the number of traversals per cell hit varied from 1 to 10, and the dose per cell hit (about 1,600 cm² on average) was estimated to be 0.01-0.1 Gy for carbon ions and 0.04-0.4 Gy for neon

ions. Cells inoculated in membrane-based inserts were irradiated with 0.13 Gy of carbon ion broadbeam (LET=108 keV/ μ m) and 0.5 Gy of γ -rays (0.2 keV/ μ m), and the inserts were then placed on corresponding companion plates, in which non-irradiated cells were cultured in the same way as irradiated cells, within 30 min following irradiation. The ratio of irradiated cells and non-irradiated cells was almost 1:2. Following co-culture up to 24 h between irradiated cells and non-irradiated cells, non-irradiated bystander cells were trypsinized, counted, and then diluted to a suitable cell density with culture medium. Diluted cell suspension was transferred into a tissue culture dish and cultured for 14 days until colonies had formed. Colonies comprising 50 or more cells were counted as survivors.

Survival of the cell population, in which about 0.02% of cells were irradiated with heavy ion microbeams, decreased at 24 h following co-culture (Fig. 1). In contrast, survival of bystander cells co-cultured with cells irradiated with carbon ion broadbeam and γ -rays decreased at 6 h or later following co-culture (Fig. 2). From these results, it is concluded that an increase in the number of cells irradiated with ionizing radiation in a cell population leads to an earlier emergence of the bystander cell-killing effect in the non-irradiated subpopulation.

References

- 1) Y. Yokota et al., JAEA Takasaki Annu. Rep. 2010 (2012) 67.
- 2) T. Funayama et al., J. Radiat. Res. 49 (2008) 71.

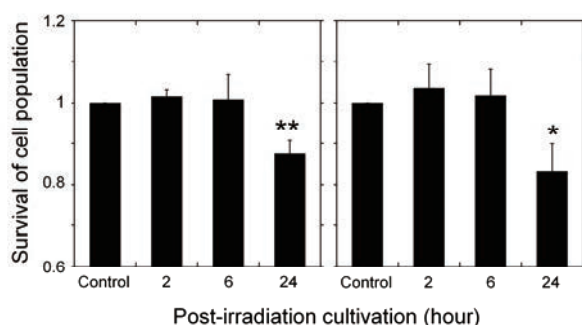


Fig. 1 Survival data of cell populations in which about 0.02% of the cells were irradiated with carbon (left side) or neon (right side) ion microbeams. Data are mean \pm SEM of 4-5 independent experiments. *: $p < 0.05$, **: $p < 0.01$. Survival of bystander cells decreased to 0.8-0.9 at 24 h following irradiation.

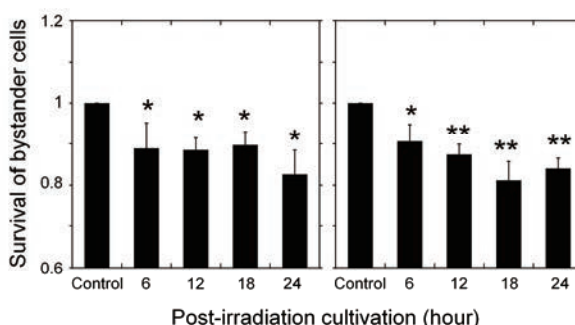


Fig. 2 Survival data of bystander cells co-cultured with cells irradiated with carbon ion broadbeam (left side) or γ -rays (right side). Data are mean \pm SEM of 3-7 independent experiments. *: $p < 0.05$, **: $p < 0.01$. Survival of bystander cells decreased to 0.8-0.9 when co-cultured with cells irradiated for 6 h or longer.

3 - 06 Interaction of Etoposide with High LET Irradiation in Lung Cancer Cells Compared to X-Ray Irradiation

K. S. Subedi^{a)}, T. Takahashi^{b)}, Y. Yoshida^{a)}, K. Ando^{a)}, T. Funayama^{c)} and T. Nakano^{a)}

^{a)} Gunma University Graduate School of Medicine, ^{b)} Saitama Medical Center, Saitama Medical University, ^{c)} Medical and Biotechnological Application Division, QuBS, JAEA

The combined use of heavy ion and chemoradiotherapy may be essential for advanced tumor in near future. Few studies have reported the heavy ion radiation-sensitizing effects of anticancer drugs¹⁾. It was also reported that etoposide in combination with X-rays had a supra-additive effect on radio-resistant tumor cell line²⁾. The purpose of this study was to investigate the mechanism of interaction of etoposide treatment combined with high LET irradiation compared to X-ray irradiation in vitro.

A 549 human lung cancer cell line was selected for experiments. Cells were irradiated using an X-ray machine (FAXITRON RX-650) operated at 100 kVp, 5.0 mA and FSD of 35.6 cm with a 0.3 mm Al filter giving a dose rate of 1 Gy/min or carbon ion beam accelerator with 18.3 MeV/nucleon carbon-ion beams at TIARA of JAEA. On 14th day of incubation colonies were fixed and stained with a crystal violet solution. The concentration required to reduce colony formation by 50% at 1 h treatment (IC₅₀) of etoposide (Nippon Kayaku Co. Ltd. Japan) was selected for combination with radiation. Colonies with 50 or more cells were counted as a single colony. Three similar and independent experiments were performed to generate a survival curve.

Figure 1 shows the cytotoxic effect of etoposide alone. Figure 2 shows that etoposide used in combination with X-ray irradiation had an additive effect on A 549 cell line. Figure 3 shows that etoposide with carbon ion irradiation have a cytotoxic effect. Supra-additive effect of etoposide in combination with carbon ion irradiation could not be demonstrated significantly in A 549 cell line.

References

- 1) T. Takahashi et al., Anticancer Res. 30 (2010) 1961.
- 2) T. Takahashi et al., Anticancer Res. 23 (2003) 3459.

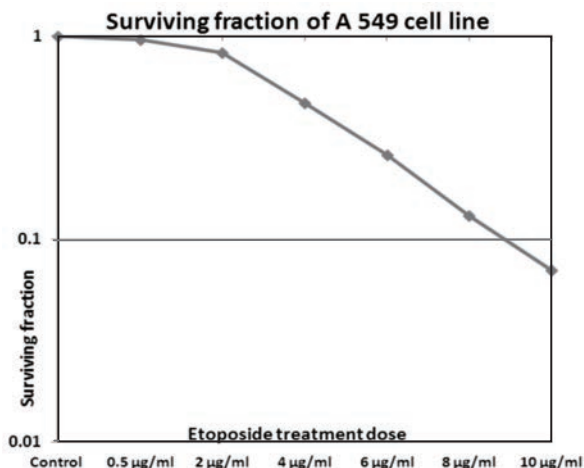


Fig. 1 Survival curve of etoposide alone.

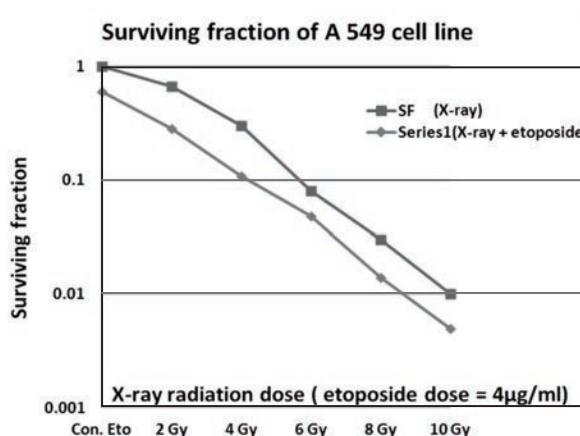


Fig. 2 Survival curves of etoposide & X-rays + etoposide.

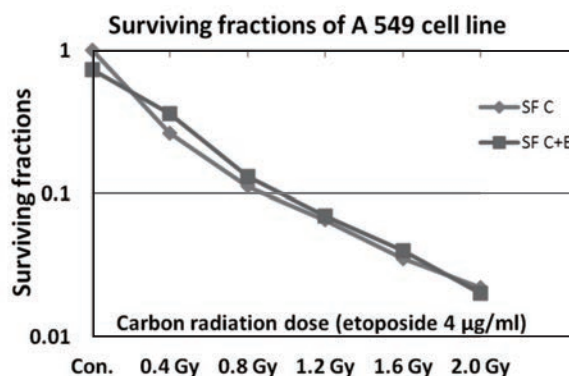


Fig. 3 Survival curves of etoposide & carbon ion beams + etoposide.

3 - 07 Mechanisms for the Induction of Radioadaptive Response by Radiation-Induced Bystander Response

H. Matsumoto^{a)}, M. Hatashita^{a)}, M. Tomita^{b)}, K. Otsuka^{b)}, M. Maeda^{b)}, T. Funayama^{c)}, Y. Yokota^{c)}, Y. Mutou^{c)}, M. Suzuki^{c)}, T. Sakashita^{c)} and Y. Kobayashi^{c)}

^{a)}Biomedical Imaging Research Center, University of Fukui, ^{b)}Central Research Institute of Electric Power Industry, ^{c)}Medical and Biotechnological Application Division, QuBS, JAEA

The objective of this project is to elucidate molecular mechanisms for the induction of radioadaptive response by bystander responses induced by low dose/low dose rate radiation using heavy ion microbeams in JAEA.

We performed the exhaustive analysis of gene expression, when radioadaptive response has been induced, using RT² ProfilerTM PCR Array System. We found several genes induced specifically and preferentially when radioadaptive response could be induced. We confirmed that *iNOS* expression was specifically induced only when radioadaptive response could be induced. Our findings strongly suggested that radioadaptive response can be induced by NO-mediated bystander responses evoked by low dose/low dose rate radiation, and that the induction of specific gene expression is required for the induction of radioadaptive response.

低線量/低線量率放射線に対して生物が示す特異的な応答様式には、放射線適応応答、放射線誘発バースタンダー応答、放射線超高感受性、遺伝的不安定性等がある¹⁾。我々は、日本原子力研究開発機構において開発された細胞局部照射装置 (HZ1) および深度制御種子照射装置 (HY1) を用いて、この放射線誘発バースタンダー応答の放射線適応応答への寄与を明らかにすることを計画した。

1. 実験方法

- (1) 細胞: *p53* 欠損ヒト非小細胞肺癌細胞 (H1299 細胞) へ正常型 *p53* 遺伝子を導入した H1299/*wtp53* 細胞を用いた。
- (2) 培養: 35 mm ディッシュの内面中央に 2.0×10^6 cells/mL の細胞懸濁液 5 μ L を 1 箇所スポットし (1.0×10^4 cells/colony)、15~20 時間培養したものを照射実験に供した。
- (3) 照射: Funayama ら²⁾の方法に従って、中央にスポットしたコロニーの 10 個の細胞に 5 粒子の 520 MeV ⁴⁰Ar¹⁴⁺ を HZ1 ポートにおいて照射した。一定時間 (3~6 時間) 培養後、520 MeV ⁴⁰Ar¹⁴⁺ を HY1 ポートにおいて 5 Gy 照射した。実験群は下記の通りである。
Group 1: 非照射細胞 (対照群)
Group 2: HZ1 照射→HY1 照射 (放射線適応応答誘導群)
Group 3: HZ1 照射のみ
Group 4: HY1 照射のみ
- (4) 全 RNA の抽出: 各実験群において最終照射から 6 時間後に細胞を回収し、全 RNA をキット (RNeasy Plus Mini Kit、キアゲン) を用いて抽出した。
- (5) 各実験群の全 RNA を RT² First Strand Kit (キアゲン) を用いて cDNA に変換し、RT² ProfilerTM PCR Array System 中の DNA Damage Signaling Pathway PCR Array および Nitric Oxide Signaling Pathway PCR Array を用いて、各実験群において特異的に発現誘導されている遺伝子を網羅的に解析した。

2. 結果および考察

- (1) HZ1 照射のみ (Group 3) あるいは HY1 照射のみ (Group 4) と HZ1 照射→HY1 照射 (適応応答誘導群、Group 2) との比較: RT² ProfilerTM PCR Array System 中の DNA Damage Signaling Pathway PCR Array および Nitric Oxide Signaling Pathway PCR Array を用いて、上記 2 群を比較した結果、放射線適応応答誘導群 (Group 2) に特異的に発現誘導されている遺伝子が数種見出された。これらの遺伝子は、細胞周期調節あるいは DNA 損傷修復に関わる遺伝子であった。またポジティブ・コントロールとなる *iNOS* 遺伝子の発現誘導は放射線適応応答誘導群 (Group 2) においてのみ確認された。
- (2) HZ1 照射のみ (Group 3) と HY1 照射のみ (Group 4) の比較: 現在解析中である。

以上の結果より、

- (1) RT² ProfilerTM PCR Array System において、放射線適応応答誘導時にのみ *iNOS* 遺伝子の発現誘導が起こることが確認され、過去の知見³⁾が異なる方法により確認された。
- (2) 放射線適応応答の誘導に必要と考えられる遺伝子が数種確認された。これらの遺伝子について、さらに精査することにより、放射線誘発バースタンダー応答による放射線適応応答の誘導のメカニズム、特に NO を介したメカニズムの解明⁴⁾を目指す。

References

- 1) H. Matsumoto et al., J. Radiat. Res. 48 (2007) 97.
- 2) T. Funayama et al., J. Radiat. Res. 163 (2005) 241.
- 3) H. Matsumoto et al., Cancer Res. 67 (2007) 8574.
- 4) H. Matsumoto et al., Curr. Mol. Pharmacol. 4 (2011) 126.

3 - 08 Analysis of Bystander Cell Signaling Pathway Activated by Heavy Ion-Microbeam III

M. Tomita^{a)}, H. Matsumoto^{b)}, K. Otsuka^{a)}, M. Maeda^{a)}, T. Funayama^{c)},
Y. Yokota^{c)}, Y. Mutou^{c)}, M. Suzuki^{c)}, T. Sakashita^{c)} and Y. Kobayashi^{c)}

^{a)} Central Research Institute of Electric Power Industry, ^{b)} University of Fukui,
^{c)} Medical and Biotechnological Application Division, QuBS, JAEA

Radiation-induced bystander responses are defined as responses in cells that have not been directly targeted by radiation but are in the neighborhood of cells that have been directly exposed. In our study, we aim to clarify the cell signaling pathway activated by high-LET radiation in the bystander cells. Normal human fibroblast WI-38 cells were irradiated with 520 MeV ⁴⁰Ar-ion microbeams or broadbeams. In our previous study, phosphorylation of Akt and accumulation of COX-2 were observed in the bystander cells 6 h after microbeam irradiation and were partially suppressed by pretreatment with a scavenger of nitric oxide (NO). These results suggested that NF-κB-dependent signaling pathway involving Akt and COX-2 play an important role in the NO-mediated bystander response. In this study, to ensure an involvement of NF-κB in the bystander signaling, we observed a phosphorylation of NF-κB in the bystander cells.

近年、低線量放射線による生物影響の機構を解明する上で、DNA 初期損傷量に依存しない「非標的効果」が注目されている。特に、放射線に直接曝露された細胞の近傍に存在する全く放射線に曝露されていない細胞において観察される「放射線誘発バイスタンダー応答」は、最も特徴的な非標的効果である¹⁾。本研究は、原子力機構の細胞局所照射装置 (HZ1) と深度制御種子照射装置 (HY1) を利用し、バイスタンダー細胞に生じるシグナル伝達経路の変化を、ヒト正常細胞を用いて明らかにすることを目的とする。

昨年度の研究において、Ar イオンマイクロビーム照射により、バイスタンダー細胞に細胞の生存シグナル伝達に関与する Akt のリン酸化、炎症反応に関与する COX-2 の蓄積が生じることを見出した。これらの応答は、一酸化窒素 (NO) の消去剤によって抑制された。Akt と COX-2 は、ともに転写因子である NF-κB を介するシグナル伝達機構に関与することが知られていることから、今年度は高 LET 重イオン線による NO を介したバイスタンダー応答のシグナル伝達経路をより確実に示すために、NF-κB のリン酸化を解析した。

WI-38 細胞を、6 穴プレート内に入れた直径 25 mm のカバーガラス上で 1 週間培養し、コンフルエントにした。照射 2 時間前に 60 mm ディッシュにカバーガラスを移した後、新しい培地もしくは NO の消去剤である carboxy-PTIO (c-PTIO, 20 μM) を添加した培地を加え培養した。マイクロビームの照射は、HZ1 ポートにおいて行い、5 粒子の 520 MeV ⁴⁰Ar¹⁴⁺ を 5 細胞のみに照射した²⁾。対照実験として、HY1 ポートにおいて 520 MeV ⁴⁰Ar¹⁴⁺ のブロードビーム 5 Gy を全体に照射した。照射 3、6 時間後にカバーガラス上の全細胞を回収した後、抗 Akt pS473 特異的抗体、抗 Akt 抗体、抗 COX-2 抗体、抗 NF-κB p65 pS536 特異的抗体、抗 β-actin を用いて western blotting を行った。

まず、昨年度と同様に照射 6 時間後に回収した細胞を用いて、NF-κB 活性化の指標である NF-κB p65 の Ser536 のリン酸化を解析した (Fig. 1)。予想に反し、NF-κB p65 のリン酸化は、照射細胞においてわずかに増加していたが、バイスタンダー細胞では変化は認められなかった。次に、NF-κB p65 のリン酸化がより早い時

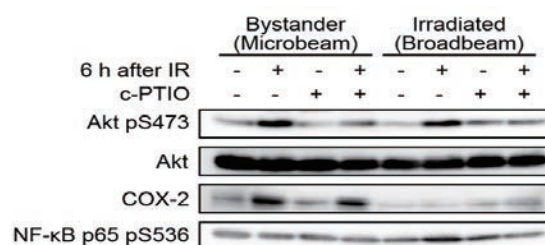


Fig. 1 Phosphorylation of Akt and NF-κB and accumulation of COX-2 in Ar-ion-irradiated or bystander WI-38 cells 6 h after irradiation. IR: Ar-ion irradiation; c-PTIO: carboxy-PTIO (20 μM).

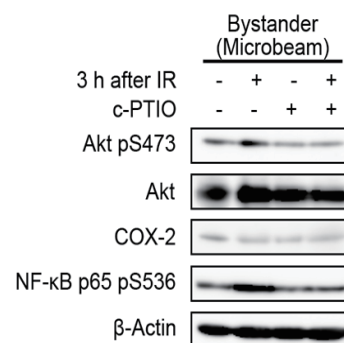


Fig. 2 Phosphorylation of Akt and NF-κB in bystander WI-38 cells 3 h after irradiation.

間に生じている可能性を考え、照射 3 時間後に細胞を回収して解析を行った (Fig. 2)。その結果、NF-κB p65 および Akt のリン酸化がバイスタンダー細胞において増加し、c-PTIO によって抑制されることを見出した。一方、COX-2 には変化は認められなかった。以上の結果から、高 LET 重イオン線によるバイスタンダー応答は、照射細胞から放出された NO により、バイスタンダー細胞において NF-κB、Akt が活性化し、COX-2 を誘導することによって生じることが明らかになった。

References

- 1) H. Matsumoto et al., *Curr. Mol. Pharmacol.* 4 (2011) 126.
- 2) T. Funayama et al., *Radiat. Res.* 163 (2005) 241.

3 - 09 Chromosomal Aberrations Induced by Intercellular Communication Mediated Bystander Effect in Normal Human Fibroblasts Induced by C-, Ne- and Ar-ion Microbeams

M. Suzuki^{a)}, N. Autsavapromporn^{a)}, T. Funayama^{b)}, Y. Yokota^{b)}, Y. Mutou^{b)}, H. Ikeda^{b)}, Y. Kobayashi^{b)} and T. Murakami^{a)}

^{a)}Research Center for Charged Particle Therapy, NIRS,

^{b)}Medical and Biotechnological Application Division, QuBS, JAEA

We have been studying the radiation-quality dependent bystander effects using heavy-ion microbeams with different ion species. Our data suggest that the bystander cell-killing effect via gap-junction mediated cell-cell communication was induced by carbon ions, but not neon and argon ions¹⁾. We must detect the lethal damage in DNA/chromosome levels induced by the bystander effect as a reproductive cell death, but still unclear what kinds of damage induce by the bystander effect in DNA/chromosome levels, relating to the cellular effects such as cell death or mutation. This year we examined micronucleus formation, which is the primary indicator of chromosomal damage, induced by the bystander effect via either gap-junction mediated cell-cell communication or secreted factor(s) to culture medium from the irradiated cells using the heavy-ion microbeams.

Normal human skin fibroblasts obtained from the Riken BioResource Center in Japan were irradiated with C-ion ($^{12}\text{C}^{5+}$ 220 MeV), Ne-ion ($^{20}\text{Ne}^{7+}$ 260 MeV) or Ar-ion ($^{40}\text{Ar}^{13+}$ 460 MeV) microbeams at the HZ1 port. Approximately 6×10^5 exponentially growing cells were inoculated into each of microbeam dish, which was made of acrylic resin ring with 36 mm diameter and attached 7.5 μm -thick polyimide film on the bottom of the ring, 2 days before the microbeam irradiation. In order to block up cell-cell communication, half of the sample dishes were treated with 18- α -glycyrrhetic acid (AGA), which was a specific inhibitor of gap-junction mediated cell-cell communication, 30 min prior to irradiations. Irradiations were carried out using the 256 (16 \times 16) - cross-stripe irradiation method described in the previous report²⁾. We can estimate that the percentage of direct irradiated cells by the microbeams in the 256-cross-stripe irradiation method is around 0.04% of total cells on the dish, when comparing to areas of the cell and the dish. The values of linear energy transfer (LET) at the sample position were estimated to be 103 keV/ μm for C ions, 380 keV/ μm for Ne ions and 1,260 keV/ μm for Ar ions, respectively. The beam size of each ion microbeam was 20 μm in diameter and the irradiations in each point were carried out to deliver 16 ions for carbon, 4 ions for neon and single ion for argon in order to lead an equivalent dose of 0.6-0.8 Gy. The fraction of micronucleated cells was examined using the cytokinesis block technique. Briefly, after irradiation cells were subcultured at the density of $\sim 3 \times 10^4$ cells per chamber flask and allowed to grow in the presence of 2 $\mu\text{g}/\text{mL}$ cytochalasin B for 72 h incubation at 37 $^\circ\text{C}$, which

treatment was not toxic to the cells. Then the cells were rinsed in PBS, fixed in ethanol, stained with Hoechst 33342 solution (1 $\mu\text{g}/\text{mL}$ in PBS) and observed under a fluorescence microscope. At least 500 cells were examined for each data point, and only micronuclei in binucleated cells were detected as a damaged cell.

Figure 1 shows the formation of micronuclei induced by carbon-, neon- and argon-ion microbeams. In any ion species, the formation of micronuclei in the absence of AGA is higher than that in the presence of AGA. The percentage of the formation of micronuclei was 4-6% in the absence of AGA, while 2-4% in the presence of AGA. The results shown in Fig. 1 were beyond our expectation, because only 0.04% of total cells in the dish was directly irradiated with the microbeams. This is clear evidence that bystander effect occurred in radio-biological effects at DNA/chromosome levels. Our data suggests that two different mechanisms play a critical role in inducing bystander effect, such as gap-junction mediated cell-cell communication in the case of the absence of AGA and secreted factor(s) to culture medium from the irradiated cells in the case of the presence of AGA.

References

- 1) M. Suzuki et al., JAEA Takasaki Annu. Rep. 2010 (2012) 72.
- 2) M. Suzuki et al., JAEA Takasaki Annu. Rep. 2006 (2008) 107.

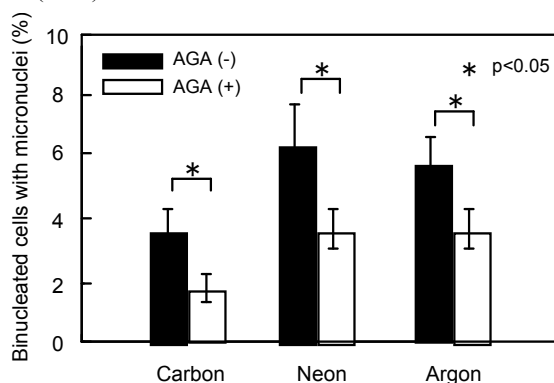


Fig. 1 The formation of micronuclei in normal human fibroblasts irradiated with C-, Ne- and Ar-ion microbeams. The irradiations in each point of the 256-cross-stripe irradiation method were carried out to deliver 16 ions for carbon, 4 ions for neon and single ion for argon. The results were the means and standard deviations from the 3 independent beam times.

3 - 10 Analysis of Bystander Effect Induced by Cell Membrane Response in Glioma Cells

S. Wada^{a)}, M. Yamamoto^{a)}, A. Yoshikubo^{a)}, T. Kakizaki^{a)}, T. Funayama^{b)}, T. Sakashita^{b)}, Y. Yokota^{b)}, Y. Kobayashi^{b)} and N. Ito^{a)}

^{a)} Department of Veterinary Medicine, Kitasato University,

^{b)} Medical and Biotechnological Application Division, QuBS, JAEA

So far, we clarified that low dose ion beam irradiation induced cell killing by bystander effect mediated-secreted factor. This phenomenon was related with sphingomyelinase (SMase). In this study we analyzed relationship between bystander effect and SMase in detail. In medium change experiment, cell killing by bystander effect was induced on the recipient cells treated by siRNA of SMase. On the other hand, this effect was completely inhibited when donor cells were treated by siRNA of SMase. This result indicates that soluble factor was secreted from donor cells by cellular membrane response that mediated by SMase.

1. はじめに

これまでに低線量炭素線照射によって得られる生存率は、高線量域の生存曲線から外挿することによって計算される低線量域での生存率よりも低い値を示し、低線量炭素線照射は高い細胞致死効果を誘導することを明らかにしてきた。また、この低線量炭素線照射による細胞致死効果の増強のメカニズムにはバイスタンダー効果の寄与が大きく、特に、照射された細胞から何らかの液性因子が分泌され、非照射細胞はこの液性因子の作用によって細胞死が誘導されることを明らかにしてきた。さらに、この液性因子による細胞致死効果には細胞膜応答分子であるスフィンゴミエリナーゼが関することも明らかにし、X線および炭素線照射によるバイスタンダー効果誘導には細胞膜応答が引き金となることが示唆され、細胞膜が放射線による細胞応答の重要なターゲットであると考えられた。

しかしながら、この細胞膜応答分子であるスフィンゴミエリナーゼがバイスタンダー効果誘導機構にどのように関与するかは詳細には明らかにされていない。そこで、本研究では、バイスタンダー効果誘導にどこでスフィンゴミエリナーゼが関与するか検討するため、スフィンゴミエリナーゼノックダウン細胞を用いて、バイスタンダー効果による細胞致死効果を解析した。

2. 実験方法

グリオーマ細胞 (A172 細胞) を用い、X線 6 Gy を照射し、細胞外放出因子による細胞致死効果を解析するため、照射 1 時間培養後に照射細胞の培養上清のみを回収し、非照射細胞に添加し 1 時間培養後に Colony formation assay を用いて、細胞致死効果を算出した (培養液交換実験)。細胞外放出因子による細胞致死効果のスフィンゴミエリナーゼの関与を解析するため、siRNA 法を用いてスフィンゴミエリナーゼノックダウン細胞を作成した。この細胞を用いて下記の条件によってバイスタンダー効果による細胞致死効果を解析した。

- ①非照射細胞の培養液を非照射細胞に添加。
- ②照射細胞の培養上清を非照射細胞に添加。
- ③スフィンゴミエリナーゼノックダウン細胞に照射後、その培養上清をスフィンゴミエリナーゼノックダウン細胞に添加。
- ④スフィンゴミエリナーゼノックダウン細胞に照射後、培養上清を非照射細胞 (ノックダウン非処

理) に添加。

⑤照射細胞 (ノックダウン非処理) の培養液をスフィンゴミエリナーゼノックダウン細胞に添加。

3. 結果および考察

Figure 1 はスフィンゴミエリナーゼノックダウン細胞を用いて X線 6 Gy 照射後に培地交換実験によるバイスタンダー効果の細胞致死効果を表している。②の条件下で生存率の低下が観察され、X線照射による液性因子を介したバイスタンダー効果が確認された。③の条件下ではバイスタンダー効果によって観察された細胞死効果が抑制され、生存率がコントロールレベルまで回復し、バイスタンダー効果による細胞致死誘導にはスフィンゴミエリナーゼが関与すると考えられた。④の条件下でも生存率はコントロールレベルであることが観察され、バイスタンダー効果誘導には照射を受ける細胞にスフィンゴミエリナーゼが必要であると考えられた。⑤の条件下では生存率の低下が観察され、②の条件で得られた生存率と同程度の値を示し、バイスタンダー効果による細胞致死効果が観察された。つまり、バイスタンダー効果誘導では照射される細胞にはスフィンゴミエリナーゼが不可欠であるが、液性因子の作用を受けるバイスタンダー細胞にはスフィンゴミエリナーゼが必須ではないと考えられた。

これらのことから、照射をうけた細胞がスフィンゴミエリナーゼの作用による細胞膜応答を介してバイスタンダー効果を誘導する液性因子を細胞外に分泌することが示唆された。

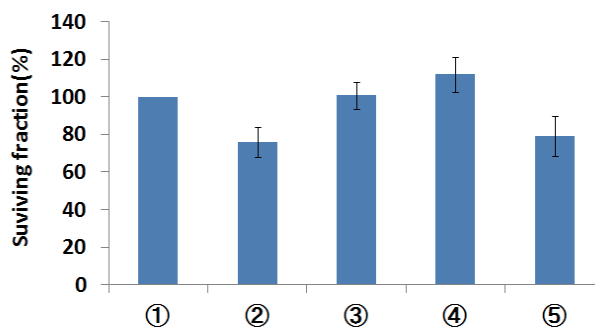


Fig. 1 Killing effect of medium change from irradiated culture cells.

3 - 11 Ion Beam Irradiation Has Different Influences on the Expression of Bcl-2 in Cultured Human Retinal Vascular Endothelial Cells Exposed to L-dopa among ^{20}Ne , ^{12}C , and ^4He

K. Akeo^{a, b)}, T. Funayama^{c)}, Y. Kobayashi^{c)} and Y. Akeo^{a)}

^{a)} Akeo Eye Clinic, ^{b)} Keio University School of Medicine,

^{c)} Medical and Biotechnological Application Division, QuBS, JAEA

Bcl-2 (B-cell lymphoma 2) is the founding member of the Bcl-2 family of apoptosis regulator protein encoded by the BCL2 gene¹⁾. These proteins govern mitochondrial outer membrane permeabilization and can be either pro-apoptotic or anti-apoptotic including Bcl-2 proper. The increase of outer mitochondrial membrane permeability (MMP) is a central event in apoptotic cell death, since it releases several apoptogenic factors such as cytochrome c into the cytoplasm that activate the downstream destructive processes. The voltage-dependent anion channel (VDAC) plays an essential role in the increase of MMP, and is regulated by the Bcl-2 family of proteins via direct interaction. Anti-apoptotic Bcl-2 family members close the VDAC, whereas some pro-apoptotic members interact with the VDAC to generate a protein-conducting channel through which cytochrome c can pass²⁾. Faucher et al. measured the expression of two Bcl-2 family members, Bax and Bcl-2, in a human endothelial like cell-line overexpressing the organic hydroperoxide-scavenging enzyme GPx, in the absence of any apoptotic/oxidant stimulus, and showed that overexpressing an antioxidant gene such as GPx in endothelial cells is able to change the basal mRNA and protein Bax levels without affecting those of p53 and Bcl-2. This phenomenon could be useful to antiatherogenic therapies which use antioxidants with the aim of protecting the vascular wall against oxidative stress injury³⁾. Deficiency of L-dopa causes degeneration of the substantia nigra in the brain and L-dopa is used in the treatment of Parkinson's disease. We proved that L-dopa produced NO and superoxide, and had the cytotoxic effects on the retinal pigment epithelial cells⁴⁾. The irradiation has the direct influence that it ionizes the important molecules such as DNA, and the indirect influence that it has the effects on H₂O or induces free radicals (O₂⁻, HO·) with high reactivity. These radicals react to the important molecules. GPx3, a plasma antioxidant enzyme, maintains genomic integrity by inactivating these reactive oxygen species, known DNA-damaging agents⁵⁾.

We previously reported that exposure to L-dopa inhibited the expression of GPx3 in human RE cells in vitro⁶⁾. Ion beam irradiations both of He and C decreased GPx3 more remarkably than Ne. The expression of GPx3 incubated with L-dopa decreased significantly after 8 h of irradiation to He, and after 4 and 24 h in case of C. On the contrary, the irradiation of Ne increased the expression of GPx3 incubated with L-dopa after 4 h of the exposure of the irradiation significantly. However, the expression of p53 was not significantly influenced by only exposure to L-dopa,

but increased just after the irradiation both of Ne and He in those cells incubated with L-dopa⁷⁾. Ion beam irradiation caused the induction of apoptosis in RE cells that affected by inactivating the reactive oxygen species because of exposure to L-dopa. We investigated how L-dopa influenced the expression of anti-apoptotic Bcl-2 genes in RE cells. We applied the ion beams as the induction of the oxidative stress that might influenced this anti-apoptotic Bcl-2 gene, and measured the expression using a real time-reverse-transcriptase polymerase chain reaction (RT-PCR).

Human RE cells incubated with L-dopa were exposed to an ionization radiation (350 MeV Ne, 220 MeV C, and 50 MeV He). We obtained the cells after of the irradiation and extracted total cellular RNA and cDNA was synthesized. We designed the primers for RT-PCR amplification of the cDNA of Bcl-2. The reactions were carried out at the following temperature: 95 °C, for denaturation; 60 °C, for annealing; and 72 °C. After mixing the cDNA, primer, and SYBR green, the expression of 18S RNA and Bcl-2 was measured using the LightCycler system as RT-PCR. The technology of this system is extremely innovative and enables rapid and simultaneous evaluation PCR experiments. Fluorometric analysis of the formed PCR products was performed as a real-time measurement either continuously or at specifically defined time points during each PCR cycle.

There were no significant differences of Bcl-2 gene expression among the irradiation of Ne, C, and He. However, exposure to L-dopa significantly inhibited the expression of Bcl-2 in human RE cells in vitro. The expression of Bcl-2 in RE cells incubated with L-dopa decreased significantly after 8 h in case of C. L-dopa damaged the expression of Bcl-2 gene inhibiting apoptosis in mitochondria. We considered the different accumulation of the energy irradiated at a point by various ions could be concerned with the effects on the expression Bcl-2 in RE cells incubated with L-dopa as well as GPx3 or p53.

References

- 1) Y. Tsujimoto et al., Science. 228(1985) 1440.
- 2) Y. Tsujimoto et al., Biochimie. 84(2002) 187.
- 3) K. Faucher et al., Mol. Cell Biochem. 277 (2005) 81.
- 4) K. Akeo et al., Pigment Cell Res. 13 (2000) 80.
- 5) B. Chen et al., Cancer Lett. 309(2011)37.
- 6) K. Akeo et al., JAEA Takasaki Annu. Rep. 2006 (2008) 108.
- 7) K. Akeo et al., JAEA Takasaki Annu. Rep. 2009 (2011) 95.

3 - 12 Ionizing Radiation Alters the Dynamics of Human Long Interspersed Nuclear Elements 1 (LINE1) Retrotransposon

A. Tanaka^{a)}, Y. Nakatani^{a)}, N. Hamada^{b)}, A. Jinno-Oue^{a)}, N. Shimizu^{a)}, S. Wada^{c)}, T. Funayama^{d)}, T. Mori^{a)}, S. Islam^{a)}, S. A. Hoque^{a)}, M. Shinagawa^{e)}, T. Ohtsuki^{f)}, Y. Kobayashi^{d)} and H. Hoshino^{a)}

^{a)} Gunma University Graduate School of Medicine, ^{b)} Nuclear Technology Research Laboratory, Central Research Institute of Electric Power Industry, ^{c)} Kitasato University School of Veterinary Medicine, ^{d)} Medical and Biotechnological Application Division, QuBS, JAEA, ^{e)} Institute for Genetic Medicine, Hokkaido University, ^{f)} Department of Microbiology and Cell Biology, Tokyo Metropolitan Institute of Medical Science

It is important to identify the mechanism by which ionizing radiation induces various genomic alterations in the progeny of surviving cells¹⁻³⁾. Ionizing radiation activates mobile elements like retrotransposons^{4, 5)}, although the mechanism of its phenomena consisting of transcriptions and insertions of the products into new sites of the genome remains unclear. In this study, we analyzed the effects of sparsely ionizing X-rays and densely ionizing carbon-ion beams on the activities of a family of active retrotransposons, long interspersed nuclear elements 1 (L1). We used the L1/reporter knock-in human glioma cell line, NP-2/L1RP enhanced GFP (EGFP), that harbours full-length L1 tagged with EGFP retrotransposition detection cassette (L1RPEGFP) in the chromosomal DNA (Fig. 1). X-rays and carbon-ion beams similarly increased frequencies the transcription from L1RP-EGFP and its retrotransposition (Fig. 2).

Short-sized de novo L1RP-EGFP insertions with 5'-truncation were induced by X-rays, while full-length or long-sized insertions (> 5 kb, containing ORF1 and ORF2) were found only in cell clones irradiated by the carbon-ion beams (Fig. 3). These data suggest that X-rays and carbon-ion beams induce different length of de novo L1 insertions, respectively. Our findings thus highlight the necessity to investigate the mechanisms of mutations caused by transposable elements by ionizing radiation.

References

- 1) W. F. Morgan et al., Radiat. Res. (1996) 146.
- 2) K. Suzuki et al., Oncogene (2003) 22.
- 3) M. A. Kadhim et al., Nature (1992) 355.
- 4) J. F. Morales et al., Mutagenesis. (2003) 18.
- 5) E. A. Farkash et al., Nucleic Acids Res. (2006) 34.

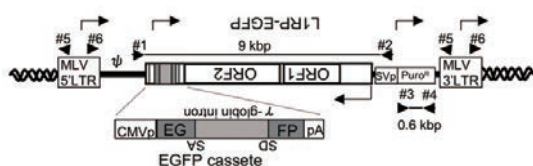


Fig. 1 Schematic diagram of an integrated pMX-L1RP-EGFP vector and locations of primers used for PCR analysis. Arrows indicate orientations of the transcription.

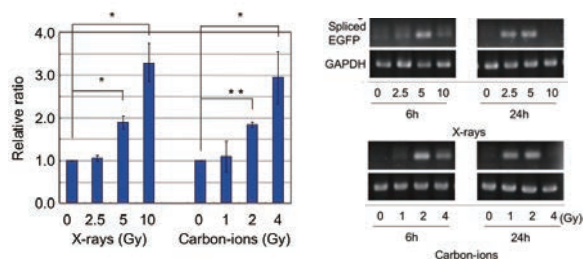


Fig. 2 Effect of irradiation on retrotransposition (A) and L1RP-EGFP RNA transcription (B).

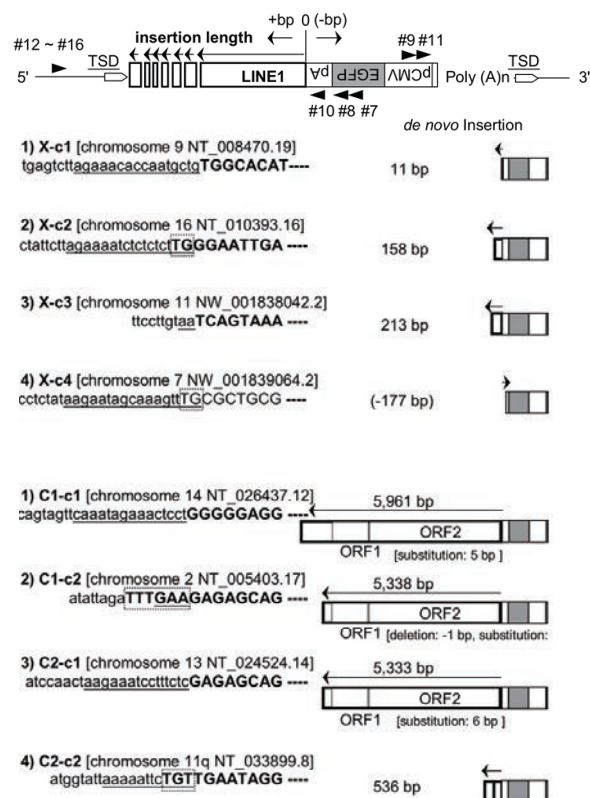


Fig. 3 Structure of retrotransposed L1RP-EGFP.

3 - 13 Degradation of Nucleus in the Heavy-ion Irradiated Silkworm Egg just after Having Reached the Peripheral Region of the Egg

K. Shirai^{a)}, C. Xu^{a)}, T. Funayama^{b)}, T. Sakashita^{b)}, Y. Yokota^{b)},
Y. Kobayashi^{b)} and K. Kiguchi^{a)}

^{a)} Faculty of Textile Science and Technology, Shinshu University,

^{b)} Medical and Biotechnological Application Division, QuBS, JAEA

The carbon ion (10 Gy) irradiated silkworm eggs can restart their development after short time delay for damage repair. However, the radiation-induced damage is not repaired perfectly. So, about 60% of the irradiated eggs stopped their development before the germ band formation. In this report, we investigate the fate of nuclei in the heavy-ion irradiated silkworm egg after restart the development.

In non-irradiated egg, the fertilized nuclei proliferated and migrate to the peripheral region of egg. Then almost all nuclei have reached the peripheral of the egg at 12 h after oviposition. Then cell division was also observed. On the other hand the heavy-ion irradiated nuclei also proliferated and migrate to the peripheral region of egg after 2 h delay. However, in the some eggs, the damaged nuclei disappeared at 14 h after oviposition. These results indicate the damaged nucleus would degrade just after having reached the peripheral region of the egg.

著者らは、昨年度の報告において、カイコ卵に 10 Gy の炭素イオンを照射した場合、約 2 時間の受精核の分裂停止後、すぐに発生（分裂）を再開することを報告した。しかしその一方で、分裂を再開した卵のほとんどが孵化することなく、途中で発生を停止することも明らかになった。今年度の研究では、致死卵全体の約 6 割を占める胚帯形成前に発生停止した卵に着目した。

これらの卵では調べた限りほぼ全ての卵で核分裂を再開するものの、漿液膜の着色以前に発生を停止する。その後、飼育環境下で長期間保護しても発生は進行しない。よって、これらの照射卵はどこかの段階で致死していることは明らかである。一方、哺乳類細胞への重イオンビームを含む放射線の照射では、しばしば細胞の増殖死が認められる。照射卵の外観からは発生の停止は確認できるものの、核または細胞が増殖死、すなわち細胞は生きた状態で留まっているのか、既に致死しているのか不明である。また、増殖を停止している場合は、障害修復は行われているのかなど疑問が生じる。本研究では、これら疑問に答える目的で、照射卵の分裂再開後の核の移動と運命を、凍結切片を作製し DAPI 染色することで調査した。

カイコ卵では発生当初、細胞分裂を伴わない核分裂のみが 1 時間に一回という割合で起こり、核は増殖しながら卵周辺（周辺細胞質）へ向かって移動する。そして産下約 12 時間後、分裂核は卵後端の周辺細胞質に到達し、ほぼ全ての場所で細胞化が認められる (Fig. 1A)。

一方、産下 8 時間後の照射卵では分裂核が分裂しながら周辺に移動する様子が観察された（データ省略）。上述のとおり、発生が 2 時間程度遅延するため、観察された核の数は非照射卵と比較して少なかった。さらに産下 12 時間後、観察された核の数は少なく、わずかであった（データ省略）。最後に産下 14 時間後の卵では、卵内には一部を除き核は観察されなくなった (Fig. 1B)。

以上、本研究の結果、照射卵の幾つかは周辺細胞質に到達した核や、その後に起こる細胞化が観

察されなかった。当初、周辺細胞質に到達した核が、その後発生を停止したままで留まることも考えられたが、この結果はこの仮説を否定する。すなわち照射により障害を受けた核が周辺細胞質に到達する前後に崩壊することを示唆する。

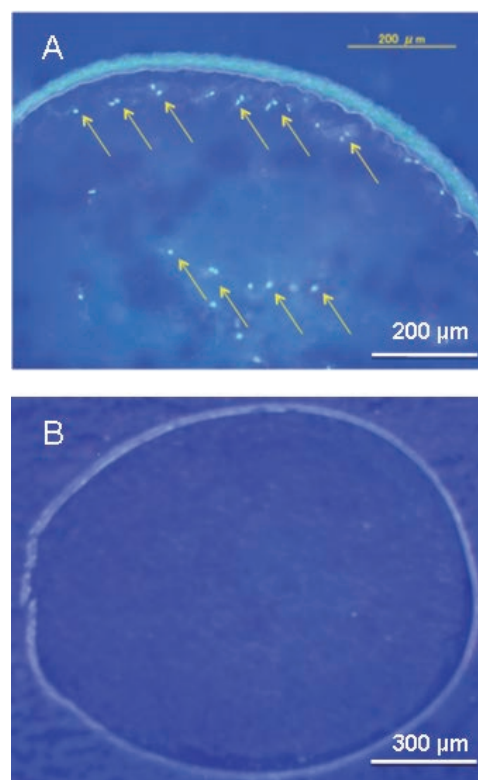


Fig. 1 Disappearance of nuclei of the heavy-ion irradiated silkworm eggs at cellular blastoderm stage. The nuclei in the silkworm egg were detected by DAPI staining. (A) The nuclei of the normal (non-irradiated) eggs at 12 h after oviposition. (B) The heavy-ion irradiated silkworm eggs. The nucleus was not observed in the eggs.

3 - 14 Neurocytotoxic Effects of Micro-beam Irradiation of Heavy Carbon-ions on the Developing Medaka Brain Measured in vivo

T. Yasuda^{a)}, Y. Hibi^{a)}, T. Funayama^{b)}, Y. Yokota^{b)}, Y. Mutou^{b)}, H. Ikeda^{b)},
Y. Kobayashi^{b)}, S. Oda^{a)} and H. Mitani^{a)}

^{a)} Graduated School of Frontier Sciences, The University of Tokyo,

^{b)} Medical and Biotechnological Application Division, QuBS, JAEA

Our previous studies showed, by staining with acridine orange (AO), that the developing brain of medaka embryos (stage 28) after exposure to gamma-rays or heavy-ions exhibited transient radiation-induced apoptosis in the marginal proliferating regions in the optic tectum (OT). In this present study, the local irradiation (diameters of 250 μm) with carbon-ion beam was applied with the following three patterns. First, the right hemisphere of OT was irradiated. Second, both hemispheres were irradiated. Third, only a center region of OT was irradiated. Our present results showed that AO-positive radiation-induced apoptosis was observed at irradiated regions of OT hemisphere at 24 hours after irradiation. However, when center region connecting hemispheres were irradiated, AO-positive apoptosis was observed not only at the irradiated region but also at all over the embryonic body, including the tail region. These finding suggests that an indirect apoptosis could be induced when the center region of OT was irradiated.

メダカ胚は体外で発生し、かつ卵殻が透明なので発生全過程を観察できる利点を有する実験材料である。またメダカ胚の脳発生は、基本的に哺乳類のそれらと同様であることが示されている。メダカ胚は哺乳類と比較して脳が小さく whole-mount のまま観察をすることが可能である。そこでメダカをモデル生物に用いて、胚の中脳で起こる放射線誘発アポトーシスをアクリジンオレンジ染色により観察を行ってきた。本実験では、メダカ後期胚期に炭素線ブロードビーム 10 Gy 照射 24 時間後の放射線誘発アポトーシスをアクリジンオレンジ染色後蛍光顕微鏡 G 領域で調べ、ガンマ線 10 Gy 照射 24 時間後の影響と比較し、線質の違いによるアポトーシス発生の様相の違いを調べた。実験には、Hd-rR 近交系メダカ胚、器官形成期直後の後期胚期(発生ステージ 28)を実験に用いた。 γ 線照射は東大・生命棟の¹³⁷Cs γ セル、線量率 10 Gy/min(室温)の条件下で照射した。炭素線は、TIARA の照射施設において、ブロードビームで 10 Gy 照射を行った。その結果、炭素線照射、 γ 線照射、共に視蓋周辺部位に特徴的なアポトーシス細胞の塊 (Fig. 1 矢印) が認められ、線質の違いによるアポトーシス発生様相はほぼ同様であった。炭素線照射胚ではこの特徴的なアポトーシス細胞の塊が γ 線照射胚よりも大きくて、それらの数も多かった (Fig. 1 矢印)。

一方、炭素線照射、 γ 線照射、共に視蓋周辺部位に特徴的なアポトーシス細胞の塊が認められ、線質の違いによるアポトーシス発生様相はほぼ同様であった。

さらに、炭素線マイクロビーム(ϕ 250 μm)で、1) 中脳の右側 1 回、2) 中脳の右と左両側 1 回ずつ計 2 回、3) 脳の中央部 1 回、3 パターンの照射を行い、照射 24 時間後に発生するアポトーシスを AO 染色により観察した。その結果、1)、2) の照射パターンでは照射野にほぼ一致した部位に放射線誘発アポトーシスが観察されたが、3) 脳の中央部のマイクロビーム照射では、照射部位以外の脳、及び胚体全部に放射線誘発アポトーシスが観察され、照射野と放射線誘発アポトーシスが起きた部位の不一致が認められた (Fig. 2)。

これらの結果、TIARA のマイクロビーム照射が、メダカ胚の脳の狙った部位へ局所的に照射することが可能であること、さらに脳の中央部のみの照射では照射野以外の部位へ影響を及ぼすことが示された。

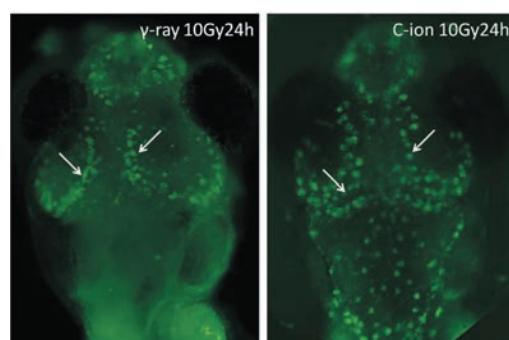


Fig. 1 Radiation-induced apoptosis by AO-staining in embryos irradiated with γ -rays and C-ions. White arrows show AO-positive aggregated apoptotic cells.

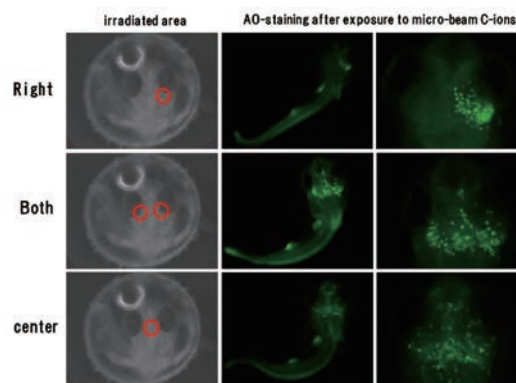


Fig. 2 AO-positive radiation-induced apoptosis was observed at irradiated regions of OT hemisphere at 24 hours after irradiation. However, when center region connecting hemispheres were irradiated, AO-positive apoptosis was observed not only at the irradiated region but also at all over the embryonic body, including the tail region.

3 - 15

Wide Overlap in Gene Expression Response to Desiccation and Ionizing Radiation in the Sleeping Chironomid Larvae

O. Gusev^{a, c)}, K. Mukae^{a)}, T. Kikawada^{a)}, T. Sakashita^{b)}, T. Funayama^{b)},
Y. Kobayashi^{b)} and T. Okuda^{a)}

^{a)} Anhydrobiosis Research Group, National Institute of Agrobiological Sciences,

^{b)} Medical and Biotechnological Application Division, QuBS, JAEA,

^{c)} Department of Invertebrate Zoology, Kazan Federal University

The Sleeping Chironomid, *Polypedium vanderplanki* can stand complete desiccation (anhydrobiosis) and also shows radio-resistance. We have recently showed that a link between anhydrobiosis and radio-resistance could be clarified by analyzing the DNA damaging effect of both desiccation and irradiation¹⁾. In the present study, by using microarrays build on the basis of *P. vanderplanki* EST database, we conducted genome-wide analysis of gene expression response to two types of ionizing radiation and desiccation.

Based on the observation that ⁴He (LET_w=16.2 keV/μm) ion beam (70 Gy) inflicts a similar damage on nuclear DNA damage occurred in normal anhydrobiotic chironomid larvae¹⁾, we compared effect of 70 Gy of gamma-rays, 70 Gy of ⁴He ions and desiccation on genome-wide mRNA expression in the larvae. The irradiation, desiccation and extraction of mRNA from the larvae were conducted as described earlier^{1,2)}.

Custom microarrays for *P. vanderplanki* (4×44k format) were prepared by Agilent Technologies Japan. Probe design for the microarrays was performed with a web-based application, eArray (Agilent) using 16,652 clones selected from Pv-EST database²⁾. All other experiments were carried out according to manufacture's manual (Agilent). Briefly, labeled cRNAs were used for hybridization using the *in situ* hybridization kit plus (Agilent Technologies). Arrays were incubated at 65 °C for 17 h in Agilent's microarray hybridization chamber. After hybridization, arrays were washed according to the Agilent protocol.

The normalized results of expression of 16652 cDNA probes were further filtered by Principle Components Analysis (PCA) and minimum up-regulation of x4 fold (compared with unstressed larvae) was defined as a threshold for definition as "up-regulated genes". We found that gamma- or ⁴He-irradiation and desiccation significantly altered gene expression in the larvae and that 553, 394 and 2,077 clones are up-regulated by these treatments, respectively (Fig. 1). The desiccation was the strongest factor affected the gene expression. Surprisingly, there was a major overlap in gene expression in the larvae stressed with radiation and desiccation. In total 43% of transcripts up-regulated by gamma irradiation and 52% of transcripts up-regulated by ⁴He were also responsive to desiccation (Fig. 1). Finally, 108 transcripts were up-regulated in all

three groups of larvae. We have further conducted transcripts scaffolding and annotation and found that the overlapped in all three groups highly upregulated transcripts represent 51 unique genes (data, not shown). The major gene groups included: long non-coding DNA (16 genes), unknown proteins (12 genes), LEA proteins (8 genes), antioxidants (6 genes), members of protein and DNA folding and reparation networks (6 genes).

Taking together, our data suggest that apart from clear similarities in nucleic acid damaging effect of desiccation and ionizing radiation, the enhanced radioresistance of the sleeping chironomid could be due to the similar regulatory pathways controlling the larvae mRNA expression in response to these stresses. Moreover, we found that the post-irradiation response in the larvae involve genes indispensable for successful anhydrobiosis, thus, involvement of the desiccation resistance in *P. vanderplanki* might be a natural factor of gradual increase of radioresistance in this species of insects.

References

- 1) O. Gusev et al., PLoS ONE. 5 (11) (2010) e140008.
- 2) R. Cornette et al., J. Biol. Chem. 285 (46) (2010) 35889-99.

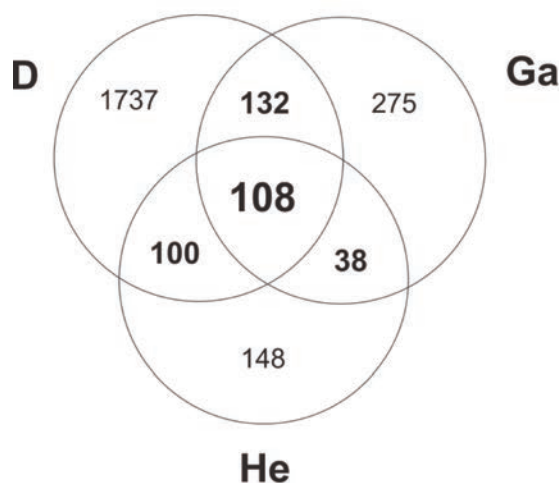


Fig. 1 Overlap in gene expression in the larvae subjected to desiccation (D), gamma irradiation (Ga) and ⁴He ions irradiation (He). Only highly up-regulated genes (more than 4 fold mRNA expression increase) were included in the analysis.

3 - 16 The Effects of THP-1 Macrophages on the Migration of Heavy-ion Irradiated Human Lung Cancer Cells

Y. Mutou-Yoshihara, T. Funayama, Y. Yokota, T. Sakashita, M. Suzuki, H. Ikeda and Y. Kobayashi

Medical and Biotechnological Application Division, QuBS, JAEA

Introduction

Heavy-ion cancer therapy has been shown to provide good treatment outcomes for patients with a various types of solid tumors¹⁾. However, it is difficult to remove all the cancer cells completely with heavy-ion cancer therapy, and the remaining cancer cell run a risk of metastasis. Immune cells accumulate around and inside the tumors, but the effects of the immune cells on the irradiated cancer cells have not been examined. In this study, we cocultured the heavy-ion irradiated lung cancer cells with immune cells and investigated the changes in migration of lung cancer cells.

Materials and methods

Human lung cancer cells (H1299/neo cells) were exposed to 2 Gy of carbon-ion broad-beam (LET=108 keV/μm), then cocultured with immune cells (THP-1 macrophage), and detected by on cytotoxicity. To determine the changes of cell migration of H1299/neo cells, the irradiated H1299/neo cells were cultured with the supernatant of THP-1 macrophages for 24 h incubation and observed by fluorescence microscope. The production of migration stimulating cytokines, tumor necrosis factor (TNF)-α and interleukin (IL)-8^{2,3)}, of THP-1 macrophages were examined using enzyme-linked immunosorbent assays (ELISA)⁴⁾.

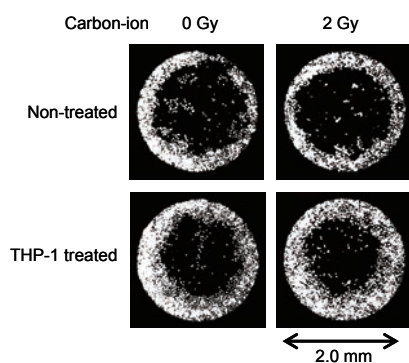


Fig. 1 Effects of THP-1 macrophages on cell migration of H1299/neo cells with heavy-ion irradiation. Fluorescently-labeled H1299/neo cells were exposed to carbon-ion beams (0 and 2 Gy), seeded into 96-well plate with cell seeding stopper, and cultured in RPMI culture medium for 24 h at 37 °C. The cell seeding stoppers were removed, and fluorescently-labeled H1299/neo cells (in a 96-well plate) were cultured with the supernatant of THP-1 macrophages for 24 h incubation. After paraformaldehyde fix, the changes of cell migration of H1299/neo cells (white dot) were observed by fluorescence microscope.

Results

While cells were irradiated with 2 Gy that hardly affect on cytotoxicity of H1299/neo cells (data not shown), the cellular morphology of H1299/neo cells changed by co-culture with THP-1 macrophages, and the cell migration of H1299/neo cells significantly increased (Fig. 1). In addition, the levels of cytokine (IL-8 and TNF-α) production under co-culture conditions elevated in 2 Gy irradiated H1299/neo cells compared with that in non-irradiated H1299/neo cells (Fig. 2).

Conclusions

These results suggested that THP-1 macrophages activate cell migration of H1299/neo with or without heavy-ion irradiation by migration stimulating cytokines. Because the production of these cytokines elevated in 2 Gy irradiated H1299/neo cells, heavy-ion beam may be involved in the increase of cell migration.

References

- 1) K. Ando and Y. Kase, Int. J. Radiat. Biol. 85 (2009) 715.
- 2) S. W. Kim et al., Cancer Res. 65 (2005) 8784.
- 3) E. M. Rosen et al., Cancer Res. 51 (1991) 5315.
- 4) Y. Mutou et al., J. H. S. 56 (2010) 675.

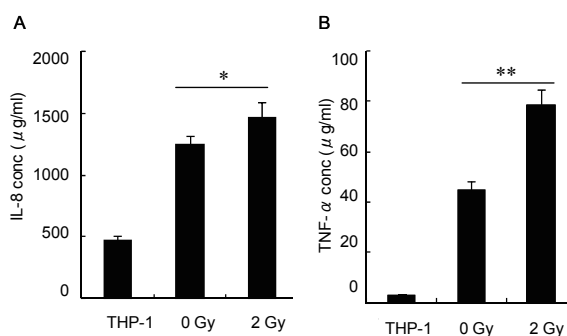


Fig. 2 Effects of heavy-ion irradiation on IL-8 and TNF-α production in H1299/neo. H1299/neo cells were exposed to carbon-ion beams (0 and 2 Gy), seeded into six-well plate, and cultured in RPMI culture medium for 24 h at 37 °C. Then, H1299/neo cells (in a six-well plate) were cocultured with THP-1 macrophages (upper inserts) in RPMI culture medium for 24 h at 37 °C. Each value represents the mean ± S.D. of triplicate cultures. **p* < 0.05 and ***p* < 0.005; significantly different from the non-treated cell in each groups (0 and 2 Gy).

3 - 17 **Effects of Carbon-ion Microbeam Irradiation on Locomotion in *Caenorhabditis elegans***

M. Suzuki^{a)}, Y. Hattori^{a, b)}, T. Sakashita^{a)}, T. Funayama^{a)}, Y. Yokota^{a)},
Y. Mutou-Yoshihara^{a)}, H. Ikeda^{a, c)} and Y. Kobayashi^{a, c)}

^{a)} Medical and Biotechnological Application Division, QuBS, JAEA,
^{b)} Graduate School of Engineering, Hiroshima University,
^{c)} Gunma University Graduate School of Medicine

Introduction

The nematode *Caenorhabditis elegans* is a good *in vivo* model system to examine radiobiological effects at behavioral level. We recently reported that locomotion (whole-body movement) using body-wall muscles was reduced after broad-beam irradiation^{1),2)}. However, it is not known whether the same effects are observed in the animals irradiated to a very limited region. In this study, we examined the region specific effects of radiation on the locomotion in *C. elegans*.

Materials and methods

Well-fed adult *C. elegans* were used in the experiments. To investigate the effects of irradiation to a very limited region of *C. elegans*, we used energetic carbon ions (¹²C, 18.3 MeV/u, LET = 119 keV/μm) generated by the HZ1 port of TIARA at JAEA. We irradiated to the following three regions of *C. elegans* independently: ‘head’ region around the nerve ring, ‘middle’ region around the bowel, and ‘tail’ region. *C. elegans* was enclosed in a polydimethylsiloxane microfluidic device³⁾ with S-basal buffer to inhibit the whole-body movement during irradiation (Fig. 1) and was irradiated with 12,000 carbon ions corresponding to 500 Gy per 20 μmφ micro-aperture area. To evaluate effects of microbeam irradiation on the locomotion of *C. elegans*, the animal was placed on an agar dish immediately after irradiation and its locomotion was video-recorded. The locomotory rate of the animal was evaluated using ‘body bends’, which is defined as the number of bends in the anterior body region at 20-sec intervals. The control animals were handled with sham manipulation in parallel with the irradiated animals, except for microbeam irradiation.

Results

We irradiated to a certain region (head/ middle/ tail) of *C. elegans* and the effects on the locomotion were evaluated. Microbeam irradiation in each case (to head, middle, and tail regions) decreased *C. elegans*'s locomotion as well as in the case of whole-body broad beam irradiation²⁾, and there were no significant differences in the degrees of the decrease between the irradiation regions (Fig. 2). This suggests that irradiation to very limited region is enough to decrease the locomotion in *C. elegans*. This may relate to the fact that the neural circuit for motor control of whole-body movement exists from the head to

the tail (upper panel in Fig. 2).

To understand the relationship between the radiation effect at behavioral level and the irradiation region in more detail, we will also focus on the pumping motion using pharyngeal muscles whose motor control circuit exists in only the pharynx.

References

- 1) M. Suzuki et al., J. Radiat. Res. 50 (2009) 119-25.
- 2) M. Suzuki et al., JAEA Takasaki Annu. Rep. 2010 (2012) 80.
- 3) Lockery et al., J. Neurophysiol. 99 (2008) 3136-43.

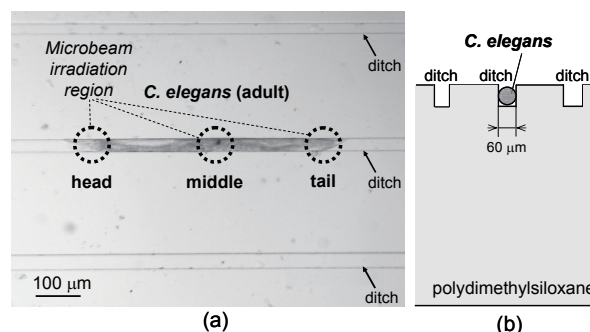


Fig. 1 Microbeam irradiation to a *C. elegans* using a microfluidic device. (a) A *C. elegans* enclosed in a microfluidic device. Dotted circle represents irradiation region. (b) The cross-section view of the microfluidic device.

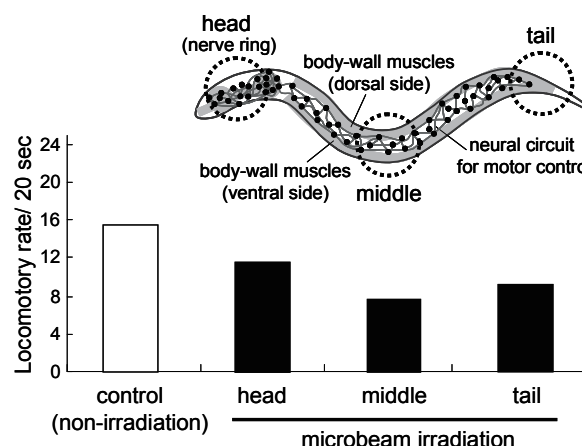


Fig. 2 Effects of carbon-ion microbeam on the locomotion in *C. elegans*. Each bar graph shows the mean locomotory rate of thirty or more animals.

3 - 18 Rapid ESR Measurement of Irradiated Fresh Papaya

M. Kikuchi^{a)}, Y. Shimoyama^{a)}, M. Ukai^{b)} and Y. Kobayashi^{a)}

^{a)} Medical and Biotechnological Application Division, QuBS, JAEA,
^{b)} Hokkaido University of Education

Electron spin resonance spectroscopy (ESR) has been authorized worldwide for irradiated food detection, such as dried spices and dried fruits. ESR detects unpaired electrons of radicals in the irradiated foods. In case of plant-derived dry foods, free radicals caused by radiation are remained in cellulose and crystalline sugars. When fresh fruits that contain water are measured by ESR method, there is difficulty on the water that at normal room temperature disturbs the resonance of unpaired electrons because the dielectric loss of microwave is caused by H₂O. To overcome the water problem, Kikuchi et al.¹⁾ have recently tried to detect radicals of irradiated fresh mangoes using a time-consuming freeze-died technique. One of the main requirements for practical application of the pretreatment is its fast, cheap and unambiguous performance for the ESR method. Then, direct ESR measurement of water-rich fruits was carried out in liquid nitrogen.

ESR spectra of radicals in fresh papaya's flesh were recorded at 77 K after 0 and 3 kGy-irradiation (Fig. 1). A singlet main peak and two side peaks were observed from the irradiated sample. Before irradiation, however, the flesh specimen showed almost ESR silent.

Figure 2 shows the dose response of main and side peaks obtained from the frozen specimen of fresh fleshes of papayas after the γ -irradiation. The main and side peak intensities from papaya flesh increased as increasing doses during 14 days after the irradiation. Therefore, we can distinguish irradiated papayas from non-irradiated ones and may estimate the absorbed doses using the peak intensity of main and side peaks. Although dose responses of the peaks were not so changed within 14 days, those profiles of ESR spectra became ambiguous gradually day by day.

ESR spectra of freeze-dry samples of the fleshes were also recorded on several irradiation doses. The freeze-dry specimens after the irradiation showed a strong main peak and weak side peaks until 14 days after irradiation. Furthermore, when the peak intensity of a dry specimen of the papaya flesh was examined using the side peaks, the dose response showed a linear dose dependency (Fig. 3). The main peak was observed in both irradiated and non-irradiated specimens of the freeze-dried flesh powder and showed no dose dependency (data not shown), suggesting that mechanical radicals are induced through powdering process. Therefore, we got two conclusions from ESR measurement of freeze-dried papaya: one is that irradiated papayas can be distinguished from non-irradiated ones by the presence of side peaks, and the other is that the estimation of absorbed doses is also possible using the intensity of the peaks.

In conclusion of this study, we propose a detection scheme for irradiated fresh papayas. First, a flesh of fresh papaya should be applied to ESR measurement under liquid nitrogen temperature for the screening of irradiation

treatment. If we cannot find any peak of main and side peak regions, the package or container batch of the papayas can be thought to be non-irradiated. If both peaks are detectable in fresh fleshes, we should conclude the papayas were irradiated. If an ESR spectrum of papaya is ambiguous at 77 K, we should try to additional ESR measurement using the freeze-dried specimen of the papaya. This rapid ESR technique is effective to identify fresh fruits as irradiated or non-irradiated²⁾.

References

- 1) M. Kikuchi et al., Spectrochim. Acta A 75 (2010) 310.
- 2) M. Kikuchi et al., Radiat. Phys. Chem. 80 (2011) 664.

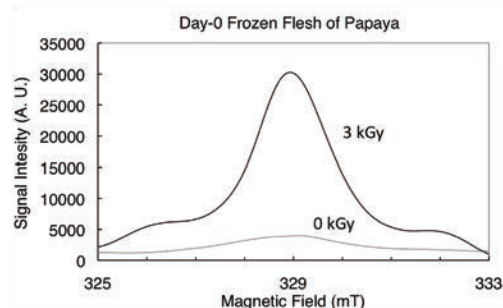


Fig. 1 ESR spectra (absorption) of a papaya.

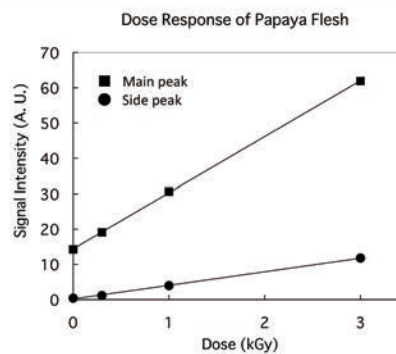


Fig. 2 Dose response of main and side peaks at 77 K.

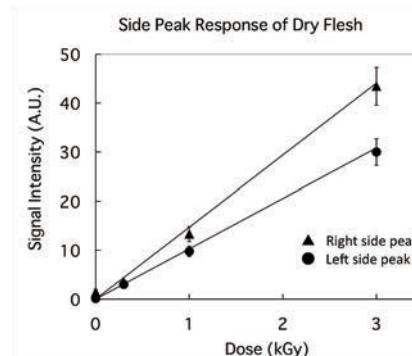


Fig. 3 Dose response of side peaks after freeze-dry.

3 - 19 ESR Studies on Decay of Radicals Induced in Irradiated Foods

Y. Kaimori^{a, b)}, Y. Sakamoto^{a)}, S. Kawamura^{a)}, K. Kishita^{a)},
M. Kikuchi^{b)}, H. Nakamura^{a)}, Y. Kobayashi^{b)} and M. Ukai^{a)}

^{a)} Hokkaido University of Education,

^{b)} Medical and Biotechnological Application Division, QuBS, JAEA

Radiation-induced radicals in irradiated foods were investigated using Electron Spin Resonance Spectroscopy (ESR). The specimens, black pepper, green coffee bean and ginseng, were exposed to ⁶⁰Co. The radiation dose level was 0.1, 5.0, 10 and 50 kGy. We succeeded to detect radiation-induced radicals as singlet ESR signal. The singlet signal intensities were increased with depending on the dose levels. After the irradiation treatment, the signal intensities were decreased rapidly. Analyses of the decay process showed that two or more kinds of radical species were induced in irradiated foods. It suggested that some radicals were decayed very fast within a few hours, and others were slowly. It showed that radiation-induced radicals are stable due to the existence of radicals being decayed slowly. We concluded that it is very useful to use ESR method for detection of irradiated foods.

食品は多種多様な分子で構成されているため、放射線による電離がランダムに生じた結果、非常に多くのラジカル種が生成する。しかし放射線照射誘導ラジカルは不安定なため、照射処理直後に消滅し、その後は比較的安定なラジカルが残ると考え、電子スピン共鳴分光法 Electron Spin Resonance Spectroscopy (ESR) を用いた照射食品検知法ではこの比較的安定なラジカルを計測している¹⁻³⁾。しかし、照射処理後のラジカルの減衰挙動についての報告がないため、どの時点から安定なラジカルが照射食品中で優勢となるか明らかとなっていない。そこで、われわれは、放射線照射処理直後のラジカルの減衰挙動について、ESR を用いて検討している。昨年度、照射誘導ラジカル由来の対電子を ESR 信号として照射処理直後から計測したので、本年度は研究をさらに進め、減衰挙動の数値シミュレーションからラジカル成分について考察した。

実験試料として、黒コショウ、コーヒー生豆、朝鮮人参を用いた。照射は、原子力機構・高崎量子応用研究所の⁶⁰Co 照射施設のガンマ線を用いて、吸収線量 0.1、5.0、10、50 kGy となるように室温で照射した。

ESR 計測により 3 種類のラジカル信号を観測できた。有機フリーラジカル(P₁)と遷移金属イオン(P₂と P₃)である。照射誘導ラジカルは、強く鋭い一本線の ESR 信号(P₁)として g 値が約 2.00 に観測できた。その信号強度は吸収線量に依存して増加した。照射処理直後から信号強度は急激に減衰し、その後は緩やかな減衰となった。

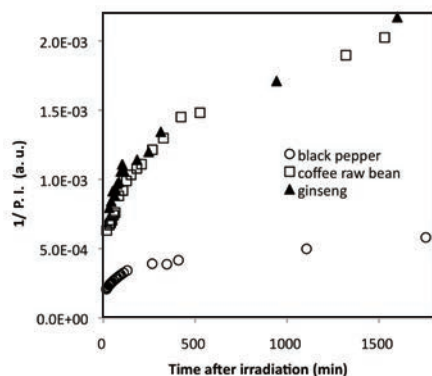


Fig. 1 Reciprocal plots of ESR peak intensities measured from 10-kGy irradiated specimens.

これにより、急激な減衰とその後の緩やかな減衰という異なる反応速度を持つラジカルの存在が示唆された。

照射により生成したラジカルが消滅していく反応は、同種分子間で起こる二次反応と仮定して解析を行った。照射により生成したラジカルが 1 種類であるとする、反応速度論では、ESR 信号強度の逆数 $1/[A]$ と時間 t が比例関係となるが、実験での照射終了直後からの ESR 信号強度の減衰挙動は、比例関係とはならなかった (Fig. 1)。

そこで、照射後経過時間に応じて、速い速度で消滅するラジカル[Radical 1]から、少し遅い速度で消滅するラジカル[Radical 2]など複数のラジカルに順に変化する状況を仮定するとき、反応速度論の理論式で表わされるグラフは曲線になり、計測した ESR 信号強度の逆数を時間の関数としてプロットした時のグラフと一致した (Fig. 2)。このことから、照射食品中に多種多様な構造をもつラジカルが残存しているとしても、その減衰プロセスは比較的単純なラジカル種を仮定する事で説明可能であることが示唆された。

照射後 3 時間以上を経過した照射食品では急激なラジカル減衰挙動の影響を受けず比較的安定なラジカルの減衰として模擬できることを改めて検証できた。

References

- 1) M. Ukai et al., Spectrochim. Acta A 69 (2008) 1417.
- 2) M. Kikuchi et al., Spectrochim. Acta A 75 (2009) 310.
- 3) M. Kikuchi et al., Radiat. Phys. Chem. 80 (2011) 664.

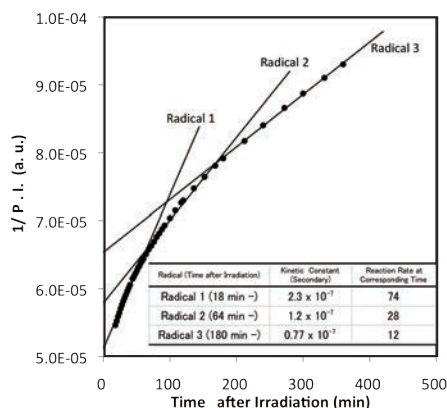


Fig. 2 Simulation analysis of 7.5-kGy black pepper using secondary reaction rate equation.

3 - 20 Improvement of Spatial Resolution of PIXE-CT Using ML-EM Algorithm in TIARA

T. Satoh, M. Koka, W. Kada, A. Yokoyama, T. Ohkubo, A. Yamazaki, Y. Ishii and T. Kamiya

Department of Advanced Radiation Technology, TARRI, JAEA

Introduction

In this study, we applied ML-EM (maximum likelihood expectation maximization) iterative algorithm¹⁾ and STIM-CT to a three dimension imaging technique of PIXE-CT in order to get better spatial resolution. The ML-EM algorithm had been developed for computed tomography such as SPECT (single photon emission computed tomography). Though it is seemingly easy to apply the ML-EM to micro-PIXE, it is necessary to take into consideration energy attenuation of incident particles and absorption of X-rays in a sample. In order to inhibit those influences, we examined a correction method using a numeric model.

Calculation

The calculation formula of the ML-EM algorithm is expressed by

$$\lambda_j^{(k+1)} = \frac{\lambda_j^{(k)} \sum_{i=1}^n y_i C_{ij}}{\sum_{i=1}^n C_{ij} \sum_{j'=1}^m C_{ij'} \lambda_{j'}^{(k)}} \quad (1)$$

where $\lambda_j^{(k)}$, j , i , y and C_{ij} are the k -th iteration image, the pixel index, the sinogram bin index, the measured sinogram and the matrix of detection probability, respectively. C_{ij} must be calculated considering the reduction of the beam energy and X-ray absorption in the sample in the case of PIXE-CT.

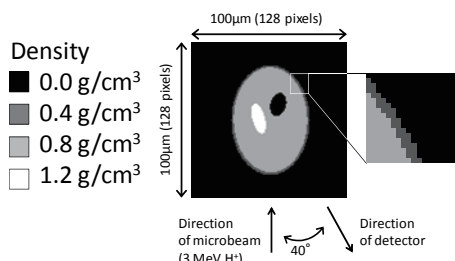


Fig. 1 Numerical model for calculation. The scanning area was 128×128 pixels ($100 \times 100 \mu\text{m}^2$). The density in each area was shown in the left table. The angle of an X-ray detector is 40° .

Figure 1 presents a numeric model used in this study. The scanning area and the corresponding number of pixels were $100 \times 100 \mu\text{m}^2$ and 128×128 , respectively, in this model. The densities in black, dark gray, light gray and white areas were set at 0.0, 0.4, 0.8 and 1.2 g/cm^3 , respectively. The ratios of major elements such as hydrogen (H), carbon (C), nitrogen (N) and oxygen (O) were respectively set as 5:2:1:2 if the protein in a cell was the simple one with only the amine and carboxyl group.

On the other hand, the X-ray absorption by trace elements such as phosphorus (P) and lead (Pb) can be disregarded. An X-ray detector was set at 40° to the beam axis. The numerical calculation was made for every angle by rotating with a step of 18° . It is difficult to reduce the step angle because the whole measuring time will increase.

Energies of protons were calculated using the Bethe-Bloch energy loss formula together with the densities and elemental ratios shown above. The energies went down from 3.0 MeV to 2.2 MeV while passing through the model. The X-ray yields at each point could be estimated from the ionization cross sections and X-ray fluorescence yields. X-ray absorption was also calculated from the defined density, the elemental ratio of the model and X-ray attenuation coefficients. The influence of the attenuation of proton energy was relatively large in the case of Pb L X-ray. On the other hand, the distribution of P was enhanced according to the direction of the detector.

Result

The sinograms and the tomograms were obtained after the foregoing calculations at each angle. Figure 2 shows the tomograms reconstructed only from geometric condition. The outer part of the distribution of P was remarkably enhanced whereas the influence is small in the case of Pb. The corrected sinogram and the appropriate tomogram could be obtained as in Fig. 3 when C_{ij} were corrected with the detection probability calculated from the beam energy and the X-ray absorption in each pixel.

Reference

- 1) K. Lange et al., J. Compt. Assist. Tomogr. 8 (1983) 306.

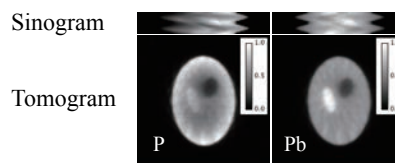


Fig. 2 The sinogram and the tomogram without the correction of C_{ij} . The number of times of calculation in ML-EM is 10.

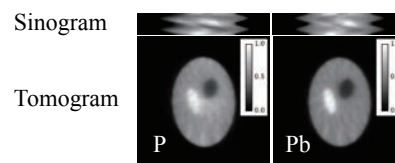


Fig. 3 The sinogram and the tomogram with the correction of C_{ij} . The emphases of the surface are reduced.

3 - 21 Measurement of Trace Elements in Histamine Receptor Deficient Mice Brain Slices by In - Air Micro-PIXE

E. Sakurai ^{b, c)}, K. Yanai ^{b)}, K. Ishii ^{a)}, S. Hiraishi ^{a)}, S. Yamauchi ^{a)}, H. Yamazaki ^{a)}, S. Matsuyama ^{a)}, N. Okamura ^{b)}, A. Yokoyama ^{d)}, W. Kada ^{d)}, M. Koka ^{d)}, T. Satoh ^{d)} and T. Kamiya ^{d)}

^{a)} Department of Quantum Science and Energy Engineering, Tohoku University,
^{b)} Department of Pharmacology, Tohoku University School of Medicine,
^{c)} Faculty of Pharmacy, Iwaki Meisei University,
^{d)} Department of Advanced Radiation Technology, TARRI, JAEA

It is well known that there are many neurons in a brain. Histaminergic neuron system was demonstrated by Watanabe *et al.* in 1983 ¹⁾. Histamine, as a neurotransmitter in the brain, plays many important physiological roles such as learning and memory, locomotor activity, sleep-awake cycle. Histamine has four subtype receptors of H1, H2, H3 and H4 in the brain ¹⁾. However, those inter-receptor communications are still unclear. In this report, we analyzed a distribution and levels of trace metals in multiple histamine receptor deficient mice ²⁾ brain slices, and as compared with neurotransmitter levels in the brain. Histamine H3 receptor antagonists for improvement in cognition function have been developed in recent years. However, H3 antagonist has unknown adverse event. To know the characterization of trace element and histamine receptor defect in the brain might be useful for good medical treatment of mental disorders. PIXE (Particle Induced X-ray Emission) is a powerful method for the analysis of trace elements. In-air micro-PIXE was developed at the Takasaki Ion Accelerators for Advanced Radiation Application (TIARA), JAEA. Micro-PIXE allows analyzing the spatial distribution of the elements quantitatively.

Figure 1 shows the beam irradiation image in region of 90×90 μm² in the brain slice of Wild type (WT: C57/BL6), H1 receptor deficient (H1KO), H3 receptor deficient (H3KO), and H1H3 double receptors deficient (H1H3DKO) mice, with the image of copper, zinc and bromine in the slices each of mice. A daily 50 mg/kg of 5-bromo-2'-deoxyuridine (BrdU) injection was given to the mice for five consecutive days before remove the brains.

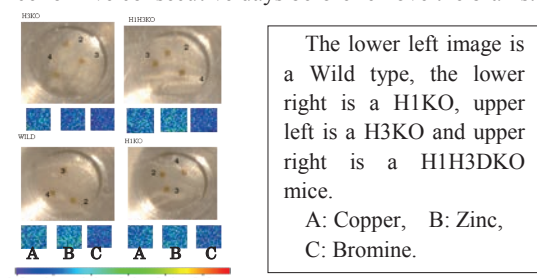


Fig. 1 Beam irradiation image with copper, zinc and bromine image (90×90 μm) of mice brain slices.

After 2-h final BrdU injection, mice brain were removed and immediately quick-frozen in dry ice to -40 °C. Each brain was cryosectioned sagittally at 16 μm thickness. The brain slices were mounted on polycarbonate films, which were processed with 5 N sulfuric acid. The brain slices were examined with beam currents of almost 120 pA. PIXE data were obtained using incident 3 MeV proton microbeams.

All experiments were performed in accordance with institutional guidelines, and experiments protocols were approved by the Animal Care Committee of Tohoku University.

Figure 2 showed the amounts of trace elements in the slices.

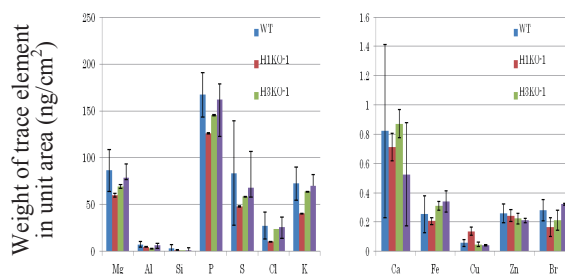


Fig. 2 Amount of trace elements in 1 cm² of brain. (■WT, ■H1KO, ■H3KO, ■H1H3DKO).

The amount of trace element except for copper shows decrease tendency in H1KO mice brain slices. Blocked histamine H1 receptor might be inhibiting neurotransmission activity. Histamine H3 receptor is a pre-synaptic autoreceptor. Thus, histamine, dopamine and 5HT (Serotonin) levels show decrease tendency when comparing to that of WT mice. Calcium level of H3KO was higher than that of H1KO mice. Blocked histamine H3 receptor might be accelerating neurotransmission activity. These results suggested that measurement of trace element level in the tissue and organ might well get valuable information for medical treatment to a disease.

References

- 1) T Watanabe *et al.*, Tohoku J. Exp. Med. 195 (2001) 197-217.
- 2) E. Sakurai *et al.*, Inflamm. Res. (2009)58 Suppl 1:41-2.

3 - 22 Comparison of Two Fluoride Regimens on Fluorine Uptake in Carious Enamel during pH-cycling

H. Komatsu ^{a)}, Y. Matsuda ^{a)}, S. Ooki ^{a)}, N. Hashimoto ^{a)}, K. Okuyama ^{a)}, H. Yamamoto ^{b)}, Y. Iwami ^{b)}, S. Ebisu ^{b)}, M. Nomachi ^{c)}, K. Yasuda ^{d)}, T. Satoh ^{e)} and M. Koka ^{e)}

^{a)} Graduate School of Dental Medicine, Hokkaido University, ^{b)} Graduate School of Dentistry, Osaka University, ^{c)} Graduate School of Science, Osaka University, ^{d)} The Wakasa wan Energy Research Center, ^{e)} Department of Advanced Radiation Technology, TARRI, JAEA

Introduction

It is well established that fluoride-containing dentifrice is a possible agent for caries prevention. On the other hand, a fluoride mouthrinse (FM) for children are recommended by some dental parties. As toothbrush with fluoride-containing dentifrices (FCDs) is the daily fluoride regimen being used by most populations, the additional regimen such as FM would be an extra application. The purpose of this study was to compare two fluoride regimens with and without FM on fluorine (F) uptake in carious enamel during pH-cycling using an in-air micro-PIGE/PIXE system at TIARA.

Material and Methods

Six extracted human teeth were used. Three sections of 170 μm thickness were obtained from each tooth. All tooth surfaces, except for the outer surface of enamel, were coated with a wax. These teeth were divided into three groups; Group A simulated to fluoride regimens without FM (Fig. 1: closed allow, twice per day). Group B simulated to fluoride regimens with FM (Fig. 1: closed allow, twice per day and open allow 5 days per week). Group C was as a control. The pH-cycling (pH 6.8-4.5) was carried out for 5 weeks for preparing artificial carious enamel using an automatic pH cycling system¹⁾. After pH-cycling, fluorine and calcium distributions of the outer enamel in each specimen were evaluated using micro-PIGE/PIXE system at TIARA²⁾. The outermost surface of the carious enamel was defined at the position containing 5% of the calcium concentration in intact enamel. For the comparison of F uptake, the average fluorine concentration in each specimen was calculated at area of 150 μm from the defined surface.

Results

Figure 2 shows the fluorine uptake into carious enamel after 5-week pH-cycling. The average fluorine concentration (ppm) in carious enamel at area of 150 μm from the defined surface for group A, B, and C were 1,117±573, 1,219±336, and 362±208, respectively. The F uptake for group C had significantly low value in comparing to that for group A and B (p<0.05, Games-Howell test). There was no difference in F uptake between group A and B (p>0.05).

Discussion

To estimate caries preventive effect of fluoride-containing dental materials (FCMs), we investigated the F uptake in carious enamel around FCMs during pH-cycling³⁾

as the F uptake resulted from the precipitation of fluorapatite Ca₁₀(PO₄)₆F₂ (i.e., remineralization). Therefore, it can be speculated that both two fluoride regimens were effective in reducing the dental caries, since F uptake for group A and B had significantly high values in comparing to that for group C. No difference in F uptake between group A and B indicated that there was no difference in caries preventive effect between two fluoride regimens. For most populations included children who have been used the fluoride-containing dentifrice as a matter of routine, additional fluoride mouthrinse may not have a benefit in preventing the dental caries. The toothbrush with fluoride-containing dentifrice as a routine measure would be recommended for caries prevention primarily.

References

- 1) Y. Matsuda et al., Dent. Mater. J. 24 (2006) 280.
- 2) H. Yamamoto et al., Nucl. Instrum. Meth. Phys. Res. B 210 (2003) 388.
- 3) H. Komatsu et al., Nucl. Instrum. Meth. Phys. Res. B 260 (2009) 2136.

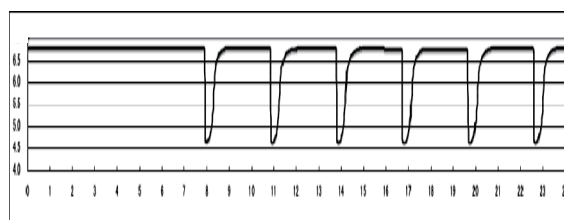


Fig. 1 Schedule of pH-cycling during one day, closed allow: injection of 2 mL 1,000 ppmF, open allow: injection of 2 mL 225 ppmF.

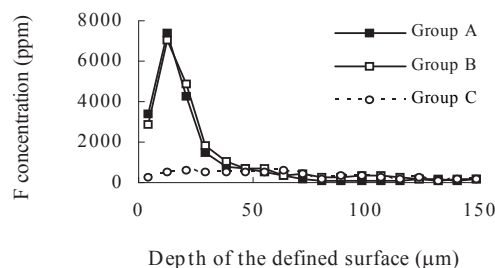


Fig. 2 The fluorine uptake into carious enamel after 5-week pH-cycling.

3 - 23 **Imaging of Metallofullerene Distribution Using Micro-particle Induced X-ray Emission for Gadolinium Neutron Capture Therapy**

Y. Yamamoto^{a)}, K. Nakai^{a)}, F. Yoshida^{a)}, M. Shirakawa^{a)}, K. Endo^{a)}, Y. Horiguchi^{b)},
Y. Nagasaki^{b)} and A. Matsumura^{a)}

^{a)} Graduated School of Comprehensive Human Sciences, University of Tsukuba,

^{b)} Graduate School of Pure and Applied Sciences, University of Tsukuba

Neutron Capture Therapy (NCT) as the radiation therapy uses nuclear reaction with thermal neutrons and the NCT agent. As the NCT agent, boron-10 and gadolinium-157 were used. However, the useful gadolinium compound for NCT has not been developed. Fullerene is a class of sphere-shaped molecule made exclusively of carbon atoms. Metallofullerene is the complexes of metal-containing fullerenes¹⁾. According to the previous studies, Gd@C82 is a type of metallofulleren which is encapsulated gadolinium atom inside fullerene, and is a potentially useful gadolinium compounds for NCT²⁾. However, the biodistribution of Gd@C82 in tumor cells is not clarified. Micro-particle induced X-ray emission (Micro-PIXE) has the high sensitivity and spatial resolution. Consequently, the purpose of this study was to analyze and clarify the biodistribution of Gd@C82 in tumor cells using Micro-PIXE.

BALB/c mice were used. Subcutaneous tumor on the rear leg of each mouse was created by subcutaneous injection of 10⁶ cells/10 μ L of CT26 undifferentiated colon carcinoma cells, respectively. Gd@C82 (5.0 mg/mL, 150 μ L) was injected intravenously into mouse via the tail vein. Two days after injection, the tumor was excised and immediately embedded using O.C.T. Compound. Tumor samples were cryosectioned at 10 μ m. Cryosectioning tumor samples were attached in polycarbonate film and freeze-dried for 12 hours. Tumor samples on the polycarbonate film were fixed on a round holder of 2 cm in diameter. Micro-PIXE was performed at Takasaki Ion Accelerators for Advanced Radiation Application (Takasaki, Japan). These sample holders were irradiated with proton beam (3 MeV) to analyze the biodistribution of Gd@C82.

The distribution of Phosphorus in tumor samples was shown in Fig. 1. The distribution of Gadolinium in tumor samples was shown in Fig. 2.

Figure 1 showed the cell distribution of the tumor specimen. We had not identified characteristic peaks of gadolinium in the spectrum of tumor samples. Therefore, the distribution of gadolinium in tumor samples had the low reliability. The result indicated that the concentration of gadolinium in tumor was very low to be detected the peak of gadolinium.

Endo et al. already reported the intra and inter cellular gadolinium imaging using cultured cells incubated with gadolinium containing medium with same methods. In this

study, gadolinium concentration of the tissue samples would be affects the results. To demonstrate Gd@C82 is potentially useful gadolinium carrier for NCT, we planning the modification of these particles to achieve prolonged blood circulating and achieve higher tumor concentrations. The bio-distribution of gadolinium compounds in tumor cells are very important and essential information for effective NCT³⁾.

References

- 1) J. Meng et al., J Nanosci. Nanotechnol. 10(12) (2010) 8610-16.
- 2) Y. Horiguchi et al., Sci. Technol. Adv. Mater. 12 (2011) 044607.
- 3) G. D. Stasio et al., Canc. Res. 61 (2001) 4272-77.

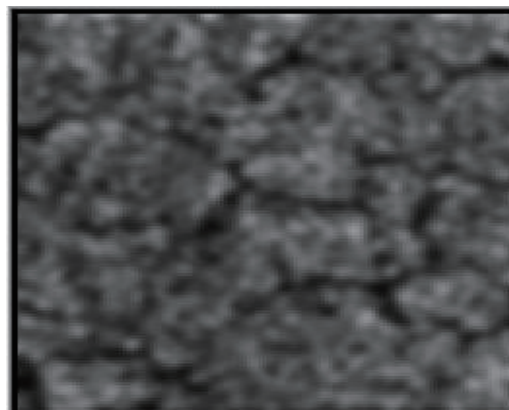


Fig. 1 The distribution of phosphorus in tumor samples (200 μ m \times 200 μ m).



Fig. 2 The distribution of gadolinium in tumor samples (200 μ m \times 200 μ m).

3 - 24 Analysis of Particles in Interstitial Pneumonia Lung Tissue Obtained by Transbronchial Biopsy

K. Dobashi^{a)}, Y. Shimizu^{b)}, S. Matsuzaki^{b)}, T. Satoh^{c)}, M. Koka^{c)}, A. Yokoyama^{c)},
T. Ohkubo^{c)}, Y. Ishii^{c)}, T. Kamiya^{c)} and M. Mori^{b)}

^{a)} Gunma University Faculty of Health Science, ^{b)} Department of Medicine and Molecular Science, Gunma University Graduate School of Medicine,
^{c)} Department of Advanced Radiation Technology, TARRI, JAEA

In-air micro particle-induced X-ray emission (PIXE) analysis was previously employed to assess the spatial distribution and content of particles in surgical lung biopsy specimens. The aim of this study was to assess the efficacy of in-air micro-analysis for transbronchial lung biopsy specimens in patients with interstitial pneumonia (IP). It is thought IP develops in association with inhaled particle. We investigated the relation between IP and occupational exposure. The elements composing lung particles and their locations could be identified by in-air micro-analysis. Si was the major component of particles. Quantitative analysis revealed that the elements composing lung particles varied among patients. For a battery making worker with suspected nickel exposure, aluminum, vanadium, and calcium were detected, but nickel was not detected. For a patient without a work history (house wife), Fe elements were detected. For a manager of car parking, inhalation of automobile exhaust fumes was suspected. The specimen obtained from him contained Fe, Mg, Al, Ti, Co, Cr, V, and Ca. Therefore, elemental analysis of transbronchial lung biopsy specimens by in-air micro-analysis can provide useful information when examining occupational and environmental factors related to IP.

1. はじめに

アスベストの吸入は、肺線維症や肺ガンの原因となり、しかも発病まで数 10 年かかることから、「静かな時限爆弾」とも言われ、大変な社会問題である。早期診断や病態解明には、肺内のアスベストの種類、量、分布などを人肺組織内で特定する必要があるが、簡単でなかった。我々は、独立行政法人日本原子力研究開発機構との共同研究で、同機構が開発した大気マイクロ PIXE 分析技術を応用して、数 mg の肺組織の中のケイ素や金属元素の二次元分布を 1 μm の解像度で画像化する分析法を開発し、世界で初めて吸入したアスベストを肺組織中に存在したままで画像化することに成功した。

今回、間質性肺炎患者から気管支鏡により採取した微量組織を用いて、肺内に存在する元素を分析することにより、本症の発症に粉塵吸入の関与の有無を検討した。

2. 実験

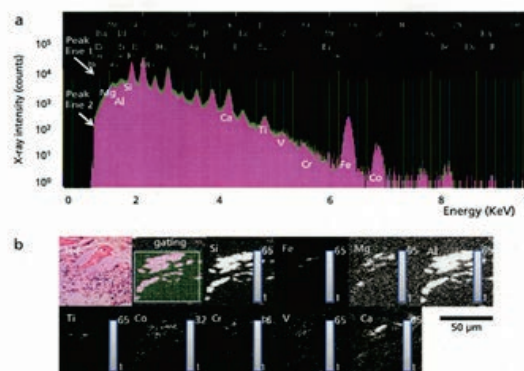
肺組織切片作成：原因不明の 4 名の特発性間質性肺炎患者から、気管支鏡により微量肺組織を採取した。これら肺組織の凍結切片を作成し、それを表面に PIXE 用のフィルムを張ったスライドガラス上に載せて乾燥させた。肺組織を含むフィルム膜とともに肺切片を切り出しアクリルホルダーに固定して、イオンビームを照射した。

3. 結果と考察

症例 4 例において、検出できる金属は異なっていた。粉塵吸入歴のない主婦の患者からは、Si に一致して Fe が、料理人の組織からは、Si に一致して Ca がそれぞれ検出された。バッテリー工場従業員では、職歴から Ni の吸入が疑われたが、Ni はほとんど検出されず、Si に一致して Al が多く検出されたことから、職業性吸入が線維化の原因とは推定できなかった。自動車駐車場の管理人では、Si に一致して、Fe、Mg、Al、Ti、Co、Cr、V 及び Ca など多種類の金属が検出された (右図)¹⁾。

これらは、いずれもディーゼル排気や高速道路沿いの大気などに多く検出される金属である。したがって、本患者では、職場での粉塵吸入と考えられ、これらの金属が線維化の発症に関与している可能性が示された。

マイクロ PIXE を使用すれば、気管支鏡により採取された微量検体から、患者の粉塵吸入の有無が推定でき、今まで原因不明とされていた患者の中から、職業性粉塵吸入が原因の患者を判別できる可能性が開かれた。



Peaks of each element and elemental map for manager of car parking. Peak line 1 indicates the spectrum for the entire beamed area and peak line 2 indicates the spectrum of the gated area (panel a) shown as white square (panel b). A serial section of irradiated area showed accumulation of lymphocytes and destroyed small airways (Hematoxylin eosine stain (H E), X400). The intensity of metals in lung tissue is shown by gray to white bars. Si is marked on the elemental map. White dots indicate the locations of elements in the TBLB specimen: Fe, Mg, Al, Ti, Co, Cr, V, and Ca are co localized with Si (panel b).

(文献 1 より転載)

Reference

- 1) Y. Shimizu et al., J Clin. Biochem. Nutr. 49 (2) (2011) 125-30.

3 - 25 Analysis of Erythrocyte Elements in Hepatitis C Patients Treated with Peginterferon-alfa and Ribavirin

T. Nagamine ^{a)}, T. Akutsu ^{a)}, M. Koka ^{b)}, T. Satoh ^{b)} and T. Kamiya ^{b)}

^{a)} Graduate School of Health Sciences, Gunma University,

^{b)} Department of Advanced Radiation Technology, TARRI, JAEA

1. Introduction

It is well known that erythrocytes (red blood cells) contain various trace elements, which are altered along with pathogenesis of disorders. Because erythrocytes can be collected via peripheral vessels non-invasively, this blood cell is a convenient sample material for in-air micro PIXE analysis^{1),2)}.

Chronic hepatitis C patients treated with Pegylated-interferon-alfa and ribavirin (PegIFN+RBV) are frequently associated with hemolytic anemia, whereas the mechanism of anemia is not determined yet. This study is aimed to evaluate the elemental changes in erythrocytes of patients treated with PegIFN and RBV by in-air micro-PIXE.

2. Material and Method

Ten patients with chronic hepatitis C (4 cases treated with PegIFN+RBV, 3 cases treated with PegIFN alone, 3 cases treated with phlebotomy), and four healthy volunteers were enrolled in this study. Whole blood was collected via peripheral vein, and the sample for PIXE analysis was prepared by the modified method of Ortega³⁾. Elemental distributions of erythrocytes were analyzed using in-air micro-PIXE at JAEA-Takasaki.

3. Results and Discussion

Elemental maps based on X-ray spectra were obtained from erythrocytes (Fig. 1, Fig. 2).

The shape of erythrocyte, so-called the donut-like, fitted well with the counterplots of P, S, Cl, K and Ca in healthy controls. In addition, these elements aggregated partially, forming small nodule. Fe distributed granularly and divided into 3-4 pieces. In patients received phlebotomy, erythrocytes became smaller in diameter, and each element distributed similar to that of healthy control.

The shape of erythrocyte became markedly blurred in patients treated with PegIFN+RBV and moderately in patients treated with Peg-IFN alone.

Each element in erythrocytes was tended to aggregate partially and distribute patchily in patients treated with PegIFN, these findings became obviously in combination with ribavirin.

Fe distribution in erythrocytes was altered in patients treated with PegIFN; Fe aggregated partially or nodularly, consequently granular pattern was disappeared. Cl, K and Ca formed small dense nodules in erythrocytes of patients treated with PegIFN+RBV. These elements aggregated patchily in patients treated with PegIFN alone. Mg and Si were detected in some controls and patients treated with PegIFN alone. Patients treated with PegIFN+RBV showed marked increment of Mg in erythrocytes. Mn was detected

in 3 out of 5 patients treated with PegIFN+RBV, but not detected in patients treated with IFN alone or the controls.

Present study showed that elemental distribution in erythrocytes was altered in hepatitis C patients treated with PegIFN, and these changes became obviously in combination with ribavirin. This finding suggests that in-air micro-MIXE is a useful tool for investigating the PegIFN+RBV-induced anemia.

References

- 1) Y. Tokita et al., JAEA Takasaki Annu. Rep. 2009 (2011) 117.
- 2) H. Kikuchi et al., JAEA Takasaki Annu. Rep. 2010 (2012) 88.
- 3) R. Ortega, Cell. Mol. Biol. 42 (1996) 77-88.

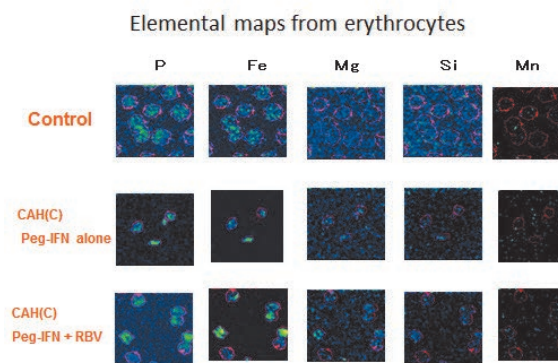


Fig. 1 Granular distribution of Fe is disappeared in patients treated with PegIFN. Mn dots were observed only in a patient treated with PegIFN+RBV.

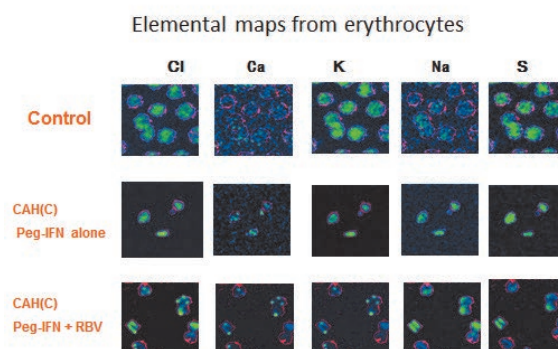


Fig. 2 In a patient treated with PegIFN alone, Cl, K, Na and S aggregate and spread patchily. Cl, Ca and K form small dense nodules in a patient treated with PegIFN+RBV.

3 - 26 Decreasing Size of Microcapsules and Increased Radiation-induced Release of Antitumor Drugs

S. Harada ^{a)}, S. Ehara ^{a)}, K. Ishii ^{b)}, T. Satoh ^{c)}, T. Kamiya ^{c)} and N. Matsuyama ^{b)}

^{a)}Iwate Medical University, School of Medicine, Department of Radiology,

^{b)}Department of Quantum Science and Energy Engineering, Tohoku University,

^{c)}Department of Advanced Radiation Technology, TARRI, JAEA

We have been developing the targeting of anticancer drug using microcapsules that release anticancer drugs with response to radiation ^{1), 2)}. First, the microcapsules are delivered around the tumors. Second, the tumors are irradiated and the microcapsules release anticancer drugs. Finally, released anticancer drugs act synergistically with radiation resulting in increased anticancer effect, and localization of anticancer drugs by microcapsules reduces adverse effects.

We have made such microcapsules by spraying the mixture of hyaluronic acid and alginate into Fe and Ca supplemented with anticancer drugs and H₂O₂ ²⁾. In order to conquer radiation-induced release of anticancer drugs, three mechanism have been used: 1) decomposition of hyaluronic acid to glucosamine; 2) destruction of polymerization by Fe; 3) generation of O₂ from irradiated H₂O₂. As for using H₂O₂, we observed severe H₂O₂-induced dermatitis when capsules were delivered subcutaneously. In addition, spraying the mixture into Ca-Fe solution resulted in large size of capsules (23 ± 2.8 μm). In this study, we used L-ascorbic acid instead of H₂O₂, which releases O₂ with response to radiation. Capsular size was reduced by adding ultrasound vibration to Ca-Fe solution.

The mixture of 0.2% alginate and 0.1% hyaluronic acid was prepared and 5 mg Carboplatin (Pt containing anticancer drug) and 1 g L-ascorbic acid were added. A droplet of this mixture was sonicated using an ultrasound disintegrator and atomized to yield a 0.1 mol solution of CaCl₂ and FeCl₂ with vibration.

The generated capsule observed in micro PIXE camera in TIARA was shown in Fig. 1-A. Their mean diameter was 1.2 ± 0.64 μm, which brought about smooth injection of capsules. The capsules were subcutaneously injected around the MM48 tumors that were inoculated in the left hind leg of C3He mice. Then 10 or 20 Gy of 400 keV soft X-ray was irradiated to tumors at Center for In Vivo science, Iwate Medical University. The capsules around the tumors ruptured with response to radiation (Fig. 1-B). Capsules added L-ascorbic acid (Fig. 2 ■, ■) ruptured with response to radiation, whose rupturing was the same level as those of H₂O₂ added (Fig. 2 ■, □). Downsizing of capsular size resulted in significant increases of rupturing. Indeed, the frequencies of rupturing in downsized microcapsules (Fig. 2 □, ■) were significantly greater than those in not downsized capsules (Fig.-2 ■, ■).

The capsules of L-ascorbic acid added did not cause dermatitis around the tumor.

The downsized capsules with addition of L-ascorbic acid will lead to the better clinical use.

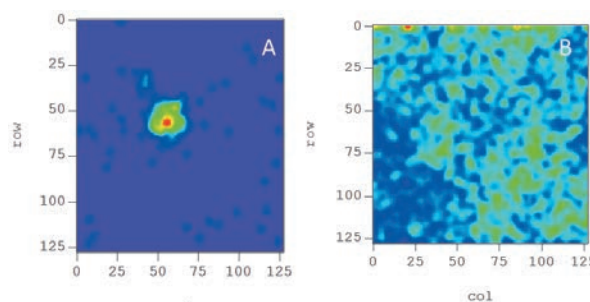


Fig. 1 Generated microcapsules observed through micro PIXE camera in TIARA. A: Before irradiation, B: After irradiation.

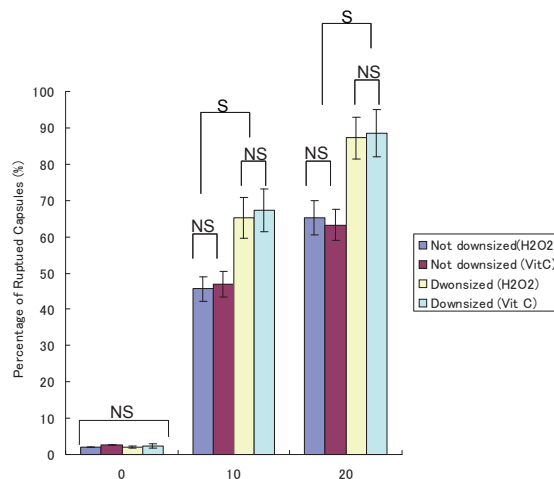


Fig. 2 Frequency of rupturing in microcapsules by irradiation.

References

- 1) S. Harada et al., Int. J. Radiat. Oncol. Biol. Phys. Vol. 75, No. 2 (2009) 455-62.
- 2) S. Harada et al., Int. J. PIXE Vol. 20, Nos. 1 & 2 (2009) 29-36.

3 - 27 Cultivation of Marine Planktons by the Artificial Seawater and Elemental Mapping by Micro Beam PIXE System of TIARA

Y. Iwata^{a)}, S. Takahashi^{a)}, K. Ishii^{b)}, T. Kamiya^{c)} and T. Satoh^{c)}

^{a)} Department of Chemistry, Faculty of Education and Human Studies, Akita University,

^{b)} Department of Quantum Science and Engineering, Graduate School of Engineering,

Tohoku University, ^{c)} Department of Advanced Radiation Technology, TIARA, JAEA

Marine planktons, *Nannochloropsis sp.* and *Brachionus plicatilis* were cultivated by the artificial seawater. These planktons were increased like cultivation in the seawater. Phytoplankton (*Nannochloropsis sp.*) was able to use as the food of the zooplankton (*Brachionus plicatilis*). Elemental abundances in these planktons were measured by normal PIXE system of NMCC. Most differences of the elemental composition by the difference in culture solution were not seen. Distribution maps for several elements, such as Na, Mg, P, S, Cl, K, Ca, Fe and Zn in *Brachionus plicatilis* were searched by 3 MeV proton bombardments by the micro beam system of TIARA. The elemental maps for major elements, such as K, Cl and S show the shape and internal structure of *Brachionus plicatilis*. The elemental maps for trace elements, Fe and Zn were also obtained by the micro beam system of TIARA. It was shown that the planktons cultivated in artificial seawater are suitable for research of a biological concentration for trace elements.

1. はじめに 海洋生物における微量金属の生物濃縮の定量的評価のため、海産の植物及び動物プランクトンを培養し、金属元素の含有量と体内分布をPIXEで調べた¹⁾。以前は、岩手県水産技術センターからろ過海水及びプランクトン類の提供を受けていたが、センターの罹災で、培養液の調製と生物種の維持、管理をすべて自身の研究室で行う状況になった。

本研究では、人工海水をベースとした培養液による植物プランクトン：*Nannochloropsis sp.* (以下藻類) 及び動物プランクトン：*Brachionus plicatilis* (以下ワムシ) を飼育し、PIXEによりこれらの生物中の元素存在度とワムシ中の元素分布を調べた。この結果、人工海水ベースで培養した生物が、ろ過海水同等以上に生物濃縮の研究に適していることがわかった。

2. 培養液の調製 人工海水は、純水 1 Lあたり Reef Salt (Sea chem社、熱帯魚用) 34 gを溶解して調製した。これを体積割合20%の純水で希釈し、栄養強化液(PES)を4 mL添加し、pHは7.8から8.0に調整した¹⁾。これを人工海水培養液とする。また、ろ過海水を用いて同様の培養液の調製を行った。以下、ろ過海水培養液とする。

藻類の増殖培養 2種の培養液に藻類保存溶液を加え、22 °C、3,200 lx (12時間明暗) の恒温槽内で、振とう・通気培養を行った。

ワムシの増殖培養 PESを添加しない人工海水培養液に、ワムシの耐久卵(クロレラ工業)を加え、27 °C、400 lx (12時間明暗) の恒温槽内で、通気培養を行った。藻類の増殖培養液を餌として与えた。

元素分析 元素存在量は、日本アイソトープ協会仁科記念サイクロトロンセンター(NMCC)で、3 MeV H⁺ビームによるnormal PIXEで行った。藻類の培養液3 mLを孔径1.0 μmのNuclepore Polycarbonate Filterでろ過し、藻類の3-5 mgをビーム径2 mmで照射した。ワムシは、3-8個体をPolycarbonate Filterの中心部に付着させ、ビーム径6 mmで照射した。

ワムシの元素分布図 元素分布図は、TIARAマイクロPIXEシステムにより取得した。ワムシ1個体をPolycarbonate膜に付着させ、照射試料とした。3 MeV

H⁺ビームをサブミクロンに絞り、ワムシ1個体350 × 350 μmをスキャンし、ワムシ1個体を1画面とした。

3. 人工海水培養液での飼育 藻類は、増殖培養開始後約3週間で、元素分析並びにワムシの餌として十分な量となった。ワムシは、ふ化率が非常に低かったが、PIXEでは微量分析が可能であるため、元素分析及び元素分布図作成には十分な個体数が確保できた。

藻類及びワムシの元素存在度 NMCCにおける元素分析により、Fe、Znなど必須微量元素を含め、藻類中の12-13元素、ワムシ中の9-10元素の定量分析が可能であった。培養液による違いは、人工海水培養液の場合Mg、Znの存在度がろ過海水培養液に比べ、いずれの生物でも1/2-2/3程度となった。それ以外の元素存在度に明確な違いは、見られなかった。以上より人工海水培養液によりろ過海水同等以上に生物濃縮の実験ができることが確認した。

ワムシ中の元素分布 TIARAマイクロPIXEシステムにより、ワムシ中のNa、Mg、P、S、Cl、K、Ca、Fe及びZnの元素分布図を作成できた。S及びFeの分布図を示す(Fig. 1)。S等の主要元素の分布図により、ワムシの概形及び体内構造が把握できた。また、元素存在量が1個体当たり0.5 ngと微量のFeの分布図も作成できた。以上から、人工海水で培養したプランクトンを利用し、生物濃縮の定量的評価が可能であることが示された。

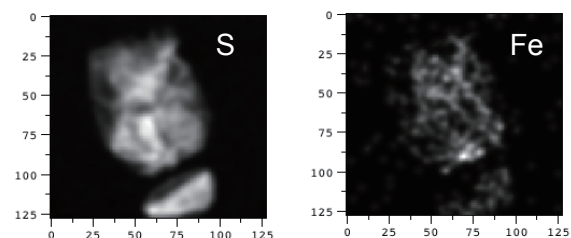


Fig. 1 Elemental maps for S and Zn in *Brachionus plicatilis* obtained by the micro beam system of TIARA.

Reference

- 1) Y. Iwata et al., J. Radioanal. Nucl. Chem. 264 (2005) 295.

3 - 28 Synthesis of Radioiodinated Antitumor Cyclic Peptide, [¹²⁵I]-Sansalvamide A Derivative

Sh. Watanabe^{a)}, K. Yamada^{b)}, N. Tsukui^{b)}, H. Hanaoka^{c)}, Y. Ohshima^{a)},
A. Yamaguchi^{d)}, H. Oku^{b)} and N. S. Ishioka^{a)}

^{a)} Medical and Biotechnological Application Division, QuBS, JAEA,
^{b)} Graduate School of Engineering, Gunma University, ^{c)} Graduate School of Pharmacy,
Chiba University, ^{d)} Graduate School of Medicine, Gunma University

Natural product which has high cytotoxicity against tumor cells is a promising lead compound of anti-tumor reagent. Sansalvamide A (SA), a cyclic peptide isolated from marine fungus, is composed of 4 amino acids and 1 hydroxy acid (Fig. 1) and exhibits cytotoxicity against colon carcinoma and melanoma¹⁾. Based on the properties, a number of SA derivatives have been enthusiastically prepared and investigated for the cytotoxicity against various cancer cell lines in vitro. In particular, Ueno et al. revealed that some halogenated SA derivatives, SA-X (X = Cl, Br, I, Fig. 1), have remarkable growth inhibition against MDA-MB-231, malignant human breast cancer cell²⁾. Evaluation in vivo is also significant in the process of exploring anti-tumor reagent. Nevertheless, its behavior and efficacy in vivo is hardly unknown, although the cytotoxicity in vitro has been well demonstrated. One of the effective ways to perform in vivo evaluation is utilization of its corresponding radiolabeled analog. In this study, we therefore considered to synthesize iodine 125 (*t*_{1/2} = 59.4 d) labeled SA derivative, [¹²⁵I] SA-I (Fig. 1).

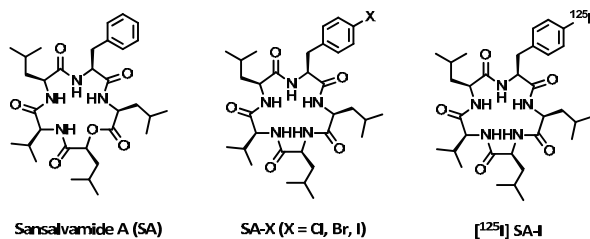


Fig. 1 Chemical structures of Sansalvamide A (SA), SA-X (X = Cl, Br, I), and [¹²⁵I]SA-I.

Synthesis of [¹²⁵I] SA-I is outlined in Fig. 2. Linear peptide **1** was obtained by stepwise elongation from oxime resin with conventional solid phase peptide synthesis using Boc-group and succeeding cleavage in the presence of MeOH and DBU. Stannylated linear peptide **2**, precursor of radioiodinated intermediate, was prepared in the presence of Pd(0) catalyst in 61% of synthetic yield. I-125 was labeled by electrophilic destannylation in the presence of chloramine T as oxidizing reagent³⁾. Radioiodinated linear peptide **3** was prepared in good labeling efficiency (88%). After saponification of methyl ester group by 0.5 M NaOH solution and subsequent deprotection of Boc-group by trifluoroacetic acid (TFA) was afforded in 73% yield (2 steps), [¹²⁵I]SA-I was synthesized in the presence of PyBOP, condensation reagent, under high diluted condition.

Reverse-phase HPLC analysis of the reactant showed radioactive peak at 15 min which was compatible with the retention time of the non-radioactive authentic compound. Consequently, the desired cyclic derivative was successfully prepared in 11% yield in this step. The overall yield from the radioiodination of **5** was 7%. To our best knowledge, this is the first compound of radiolabeled SA derivative.

Since electrophilic destannylation is commonly used in radiohalogen labeling, the synthetic route reported in this study is applicable for preparation of various radiohalogenated SA derivatives. Thus, labeling of appropriate radiohalogens such as ⁷⁶Br for PET and ¹³¹I for radionuclide therapy is potent to give useful compounds for not only in vivo evaluation but nuclear medicine.

In vivo evaluation using [¹²⁵I]SA-I is now being undertaken. Preparation via direct radioiodination using cyclic stannyl precursor is also under investigating in order to improve radiolabeling yield.

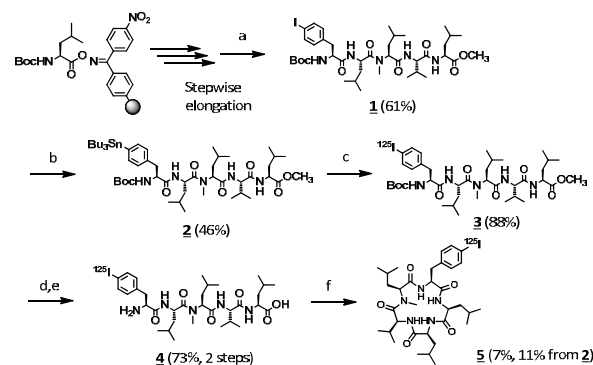


Fig. 2 Synthetic route of [¹²⁵I]SA-I. Reagents and Conditions; (a) DBU, 5%MeOH/THF, r.t., 2 h; (b) (SnBu₃)₂, Pd(PPh₃)₄, toluene, reflux, 4 h; (c) Chloramin T, 50%MeOH/1% AcOH, r.t., 30 min.; (d) 0.5M NaOH, r.t., overnight; (e) 25%TFA/CH₂Cl₂, r.t.; (f) PyBOP, DIEA, DMF, r.t., 2.5 h.

References

- 1) G. Belofsky et al., Tetrahedron Lett. (1999) 2913-16.
- 2) H. Ueno et al., Peptide Sci. 2007 (2008) 281-84.
- 3) D. S. Wilbur et al., Bioconjugate Chem. (1993) 574-80.

3 - 29 Development of a ^{76}Br -labeled Amino Acid Derivative for PET Imaging of Tumor

H. Hanaoka^{a)}, Sh. Watanabe^{b)}, H. Tominaga^{a)}, Y. Ohshima^{b)}, Sa. Watanabe^{b)}, K. Yamada^{c)}, Y. Iida^{a)}, N. S. Ishioka^{b)} and K. Endo^{a)}

^{a)} Graduate School of Medicine, Gunma University, ^{b)} Medical and Biotechnological Application Division, QuBS, JAEA, ^{c)} Graduate School of Engineering, Gunma University

Positron emission tomography (PET) with ^{18}F -fluorodeoxyglucose (FDG) is widely used for imaging of tumor. However, FDG accumulates not only in the tumor but also in the inflammation or the benign region. Recently, radiolabeled amino acid derivatives have received attention since they are more specific tracer for malignant tumors than FDG, and some of them are becoming to use in clinical phase. However, since these tracers were labeled with short half-life positron emitter such as ^{11}C and ^{18}F , they are not suitable for widespread use.

^{76}Br is an attractive positron emitter (β^+ =57%, electron capture=43%) since it has a longer half-life ($t_{1/2}$ =16.1 h) than ^{18}F and substitution of ^{18}F with ^{76}Br would be easy because both bromine and fluorine belong to the halogen group. Several reports have demonstrated that PET imaging with ^{76}Br -labeled tracers is feasible, not only for use in experimental models but also for clinical diagnosis. Thus, ^{76}Br use could potentially increase the availability of PET using radiolabeled amino acid derivatives in many hospitals. In this study, amino acid derivative labeled with ^{76}Br was prepared and evaluated as a potential PET tracer for imaging tumors.

Alpha-methyl phenylalanine (α -Me-Phe) was selected as the mother compound considering tumor specificity (α -methylation) and stability in vivo (phenylalanine) (Fig. 1). Para position of α -Me-Phe was selected for labeling with ^{76}Br .

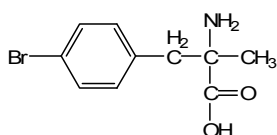


Fig. 1 Structure of *p*-Br- α -Me-Phe.

No-carrier-added ^{76}Br and ^{77}Br , the latter of which is suitable radiobromine for basic studies due to its longer half-life ($t_{1/2}$ =57.1 h), were produced according to a process reported by Tolmachev et al.¹⁾ with some modifications. Irradiation was performed using proton beams with energy of 20 MeV using an AVF cyclotron. Separated radiobromine was trapped into 15 mL of Milli-Q water. Radiobromine was characterized by gamma-ray spectrometry using an HP-Ge detector (crystal diameter, 58 mm; length, 67.3 mm) coupled to a multichannel analyzer. Radioactivity was determined based on the gamma-ray energy (^{76}Br : 559 keV; ^{77}Br : 239 keV). The stannyl precursor of Br- α -Me-Phe, tri-*n*-butylstannyl- α -Me-Phe was prepared for radiolabeling. Precursor was radiobrominated with N-chlorosuccinimide as an oxidant, and the radiolabeling yield of $^{76/77}\text{Br}$ - α -Me-Phe was approximately 25 - 40%. In stability study, almost all of

^{77}Br - α -Me-Phe remained intact over 24 h after incubation in the serum, indicating that ^{77}Br - α -Me-Phe was stable. Biodistribution studies of ^{77}Br - α -Me-Phe in nude mice bearing colorectal cancer cell line, LS-180, showed a marked accumulation in the tumor at 3 h after injection, and resulting in high tumor-to-blood and tumor-to-muscle ratios of 3.94 ± 0.66 and 3.95 ± 0.51 , respectively (Table 1).

Table 1 Biodistribution of ^{77}Br - α -Me-Phe in tumor bearing mice.

	30 min	1 h	3 h
Blood	4.00 ± 0.24	3.18 ± 0.17	3.23 ± 0.28
Liver	5.02 ± 0.31	4.03 ± 0.21	4.17 ± 0.46
Kidney	30.64 ± 3.20	32.60 ± 2.53	25.72 ± 3.35
Intestine	2.55 ± 0.23	2.32 ± 0.45	2.25 ± 0.24
Pancreas	31.89 ± 7.13	23.42 ± 3.41	26.24 ± 5.11
Lung	4.15 ± 0.25	3.45 ± 0.10	3.34 ± 0.14
Muscle	3.28 ± 0.20	3.18 ± 0.16	3.25 ± 0.34
Tumor	9.62 ± 1.02	9.25 ± 0.91	13.25 ± 3.05
Tum/Bld	2.43 ± 0.40	2.91 ± 0.22	3.94 ± 0.66
Tum/Mus	2.96 ± 0.48	2.91 ± 0.22	3.95 ± 0.51

^{76}Br - α -Me-Phe PET showed a clear image of the tumor (Fig. 2), which was almost same with ^{18}F -labeled α -methyl-tyrosine, which has been already used in clinical practice.

These findings indicated that ^{76}Br - α -Me-Phe would be a potential tracer for imaging tumor.

On the other hand, ^{77}Br - α -Me-Phe showed slow clearance from the blood and high accumulation in the non targeted organs (Table 1). Since ^{77}Br - α -Me-Phe was not metabolized in vivo, this slow clearance was probably because its high lipophilicity. Thus, novel designs in reduction of accumulation and retention in non target organs would be need for clearer tumor imaging.

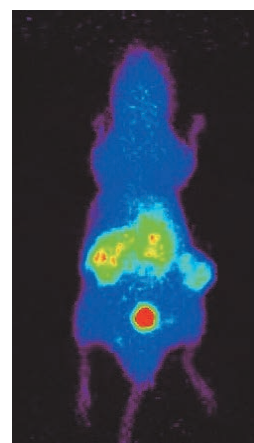


Fig. 2 PET image with ^{76}Br - α -Me-Phe.

Reference

- 1) V. Tolmachev et al., Appl. Radiat. Isot. Rep. 49 (1998) 1537.

3 - 30 The Process to Improve the Production of ^{13}N -labeled Nitrogen Gas Tracer for the Imaging of Nitrogen Fixation in Soybean Nodules

S. Ishii^{a)}, N. Suzui^{a)}, Yong-Gen Yin^{a)}, N. Kawachi^{a)}, H. Yamazaki^{a, b)}, A. Koyanagi^{a, b)},
N. Ohtake^{c)}, T. Ohyama^{a, c)} and S. Fujimaki^{a)}

^{a)} Medical and Biotechnological Application Division, QuBS, JAEA,

^{b)} Faculty of Science and Technology, Tokyo University of Science,

^{c)} Graduate School of Science and Technology, Niigata University

The nodule is a symbiotic organ of leguminous plants with rhizobium. Soybean plants utilize nitrogen (N) fixed by nodules from atmospheric N_2 . Until now, ^{15}N , a stable isotope, has long been used for studies of N_2 fixation. However, because this method is invasive, it is difficult to analyze a quick response to environmental (ex. temperature, light) changes.

The purpose of our study is to visualize the N_2 fixation in the nodules using PETIS under various ambient conditions and translocation of fixed N from nodules to the aerial part noninvasively and analyze the PETIS images obtained quantitatively. Previously, we developed a production method of highly purified ^{13}N -labelled nitrogen gas tracer using a gas chromatograph, and successfully visualized nitrogen fixation in intact nodules¹⁾. However, the experimental condition was not completely natural: that is, the composition of the feeding gas to the plant was $\text{N}_2:\text{O}_2:\text{He} = 10:20:70$, in which the proportion of (nonradioactive) nitrogen was purposely lowered from the atmospheric composition to achieve a higher specific radioactivity of ^{13}N . Moreover, a much higher radioactivity of the tracer, presumably more than 30 MBq, is required for the next experiments for visualization of the transport of fixed nitrogen to the aerial part. Therefore, our new objective has been set to obtain a tracer gas with the atmospheric composition and a higher radioactivity.

To reach new goal, in this study, we didn't purify the ^{13}N -labelled nitrogen using gas chromatograph. The crude tracer gas mixed with the ambient air was applied to test plants. This might provide very high radioactivity but also possible contamination of ^{13}N -labelled dinitrogenmonoxide (N_2O) as a byproduct.

^{13}N was produced using the $^{16}\text{O}(\text{p}, \alpha)^{13}\text{N}$ nuclear reaction. CO_2 was filled in a target chamber and irradiated with proton ions at energy of 18.3 MeV and electric current of 5 μA for 10 min delivered from the cyclotron (TIARA). The irradiated target gas was collected into a plastic bag with soda lime powder (a strong absorber for CO_2) and small amount of ambient air. The resultant radioactive gas was collected to a syringe by injecting water into the bag. Finally, approximate 200 MBq of ^{13}N was obtained in a few tens milliliter of ambient air. This gas was fed to the underground part of soybean plants for 10 min. In some cases, nonradioactive N_2O was mixed to the tracer gas before the feeding to dilute ^{13}N -labelled N_2O in order to distinguish possible images of ^{13}N -labelled N_2O and of ^{13}N -labelled N_2 . The serial images by PETIS were collected for 1 h (360 frames \times 10 seconds). As a result, a strong unidentified signal was observed in the hydroponic culture as well as a moderate signal in the nodules (Fig. 1). We think this showed ^{13}N -labelled N_2O was solved into the culture. Moreover, the signal in the nodules decreased to almost 1/3 of the original intensity when nonradioactive N_2O was added to the tracer gas in advance. This probably indicates that the 2/3 of the original signal was derived from the ^{13}N -labelled N_2O .

In conclusion, ^{13}N -labelled N_2O must be removed by all means, but in the same time, high yields of radioactivity must be achieved. We are now trying a new production method to reduce N_2O to N_2 directly in a short time.

Reference

- 1) S. Ishii et al., Soil Sci. Plant Nutr. 55 (2009) 660-66.

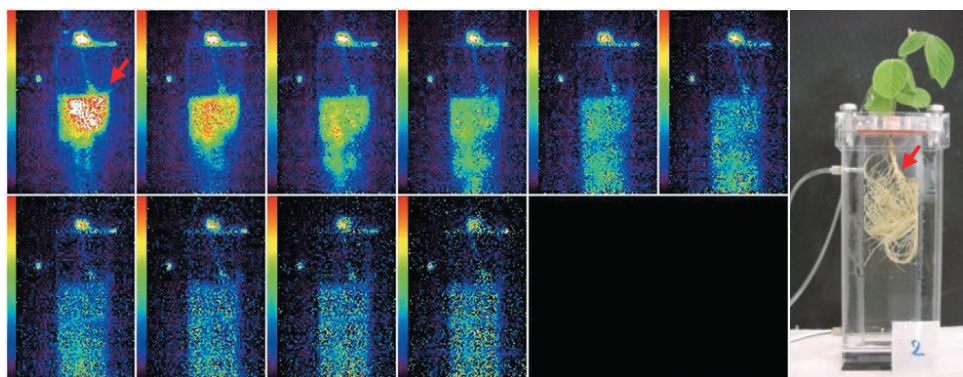


Fig. 1 Serial images of the distribution of ^{13}N (integrated by every 4 min) [Left]. Photograph in the same view [Right]. The red arrows indicate the main nodules.

3 - 31 Real-Time Imaging and Analysis of Differences in Cadmium Dynamics in Rice Cultivars (*Oryza sativa*) Using Positron-Emitting ¹⁰⁷Cd Tracer

S. Ishikawa^{a)}, N. Suzui^{b)}, S. Ito-Tanabata^{b, c)}, S. Ishii^{b)}, M. Igura^{a)}, Tadashi Abe^{a)}, M. Kuramata^{a)}, N. Kawachi^{b)} and S. Fujimaki^{b)}

^{a)} Soil Environment Division, NIAES, ^{b)} Medical and Biotechnological Application Division, QuBS, JAEA, ^{c)} Agricultural Research Institute

Rice is a major source of dietary intake of cadmium (Cd) for populations that consume rice as a staple food. Understanding how Cd is transported into grains through the whole plant body is necessary for reducing rice Cd concentrations to the lowest levels possible, to reduce the associated health risks. In this study, we have visualized and quantitatively analyzed the real-time Cd dynamics from roots to grains in typical rice cultivars that differed in grain Cd concentrations. We used positron-emitting ¹⁰⁷Cd tracer and an innovative imaging technique, the positron-emitting tracer imaging system (PETIS). In particular, a new method for direct and real-time visualization of the Cd uptake by the roots in the culture was first realized in this work.

Imaging and quantitative analyses revealed the different patterns in time-varying curves of Cd amounts in the roots of rice cultivars tested. Three low-Cd accumulating cultivars (*japonica* type: Nipponbare, Koshihikari, Sasanishiki) showed rapid saturation curves, whereas three high-Cd accumulating cultivars (*indica* type: Choko-koku, Jarjan, Anjana Dhan) were characterized by curves with a peak within 30 min after ¹⁰⁷Cd supplementation, and a subsequent steep decrease resulting in maintenance of lower Cd concentrations in their roots (Fig. 1). This difference in Cd dynamics may be attributable to OsHMA3 transporter protein, which was recently shown to be involved in Cd storage in root vacuoles and not functional in the high-Cd accumulating cultivars¹⁻³⁾.

Moreover, the PETIS analyses revealed that the high-Cd accumulating cultivars were characterized by rapid and abundant Cd transfer to the shoots from the roots (Fig. 2),

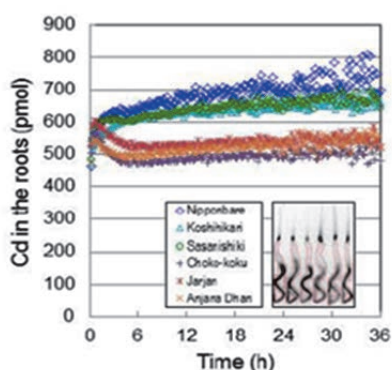


Fig. 1 Imaging and analysis of ¹⁰⁷Cd uptake by the roots of rice cultivars (vegetative stage). Time courses of Cd amounts in the roots surrounded by red lines in the black and white photograph.

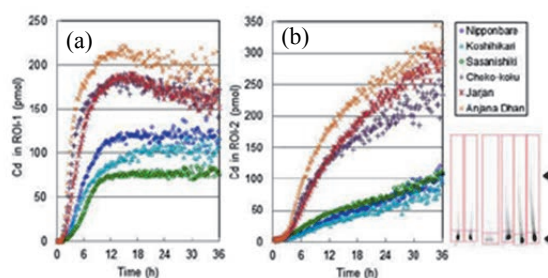


Fig. 2 Imaging and analysis of ¹⁰⁷Cd transport into shoots and of six rice cultivars (vegetative stage). (a) Time course of Cd amounts in ROI-1 (shoot bases). (b) Time course of Cd amounts in ROI-2 (leaf sheaths and leaf blades). The relevant portion of each ROI is surrounded by red lines in the black and white photograph. Cd in ROI (pmol) in Figure indicates the sums of radioactive ¹⁰⁷Cd and nonradioactive Cd.

a faster transport velocity of Cd to the panicles, and Cd accumulation at high levels in their panicles, passing through the nodal portions of the stems where the highest Cd intensities were observed (Fig. 3).

This is the first successful visualization and quantification of the differences in whole-body Cd transport from the roots to the grains of intact plants within rice cultivars that differ in grain Cd concentrations, by using PETIS, a real-time imaging method.

References

- 1) H. Miyadate et al., *New Phytol.* 189 (2011) 190-99.
- 2) D. Ueno et al., *Proc. Natl. Acad. Sci. USA* 107 (2010) 16500-505.
- 3) D. Ueno et al., *J Exp Bot* 62 (2011) 2265-72.

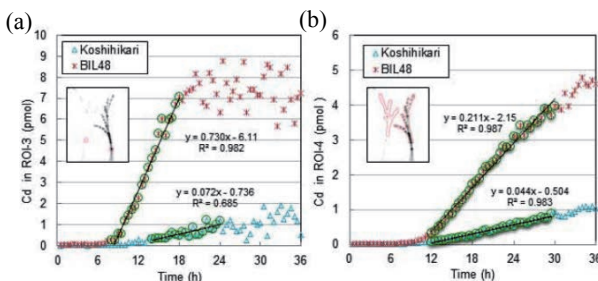


Fig. 3 Imaging and analysis of ¹⁰⁷Cd transport into the panicle for Koshihikari and BIL48. (a) Time course of Cd amounts in ROI-3 (neck nodes of panicles). (b) Time course of Cd amounts in ROI-4 (panicles). BIL48 carries the QTL (quantitative trait locus) responsible for high Cd accumulation derived from Jarjan with the Koshihikari genetic background.

3 - 32 Imaging of Root Exudates Secreted from Soybean Root to Soil by Using Carbon-11-Labeled Carbon Dioxide and PETIS

Y-G. Yin ^{a)}, N. Suzui ^{a)}, N. Kawachi ^{a)}, S. Ishii ^{a)}, H. Yamazaki ^{a, b)},
A. Koyanagi ^{a, b)} and S. Fujimaki ^{a)}

^{a)} Medical and Biotechnological Application Division, QuBS, JAEA,
^{b)} Faculty of Science and Technology, Tokyo University of Science

1. Introduction

The root of higher plant has important role in absorb essential nutrients critical to life. On the other hand, the root evolved special abilities to uptake of nutrients from the rhizosphere environment because that is fixed in the soil. As one example, the roots secrete organic acids to surrounding of rhizosphere for solubilization of the insoluble mineral in soil and absorb directly or indirectly of the nutrition. Previously, our group has reported that imaging of cadmium (Cd) uptake from hydroponic culture solution to root for study the mechanism of mineral metabolism by using a positron-emitting tracer imaging system (PETIS) in plant. In this study, we performed the imaging of organic matter which is exudate from root to soil cultivation by using carbon-11-labeled carbon dioxide (¹¹CO₂) gas tracer with PETIS.

2. Materials and Methods

Seeds of soybean (*Glycine max*) cultivar Jack were germinated in culture room at 26 °C under a light intensity of 650 μmol photon/m²/s with a 12/12 h light/dark cycle. Seedling was transplanted into the root-box and grown in soil. Two parts of the root-box made from oblong biological dishes each was wrapped by the nylon mesh. The root-box was crammed soil into the inside of each two parts, which structures can be open and close. Five-week-old plants were performed imaging experiments with the PETIS.

The aerial part of soybean was covered with a gas cell for feeding 220 MBq of ¹¹CO₂ gas transiently (Fig. 2A). At first step of imaging, ¹¹C-photoassimilate translocation from leaf to root was imaged for 60 minutes at root-box area with root. Then, the plant including root was removed from the

root-box. At second step of imaging, the PETIS was restarted for 60 minutes in state of without root of the root-box (Fig. 1).

3. Results and Discussion

Figures 2B and C show PETIS image data of ¹¹C-activities of root and root exudates of soybean in root-box area. As shown in Fig. 2A, we selected the PETIS imaging area in underground part of soybean including the root-box. In Fig. 2B, we can see the ¹¹C-activities of root in the state of root within root-box. These ¹¹C-activities were translocated from the photoassimilate of leaves, and its highest in primary root. In Fig. 2C, the ¹¹C-activities indicate the root exudates in soil of root-box that were secreted from root. The total ¹¹C-activities of root exudates show approximately 2.7% of total ¹¹C-photoassimilate of root in root-box area.

For analysis of the exudates of ¹¹C-assimilate in rhizosphere soil, we were selected many regions of interests (ROIs), then quantitated the root exudate in each ROIs. The results of ¹¹C-activities ratio of root exudates of soil in each ROIs show almost 0.8-3.7% of activities of root image respectively, and they are highest in root tips area.

In this study, we report for a new method based on the use of PETIS and tracer gas of ¹¹CO₂ for detect and quantitative of carbon secretion by root grown in soil.

References

- 1) N. Kawachi et al., JAEA Takasaki Annu. Rep. 2010 (2012) 93.
- 2) N. Suzui et al., JAEA Takasaki Annu. Rep. 2010 (2012) 95.

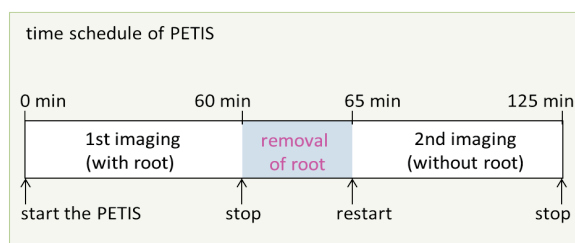


Fig. 1 Time schedule and methods in PETIS experiments. At 1st 60 minutes, the root-box was imaged by PETIS in state of root-box with root. At 2nd imaging, we removed the root from root-box (without root) and then has imaged for 60 minutes.

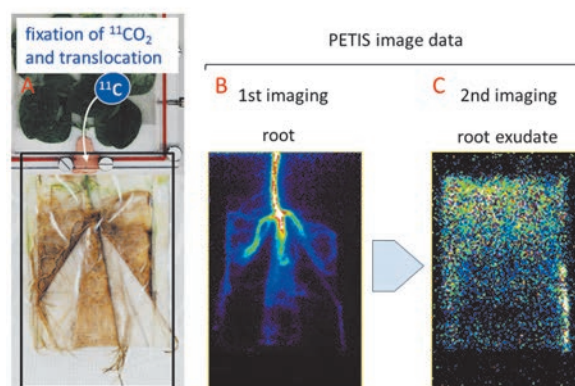


Fig. 2 Image data of PETIS experiment. A, setup of soybean aerial part for feeding ¹¹CO₂ gas. B, ¹¹C-activities in root. C, ¹¹C-activities of root exudates in soil.

3 - 33 A New Method to Analyze Individual Photosynthetic Abilities of Young Plant Seedlings Using Positron-Emitting Tracer Imaging System (PETIS)

N. Kawachi^{a), d)}, A. Koyanagi^{a), b), d)}, N. Suzui^{a), d)}, S. Ishii^{a), d)}, Yong-Gen Yin^{a), d)}, H. Yamazaki^{a), b), d)}, A. Iwasaki^{c), d)}, K. Ogawa^{c), d)} and S. Fujimaki^{a), d)}

^{a)} Medical and Biotechnological Application Division, QuBS, JAEA, ^{b)} Faculty of Science and Technology, Tokyo University of Science, ^{c)} Plant Redox Regulation Research Group, Research Institute for Biological Sciences Okayama, ^{d)} JST, CREST

Elucidation of carbon kinetics, in particular, those related to photosynthetic carbon dioxide (CO₂) fixation and photoassimilate translocation, in higher plants is important from the viewpoint of atmospheric CO₂ level mitigation and from the agricultural viewpoint of growth and development of the plant body. Previously, we have reported the use of radiotracer imaging for studying the carbon kinetics of photosynthesis and photoassimilate translocation in a plant body. We had employed the positron-emitting tracer imaging system (PETIS) in combination with carbon-11-labeled carbon dioxide (¹¹CO₂) as the tracer gas^{1,2)}. In the present study, we have developed a new method based on PETIS and ¹¹CO₂ to evaluate individual photosynthetic abilities of young seedlings planted collectively on a petri dish with agar culture medium and thus investigate the effect of genetic modification or treatment on plant biomass enhancement.

A chamber (374 x 414 x 70 mm³) with an inlet, an outlet, light sources and small two fans was designed for uniform feeding of ¹¹CO₂ to the test plants. A petri dish with agar medium including sixteen *Arabidopsis thaliana*, the most popular model used in experimental plant studies, seedlings (10 days after sown) each was placed into the chamber. After the tracer gas was uniformly distributed in the chamber, the cover of petri dish was displaced by pulling with a string connected to the cover from outside, after that the plants were exposed to the tracer gas.

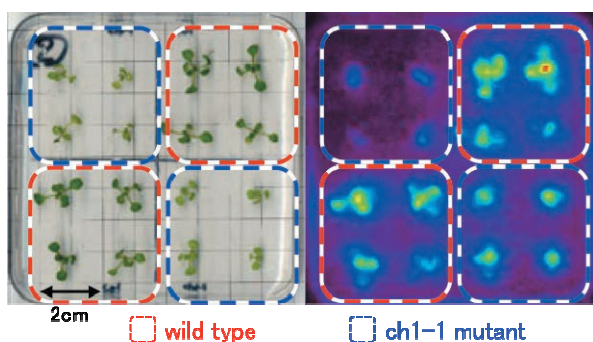


Fig. 1 Photograph of petri dish with agar culture including sixteen wild-type and ch1-1 mutant *Arabidopsis thaliana* young plants (left) and PETIS image showing individual photosynthetic ability of seedlings (right).

The ¹¹C images obtained with PETIS acquisition showed very little variation, and the average rate of carbon fixation by wild-type plants was accurately estimated (standard error: ~6%) by mathematical analysis, which proved the good quantitative capability of the present experimental system and analysis method for evaluating a genetically homogeneous line (Fig. 1). Then, eight *chl-1* mutant plants, which lacked chlorophyll *b* and had low carbon fixation activity, were analyzed by this method, together with eight wild-type plants. The carbon fixation rate for the *chl-1* mutants was analyzed 53 ± 4 % lower than that for the wild-type plants in Fig. 2.

In conclusion, we report for the first time a method based on the use of PETIS and tracer gas of ¹¹CO₂ for the quantitative and statistical evaluation of carbon fixation by small plant individuals.

We plan to apply the method for analysis on the relationship between the individual carbon fixation ability and the expression of genes suggested to be involved with the photosynthesis. Furthermore, evaluation of the rate constants of photoassimilate translocation is in progress.

References

- 1) N. Kawachi et al., JAEA Takasaki Annu. Rep. 2010 (2012) 93.
- 2) N. Kawachi et al., Nucl. Instrum. Meth. Phys. Res. A 648 (2011) 317.

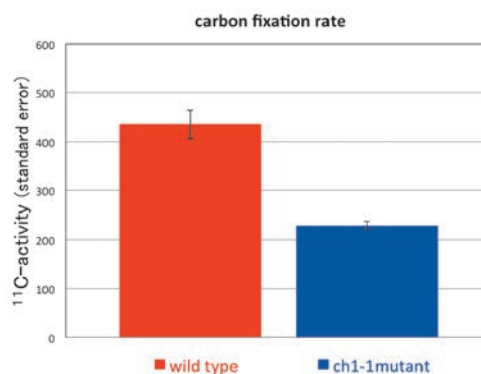


Fig. 2 Differences in carbon fixation rate between wild-type and ch1-1 mutant *Arabidopsis thaliana* plants. Error bars indicate the standard error (SE) around the mean.

3 - 34

Production of Cs-129 Tracer by Using Ion Beam Bombardment for Positron Imaging Applications

N. Suzui, Y.-G. Yin, N. Kawachi and S. Fujimaki

Medical and Biotechnological Application Division, QuBS, JAEA

Introduction

A vast land area was contaminated with radiocesium by the accident of the Tokyo Electric Power Company, Inc. Fukushima Daiichi Nuclear Power Station. For production of safe foods and decontamination of the soil using cleanup plants, it is strongly required to elucidate the total dynamics of radiocesium from the soil to the plant parts under various environmental/agricultural conditions. We have previously made clear some key dynamics and mechanisms of soil-to-fruit transport of cadmium, one of the most serious soil contaminant in the world, by using a positron-emitting tracer imaging system (PETIS)¹⁾. Moreover, we also successfully evaluated a few rice cultivars as candidates for a cleanup plant with their uptake capacities for cadmium by using PETIS²⁾. Based on these experiences, we are trying to establish new technologies of radiotracer imaging which can visualize and analyze the movement of radiocesium in the soil-plant system. However, the radiocesium nuclides in the present environment, Cs-134 and Cs-137, are both NOT positron-emitting nuclides and thus NOT available for PETIS. Our objective in the present project is to establish a production method for Cs-129, a positron-emitting radionuclide, by using ion beam bombardment, and to realize positron imaging of radiocesium in intact plants.

In a previous study, we found that Cs-129 (half-life: 32 hour, positron emission rate: 0.0027% per decay) can be produced when sodium iodide (NaI) target is bombarded with 50 MeV of helium ion beam through the $^{127}\text{I}(\alpha, 2n)^{129}\text{Cs}$ nuclear reaction. In this study, potassium iodide (KI) was also examined because sodium ion is toxic for plants.

Results and Discussion

Target plates with a thickness of 0.55 mm were made by pressing pure chemical reagents of NaI and KI for ion beam bombardment. These targets were irradiated with helium ion beam for 20 minutes, and 12 hours later, solved in pure water and purified with an anion-exchange column for removal of iodide ions (Fig.1). Finally, the collected solution was subjected to nuclide analysis using a Ge semiconductor detector. As a result, Cs-129 was identified as the main product from the both targets, but some by-products were also detected. The harvested amounts of Cs-129 after purification with the anion-exchange column were 1.2 - 1.6 MBq (Table 1). We estimate that approximately 13 MBq of Cs-129 in total is required to obtain serial images of sufficient quality by every 1 hour from the PETIS measurements. Therefore, the present results suggest that the positron imaging with Cs-129 tracer and intact plants is feasible by approximately 3 hours of ion beam bombardment. In the next step, we will develop a good purification method to remove the radioactive by-products.

Acknowledgements

We thank Dr. Satoshi Watanabe (Medical Radioisotope Application Group) for his help in the irradiation experiments.

References

- 1) S. Fujimaki et al., *Plant Physiol.* (2010) 1796-1806.
- 2) S. Ishikawa, N. Suzui et al., *BMC Plant Biol.* (2011) 172:1-12.

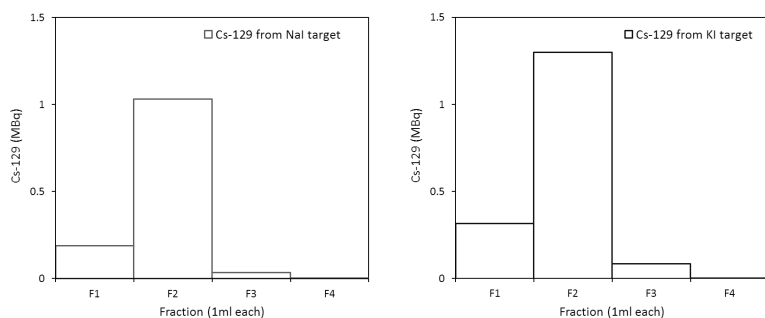


Fig. 1 Fractions from anion-exchange columns for purification of Cs-129 after ion beam bombardment of NaI [Left] and KI [Right].

Table 1 Conditions of bombardment and yields of Cs-129.

Target material	Beam species and energy (mmol)	Beam current (μA)	Irradiation time (min)	Yield (MBq)	Efficiency (MBq/μA/min/mmol)
NaI	1.0 α 50 MeV	1	20	1.6	0.075
KI	0.77 α 50 MeV	1	20	1.2	0.078

3 - 35 Development of Ion Beam Breeding Technology in Plants and Creation of Useful Plant Resources

Y. Hase^{a)}, S. Nozawa^{a)}, T. Okada^{b)}, I. Asami^{c)}, T. Nagatani^{d)},
Y. Matsuo^{e)}, A. Kanazawa^{f)}, K. Honda^{g)} and I. Narumi^{a)}

^{a)} Medical and Biotechnological Application Division, QuBS, JAEA, ^{b)} Gunma Agricultural Technology Center, ^{c)} Aichi Agricultural Research Center, ^{d)} Kagoshima Biotechnology Institute, ^{e)} Saga Prefectural Agricultural Fruit Tree Experiment Station, ^{f)} Research Faculty of Agriculture, Hokkaido University, ^{g)} Faculty of Agriculture and Life Science, Hirosaki University

This study is aimed to develop ion beam breeding technology and useful plant resources. In particular, our current research is focused on the step-wise improvement of traits in flower and ornamental plants. We also focus on improvement of trees and functional ingredients in crops because little knowledge has been accumulated in this area. Here, we describe recent progress made in these studies.

Chrysanthemum variety 'Konatsunokaze', which has unique round-shaped petals, was developed by Gunma Agricultural Technology Center. In order to obtain color variants with a similar petal shape, leaf cultures of chrysanthemum strain '07-33' were irradiated with carbon ions with doses of 0.1–5.0 Gy. In total, 1,769 regenerated plants were obtained from 1,941 cultured leaf segments. The chrysanthemum strain '07-33' has light pink flowers. So far, dark pink, white and cream flower mutants, bicolor (pink/white) mutants, and mutants with doubled flowers were obtained.

Spray variety of chrysanthemum 'Pretty Lala (pink flower)', which was developed by Aichi Agricultural Research Center, was irradiated with carbon ions. A mutant with dark pink flowers and a mutant with striped pink flowers were obtained from 700 regenerated plants. As for the irradiation of chrysanthemum strain 'Princess (tentative name)', eighty variants were obtained from about 1,500 regenerated plants. Cutting was performed to obtain non-chimeric mutants. Finally, ten mutant lines were selected. Further characterization of mutant traits and re-irradiation of these mutants will be performed.

We carried out further improvement of chrysanthemum variety 'Araddin'. Two mutant lines were selected last year according to the number of adventitious buds, flower quality and the growth under a low temperature condition. In this year, growth characteristics of two mutant lines were examined under a low temperature condition by 4 degree than the standard cultivation condition in Kagoshima prefecture. The mutant lines flowered 12 days earlier than 'Araddin' did. Number of adventitious bud was slightly lower than that of 'Araddin'. Flower quality was as good as 'Araddin'.

In order to develop ion beam breeding technology in trees, improvement of Japanese mandarin orange has been carried out. The cut surfaces of hypocotyls of cultivar 'Imamura-unshu' were exposed to carbon ions with the doses of 2 and 4 Gy. The mean plant height decreased as

the dose increased. The mean plant height and internode of non-irradiated plants was 70.6 cm and 2.1 cm, respectively. Of 1,119 regenerated plants, 114 plants that were shorter than 30 cm and 149 plants with shorter internode less than 1.6 cm were selected.

Soybean is an important crop that provides food, oil, forage and industrial raw materials. Genome sequence of soybean revealed that ~75% of genes present in multiple copies¹⁾. It is likely that gene duplication lowers the efficiency of mutant production. We carried out a detailed analysis of mutagenic effect of carbon ions in soybean. We identified chlorophyll-deficient mutants in M₂ generation of plants irradiated with 2.0–7.5 Gy. We also found some plants that had a similar chlorophyll-deficient phenotype even in M₁ generation. We examined the heritability of such an altered phenotype and found that all the progeny of a plant designated 'M1a' had the altered phenotype. Interestingly, two of seven progeny plants had an extremely early-flowering phenotype in addition to the chlorophyll deficiency. These traits were also maintained in M₃ generation. The chlorophyll-deficient plants, which were found in M₂ generation, mostly had a late-flowering phenotype or a low growth rate. In the next generation, some plants having altered leaf morphology or an altered degree of chlorophyll deficiency were newly found. These results suggest that mutations accumulate and/or an altered phenotype become evident after passing through generations of post-irradiation in soybean.

In order to create useful plant resources in terms of functional ingredients, dry seeds of traditional pepper variety 'Hirosaki Zairai' in Aomori prefecture, were irradiated with carbon ions. Four mutants with shorter internodes, two mutants with increased branching and two mutants having fleshy fruits were obtained. Further genetic analysis of these mutants and the fixation of useful mutant traits will be performed. Although some morphological alterations were observed even in M₁ generation, there was no clear relationship between morphological alterations found in M₁ and M₂ generations of each line.

Reference

- 1) J. Schmutz et al., Nature 463 (2010) 178.

3 - 36 Ion Beam Irradiation on Rice Seeds for the Mutation Breeding Project of the Forum for Nuclear Cooperation in Asia (FNCA)

A. Tanaka^{a)}, S. Nozawa^{a)}, Y. Hase^{a)}, I. Narumi^{a)}, H. Ishikawa^{b)} and A. Koike^{b)}

^{a)} Medical and Biotechnological Application Division, QuBS, JAEA,
^{b)} Nuclear Safety Research Association

1. Introduction

From 2009, ion beams have been utilized for the Sub-Project on Composition or Quality in Rice (FY 2007–2012) under the Mutation Breeding Project of the Forum for Nuclear Cooperation in Asia (FNCA) of MEXT (Ministry of Education, Culture, Sports, Science and Technology)¹⁾. This sub-project contributes to increase food production and to improve food quality in Asia, by developing new rice mutant varieties that are more resistant to disease, insects, and drought, or give higher yields and offer higher quality. Eight participant countries, i.e., Bangladesh, China, Indonesia, Korea, Malaysia, The Philippines, Thailand and Vietnam joined this project and irradiated seeds of their own rice varieties with ion beams.

2. Materials and Methods

In general, hulled dry seeds of rice varieties of participant countries were irradiated with 320 MeV carbon ions at TIARA. After irradiation, seeds were rightly sent back to the participant countries and grown to obtain the offspring.

At the FNCA workshop on Mutation Breeding held in Thailand in February 2012, we have deeply discussed the appropriate population size for mutation induction and concluded that at least several seeds from each 5 panicles from each 1,000 M_1 plants should be harvested in order to obtain mutants efficiently from 5,000 initial mutated cells. We also discussed how to overcome problems of fungal infection and low germination rate of irradiated seeds that happened in Bangladesh and Malaysia. It was recommended to soak seeds in 1% fungicide (benomyl) solution for one night for disinfection. To avoid reduction of seed viability, the seeds must be sown as soon as possible after irradiation with ion beams, although rice seeds can be stored longer, even a year under low temperature (5–15 °C) and dry condition.

3. Results and Discussion

In FY2011, most of participant countries finished to decide the best doses for mutation induction and have started to harvest descendant plants and mutant screening. For example, in Malaysia, in order to obtain mutants useful for minimal water requirement and improvement of nutrient content, dozens of mutagenized M_2 lines derived from ‘MR219’ variety irradiated with carbon ions were planted for further experiment (Fig. 1). In Bangladesh, the M_2 families derived from carbon ion-irradiated seeds of a local salt tolerant variety ‘Ashfal’ were evaluated. Since the

‘Ashfal’ is a highly photosensitive variety, none of the non-irradiated plants flowered under long day conditions. However, several photo-insensitive mutants were obtained that flowered even under long day conditions (Fig. 2). These mutants are slightly dwarf and showed early maturing and high yield. These mutants are useful materials to develop new rice variety in Bangladesh.



Fig. 1 M_2 lines derived from ‘MR219’ variety irradiated with carbon ions were planted in order to evaluate their mutant characters.

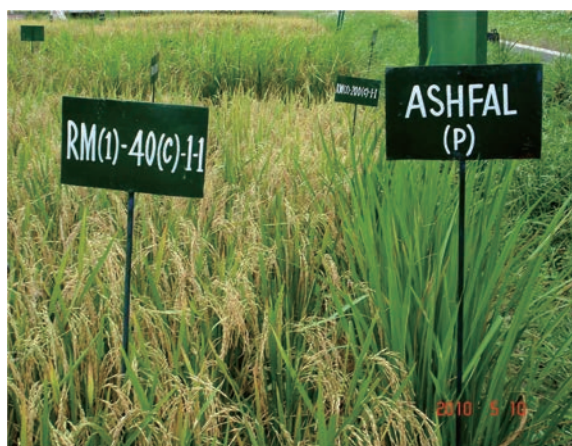


Fig. 2 Parental variety ‘Ashfal’ (right) and photo-insensitive mutant line that shows early maturing and high yield (left) under long day conditions (*boro* season, December to May).

Reference

- 1) A. Tanaka et al., JAEA Takasaki Annu. Rep. 2010 (2012) 101.

3 - 37 Generating New Ornamental Plant Varieties Using Ion Beams

A. Zaiton^{a)}, A. H. Affrida^{a)}, S. Shakinah^{a)}, S. Nozawa^{b)}, I. Narumi^{b)},
Y. Hase^{b)} and Y. Oono^{b)}

^{a)} Agrotechnology and Biosciences Division, Malaysian Nuclear Agency,
^{b)} Medical and Biotechnological Application Division, QuBS, JAEA

Chrysanthemums, which belong to genus *Chrysanthemum*, consist of approximately 30 species of perennial flowering plants. It is one of the leading cut flowers in Malaysia's cut flower industry. Due to the increasing demand of chrysanthemum cut flower, there is a need for new variety of chrysanthemum in order to compete to the ever-competitive cut flower market.

Induced mutation breeding using ionizing radiation is one of the effective methods in plant breeding that resulted in generation of new mutated alleles and most unique feature¹⁾. Attempt was carried out to apply mutation breeding technique using ion beam radiation to produce new variety of chrysanthemum.

A pink variety of *Chrysanthemum morifolium* (Fig. 1) was used in this experiment. The ray florets were surface-sterilized and cultured on 6-cm sterile petri dishes containing MS medium²⁾ supplemented with 0.5 mg/L α -naphthalene acetic acid (NAA) and 2.0 mg/L 6-benzylaminopurine (BAP). The samples, covered with Kapton films, were irradiated with 320 MeV $^{12}\text{C}^{6+}$ ion beams at 0, 0.5, 0.8, 1, 2, 5, 8, 10, 15, 20 and 30 Gy from the TIARA AVF cyclotron. The irradiated petals were transferred onto fresh media and incubated at $25\pm 2^\circ\text{C}$ under 16-h photoperiod for proliferation.



Fig. 1 *Chrysanthemum morifolium* pink.

Data on callus formation and shoot regeneration was recorded at 4th and 8th weeks after the irradiation of petals. From the observation, degree of callus formation decreased tremendously from 5 Gy to 8 Gy (Fig. 2).



Fig. 2 Differences in callus formation at 5 Gy and 8 Gy.

The dose response curve is shown in Fig. 3. The percentage of survived cultures decreased at doses higher than 5 Gy, and dropped to 50% at 10 Gy as early as 4 weeks. At doses higher than 15 Gy, less than 10% of the petals could produce callus, and the growth was very slow and not vigorous. At week 8, petals at doses above 8 Gy formed almost no callus and shoots.

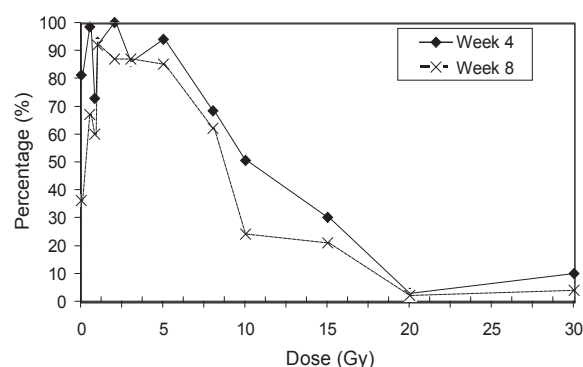


Fig. 3 Percentage of callus formation at week 4 and week 8.

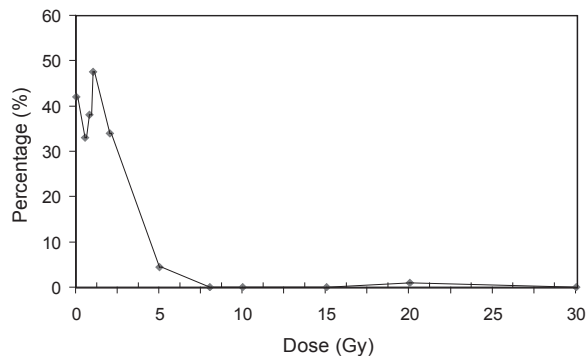


Fig. 4 Percentage of shoot regeneration at week 8.

Higher doses also affected shoot regeneration. The percentage of shoot formation was between 33 to 47.5% for doses below 2 Gy. The percentage dropped to lower than 5% at 5 Gy, whilst at doses higher than 8 Gy, no shoot formation was recorded (Fig. 4).

The experiment will be repeated to determine the accurate optimum irradiation dose for this variety. Meanwhile all shoots generated are being sub-cultured and will be planted in the nursery.

References

- 1) T. Murasige et al., *Physiol. Plant* 15 (1962) 473.
- 2) Q. Y. Shu et al., *Mol. Plant Breed.* 5 (2007) 193.

3 - 38 Mutational Effects of Carbon Ions near the Range End and Development of an Efficient Mutagenesis Technique Using Ion Beams

Y. Hase, R. Yoshihara, S. Nozawa and I. Narumi

Medical and Biotechnological Application Division, QuBS, JAEA

The accelerated heavy ions deposit most of their energy close to the end of their range. Little is known about the mutational effects of ion beams near the range end, especially in plants. In previous studies, we showed that the carbon ions near the range end (mean LET, 425 keV/μm) had higher cell killing effect than 208 MeV carbon ions (mean LET, 113 keV/μm)¹⁾. To irradiate the whole seeds with carbon ions near the range end, the seeds were sequentially exposed to five different carbon ion beams (89, 77, 64, 49 and 30 MeV). Doses corresponding to the shoulder of the survival curves were 180 and 80 Gy for 208 MeV carbon ions and carbon ions near the range end, respectively. We also showed that the difference of radiation sensitivity between the Arabidopsis wild type and ligase IV mutant, deficient in non-homologous end joining repair, was greatly diminished in the case of carbon ions near the range end. This result suggested that the carbon ions near range end induce more irreparable DNA lesions than 208 MeV carbon ions.

To further characterize the mutational effects of carbon ions near the range end, we analyzed the mutations occurred in the Arabidopsis *GLI* gene with the emphasis on large deletions²⁾. Arabidopsis seeds obtained by crossing the wild type with *gli-1* mutant were used as a material. The DNA markers that can distinguish the wild type and *gli-1* sequence were used to detect deletions. The frequency of glabrous mutant sectors, which is caused by inactivation of *GLI* gene, was not significantly different between 208 MeV carbon ions and carbon ions near the range end (Table 1). However, the carbon ions near the range end induced deletions (> 6.7 kb) more frequently by 6 times than 208 MeV carbon ions. To accumulate the knowledge about the LET dependency of the frequency of large deletions, we also examined the mutational effects of 316 MeV neon ions. The frequency of deletions was higher by more than 6 times than the frequency in 208 MeV

carbon ions (Table 1). The frequency of deletions thus appears to be affected by LET. Most of the deletions were assumed to be more than 88 kb. The total length of deletions remains to be evaluated.

We previously showed that the frequency of flower color mutants was increased by ion beam irradiation combined with sucrose pretreatment in petunia³⁾. Sucrose treatment promotes pigment biosynthesis in petunia seedlings. Our result suggests that the condition of the cells, possibly profile of gene expression, alters the mutation frequency of particular phenotypes. To gain more insight into the relationship between gene expression status and mutation frequency, we prepared transgenic Arabidopsis plants that have *GLI* gene driven by a chemical-inducible promoter. The *GLI* cDNA was cloned into the hormone (dexamethazone and estrogen)-based chemical-inducible expression vectors. Arabidopsis *gli-1* mutant, which has no trichome on leaf surface, was transformed with these vectors. We confirmed that the transgenic plants develop trichomes upon hormone administration. This indicates that the expression status of *GLI* gene can be controlled by hormone administration. At present, the induction of trichome development is unstable and the methods for hormone administration have to be improved for further experiments. We are going to compare the mutation frequency on *GLI* gene between hormone-treated and non-treated transgenic plants.

A part of these studies were supported by Grant-in-Aid for Young Scientists (B) 23780008, JSPS.

References

- 1) Y. Hase et al., JAEA Takasaki Annu. Rep. 2010 (2012) 103.
- 2) Y. Hase et al., Mutat. Res. 731 (2012) 41.
- 3) Y. Hase et al., Plant Biotechnol. (2010) 99.

Table 1 Frequency of plants with glabrous mutant sectors and mutant sectors with deletions around *GLI* locus.

Ion beams ^a	Mean LET (keV/μm)	Total number of plants examined	Number of plants with a glabrous mutant sector	Number of mutant sectors with deletion (> 6.7 kb) around <i>GLI</i> locus
208 MeV carbon	113	,873	24 (2.7×10^{-2})*	1 (1.1×10^{-3})**
89 ~ 30 MeV carbon	425	1,065	29 (2.7×10^{-2})*	7 (6.6×10^{-3})**
316 MeV neon	352	1,147	36 (3.1×10^{-2})*	8 (7.0×10^{-3})**
Non-irradiated	—	,440	0 (0.0×10^{-2})*	—

^a The values represent total energy at sample surface.

* Significantly higher than the frequencies in 208 MeV carbon and 89 ~ 30 MeV carbon.

** Significantly higher than the frequency in 208 MeV carbon.

3 - 39 Effect of Carbon Ion Beam Irradiation on Callus Growth in Arabidopsis and Rice

H. Saika ^{a)}, R. Yoshihara ^{b, c)}, A. N. Sakamoto ^{b)} and S. Toki ^{a, d)}

^{a)} Agrogenomics Research Center, National Institute of Agrobiological Sciences, ^{b)} Medical and Biotechnological Application Division, QuBS, JAEA, ^{c)} Research Center for Environmental Genomics, Kobe University, ^{d)} Kihara Institute of Biological Research, Yokohama City University

To date, many commercial varieties of various kinds of plants have been developed by ion beam breeding. However, to further improve the ion beam breeding system, it is important to gather more basic information on the mutagenic effects of ion beams in plants. To this end, we try to establish a novel mutation detection system using a conditional negative selection marker to stop cell growth. In this system, mutations not only in the marker gene but also in the whole genome can be analyzed since each mutant cell in which the marker gene is disrupted can be clonally propagated independently. Cultured cells such as callus that can clonally propagate efficiently and easily are well-suited to this system. In the present study, we checked the sensitivity of callus of the model plants *Arabidopsis* (*Arabidopsis thaliana*, var. Col.) and rice (*Oryza sativa* L. cv. Nipponbare) to carbon ion beams.

One-month-old root segments of *Arabidopsis* were cultured on callus induction medium. At 7 days after induction, callus was irradiated with various doses of carbon ion beams (¹²C⁶⁺, 320 MeV). After 19-days irradiation, callus was cultured on regeneration medium for 3 weeks at

22 °C and regeneration frequency was evaluated. In rice, dehulled mature seeds were cultured on callus induction medium for 18 days at 33 °C. Callus with a diameter of smaller than 2 mm was irradiated with various doses of carbon ion beam (¹²C⁶⁺, 320 MeV). Irradiated calli were cultured on callus induction medium for 21 days at 33 °C, and the fresh weight of each callus was measured.

In *Arabidopsis*, doses higher than 7.5 Gy ion beam irradiation led to a decrease in shoot regeneration frequency, although no obvious differences in callus growth were observed (Fig. 1), suggesting that the optimal dose to halt cell growth in *Arabidopsis* callus was not determined. On the other hand, the fresh weight of rice calli exposed to 20 and 40 Gy ion beams was 15-20 mg, while that of calli exposed to less than 20 Gy ion beam was 30-35 mg at 21 days after irradiation (Fig. 2), suggesting that cell growth in rice callus was suppressed efficiently by irradiation with carbon ion beam >20 Gy. Thus, we confirmed that carbon ion beam of 10-15 Gy is the optimal dose for mutation analysis in rice callus.

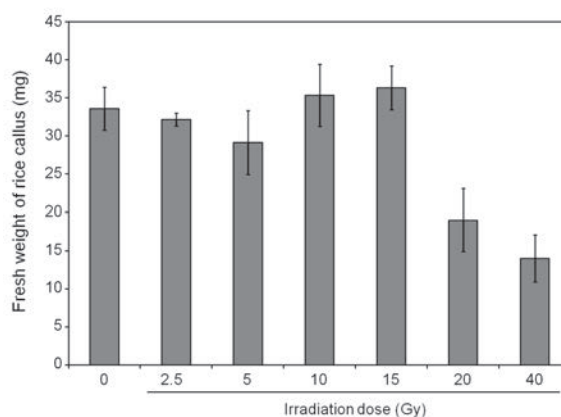
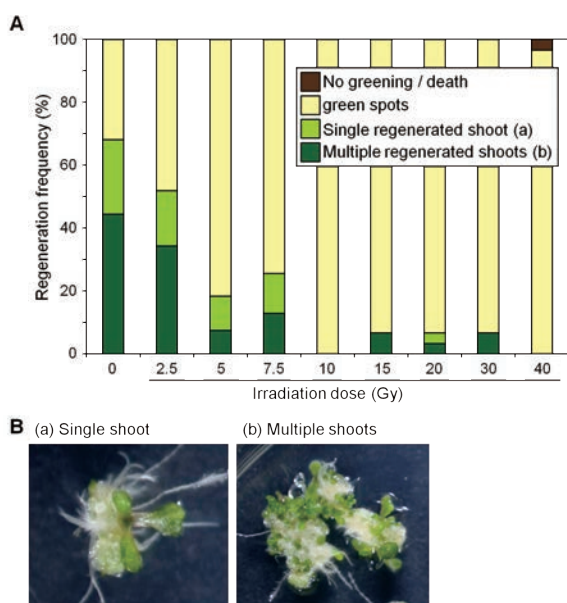


Fig. 2 Fresh weight in rice callus exposed to various doses of carbon ion beams.

Fig. 1 (A) Regeneration frequency in *Arabidopsis* callus exposed to various doses of carbon ion beams. Regeneration frequency was evaluated according to the following criteria: No greening, green spots, single shoot and multiple shoots. (B) Representative images of single (a) and multiple (b) regenerated shoots.

3 - 40 Developing Protocol for Screening of Drought/Salt Tolerant Mutants with Ion Beam Mutagenesis in *Populus* sp.

K. K. Biswas^{a)}, T. Mohri^{b)}, S. Kogawara^{b)}, I. Narumi^{a)} and Y. Oono^{a)}

^{a)} Medical and Biotechnological Application Division, QuBS, JAEA,

^{b)} Forestry and Forest Products Research Institute

Poplars are economically important trees that are favored for plantation forestry due to their capacity for rapid juvenile growth, which allows us to harvest them in a short span of time. However the rapid growth of poplar is dependent on access to plantation sites with sufficient water and this is problematic, particularly in less rainfall area.

The patterns of episodic drought over the last decade suggest that the development of drought tolerant mutant plants could be a promising approach to increase sustained vegetation biomass and forest productivity¹⁾. But, long time life cycle of woody species remains as an obstacle in quick establishment of drought tolerant woody plants. To overcome this problem, a forward genetics approach has been taken for developing drought/salt tolerant mutants by means of ion beams and *in vitro* regeneration system in *Populus*. It is believed that induced mutation through a combination of ion beam irradiation and *in vitro* regeneration has a great potential to produce new cultivars with wider mutation spectrum²⁾. Thus, the objective of this study is to develop plants by use of ion beams.

Surface-sterilized explants of *Populus* from newly growing canes of 3-to 4-month-old plants were cultured for one week in Murashige and Skoog (MS) based shoot regeneration medium and subjected to ion beam and gamma ray irradiation. Survival ability and suitable dose for screening mutants were evaluated four-to-five weeks after irradiation. Newly regenerated shoots were further cultured in rooting medium and the plants with healthy root system were used for screening of drought/salt tolerant mutants. Tolerance level to salt was monitored by ability of regenerated shoots for growth and root development in NaCl-supplemented rooting medium.

For screening of drought/salt tolerant mutants, *in vitro* regeneration system had been established (Fig. 1). About 87% of the shoot explants produced regenerated shoots in shoot regeneration medium, whereas 77% regenerated shoots developed roots in root induction medium. Survival rate of the regenerated plants in soil was about 88%.

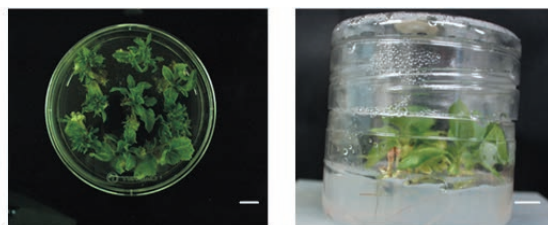


Fig. 1 *In vitro* regeneration in *Populus*. Bars:1 cm.

Results shown in Fig. 2 indicate that the suitable dose of ion beams to screen mutants ranged between 2.5 Gy to 3 Gy for shoot explants in poplar. *In vitro* regenerated wild type poplar shoots did not develop any root system in rooting medium supplemented with 75 mM NaCl. Thus, the initial goal of this study to screen drought/salt tolerant mutants could be achieved by the use of well-established ion-beam facilities at Japan Atomic Energy Agency.

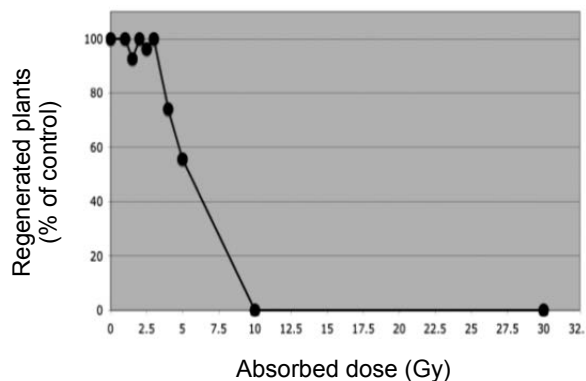


Fig. 2 Dose response curve with ion-beam irradiation to shoot explants in *Populus*.

References

- 1) S. B. Rood et al., *Tree Physiol.* 23 (2003) 1113.
- 2) S. Nagatomi et al., *Acta Horticulturae* 508 (2000) 69.

3 - 41

Effects of Gamma Ray Irradiation on *Rumex obtusifolius* L.

S. Kitano^{a)}, A. Miyagi^{b)}, Y. Oono^{c)}, Y. Hase^{c)}, I. Narumi^{c)},
H. Uchimiya^{b)} and M. Kawai-Yamada^{a,b)}

^{a)} Graduate School of Science and Engineering, Saitama University,
^{b)} Institute for Environmental Science and Technology, Saitama University,
^{c)} Medical and Biotechnological Application Division, QuBS, JAEA

Rumex obtusifolius, a member of Polygonaceae, highly accumulates oxalate in leaves. Animals should restrict their intake because high level of oxalate causes of the poisoning. Therefore, *R. obtusifolius* well growing in the meadow is a target of weeding. In this study, we aim to develop a low oxalate *R. obtusifolius* plant that can be used as a pasture by radiation breeding. Plant seeds irradiated with several doses of gamma rays were used to determine the germination rate and the lethal dose. As a result, the germination rate was not affected at doses up to 2,000 Gy. However, the growth abnormality was shown in the lower dose. In the doses above 700 Gy, almost plants died after 1st leaf expansion. In conclusion, the 50% lethal dose (LD50) of gamma rays was estimated to be 213 Gy for *R. obtusifolius*.

エゾノギシギシ(タデ科)はヨーロッパ原産の多年生草本である。繁殖力が強く牧草地に繁茂する性質があるため、播種やバイオマス維持等のコスト削減が見込めることから、新規の牧草としての利用が期待できる。しかし、この植物の代謝的特徴として、葉に可溶性シュウ酸を高蓄積することが知られている。シュウ酸は、植物にとっては被食防御などに役立つ一方、動物が過剰摂取をすると害になる。そのため、エゾノギシギシの牧草化において、低シュウ酸系統の作出が必須である。そこで、本研究では、ガンマ線照射によって、低シュウ酸個体の作出を目指して研究を行っている。

斗型の葉や左右非対称に変形した葉が見られることが多く、このような個体では多くが第2葉の形成が出来なかった。また、個体の致死率(Fig. 3)から求めた結果、LD50は213 Gyとなった。

今後、ガンマ線照射個体の葉の代謝物の測定を行い、低シュウ酸個体の探索を行う。また、メタボローム解析を行い、ガンマ線が代謝に及ぼす影響を調べる。

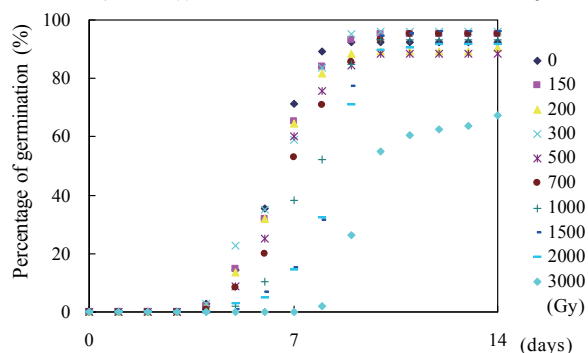


Fig. 1 Germination rate of seeds irradiated with gamma rays.

ガンマ線照射によるエゾノギシギシ変異体の作出にあたり、放射線育種を行うための線量の目安を得るために50%致死線量(LD50)を探索する必要がある。そこで、4 °Cで低温処理したエゾノギシギシの種子に0 - 3,000 Gyのガンマ線を照射し、各線量あたり100粒ずつをインキュベーター内で培養して発芽率を調べた。その結果、2,000 Gyまでの線量を照射した種子の発芽率は、非照射のものと同変らなかった(Fig. 1)。しかし、その後、培養土に移して培養室(光量60 μmol/m²s、連続光、22 °C)で育成を続けた結果、700 Gy以上のガンマ線を照射した個体は、子葉は展開するものの、本葉の形成が出来ないまま赤く変色し枯死した(Fig. 2a)。700 Gy未満の線量でも、第一葉にFig. 2bの矢印で示したような漏

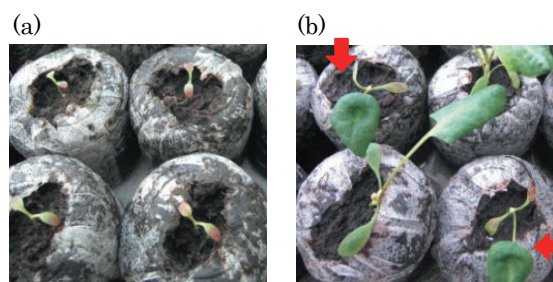


Fig. 2 *R. obtusifolius* irradiated with gamma rays. One month-old plants after 2,000-Gy (a) and 200-Gy (b) irradiation. Arrows indicate abnormal cup-shaped cotyledons.

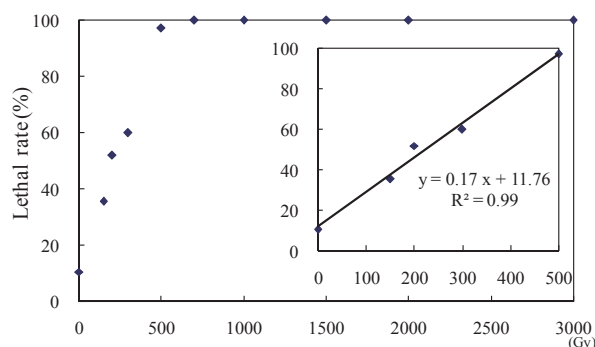


Fig. 3 Lethal rate of *R. obtusifolius* irradiated with gamma rays. A plant that did not expand 2nd and later leaves was defined as a dead plant.

Reference

1) A. Miyagi et al., Metabolomics 6 (2010) 497.

3 - 42 Production of Mutants by Ion Beam Irradiation in *Dahlia* spp.

Y. Uyama^{a)}, H. Ohya^{a)}, Y. Amano^{a)}, K. Kashimoto^{a)}, S. Hatano^{a)}, S. Nozawa^{b)},
R. Yoshihara^{b)}, Y. Hase^{b)} and I. Narumi^{b)}

^{a)} Research & Development Center, Miyoshi & Co., Ltd,

^{b)} Medical and Biotechnological Application Division, QuBS, JAEA

In order to obtain horticulturally useful mutants of *Dahlia* spp., tissue-cultured shoots were irradiated with ion beams at TIARA. The shoots were irradiated with carbon ions ($^{12}\text{C}^{6+}$, 320 MeV) in the range of doses from 1 to 5 Gy. Irradiated shoots were transplanted to culture vessel for rooting. Two hundred forty seven plants were acclimated and then settle planted in the field. After blooming, we investigated mutants by focusing mainly on flower shape and color. As a result, several flower shape and flower color mutants are obtained even from 1-Gy irradiated shoots. We are planning to obtain more mutants by increasing study population. Thereafter, we will propagate horticulturally useful mutants and investigate the stability of their characteristics.

ダリア (*Dahlia* spp.) はメキシコ原産のキク科の多年草である。交配による品種改良が進み、様々な花色、花形を持つ品種が生み出されてきた。その一方で現在見られるダリアのバリエーションの幅から、交配育種では得る事が難しいと考えられる花色や花型がある。

そこで本研究では、優れた変異原として期待されるイオンビームを利用し、通常では現れないような表現型のダリア品種を作出することを目標とした。

供試品種は株式会社ミヨシ保有系統を用いた。高崎量子応用研究所のイオン照射研究施設 (TIARA) の AVF サイクロトロンで、ダリアのシュートに炭素イオンビーム ($^{12}\text{C}^{6+}$, 320 MeV) を各々の線量で照射した。照射に際し、直径 6 cm のシャーレに寒天培地を張り、その中に無菌培養したダリアのシュートを成長点が重ならないよう配置し、カプトン膜で封をした。以前の試験結果から 5 Gy 区以上ではビトロ内で明確なシュート伸長の停滞が確認されたことから、今回は照射線量を絞り込み 1-5 Gy の範囲とした。

照射数日後に培養容器に移し替え、培養を継続した。今回は照射シュートから新たな増殖は行わず、照射シュート当代を発根させた。その発根シュートを野外順化し、1-5 Gy で照射した 247 個体を定植した。その後、開花した際に花色や花形に変化が見られる個体があるか調査を行った。

その結果、1 Gy で既に変異体と見られる個体が複数得られた (Table 1)。得られた変異体は花形の形状が変わったもの、花色が変わったもの等である (Fig. 1)。

今後はまだ開花調査していない照射済シュートを野外に定植し、更なる変異体の獲得を目指す。そして得られた変異体の中で園芸的価値が高いと思われるものについては増殖を行い、その性質の安定性を確認する予定である。

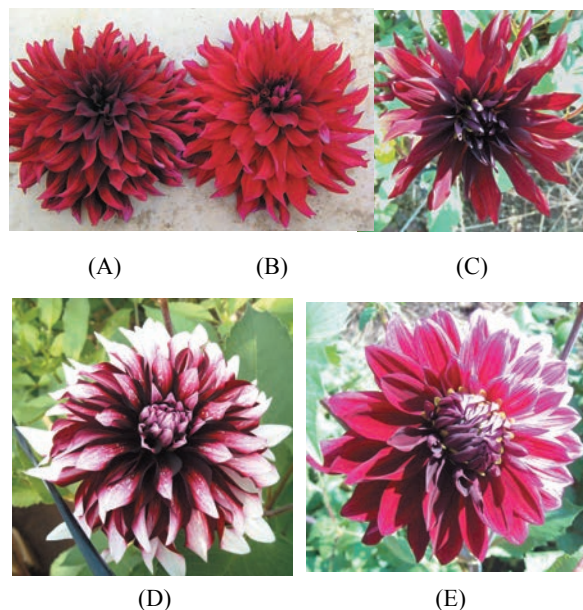


Fig. 1 Flowers of original (A) and mutants (B)-(E) of *Dahlia* spp.

Table 1 Field investigation result of ion beam irradiated *Dahlia* spp.

Dose (Gy)	Number of plants	Number of mutants	Mutation rate (%)	Note
1	118	3	2.54	Flower color mutation, flower shape mutation.
1.5	96	2	2.08	Flower shape mutation.
2	23	0	0	No mutant was obtained despite we had obtained flower color mutants in our previous investigation.
5	10	1	10	Flower shape mutation.

3 - 43 Analysis of Mutant Frequencies for Different LET Radiations in *Deinococcus radiodurans*

K. Satoh^{a)}, K. Tejima^{a)}, T. Onodera^{a, b)} and I. Narumi^{a)}

^{a)} Medical and Biotechnological Application Division, QuBS, JAEA,

^{b)} Graduate School of Life Sciences, Tokyo University of Pharmacy and Life Sciences

Introduction

Ionizing radiation induces DNA double-strand breaks (DSBs), which is a particularly serious form of DNA damage and has an especially deleterious effect in cells. Ion beams have a high linear energy transfer (LET, keV/μm) and give DNA damage containing DSBs locally (clustered damage) than gamma rays do. *Deinococcus radiodurans* exhibits extraordinary resistance to the lethal effects of ionizing radiations. This resistance has been attributed to its highly proficient DNA repair capacity¹⁾. Previously, it had been reported that *D. radiodurans* possessed accurate, an “error-free”, DNA repair mechanism since there were no significant increase in antibiotics-resistant mutant frequency depending on gamma radiation dose²⁾. However, the accuracy of DNA repair mechanism has not been fully verified. In this study, we investigated antibiotics-resistant mutant frequencies for different LET radiations in *D. radiodurans*.

Experimental procedures

D. radiodurans cells were cultivated at 30 °C in TGY broth with agitation to early stationary phase. Cells were harvested, washed and resuspended in 100 mM Tris-HCl (pH 7.0) containing 2.5% glycerol. Aliquots (1 mL) of the cell suspensions were adhered onto cellulose membrane, frozen and dried *in vacuo*. Freeze-dried cells were irradiated with five kinds of ion beams (⁴He²⁺ [50 MeV; 19.4 keV/μm], ¹²C⁶⁺ [320 MeV; 86.2 keV/μm], ¹²C⁵⁺ [220 MeV; 121.8 keV/μm], ²⁰Ne⁸⁺ [350 MeV; 440.8 keV/μm] and ⁴⁰Ar¹³⁺ [460 MeV; 1,649.6 keV/μm]) accelerated by an AVF cyclotron, or with ⁶⁰Co gamma rays (0.2 keV/μm) at Food Irradiation Facility, JAEA. The irradiation dose ranged from 2 to 20 kGy. Irradiated cells were cultivated at 30 °C in TGY broth with agitation to early stationary phase. Cells were harvested, diluted appropriately with 10 mM sodium phosphate, spread onto either TGY agar or TGY agar supplemented with rifampicin (50 μg/mL), and incubated at 30 °C for 3 or 4 days prior to the enumeration of colonies. The mutant frequency was determined by calculating the number of rifampicin-resistant (Rif^R) colonies divided by the total number of viable cells.

Results and discussion

The cells exhibited sensitivities to five kinds of ion beams depending on radiation dose. The lethal effects to ion beams were almost equal to that of gamma rays (Fig. 1)³⁾. Rifampicin is one of the antibiotics that inhibit RNA synthesis by directly interacting with the RNA polymerase

beta subunit protein encoded by *rpoB* gene. By genetically altering the *rpoB* gene in genome, Rif^R mutant can be generated. Unlike the previous study²⁾, the Rif^R mutant frequencies increased depending on radiation dose (Fig. 1). The highest Rif^R mutant frequencies were observed at a dose range that gives 10⁻¹ to 10⁻² of surviving fraction. There is the possibility that this dose range is the best dose to generate the mutants of interest for research and breeding purpose. The decrease in Rif^R mutant frequency at high doses might be due to a frequent generation of severe mutations that exert deleterious effects on cell survival. These results suggest that the DNA repair mechanism of *D. radiodurans* is not necessarily “error-free”.

References

- 1) I. Narumi, Trends Microbiol. 11 (2003) 422.
- 2) D. M. Sweet & B. E. B. Moseley, Mutat. Res. 34 (1976) 178.
- 3) K. Satoh et al., JAEA Takasaki Annu. Rep. 2009 (2011) 80.

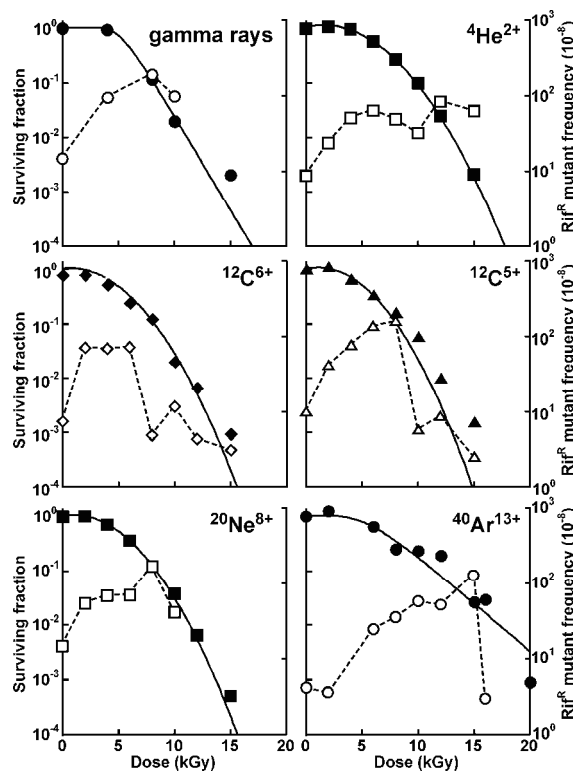


Fig. 1 Survival curves and Rif^R mutant frequencies for different LET radiations. Closed and open symbols indicate surviving fraction and mutant frequency, respectively.

3 - 44 Functional Analysis of Universally Conserved Genes, *ygjD* and *yeaZ* Orthologs, in DNA Repair of *Deinococcus radiodurans*

T. Onodera ^{a, b)}, K. Satoh ^{a)}, T. Ohta ^{b)} and I. Narumi ^{a)}

^{a)} Medical and Biotechnological Application Division, QuBS, JAEA,

^{b)} Graduate School of Life Sciences, Tokyo University of Pharmacy and Life Sciences

The *ygjD* and *yeaZ* orthologs are highly conserved in eubacteria, and the former is also widely found in the genomes of archaea and eukaryotes. These orthologs are known as essential genes for *Escherichia coli* and *Saccharomyces cerevisiae* but not in *Synechocystis* sp. PCC6803 and *Thermus thermophilus*. It was recently reported that the *ygjD* and *yeaZ* orthologs were related to DNA metabolism in *E. coli* ¹⁾, mitochondrial DNA maintenance and transcriptional regulation in *S. cerevisiae* ²⁾. However, its actual function is still poorly understood. *D. radiodurans*, well known as a radioresistant bacterium, possesses the both orthologs, hereafter *DrygjD* and *DryeaZ*. In this study, we generated *DrygjD* and *DryeaZ* deletion mutants and their complementation strains. To investigate gene disruption effects, generated strains were then challenged with mitomycin C (MMC), which causes interstrand DNA cross-links.

DrygjD and *DryeaZ* deletion mutants were generated by replacement with antibiotic resistance genes. We also constructed five plasmids as follows. PCR fragment containing the structural gene of *DrygjD* was inserted into an *NdeI-BamHI* site of pRGL1 carrying the *D. radiodurans* *groE* promoter to yield plasmid pGroDrygjD. PCR fragment containing *DrygjD* with a 260-bp upstream region was inserted into a *BlnI-BamHI* site of pRADN2 ³⁾ to yield plasmid pIntDrygjD. A 250-bp upstream region of *DR0380* was replaced by the *groE* promoter region of pGroDrygjD to yield plasmid pUPDrygjD. PCR fragment containing the structural gene of *DryeaZ* was inserted into an *NdeI-BamHI* site of pRGL1 to yield plasmid pGroDryeaZ. *MscI/FspI*-digested pGroDryeaZ was then ligated with a *HincII* fragment of pKatHPH4 to yield plasmid pGroDryeaZ-Hyg2. A 250-bp upstream region of *DryeaZ* was inserted into a *BlnI-BamHI* site of pRADN2 to yield plasmid pIntDreaZ. *MscI/FspI*-digested pIntDreaZ was ligated with a *HincII* fragment of pKatHPH4 to yield plasmid pIntDryeaZ-Hyg2. *DrygjD* and *DryeaZ* disruptant strains were transformed with the above-mentioned plasmids.

We successfully constructed *DrygjD* disruptant, *DryeaZ* disruptant and *DrygjD DryeaZ* double-disruptant strains. This result clearly indicated that neither *DrygjD* nor *DryeaZ* genes is essential for cell viability in *D. radiodurans*. These gene disruptant strains exhibited extreme sensitivity to MMC compare to the wild-type strain (Fig. 1). The deficiency of *DrygjD* and *DryeaZ* genes was complemented to restore the wild-type phenotype by introducing plasmids

that express these genes (Fig. 2). These results suggest that *DrygjD* and *DryeaZ* genes are involved in DNA repair and especially play a critical role in the MMC-induced DNA damage in *D. radiodurans*.

References

- 1) J. I. Handford et al., J. Bacteriol. 191 (2009) 4732.
- 2) J. Obero et al., Nucleic Acids Res. 37 (2009) 5343.
- 3) H. Ohba et al., Gene. 363 (2005) 133.

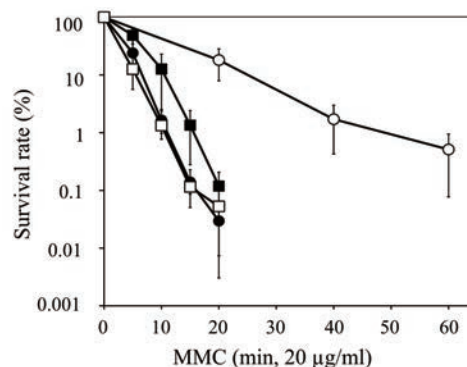


Fig. 1 Sensitivity of gene disruptant strains to MMC. Each plotted data are the mean \pm standard error of three independent experiments; n = 4. Symbols: open circles, wild-type; filled circles, *DrygjD* disruptant strain; open squares, *DryeaZ* disruptant strain; closed squares, *DrygjD DryeaZ* double-disruptant strain.

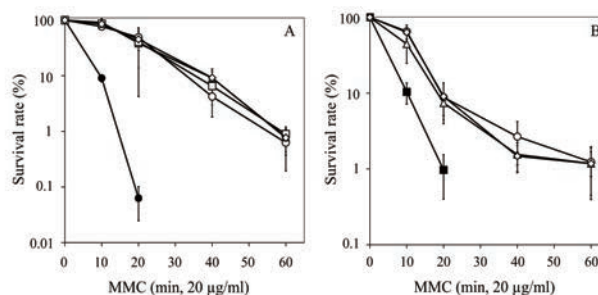


Fig. 2 Sensitivity of *DrygjD* and *DryeaZ* deficient mutants expressing wild-type *DrygjD* and *DryeaZ* genes to MMC. Each plotted data are the mean \pm standard error of three independent experiments; n = 3. (A) Symbols: open circles, WT/pRADN1; filled circles, Δ *DrygjD*/pRADN1; open triangles, Δ *DrygjD*/pGroDrygjD; open squares, Δ *DrygjD*/pIntDrygjD. (B) Symbols: open circles, WT/pRADN1-Hyg2; filled squares, Δ *DreaZ*/pRADN1-Hyg2; open triangles, Δ *DryeaZ*/pGroDryeaZ; open diamonds, Δ *DreaZ*/pIntDreaZ.

3 - 45 DNA Damage Evaluation System of the High-LET Ion Beam Using the Polymerase Chain Reaction

Y. Matuo ^{a)}, Y. Izumi ^{a)}, Y. Hase ^{b)}, A. Sakamoto ^{b)}, S. Nozawa ^{b)},
I. Narumi ^{b)} and K. Shimizu ^{c)}

^{a)} Research Institute of Nuclear Engineering, University of Fukui,
^{b)} Medical and Biotechnological Application Division, QuBS, JAEA,
^{c)} Radioisotope Research Center, Osaka University

We have been studying ion beam-induced mutations in budding yeast *S288c* (*RAD⁺*) as a model of eukaryote cell. In previous studies, the yeast cells were irradiated with carbon ions (¹²C⁵⁺; 220 MeV) and gamma-rays. The remarkable feature of yeast mutations induced by high linear energy transfer (LET) ion beams was that the mutation sites were localized near the linker regions of nucleosomes, whereas mutations induced by gamma-ray irradiation were located uniformly through the marker gene¹⁾. High-LET radiation deposits high-density energy locally compared to low-LET radiation. It has been thought that high-LET radiation induces a large number of single and double-strand breaks (DSBs) compared to low-LET radiation. DSBs are more difficult to repair than the other DNA lesions²⁾. It is thought that the effect of high-LET radiation on the living cells is larger than that of low-LET radiation. We report a new method to evaluate DNA lesions caused by high-LET radiation using the polymerase chain reaction (PCR). PCR is one of the most reliable methods for detecting DNA damage as the amplification stops at the site of the damage. In this study, the 804-bp region of *URA3* gene was amplified by PCR using a specific oligonucleotide primer set. Thereafter, the DNA fragments (1 µg/mL), which were dissolved in TE buffer (10 mM Tris-HCl, 1 mM EDTA, pH 7.4), were irradiated with carbon ions at the doses of 0.1 to 1 Gy. The carbon ion beams were generated with the cyclotron at TIARA (Japan Atomic Energy Agency). For the purposes of comparison, DNA fragments were also irradiated with ⁶⁰Co gamma rays (Chiyoda Technol).

Real-time PCR was used to detect DNA damage on the *URA3* DNA fragment. The PCR device adopted was an Eco Real-Time PCR System (Illumina). The amount of template DNA was 0.1 ng. The PCR leads to an increase in fluorescence intensity at each cycle, which allows the quantification of undamaged template DNA that was used in PCR amplification. In this system, SYBR Green (Sigma-Aldrich), which is an asymmetrical cyanine dye preferentially bound to double-stranded DNA, was used to monitor DNA synthesis. Figure 1 shows the percentage of undamaged template DNA after exposure to radiation with different LET. The percentage of undamaged template DNA tended to decrease with an increase in absorbed dose of radiation. Interestingly, the higher LET radiations resulted in the higher rate of decrease in undamaged template DNA. This result suggests that different types of lesions are produced on DNA depending on the LET value of radiations. DNA lesions such as apurinic/aprimidinic (AP) site, single-strand breaks (SSBs) and DSBs are considered to be severe factors to delay and/or inhibit the PCR amplification. For example, it is known that PCR polymerases stall at the AP site preventing further replication. Similarly, DNA carrying SSBs or DSBs is not suitable as a template DNA for the PCR amplification. To characterize ion beam-induced DNA damage in more detail, it is necessary to classify the types of the damage by an easy and simple method. Therefore, further improvement of the experimental system developed in this study is needed to evaluate the types of DNA damage.

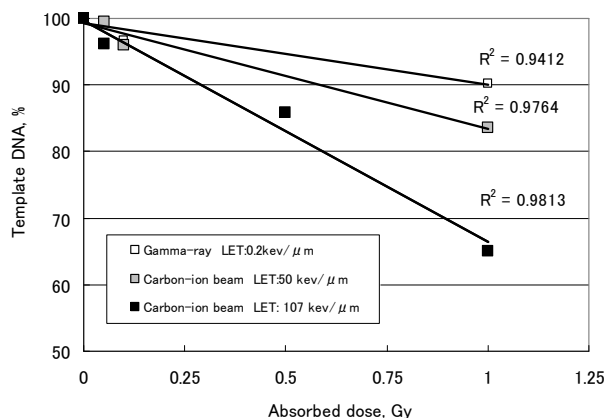


Fig. 1 The percentage of undamaged template DNA after exposure to radiation with different LET.

References

- 1) Y. Matuo et al., *Mutat. Res.* 602 (2006) 7.
- 2) K. H. Karlsson et al., *Radiat. Res.* 161 (1999) 517.
- 3) J. A. Sikorsky et al., *Biochem. Biophys. Res. Commun.* 355 (2007) 431.

3 - 46

Application of Bio-pesticide with Plant Growth Promoter Made from Oligo-chitosan

M. Aino ^{a)}, K. Matsuura ^{a)}, N. Nagasawa ^{b)}, F. Yoshii ^{b)}, M. Taguchi ^{b)},
K. Satoh ^{c)} and I. Narumi ^{c)}

^{a)} Hyogo Prefectural Center for Agriculture, Forestry and Fisheries,
^{b)} Environment and Industrial Materials Research Division, QuBS, JAEA,
^{c)} Medical and Biotechnological Application Division, QuBS, JAEA

Chitosan is a linear polysaccharide composed of randomly distributed β-(1-4)-linked D-glucosamine (deacetylated unit) and N-acetyl-D-glucosamine (acetylated unit). By γ-ray irradiation of chitosan in diluted solutions, low molecular weight chitosan (oligo-chitosan) can be obtained. Oligo-chitosan has potential use in agriculture. In this study, the possibility of oligo-chitosan as a plant growth promoter in tomato was investigated. The combination of oligo-chitosan and bio-pesticide was totally ineffective when tomato was treated at the same time. On the other hand, the suppression effect against the pathogen significantly increased when tomato was treated with oligo-chitosan 1 day before transplant to soil contaminated by the pathogen. This result strongly suggests that oligo-chitosan enhances pathogen resistance in tomato seedling treated with bio-pesticide.

内生細菌を用いて植物に誘導抵抗を起こさせ、病原菌の侵入を防ぐ技術が開発されている。農薬を使用せず環境負荷を低減する技術して注目を集めている。しかし、誘導抵抗は長時間持続させることが困難であり、本防除法の普及に大きな障壁となっている。そこで、植物に生理活性を有するオリゴキトサンを用いて、トマトに生じる抵抗性誘導現象の増強及び持続が可能かどうかを検討したので報告する。

供試内生細菌は *Pseudomonas fluorescens* FPH9601 及び *P. fluorescens* FPT961 の 2 菌株を用い、ライブコート技術を用いて、トマト (品種: 麗夏) に 2 菌株同時に種子コーティングした。青枯病菌は兵庫農技総セ保存菌株 HAIP010 を用い、標準寒天培地上で 28 °C、24 時間培養後、滅菌蒸留水に懸濁し使用した。オリゴキトサンは原子力機構作製のオリゴキトサン・エチルアルコール溶液を用い、エバポレータでエチルアルコールを除いて使用した。

①同時処理の効果

青枯病菌の菌密度が 10⁷ CFU/mL になるように調整したパーミキュライトをガラス円筒管 (直径 3 cm×高さ 10 cm) に充填した。ライブコート処理したトマト種子を播種し、覆土後、速やかにオリゴキトサン水溶液 (1, 10, 100 及び 1,000 ppm) を 10 mL 添加した。人工気象内で 28 °C、24 時間照明 (20,000 lux) で 11 日間保持した後、病徴の有無で調査をした。その結果、オリゴキトサン単独処理ではトマト青枯病に対する防除効果は処理した全ての濃度において効果がなかった (Fig. 1)。また、オリゴキトサンと内生細菌同時処理 (ライブコート処理) においても、オリゴキトサンにより増強効果は認められず。オリゴキトサン濃度を高めても認められなかった (Fig. 1)。

②定植 1 日前処理の効果

パーミキュライトをセル成型トレイ (400 穴) に充填し、ライブコート処理をしたトマト種子を播種、28 °C、24 時間照明 (20,000 lux) で 10 日間保持した。トマト苗 (本葉 1 葉期) にオリゴキトサン水溶液 (100 ppm) を十分量散布した。散布 1 日後、トレイ底部から伸長する根部に青枯病菌が感染するように、青枯病菌汚染パーミキュライト (菌密度 10⁷ CFU/mL) 上にトレイを

置き、32 °C にした人工気象器で育苗、経時的に観察した。オリゴキトサン単独処理では無処理と変わらず、発病抑制効果は確認できなかった。内生細菌とオリゴキトサン処理では、発病抑制効果が高く、長時間持続した (Fig. 2)。これらの結果から、オリゴキトサンの処理時期は同時処理では効果が表れず、抵抗性誘導を生じた植物体に処理すると、その効果が発揮するものと考えられた。

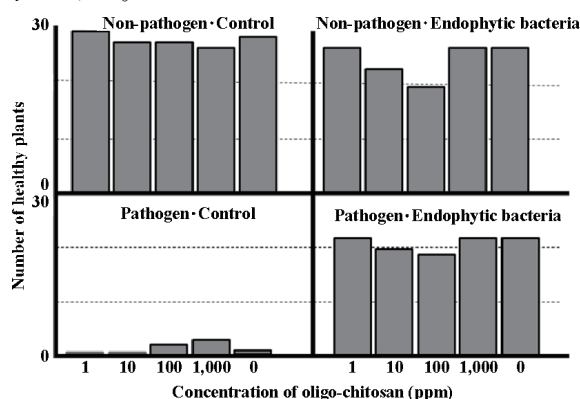


Fig. 1 Suppression effect against the pathogen by the combination of oligo-chitosan and endophytic bacteria (at the same time).

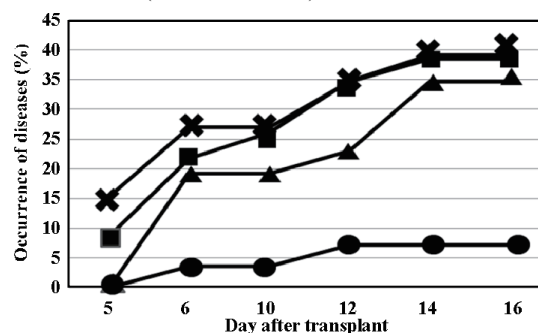


Fig. 2 Suppression effect against the pathogen by the combination of oligo-chitosan and endophytic bacteria (1 day before transplant). x: control, ■: oligo-chitosan, ▲: endophytic bacteria, ●: oligo-chitosan + endophytic bacteria.

3 - 47 Phenotypic Characterization of High Temperature Tolerant Mutants of *Bradyrhizobium japonicum* USDA110 Generated by Ion-beam Irradiation

K. Takeda ^{a), b)}, K. Tejima ^{b)}, K. Satoh ^{b)}, I. Narumi ^{b)} and T. Yokoyama ^{c)}

^{a)} United Graduate School of Agricultural Science, Tokyo University of Agriculture and Technology,

^{b)} Medical and Biotechnological Application Division, QuBS, JAEA,

^{c)} Institute of Agriculture, Tokyo University of Agriculture and Technology

Biofertilizer is defined to be “a substance that contains living microorganisms which, when applied to seed, plant surfaces, or soil, colonizes the rhizosphere or the interior of the plant and promotes growth by increasing the supply or availability of primary nutrients to the host plant” ¹⁾. In Asian countries, to increase crop yield under low input of chemical fertilizers, biofertilizers have been developed by many researchers in agricultural institutes. However, several researchers pointed out constraints on biofertilizers application. Major constraint is a viability loss of beneficial microorganisms in biofertilizers caused by high temperature and drought stress during both storage and transportation. Therefore, we have tried to improve high temperature tolerance of *Bradyrhizobium japonicum* USDA110, which is a superior inoculant to soybean in the temperate regions.

Consequently, we have obtained 20 high temperature tolerant mutants, which can survive at 43 °C for at least 7 days. In this report, we show the phenotypic characteristics of 3 mutants (strains M4, M5 and M6) that exhibit relatively higher tolerance among the mutants obtained.

As shown in Fig. 1, the colony of M4, M5 and M6 was smooth with glossy pale pink color unlike wild type (WT). The colony sizes of the mutants were clearly bigger than that of WT when incubated at 30 °C. Figure 2 shows the change in pH of YM agar containing bromothymol blue (BTB) as a pH indicator after cultivating the strains at 30 °C for 10 days. WT seemed to secrete alkali-producing substances into YM agar as expected as a member of the genus *Bradyrhizobium*. On the other hand, the media of M4, M5 and M6 turned yellow probably resulting from a greater secretion of acid-producing substances than alkali-producing substances.

The number of viable cells of these 4 strains in YM broth at 30 °C was monitored by the dilution plate method. Using a growth curve, the generation time for each strain was calculated. The generation time of WT at 30 °C was 5.97 h, and those of M4, M5 and M6 were 4.14, 4.34 and 4.35 h, respectively. The generation time of high-temperature tolerant mutants at 30 °C was about 1.5 h shorter than that of WT (Fig. 3).

Symbiotic functions with soybean (*Glycine max* cv. Enrei) were also investigated. Inoculated plants were grown for 4 weeks in a 300 mL glass jar under 14 h light

(25 °C)/10 h dark (18 °C) photoperiod intervals with 60% moisture level. After harvesting, nodule numbers, dry weights of shoots, roots, and root nodules were measured. In order to evaluate nitrogenase activity, acetylene reduction activity was also determined. As results, M5 and M6 seemed to form more nodules than WT, and the size of these nodules was a little smaller than that of WT. On the contrary, M4 tended to form bigger nodules with lower numbers compared to WT. Nitrogenase activity of M4, M5 and M6 were seemed to be slightly higher than WT, although there were no significant differences ($p < 0.05$).

There might be a link between high temperature tolerance and these phenotypic changes. Therefore, we intend to identify factors causing these changes.

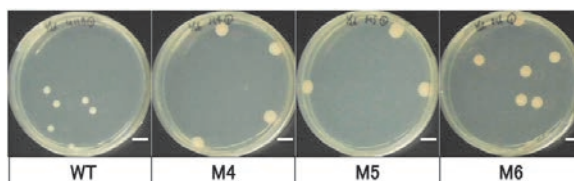


Fig. 1 Colony morphology after cultivating at 30 °C for 21 days. Bars indicate 1 cm.

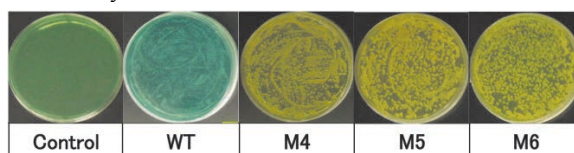


Fig. 2 Change in pH of YM agar containing BTB after cultivating at 30 °C for 10 days. Control, YM agar containing BTB without bacteria (Green, pH 6.8); Blue, above pH 7.6; Yellow, below pH 6.0.

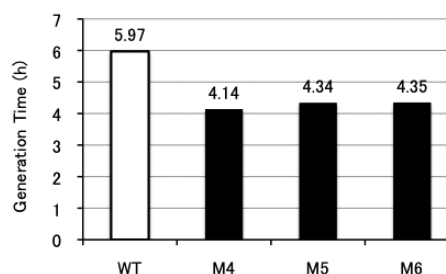


Fig. 3 Difference in generation time at 30 °C.

Reference

1) J. K. Vessey, Plant Soil 255 (2003) 571.

3 - 48 FACS-based Screening for Yeast Clone Highly Expressing Cellulase

K. Ninomiya^{a)}, T. Nomura^{a)}, K. Satoh^{b)}, I. Narumi^{b)} and N. Shimizu^{a)}

^{a)} Division of Material Engineering, Graduate School of Natural Science and Technology, Kanazawa University, ^{b)} Medical and Biotechnological Application Division, QuBS, JAEA

By using immunocytochemistry and fluorescence-activated cell sorter (FACS), yeast population highly expressing cellulase on the cell surface was enriched from the mutant population prepared by irradiation with carbon ion beams (220 MeV $^{12}\text{C}^{5+}$, 100 Gy). Enzymatic activity of the enriched clones was quantified *in vitro* by a conventional biochemical method. Repeated FACS after irradiation with carbon ion beams was effective for selecting yeast population of interest.

【緒言】 近年、非食用バイオマスであるセルロースを原料としたエタノール発酵生産への関心が高まっている。セルロース糖化酵素であるセルラーゼを発現する酵母を用いた“セルロースからの直接エタノール発酵生産”では、酵母のセルラーゼ発現量が生産コストを下げるための律速段階の1つと言われている。我々は、セルラーゼ高発現酵母を育種するために、細胞表面に発現したセルラーゼの酵素量を蛍光免疫染色で蛍光強度に置き換えることにより、fluorescence-activated cell sorter (FACS) を用いて、セルラーゼ高発現株を蛍光強度の高い細胞集団として high-throughput に分取することを試みてきた。今回は FACS による濃縮を繰り返した後、クローンの単離及び得られた酵母クローンについての酵素活性を測定した結果を報告する。

【実験方法】 使用菌株及び変異導入: 3種のセルラーゼ endoglucanase II (EGII)、cellobiohydrazin II (CBHII)、 β -glucosidase を細胞表面に発現した酵母 *Saccharomyces cerevisiae* MT8-1/pEG23u31H6/pFCBH2w3/pBG211 株¹⁾ (MT8-1III 株) を用いた。また、MT8-1III 株に炭素イオン (220 MeV $^{12}\text{C}^{5+}$) を 100 Gy 照射し (以下、イオンビーム照射)、変異株集団を調製した。酵母の培養は SD 培地を用いて 30 °C で行った。

セルラーゼ高発現株の選抜: 酵母表面のセルラーゼ分子の量を蛍光量として評価するため、EGII ならびに CBHII のタグとして融合発現させた RGSHis₆ 及び FLAG に対する一次抗体、それぞれの一次抗体に特異的な Alexa Fluor 488 (FITC) 及び R-phycoerythrin (PE) 標識二次抗体を用いて二重染色を行った。蛍光免疫染色を行った酵母株は、FACS を用いて蛍光強度を測定し、FITC ならびに PE の蛍光強度の高い細胞集団を目的集団として cell sorting を行なった。一連の cell sorting 操作が終了した後の細胞集団は、リン酸膨潤セルロース (PASC) を単一炭素源とした SD 寒天培地を用いたコロニー単離によりクローン化した。

セルラーゼ活性測定: セルラーゼ活性としては、PASC を基質とした EGII 及び CBHII の活性をまとめて評価した。PASC が加水分解されて生じる還元末端の増加速度を 3,5-dinitrosalicylic acid 法を用いて測定した。1 $\mu\text{mol}/\text{min}$ で還元末端を生じる酵素活性を 1 U、また $\text{OD}_{600}=10$ の酵母細胞懸濁液 1 mL を 1 OD unit とし、酵母細胞の持つセルラーゼ活性を U/OD unit と定義した。

【結果と考察】 FACS によるセルラーゼ高発現酵母細胞集団の濃縮作業として、(A) イオンビーム照射なし+FACS 選抜なし (control)、(B) イオンビーム照射なし+FACS 選抜あり、(C) イオンビーム照射あり+FACS 選抜あり、(D) FACS 選抜+イオンビーム照射あり+FACS 選抜あり、の4つの操作を行った。その結果、2回の選抜操作 (2nd round) 後、操作 (D) で濃縮された酵母集団が最もセルラーゼが高く、(A) の control が 2.6×10^{-3} U/OD unit に対し、選抜後 5.9×10^{-3} U/OD unit と約 2.3 倍の結果が得られた (Fig. 1)。さらに、操作 (D) で濃縮された酵母集団をクローン化し、セルラーゼ活性を測定した。親株の MT8-1III 株 (WT) のセルラーゼ活性が 3.5×10^{-3} U/OD unit であったのに対し、最も活性が高かったクローンは 9.1×10^{-3} U/OD unit と約 2.6 倍の活性であった (Fig. 2)。

Reference

- 1) Y. Fujita et al., Appl. Environ. Microbiol. 68 (2002) 5136.

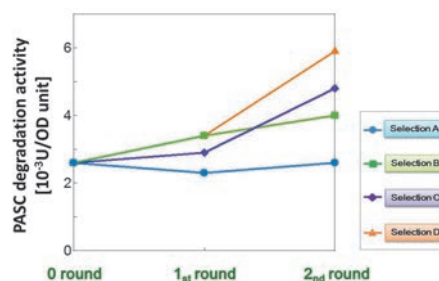


Fig. 1 Cellulase activities of yeast population enriched by FACS sorting.

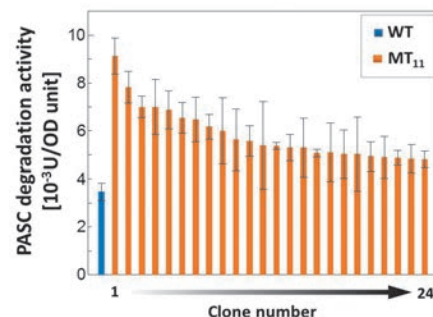


Fig. 2 Cellulase activities of yeast clones obtained by colony isolation from PASC plate following FACS sorting. WT and MT indicate parental strain for ion beam irradiation (MT8-1III) and each isolated strain, respectively. Each point represents the average result obtained from three independent experiments.

3 - 49 Benomyl-tolerant Mutation of Entomopathogenic Fungi Induced by Carbon Ion Beams

T. Saito^{a)}, S. Shinohara^{a)}, K. Satoh^{b)} and I. Narumi^{b)}

^{a)} Faculty of Agriculture, Shizuoka University,

^{b)} Medical and Biotechnological Application Division, QuBS, JAEA

Entomopathogenic fungi, *Isaria fumosorosea* and *Beauveria bassiana*, are important agents to control insect pests, but the fungi are highly susceptible to conventional fungicides for plant diseases such as powdery mildew. The purpose of this study is to generate mutants tolerant to benomyl, a major fungicide, using carbon ion beams. We have obtained some benomyl-tolerant mutants that were selected on medium supplemented with the fungicide (1,000 ppm). In this study, IC₅₀ (half maximal inhibitory concentration) of benomyl was determined for the mutants obtained. As compared to wild type, *I. fumosorosea* and *B. bassiana* mutants were more than 3,000-fold and approximately 200-fold tolerant to the fungicide, respectively. The *B. bassiana* benomyl-tolerant mutants showed a cross-tolerance to thiophanate-methyl. On the other hands, the *I. fumosorosea* benomyl-tolerant mutants showed a cross-tolerance to myclobutanil, but not to thiophanate-methyl. Some mutants of *I. fumosorosea* and *B. bassiana* exhibited high mortalities for nymphs of the sweetpotato whitefly, *Bemisia tabaci*, and adults of the onion thrips, *Thrips tabaci*, respectively. It is suggested that the fungicide-tolerant mutants maintained a high virulence serve as highly potential biological control agents in integrated pest management programs.

昆虫病原糸状菌を用いて害虫を防除する微生物的防除法は殺菌剤と併用しにくいという難題を抱えている。この抜本的な解決策として、殺菌剤耐性という新機能を有する昆虫病原糸状菌を創出することが考えられる。本研究の目的は、炭素イオンビームの照射による突然変異育種技術を用いて、殺菌剤耐性の昆虫病原糸状菌 (*Isaria fumosorosea* および *Beauveria bassiana*) 変異体を創出することである。

これまでの研究によって、ベノミル剤耐性変異体が選抜されている^{1,2)}。ここでは、それらの詳細な耐性レベルを検定により明らかにした。さらに、他剤に対する交差耐性ならびに病原力を調査した。

耐性レベル (IC₅₀) : ベノミル剤を添加したサブロー寒天培地 (直径 9 cm) の中央に菌叢片 (直径 4 mm) を接種し、20 °C (全暗) で 7 日間培養したのちコロニー直径を測定した。3 濃度以上のデータを基にして IC₅₀ 値を算出した。その結果、耐性レベルは *I. fumosorosea* で 3,000 倍以上 (IC₅₀: > 5,000 ppm)、*B. bassiana* で 200 倍以上 (IC₅₀: > 500 ppm) 高まった (Table 1)。

交差耐性 : ベノミル剤耐性変異体は他剤 (常用濃度) に対して交差耐性を示すかどうか前述と同様の方法で調べた。その結果、チオファネートメチル (ベノミルと同系) に対して *B. bassiana* 変異体は顕著な交差耐性を示したが、*I. fumosorosea* 変異体は交差耐性を示さなかった (Table 2)。*I. fumosorosea* の BPF2 はミクロブタニルに対して顕著な交差耐性を示した。

病原力 : *I. fumosorosea* 変異体はタバココナジラミバ イオタイプ B (幼虫) に、*B. bassiana* 変異体はネギアザミウマ (成虫) に対する病原力を調べた。*I. fumosorosea* 変異体は、低濃度 (1×10⁶ 分生子/mL) の場合、親株の病原力を下回ったが、高濃度 (1×10⁷ 分生子/mL) の場合は親株と同等の病原力を示した (Table 3)。*B. bassiana* 変異体でも親株と同等の病原力を示す菌株が得られた。

本研究によって、ベノミル剤耐性と病原力を併せ持つ昆虫病原糸状菌の変異体を得られた。これらの変異体は実用レベルに達していると考えられる。変異体の中には他剤に対しても交差耐性を示すものがあつたこと

から、耐性の範囲はベノミル剤にとどまらないと考えられる。今後、変異の安定性などにも変異の遺伝子学的な解析を進めたい。

References

- 1) T. Saito et al., JAEA Takasaki Annu. Rep. 2009 (2011) 76.
- 2) T. Saito et al., JAEA Takasaki Annu. Rep. 2010 (2012) 112.

Table 1 IC₅₀ of benomyl for the mutants.

Fungus	Isolates	IC ₅₀ (ppm)	RR*
<i>I. fumosorosea</i>	Wild type	1.4	
	R1-1B8	> 5,000	> 3,571
	R1-1B9	> 5,000	> 3,571
	④B34P-1	> 5,000	> 3,571
	⑨BI300-4-2-1	2,851	2,036
	TPf22	2,612	1,866
	BPF2	1,107	791
<i>B. bassiana</i>	Wild type	2.6	
	②BB22	526	202
	②BB24	498	192

* IC₅₀ value of mutant / IC₅₀ value of wild type

Table 2 Tolerance to six fungicides for the benomyl-tolerant mutants.

Fungicide	<i>I. fumosorosea</i>		<i>B. bassiana</i>	
	R1-1B8	BPF2	②BB22	②BB24
Benomyl	2.7	4.3	11.0	13.4
Thiophanate-methyl	0.5	1.2	3.5	4.5
Diethofencarb	0.5	1.2	0.2	0.4
Polycarbamate	0.8	1.0	0.2	0.8
Myclobutanil	1.2	2.3	0.9	0.4
Iprodione	0.4	1.4	0.5	0.7

Values indicate growth of mutant / growth of wild type.

Table 3 Percent mortality of whitefly nymphs caused by the benomyl-tolerant mutants of *I. fumosorosea*.

Inoculums (conidia/mL)	Mutants		Wild type
	R1-1B8	R1-1B9	
1 × 10 ⁶	52	77	97
1 × 10 ⁷	98	97	99
Water	13	13	13

3 - 50 Identification of Mutation Sites in High Ethyl Caproate Producing Sake Yeasts Generated by Ion Beam Breeding

T. Masubuchi^{a)}, C. Takashima^{b), c)}, O. Kamiyama^{a)}, H. Ikenaga^{b)},
K. Satoh^{c)} and I. Narumi^{c)}

^{a)} Gunma Industrial Technology Center, ^{b)} Maebashi Institute of Technology,
^{c)} Medical and Biotechnological Application Division, QuBS, JAEA

In the previous study, we have obtained high ethyl caproate producing Sake yeasts “No.227” and “No.1333” by carbon-ion irradiation. In this study, to identify the mutation sites of the mutant strains, the specific region (226 bp; nucleotide positions 3,642–3,867) in the fatty acid synthase gene *FAS2* that might be involved in the higher production of ethyl caproate was sequenced and compared with the corresponding sequence in the parental strain “Kyokai-901”. Consequently, strains No.227 and No.1333 carried G/A and A/C mutations, respectively, at nucleotide position 3,748 as a heterozygous state. This result strongly suggested that the higher production of ethyl caproate in strains No.227 and No.1333 is attributed to a dominant mutation in *FAS2* gene.

群馬県では、オリジナルの吟醸用清酒酵母を開発するために、平成 20 年度より炭素イオンビーム照射による優良清酒酵母の選抜を行っている¹⁾。これまでに、吟醸香成分の一つであるカブロン酸エチルを高生産する優良清酒酵母 (No.227 及び No.1333 株) を選抜している。清酒酵母でのカブロン酸エチルの生合成は、脂肪酸生合成経路で生成・蓄積されたカブロン酸がアルコール発酵によって生成したエタノールとエステル化することで生成される。そこで本研究では、優良清酒酵母のカブロン酸生合成に関与する脂肪酸生合成関連遺伝子 *FAS2* に着目し、*FAS2* 遺伝子の DNA 塩基配列について解析を行い、カブロン酸エチルを高生産する要因を明らかにすることを目的とした。

これまでに、変異原エチルメタンスルホン酸 (EMS) による突然変異育種で作出された変異株は、*FAS2* 遺伝子 (5,664 bp) の 3,748 番目の塩基 G が A に変異し、その結果、*FAS2* タンパク質の 1,250 番目のアミノ酸の Gly が Ser に変異していることが報告されている²⁾。そこで、この突然変異部位に着目し、群馬県で EMS を変異原として作出し、既に実用化しているカブロン酸エチル高生産清酒酵母 KAZE-2 号、イオンビーム照射に使用した親株である協会 901 号、及びイオンビーム照射により作出した優良清酒酵母 No.227 及び No.1333 株の 4 種の清酒酵母について、ゲノム DNA を抽出し、PCR により *FAS2* 遺伝子の特定領域 (226 bp; 3,642~3,867 番目の領域) を増幅した。増幅した *FAS2* 遺伝子領域の DNA 塩基配列を決定し、得られた DNA 塩基配列を比較することで変異部位を同定した。

FAS2 遺伝子領域 DNA 塩基配列解析の結果、協会 901 号は、3,748 番目の塩基 G に変異は見られなかった (Fig. 1A)。一方、KAZE-2 号及び No.227 株では、3,748 番目の塩基に G 及び A のシグナルが見られ (Fig. 1B 及び C)、相同染色体間で相違を持つ。これにより、相同染色体の片方では、*FAS2* タンパク質の 1,250 番目のアミノ酸の Gly が Ser に変異していると考えられた。さらに、No.1333 株では、3,748 番目の塩基に A 及び C のシグナルが見られ (Fig. 1D)、相同染色体間で相違を持つ。これにより、*FAS2* タンパク質の 1,250 番目のアミノ酸の

Gly が Ser あるいは Arg に変異していると考えられた。

以上の結果から、KAZE-2 号、No.227 及び No.1333 株は、親株である協会 901 号とは異なり、相同染色体の片方あるいは両方に突然変異を持つことを明らかにした。本研究で同定した *FAS2* 遺伝子領域の突然変異はヘテロであるが、変異型 *FAS2* 遺伝子を持つことによって、有用形質としてカブロン酸エチルを高生産すると考えられた。

References

- 1) 増淵 隆 et al., 放射線と産業 128 (2010) 43.
- 2) R. Akada et al., J. Biosci. Bioeng. 92 (2001) 189.

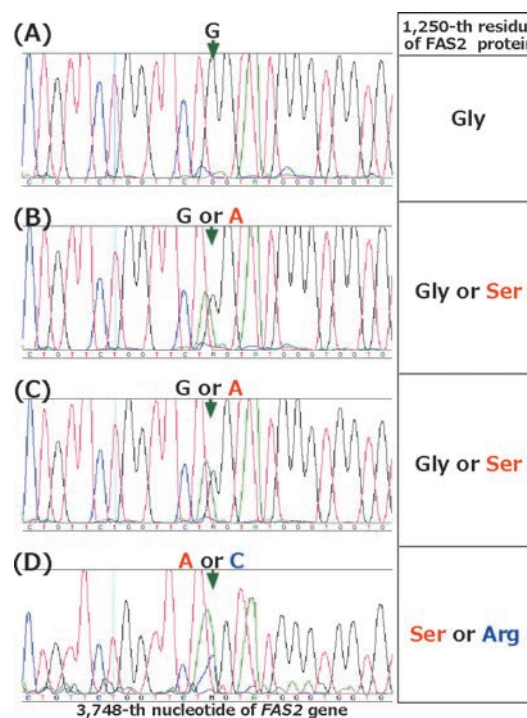


Fig. 1 Sequence analysis of the specific region in *FAS2* gene. (A) Kyokai-901. (B) KAZE-2. (C) No.227. (D) No.1333.

3 - 51 Effects of Ion Beam Radiation on Genome Integrity in *Saccharomyces cerevisiae*

T. Nunoshiba^{a)}, Y. Hirasawa^{a)}, A. Yamauchi^{a)}, K. Satoh^{b)}, K. Tejima^{b)},
T. Onodera^{b)} and I. Narumi^{b)}

^{a)} Graduate School Department of Life Science, International Christian University,
^{b)} Medical and Biotechnological Application Division, QuBS, JAEA

The LOH (loss of heterozygosity) induction by various ion beam radiations was investigated in diploid *Saccharomyces cerevisiae*. The ion beams $^{12}\text{C}^{5+}$, $^{12}\text{C}^{6+}$, $^4\text{He}^{2+}$ and $^{40}\text{Ar}^{13+}$ at the lowest dose (75, 75, 200 and 150 Gy, respectively), which had 30-50% lethality, induced LOH with 10-fold higher frequency. The LOH induction was predominantly (~90%) resulted from gene conversion or crossover through homologous recombination, and followed by chromosome loss through chromosome mis-segregation. Induction of LOH by $^{12}\text{C}^{5+}$ was also examined in *S. cerevisiae* deficient in AP endonuclease (Apn1), translesion DNA polymerases Pol η encoded by Rad30 and Pol ζ encoded by Rev3 and Rev7. Pol ζ may be involved in the induction of LOH, because a slight induction of LOH by $^{12}\text{C}^{5+}$ was observed in the rev3-deficient strain.

生物は常に DNA に損傷を被る環境に曝されており、生命維持や種の保存はいかなる仕組みで損傷 DNA を効率良く正確に修復するかに懸かっている。生命維持の根幹機能であるゲノム情報の維持機構を明らかにすることは、巧妙な生命現象を理解する上で非常に重要である。これまで微生物を用いた放射線のゲノムへの影響を検討する指標として突然変異が用いられてきたが、大腸菌などとは異なり出芽酵母は 1 倍体と 2 倍体の両方を用いることができることから、ヘテロ接合性喪失 (LOH: loss of heterozygosity) を指標とすることが出来る。我々はすでに突然変異マーカー遺伝子 *CAN1* の一方のアレルに変異をもつ 2 倍体細胞を構築し、LOH 検出系を樹立した。この菌株では LOH 誘発頻度とともに起こった LOH が 2 次的な突然変異によるのか、相同組換えに依存する遺伝子変換や交叉によるのか、または染色体の不均衡な分配に起因する染色体喪失によるのかをも推定することができる。そこで本研究ではこの系を用い、イオンビームによって出芽酵母のゲノムやゲノム維持機構への影響に関する基礎的知見を得ることとともに、DNA 修復や損傷乗り越え DNA 合成酵素の役割についても検討した。

実験では YPD 培地中で 30 °C、17 時間培養した出芽酵母細胞 (1×10^7 cells) をセルロースメンブレンにトラップし、シャーレに載せた後、カンプトン膜を掛けて、線エネルギー付与の異なるイオンビームを照射した。メンブレンをチューブに移し、照射した細胞を 1 mL の ddH₂O に回収した。この菌懸濁液を適当に希釈し、生存率を求めるとともに、回収した細胞 20 μL を YPD 培地 2 mL に加え、30 °C、17 時間培養したのち、栄養培地と選択培地に撒いて LOH 誘発頻度を求めた。

野生株の場合、非照射が概ね $2-3 \times 10^{-4}$ であるのに対し、 $^{12}\text{C}^{5+}$ 、 $^{12}\text{C}^{6+}$ は照射最小線量の 75 Gy でそれぞれ 4.5×10^{-3} 、 4.7×10^{-3} と 10 倍以上の頻度で LOH を誘発し、それ以上の線量による大きな LOH 誘発頻度の上昇は見られなかった (Fig. 1)。 $^4\text{He}^{2+}$ についても非照射が 5×10^{-4} であるのに対し照射最小線量の 200 Gy で 4.5×10^{-3} と約 10 倍、 $^{40}\text{Ar}^{13+}$ でも非照射が 2×10^{-4} であるのに対し照射最小線量の 150 Gy で 1.9×10^{-3} と 10 倍の頻度で LOH を誘発し、それ以上の線量による大きな LOH 誘発頻度の上昇は見られなかった。これらの $^{12}\text{C}^{5+}$ 、 $^{12}\text{C}^{6+}$ 、 $^4\text{He}^{2+}$ 及び $^{40}\text{Ar}^{13+}$ 照射最小線量による致死効果はいずれも 30-

50% 程度であった。いずれの核種も致死作用、LOH 誘発性にそれほど大きな差は見られなかった。LOH 誘発機構としては、LOH の 90% 程度は相同組換え依存の遺伝子変換や交叉によるもので、残る 10% 程度は染色体喪失によるもので、イオンビーム照射が染色体不均等分配を引き起こす可能性は確認できなかった。また、 $^{12}\text{C}^{5+}$ については DNA 脱塩基 (AP) 部位の DNA 修復に関わる AP endonuclease (Apn1) 欠損株、translesion DNA polymerase である Pol η (Rad30) 及び Pol ζ (Rev3) 欠損株についても検討した結果、Apn1 欠損株及び Rad30 欠損株については野生株と大きな差は見られなかったが、Rev3 欠損株では、非照射で 1.9×10^{-3} と他の株より高頻度で LOH が高いものの、照射によっても 75 Gy、150 Gy でそれぞれ 4.9×10^{-3} 、 6×10^{-3} と 2-3 倍の LOH 誘発しか見られず、これらの LOH 誘発に translesion DNA polymerase Pol ζ の関与が窺えた (Fig. 2)。

今後、LOH 誘発における translesion DNA polymerase 特に Pol ζ の役割について検討を加える予定である、また、この系を用いた放射線防護剤や増感剤スクリーニングへの応用についても検討する予定である。

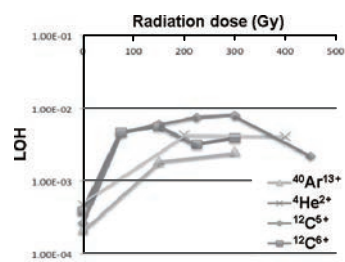


Fig. 1 LOH inducing ability of ion beam radiation in *S. cerevisiae*.

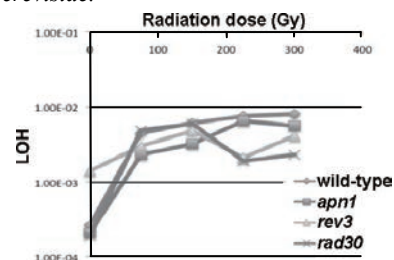


Fig. 2 LOH inducing ability of $^{12}\text{C}^{5+}$ in wild-type, *apn1*, *rad30* and *rev3* disruptant strains of *S. cerevisiae*.

3 - 52 The Effect of γ -sterilization of Biofertilizer's Carrier on Bacterial Inoculants Survival

K. Tejima ^{a)}, T. Yokoyama ^{b)}, K. Satoh ^{a)}, K. Takeda ^{a, c)} and I. Narumi ^{a)}

^{a)} Medical and Biotechnological Application Division, QuBS, JAEA,

^{b)} Institute of Agriculture, Tokyo University of Agriculture and Technology,

^{c)} United Graduate School of Agricultural Science, University of Agriculture and Technology

Biofertilizer is a substance that holds beneficial microorganisms for plant growth (e.g. Rhizobia) in the carrier such as peat, perlite, charcoal and soil. To use biofertilizer more efficiently, it is necessary to keep the amount of viable inoculants in the biofertilizer for a definite period of time. The inoculants survival in the biofertilizer could be affected by the physical and chemical properties of carrier materials and by the competition with native microbes in the carrier. Gamma-irradiation is expected to sterilize the carrier materials without changes in physical and chemical properties. We have reported the long-term storage of rhizobial biofertilizer made with γ -sterilized carriers ¹⁻³⁾. To demonstrate the effectiveness of γ -sterilization in the other nitrogen-fixing bacteria, the survivals of inoculants were monitored to assess the shelf life of biofertilizer.

As biofertilizer's carriers, Japanese peat soil "Keto-tsuchi" and topsoil of Andosol (Japanese typical cultivated soils) were prepared. To make the soil-based artificial carriers, Andosol was mixed with charcoal powder (3:1). Before sterilization, 20% (w/w) of demineralized water was added to biofertilizer's carriers. The prepared biofertilizer's carriers (6 g) were packed in polyethylene bags (for γ -sterilization) or polystyrene bags (for autoclave-sterilization). Following the sterilization of the carrier by γ -irradiation (50 kGy) or autoclaving (121 °C for 45 min; 3 times every 24 h), 1 mL of water suspension of *Bacillus pumilus* strain TUAT1 or *Azospirillum* sp. strain MAFF210364 was inoculated. As results, the initial

density of inoculants in the biofertilizer was adjusted to 7.7×10^7 cells g^{-1} and 2.0×10^7 cells g^{-1} for strains TUAT1 and MAFF210364, respectively. After storage the package of biofertilizer at 4 °C or 30 °C, viable inoculants in the biofertilizer were enumerated by the dilution plate method¹⁾.

The inoculant density in the *B. pumilus* biofertilizer made with autoclaved Keto-tsuchi rapidly decreased both at 4 °C and 30 °C compared to that with γ -sterilized Keto-tsuchi (Fig. 1). Especially, storage at 30 °C was detrimental to maintaining the inoculant density. We could not observe any survived cell after 1-week storage at 30 °C. Thus, γ -sterilization was superior to autoclave-sterilization in maintaining the survival of inoculants in the *B. pumilus* biofertilizer made with Keto-tsuchi carrier. The inoculant density in the biofertilizer made with Andosol carrier was maintained both in the γ -sterilized and autoclaved carriers stored at 30 °C for 20 weeks. On the other hand, the inoculant density in the *Azospirillum* biofertilizer made with autoclaved carriers was comparable to that of γ -sterilized carriers for 15 weeks (Fig. 2).

References

- 1) K. Tejima et al., JAEA Takasaki Annu. Rep. 2009 (2011) 83.
- 2) K. Tejima et al., JAEA Takasaki Annu. Rep. 2010 (2012) 114.
- 3) K. Tejima et al., Radioisotopes (2012) 161.

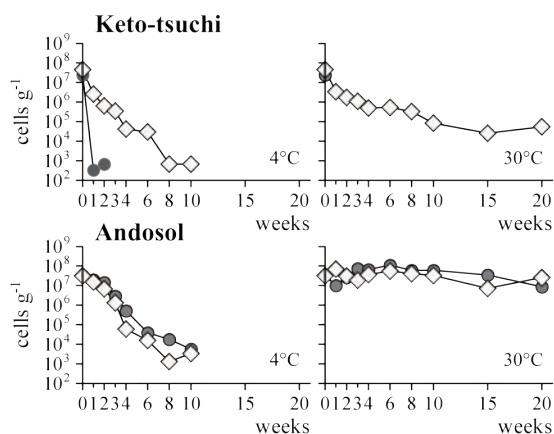


Fig. 1 Survival of *Bacillus pumilus* strain TUAT1 in biofertilizer stored at 4 °C and 30 °C.

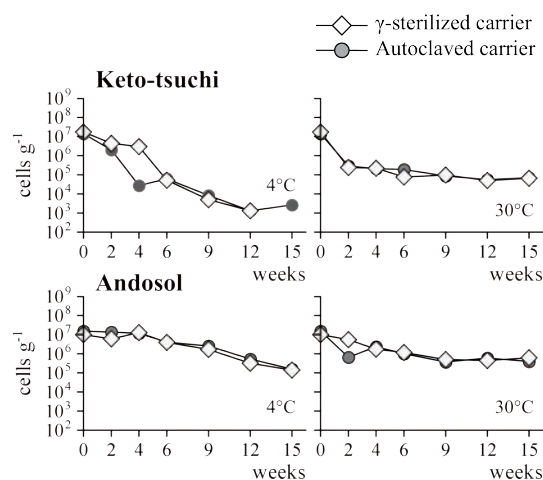


Fig. 2 Survival of *Azospirillum* sp. strain MAFF210364 in biofertilizer stored at 4 °C and 30 °C.

4. Advanced Materials, Analysis and Novel Technology for Facilities

4-01	Preparation of Gasochromic Transition Metal Oxide Thin Films by Pulsed Laser Deposition	117
	S. Yamamoto, T. Hakoda, K. Kawaguchi and M. Yoshikawa	
4-02	Three-dimensional Micro-assembly on the Single Particle Nano-fabrication Technique	118
	K. Takano, A. Asano, H. Marui, Y. Maeyoshi, M. Omichi, A. Saeki, M. Sugimoto, S. Tsukuda, T. Kamiya and S. Seki	
4-03	Fabrication of Poly(vinylphenol)/Ti-O Hybrids Nanowires by High Energy Ion Beam	119
	S. Tsukuda, M. Sugimoto, A. Idesaki, M. Yoshikawa, S. Seki and S.-I. Tanaka	
4-04	Formation of Nano Fiber Including Au Particles by Ion Beam Irradiation	120
	M. Sugimoto, M. Yoshikawa, S. Tsukuda, A. Asano and S. Seki	
4-05	Production of Platinum Nanoparticles Using a Few Tens keV Electron Beams	121
	T. Hakoda, Y. Isozumi, S. Yamamoto, H. Aritani and M. Yoshikawa	
4-06	Stability of Silicon Carbide Membrane Prepared from Polymer Precursor in Steam	122
	A. Takeyama, M. Sugimoto and M. Yoshikawa	
4-07	Ion Beam Synthesis of Carbon Doped β -FeSi ₂ Nanocrystals Embedded in Si and Their Photoluminescence Enhancement	123
	Y. Maeda, B. Matsukura, T. Nakajima, K. Nishimura, K. Narumi and S. Sakai	
4-08	Synthesis of Highly-mismatched ZnTeO Alloys with Multiple Band Gaps by Oxygen Ion Implantation	124
	T. Tanaka, S. Kusaba, Y. Nagao, K. Saito, Q. Guo and M. Nishio	
4-09	Microscopic Observation for Damage of Hybrid Type Boron-Doped Carbon Stripper Foil by Ion Beam	125
	Y. Yamazaki, M. Yoshimoto, O. Takeda, M. Kinsho, T. Taguchi, S. Yamamoto, T. Kurihara and I. Sugai	
4-10	Mach-Zehnder Polymer Waveguides Fabricated Using Proton Beam Writing ...	126
	K. Miura, T. Satoh, Y. Ishii, M. Koka, H. Kiryu, Y. Ozawa, K. Takano, T. Ohkubo, A. Yamazaki, W. Kada, A. Yokoyama, T. Kamiya and O. Hanaizumi	
4-11	Multiplex Energy Proton Irradiation Effects on Hydriding Property of a Hydrogen Storage Alloy	127
	H. Abe, K. Muraki, M. Kishimoto, H. Uchida and T. Ohshima	
4-12	Fabrication of Microstructure at a Fluoropolymer Surface by Ion Microbeam ...	128
	A. Kitamura(Ogawa), T. Satoh, M. Koka, T. Kamiya and T. Kobayashi	
4-13	Electroplating of Ni Microstructures on the Cross Section of Cu Wire Using PMMA Mother Fabricated by Proton Beam Writing	129
	Y. Tanabe, T. Iwamoto, J. Takahashi, H. Nishikawa, T. Satoh, Y. Ishii and T. Kamiya	

4-14	Epitaxial Transformation of Evaporated-Ti Thin Films during Nitriding Processes due to Ion-Implantation	130
	Y. Kasukabe, Y. Chen, S. Yamamoto and M. Yoshikawa	
4-15	Gamma-ray Induced Defect Formation in High-purity α -Quartz	131
	K. Kajihara	
4-16	Thermal Stability of Fe ₂ MnSi/Ge(111) Heteroepitaxial Interfaces	132
	Y. Maeda, B. Matsukura, T. Nakajima, K. Narumi and S. Sakai	
4-17	MFM Observation of Micrometer-sized Magnetic Patterns Produced by Heavy Ion Microbeam Irradiation in FeRh Films	133
	K. Aikoh, A. Tohki, T. Matsui, A. Iwase, T. Satoh, K. Takano, M. Koka, Y. Saitoh and T. Kamiya	
4-18	Nuclear Reaction Imaging of Boron Doped Iron	134
	H. Shibata, Y. Kohno, T. Satoh, T. Ohkubo, A. Yamazaki, Y. Ishii, A. Yokoyama and M. Koka	
4-19	Ion Scattering Spectroscopy of Polarity-controlled ZnO Surfaces by 1 - 2 MeV C ⁺ Ions	135
	K. Motohashi, Y. Saitoh, N. Miyawaki and T. Kamiya	
4-20	He ⁺ Ion Implantation Effect on Cathodoluminescence of Plagioclase	136
	H. Nishido, M. Kayama, S. Toyoda and K. Komuro	
4-21	Reconstruction of the Tectonic Activity in the Southwestern Tarim Basin	137
	A. Karasuda, R. Tada, Z. Hongbo, S. Toyoda and T. Yoshida	
4-22	Development of Spin-Polarized Positron Beam and Its Application to Spintronics Study	138
	A. Kawasuso, M. Maekawa, Y. Fukaya, A. Yabuuchi and I. Mochizuki	
4-23	Thermal Stability of Vacancies in Zr-Doped Stainless Steels	139
	A. Yabuuchi, M. Maekawa and A. Kawasuso	
4-24	Observation of Spatial Distribution of Vacancy Defects in Semiconductor by Positron Microbeam and Electron Beam Induced Current Measurement	140
	M. Maekawa and A. Kawasuso	
4-25	Atomic Displacement of Pb/Ag(111) Surface Studied by Reflection High-energy Positron Diffraction	141
	Y. Fukaya, I. Matsuda, M. Maekawa, I. Mochizuki, A. Kawasuso, K. Wada and T. Hyodo	
4-26	Phase Transition of Quasi One-dimensional Nanowire on Pt/Ge(001) Surface Studied by Reflection High-energy Positron Diffraction	142
	I. Mochizuki, Y. Fukaya, M. Maekawa, A. Kawasuso, K. Wada and T. Hyodo	
4-27	Pulse Radiolysis of Water by Energetic Heavy Ion	143
	M. Taguchi, K. Iwamatsu, Y. Sugo, S. Kurashima, S. Yamashita and Y. Katsumura	
4-28	Transient Absorption of Pyrene-Dodecane Solution Measured by Microsecond Ion Beam Pulse Radiolysis	144
	T. Kondoh, J. Yang, K. Kan, Y. Yoshida, H. Shibata, S. Kurashima, K. Iwamatsu and M. Taguchi	

4-29	Solvent Effect on the Radiation Induced Copolymerization of Maleimide with Styrene	145
	S. Nakagawa, M. Taguchi and A. Kimura	
4-30	Improvement of Source Neutron Spectrum Measurement Down to a Few MeV	146
	Y. Shikaze, Y. Tanimura, Y. Tatebe, H. Yoshitomi, M. Yoshizawa, H. Harano, T. Matsumoto and K. Mizuhashi	
4-31	Measurements of Low Energy Neutron Spectra of Quasi-Monoenergetic Neutron Fields by the TOF Method at TIARA	147
	T. Matsumoto, A. Masuda, H. Harano, Y. Unno, M. Hagiwara, T. Sanami, Y. Shikaze, Y. Tanimura, M. Yoshizawa, M. Baba and K. Mizuhashi	
4-32	Measurements of Neutron and Charged Particle Production Cross Sections on Be and Fe Bombarded with 13 MeV/nucleon ²⁰ Ne Beam	148
	Y. Iwamoto, M. Hagiwara, N. Matsuda, N. Shigyo, T. Nishizawa, T. Sanami, H. Nakashima and Y. Sakamoto	
4-33	Measurement of Thick Target Neutron Yields by 10 MeV Deuteron Incidence on Tungsten	149
	N. Shigyo, T. Nishizawa, K. Ishibashi, Y. Iwamoto, N. Matsuda, Y. Sakamoto and M. Hagiwara	
4-34	Development of Spatial Resolution Test-chart and Novel Fluorescent Converter Plates for Neutron Radiography	150
	T. Sakai, R. Yasuda, H. Iikura, T. Nojima, M. Matsubayashi, M. Koka, T. Satoh, T. Ohkubo, Y. Ishii and S. Yamamoto	
4-35	Response Studies of CR-39 Track Detectors Irradiated Heavy Ions under Vacuum	151
	A. Hattori, M. Kanasaki, H. Sakaki, Y. Fukuda, A. Yogo, S. Jinno, S. Kurashima, T. Kamiya, K. Kondo, K. Oda and T. Yamauchi	
4-36	Measurement of Radio Wave Reflection Due to Rock Salt and Ice Irradiated by an Electron Beam for an Ultra-high-energy Neutrino Detector	152
	T. Tanikawa, M. Chiba, T. Kamijo, F. Yabuki, O. Yasuda, H. Akiyama, Y. Chikashige, T. Kon, Y. Shimizu, M. Utsumi and M. Fujii	
4-37	Effect of Temperature on the Response of Alanine Dosimeters under Low Dose and Long Time Irradiation	153
	H. Seito, Y. Nagao, Y. Momoki, H. Kaneko, K. Nakagawa and T. Kojima	
4-38	Status Report on Technical Developments of the JAEA AVF Cyclotron	154
	S. Kurashima, H. Kashiwagi, N. Miyawaki, S. Okumura, K. Yoshida, Y. Yuri, T. Yuyama, T. Ishizaka, I. Ishibori and T. Nara	
4-39	Development of Beam Generation and Irradiation Technology for Electrostatic Accelerators	155
	K. Yamada, A. Chiba, A. Yokoyama, Y. Saitoh, Y. Ishii, T. Satoh, T. Ohkubo and S. Uno	

4-40	Fast Single-Ion Hit System for Heavy-Ion Microbeam at TIARA Cyclotron (V)	156
	W. Yokota, T. Satoh, S. Okumura, S. Kurashima, N. Miyawaki, H. Kashiwagi, K. Yoshida, M. Koka, A. Yokoyama, W. Kada and T. Kamiya	
4-41	Use of Gafchromic Dosimetry Films to Measure a Large-Area Ion-Beam Distribution	157
	T. Ishizaka, K. Imai, Y. Yuri, T. Yuyama, I. Ishibori and S. Okumura	
4-42	Detection Method for Dose Distribution of Focused Proton Beam by Using Common Polymer Film	158
	M. Omichi, K. Takano, T. Satoh, T. Kamiya, Y. Ishii, T. Ohkubo, M. Koka, W. Kada, M. Sugimoto, H. Nishikawa and S. Seki	
4-43	Development of Visible Light Measurement Techniques for Detention of Single-ion Hit	159
	A. Yokoyama, W. Kada, T. Satoh, M. Koka, S. Yamamoto, T. Kamiya and W. Yokota	
4-44	Development of Transmission Thin Diamond Sensors for the Single Hit Detection of High-energy Ions	160
	W. Kada, T. Kamiya, N. Iwamoto, S. Onoda, V. Grilj, N. Skukan, T. Makino, M. Koka, T. Satoh, M. Jakšić and T. Ohshima	
4-45	Quantitative Evaluation of Charge State for Internuclear Distance of Constituent Ions Dissociated from C_2^+ Ion Moving in a Solid	161
	A. Chiba, Y. Saitoh, K. Narumi, K. Yamada and T. Kaneko	
4-46	Ion Induced Luminescence from Sapphire Irradiated with Swift Cluster Ion Beams - Cluster Ion Size and Energy Dependences -	162
	H. Shibata, Y. Saitoh, A. Chiba, K. Yamada, K. Narumi and M. Taguchi	
4-47	Visualization of a Single Cluster Particle Track in Polystyrene Films	163
	A. Asano, K. Takano, A. Chiba, Y. Saitoh, H. Marui, M. Omichi, Y. Maeyoshi, Y. Honsho, A. Saeki, K. Yamada, K. Narumi and S. Seki	
4-48	Electronic Stopping Power Connected with Average Charge Reduction for Swift Carbon Cluster Ions in Carbon	164
	T. Kaneko, K. Ihara, M. Kohno, Y. Saitoh, A. Chiba and K. Narumi	
4-49	Reduction of Charging Effects on Negative Secondary Ion TOF Mass Spectra of PMMA Using Cluster Ion Impacts	165
	K. Hirata, Y. Saitoh, A. Chiba, K. Yamada, K. Narumi and T. Kamiya	
4-50	Cluster Effect on Damage Accumulation in a Si Crystal Bombarded with 10-540-keV C_{60} Ions	166
	K. Narumi, H. Naramoto, K. Yamada, A. Chiba, Y. Saitoh and Y. Maeda	
4-51	Cluster Effect on Projected Range of 30-keV C_{60}^+ in Silicon	167
	Y. Morita, K. Nakajima, M. Suzuki, K. Narumi, Y. Saitoh and K. Kimura	

4 - 01 Preparation of Gasochromic Transition Metal Oxide Thin Films by Pulsed Laser Deposition

S. Yamamoto, T. Hakoda, K. Kawaguchi and M. Yoshikawa

Environment and Industrial Materials Research Division, QuBS, JAEA

Liquid organic-hydrides such as cyclohexane, decalin are promising carriers of storage and supply of hydrogen gas for fuel cells. Organic-hydrides are highly flammable and volatile. For example, cyclohexane leakage of 1.3% (the lower combustion limit) in air may lead an explosive atmosphere of easy ignition. In addition, organic-hydrides are treated in a dehydrogenation reactor with production of hydrogen. The monitoring of leakage of hydrogen and organic-hydride gases at storage or usage sites is strongly required for safe operation. In explosive atmospheres, optical gas detection with gasochromic materials such as tungsten trioxide (WO_3)¹⁾ is more appropriated because they have not any ignition sources such as electrical circuits.

In the present study, we prepared 10 different kinds of transition metal (titanium, vanadium, cobalt, nickel, copper zirconium, niobium, molybdenum, silver and tantalum) oxide films using a pulsed laser deposition (PLD) on SiO_2 substrates in order to find suitable gasochromic oxide materials for optical detection of hydrogen and organic-hydride. The PLD was performed by the second harmonic Q-switched Nd:YAG laser with a wavelength of 532 nm in the presence of oxygen gas. A typical laser fluence and repetition rate were 150 mJ cm^{-2} and 10 Hz, respectively. To evaluate the gasochromic coloration of oxide films, the films were coated with a Pt layer (8 nm) by sputtering method. And then, optical transmittance spectra (wavelength: 350 - 850 nm) were measured using a spectrometer while nitrogen gas including 1% hydrogen (1% H_2/N_2). The films were characterized using X-ray diffraction (XRD) and Rutherford backscattering spectroscopy (RBS). The RBS analysis using a 3 MV single-stage-accelerator at JAEA Takasaki was employed to determine the composition of the films.

The results of the optical transmittance spectra measurements of the oxide films exposing to hydrogen, significant optical transmittance changes were observed in molybdenum (Mo) oxide, vanadium (V) oxide and nickel (Ni) oxide films. Figure 1 shows the optical transmittance change ratio of (a) Pt/Ni oxide film and Pt/Mo oxide film induced by 1% H_2/N_2 . It can be seen that the Pt/Ni oxide film becomes transparent and the Pt/Mo oxide film becomes blue in color. Also, the color of V oxide film turned from yellow semi-transparent to blue exposing to hydrogen. In addition, these oxide films show optical transmittance changes reversibly in exposing to hydrogen and air. The results of XRD and RBS indicated the Ni oxide film on SiO_2 substrate has amorphous structure and the following composition, O/Ni atomic ratio of 1.5 corresponding to stoichiometric Ni_2O_3 determined by RBS spectra shown in

Fig 2. Furthermore, the composition of gasochromic Mo oxide and V oxide films was determined by XRD and RBS analysis. In summary, in addition to WO_3 , MoO_3 , V oxide with O/V atomic ratio of 0.23 and Ni_2O_3 films have potential for optical detection of hydrogen and organic-hydrides.

Reference

- 1) K. Yoshimura et al., Appl. Surf. Sci. 257 (2011) 4428-31.

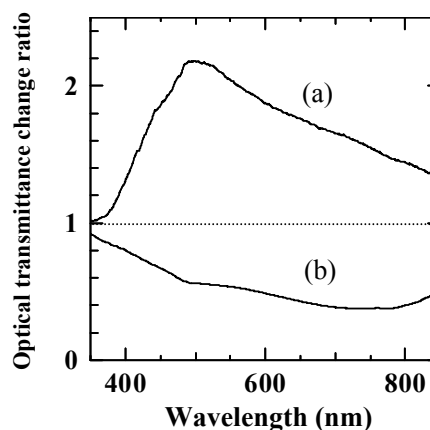


Fig. 1 Change ratio of optical transmittance induced by 1% H_2/N_2 exposure. (a) Pt/ Ni_2O_3 film, (b) Pt/ MoO_3 film.

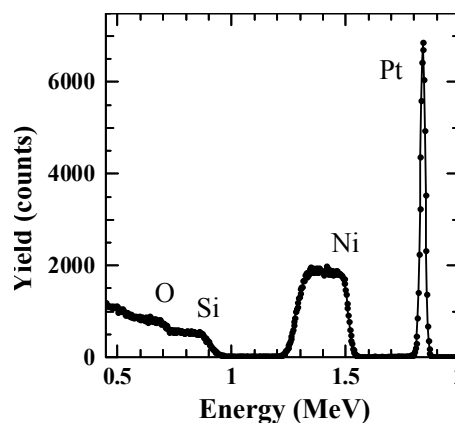


Fig. 2 Two MeV $^4\text{He}^+$ RBS spectrum from a Pt (8 nm)/ Ni_2O_3 (320 nm) film on SiO_2 substrate. The film was prepared by pulsed laser deposition at RT.

4 - 02 Three-dimensional Micro-assembly on the Single Particle Nano-fabrication Technique

K. Takano^{a)}, A. Asano^{a)}, H. Marui^{a)}, Y. Maeyoshi^{a)}, M. Omichi^{a, b)},
A. Saeki^{a)}, M. Sugimoto^{c)}, S. Tsukuda^{d)}, T. Kamiya^{e)} and S. Seki^{a)}

^{a)} Division of Applied Chemistry, Graduate School of Engineering, Osaka University, ^{b)} Department of Material Engineering, Anan National College of Technology, ^{c)} Environment and Industrial Materials Research Division, QuBS, JAEA, ^{d)} Institute of Multidisciplinary Research for Advanced Materials, Tohoku University, ^{e)} Department of Advanced Radiation Technology, TARRI, JAEA

The direct formation technique of 1-D polymer nanostructures using single heavy ion induced cross-linking reactions, Single Particle Nanofabrication Technique (SPNT), has been developed as a unique microprocessing technique^{1,2)}. The energy of the heavy ion was set at from several to hundreds MeV order, where the electronic stopping power is dominant in the Linear Energy Transfer (LET). Cross-linking reactions along an ion trajectory in the target polymer are promoted by knocked-on secondary electrons, and the reactions are distributed radially from the trajectory. Although the large LET is transferred into the polymer by the irradiations, the properties of polymer nanostructures were almost similar or enhanced to the intrinsic properties. In the processing with SPNT, the cross-linking reaction is promoted sufficiently to form the structures without post-exposure treatment, such as a baking which is needed in photolithographic process. However, there were problems that the nanostructures were distorted and lying down on the substrate at the development.

To avoid the collapse of the nanostructures made up of silicon or polymers, the supercritical drying using supercritical carbon dioxide (CO₂) under high pressure has been proposed as new drying method for the microprocessing with high aspect ratio³⁾. However, the supercritical drying for the polymer nanostructures has not been widely applied. Because swelling effects for the polymer nanostructures have not been clearly understood. In this study, a fabrication of polymer nanostructures with unlying on the substrate was tried by a combination of the SPNT and the supercritical drying. And the swelling effect was investigated by an observation the formed structures.

The target films with 20 μm thickness were fabricated by spin-coat method on a silicon wafer, using SU-8 photoresist which is high sensitively for the ion beam irradiations⁴⁾. The radiation-induced cross-linking efficiency (G-value) of SU-8 photoresist is to be over 3.5 (100 eV)⁻¹. The films were irradiated with scanning ¹⁹²Os³⁰⁺ beam with the energy of 490 MeV at LD beam-line connected to the cyclotron accelerator at Takasaki Ion Accelerators for Advanced Radiation Application facility (TIARA), of JAEA/Takasaki. The ion fluence of the beam was adjusted by adjusting the irradiation time to be 1 × 10⁸ ions/cm². After the developing of the irradiated films, the supercritical drying with liquid carbon dioxide was performed at 12 MPa, 40 °C, using a supercritical rinser & dryer SCR6 developed by

Rexxam Co., Ltd. A drying in atmosphere was also performed to compare with the case of the supercritical drying. The formed nanostructures were observed by Scanning Electron Microscopy (SEM) tilting the sample without any surface treatments.

In the case of the drying in atmosphere, lying nanostructures were confirmed to be formed on the substrate as shown in Fig. 1(a). The radii of the structures were estimated with the ellipse model⁵⁾ to be 15.6 nm which was consistent in the estimation with the formulation¹⁾. On the other hand, the nanostructures which assembled and bended in three-dimensionally were formed by the supercritical drying as shown in Fig. 1(b). Not only less driving the surface tension from the supercritical CO₂ but also a swelling of epoxy matrix with uncrosslinking is considered to be induced by the high pressure CO₂⁶⁾. It is expected that there is a possibility of controlling the structure shape optimizing the parameters for the swelling at the supercritical drying, and applying this technique to three-dimensional microprocessing of other polymer materials.

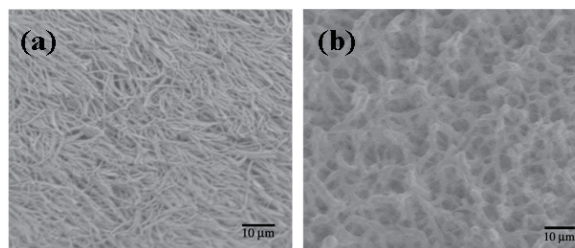


Fig. 1 SEM images of epoxy nanostructures formed by the SPNT with 490 MeV ¹⁹²Os³⁰⁺ beam at 3 × 10⁹ ions/cm². The observations were performed after the drying in atmosphere (a) or supercritical drying (b).

References

- 1) S. Seki et al., Phys. Rev. B 70 (2004) 144203.
- 2) S. Seki et al., Adv. Mater. 13 (2001) 1663.
- 3) H. Namatsu et al., Microelectron. Eng. 46 (1999) 129.
- 4) S. Seki et al., J. Photopolym. Sci. Tech. 21 (2008) 541.
- 5) S. Tsukuda et al., Surf. Coatings Tech. 201 (2007) 8526.
- 6) J. S. Chiou et al., J. Appl. Polym. Sci. 30 (1985) 2633.

4 - 03 Fabrication of Poly(vinylphenol)/Ti-O Hybrids Nanowires by High Energy Ion Beam

S. Tsukuda^{a)}, M. Sugimoto^{c)}, A. Idesaki^{c)}, M. Yoshikawa^{c)}, S. Seki^{b)} and S.-I. Tanaka^{a)}

^{a)} Institute of Multidisciplinary Research for Advanced Materials, Tohoku University,

^{b)} Division of Applied Chemistry, Graduate School of Engineering, Osaka University,

^{c)} Environment and Industrial Materials Research Division, QuBS, JAEA

In recent years, design and synthesis of organic-inorganic hybrid materials have attracted great interests in the fields of materials sciences. Sol-gel process is popular route to synthesize inorganic oxides materials. These materials, synthesized via the sol-gel processes, combine the properties of their constituents, such as chemical and thermal stability, hardness, photocatalytic function, and low processing temperatures. Direct pattern writing of novel sol-gel materials has also been reported by electron beam lithography with high spatial resolution. Single particle nanofabrication technique (SPNT) is useful technique to fabricate one dimensional polymer nanostructures by crosslinking reaction within an ion track along the single ion path¹⁻³⁾. In this paper, we report the direct formation of the poly(4-vinylphenol)/Ti-O hybrids nanowires by ion irradiation to the sol-gel hybrid films. The number density of the hybrid nanowires were also controlled by changing the number of incident ions.

The negative tone hybrid sol-gel materials were composed by typical sol-gel synthesis. Poly(4-vinylphenol) (PHS) were dissolved in EtOH at 5 wt%, and titanium isopropoxide (TIP) were added to the solutions with 1 wt% against dissolved PHS. EtOH was used as solvent, distilled water for hydrolysis and HCl as catalysts. The mixture was stirred at room temperature for 12 h. The sol-gel materials (PHS/TIP) were spin-coated on Si substrates. The chemical composition analysis of the films was carried out using X-ray photoelectron spectrometer (XPS), operating with Mg Ka radiation at 10 mA and 10 kV. Figure 1 shows XPS spectra of Ti 2p region for the PHS/TIP hybrid film. Ti 2p photoelectron peaks appeared at 460.1 and 465.8 eV for Ti 2p_{3/2} and Ti 2p_{1/2}, respectively. The O 1s several peaks were also detected. These peaks were attributed to chemical bonds both TiO₂ and PHS.

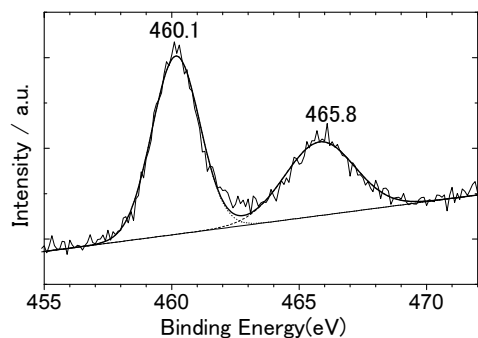


Fig. 1 XPS spectra of Ti 2p for the hybrid PHS/TIP film.

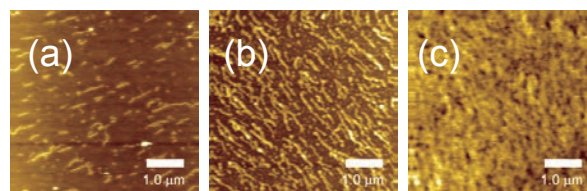


Fig. 2 AFM micrographs of PHS/TIP nanowires formed by 450 MeV Xe ion beam irradiation to the thin films (thickness: 850 nm) with the fluence of (a) 1.0×10^9 , (b) 5.0×10^9 and (c) 1.0×10^{11} ions/cm².

These hybrid films were subsequently placed in a vacuum chamber and exposed to 450 MeV ¹²⁹Xe²³⁺ beam at the Takasaki Ion Accelerators for Advanced Radiation Application (TIARA) cyclotron accelerator facility of the Japan Atomic Energy Agency. Ion irradiation at low fluence without overlapping between ion tracks produces single ion events in the target materials. The crosslinking reactions along the ion track result in the formation of a cross-linked nanowire in the thin films. After irradiation, the samples were developed using EtOH for 2 minutes. The irradiated part of the film was insoluble in EtOH. Therefore, the hybrid nanowires based on PHS/TIP were successfully isolated on the substrate after development procedures. However, the average radial sizes of PHS/TIP hybrid nanowires were decreased compared with that of the PHS nanowires. These results indicate that the cross-linking efficiency $G(x)$ is decreased in the hybrid films, because of the inhibition of cross-linking reaction by including TIP.

The number density of nanowires was also depended on the number of incident ions (fluence), because the one nanowire was formed along the single ion path. Figure 2 shows the results aimed to control of number density of hybrid nanowires by changing the ion fluence. The relative number density of nanowires was increased with number of incident ions from 1.0×10^9 to 1.0×10^{11} ions/cm², clearly. Especially, the surface of substrate was completely covered with the hybrid nanowires formed by ion irradiation at 1.0×10^{11} ions/cm². Therefore, it is suggested that the surface modification by the nanowires is very useful to control the relative surface area and surface properties.

References

- 1) S. Seki et. al., Adv. Mater. 13 (2001) 1663-65.
- 2) S. Tsukuda, et al., Appl. Phys. Lett. 87 (2005) 233119-1-3.
- 3) S. Tsukuda, et al., J. Photopolym. Sci. Technol. 22 (2009) 245-48.

4 - 04 Formation of Nano Fiber Including Au Particles by Ion Beam Irradiation

M. Sugimoto^{a)}, M. Yoshikawa^{a)}, S. Tsukuda^{b)}, A. Asano^{c)} and S. Seki^{c)}

^{a)} Environment and Industrial Materials Research Division, QuBS, JAEA,

^{b)} Institute of Multidisciplinary Research for Advanced Materials, Tohoku University,

^{c)} Department of Applied Chemistry, Osaka University

Ion beams are used for high-density energy deposition in polymer materials. Single ion bombardment can release active intermediates at high density within a limited area along the single ion track. In crosslinking-type polymers, the crosslinking reactions along the ion track result in the formation of a cross-linked part in the thin films. The non-crosslinked area can be removed by a development procedure, utilizing the change in solubility due to the gelation of polymer¹⁾. Recently we succeeded in obtaining the palladium folded nano fiber synthesized from the polymer-blend thin film with Si-based polymer and palladium acetate²⁾. In this synthesis method, the amount of folded palladium in the nano fiber was insufficient for applying as a catalyst material. In this research, we report a synthesis method of nano fiber including Au nano particles produced by single ion irradiation of poly(vinylpyrrolidone) (PVP) and chloroauric acid (HAuCl₄).

PVP was dissolved in 2-propanol at 5 mass%, then HAuCl₄ was also dissolved at 0.125, 0.25, 0.50, 0.75 mass%. This mixed solution was spin coated on a Si substrate. The thin film of PVP was subsequently placed in a vacuum chamber and irradiated to 490 MeV ¹⁹²Os³⁰⁺ beams at ion fluence of 1.0×10^9 ions/cm². The irradiated films were treated using 2-propanol for 1 minute and the insoluble irradiated part of the film was developed as nano fiber. The sizes and shapes of the nano fibers were observed using atomic force microscope (AFM Seiko Instruments Inc. (SII) SPA-400).

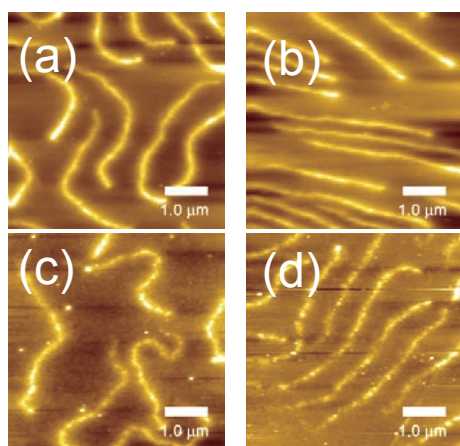


Fig. 1 AFM micrographs of nano fiber formed by 490 MeV Os ion beam irradiation to PVP included Au nano particles thin films with the fluence of 1.0×10^9 ions cm⁻². The concentrations of HAuCl₄ were (a) 0.125, (b) 0.25, (c) 0.50, and (d) 0.75 mass%.

The nano fibers based on PVP including Au particles (PVP/Au) were successfully formed and isolated on the Si substrate as shown in Fig. 1. These nano fibers were synthesized from the PVP film of similar thickness, but it was observed that a tendency to decrease of the length of the nano fiber with increasing in the HAuCl₄ concentration. Especially in the case of the HAuCl₄ concentration at 0.75 mass%, the nano fibers were cut partially and observed as discontinuous form. Relationship between the concentration of HAuCl₄ and radii of PVP/Au nano fibers is presented in Fig. 2. The value of radius decreased with the concentration of HAuCl₄. These results indicate the including Au nano particles inhibits cross-linking reaction, resulting in reduced cross-linking efficiency of the PVP/Au film compared with that of PVP. The significant decrease in cross-linking efficiency between PVP and PVP/Au influences the radial sizes.

It is expected that this synthesis method will enable to fabricate the nano fiber containing metal particles of high concentration by improving cross-linking efficiency.

References

- 1) S. Seki et al., Adv. Mater. 13 (2001) 1663-65.
- 2) M. Sugimoto et. al., Ceramic Trans. 213 (2010) 105-11.

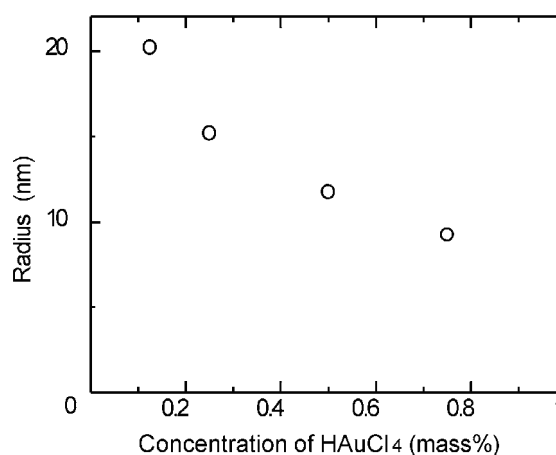


Fig. 2 Relationship between the concentration of HAuCl₄ and the radii of PVP/Au nano fiber. The radii of the nano fiber were determined by AFM.

4 - 05 Production of Platinum Nanoparticles Using a Few Tens keV Electron Beams

T. Hakoda^{a)}, Y. Isozumi^{b)}, S. Yamamoto^{a)}, H. Aritani^{b)} and M. Yoshikawa^{a)}

^{a)}Environment and Industrial Materials Research Division, QuBS, JAEA,

^{b)}Department of Applied Chemistry, Saitama Institute of Technology

Reduction of noble metal ions and subsequent production of noble metal particles in a solution has been performed as a radiation-induced reduction method using high energy ionizing radiation such as a few MeV electron beams (EBs) and ⁶⁰Co γ -rays. The size of produced particles is reported to be smaller as increasing the dose rate of ionizing radiation¹⁾. Electron beams with energies below 100 keV, low energy EBs, have been frequently used for surface curing because they have shorter penetration range and can irradiate at higher dose rates. In the present study, reduction of noble metal ions and subsequent formation of metal particles was performed using a few tens keV EBs to study the effect of low energy EBs on the production of nano-sized particles, nanoparticles, of noble metals²⁾.

A solution containing 0.5 mmol/L PtCl₄²⁻ ion and 5–20 v% ethanol, which is an OH radical scavenger, was prepared as a sample solution. The sample solution (10 mL) in a cup with a diameter of 45 mm was irradiated with 55-keV and 0.17-mA EBs. The dose of the sample solution varied from 2 to 6 kGy by changing irradiation time of 20–60 s. Nitrogen gas was introduced between an irradiation window and the sample solution to remove oxygen dissolved in the irradiated solution. After EB irradiation, the morphology of produced Pt particles was observed by transmission electron microscope (TEM) and scanning electron microscope (SEM) analysis after fixation on a collodion mesh. The concentration of PtCl₄²⁻ ions was measured by atomic absorption spectrometry of the sample solution after filtration of produced Pt particles.

The color of whole solution turned from yellow into black after EB irradiation. This result suggests that the reduction of PtCl₄²⁻ ions should proceed in whole solution

even by irradiating only the surface layer of the solution. The reduction rate of PtCl₄²⁻ ions was obtained from the change in their concentration before and after irradiation. The reduction rate increased with dose and reached to 50, 82, and 70% in presence of 5, 10, and 20 v% ethanol, respectively, at a dose of 6 kGy.

The TEM micrographs of Pt particles were obtained for a solution containing 10 v% ethanol at different doses. As shown in Fig. 1 (a), the TEM micrograph showed Pt particles with sizes of 2-5 nm and their aggregated particles at 2 kGy. As increasing dose, the aggregated particles were frequently observed in the TEM and SEM micrographs (Fig. 1 (b)). These results suggest that Pt particles with sizes of 2-5 nm, which are Pt nanoparticles, would be produced as primary particles through reduction of PtCl₄²⁻ ions. The coarse particles will be produced through the aggregation of primary particles. Based on these results, low energy EBs can be used as a source of ionizing radiation for production of noble metal nanoparticles.

The Pt nanoparticles, produced by a few tens keV EB irradiation, loaded tungsten trioxide (WO₃) powders were prepared to examine their catalytic activity. The prepared Pt/WO₃ demonstrated the gasochromic property in exposure to H₂ gas through reaction of WO₃ with hydrogen atoms dissociating over Pt nanoparticles (Fig. 2). The colored Pt/WO₃ powders showed discoloration after exposure to air through catalytic oxidation of absorbed hydrogen atoms. This result suggests that the Pt nanoparticles should have hydrogen dissociation activity and oxidation activity.

References

- 1) S. Seino et al., J. Nanopart. Res. 10 (2008) 1071.
- 2) Y. Isozumi et al., RADIOISOTOPES (in press).

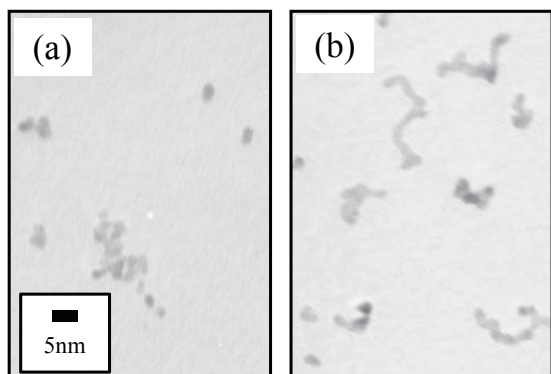


Fig. 1 TEM micrograph of Pt particles in a sample solution containing 10 v% ethanol after 55-keV EB irradiation at doses of 2 kGy (a) and 6 kGy (b).

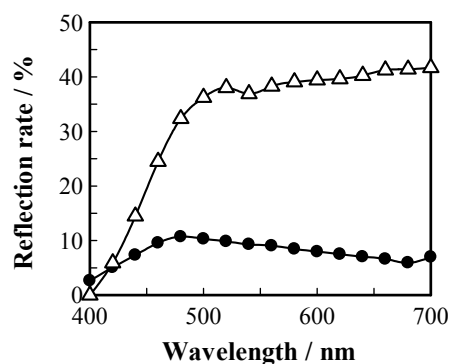


Fig. 2 Reflection spectra of visible lights for Pt/WO₃ powders before (Δ) and after exposure to 1 v% H₂/N₂ gas (\bullet).

4 - 06 Stability of Silicon Carbide Membrane Prepared from Polymer Precursor in Steam

A. Takeyama, M. Sugimoto and M. Yoshikawa

Environment and Industrial Materials Research Division, QuBS, JAEA

Inorganic membrane prepared from precursor-derived silicon carbide (SiC) has been a promising candidate as a membrane usable for hydrogen separation in harsh condition. When SiC membrane is used for hydrogen separation in Iodide Sulfur (IS) process or steam reforming of methane, it is attacked by corrosive gases such as hydrogen iodide or steam in the temperature range from 723 K to 873 K. In this report, SiC membrane prepared using our developed method¹⁾ was exposed to steam and its gas permeances were measured.

Alpha alumina tubes coated with thin gamma alumina layer were used as supports. Coating solution was prepared by dissolving polymer precursor polycarbosilane (PCS) into cyclohexane. PCS film was coated on the porous support by our developed method using 10 mass% PCS solution. Curing and cross-linking of coated PCS film was carried out by an electron beam irradiation in helium atmosphere. Subsequently, the pyrolysis at 973 K or 1,073 K for 30 minutes in argon atmosphere was performed. A series of preparation procedure was repeated three times to layer SiC film on the support. Prepared membrane was exposed to steam at 773 K for 10 hours. Water vapor pressure was about 47 kPa. Single gas permeances of hydrogen (H₂) and nitrogen (N₂) of the membrane before/after the exposure were measured in the temperature range from room temperature to 523 K.

Figure 1 shows H₂ and N₂ permeances of SiC membrane prepared via the pyrolysis at 973 K. Arrhenius plot of H₂ permeance of as-prepared membrane (solid line) means H₂ permeated through the membrane by molecular sieving mechanism. In contrast, after the exposure to steam, H₂ permeance as well as N₂ permeance (dashed line) was decreased as the temperature raised. This indicates gases

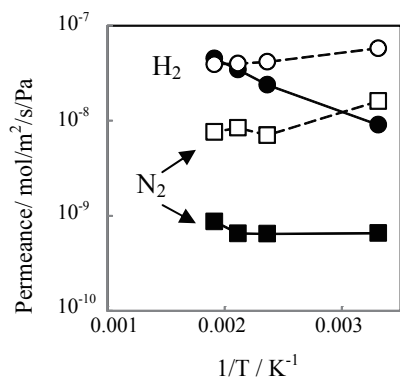


Fig. 1 Gas permeances of SiC membrane. Circles and squares are for H₂ and N₂ permeances. Solid and dashed lines are for the membranes before/after the exposure to steam. Pyrolysis temperature was 973 K.

diffused through large sized pores formed as a result of degradation of SiC film by Knudsen diffusion. Figure 2 shows the gas permeation behavior of SiC membrane prepared via the pyrolysis at 1,073 K. Lower H₂ permeance of as-prepared membrane (solid line) than that shown in Fig. 1 means the membrane was so dense that smaller amount of H₂ was allowed to pass through it. Arrhenius plot of H₂ permeance indicates H₂ passed through the membrane by molecular sieving mechanism. After the exposure to steam, both H₂ and N₂ permeances were increased (dashed lines) and H₂ permeance still followed Arrhenius plot. This gas permeation behavior indicates only a few large sized pores were formed by the exposure.

Crystalline silicon carbide is oxidized in steam following the reaction, $\text{SiC} + 3\text{H}_2\text{O} = \text{SiO}_2 + 3\text{H}_2 + \text{CO}^{2)}$. Though a sign of Gibbs energy of this reaction is negative, the reaction could be retarded by thin SiO₂ film formed on the surface of SiC³⁾. Since our SiC film prepared via the pyrolysis at 1,073 K possessed well-grown Si-C network, uniform SiO₂ film formed on the surface likely retarded the oxidation which resulted in the formation of large sized pore in SiC film. Pyrolysis at high temperature is desirable to prevent the oxidation and further optimization of the preparation condition to improve the gas permeation behavior of SiC membrane is required.

References

- 1) A. Takeyama et al., Mater. Trans. 52 (2011) 1276.
- 2) M. Fukushima et al., J. Ceram. Soc. Jpn. 114 (2006) 1155.
- 3) T. Shimoo et al., J. Ceram. Soc. Jpn. 107 (1999) 263.

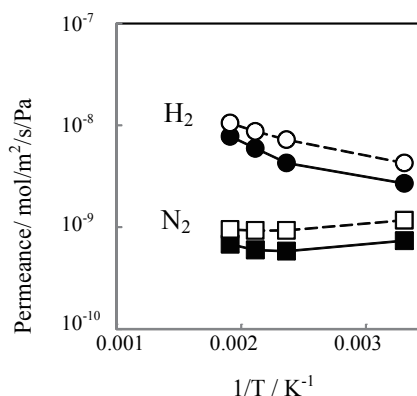


Fig. 2 Gas permeances of SiC membrane. Circles and squares are for H₂ and N₂ permeances. Solid and dashed lines are for the membranes before/after the exposure to steam. Pyrolysis temperature was 1,073 K.

4 - 07 Ion Beam Synthesis of Carbon Doped β -FeSi₂ Nanocrystals Embedded in Si and Their Photoluminescence Enhancement

Y. Maeda^{a, b)}, B. Matsukura^{a)}, T. Nakajima^{a)}, K. Nishimura^{a)}, K. Narumi^{b)} and S. Sakai^{b)}

^{a)} Department of Energy Science and Technology, Kyoto University,
^{b)} Advanced Science Research Center, JAEA

A specific luminescence of β -FeSi₂ nanocrystals has been observed at 0.803-5 eV (A band due to recombination of indirect excitons) and expected to be applied to Si based light emitters at telecom wavelengths¹⁾. Other effective elements for enhancement of the A band luminescence have not been found except for Al and B²⁻⁴⁾. Carbon in the β -FeSi₂ lattice was predicted to form isoelectronic traps (IET) because of large difference in electronegativity between C and Si⁵⁾. We can actively expect enhancement of luminescence efficiency by bound excitons (BEX) due to the IET.

In this study, we investigated ion beam synthesis of carbon doped β -FeSi₂ nanocrystals embedded in Si and photoluminescence (PL) properties, and found pronounced PL enhancement by C doping.

Beta-FeSi₂ nanocrystals were formed at the surface of Si substrate by using ion beam synthesis, in which 200 keV-⁵⁶Fe⁺ ions with the dose of 10¹⁷ ions/cm² were implanted into Si(001) substrates. The Fe implanted substrates were annealed at 800 °C for 2 h by a rapid thermal anneal process (RTA). We employed C₆₀⁺ cluster ions in order to realize very shallow implantation. Sixty keV-C₆₀⁺ ions with doses of 5 × 10¹¹-5 × 10¹³ C₆₀⁺/cm² were implanted into the surface layer where β -FeSi₂ nanocrystals precipitate.

PLs excited with an Ar⁺ ion laser of 514.5 nm were measured with a monochromator and a Liquid N₂ cooled Ge-pin photodetector. All the spectra were detected at the constant optical condition in order to compare their intensities.

Figure 1 shows some PL spectra at 10 K corresponding to the dose of C₆₀⁺ ions. The spectrum showed two components of the A band at 0.803 eV and the C band at 0.763 eV. Both intensities of the A and C bands were observed to be dependent upon the dose.

In comparison with the non-doped sample, especially only the sample implanted by 10¹³ C₆₀⁺ ions/cm² showed pronounced enhancement by 260% of the A band luminescence. The intensity rapidly decreased as the dose increased from 10¹³ C₆₀⁺ ions/cm². This critical dose of 10¹³ ions/cm² at 60 keV corresponds to ~1 at% C in the nanocrystal. Using the density of 2 × 10¹⁷ cm⁻³ and the average size of 14 nm for spherical nanocrystals obtained by electron microscopic observations and the β -FeSi₂ unit cell volume of 602.9 Å³, we can know that average number of C atom doped in the unit cell of β -FeSi₂ is one atom at the critical dose. One C atom doping into β -FeSi₂ lattice can

realize effective formation of BEX due to the IET, so that pronounced enhancement of PL may be caused by quasi direct recombination of BEX.

Next we measured the exciton binding energy of C-doped β -FeSi₂ nanocrystal from a peak shift of the A band emission as a function of the C₆₀⁺ dose, and found that the binding energy was enhanced up to 1.8 meV by doping of 10¹³. This dose corresponds to that for the maximum enhancement of PL in Fig. 1. This result also suggests the presence of the BEX due to C atoms in the nanocrystal⁷⁾.

References

- 1) Y. Maeda, Appl. Surf. Sci. **254** (2008) 6242.
- 2) Y. Terai and Y. Maeda, Appl. Phys. Lett. **84** (2004) 903.
- 3) Y. Terai and Y. Maeda, Opt. Mater. **27/5** (2005) 925.
- 4) T. Nakajima et al., Phys. Procedia **23** (2012) 25.
- 5) S. Kondo et al., Phys. Procedia **11** (2011) 142.
- 6) R. Lange et al., J. Appl. Phys. **107** (2010) 103508.
- 7) Y. Maeda et al., Phys. Status Solidi (a) (in press).

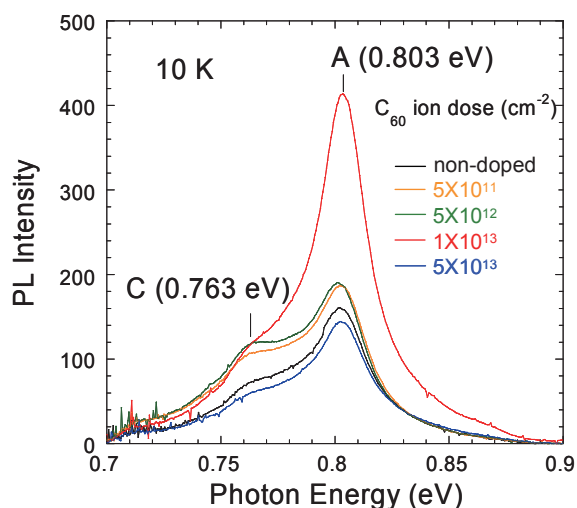


Fig. 1 Photoluminescence spectra of carbon doped β -FeSi₂ as a function of the C₆₀⁺ ion dose. A: intrinsic light emission band of β -FeSi₂¹⁾, C: light emission band by conduction band to acceptor impurity transition (tentative)⁵⁾.

4 - 08 Synthesis of Highly-mismatched ZnTeO Alloys with Multiple Band Gaps by Oxygen Ion Implantation

T. Tanaka ^{a, b)}, S. Kusaba ^{a)}, Y. Nagao ^{a)}, K. Saito ^{a)}, Q. Guo ^{a)} and M. Nishio ^{a)}

^{a)} Department of Electrical and Electronic Engineering, Saga University,

^{b)} PRESTO, Japan Science and Technology Agency

The concept of multiband or intermediate band solar cell (IBSC) has recently attracted a renewed attention as a viable approach to achieving high solar power conversion efficiencies ¹⁾. Highly mismatched alloys (HMAs) is a class of materials whose fundamental properties are dramatically modified through the substitution of a relatively small fraction (up to 5%) of host atoms with an element of very much different electronegativity, for example Nitrogen in GaAs and oxygen in ZnTe. In ZnTe, the incorporation of a small amount of isoelectronic oxygen leads to the formation of a narrow, oxygen-derived band of extended states located well below the conduction band edge of the ZnTe ¹⁻³⁾. The three absorption edges of ZnTe_{1-x}O_x(ZnTeO) cover the entire solar spectrum providing a material envisioned for the multi-band, single junction, high efficiency photovoltaic devices.

In this study, we synthesized ZnTeO alloys by O ion implantation into ZnTe, and characterized the optical properties of the ZnTeO alloys.

ZnTe_{1-x}O_x was synthesized using the combination of oxygen ion implantation and pulsed laser melting (PLM). Multiple energy implantation using 200, 80 and 30 keV O⁺ was carried out into ZnTe (100) wafers and ZnTe films on α -Al₂O₃(001) substrates to form \sim 0.4 μ m thick layers with relatively constant O concentrations. The O composition x was changed between 0.5 and 5%. The O⁺-implanted samples were pulsed laser melted in air using a KrF laser (λ =248 nm) with a FWHM pulse duration of \sim 38 ns. The fluence at the sample was 0.615 J/cm².

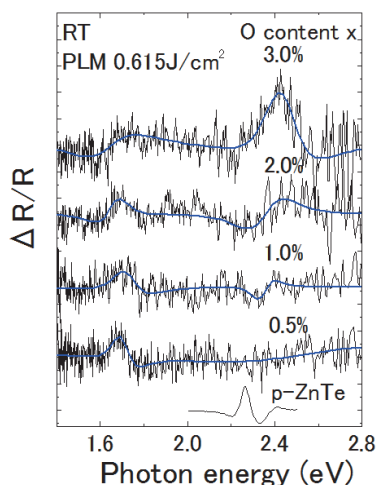


Fig. 1 Photo-modulated reflectance spectra of ZnTeO samples. Blue lines show the fitting results by the Aspnes equation.

Figure 1 shows a series of photo-modulated reflectance (PR) spectra of ZnTeO samples. Two optical transitions at \sim 1.7 and 2.45 eV, distinctly different from the fundamental band gap transition ($E_M=2.26$ eV) of the matrix, can be clearly observed. The two observed optical transitions can be attributed to transitions from the valence band to the two conduction subbands, E^+ (\sim 2.45 eV) and E^- (\sim 1.7 eV) formed as a result of the hybridization of the localized O states and the extended conduction band states of ZnTe. The values of the band gap were determined by fitting the PR spectra to the Aspnes third-derivative functional form, and the fitting results are shown by blue lines in Fig. 1.

Figure 2 shows the absorption coefficients of ZnTeO calculated from the optical transmission and reflectance spectra of ZnTeO/ α -Al₂O₃(001) samples. It can be seen that the absorption coefficients associated with the transition from the valence band to the E^- band exceed 2×10^4 cm⁻¹, confirming the suitability of this material for thin-film PV device applications, and the absorption coefficient increases with increasing O content x. In addition, the increase of the slope of absorption coefficients was observed at around 2.4 eV due to the increased electron transition from valence band to the E^+ band. These fundamental results offer a potential in using these alloys for intermediate band solar cells.

References

- 1) K. M. Yu et al., Phys. Rev. Lett. 91 (2003) 246403.
- 2) T. Tanaka et al., Jpn. J. Appl. Phys. 50 (2011) 082304.
- 3) T. Tanaka et al., Appl. Phys. Lett. 100 (2012) 011905.

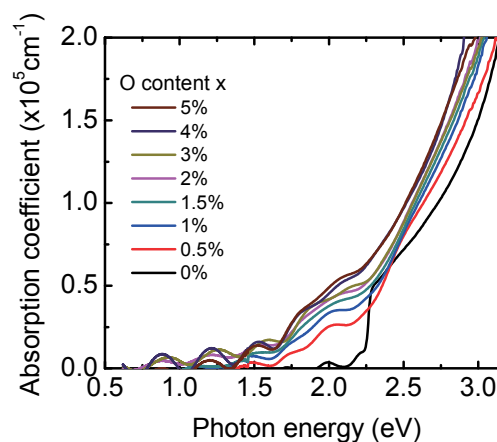


Fig. 2 Absorption coefficients of ZnTeO samples with various O content x.

4 - 09 Microscopic Observation for Damage of Hybrid Type Boron-Doped Carbon Stripper Foil by Ion Beam

Y. Yamazaki^{a)}, M. Yoshimoto^{a)}, O. Takeda^{a)}, M. Kinsho^{a)}, T. Taguchi^{b)},
S. Yamamoto^{c)}, T. Kurihara^{d)} and I. Sugai^{d)}

^{a)} Accelerator Division, J-PARC, JAEA, ^{b)} Material Science Research Division, QuBS, JAEA,
^{c)} Environment and Industrial Materials Research Division, QuBS, JAEA,
^{d)} High Energy Accelerator Research Organization, KEK

A charge stripper foil is a key technology for multi-turn injection of high power proton synchrotron. Typically carbon-based material is used to strip two electrons off the incident H⁺. Recently, the proton injection into high power ring accelerators such as J-PARC demands much longer lifetime for the stripping foils to reduce beam dead time. J-PARC RCS (Rapid Cycling Synchrotron) applied the hybrid type thick boron-doped carbon (HBC) foil which is developed with the arc-discharge method by Sugai¹⁾. HBC foil is much better than a normal carbon foil in respect of uniformity, dynamic strength of large area foil and durability against irradiation of ions. The foil thickness is about 1 μm (200 μg/cm²) giving rise to a conversion efficiency of 99.7%. The usual foil is composed of two pieces of foil because the double foil can endure against beam irradiation as compared to the single one²⁾.

Although typical foil thickness is 200 μg/cm² for the practical usage, in this study we used foil thickness of 15 μg/cm² for the sake of ease for TEM (Transmission Electron Microscope) observation. We selected Ar⁺ as irradiated ion instead of H⁺ in order to affect damage in a short period of time. Ar⁺ of 300 keV, which we use as irradiated ion from ion implanter in TIARA this time, can deliver the energy deposition by the ion beam into this thickness foil without ion implantation. HBC foils were prepared by the controlled direct current arc discharge method. The cathode(-) was a boron-doped (25%) carbon rod of 10 mm diameter while the opposite electrode(+) was a pure graphite rod of 15 mm diameter. The distance between the evaporation source of the carbon rods and the substrate on the flat glass was 250 mm. The major atomic composition of HBC foils were analyzed using RBS (Rutherford Backscattering Spectrometry) with the H⁺ probe

beam with energy of 3 MeV from a 3-MV single ended accelerator, the size of 1 mm diameter and the current of 15 nA. It is possible to obtain the boron to carbon ratio and the foil thickness information. In HBC foil, the boron to carbon ratio is close to the rod's component³⁾.

We have great interest how the irradiated area of the foil changes microscopically. In TIARA we have TEM (JOEL JEM-4000F:400 keV) system which can inject ion beams from the ion implanter. We tried to observe the time variation by Ar ion irradiation (300 kV, 20 nA, <3 mmφ) for these foils in the TEM system. HBC had generally amorphous phase, but they involved a lot of micro graphite grains of a few nanometer and many boron-rich micro grains before irradiation of ions. In particular, it seems that grain size of boron-rich area became much larger by irradiation as shown in Fig. 1. In Fig. 2, it is also observed that boron-rich grains grow up and generated pinholes more than 100 nm. On the other hand, HBC foils were shrunk the volume by the ion bombardment macroscopically. We guess that these phenomena were destructive mechanisms of the HBC foil. Figure 1 shows variance of the surface appearances for each of foils irradiated by Ar⁺.

In this study some results with microscopic analysis methods, such as RBS and TEM, were obtained for HBC foils before and after Ar⁺ ion irradiation. In future, we will try to evaluate atomic component and structure for boron-rich area in HBC foil, and reveal relation between boron and carbon in the foil.

References

- 1) I. Sugai et al., Nucl. Instrum. Meth. A 561 (2006) 16.
- 2) I. Sugai et al., Nucl. Instrum. Meth. A 613 (2010) 457.
- 3) Y. Yamazaki et al., IPAC10. Proc. (2010) 3924.

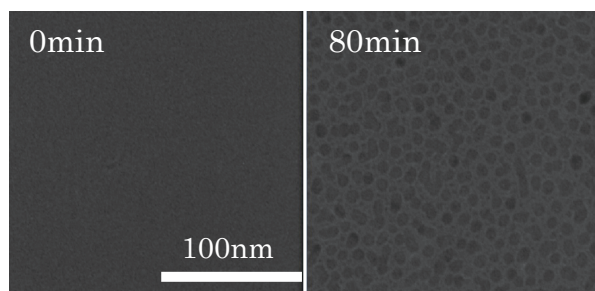


Fig. 1 The time variation by Ar ion irradiation (300 kV, 20 nA) for the boron-rich area of HBC foil in the TEM system. Left side is before irradiation, and right is after irradiation for 80 min.

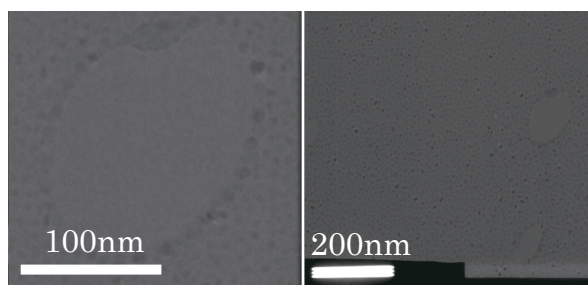


Fig. 2 Some large pinholes by Ar ion irradiation of HBC foil in the TEM system.

4 - 10 Mach-Zehnder Polymer Waveguides Fabricated Using Proton Beam Writing

K. Miura^{a)}, T. Satoh^{b)}, Y. Ishii^{b)}, M. Koka^{b)}, H. Kiryu^{a)}, Y. Ozawa^{a)}, K. Takano^{c)}, T. Ohkubo^{b)}, A. Yamazaki^{b)}, W. Kada^{b)}, A. Yokoyama^{b)}, T. Kamiya^{b)} and O. Hanaizumi^{a)}

^{a)} Graduate School of Engineering, Gunma University, ^{b)} Department of Advanced Radiation Technology, TARRI, JAEA, ^{c)} Graduate School of Engineering, Osaka University

Proton beam writing (PBW) has recently attracted much attention as a next generation micro-fabrication technology¹⁾. It is a direct-writing technique and does not need any masks to transfer micro-patterns to the surfaces. Furthermore, the importance of planar polymer optical waveguides is recently increasing in fields such as optical fiber telecommunication and optical interconnection. Optical waveguides can be directly drawn in poly(methyl methacrylate) (PMMA) using the PBW technique because the refractive index of a PMMA can be increased by proton irradiation²⁾. In our previous work, we demonstrated the first single-mode straight-line and Y-junction PMMA-based waveguides fabricated using PBW and working at $\lambda=1.55\ \mu\text{m}$ ³⁾. Such single-mode waveguides and Y junctions are important components for constructing Mach-Zehnder (MZ) type thermo-optic switches for long-haul optical-fiber telecommunication systems⁴⁾. In this study, we fabricated PMMA-based MZ waveguides utilizing PBW for the first time as the next step to construct thermo-optic switches.

A 15- μm -thick SiO_2 film was deposited as the under cladding on an Si substrate ($20\ \text{mm} \times 40\ \text{mm} \times 0.5\ \text{mm}$) using radio-frequency magnetron sputtering. A 10- μm -thick PMMA (Microchem, 950A11; 11% PMMA in Anisole) film was spin-coated onto the SiO_2 film. We drew cores of a MZ waveguide in the PMMA film using the 3-MV single-ended accelerator in TIARA. The proton (H^+) beam energy was 1.7 MeV, and the beam current was $\sim 50\ \text{pA}$. The beam diameter was focused to $\sim 1.1\ \mu\text{m}$, and the total dose was set to $100\ \text{nC}/\text{mm}^2$. A MZ waveguide was drawn by symmetrically coupling two Y junctions with $w = 8\ \mu\text{m}$ in order for it to work as a single-mode waveguide⁵⁾, and we set its branching angle to 2° in order to obtain a low branching loss⁵⁾. The two Y-junction waveguides were drawn by controlling both H^+ beam scanning and stage translation. Figure 1(a) presents a photograph and schematic of the sample. The waveguide was $\sim 40\ \text{mm}$ long. Figure 1(b) presents a microscopic image of two straight lines at the center of the sample, and Fig. 1(c) presents that of a Y-junction part after drawing. We can observe the cores of the MZ waveguide from these images. A 10- μm -thick PMMA film was subsequently deposited again on the sample as an upper cladding by spin-coating under the same conditions as the first PMMA layer.

We cleaved both sides of the sample to observe near field patterns (NFPs) of the waveguides. We used a wavelength-tunable laser for our NFP measurements, and

we observed their NFPs by using a vidicon camera. Figure 2 presents the NFP of the waveguide at $\lambda=1.55\ \mu\text{m}$. Its mode-field diameter was almost $10\ \mu\text{m}$. We regarded it as a single-mode waveguide because a fundamental mode was observed and no higher-order modes were observed from it when the excitation condition was changed³⁾. We thus succeeded in fabricating for the first time a PMMA-based single-mode MZ waveguide for $\lambda=1.55\ \mu\text{m}$ using PBW. Such a single-mode operation is very important in order to construct our objective MZ type thermo-optic switch for optical-fiber telecommunication⁴⁾. As the next step to realize this type of optical switch, we are working to form a Ti thin-film heater and Al electrodes on the MZ waveguide by using photolithography and wet-etching processes.

References

- 1) N. Uchiya et al., Nucl. Instrum. Meth. Phys. Res. B 260 (2007) 405.
- 2) I. Rajta et al., Nucl. Instrum. Meth. Phys. Res. B 260 (2007) 400.
- 3) K. Miura et al., Key Eng. Mater. 497 (2011) 147.
- 4) O. Hanaizumi et al., Key Eng. Mater. 459 (2011) 153.

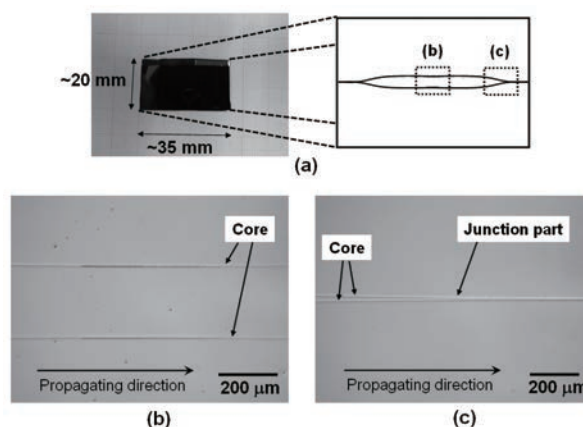


Fig. 1 (a) Photograph and schematic of the sample, and microscopic images of (b) two straight lines at the center and (c) a Y-junction part of the sample after drawing (without an upper cladding).



Fig. 2 NFP of the MZ waveguide ($\lambda=1.55\ \mu\text{m}$).

4 - 11 Multiplex Energy Proton Irradiation Effects on Hydriding Property of a Hydrogen Storage Alloy

H. Abe ^{a)}, K. Muraki ^{b)}, M. Kishimoto ^{b)}, H. Uchida ^{b)} and T. Ohshima ^{a)}

^{a)} Environment and Industrial Materials Research Division, QuBS, JAEA,

^{b)} Course of Applied Science, Graduate School of Engineering, Tokai University

We investigated the structure changes of a hydrogen storage alloy by ion irradiations, and its absorption property in order to obtain basic data and to elucidate relevant mechanisms of hydrogen absorption by the influence of the irradiation. In previous studies, the induction of vacancies in the hydrogen absorption alloy was found to be effective to increase the hydrogen absorption rate¹⁻³⁾. As well known, the rate of hydrogen absorption strongly depends on the surface state of the hydrogen storage alloy because the dissociation of hydrogen molecules or water molecules needs electron change with the surface in the H₂ gas or electrochemical reaction process⁴⁾. In this study, the samples of MnNi_{13.48}Co_{0.73}Mn_{0.45}Al_{0.34} (Mm = La_{0.35}Ce_{0.65}) alloys were irradiated using the 400 kV ion implanter at TIARA. The samples were irradiated with proton beams with the energy from 30 to 350 keV (30, 100 and 350 keV) in case of multiplex energy irradiation, and each samples with the 30 keV, 100 keV and 350 keV, respectively in case of mono-energetic irradiation. Figure 1 shows distribution of vacancy concentration induced by 30 to 350 keV proton beam irradiation calculated using a SRIM simulation code⁵⁾. The hydrogen absorption rate measurements were performed for the irradiated samples using the electrochemical apparatus method. An alkaline treatment was made by heating the sample at 398 K for 30 minutes in a 6M-KOH solution. The hydrogen absorption rate was measured electrochemically in the 6M-KOH with an open cell as the current density at a constant potential of -0.93 V at room temperature, for 0 to 120 minutes.

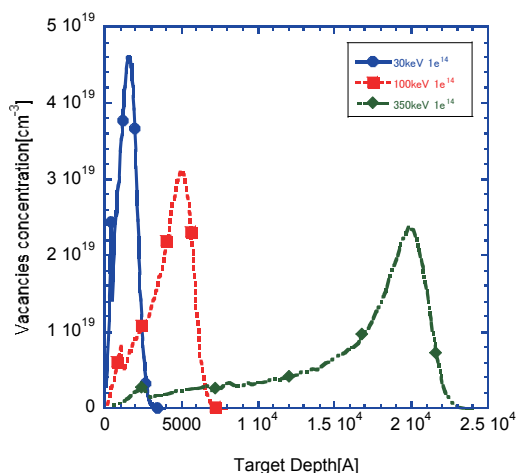


Fig. 1 Distribution of vacancy concentration induced by H ions with a dose of 10¹⁴ cm⁻² at irradiation energies of 30, 100 and 350 keV.

Figure 2 shows hydriding curves for samples with multiplex energy irradiation of proton and mono-energetic proton irradiation. In the mono-energetic irradiation cases, initial hydrogen absorption rate (H/M value) has energy dependence.

However, multiplex energy irradiated sample has higher H/M value than another mono-energetic irradiated samples. From the obtained results, the initial hydrogen absorption rate was found to be improved by the multiplex energy irradiation of proton beam rather more effectively than the mono-energetic proton beam irradiation. The proton beam with high permeability has introduced the defect from the irradiation surface to the deep domain by wide range energy irradiation. These effects can be interpreted in terms of the induced vacancy defects by multiplex energy proton irradiation and are considered to be a cause of the improvement in hydriding property of the hydrogen storage alloy. As mentioned above it is found that the multiplex energy proton irradiation was useful for material modification with the sensitive surface.

References

- 1) H. Abe et al., Nucl. Instrum. Meth. B 206 (2003) 224.
- 2) H. Abe et al., J. Alloys Comp. 404-406 (2005) 288.
- 3) H. Abe et al., Trans. Mater. Res. Soc. Jpn. 36 (1) (2011) 133.
- 4) H. Uchida, Int. J. Hydrogen Energy 24 (1999) 861.
- 5) J. F. Ziegler, Handbook of Ion Implantation Technology, (Elsevier, Amsterdam) (1992) 1.

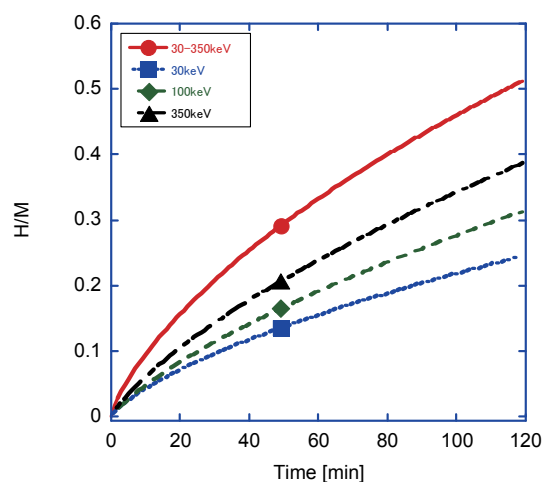


Fig. 2 Hydriding curves for samples with proton irradiation.

4 - 12 Fabrication of Microstructure at a Fluoropolymer Surface by Ion Microbeam

A. Kitamura(Ogawa)^{a)}, T. Satoh^{a)}, M. Koka^{a)}, T. Kamiya^{a)} and T. Kobayashi^{b)}

^{a)} Department of Advanced Radiation Technology, TARRI, JAEA,

^{b)} Advanced Science Institute, RIKEN

Polytetrafluoroethylene (PTFE) $(-CF_2-)_n$ is used in various industrial applications because of its desirable physical and chemical properties. Because PTFE is chemically inert under most conditions, a few suitable microfabrication techniques are available and all these go through an etching process from the top-surface. Some effective techniques are synchrotron radiation or ion beam irradiation¹⁾. For example, microprotrusions were formed with high density on a PTFE surface using 80 keV N_2^+ ion beam irradiation²⁻⁴⁾. In this report, an independent microstructure were fabricated at the original PTFE surface only using 3 MeV proton microbeam irradiation.

PTFE sheets (Nichias Corp.), which range from 50 to 500 μm in thickness, were used in this study. A 3 MeV proton beam from the 3-MV single-ended accelerator focused to about 1 μm in diameter on the surface of the sample using the light-ion microbeam system at TIARA. The beam current was 200 pA. The scan rate was also controlled from 40 to 200 $\mu\text{m}/\text{s}$. The scan pattern was a circle 50 μm in diameter. The surface morphology of the samples was observed by scanning electron microscopy (SEM) after the surfaces were coated with a layer of gold using a plasma coater.

Figure 1 shows the PTFE surfaces after 10 cycles of proton beam scanning along the circle. The scan rate was 40 $\mu\text{m}/\text{s}$. For the 100- μm -thick sample, the scanned area was roundly swelled (Fig. 1(a)). The thermal deformation along the circle was also observed at the back surface of this sample. While for the 500- μm -thick sample, the shape was jagged (Fig. 1(b)), and the back side did not change. The morphological change was caused by the volume expansion due to both the temperature elevation and the gas generation along the proton trajectories inside the PTFE samples.

When the beam was once scanned spirally at 40 $\mu\text{m}/\text{s}$ from the center to a 25 μm radius on the 500- μm -thick sample, a conical structure was formed (Fig. 2(a)). The height was around 250 μm , and it covered with jagged holes. Figure 2(b) and 2(c) show the cut surfaces of the top and bottom of the cone, respectively, and indicate that the cone was porous. Figure 2(c) shows that the base of the cone was 50 μm in diameter, which corresponds to the scan area. The structure was formed by swelling the sample sequentially from the center according to the spiral beam scanning.

The main feature of these structures was that they were formed by swelling of PTFE samples. The shape and the fabrication process were quite unique because most common microfabrication techniques use excavation of the PTFE

surface. The observation of morphological change with the beam scan rate and the scan way and the chemical analysis are in progress.

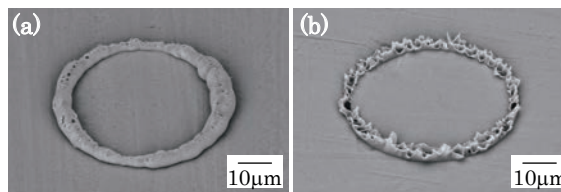


Fig. 1 SEM images of the PTFE surfaces after 10 cycles of proton beam scanning along a circle 50 μm in diameter for the (a) 100- μm - and (b) 500- μm -thick samples.

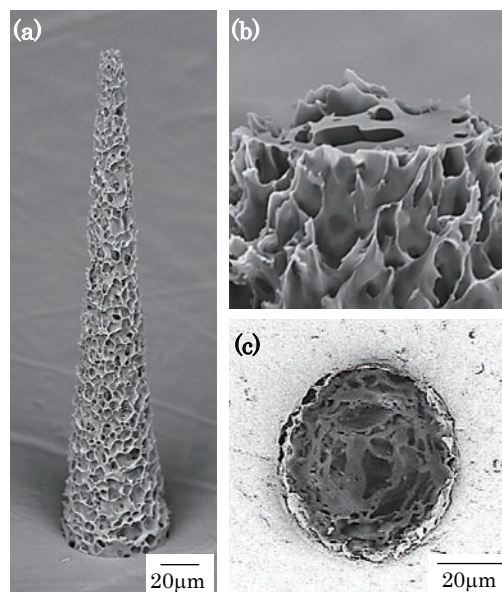


Fig. 2 (a) SEM image of PTFE surfaces after spiral scanning from the center for the 100- μm -thick samples, (b), (c) SEM images of the cut surfaces of the top and bottom of the cone, respectively.

References

- 1) N. Miyoshi et al., Radiat. Phys. Chem. **80** (2011) 230-35.
- 2) A. Kitamura et al., Trans. Mater. Res. Soc. Jpn. **33**, 4 (2008) 1035-38.
- 3) A. Kitamura et al., Surf. Coat. Technol. **203** (2009) 2406-09.
- 4) A. Kitamura et al., Surf. Coat. Technol. **206** (2011) 841-44.

4 - 13 Electroplating of Ni Microstructures on the Cross Section of Cu Wire Using PMMA Mother Fabricated by Proton Beam Writing

Y. Tanabe^{a)}, T. Iwamoto^{a)}, J. Takahashi^{a)}, H. Nishikawa^{a)}, T. Satoh^{b)},
Y. Ishii^{b)} and T. Kamiya^{b)}

^{a)}Department of Electrical Engineering, Shibaura Institute of Technology,
^{b)}Department of Advanced Radiation Technology, TARRI, JAEA

Proton Beam Writing (PBW) is a direct-write technique using focused beam of MeV protons, which has several advantages in comparison with other lithographic techniques¹⁾. We can expose and develop typical resists such as PMMA and SU-8 to fabricate high aspect-ratio structures^{1, 2)}. We have previously reported on Ni electroforming using high-aspect-ratio PMMA microstructures by PBW^{3,4)}, so that the Ni microstructures can be used as a mold for imprint lithography. In this study, we report Ni microstructures fabricated on the cross section of Cu wires aiming at the use for imprint lithography.

A PMMA layer with a thickness of 20 μm was spin coated on a polished end of Cu wire with diameter of 1.0 mm. Then, PBW was performed with a beam size of 1.1 μm at beam energy of 3.0 MeV using a microbeam line of the Takasaki Ion Accelerators for Advanced Radiation Application (TIARA). PMMA with a relatively lower molecular weight of 120 K was used to assure well defined structures after development. After exposure by PBW, the PMMA sample was developed with IPA-water (7:3) and rinsed in deionized water²⁻⁴⁾. Electroplating was performed using a nickel sulfamate bath at a current of 40 A/m^2 ²⁻⁴⁾. The electroplated Ni surface was mechanically polished to obtain a smooth surface, before the removal of PMMA mother.

Figure 1 shows an optical microscope image of the PMMA surface after PBW and development. A 4- μm wide line with a pitch of 25 μm with a depth of 20 μm was successfully made on the cross section of the Cu wire. Figure 2 (a) and (b) show SEM images of Ni microstructures by electroplating on the PMMA mother in Fig. 1. The central part of the Ni pattern was lost at the polishing step. Improved process was needed to avoid such broken Ni structures. We also performed UV imprint lithography using the Ni microstructures as a mold. Figure 3 shows the result of the UV imprint using a photosensitive polymer (PAK-01, Toyo Gosei Co., Ltd.) on glass. Due to the small cross section of mold less than 1 mm, patterns were easily transferred by a mask aligner without application of pressure on the Ni mold.

References

- 1) F. Watt et al., *Mater. Today*, 10, 6 (2007) 20-29.
- 2) N. Uchiya et al., *Microsystem Tech.* 14 (2008) 1537-40.
- 3) Y. Seki et al., *Microsystem Tech.* 86 (2009) 945-48.
- 4) Y. Tanabe, et al., *Microelectron. Eng.* 88 (2011) 2145-48.

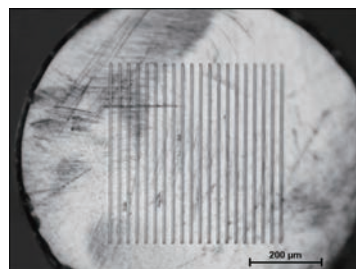
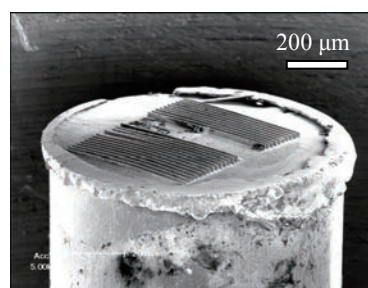
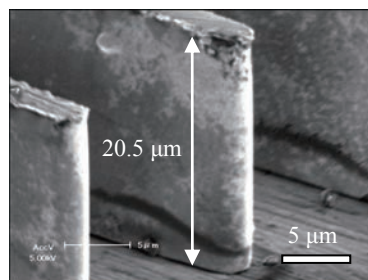


Fig. 1 Optical microscope image of a line and space pattern written by PBW at 3.0 MeV on 20- μm thick PMMA coated on the cross section of Cu wire.



(a) Ni pattern on a Cu wire edge.



(b) Magnified image of Ni pattern.

Fig. 2 SEM images of Ni microstructures fabricated by electroplating using the PMMA pattern formed on the edge of Cu wire shown in Fig. 1.

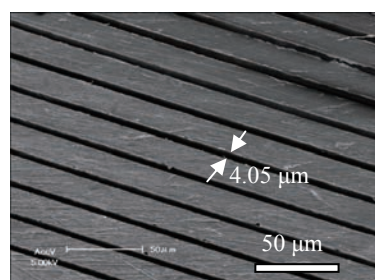


Fig. 3 SEM images of the UV imprinted grooves using a photosensitive polymer on glass using the mold on the edge of Cu wire shown in Fig. 2.

4 - 14 Epitaxial Transformation of Evaporated-Ti Thin Films during Nitriding Processes due to Ion-Implantation

Y. Kasukabe^{a), b)}, Y. Chen^{b)}, S. Yamamoto^{c)} and M. Yoshikawa^{c)}

^{a)} Center for International Exchange, Tohoku University, ^{b)} Department of Metallurgy, Tohoku University, ^{c)} Environment and Industrial Materials Research Division, QuBS, JAEA

Properties of non-stoichiometric titanium nitrides (TiN_y) such as electrical conduction, covalency, hardness, etc. depend not only on chemical composition, but also on orientation relationships between TiN_y films and substrates. Therefore, much interest has been focused on atomistic growth processes of TiN_y films¹⁾. In order to clarify atomistic transformation processes of Ti films, especially from the $(\bar{2}1\cdot0)$ -oriented hcp-Ti to the (110)-oriented TiN_y , due to N-implantation, in-situ observations by using transmission electron microscope (TEM) and electron energy loss spectroscopy have been carried out, along with the characterization of the electronic structure by molecular orbital calculations. The N_2^+ ions with 62 keV are implanted into hcp-Ti and TiH_x with preferred orientations in the 400 kV analytic high resolution TEM combined with ion accelerators at JAEA-Takasaki²⁾.

TEM observation clarified that (110)-oriented TiN_y films were epitaxially formed by the partial inheritance of atomic arrangement of $(\bar{2}1\cdot0)$ -oriented hcp-Ti and by the occupation of octahedral sites of hcp-Ti by N atoms. The transformation mechanism from the $(\bar{2}1\cdot0)$ -oriented hcp-Ti to the (110)-oriented TiN_y , which is concerned with the transformation between the hcp and fcc Ti sublattices, can be explained with the schematic model shown in Fig. 1. The various circles represent Ti atoms in hcp-Ti lattices. In this schematic model, the Ti atom indicated by H is defined as the origin in the basal plane of hcp-Ti. Starting from the origin H along c-axis, those consecutive $(00\cdot1)$ planes of hcp-Ti are defined as A_1 , B_1 , A_2 , and B_2 planes,

which correspond to the basal planes in the so-called ABAB packing of hcp-Ti. The open circles are on the A_1 and A_2 planes, on which the Ti atoms have the same packing position along the c-axis. The solid circles are on the B_1 plane, which is in the middle of A_1 and A_2 planes. The gray circles are on the B_2 plane, which is above the A_2 plane. The Ti atoms on B_1 and B_2 planes have the same packing position along the c-axis. Since the occupation of the octahedral (O-) site by N atoms leads to the forming of the strain in the hcp-Ti lattice, the invasion of N atoms induces the movement of open circles on the A_2 plane to the direction represented by the arrows and finally to the dotted open circles, and the movement of gray circles on the B_2 plane to the dotted gray circles. For example, the open circle indicated by F moves to the dotted open circle indicated by T, which is in the center of gravity of triangle BEF. However, the open circles on the A_1 plane and solid circles on the B_1 plane do not change their positions during this transformation. As the dotted open circles represent Ti atoms on the C plane in the so-called ABCABC packing of fcc-Ti lattice after the hcp-fcc transformation, and the dotted gray circles represent Ti atoms on the A plane in the ABCABC packing. This movement from the ABAB packing of hcp-Ti to the ABCABC packing of fcc-Ti sublattices leads to the formation of fcc-Ti sublattice, a unit cell of which is represented by AMWP-JQRS. During this transformation, a shadowed parallelogram AUJV in the $(\bar{2}1\cdot0)$ plane in hcp-Ti is preserved, which partially corresponds to the atomic arrangement of the (110) plane represented by a rectangle AJRW in the transformed fcc-Ti sublattice. It is noticeable that a shadowed triangle HUJ, which corresponds to the $(00\cdot1)$ plane of hcp-Ti and the (111) plane of the transformed fcc-Ti sublattice, is perpendicular to the shadowed parallelogram AUJV, which corresponds to the $(\bar{2}1\cdot0)$ plane in the hcp-Ti and the (110) plane in the fcc-Ti. Thus, it is considered that the shear in the $\langle 01\cdot0 \rangle$ direction of hcp-Ti promoted by the forming of the strong Ti-N bonds is the origin for the hcp-fcc transformation of Ti sublattices. Furthermore, the inheritance of partial atomic arrangements and the movement of the N atoms to O-sites in the transformed fcc-Ti sublattice, are responsible for the epitaxial growth of TiN_y .

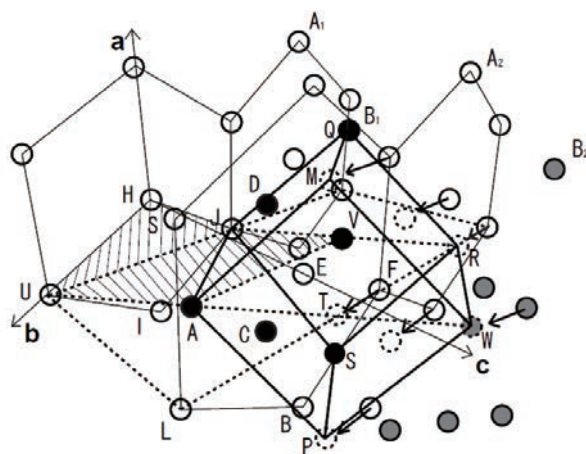


Fig. 1 The schematic illustration of the transformation from the $(\bar{2}1\cdot0)$ -oriented hcp-Ti to the (110)-oriented TiN_y .

References

- 1) S. Hao et al., Phys. Rev. B 74 (2006) 035424-1.
- 2) H. Abe et al., JAERI-Research 96-047 (1996) 1.

4 - 15

Gamma-ray Induced Defect Formation
in High-purity α -Quartz

K. Kajihara

Department of Applied Chemistry, Graduate School of Urban Environmental Sciences,
Tokyo Metropolitan University

Gamma-ray induced intrinsic defect formation was examined using high-purity synthetic α -quartz (crystalline SiO_2) of low metallic impurity concentrations. Radiation-induced optical absorption at visible-ultraviolet spectral region which is due to metallic impurities and commonly observed in conventional synthetic α -quartz is greatly suppressed. The main radiation-induced defects are Si-Si bonds exhibiting optical absorption at 7.6 eV, suggesting that the main defect formation mechanism is the Frenkel mechanism, which is intrinsic and is depicted by displacement of bridging oxygen atoms in regular Si-O-Si bonds. However, formation of a part of Si-Si bonds is most likely related to impurities. Formation of interstitial oxygen molecules, which are one of the main form of the anion part of the Frenkel pair in amorphous SiO_2 , is not confirmed.

赤外域から深紫外域にわたる広い透明領域を有し、化学的に安定で、かつ大きな結晶が容易に入手できる典型元素の結晶性酸化物である α -石英は、酸化物での照射欠陥形成を調べるうえで重要なモデル物質である。しかし、従来の α -石英は天然石英を原料とするため、Al や Na などの金属不純物を含んでおり、不純物によらない欠陥形成を調べるのが困難であった。今回の実験では、近年開発された、精製したシリカを原料とするため金属不純物をほとんど含まない高純度 α -石英を用い、不純物に妨害されずに真性欠陥過程を調べることを目的とした。

両面光学研磨した高純度 α -石英(A)に6通りの異なる線量で ^{60}Co γ 線照射を行った。照射後、試料の可視・紫外・真空紫外光吸収測定を行った。また、赤外発光測定によってFrenkel過程によって生成する可能性のある格子間酸素分子の有無を調べた。

高純度 α -石英(A)は ^{60}Co γ 線照射後もほぼ無色であり、不純物を含む α -石英(B)にみられる可視紫外域の光吸収(“smoky coloration”)はほとんど生じなかった(Fig. 1)。光吸収測定によって、Si-O-Si結合からOがはずれて形成されるSi-Si結合に帰属される7.6 eV光吸収帯が生じ、その強度が照射時間とともに増大することが確認された。また、Si-Si結合濃度(C)の吸収線量(D)依存性(Fig. 2)には、Dの小さい領域ですみやかに飽和する成分と、Dの大きい領域でDに比例して増大する成分の二種類が観察された。前者の成分の濃度は試料に含まれる不純物の濃度($C_0 \sim 10^{15} \text{ cm}^{-3}$)に近く、不純物がこの過程を促進していることが示唆される。後者の成分の最終的な濃度は不純物濃度よりも大きく、この過程が真性欠陥過程であることを強く示唆する。後者の成分のD依存性から求めた形成効率($\sim 7 \times 10^{-7}$)は、 α -石英と同じ組成をもつが歪んだSi-O-Si結合を含むシリカガラスでの値($\sim 1 - 3 \times 10^{-5}$)^{1,2)}よりも1桁以上小さいことが示された。以上より、Si-Si結合の形成が不純物の関与しない真性過程であること、この過程(Frenkel過程)はSi-O-Si結合に歪のない α -石英でも進行することが明確に示された。一方で、格子間酸素分子(O_2)の生成は確認できなかった。シリカガラスでのFrenkel過程は格子間 O_2 の形成を伴う¹⁻³⁾。一方で、格子間 O_2 の生成には、Si-O-Si結合からはずれたOの二量化が必要であるが、 α -石英ではこの二量化が抑制されていることが示唆される。

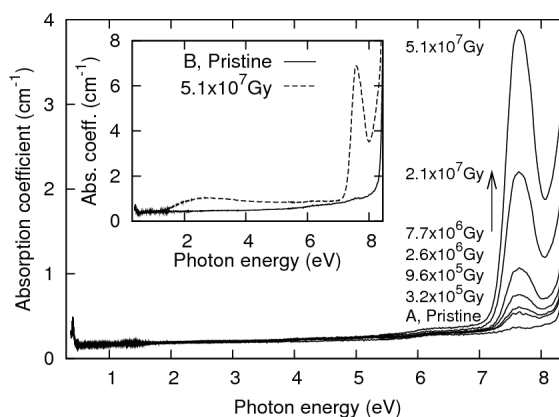


Fig. 1 Optical absorption spectra of high-purity α -quartz (A) irradiated at various γ -ray doses. The inset shows optical absorption spectra of conventional α -quartz (B).

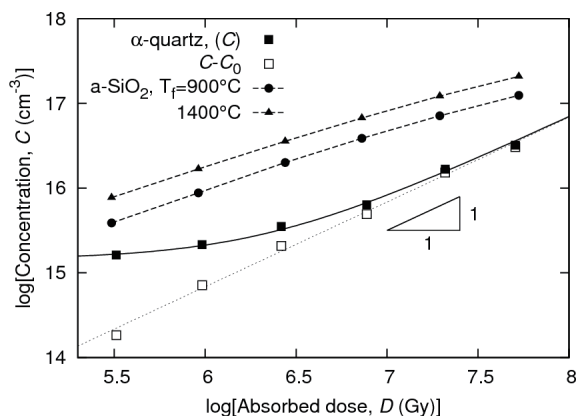


Fig. 2 Variation of concentration of Si-Si bond with γ -ray dose in high-purity α -quartz (A). Data for fluorine-doped synthetic silica glasses annealed at 900 and 1400 $^{\circ}\text{C}$ ^{2,3)} are also shown.

References

- 1) K. Kajihara et al., Chem. Lett. 36 (2007) 266.
- 2) K. Kajihara et al., Phys. Rev. B 78 (2008) 094201.
- 3) K. Kajihara et al., Mater. Sci. Eng. B 96 (2009) 161.

4 - 16

Thermal Stability of Fe₂MnSi/Ge(111) Heteroepitaxial Interfaces

Y. Maeda^{a, b)}, B. Matsukura^{a)}, T. Nakajima^{a)}, K. Narumi^{b)} and S. Sakai^{b)}

^{a)} Department of Energy Science and Technology, Kyoto University,

^{b)} Advanced Science Research Center, JAEA

Heteroepitaxial interfaces between Heusler alloy L₂₁ type Fe₂MnSi (FMS) and semiconductors, Si, SiGe or Ge have been expected as injectors or filters of spin polarized electrons which can be applied to Spin-Field Effect Transistors (FETs), since FMS has highly or fully polarized spin states and still at the less Mn concentration high spin polarization can be maintained^{1,2)}. Using a low temperature molecular beam epitaxy (LTMBE) method carried out at the deposition temperature lower than 300 °C, we have realized FMS/Ge(111) heterointerfaces with atomically scaled flatness required for spin-FETs³⁾. Thermal stability of the heteroepitaxial interface is a crucial factor for device fabrication. In Fe₃Si/Ge, we found that the thermal stability of atomic scale flatness at the interface was strongly dependent on chemical stoichiometry of the alloy⁴⁻⁶⁾.

In this study, we investigated the thermal stability of heteroepitaxial interfaces of FMS with three Mn contents using Rutherford backscattering spectrometry (RBS).

Fifty-nm-thick FMS(111) films with 9, 18 and 21at%Mn were epitaxially grown on Ge(111) substrates at 200 °C by the LTMBE method¹⁾. To investigate thermal stability of the heteroepitaxial interface, the FMS(111)/Ge(111)samples were annealed at 300, 400 and 450 °C in a vacuum for 2 h. Two MeV-⁴He⁺ RBS were measured at the backscattering angle of 165°. The depth profiles of compositions were obtained from the RBS spectra by simulation using a SIMNRA code.

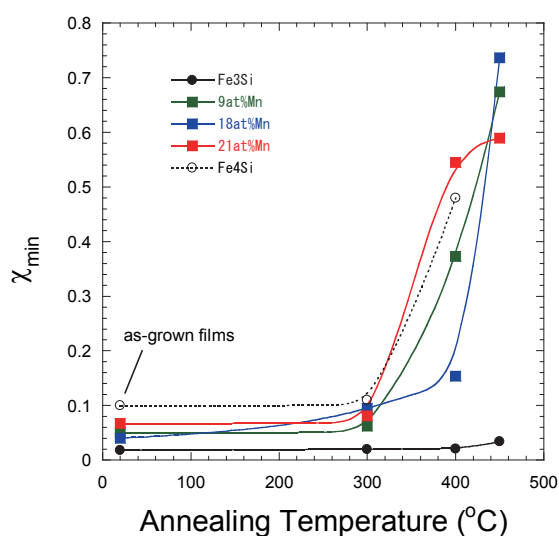


Fig. 1 Change of χ_{\min} at the heteroepitaxial interfaces of FMS/Ge(111) with different Mn content after 1 h annealing at each temperature.

Figure 1 shows a minimum yield (χ_{\min}) obtained from a ratio of back scattering yields between random and aligned RBS spectra near the interfaces after annealing at each temperature. The increase of χ_{\min} means disordering of epitaxy at the interface. The thermal stability of high grade epitaxy in stoichiometric Fe₃Si was maintained up to 450 °C, while in Fe₄Si: iron-rich Fe₃Si pronounced disordering was caused above 300 °C. This observed structural disordering has been confirmed to originate from interdiffusion of Fe and Ge atoms between alloy films and Ge substrates⁴⁾.

Also in the FMS films, we observed pronounced disordering above 300 °C as well as in Fe₄Si in Fig. 1. Analysis of composition in depth at each annealing temperature indicated that the disordering (increase of χ_{\min}) observed above 300 °C was caused by pronounced interdiffusion of Fe, Mn and Ge atoms at the interface. This disordering behavior showed small dependence upon the Mn content of FMS films. This result suggests that disordering in the FMS films may be caused by a mechanism that is different from the mechanism observed in the Fe₃Si films.

Now we are discussing the possible mechanism of disordering due to lattice mismatching at the heteroepitaxial interface⁵⁾, chemical instability of Mn atoms at the B site of L₂₁ lattice⁶⁾ or vacancy site jump model⁷⁾.

References

- 1) M. Miyao et al., *Thin Solid Films* **517** (2008) 181.
- 2) K. Hamaya et al., *Phys. Rev. Lett.* **102** (2009) 137204.
- 3) K. Ueda et al., *Appl. Phys. Lett.* **93** (2008) 112108.
- 4) Y. Maeda et al., *Appl. Phys. Lett.* **91** (2007) 171910.
- 5) Y. Maeda, *MRS Proc.* **1119E** (2009) 1119-L05-02-05.
- 6) Y. Maeda et al., *Thin Solid Films* **519** (2011) 8461.
- 7) S. Denzler and J. Hafner, *Phys. Rev. B* **73** (2006) 174303.

4 - 17 MFM Observation of Micrometer-sized Magnetic Patterns Produced by Heavy Ion Microbeam Irradiation in FeRh Films

K. Aikoh^{a)}, A. Tohki^{a)}, T. Matsui^{b)}, A. Iwase^{a)}, T. Satoh^{c)}, K. Takano^{c)},
M. Koka^{c)}, Y. Saitoh^{c)} and T. Kamiya^{c)}

^{a)} Department of Materials Science, Osaka Prefecture University,

^{b)} Research Organization for the 21st Century, Osaka Prefecture University,

^{c)} Department of Advanced Radiation Technology, TARRI, JAEA

Recently, we have reported that energetic ion irradiation induces the change in magnetic properties of FeRh intermetallic compound and this irradiation effect is well correlated with the energy deposited through the elastic collisions¹⁾; with increasing the elastically deposited energy, the magnetization of the ferromagnetic state, which appears after the irradiation with a small fluence, increases, reaches a maximum value and then decreases. As the irradiation effect appears only within irradiated regions, we have used ion microbeam irradiation to produce micrometer-sized and two-dimensional magnetic patterns on the surface of FeRh thin films^{2,3)}.

Fe₄₇Rh₅₃ thin films about 80 nm thick were deposited on MgO(100) substrates at 973 K by means of ion-beam sputtering. The thin films nearly show the anti-ferromagnetic state at room temperature. To realize the lateral magnetic modification on the sample surface, the ion-microbeam irradiation was performed by using 3 MeV tandem accelerator at TIARA-JAEA. The focused 10 MeV iodine ion microbeam, which had a rectangular shape of 2 μm × 4 μm, was scanned on the FeRh thin film surface. By using such a beam, several different magnetic patterns could be drawn; a typical example was 10 μm × 10 μm squares with 5 μm intervals in the x and y directions over the 200 μm × 200 μm area. After the irradiation, the surface roughness and the magnetic state were observed by means of atomic force microscopy (AFM) and magnetic force microscopy (MFM), respectively.

AFM and MFM images of micro-ionbeam irradiated areas are shown in Fig. 1. The AFM images in Fig. 1(a) shows that the ion microbeam does not create any topographic modification at the FeRh surface, while an array with 2 μm × 4 μm bright rectangles at designated regular intervals is seen in the MFM image (Fig. 1(b)). As the bright areas in the MFM image correspond to the ferromagnetic areas, the observed MFM image clearly shows the presence of micrometer-sized magnetic modification. The size of each bright area is just the same as that of the ion microbeam.

Another ferromagnetic pattern that was produced by the 10 MeV iodine microbeam with a different shape and interval is shown in Figs. 1(c) and 1(d). The AFM image in Fig. 1(c) does not show any topographic structure. As can be seen in Fig. 1(d), however, an array with 10 μm

squared rectangular ferromagnetic areas at the interval of about 5 μm is observed.

The present experimental result shows that the ion microbeam is a useful tool for the fabrication of two-dimensional and micrometer-sized magnetic patterns on FeRh samples. To investigate the details in magnetic structure for each micrometer-sized magnetic area, we performed the observation by means of photoemission electron microscopy (PEEM) at SPing-8 synchrotron radiation facility. The result has been reported elsewhere³⁾.

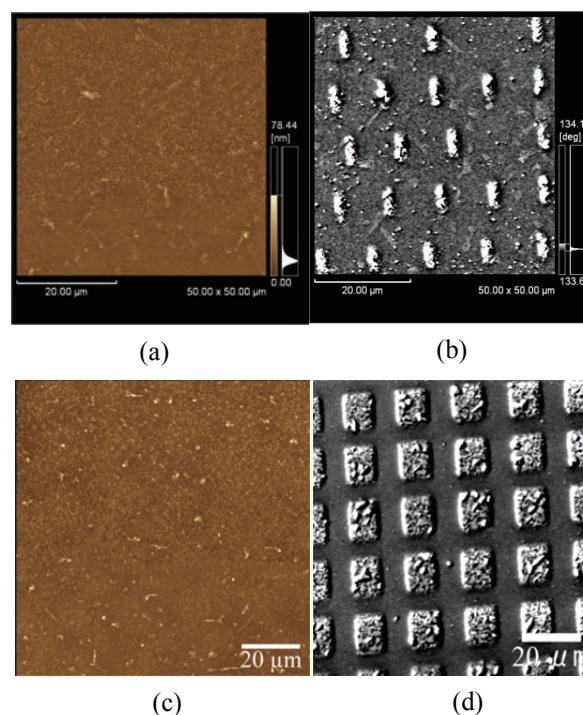


Fig. 1 Micrometer-sized patterns at FeRh thin film surfaces using a 10 MeV iodine ion microbeam; (a) and (c) are AFM images, and (b) and (d) are MFM images.

References

- 1) N. Fujita et al., J. Appl. Phys. 107 (2010) 09E302.
- 2) N. Fujita et al., Jpn. J. Appl. Phys. 49 (2010) 060211.
- 3) K. Aikoh et al., J. Synchrotron Radiat. 19 (2012) 223-26.

4 - 18 Nuclear Reaction Imaging of Boron Doped Iron

H. Shibata^{a)}, Y. Kohno^{b)}, T. Satoh^{c)}, T. Ohkubo^{c)}, A. Yamazaki^{c)}, Y. Ishii^{c)},
A. Yokoyama^{c)} and M. Koka^{c)}

^{a)} Graduate School of Engineering, Kyoto University,

^{b)} Department of Materials Science and Engineering, Muroran Institute of Technology,

^{c)} Department of Advanced Radiation Technology, TARRI, JAEA

An addition of a trace amount of boron to iron improves mechanical properties. Behavior of boron additive, however, is not sufficiently understood because of the difficulty of microscopic analysis, although boron treatment substantially may prevent hydrogen from segregating at grain boundaries. Recently imaging of boron distribution in a cancer cell has been also required to elucidate the buildup mechanism for boron neutron capture therapy (BNCT). These requirements to analyze the behavior of several tens ppm boron with a good spatial resolution stimulates us for developing an imaging technique of a trace amount of boron distribution by using particle induced gamma ray emission (PIGE) or α -particle detection by nuclear reaction.

A proton micro-beam from 3 MV single-ended electrostatic accelerator of TIARA facility was used for microanalysis of a trace amount of boron. The imaging techniques of a trace amount of boron (several tens ppm) distribution by detecting 428 keV γ -ray emitted from $^{10}\text{B}(p, \alpha')\gamma\ ^7\text{Be}$ or α -particle from $^{11}\text{B}(p, \alpha)\ ^8\text{Be}$ nuclear reaction have been developed. In the case of γ -ray measurement, X-rays from the same sample was also measured simultaneously for heavier elemental analysis. A typical current of several pA at the beam diameter of about 2~3 μm was used for mapping area of 20 $\mu\text{m} \times$ 200 μm in this experiment. The overall spatial resolution of the proton beam can be kept nearly 3 μm .

A hp-Ge γ -ray detector (Ortec 1601-1231- S-2), which has 100 cm^3 crystal volume, is remodeled by Raytech corporation. The endcap of the detector is converted to L-shape to set the detector crystal just behind the sample. The resolution of this detector is 1.7 keV at 1.33 MeV with a cooled FET pre-amplifier. A Si(Li) detector is also installed for micro-PIXE analysis of heavier elements. The simultaneous measurements of X-ray and γ -ray can be performed in this study.

In order to obtain quantitative information of depth profile of boron distribution, γ -ray images dependent on incident beam energy were measured. 1.5~2.3 MeV proton micro-beams were used to determine depth position of boron by measuring γ -rays from the inside of the specimen in FY2011. An iron specimen (10 \times 10 \times 1 mm) used in this study contained 100 ppm boron and trace amounts of C, Si, Mn, P, S, N, Cr, W, Co and V. Gamma-ray from BN specimen was measured for each incident energy to normalize to the same beam intensities.

Figure 1 shows total cross section of $^{10}\text{B}(p, \alpha')\gamma\ ^7\text{Be}$ reaction measured by Mateus et al¹⁾. One broad resonance peaked at 1.5 MeV superposing smooth slope beginning from around 700 keV can be seen in this energy region. Irradiation was performed in the energy range from 1.5 to 2.3 MeV in 100 or 200 keV interval.

Penetration depths of protons for nuclear reaction were

~8 μm for 1.5 MeV incident energy, ~10 μm for 1.7 MeV, ~13 μm for 1.9 MeV, ~14 μm for 2.0 MeV and ~19 μm for 2.3 MeV that were calculated by using SRIM considering nuclear reaction threshold of about 750 keV shown in Fig. 1. The relation between these images is clearly understood because of 1~5 μm depth intervals.

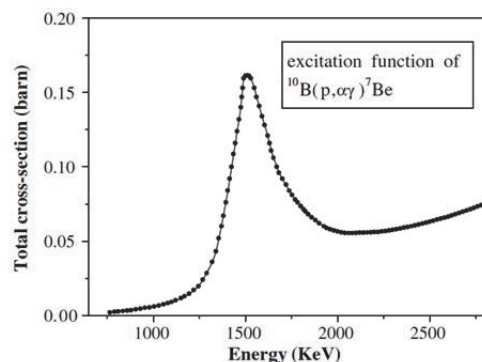


Fig.1 Total cross-section of $^{10}\text{B}(p, \alpha')\gamma\ ^7\text{Be}$ reaction¹⁾.

Typical γ -ray images taken by (a) 1.5, (b) 1.7, (c) 1.9, (d) 2.0 and (e) 2.3 MeV proton irradiation are shown in Fig. 2. Several tens micron of segregated boron blocks were observed at each incident energy, and some correlations between boron images at different incident energies could be clearly seen. This segregation may appear along with iron grain boundaries. Sizes of these blocks are from several μm to ~10 μm . In this study, any iron grains cannot be imaged, therefore, these blocks cannot be determined their locations. The intensities of γ -ray signals are not calibrated to the absolute value of boron density in Fig. 2, however, concentration of boron in a block will be estimated by using boron intensities from BN measurement.

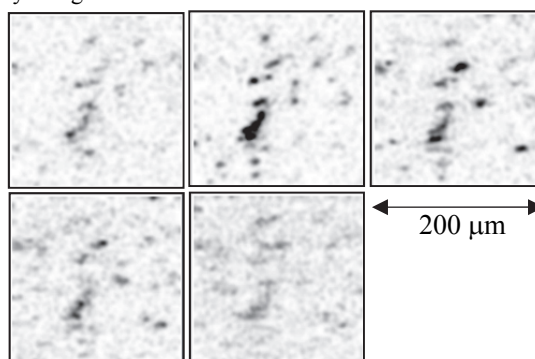


Fig. 2 Typical γ -ray images of 100 ppm boron contained steel specimen bombarded by (a) 1.5, (b) 1.7, (c) 1.9, (d) 2.0 and (e) 2.3 MeV proton micro-beam.

Reference

- 1) R. Mateus et al., Nucl. Instrum. Meth. Phys. Res. B 219-220 (2004) 519-23.

4 - 19 Ion Scattering Spectroscopy of Polarity-controlled ZnO Surfaces by 1-2 MeV C⁺ Ions

K. Motohashi^{a)}, Y. Saitoh^{b)}, N. Miyawaki^{b)} and T. Kamiya^{b)}

^{a)} Department of Biomedical Engineering, Toyo University,

^{b)} Department of Advanced Radiation Technology, TARRI, JAEA

Well-defined surfaces of compound semiconductors are recently becoming available with the development of crystal growth techniques. The lattice polarity of some binary compound semiconductors can be precisely controlled during growth, which is an essential factor in commercial use. The polarity-controlled crystal has two different surfaces terminated with different kinds of atoms. The lattice polarity of such surfaces has been analyzed by coaxial impact collision ion scattering spectroscopy¹⁾. One can quantitatively analyze the lattice polarity of the surfaces by measuring the angular and/or energy distribution of backscattered ions. This is because head-on collisions are significantly influenced by the atoms of the first layer²⁾.

Moreover, an almost total reflection of a 2.5-MeV proton beam on an evaporated Au layer was found at slightly smaller angles than the mirror reflection angle³⁾. Focusing of 2-MeV He⁺ ions by means of tapered glass capillary optics was achieved by Nebiki et al⁴⁾. Although it has generally been considered that small-angle scattering on the surfaces play an important role, the details of the processes have not been clarified yet. We studied the mechanism of collisions between MeV carbon ions and polarity-controlled ZnO surfaces aligned to the *c*-axis in order to investigate the efficient reflection of swift ions on solid surfaces as mentioned above.

The experiment was performed at the TC beam line of the 3-MV tandem accelerator at the JAEA Takasaki institute. C⁺ (1-2 MeV) ions of diameter 1 mm were introduced into the vacuum chamber. A continuous primary beam with a current of ~50 pA was modulated to a 10-kHz pulsed beam by a pair of parallel plates after attenuating the fluence rate to 1/300 or 1/30. Free-standing ZnO single crystals with two opposite surfaces, so-called "Zn and O faces," were set on a manipulator in the chamber. The angle of incidence was fixed at 2°. The two crystals were of the same dimensions 10 mm × 10 mm × 0.5 mm. The energy of the ions scattered at 3° with respect to the beam axis was measured by a conventional Si surface barrier detector. The energy distribution was recorded by a multichannel analyzer. The vacuum in the chamber was maintained below 4 × 10⁻⁶ Pa.

Figure 1 shows the energy distribution of the scattered ions after incidence of 1-MeV C⁺ ions on the ZnO surfaces. The distributions on the two opposite surfaces are significantly different despite the almost equal integrated intensities. A larger energy loss of scattered ions on the Zn face compared to the O face suggests that multiple collisions with surface atoms play key roles; however, the almost

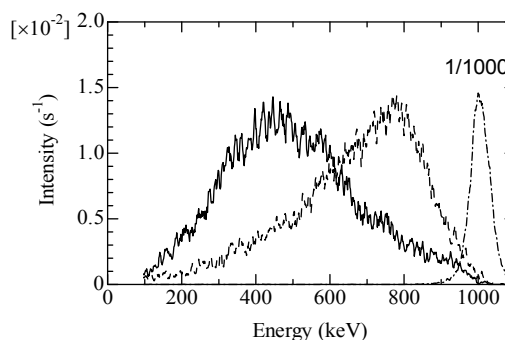


Fig. 1 Energy distribution of scattered ions after incidence of 1 MeV C⁺ ions on ZnO surfaces. —; (0001) Zn face, - - -; (000-1) O face, and ····; primary beam (1/1000).

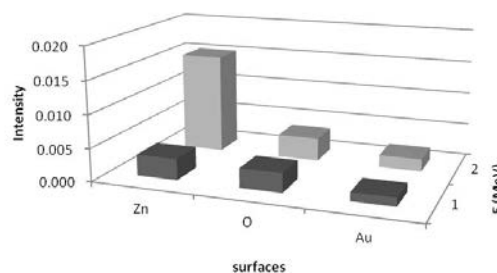


Fig. 2 Comparison of scattered ion intensities on the Zn and O faces of ZnO crystals and a polycrystalline Au film.

equal intensity of reflected ions on the two opposite surfaces seems to be contrary to this reasoning. Figure 2 compares the intensities of ions scattered on three different surfaces of Zn and O faces of the ZnO crystals and a polycrystalline Au film. The intensity on the Zn face of the ZnO crystals significantly increased at 2 MeV, although there was a small increase in intensity in the case of the O face of the ZnO and Au surfaces. The details of this finding have not been clarified yet. However, efficient reflection of MeV ions is expected on polarity-controlled ZnO surfaces.

References

- 1) M. Sumita et al., *Appl. Phys. Lett.* **75** (1999) 674.
- 2) T. Ohnishi et al., *Mater. Sci. Eng.* **B56** (1998) 256.
- 3) J. A. van Kan, Dr. thesis, Vrije Universiteit, Amsterdam (1996).
- 4) T. Nebiki et al., *J. Vac. Sci. Technol. A* **21** (2003) 167.

4 - 20 He⁺ Ion Implantation Effect on Cathodoluminescence of Plagioclase

H. Nishido^{a)}, M. Kayama^{b)}, S. Toyoda^{c)} and K. Komuro^{d)}

^{a)} Research Institute of Natural Sciences, Okayama University of Science, ^{b)} Department of Earth and Planetary Systems Science, Graduate School of Science, Hiroshima University,

^{c)} Department of Applied Physics, Okayama University of Science,

^{d)} Earth Evolution Sciences, University of Tsukuba

Cathodoluminescence (CL) is the emission of photons of UV to IR wavelengths from a material stimulated by an incident electron beam. CL properties of minerals depend on radiation dose of alpha particles, implying its geoscientific applications for a geodosimetry. CL microscopy and spectroscopy has been extensively investigated to clarify radiation-induced damages on quartz, zircon and cordierite and estimate natural radiation dose on them, but less on feldspar in spite of an important rock-forming mineral. In this study, He⁺ ion implantation at 4.0 MeV, corresponding to the energy of alpha particles from disintegration of ²³⁸U, on albite (sodium feldspar) from various localities was conducted to specify radiation-induced centers and to reveal their dependence on mineralogical features^{1,2)}.

He⁺ ion implantation at 4.0 MeV was carried out for single crystals of albite from Minas Gerais, Brazil (Ab1), from Itoigawa, Japan (Ab2), and from Tanogami, Japan (Ab3) using a 3 MV tandem accelerator at Takasaki Advanced Radiation Research Institute of the Japan Atomic Energy Agency, where the radiation dose was controlled under 10 sets of conditions in the range from 2.18×10^{-6} to 6.33×10^{-4} C/cm². CL imaging and spectroscopy were carried with a scanning electron microscopy-cathodoluminescence (SEM-CL) of an SEM (JEOL: JSM-5410) combined with a grating monochromator (Oxford: Mono CL2) at the Okayama University of Science. All CL measurements were obtained at 15 kV accelerating voltage and 1.0 nA beam current in a scanning mode. Raman spectra were measured using a micro-Raman microscope (Nicolet Almega XR).

Feldspar has many types of luminescence centers (Mn²⁺, Fe³⁺) and defect centers (Al-O-Al)³⁾. CL spectra of all He⁺-ion-implanted Ab1, Ab2 and Ab3 have emission bands at 700-750 nm, of which the intensities increase with the enhanced radiation dose. These red CL emissions can be assigned to radiation-induced defect center. CL images of these implanted samples consist of a red CL halo on the implanted surface of approximately 14 μm thickness, which is consistent with a theoretical range of alpha particles at 4.0 MeV. Two-D Raman mapping of the peak at 508 cm⁻¹ for CL halo area shows minimum intensity and maximum full width at half maximum at ~14 μm from the implanted surface, implying production of the radiation-induced defect center by a partial destruction of framework structure in albite.

Deconvolution of CL spectra obtained from the implanted Ab1, Ab2 and Ab3 successfully separates the red emission bands into a Gaussian component at 1.861 eV attributed to the radiation-induced defect center. The emission intensity of the component at 1.861 eV linearly correlates with the radiation dose as a function of the defect density (Fig. 1). There is no difference in the gradient of the linear approximations among albite from various localities, suggesting almost no dependence of the intensity on the mineralogical features such as concentration and distribution of other emission center, the presence of microstructures or textures, and crystallographic orientation. The CL spectral deconvolution has a high potential for quantitative estimation of the radiation dose of alpha particles from natural radionuclides on albite for a geodosimetry. This might allow new and progressive applications to the geosciences and radiation physics, for example, estimating leakage of nuclear waste from geologic disposal facilities. Another example would be sedimentary dating of feldspar that coexisted with natural radionuclide, if annual dose rate of the natural radionuclide could be evaluated.

References

- 1) M. Kayama et al., *Am. Mineral.* 96 (2011) 195.
- 2) M. Kayama et al., *Spectros. Lett.* 44 (2011) 469.
- 3) M. Kayama et al., *Am. Mineral.* 95 (2010) 1783.

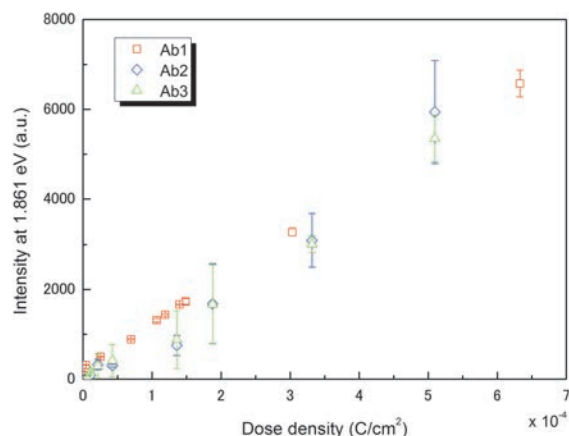


Fig. 1 Integral intensities of Gaussian components at 1.861 eV obtained using CL spectral deconvolution for the He⁺ ion implanted albite (Ab1, Ab2, Ab3) against dose density of the implantation.

4 - 21 Reconstruction of the Tectonic Activity in the Southwestern Tarim Basin

A. Karasuda ^{a)}, R. Tada ^{a)}, Z. Hongbo ^{b)}, S. Toyoda ^{c)} and T. Yoshida ^{a)}

^{a)} Department of Earth and Planetary science, The University of Tokyo,

^{b)} Institute of Surface Geochemistry, School of Earth Sciences and Engineering, Nanjing University,

^{c)} Department of Applied Physics, Okayama University of Science

Tectonics-climate linkage is one of the most important subjects of the paleoclimate research, but it is very difficult to reconstruct detailed tectonic activity of the past. In this research, we try to reconstruct tectonic activity from provenance changes of the river sediments estimated by the electron spin resonance (ESR) and crystallinity of quartz. We found provenance changes of the river sediments for the two times. These changes seem to reflect exposure of different types of rocks due to the tectonic activity.

古気候においてテクトニクスと気候の関係性を知る事が重要な課題であるが、詳細な過去のテクトニクス運動を復元することが困難なため両者の比較が困難であった。そこで今回我々は堆積物中の石英について電子スピン共鳴 (ESR) 信号強度と結晶化度 (CI) を供給源推定の指標として用いることで、河川堆積物の供給源変動を明らかにし、河川供給源変動を引き起こすテクトニクス運動の推定を行った。

石英の ESR 信号強度は年代と比例関係であることが知られており ¹⁾、石英の結晶化度 (CI) は石英の晶出過程を反映していることが知られている ²⁾。この2つの手法の特徴は供給源の年代と岩系を推定することが可能なため、具体的な供給源推定が可能な点がこの指標のメリットである。

本研究では大陸地殻同士の衝突によるテクトニクス活動が活発な中央アジアタリム盆地南西部 Yecheng section の河川堆積物を用いた (Fig. 1)。Yecheng section では古地磁気層序より堆積年代が 4.6-1.8 Ma (Megaannum: 百万年前) と判明している ³⁾。今回は堆積物層より礫岩マトリックス 11 サンプルについて、酢酸 (10%) による炭酸塩除去 (8 時間)、0.3 mol/L クエン酸ナトリウムと 1 mol/L 炭酸水素ナトリウムを 8:1 で混合した溶液による鉄、マンガン酸化物除去 (80 °C, 8 時間)、過酸化水素水 (10%) による有機物除去 (60 °C, 8 時間) を行った後、粒度分画 (64-512 μm)、γ線照射 (2.5 kGy)、加熱 (300 °C, 15 分) の後に石英の ESR 信号強度と結晶化度 (CI) の測定を行った。

その結果、この時代においては2回の大きな供給源変動イベントが観察された (Fig. 2)。変動が発生した時代は先行研究の古地磁気層序より 3.5, 3.0 Ma であった。また ESR 信号強度と CI の二軸プロットを行うと供給源が大きく3つに区別されることが分かった (Fig. 3)。これらの変動の原因は新しい岩帯の露出が考えられるため、先行研究 ³⁾ より 3.5 Ma 以降に産出が見られる変成岩、火成岩について同じく石英の ESR 信号強度と CI の測定を行い前の結果に

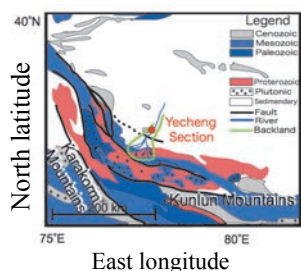


Fig. 1 Research area.

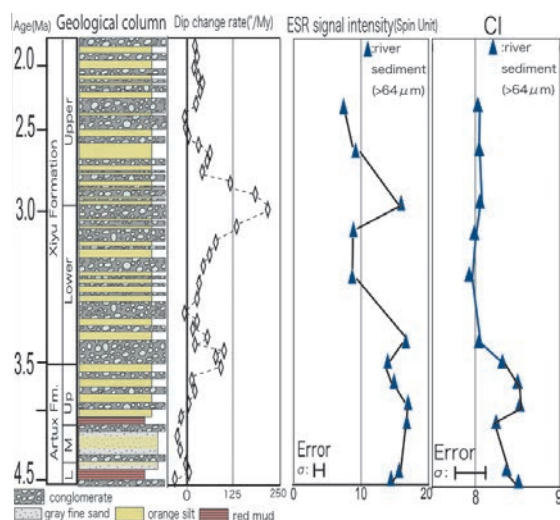


Fig. 2 ESR and CI data with geological column and Dip change.

重ね合わせると、3.5 Ma と 3.0 Ma では火成岩 3.5 Ma 以降は変成岩の影響を強く受けていることが判明した。

以上の結果よりテクトニクス復元を行うと、火成岩が逆断層に付随する形で見られるため、この逆断層が 3.5, 3.0 Ma に大きな変動があったと考えられる。また、変成岩は逆断層の北にある褶曲の軸中心部に見られるため、3.5 Ma 以降にこの褶曲活動が活発化することで露出が起きたと考えられる。

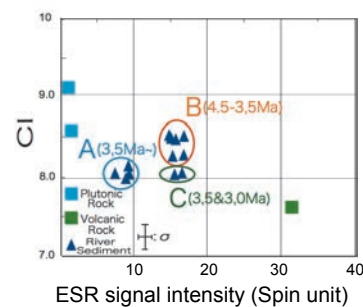


Fig. 3 Plot data of ESR and CI.

References

- 1) S. Toyoda, T. Naruse, Jpn. Geomorphology 23, (2002) 811-20.
- 2) K. Murata and M. Norman, Am. J. Sci. 276 (1976) 1120-30.
- 3) Zheng et al., Geol. Soc. Lond. Spec. Publ. 342 (2010) 67-78.

4 - 22 Development of Spin-Polarized Positron Beam and Its Application to Spintronics Study

A. Kawasuso, M. Maekawa, Y. Fukaya, A. Yabuuchi and I. Mochizuki

Advanced Science Research Center, JAEA

Spin-polarized positron beam is useful in studying spintronics materials. We have been producing a ^{68}Ge - ^{68}Ga positron source which emits highly spin-polarized positrons as compared to the conventional ^{22}Na source. In 2011 fiscal year, we accomplished the construction of a spin-polarized positron beam apparatus in which the above ^{68}Ge - ^{68}Ga source was installed. Furthermore, to establish the foundation of spin-polarized positron annihilation spectroscopy (SP-PAS), we have also studied some ferromagnets.

Figure 1 shows a picture of the constructed spin-polarized positron beam line. The beam line is directly connected to the ion irradiation chamber. After activating through proton bombardment, the source is transferred to the slow positron generation chamber. Current source activity is approximately 300 MBq. The moderator is composed of tungsten meshes and plates. Slow positrons generated at the moderator are electrostatically accelerated and transported to the sample chamber. The beam flux is 5×10^3 e^+ /sec and the polarization is approximately 0.35. Using a magnetic or electrostatic deflector as an energy selector, a longitudinally or a transversely polarized positron beam is obtained.

To examine the feasibility of SP-PAS to apply magnetic materials for the spin-electronic devices, we have performed the SP-PAS measurements of high quality for the simple ferromagnets (Fe, Co, Ni, and Gd). Figure 2 shows the differential Doppler broadening of annihilation radiation (DBAR) spectra (electron momentum distributions) between positive and negative magnetic field with respect to positron spin direction obtained for polycrystalline Fe, Co, Ni and Gd. The residuals are not zero. This is called field-reversal asymmetry.

Roughly speaking, the field-reversal asymmetry appears due to enhanced annihilation between spin-up positrons and

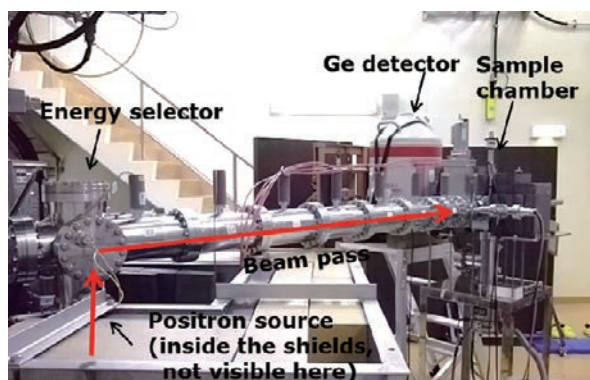


Fig. 1 Picture of the spin-polarized positron beam line in which a ^{68}Ge - ^{68}Ga source is installed.

spin-down 3d, 4s (Fe, Co, Ni) and 4f, 5d, 6s (Gd) unpaired electrons. The field-reversal asymmetry of the Fe sample is the strongest, while it is slightly weaker for the Co sample, and only a small effect is observed for the Ni and Gd samples. Actually, the experimental results are well-reproduced by the first principles calculation considering polarization of electrons and positrons as shown by the solid lines.

The relative amplitude of the differential DBAR spectra of the Fe, Co and Ni samples seems to coincide with the trend of effective magnetization of these metals. If the area intensity of the Fe sample is normalized to 2.2, those of Co and samples are 1.8 and 0.4. These are comparable to the effective magnetizations of these materials. This result indicates that the magnetization of a magnetic substance can be estimated from the field reversal asymmetry of DBAR spectrum using a reference sample with known magnetization. Considering the fact that the electron polarization of Fe is at most about 40% near the Fermi level, the determination of electron polarizations of half-metals by the present method is feasible.

References

- 1) A. Kawasuso et al., Phys. Rev. B **83** (2011) 100406(R)-1-100406(R)-4.
- 2) A. Kawasuso et al., Phys. Rev. B **85** (2012) 024417-1-024417-6.

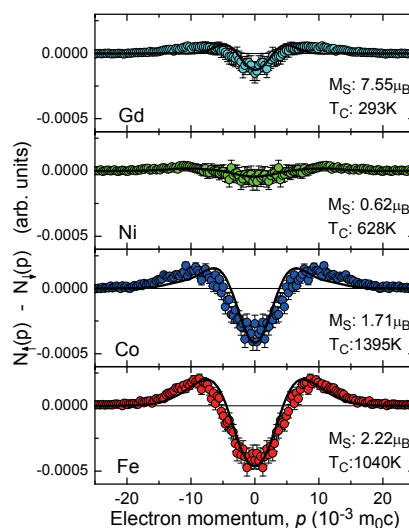


Fig. 2 Differential DBAR spectra of the Fe, Co, Ni and Gd samples obtained in the external magnetic field of 1 T at room temperature. These spectra are folded at $p=0$ to enhance the statistics. Solid lines denote calculated differential DBAR spectra. The amplitudes are adjusted to levels comparable with the experiments.

4 - 23

**Thermal Stability of Vacancies
in Zr-Doped Stainless Steels**

A. Yabuuchi, M. Maekawa and A. Kawasuso

Advanced Science Research Center, JAEA

It has been reported that radiation-induced segregation to cause stress corrosion cracking is inhibited by addition of Zr to stainless steels¹⁾. This effect is thought to be due to the binding of mobile vacancies to oversized Zr atoms. As a result, the flow of vacancies to grain boundaries is decreased and the grain boundary segregation caused by inverse Kirkendall effect is suppressed. In this report, solute-vacancy binding effect was evaluated for type 316L stainless steels doped with oversized Zr atoms by means of positron annihilation lifetime spectroscopy.

Alloy ingot of 316L-0.5at%Zr was prepared by vacuum arc melting. The ingot was annealed at 1150 °C for 2 h in vacuum and subsequently quenched in ice water. To serve as a reference, unaltered 316L specimen was also annealed and water-quenched at the same temperature. Both specimens were then irradiated with 2 MeV electrons at a fluence of $1.5 \times 10^{18} \text{ e/cm}^2$ at approximately 50 °C and were then isochronally annealed in vacuum with a temperature step of 50 °C for a duration of 15 min.

Based on the two-state trapping model, τ_2 is related to the positron lifetime at vacancies ($\tau_2 = \tau_v$). The positron trapping rate to vacancies is given by $\kappa = (I_2/I_1)(\tau_b^{-1} - \tau_2^{-1})$, where τ_b and τ_v are positron lifetimes for bulk and vacancies. The first lifetime is given by $\tau_1^{\text{TM}} = 1/(\tau_b^{-1} + \kappa)$. The reference specimen (annealed 316L alloy) had a one lifetime value of 105 ps. This is attributed to the bulk positron lifetime²⁾. Thus, before irradiation, the vacancy concentration was under the detection limit ($< 10^{-7}$). Figure 1 shows the isochronal annealing behavior of positron lifetimes (τ_1 and τ_2) and intensities (I_2) after

irradiation. In both specimens, τ_1 and τ_1^{TM} agree each other, suggesting the validity of the two-component trapping model. The vacancy-related lifetimes (τ_2) do not increase during annealing. This suggests that vacancy clustering is not a major annealing process. That the I_2 value of the additive-free 316L alloy after irradiation is the larger than that of the 316L-Zr alloy can be interpreted as follows. In this study, the 316L-Zr alloy was prepared by vacuum melting, but the additive-free 316L alloy was not. As an analogous example, vacuum melting in steels decreases carbon concentration. Additionally, it has been reported that there are strong interactions between vacancies and carbon atoms in pure Fe³⁾. Thus, it is considered that this result reflects the differences in carbon concentrations in both specimens.

Figure 2 shows the positron trapping rates, which are proportional to vacancy concentration, obtained for both specimens after irradiation as a function of annealing temperature. Focusing on the annealing process, the positron trapping rate of the additive-free 316L specimen decreases drastically at 300 °C. The recovery temperature seems to increase by adding Zr, indicating that Zr atoms stabilize the vacancies in stainless steels. The results show that the Zr addition stabilizes vacancies, suppressing the flow of vacancies to grain boundaries. The decrease in the flow of vacancies will inhibit radiation-induced grain boundary segregation.

References

- 1) T. Kato et al., J. Nucl. Mater. 189 (1992) 167.
- 2) P. Hautojärvi et al., Solid State Commun. 29 (1979) 855.
- 3) P. Hautojärvi et al., Phys. Rev. Lett. 44 (1980) 1326.

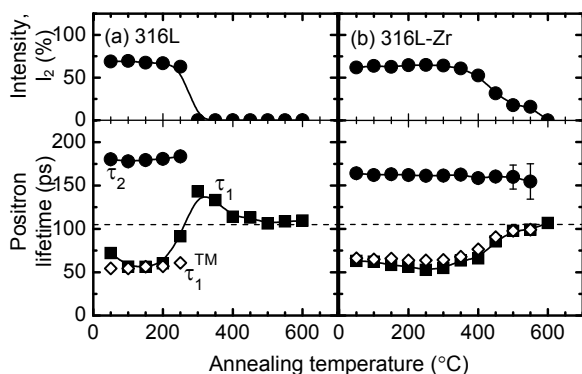


Fig. 1 Positron lifetimes (τ_1 and τ_2) and intensity (I_2) obtained for each specimen after electron irradiation as a function of annealing temperature. The positron lifetime obtained for unirradiated 316L is depicted by a horizontal dashed line. Error bars of τ_1 are smaller than the sizes of the symbols.

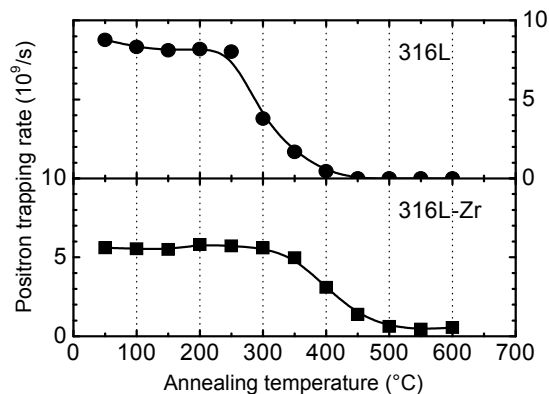


Fig. 2 Positron trapping rates (κ) obtained for each specimen after electron irradiation as a function of annealing temperature.

4 - 24 Observation of Spatial Distribution of Vacancy Defects in Semiconductor by Positron Microbeam and Electron Beam Induced Current Measurement

M. Maekawa and A. Kawasuso

Advanced Science Research Center, JAEA

Two dimensional mapping of lattice defects on the semiconductor wafer is important to supply high-quality substrates or improve the yield of device fabrication in the semiconductor process. Scanning positron microbeam (SPM) is expected to be a powerful tool for the observation of such defects, because the SPM can provide spatial distribution of vacancy defects near the subsurface region. We have constructed a positron microprobe by using a specially-fabricated small source (active diameter of ~2 mm, 330 MBq of ^{22}Na) and a solid neon moderator^{1,2)}. The slow positron beam was focused on the sample by a objective lens. Minimum beam diameter of 1.9 micron was estimated.

Electron beam induced current (EBIC) measurement is also known as a method to obtain the spatial distribution of defects^{3,4)}. This method is based on a phenomenon that the induced current, which is generated when electron-beam probe is irradiated to a semiconductor sample, is reduced due to the recombination at defects. That is, EBIC image reflects the spatial distribution of electron traps, which cannot be observed only by the SPM directly. From the comparison of the above two methods, one can know if that electron traps are associated with vacancy defects or not.

To demonstrate the superiority of the above-mentioned method in defect evaluation, we added the EBIC measurement system to our SPM. Figure 1 shows the schematics of the constructed measurement system. A partially proton-implanted Si was used as a sample. Figure 2 shows the tentative results of the positron and EBIC measurements. Only at the implanted region, the peak intensity of annihilation gamma ray, S parameter, is increased. This is attributed to the annihilation at the vacancy-type defects. On the other hand, EBIC contrast decrease. This means that the recombination of induced current was occurred at the irradiation defects. From this result, vacancy defects created by the ion irradiation may become the origin of the electron level. Complementally use of SPM and EBIC may be a good way to recognize the origin of the electron states.

References

- 1) M. Maekawa et al., *App. Surf. Sci.* 255 (2008) 39-41.
- 2) M. Maekawa et al., *J. Phys. Conf. Ser.* 225 (2010) 012033.
- 3) H. J. Leamy, *J. Appl. Phys.* 53 (1982) R51.
- 4) P. R. Wilshaw, *Ultramicroscopy* 31 (1989) 177.

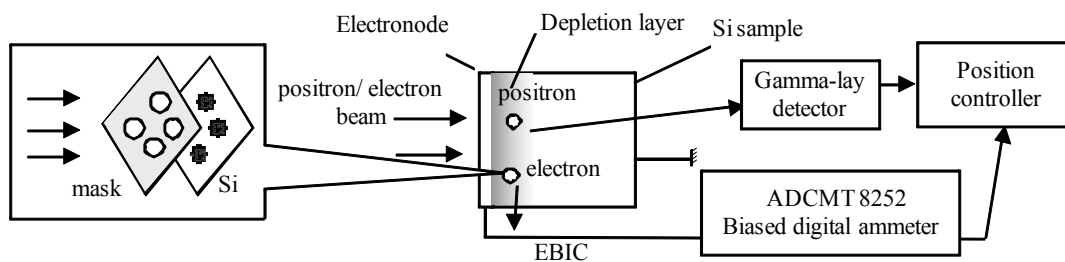


Fig. 1 Schematics of the sample and the measurement system.

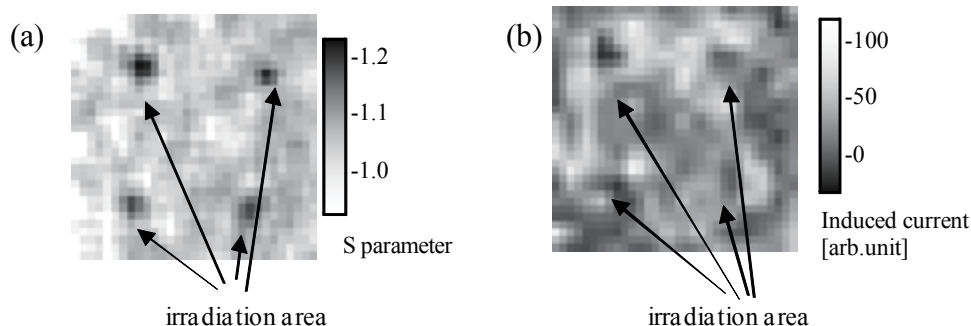


Fig. 2 (a) Spatial distribution of S parameter of partially ion irradiation sample and (b) EBIC image of the same sample.

4 - 25 Atomic Displacement of Pb/Ag(111) Surface Studied by Reflection High-energy Positron Diffraction

Y. Fukaya^{a)}, I. Matsuda^{b)}, M. Maekawa^{a)}, I. Mochizuki^{a)}, A. Kawasuso^{a)},
K. Wada^{c)} and T. Hyodo^{c)}

^{a)} Advanced Science Research Center, JAEA, ^{b)} ISSP, The University of Tokyo, ^{c)} IMSS, KEK

Breaking the spatial inversion symmetry at a surface, the effective magnetic fields are generated and hence the spin-degenerated surface bands are split into spin-polarized states through the spin-orbit interaction. This is called Rashba effect¹⁾, which is one of the key techniques to yield the functional materials for spintronics. Recently, markedly large Rashba energy (200 meV) was observed for the Bi/Ag(111) surface alloys²⁾. After that, it was found that various surface alloy phases, e.g. Pb/Ag(111) and Sb/Ag(111), show the giant Rashba effects. The first-principles calculations suggested that the height of the topmost heavy element is closely related to the magnitude of the Rashba energy³⁾. However, the relationship is not yet confirmed experimentally. In this paper, the heights of the Pb atoms on crystalline Ag films with various film thicknesses were investigated using reflection high-energy positron diffraction (RHEPD).

The substrates were cut from a mirror-polished Si(111) wafer. To make crystalline Ag(111) thin films, Ag atoms were deposited onto the Si(111)-7×7 surface at 130 K. After the annealing up to room temperature, well-ordered Ag(111) thin films were formed. The $\sqrt{3}\times\sqrt{3}$ structure was formed by the deposition of the Pb atoms of 1/3 monolayer (ML) on the Ag(111) thin film surfaces. Here, 1 ML is defined as 1.38×10^{15} cm⁻².

The RHEPD experiments were carried out using the positron beams from a ²²Na positron source of JAEA and a linac at the Slow Positron Facility of the Institute of Materials Structure Science, KEK. The positron beam energy was 10 keV. To measure the rocking curves, the glancing angle was varied up to 6° by rotating the sample holder.

Figure 1(a) displays a sequence of the RHEPD rocking curves of the specular spots from the Pb/Ag(111) surface alloys with various Ag film thicknesses (t) under the one-beam condition. In this condition, the rocking curve depends mainly on the atomic heights. Although the rocking curves show only a slight dependence on the Ag film thickness, the intensities in the glancing angle region of 2.0°-4.5° are gradually decreased with increasing the Ag film thickness. This indicates that the atomic heights are changed with the Ag film thickness.

To determine the shift of the Pb atoms with the Ag thickness, the RHEPD intensities were calculated based on the dynamical diffraction theory. The solid lines in Fig. 1(a) indicate the rocking curves calculated using the optimum heights of the Pb atoms at each film thickness. The calculated curves can reproduce the experimental curve

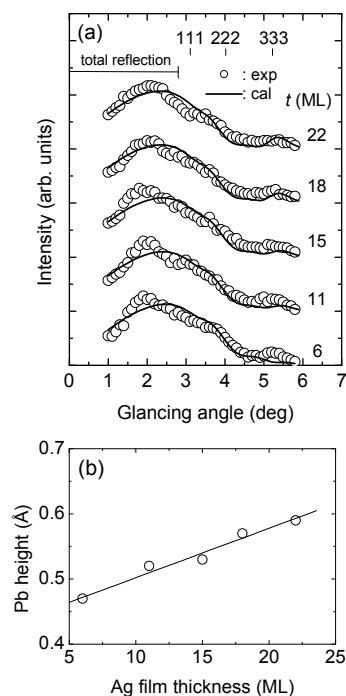


Fig. 1 (a) RHEPD rocking curves from the $\sqrt{3}\times\sqrt{3}$ of Pb/Ag(111) surfaces at $t = 6$ -22 ML. The circles indicate the measured curves. The solid lines show the calculated curves using the optimum heights of the Pb atoms. (b) Pb heights from the first Ag layer for Pb/Ag(111) surfaces as a function of the Ag thickness.

at each film thickness. The optimum height at each film thickness is plotted in Fig. 1(b). The height of the Pb atoms increases with increasing the Ag film thickness. The height of the Pb atoms at the Ag film thickness of 22 ML is close to that for the Ag bulk. Thus, the height of the Pb atoms is significantly affected by the Ag film thickness. The surface electronic band structures were also measured using angle-resolved photoemission spectroscopy (ARPES). The ARPES intensity maps indicate that band dispersions of spin-split surface states are changed depending on the Ag film thickness. The relationship between the atomic height and the spin splitting is explained by considering the hybridization between the quantum well states and surface states.

References

- 1) E. I. Rashba, Sov. Phys. Solid State **2** (1960) 1109.
- 2) C. R. Ast et al., Phys. Rev. Lett. **98** (2007) 186807.
- 3) G. Bihlmayer et al., Phys. Rev. B **75** (2007) 195414.

4 - 26 Phase Transition of Quasi One-dimensional Nanowire on Pt/Ge(001) Surface Studied by Reflection High-energy Positron Diffraction

I. Mochizuki^{a)}, Y. Fukaya^{a)}, M. Maekawa^{a)}, A. Kawasuso^{a)}, K. Wada^{b)} and T. Hyodo^{b)}

^{a)} Advanced Science Research Center, JAEA,

^{b)} Institute of Materials Structure Science, High Energy Accelerator Research Organization (KEK)

Self-assembled nanowires have attracted a great deal of interests as not only potential applications in nano-devices, but also fundamental understandings of one-dimensional properties. Defect-free nanowires with single-atom width are fabricated on the Ge(001) surface by the adsorption of Pt atoms. We have investigated the Pt/Ge(001) surface by using reflection high-energy positron diffraction (RHEPD)¹⁾, and have shown that the atomic arrangement is explained by the nanowire (NW) model²⁾ (Fig. 1). Recently, van Houselt et al.³⁾ have reported that the nanowires undergo the Peierls-type structural phase transition (SPT) around 80 K by using scanning tunneling microscopy/spectroscopy. Whereas, the atomic displacements and the electronic band dispersions in the SPT are still unrevealed. In this study, we investigated atomic and electronic structures of the Pt/Ge(001) surface by using RHEPD and angle resolved photoemission spectroscopy (ARPES).

To produce a Ge(001)-(4×2)-Pt structure, 1.2 monolayers (ML) of Pt atoms were deposited on the clean Ge(001) surface kept at 620 K, where 1 ML corresponds to 6.3×10^{14} atoms/cm². The RHEPD experiments were performed using a positron beam of 10 keV generated from a ²²Na source and an intense positron beam in the Slow Positron Facility of the High Energy Accelerator Research Organization (KEK). The incident azimuth was set at the 22.5° away from the [110] direction. The ARPES measurements were performed with a polarized radiation of $h\nu = 24$ eV at the BL-18A beamline of the KEK Photon Factory (Institute for Solid State Physics, The University of Tokyo).

Figure 2 shows the RHEPD rocking curves from the Pt/Ge(001) surface up to a glancing angle (θ) of 4°. The intensities at $\theta = 2.3^\circ - 3.2^\circ$ are enhanced with increasing temperature from 35 K (black-open circles) to room temperature (gray-open circles). From the calculations of

the rocking curves (solid lines) based on the dynamical diffraction theory, we have confirmed that the change is derived from the height difference between the topmost Ge dimer atoms. Figure 3 shows temperature dependence of the specular spot intensity at $\theta = 2.5^\circ$. The intensity gradually increases from 80 to 110 K, indicating the progress of the SPT, and thereafter, a conventional Debye-Waller-like temperature dependence is observed.

From the ARPES measurements, we have observed the change in electronic band dispersions due to the SPT. In the present results, the SPT for the Pt/Ge(001) surface might be categorized as a new type of the Peierls transition, where the formation and fluctuation of charge density waves trigger the atomic displacements of the topmost Ge dimers.

References

- 1) I. Mochizuki et al., Phys. Rev. B 85 (2012) 245438.
- 2) D. E. P. Vanpoucke et al., Phys. Rev. B 81 (2010) 085410.
- 3) A. van Houselt et al., Surf. Sci. 602 (2008) 1731.

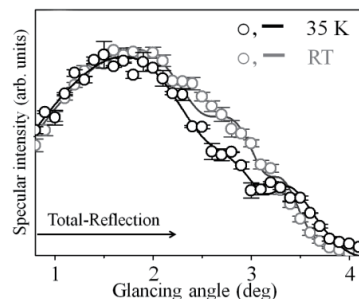


Fig. 2 Comparison of RHEPD rocking curves between above and below the SPT temperature. The solid lines are the calculated curves for the NW model.

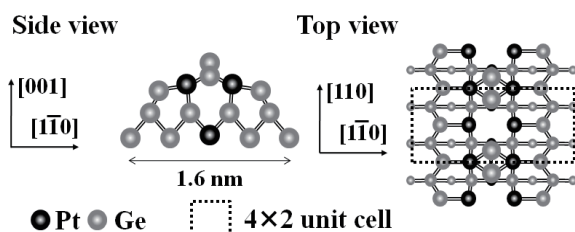


Fig. 1 Ball-and-stick representations of the NW model. Black and gray balls show Pt and Ge atoms, respectively. The dotted square indicates the 4×2 unit cell.

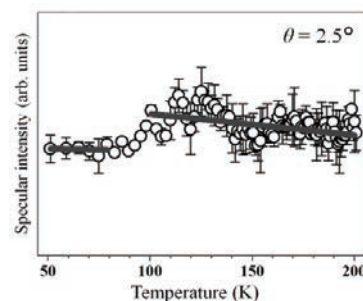


Fig. 3 Temperature dependent specular spot intensity curve from 50 to 200 K. The solid lines indicate the calculated temperature dependences assuming Debye temperatures of 210 and 130 K above and below the SPT temperature, respectively.

4 - 27 Pulse Radiolysis of Water by Energetic Heavy Ion

M. Taguchi^{a)}, K. Iwamatsu^{a, b)}, Y. Sugo^{c)}, S. Kurashima^{d)},
S. Yamashita^{a)} and Y. Katsumura^{b)}

^{a)} Environment and Industrial Materials Research Division, QuBS, JAEA,

^{b)} The University of Tokyo, ^{c)} Medical and Biotechnological Application Division, QuBS, JAEA,

^{d)} Department of Advanced Radiation Technology, TARRI, JAEA

Heavy ion beam, one of the high Linear Energy Transfer (LET) radiations, induces specific chemical effects being different from those by low LET radiations such as X-rays, γ -rays and electron beams. The effects of low LET radiations are well known but those of high LET radiations are not fully elucidated, these effects are attributed to the dense energy deposition along the trajectory leading to dense and heterogeneous distributions of the reactive species produced, so called "track structure". The degree of water molecule decomposition depends on the type and LET value of radiations. However, the degradation of water molecules by high LET radiations has not been clearly understood. The purpose of this study is to clarify chemical reactions of OH (hydroxyl) radical, which is the most important reactive species in water, induced by heavy ions.

The ions used in this study were H^+ (20 MeV), He^{2+} (50 MeV), and C^{5+} (220 MeV) ions provided from the AVF cyclotron at the Takasaki Ion Accelerators for Advanced Radiation Application (TIARA) facility in JAEA/Takasaki. Ion beams were pulsed into 50 μs by a chopping system¹⁾. NaBr was selected as a probe reagent for OH radicals since OH radical reacts with Br^- to produce $Br_2^{\bullet-}$, which has large extinction coefficient, as shown in reaction scheme. The aqueous solution was saturated with oxygen gas. NaBr aqueous solutions (0.1~100 mM) were irradiated with the pulsed ions, and $Br_2^{\bullet-}$ was observed by the time-resolved spectroscopic method at 375 nm²⁾. The energy dependence, in other words, the LET dependence of the ions was investigated by setting Al films, which has several thicknesses, above sample cell.

The optical density of $Br_2^{\bullet-}$ sharply increased within the pulse and then decreased bimolecularly (Fig. 1). Peak

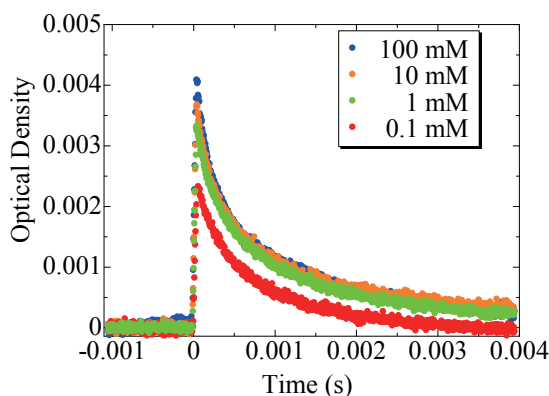
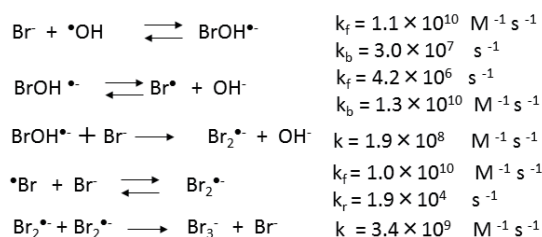


Fig. 1 Time profile of absorbance (375 nm) of $Br_2^{\bullet-}$ in NaBr aqueous solution irradiated with H^+ (LET=4.65 eV/nm).

Reaction scheme



values of the optical density of $Br_2^{\bullet-}$ decreased slightly with decreasing in the NaBr concentration. The formation yield of $Br_2^{\bullet-}$ was estimated from the peak values of the optical density and expressed in the G -value (molecules/100 eV). The G -value of $Br_2^{\bullet-}$ is strongly related to the yield of the OH radical. G -values of $Br_2^{\bullet-}$ in 100 mM NaBr aqueous solution decreased with the increase in LET value of incident ions as shown in Fig. 2. The G -values also depend on the kind of the incident ions. The observed G -values of $Br_2^{\bullet-}$ were smaller than those of OH radicals theoretically estimated by Monte Carlo method³⁾. The heavy ions induce dense initial distributions of radicals around their trajectory, resulting in the increase in the recombination of OH radicals with vicinal radicals. Theoretical analysis based on reaction kinetics model is in progress.

References

- 1) M. Taguchi, et al., Radiat. Phys. Chem. 78 (2009) 1169.
- 2) K. Iwamatsu, et al., Trans. Mater. Res. Soc. Jpn. 36 (2011) 329.
- 3) M. Taguchi, et al., Radiat. Res. 171 (2009) 254.

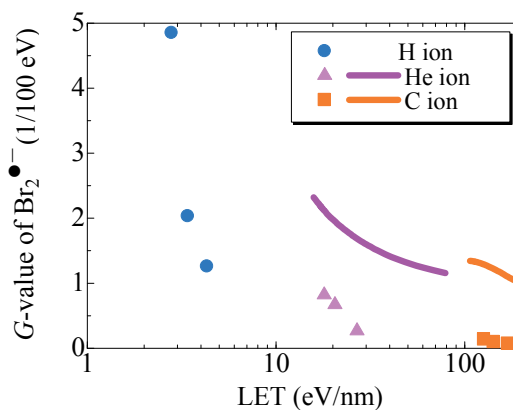


Fig. 2 LET dependence of $Br_2^{\bullet-}$ yields for 100 mM NaBr aqueous solution irradiated with pulsed H, He, and C ions.

4 - 28 Transient Absorption of Pyrene-Dodecane Solution Measured by Microsecond Ion Beam Pulse Radiolysis

T. Kondoh^{a)}, J. Yang^{a)}, K. Kan^{a)}, Y. Yoshida^{a)}, H. Shibata^{b)},
S. Kurashima^{c)}, K. Iwamatsu^{d)} and M. Taguchi^{d)}

^{a)} ISIR, Osaka University, ^{b)} Faculty of Engineering, Kyoto University,

^{c)} Department of Advanced Radiation Technology, TARRI, JAEA,

^{d)} Environment and Industrial Materials Research Division, QuBS, JAEA

Microsecond time resolved ion-beam pulse radiolysis system was developed at TIARA facility to measure the initial process of ion-beam induced reactions in the ion tracks. Time dependent behavior of optical absorption of pyrene-dodecane solution irradiated with 350 MeV Ne⁸⁺ ions was measured by the ion pulse radiolysis.

重粒子線がん治療やイオンビーム照射による植物の品種改良、イオン注入による材料改質などの応用技術が注目されている。これらのイオンビーム応用技術には、高LET放射線であるイオンビームが生成する高密度イオン化の効果を応用したものが多いが、イオンビームの高密度イオン化による活性種反応の初期過程は直接観測され理解されたというわけではない。高密度に生成した活性種は高速に反応していると生成物分析の結果から考えられている。高密度イオン化状態での時間挙動や反応性を解明するために、イオンパルスラジオリシスを開発している。パルスラジオリシスでは、重イオンが生成した活性種を光吸収で観測するが、重イオンの場合エネルギー付与の空間構造の特異性から測定システムの構築は困難だった。さらにTIARAサイクロトロンが発生した350 MeV Ne⁸⁺重イオンでは、20個程度の重イオンを含んだパルスが50 nsの間隔で照射されるため、数100 nsから数 μ sにわたる化学反応の観測は困難であり、一方50 ns以下の反応の観測にはビームのパルス強度が小さい。原子力機構の田口らはこれらの困難を克服するために、チョッパーのゲート幅を変化させることにより、シングルパルスから数千パルスにわたるパルス列を得て、これを大きな一つのマクロパルスとして試料に照射して、マクロパルスのパルス幅より長いマイクロ秒の時間領域で活性種の光吸収時間挙動を観測可能なマイクロ秒重イオンパルスラジオリシスを開発した¹⁾。核燃料サイクルにおける抽出剤溶媒であるドデカンに重イオンを照射した場合の高密度イオン化の基礎過程を解明するために、この測定システムを用いた。チョッパーのゲート幅を50 μ sとすることにより、マクロパルス内には約1,000個のマイクロパルスがある。HYポートに輸送されたビームは、試料に入射して溶媒の活性種や溶質との反応を誘起する。これを観測するために分析光には高出力・高安定な半導体レーザーを用いた。測定波長はレーザーの発振波長で決まり、今回はピレンラジカルカチオンの光吸収ピークがある447 nmで測定した。350 MeV Ne⁸⁺イオンビームをドデカンおよび100 mMピレン-ドデカン溶液に照射し、447 nmで測定した結果をFig. 1に示した。50 μ sまでに重イオンマクロパルスにより光吸収が生成した。ドデカンも100 mMピレン-ドデカン溶液もパルス終了直後に速い光吸収の減衰が観測された。ドデカンはその後ノイズによる変動があるが非常に緩やかな減少

を示した。一方ピレン溶液では、同様のノイズが見られたが、その後数百 μ sで減衰した。当初溶液を用いればピレンラジカルカチオンによる光吸収増大が観測されると推測していたが、ピレンによる吸収増大は見られなかった。現状では、高密度イオン化状態でのクロス再結合を生き残った長寿命のドデカンの三重項励起状態がピレンに捕捉されたと推測しているが、結論には至っていない。今後スペクトル測定や他の線種で同様に測定し、ドデカン中の高密度イオン化状態の研究を行う。また1つの手法として、高粘性液体、たとえばイオン液体を用いることにより、トラック内の拡散律速反応を1,000倍程度遅らせて観測する手法を検討した。その結果をFig. 2に示した。DEME-TFSAと比較して20 mMピレン溶液でピレンラジカルカチオンと思われる大きな光吸収帯が観測された。

Reference

- 1) M. Taguchi et al., Radiat. Phys. Chem. 78 (2009) 1169-74.

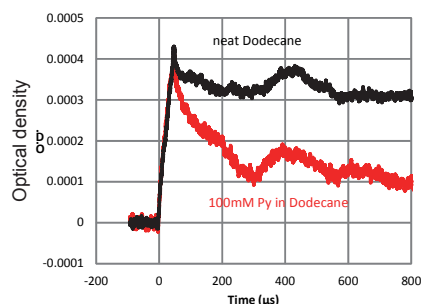


Fig. 1 Transient absorption of neat-dodecane(black) and 100 mM pyrene dodecane solution(red) at 447 nm.

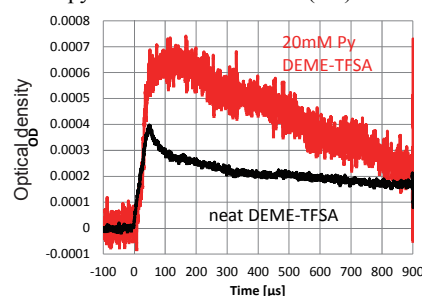


Fig. 2 Transient absorption of neat-DEME-TFSA (black) and 20 mM pyrene DEME-TFSA solution (red) at 447 nm.

4 - 29

Solvent Effect on the Radiation Induced Copolymerization of Maleimide with Styrene

S. Nakagawa ^{a)}, M. Taguchi ^{b)} and A. Kimura ^{b)}

^{a)} Tokyo Metropolitan Industrial Research Institute,

^{b)} Environment and Industrial Materials Research Division, QuBS, JAEA

Methanol, ethanol, and 2-propanol solutions including with styrene and maleimide were irradiated with 1 MeV electron, 320 MeV C-ion, and 107 MeV He-ion beams. The efficiency of polymerization increased in the order of methanol, ethanol, and 2-propanol. On the contrary, the yield of polymer increased with decreasing dose rate, remarkably appeared in methanol.

2-プロパノール中でマレイミド (C₂H₂(CO)₂NH) とスチレンを放射線共重合したところ、平均分子量およびポリマー生成量は線量率が減少するほど増加し、この効果は LET の大きい重イオンビームほど顕著であった。また、ポリマー生成量は LET が高いと減少するが、高 LET 線源により低線量率で照射すると高分子量のポリマーが生成することがわかった¹⁾。時間的空間的なラジカル分布が、ポリマーの分子量や生成効率に影響を与えると考えられる。一方、溶媒ラジカルのヒドロキシマレイミドへの付加反応の効率は 2-プロパノールに比較してメタノールでは 1/2 以下であった²⁾。そこで、溶媒ラジカルのマレイミド付加反応の効率が放射線重合に及ぼす影響について検討することとした。

マレイミドおよびスチレンをメタノールおよびエタノールに溶かし(各 0.5 mol/L)、窒素置換した試料に原子力機構高崎量子応用研究所において、1 MeV 電子線および重イオン (C イオン-320 MeV, He イオン-107 MeV) を照射した。照射により白色微粒子が生成した。微粒子をメンブランフィルターで回収し、生成物の質量を測定した。また、テトラヒドロフランに溶解し、分子量分布をゲル浸透クロマトグラフで分析した。

Figure 1 に、0.1 mA の電子線照射により試料溶液 1 mL 中に生成したポリマー量を吸収線量に対してプロットする。エタノールでは、メタノールに比べてポリマー生成効率が大きくなっていることがわかる。Figure 1 の傾きから得られる 1 kGy あたりのポリマー生成量を Table 1 に示す。電子線照射および 20 nA、2 nA のイオンビーム照射ともメタノール<エタノール<2-プロパノールの順で、生成効率が增加することがわかる。しかし、20 nA 照射と比較した 2 nA 照射の線量率低下によるポリマー生成効率の増加率は、メタノールが最も顕著である。

Figure 2 に、2 nA の C イオンビームを 2,400 秒照射した試料の分子量分布を示す。メタノール中ではエタノール中と比較して、高分子量のポリマーが生成していることがわかった。メタノールのラジカルはマレイミドへの付加反応が起きにくい、重合成長ラジカルの密度も低いため、再結合による重合の停止反応の効率も低くなると考えられる。このため、低線量率照射や重イオンビームによる生成ラジカルの減少によるポリマーの高分子化の効果がより顕著になったと推測される。

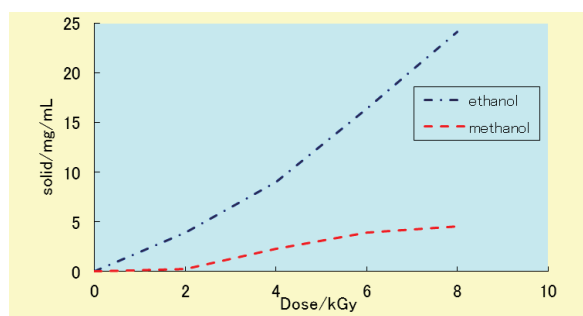


Fig. 1 Dose dependence of the polymer yields per unit volume of the solution obtained by irradiation of 1 MeV electron beam (0.1 mA).

Table 1 The yield of polymer by 1 kGy irradiation of electron and ion beams.

irradiation source	dose rate	2-propanol	ethanol	methanol
electron	0.1 mA	4.77	2.49	0.61
He-107MeV	20 nA	2.21	0.48	0.11
He-107MeV	2 nA	9.06 (4.1) ^{a)}	6.96 (14.5) ^{a)}	2.97 (27.0) ^{a)}
C-320MeV	20 nA	0.71	0.28	0.07
C-320MeV	2 nA	3.67 (5.2) ^{a)}	1.94 (6.9) ^{a)}	1.43 (20.4) ^{a)}

a: The ratio of the dose rate effect on each irradiation source.

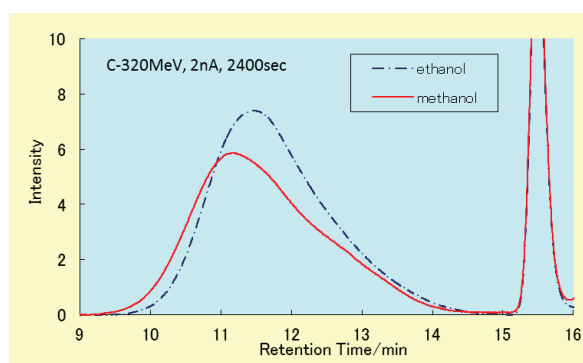


Fig. 2 Molecular weight distribution of the polymer obtained by irradiation of 320 MeV C ion beam (2 nA).

References

- 1) S. Nakagawa et al., Radiat. Phys. Chem. 80 (2011) 1199-202.
- 2) S. Nakagawa, Radiat. Phys. Chem. 79 (2010) 705-09.

4 - 30

Improvement of Source Neutron Spectrum Measurement Down to a Few MeV

Y. Shikaze^{a)}, Y. Tanimura^{a)}, Y. Tatebe^{a)}, H. Yoshitomi^{a)}, M. Yoshizawa^{a)},
H. Harano^{b)}, T. Matsumoto^{b)} and K. Mizuhashi^{c)}

^{a)}Department of Radiation Protection, NSRI, JAEA, ^{b)}National Metrology Institute of Japan,
National Institute of Advanced Industrial Science and Technology,
^{c)}Department of Advanced Radiation Technology, TARRI, JAEA

The neutron standard fields of Japan above 20 MeV have been developed using the quasi-monoenergetic neutron irradiation fields with 45, 60 and 75 MeV peaks at TIARA¹⁻³⁾ in Takasaki Advanced Radiation Research Institute, Japan Atomic Energy Agency. The energy spectrum of the source neutron has a continuous distribution below the main peak. For precise response evaluation to the peak energy neutrons, contribution of the neutrons in the continuous distribution must be subtracted from the total response of the neutron detectors or monitors to be calibrated. Therefore, energy spectrum measurement of the quasi-monoenergetic source neutron is necessary.

The neutron energy spectrum was measured by the time-of-flight (TOF) method using the organic liquid scintillation detector (BC501A) since neutrons could be separated from gamma-rays by using the rise time difference of the detector signals. The measurement of the energy spectrum below 10 MeV was generally difficult due to various restrictions on the measurement circuit modules. Then, the measurement system was improved so as to extend the energy range down to a few MeV in the previous experiments. Using the improved measurement system, precise measurement of the source energy spectrum down to 4.5 MeV was performed.

In the TOF measurement, the anode signal of the photomultiplier tube (PMT) of the detector was used as the stop signal, and the chopper signal of the cyclotron was used as the start signal. In the improved measurement system, the method with two different amplifier's gains was applied. The dynode signal of the detector was divided into two signals. They were led to amplifiers with different gain. One amplifier's gain was set to normal gain and other set to 10 times gain. The high gain was used for spectrum measurement in the lower energy range. At TIARA, 45 MeV quasi-monoenergetic neutron beam was used for the measurement. TOF, pulse height and rise time of the signals for both measurement circuit systems were recorded together with counts of the neutron fluence monitor by using the MPA-3 data acquisition system.

In the analysis, overlap of the next beam bunch was excluded by event selection in the two-dimensional distribution on TOF versus pulse height. A TOF region corresponded to only one beam bunch was selected. Lower pulse height region was excluded to reject the overlap events. In the analysis, energy dependent (TOF dependent) lower limit of the pulse height could be applied since maximum

pulse height of the overlap events of low energy was lower than the Analogue-to-digital converter threshold. After the event selection, the TOF was converted into the neutron energy. The pulse height was also calibrated to calculate detection efficiency of the BC501A detector. The neutron energy spectra were obtained by correcting the detection efficiency and the live time and by normalization of the beam intensity. Finally, the neutron energy spectrum was obtained by combining both spectra for normal gain and high gain data.

Figure 1 shows the finally obtained neutron energy spectrum after combining both spectra for different gain. The lower energy range of the spectrum measurement was extended down to 4.5 MeV. The neutron fluence of the main energy peak agreed with the result of the absolute measurement within 5%.

In conclusion, the quasi-monoenergetic source neutron spectrum with 45 MeV peak was successfully measured and evaluated precisely down to 4.5 MeV by using the improved measurement system.

References

- 1) M. Baba et al., Nucl. Instrum. Meth. Phys. Res. A 428 (1999) 454.
- 2) Y. Shikaze et al., Radiat. Prot. Dosim. 126 (2007) 163.
- 3) Y. Shikaze et al., J. Nucl. Sci. Tech. Suppl. 5 (2008) 209.

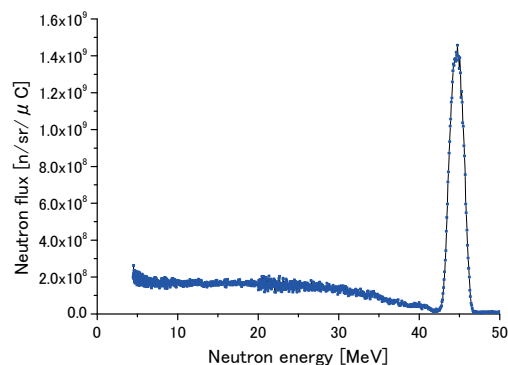


Fig. 1 Measured energy spectrum of 45 MeV quasi-monoenergetic neutron beam at TIARA. Energy range of the spectrum was extended down to 4.5 MeV.

4 - 31 Measurements of Low Energy Neutron Spectra of Quasi-Monoenergetic Neutron Fields by the TOF Method at TIARA

T. Matsumoto ^{a)}, A. Masuda ^{a)}, H. Harano ^{a)}, Y. Unno ^{a)}, M. Hagiwara ^{b)}, T. Sanami ^{b)}, Y. Shikaze ^{c)}, Y. Tanimura ^{c)}, M. Yoshizawa ^{c)}, M. Baba ^{d)} and K. Mizuhashi ^{e)}

^{a)}National Metrology Institute of Japan, National Institute of Advanced Industrial Science and Technology, ^{b)}High Energy Accelerator Research Organization, ^{c)}Department of Radiation Protection, NSRI, JAEA, ^{d)}CYRIC, Tohoku University, ^{e)}Department of Advanced Radiation Technology, TARRI, JAEA

Precise measurements for high energy neutrons are important in studies on the neutron dose estimation around large accelerator facilities such as J-PARC, nuclear data, exposure in aircrafts and neutron induced soft error rate in semiconductor devices. High energy quasi-monoenergetic neutron fields at energies of 45 MeV, 60 MeV and 75 MeV at cyclotron facility in TIARA are promising candidates for reference fields in order to calibrate measuring devices ¹⁾. The peak neutron fluence was measured with a proton recoil telescope and a liquid scintillator ^{1,2)}. However, it is also necessary to precisely evaluate neutron spectra of the low energy region in the field, because most of neutron dosimeters have large sensitivity for low energy neutrons. In TIARA, quasi-monoenergetic neutrons were produced by the ⁷Li(p, n) reaction. In the previous experiments with the TOF method, it was difficult to measure the neutron spectra below approximately 10 MeV by limitations for pulse intervals of ion beams from the AVF cyclotron and the distance from the neutron production target. In the present experiments, it was possible to measure the neutron spectrum below 10 MeV by the TOF method, because ion pulse with intervals from the AVF cyclotron improved to over 10 μs by using S- and P-chopper system developed by Kurashima et al ³⁾. The neutron spectrum of low energy region in the field was measured with a time of flight (TOF) method using a liquid organic scintillator (3"×3" NE213). The NE213 was placed 13.7 m away from the target. The response function of the NE213 was determined by calculation with the SCINFUL-QMD code ⁴⁾. Figure 1 shows the neutron spectrum obtained by the TOF method. The evaporation spectrum is also shown below 4 MeV. In Fig. 1, minimum energy is 1.8 MeV. However, it is possible to measure neutrons with energy range from 1 keV to 1 MeV by using a ⁶Li-glass scintillator. We also obtained the neutron spectrum measured with a Bonner sphere spectrometer by means of an unfolding method ⁵⁾. After measurements with the ⁶Li-glass scintillator, the TOF and unfolding methods will be compared.

A new calibration method with the TOF method was also developed in high energy quasi-monoenergetic neutron fields. This method can remove effects due to the low energy neutrons in the fields from calibration results. Figure 2 shows the TOF spectrum measured with the neutron survey meter "PRESCILA⁶⁾" in the 60 MeV

quasi-monoenergetic neutron field. The peak due to the 60 MeV neutrons are successfully observed. However, the calibration method is not applied to the neutron detector with a neutron moderator.

A sandwich spectrometer has been also developed to measure the low energy neutrons in the quasi-monoenergetic neutron field. The spectrometer consists of a ³He proportional counter and two Si detectors. It is necessary to more precisely evaluate the low energy neutron spectra to improve the reliability of the experimental results.

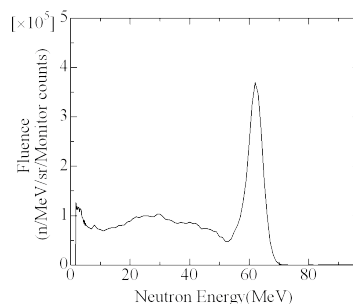


Fig. 1 Neutron spectrum measured by the TOF method in the 60 MeV quasi-monoenergetic neutron field.

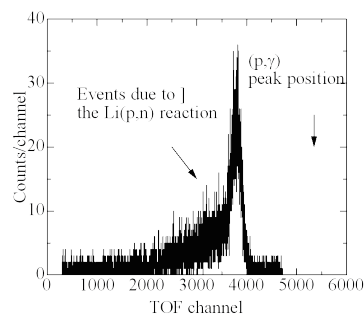


Fig. 2 TOF spectrum measured with the PRESCILA.

References

- 1) H. Harano et al., Radiat. Meas. 45 (2010) 1076-82.
- 2) Y. Shikaze et al., Nucl. Instrum. Meth. Phys. Res. A 615 (2010) 211-19.
- 3) S. Kurashima et al., Proc. CYCLOTRONS 2010, MOPCP090 (2010) 233-35.
- 4) D. Satoh et al., JAEA-Data/Code 2006-023 (2006) 43p.
- 5) M. Reginatto, et al., Nucl. Instr. Methods A476 (2002) 242-46.
- 6) R. H. Olsher, et al., Health Phys. 86(6) (2004) 603-12.

4 - 32 Measurements of Neutron and Charged Particle Production Cross Sections on Be and Fe Bombarded with 13 MeV/nucleon ²⁰Ne Beam

Y. Iwamoto ^{a)}, M. Hagiwara ^{b)}, N. Matsuda ^{a)}, N. Shigyo ^{c)}, T. Nishizawa ^{c)},
T. Sanami ^{b)}, H. Nakashima ^{a)} and Y. Sakamoto ^{a)}

^{a)} Division of Nuclear Data and Reactor Engineering, NSED, JAEA,

^{b)} Radiation Science Center, KEK,

^{c)} Department of Applied Quantum Physics and Nuclear Engineering, Kyushu University

There is currently an interest in low-energy heavy ion reactions with the availability of newly developing techniques such as the acceleration of intense (~1 particle μ A) and low-energy (~15 MeV/nucleon) rare isotope beams at Michigan State University (MSU). It will be sometimes desirable to allow personnel to work around experimental endstations where heavy ions interact with targets. It is useful to predict radiation levels around such new facilities easily and reliably.

The Monte Carlo-based heavy ion transport code system PHITS¹⁾ has been typically used to predict radiation levels around high-energy (above 100 MeV/nucleon) heavy-ion accelerator facilities. However, predictions by PHITS around low-energy (10 MeV/nucleon) heavy-ion reactions have not yet been investigated due to lack of experimental data. In this report, we describe the measurements of neutron and charged particle production double differential cross sections (DDXs) from 15- μ m-thick ⁹Be and 1- μ m-thick ^{nat}Fe targets bombarded with 13 MeV/nucleon ²⁰Ne and comparisons between the experimental data and calculation results.

The experiments were carried out at the HB-1 beam line at the AVF cyclotron of TIARA. The target was installed in a vacuum chamber. For the neutron measurement, the NE213 organic liquid scintillators (5.08 cm in diameter and 5.08 cm in length) were placed in directions of 15°, 30°, 60°, 90° and 120° at a distance of 2.0 m from the target to measure the light outputs for neutrons. Neutron energy was determined by the time-of-flight (TOF) method. A 2-mm-thick plastic scintillator NE102A placed in front of the neutron detector tagged events induced by a charged particle. The events of neutrons and γ -rays were separated

by using a pulse shape discrimination technique and neutron energy spectra were analyzed by the TOF method.

For charged particle measurements, the telescope detectors composed of three Si strip detectors (SSDs) with different thickness (40, 250 and 1,000 μ m) and a 2 cm thick lutetium yttrium orthosilicate LuY2-xSiO5:Ce (LYSO) scintillator were placed in directions of 30°, 60°, and 90° in a vacuum chamber. Each charged particle was identified by the two dimensional plot with light outputs of the detector. The energy of charged particle was determined by the pulse height related with the deposit energy in detectors.

Figure 1 shows the neutron energy spectra with comparison between measured and calculated results using the JQMD model and the evaporation model, GEM. The calculated results generally overestimated the measured data due to the emission of many neutrons following the decay of excited fragments with high energies. Figure 2 shows the triton production DDXs for Be target. Calculated results at 30° give good agreement with the experimental data, while that at 90° gives large underestimation. From Fig. 3, it was found that JQMD+GEM model could not produce heavier particles due to the poor fragment production process in the models.

We conclude that present JQMD+GEM model should not be applied to the low-energy heavy-ion incident reactions. Our data will be used for the model improvement of the nuclear reaction and the fragmentation production reaction.

Reference

- 1) K. Niita et al., JAEA-Data/Code 2010-022 (2010).

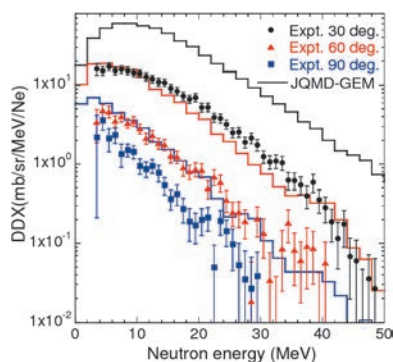


Fig. 1 Neutron DDX for Be target.

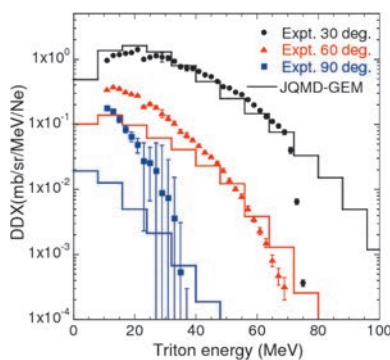


Fig. 2 Triton DDX for Be target.

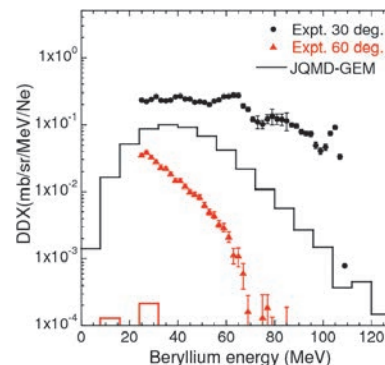


Fig. 3 Beryllium DDX for Be target.

4 - 33 Measurement of Thick Target Neutron Yields by 10 MeV Deuteron Incidence on Tungsten

N. Shigyo ^{a)}, T. Nishizawa ^{a)}, K. Ishibashi ^{a)}, Y. Iwamoto ^{b)}, N. Matsuda ^{b)},
Y. Sakamoto ^{b)} and M. Hagiwara ^{c)}

^{a)} Department of Applied Quantum Physics and Nuclear Engineering, Kyushu University,

^{b)} Division of Nuclear Data and Reactor Engineering, NSED, JAEA,

^{c)} High Energy Accelerator Research Organization, KEK

The collision of deuteron beam having around tens of MeV with a light element target has promise as an intense neutron generator. Estimation of neutrons generated by bombardment of accelerator components and beam dumps with beam is essential for radiation safety. Thick target neutron yields (TTNYs) has been measured for some elements for 5- and 9-MeV deuteron incidence¹⁾. However, there is no experimental data in the energy region for a tungsten, which is one of possible materials of beam dump. In this study, we measured TTNY of 10 MeV deuteron incidence on a thick tungsten target.

The experiment was performed at the 1st heavy ion room of TIARA. Experimental setup is illustrated in Fig. 1. The intensity of deuteron beam was about 100 nA. The thickness of a tungsten target was 0.15 mm, in which a 10 MeV deuteron completely stopped. The target was put in a vacuum chamber in order to avoid energy loss of deuteron in the air. A 20 mm thick aluminum flange was set downstream of the target at 0° as a beam stopper for other thin target experiments.

Two NE213 scintillators with 5.08 cm thickness and 5.08 cm diameter were adopted as neutron detectors. Measurement directions were 0°, 15°, 30° and 60°. Flight paths between the target and detectors were from 2.0 to 5.0 m depending on available area in the room.

In order to evaluate neutrons scattered from the floor, wall and other apparatus in the room, a 30 cm-long-iron block was set between the target and each detector.

Time difference between timing signal of neutron detectors and deuteron beam pick-up from the accelerator, and light outputs of neutron detectors were stored and analyzed after the experiment. Because the NE213 scintillator is also sensitive to γ -rays, neutron events were separated from γ -ray ones using pulse shape discrimination.

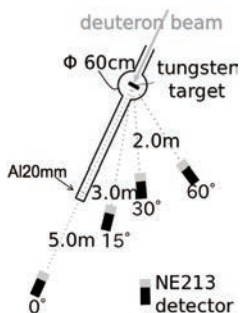


Fig. 1 Experimental setup at the 1st heavy ion room.

Detection efficiency was obtained by calculation with SCINFUL-QMD²⁾. Neutron energy was determined by time-of-flight technique. The energy spectra of neutrons from the target were obtained by subtraction of spectra with the iron block measurement from those without the block.

Measured data are shown in Fig. 2. The effect of neutron attenuation by the 20 mm aluminum flange was corrected at 0°. TTNY data below 6 MeV at 0° was not analyzed because neutron events by collision of deuteron with accelerator components were overlapped on the TOF spectrum. These events were not observed at 15°, 30° and 60°. It seemed that accidental collisions of beam with accelerator components occurred on upstream of the target. Calculation results by PHITS³⁾ with QMD model and TALYS⁴⁾ with An-Cai deuteron optical potential are also given. Both calculations reproduce trend of experimental data, however, overestimate at 15°, 30° and 60°.

References

- 1) N. Shigyo et al., J. Kor. Phys. Soc. 59 (2011) 1725.
- 2) D. Satoh et al., JAEA-Data/Code 2006-023 (2006).
- 3) K. Niita et al., JAEA-Data/Code 2010-022 (2010).
- 4) A.J. Koning et al., Proc. Int. Conf. Nucl. Data Sci. Tech. Nice, France 2007 (2008) 211.

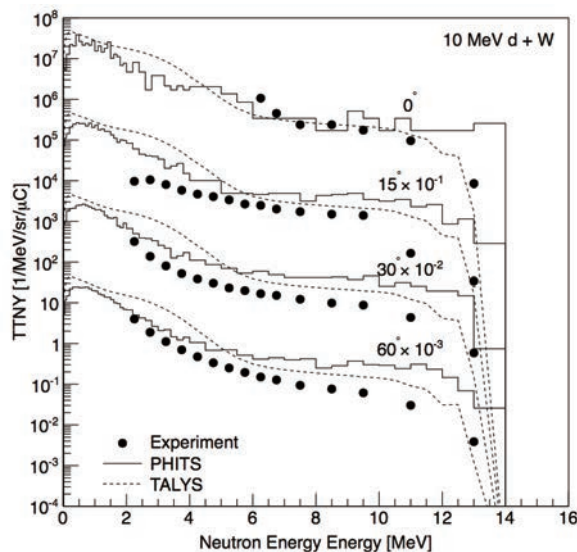


Fig. 2 TTNY from 10 MeV deuteron incidence on a tungsten target. Marks, solid and dashed lines stand for experimental data, calculation by PHITS and TALYS codes, respectively.

4 - 34 Development of Spatial Resolution Test-chart and Novel Fluorescent Converter Plates for Neutron Radiography

T. Sakai^{a)}, R. Yasuda^{a)}, H. Iikura^{a)}, T. Nojima^{a)}, M. Matsubayashi^{a)}, M. Koka^{b)},
T. Satoh^{b)}, T. Ohkubo^{b)}, Y. Ishii^{b)} and S. Yamamoto^{c)}

^{a)} Materials Science Research Division, QuBS, JAEA,

^{b)} Department of Advanced Radiation Technology, TARRI, JAEA,

^{c)} Environment and Industrial Materials Research Division, QuBS, JAEA

We have developed spatial resolution test-chart and novel fluorescent converter plates for neutron radiography. Both devices are coated by a thin Gd layer as a neutron absorber. The layer is optically transparent and expected to play a role of neutron converter for fluorescent plates. Our preliminary result shows that the developed fluorescent converter is very promising.

中性子ビームの透過強度分布をイメージ(像)として撮影する中性子ラジオグラフィ(NRG)法は、学術研究や産業利用をはじめ、水や水素などを可視化する非破壊分析法として良く用いられている手法の一つである¹⁾。特に、燃料電池研究などにおいては、10 μm 程度の高い空間分解能が必要とされており、高解像度化のための技術開発が望まれている。一方、プロトンマイクロビームによる微細加工技術は、レジスト材に対してアスペクト比の高い加工が可能であり、中性子光学用の素子を作製するのに有効な手法と考えられる。

昨年度においては、プロトンマイクロビームを利用して NRG の空間分解能を評価するためのテストチャートとして、線幅 50 μm から 3 μm までのラインペア(Line & Space)の作製に成功した²⁾。今年度においては、作製したテストチャート上に中性子吸収体の成膜を行った。中性子吸収体としては、吸収断面積の大きい Gd を選択し、レーザーアブレーション蒸着により、微細加工済の PMMA 基板に 1~2 μm 厚で成膜を行った。顕微鏡観察を行った結果を Fig. 1 に示す。蒸着した Gd は酸化物になっているようで、透明であった。

さらに、光学的に透明な中性子吸収体を成膜できることを利用して、中性子ビームを可視光に変換する蛍光コンバーターの高度化を行った。蛍光コンバーターは、中性子を捕捉して α 粒子を放出する核種(${}^6\text{Li}$, ${}^{10}\text{B}$ など)と蛍光物質の混合物であり、高分解能化のためにはコンバーター材を極力薄くする必要があるが、発光量は厚さに依存するため、従来は数十 μm 程度まででしか薄くできなかった。一方、Gd はオージェ電子放出を伴う中性子捕捉断面積が非常に大きいため、コンバーター材の表面を薄くコーティングすることで、発光量の向上が見込め、薄いコンバーター材でも十分な明るさを得ることができると思われる。そこで、 ${}^6\text{LiF}$ と ZnS(Ag) からなる 15 μm 厚の蛍光コンバーター材に、1 μm 厚の Gd 蒸着を施した。NRG に適用できるかの確認実験は京都大学原子炉実験所で行った。その結果、膜厚当たりの発光量増加が認められ、高分解能用の蛍光コンバーターとして十分利用できることが判った。Figure 2 に中性子ビームによる発光を示す。

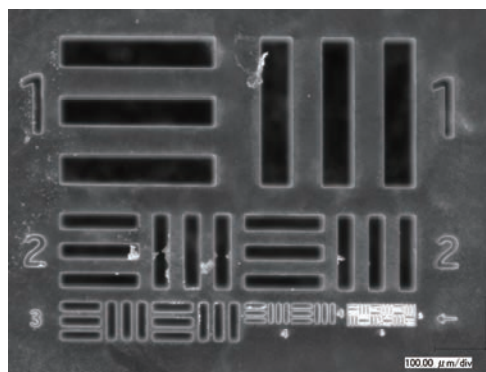


Fig. 1 Microscopic photograph of a fabricated test-chart on 75 μm -thick PMMA sheet. The surface is coated by 2 μm -thick neutron absorber (Gd).

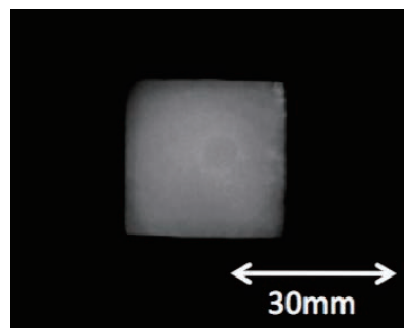


Fig. 2 Photograph of light emission from the fabricated fluorescent converter plate during neutron beam bombardment. The thickness of converter material is 15 μm .

今後、研究炉 JRR-3 の再稼働後、空間分解能評価用のテストチャートに関しては、実素子として活用する予定である。また、新規に開発した蛍光コンバーターの特性評価も同様に行う予定である。本研究は、科研費(22604010)の助成を受けたものである。

References

- 1) (社)日本アイソトープ協会 理工学部会 中性子ラジオグラフィ専門委員会編、「中性子イメージング技術の基礎と応用」(2009年)。
- 2) T. Sakai et al., JAEA Takasaki Annu. Rep. 2010 (2012) 165.

Response Studies of CR-39 Track Detectors Irradiated Heavy Ions under Vacuum

A. Hattori^{a)}, M. Kanasaki^{a, b)}, H. Sakaki^{b)}, Y. Fukuda^{b)}, A. Yogo^{b)}, S. Jinno^{b)},
S. Kurashima^{c)}, T. Kamiya^{c)}, K. Kondo^{b)}, K. Oda^{a)} and T. Yamauchi^{a)}

^{a)} Graduate School of Maritime Sciences, Kobe University,

^{b)} Advanced Beam Technology Division, QuBS, JAEA,

^{c)} Department of Advanced Radiation Technology, TARRI, JAEA

CR-39 is a one of the well-known ion track detector with excellent dynamic range in ion track diagnosis. For example, the CR-39 is possible to diagnosis for low-LET particles such as a proton under 27 MeV. Furthermore, this detector has diagnostic sensitivity only for ions; there is no sensitivity in electrons and X-rays.

In recent years, laser-driven acceleration systems have generated beams with energies up to tens-MeV ions¹⁾ from laser-plasma interaction. These ions are combined with X-ray and high energy electrons. So, for the ion diagnostics in the laser-driven ion acceleration, these characteristics of the CR-39 are useful in many experiments. Because we equip the CR-39 under vacuum environment, we have to study that the characteristic change of the CR-39 on this environment for accurate measurement. Previously, we experimentally verified about a reduction of the detection sensitivity called "vacuum effect" which was checked with a just low energy and light-ion such as proton and helium^{2,3)}. In this paper, we report the vacuum effect with a heavy-ion, such as carbon.

The vacuum effect was measured by using multilayer (three layer) stack of CR-39 (HARZLAS TD-1: produced by FUKUBI chemistry industry). And carbon ion of 320 MeV was irradiated to the stack in a vacuum chamber of JAEA TIARA cyclotron.

This effect occurs depending on the time length of pre-irradiation storage in vacuum. In order to change the vacuum expose time, after the stacks were held in the vacuum ($<6.7 \times 10^{-4}$ Pa) for two hours, we irradiated every eight domains one by one sequentially in every hour. That is, the irradiation data of time-of-exposure from 2 to 10 hours is measured. Finally, One hour passed after the end of irradiation, the vacuum was leaked and the stacks took out from the chamber.

The analysis result is shown in Fig. 1. Vertical axis is the radius of a particle track (etch pit), on the 1st, 2nd and 3rd layer of the stacks, horizontal axis is the vacuum exposure time before irradiation. It is shown that the time contributes as one of the reduction parameter in the carbon's etch pit radius; this means that the vacuum effect is also seen in case of heavy ion irradiation very clearly.

From now on, it will be required that the response function of the detection sensitivity that depends on the vacuum exposure time will be researched.

References

- 1) Y. Fukuda et al., Phys. Rev. Lett. 103 (2009) 165002.
- 2) T. Yamauchi et al., Nucl. Tracks Radiat. Meas. 20 (4), (1992) 615-17.
- 3) B. Dorschel et al., Radiat. Meas. 40 (2005) 234-39.

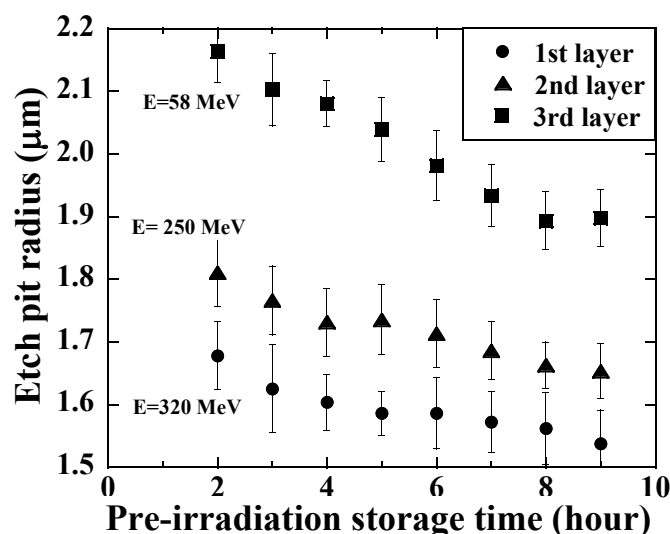


Fig. 1 Etch pit radius in dependence on pre-irradiation storage times in the vacuum with carbon ions.

4 - 36 Measurement of Radio Wave Reflection Due to Rock Salt and Ice Irradiated by an Electron Beam for an Ultra-high-energy Neutrino Detector

T. Tanikawa^{a)}, M. Chiba^{a)}, T. Kamijo^{a)}, F. Yabuki^{a)}, O. Yasuda^{a)}, H. Akiyama^{b)}, Y. Chikashige^{b)}, T. Kon^{b)}, Y. Shimizu^{b)}, M. Utsumi^{c)} and M. Fujii^{d)}

^{a)} Graduate School of Science and Engineering, Tokyo Metropolitan University,
^{b)} Faculty of Science and Technology, Seikei University,
^{c)} Department of Applied Science and Energy Engineering, School of Engineering, Tokai University,
^{d)} School of Medicine, Shimane University

Ultra-high-energy (UHE) cosmic rays ($E > 4 \times 10^{19}$ eV) interacts with cosmic microwave background radiation. The interaction generates neutrino (UHEν) in this Greisen, Zatsepin, and Kuzmin (GZK) cut-off process¹⁾. The UHEν generated in this process is called GZKν. The energy of GZKν is between 10^{16} and 10^{20} eV. Since flux of GZKν is very low ($\approx 1/\text{km}^2$ day), we need a huge detector (50 Gt) to detect them. GZKν gives temperature rise along the hadronic and electromagnetic shower when it enters into rock salt or ice. To realize such a huge detector we plan to utilize a salt dome in Fig. 1, the Antarctic ice sheet and the moon crust. Permittivities of them are increased proportionally to the temperatures in ionization processes of the GZKν shower. It is expected by Fresnel's formula that radio wave reflects at the irregularity of the permittivity in the medium²⁾. In order to check this, the experiment by an electron beam was conducted.

Open end of the coaxial tube (19.94 mm inner diameter of external conductor, filled with rock or ice) was irradiated by a 2 MeV perpendicular electron beam produced by the electron accelerator located at Takasaki Advanced Radiation Research Institute, Japan Atomic Energy Agency. The electron beam heated up the medium 5 mm deep from the upper open end. Radio wave of 435 MHz with 10^{-4} W was introduced to the coaxial tube and measured the reflection from the open end. The permittivity of the measured rock salt powder and ice was almost equal ($\epsilon' \approx 3.2$). Temperature at position of 2 mm from the upper open end was measured by a thermo couple. Power difference of reflected radio wave was measured by null method and a minute gap from zero without the irradiation was recorded by a spectrum analyzer.

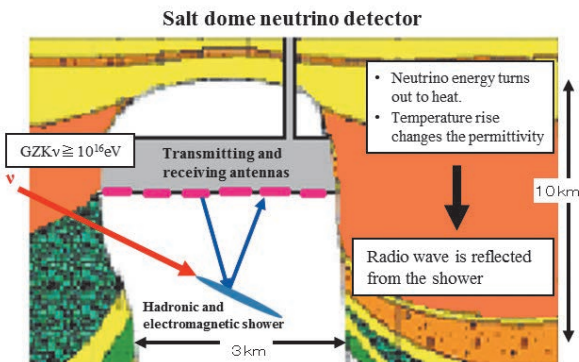


Fig. 1 Radar system for salt dome.

In order to increase signal to noise ratio, the time domain data was taken with a step of 0.125 ms and transformed by FFT with 1,024 points (=128 ms). The electron beam was the energy of 2 MeV and the current of 1 mA. The energy for 0.128 s of the beam irradiated to the dielectric material in this experiment was 3.5×10^{18} eV (≈ 0.54 J/s).

Refractive index n_2 (square root of permittivity) near the open end becomes larger than n_1 far from the open end. The reflected power ratio of radio wave (Γ) is presented by Fresnel's formula Eq. 1.

$$\Gamma = \frac{(n_1 - n_2)^2}{(n_1 + n_2)^2} \tag{1}$$

The measured Γ was proportional to the square of temperature rise from the room temperature (ΔT) in Fig. 2. They are consistent with expected values from Fresnel's formula Eq. 1 for rock salt. In the case of ice, Γ was 10 times larger than expected value from Fresnel's formula.

We found the radio wave reflection effect in ice as well as in rock salt for an UHEν detector. Hence, the Antarctic ice sheet or a salt dome could be a good candidate of detection media. And, from this result, the radio wave reflection by entrance of GZKν to energy is calculable.

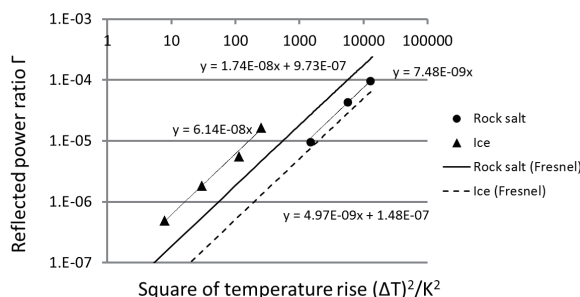


Fig. 2 Γ vs. $(\Delta T)^2$. Measured values of Γ (with the error of $\pm 3\%$) are compared with Fresnel's formula. A coaxial tube filled with rock salt or ice was irradiated by the electron beam for 60 s. Γ and ΔT values are at 60 s. Ice was cooled to 223 K by dry ice and rock salt to 288 K at first.

References

- 1) K. Greisen, Phys. Rev. Lett. 16 (1966) 748; G.T. Zatsepin, V.A. Kuzmin, Zh. Eksp. Teor. Fiz. Pis'ma Red. 4 (1966) 114 (Sov. Phys. JETP Lett. 4 (1966) 78).
- 2) M. Chiba et al., Nucl. Instrum. Meth. A662 (2012) S222-25, doi:10.1016/j.nima.2010.11.165.

4 - 37 Effect of Temperature on the Response of Alanine Dosimeters under Low Dose and Long Time Irradiation

H. Seito^{a)}, Y. Nagao^{a)}, Y. Momoki^{b)}, H. Kaneko^{a)},
K. Nakagawa^{b)} and T. Kojima^{a)}

^{a)} Department of Advanced Radiation Technology, TARRI, JAEA,
^{b)} Graduate School of Human Development and Environment, Kobe University

Applications of alanine dosimeter are widened to dosimetry in space environment and so on. The space environment provides various parameters that are not experienced on Earth, such as high temperature and severe radiation. Effect of temperature during and after irradiation between 20 °C and 80 °C on the dose response of alanine dosimeters was investigated under low dose of about 10-20 Gy and long time of about 100 hours irradiations¹⁾. Alanine dosimeters were manufactured with a composition of DL- α alanine and polystyrene with dimensions of 3 mm diam. and 30 mm long held in a 4 mm thick polystyrene capsule for electron equilibrium. The gamma-ray irradiation was carried out using a ⁶⁰Co plaque source at a dose rate of about 0.1 Gy/h in air in the air-conditioned irradiation box. The temperature dependence of dose response of alanine dosimeters is shown in Fig. 1. The response is normalized to that at 20 °C. The broken line shows a straight line with a temperature coefficient of +0.24 %/°C reported by Kojima et al.²⁾. Differences in dose response to that irradiated at 20 °C were within $\pm 2\%$ for irradiation temperature of 60 °C or less, and $\pm 5\%$ at irradiation temperature of 80 °C, although the response was nonlinear to dose and 5-8% lower than that calculated based on the irradiation temperature coefficient of +0.24 %/°C. Fading curves for storage at different temperature after irradiation at 20 °C are shown in Fig. 2. The dose response decreases with elapsed time only for the storage temperatures of 40 - 80 °C. On the other hand dose responses are almost constant for storage at almost equivalent temperatures to irradiation temperature. This result implies that the attenuation of radical generated in alanine at high temperatures is occurred during irradiation. The apparent ESR signal for the number of radical generated in alanine during irradiation under high temperature was estimated on the basis of result as shown in Fig. 2. The estimated dose response of alanine dosimeters is shown in Fig. 3. The responses at 40 °C, 60 °C, and 80 °C are corrected using fitting parameters for fading curves at three storage temperatures: 40 °C, 60 °C, and 80 °C. Irradiation temperature coefficient is calculated as $+0.27 \pm 0.03$ %/°C from linear fitting in Fig. 3. This result is consistent with the previously reported coefficient, 0.24 %/°C. When a stable radical of the dose response under high irradiation temperature was estimated on the basis of the effect of storage temperature after irradiation taking into account the known irradiation temperature coefficient, dose evaluation using alanine dosimeter should be more accurate even

suffering from combined temperature effects during and after irradiation.

References

- 1) Y. Nagao et al., *Radioisotopes* 61 (2012) 173.
- 2) T. Kojima et al., *Appl. Radiat. Isot.* 43 (1992) 863.

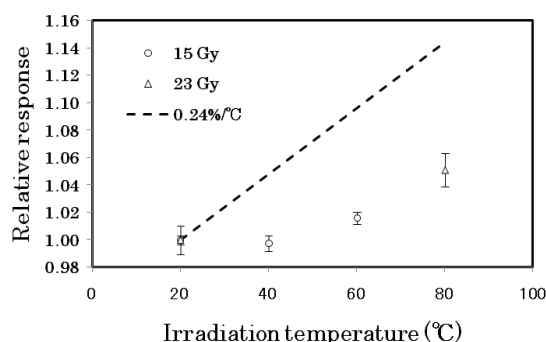


Fig. 1 Dose response of alanine dosimeters as a function of irradiation temperature.

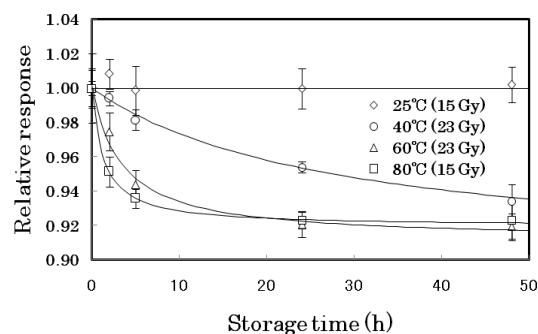


Fig. 2 Fading curves for storage at different temperatures after irradiation at 20 °C.

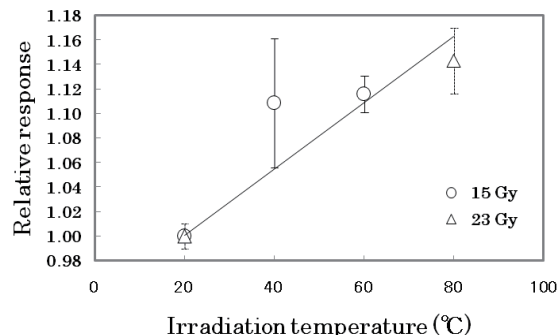


Fig. 3 Estimated dose response of alanine dosimeters as a function of irradiation temperature.

4 - 38 Status Report on Technical Developments of the JAEA AVF Cyclotron

S. Kurashima, H. Kashiwagi, N. Miyawaki, S. Okumura, K. Yoshida, Y. Yuri, T. Yuyama, T. Ishizaka, I. Ishibori and T. Nara

Department of Advanced Radiation Technology, TARRI, JAEA

Beam manipulation for measurement of the whole transverse acceptance

In acceptance measurement, an arbitrary small portion in the beam from an ion source is cut out by a pair of position and angle slit so that a small area in a phase plane is injected to the cyclotron. The positions of the slits are scanned to determine the distribution of relative transmission in the phase plane. Since the injection-beam emittance does not cover the whole acceptance, only the part of acceptance overlapped with the emittance was able to be measured¹⁾. Therefore the injection beam needs to be scanned in the phase planes using a steering magnet to expand the effective emittance. The result of a test experiment showed that the beam was manipulated by the magnet in the horizontal and vertical phase planes with little emittance distortion, and the beam was able to be scanned in synchronization with the acceptance measurement.

Beam phase measurement for investigation of influence of the buncher on the beam phase width

The beam intensity distribution in the acceleration phase was measured to investigate influence of the buncher on the beam phase width. The measurement was carried out with two scintillation detectors²⁾ which is located inside and outside the cyclotron and the buncher was operated to maximize the beam current. The peak height with the buncher was several times as high as that without the buncher for the both measuring positions since the buncher compresses the DC beam to increase the beam current accelerated with the cyclotron. However, although the full beam phase width with the buncher had been expected to be narrower than that without the buncher, the difference of that was not observed, and then the full beam phase width was expanded up to the full acceptance of the acceleration phase resulting in a wide energy spread. Since the beam in the cyclotron was expanded in radial direction due to the energy spread, a part of the accelerating beam can only pass through the deflector electrode with the small radial acceptance. As a result, the measured beam phase widths outside the cyclotron were narrower than those inside the cyclotron. Therefore the influence of the buncher on the beam phase width disappears by the typical buncher operation to maximize the beam current and the full beam phase width in the cyclotron can be narrowed by mechanically restricting the radial acceptance.

Quick change of heavy-ion beams using scaling method

Heavy ion microbeams of carbon, neon and argon formed

by using a micro aperture system are used frequently at the HZ port. The average beam time, less than three hours, is shorter than the cyclotron tuning time of three hours and this means frequent retuning of the cyclotron causing inefficient use of the facility. In order to reduce the tuning time, the scaling method has been introduced to change the ion species having various mass to charge ratios (M/Q) in a short-time via a limited operation described below. An acceleration frequency and high voltage values of equipment such as an ion source, dee electrodes and a deflector electrode are scaled proportionally to the difference of M/Q . The cyclotron requires retuning of trim coils, which create the isochronous field, without changing a magnetic field strength at the extraction radius. No change is basically required in the beam transport line since the magnetic rigidities of the ion beams are kept constant. The key point of the scaling method is short-time retuning of the trim coils, and a beam phase measurement system using a lock-in amplifier has been developed to confirm isochronism quickly. After usual tuning of a 220 MeV $^{12}\text{C}^{5+}$ beam, a 255 MeV $^{20}\text{Ne}^{7+}$, a 335 MeV $^{20}\text{Ne}^{8+}$ and a 440 MeV $^{40}\text{Ar}^{13+}$ beams were extracted from the cyclotron in sequence using the scaling method. The trim coils were tuned well for all ion species as shown in Fig. 1. The beam change to the other ion species was completed within 20 minutes.

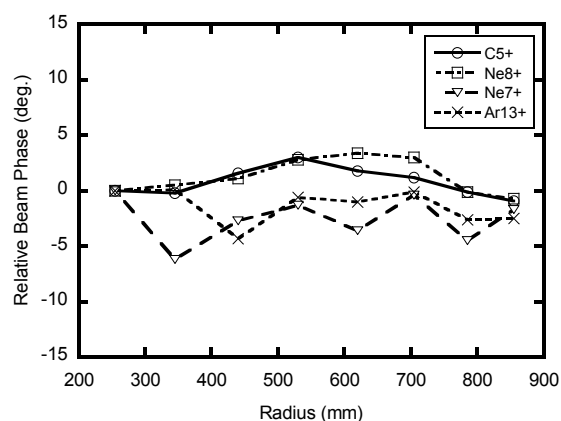


Fig. 1 Relative beam phase in the cyclotron measured by the phase probe and the lock-in amplifier. Good isochronism was confirmed for each ion species.

References

- 1) H. Kashiwagi et al., Proc. 8th Annu. Meet. Part. Accel. Soc. Jpn. 8 (2011) MOPS079.
- 2) N. Miyawaki et al., Proc. 5th Annu. Meet. Part. Accel. Soc. Jpn & 33rd Linear Accel. Meet., (2008) 400-03.

4 - 39 Development of Beam Generation and Irradiation Technology for Electrostatic Accelerators

K. Yamada, A. Chiba, A. Yokoyama, Y. Saitoh,
Y. Ishii, T. Satoh, T. Ohkubo and S. Uno

Department of Advanced Radiation Technology, TARRI, JAEA

Cluster Ion Acceleration

We investigate the charge exchange and destruction mechanism on the MeV energy cluster ions colliding with gas targets to select the suitable charge exchange gas which has a small destruction cross section (σ_d) and a large charge exchange cross section without destruction¹⁾. In this financial year, the destruction cross sections for 0.065-0.750 MeV/atom carbon cluster ions C_n ($n=4, 8$) in collisions with a helium, a nitrogen and a xenon gas targets were evaluated from a beam transmission through the tandem accelerator. As a result, it was revealed that there was no energy dependence of the cross sections in the energy range studied shown in the Fig. 1, whereas they depended on target gases and cluster sizes as we reported previously²⁾. The results indicate helium gas should be effective for cluster ion acceleration over the energy region of the TIARA 3 MV tandem accelerator. Next financial year, we will improve the measurement accuracy for the production cross sections to consider a charge exchange mechanism of a cluster ion.

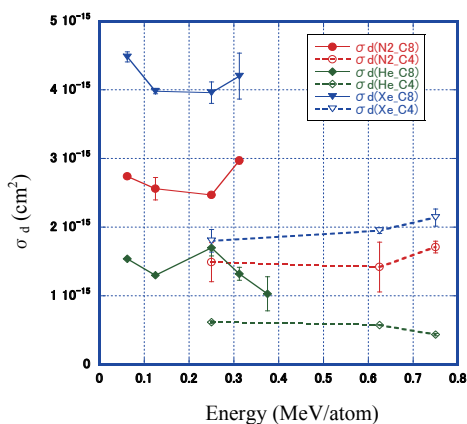


Fig. 1 The destruction cross section of C_n ($n=4, 8$).

Beam Line for Cluster Ion Experiments

We have developed a new beam line connected to 400 kV Ion Implanter for the cluster ion experiments. The existing bending magnet (BM I-1) was replaced with a new switching magnet which has 0° and $\pm 45^\circ$ beam lines to transport ion beam to -45° beam line of the opposite side of IA line. The maximum magnetic field of the switching magnet is 1.4 T (93.2 MeVamu at $\pm 45^\circ$ line). Therefore, it can bend C_{60}^+ up to 120-keV for the $\pm 45^\circ$ beam line. The deflection electrodes and double slits were installed to produce pulsed ion beams. The cluster beam was experimentally transported to the -45° beam line, and the beam current was comparable with the IA line. We will provide the beam line to users from the next fiscal year.

Emittance Measurement Using the Fine Cu Wire

The enhancement of brightness of proton beam that is accelerated by Singled-ended Accelerator is attempted in order to increase beam current and reduce the beam size at focusing point in Light Ion Microbeam System. The parameter optimization of the ion source in the accelerator is a key point for the enhancement. The emittance and brightness of the proton beam are measured to evaluate the effect of ion source parameters in the accelerator. In 2011 fiscal year, the estimation of 1 MeV proton beam emittance was carried out using a fine Cu wire with 0.1 mm in diameter that was moved by a stepping motor. The emittance was estimated by numerical analyses on the measurement data of beam current as a function of the wire position. The wire position and the beam current according to its position were measured by moving the fine wire in perpendicular direction to the beam passing through a multi-hole slit. In the experiments, the two sets of the relation were obtained at two different wire positions with 400 mm apart to traveling beam direction so as to calculate divergence angle of the proton beam. The 70% X-direction emittance diagram of 1 MeV proton beam was shown in Fig. 2 as a calculation result. The emittance was estimated to be 1.9 mm mrad at this diagram. This result showed the emittance was measured using the thin Cu wire.

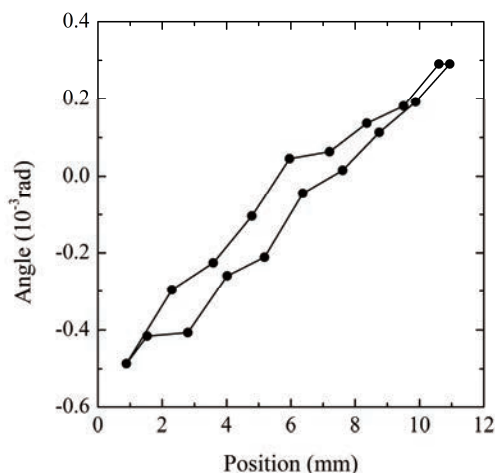


Fig. 2 The 70% X-direction emittance diagram at 1 MeV proton beam.

References

- 1) A. Yokoyama et al., JAEA Takasaki Annu. Rep. 2010 (2012) 158.
- 2) Y. Saitoh et al., Rev. Sci. Instrum. 80 (2009) 106104.

4 - 40 Fast Single-Ion Hit System for Heavy-Ion Microbeam at TIARA Cyclotron (V)

W. Yokota, T. Satoh, S. Okumura, S. Kurashima, N. Miyawaki, H. Kashiwagi,
K. Yoshida, M. Koka, A. Yokoyama, W. Kada and T. Kamiya

Department of Advanced Radiation Technology, TARRI, JAEA

The fast single-ion hit system on the HX course of the TIARA cyclotron was continuously improved for higher quality of microbeam and single-ion hit. The paper reports progress in the major subjects of (1) reduction of the miss hit in the single-ion-hit irradiation, (2) development of the real-time detection system of single-ion-hit position and (3) new microbeam development, following the impact of the Great East Japan Earthquake.

The components of the microbeam system such as the quadrupole focusing magnet, the irradiation chamber and the optical microscope are connected vertically in a line hanging on the steel frame, which is fixed on the concrete floor, through interleaved rubber pads to insulate vibration. Therefore, they can easily sway and were thought to be damaged by the large quake with seismic intensity of 5.5. It was also a question if the cyclotron system would function normally. The test operation of the microbeam system was carried out as a part of a check of the whole cyclotron system in May, 2011 after normality of radiation safety system and the utility of the TIARA were ensured. The result was remarkable and indicates that the microbeam system did not suffer a detectable damage: An ion beam of 260 MeV- $^{20}\text{Ne}^{7+}$ was accelerated and transported to the end of the HX course smoothly using the operation parameters of the last experiment before the earthquake. Microbeam formation was also well proceeded and beam size reached about 2 μm without any trouble.

A ratio of the miss hit is strongly dependent on tuning of beam transportation and the curvature of the micro slit edge as reported before¹⁾. This means that the beam state at the micro slit such as incident angle or relative position to a couple of baffles of the micro slit can affect a frequency of the miss hit. In order to pass the beam perpendicularly to the micro slit by balancing current of the beam hitting the baffles, they were electrically insulated and the current was measured. The difference of current on the baffles was small and did not significantly change unless the beam was intentionally moved largely. This indicates that the beam size was much bigger than the baffles and this method is not adequate to see the beam state. Real-time ion-hit position detection using $\text{CaF}_2:\text{Eu}$ explained in next paragraph will be another method, which enable us real-time search of beam transportation condition for less scattering of ions at the slit that causes the miss hit¹⁾.

In the development of the real-time detection system of single-ion-hit position, scintillation from $\text{CaF}_2:\text{Eu}$ as thick as ions stopped in it was detected at a rate of several hits per second for 260 MeV- $^{20}\text{Ne}^{7+}$. The spatial accuracy of position might be over several microns because the ions were scattered in the scintillator. It is expected to be useful, however, for real-time position detection for a wide view to monitor ion scattering by the micro slit because the scattering leads deviation of hit position by some hundreds of microns from a targeted position. Such detection will realize easy tuning of beam transportation and the micro slit gap for less scattering, and permit quick improvement in quality and efficiency of irradiation experiments with use of single-ion hit. There is also a possibility to detect feebler scintillation by a single-ion or that from the thinner $\text{CaF}_2:\text{Eu}$ for a higher spatial resolution by raising sensitivity of the light detection system.

The new microbeam development of carbon beam is required from radiation biology study and 220 MeV- $^{12}\text{C}^{5+}$ was already focused to microbeam in 2009. The 320 MeV- $^{12}\text{C}^{6+}$ microbeam formation was the second trial. In the case of 220 MeV- $^{12}\text{C}^{5+}$, the tuning of formation was difficult because the secondary electron image from a copper grid was not clear due to low secondary electron emission and the beam size was not smaller than 2 μm . The secondary electron emission and beam intensity are further lower for 320 MeV- $^{12}\text{C}^{6+}$ and microbeam formation is more difficult, therefore, the ion source and the cyclotron were tuned to obtain the beam intensity as high as possible. The secondary electron image of a copper grid was too faint nevertheless, and microbeam formation was carried out monitoring scintillation from $\text{CaF}_2:\text{Eu}$. The beam size estimated by means of CR-39 irradiation was about 50 $\mu\text{m} \times 5 \mu\text{m}$. This extremely flat shape might be caused by beam optics of transportation upstream of the micro slit, which should be improved in next experiment. The result also indicates a prospect that 320 MeV- $^{12}\text{C}^{6+}$ beam can be focused as small as 5 $\mu\text{m} \times 5 \mu\text{m}$ by $\text{CaF}_2:\text{Eu}$ scintillation observation instead of secondary electron image of a grid.

Reference

- 1) W. Yokota et al., JAEA Takasaki Annu. Rep. 2010 (2012) 159.

4 - 41

Use of Gafchromic Dosimetry Films to Measure a Large-Area Ion-Beam Distribution

T. Ishizaka, K. Imai, Y. Yuri, T. Yuyama, I. Ishibori and S. Okumura

Department of Advanced Radiation Technology, TARRI, JAEA

A research and development (R&D) study is now in progress on the heavy-ion uniform-beam formation using multipole magnets at TIARA^{1,2)}. It is important to evaluate the quality of the uniform beam precisely for the R&D study and future applications. We are, therefore, developing techniques to measure the two-dimensional intensity distribution of a large-area ion beam expanded on the target. Radiochromic films of Gafchromic HD-810 and EBT2 (Ashland Inc.) have been employed as one of possible techniques for the present purpose. The film, whose color turns blue due to radiation exposure, is widely used for dose evaluation in radiation therapy. It has various characteristics such as high spatial resolution, large area, relatively low-dose range, easy handling. Previously, it was shown that the HD-810 film was available for electron beams³⁾. It is, thus, expected that it can be applied to ion beams as well. The coloring response was investigated as a change in the optical density when the HD-810 and EBT2 films are irradiated with ion beams.

The following procedure was taken for film evaluation:³⁾ First of all, the film was uniformly irradiated with an ion beam. The irradiation time ranged from 10^{-3} ~ 10^1 s, depending on the fluence and intensity of the beam. An electrostatic beam chopper was used for precise control of the irradiation time. Then, the coloring response of the irradiated film was digitized by general-purpose scanners to extract 16-bit RGB intensity values from the TIFF image. Finally, the optical density was determined for each of the three color components. An analysis program has been developed for systematic data processing. The effect of image manipulations such as the resolution change and rotation was also investigated on the optical density.

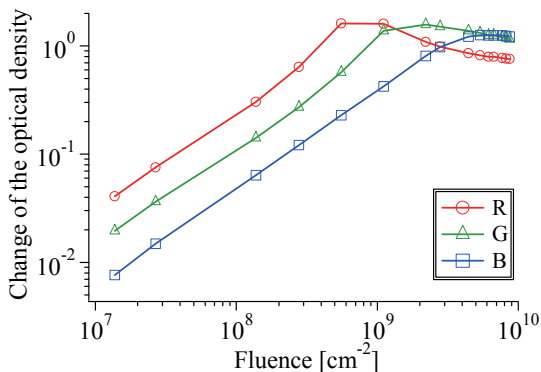


Fig. 1 Optical density of a Gafchromic film HD-810 as a function of the fluence of 520-MeV ⁴⁰Ar beam. Irradiated films were scanned by a scanner, LiDE50 (Canon).

We used three different kinds of ion beams, 10-MeV H, 520-MeV Ar, and 490-MeV Xe for the film calibration. Figure 1 shows the response of HD-810 films irradiated with 520-MeV Ar beams and then read by a scanner, LiDE50 (Canon). The optical densities of all three colors increase linearly with the particle fluence for the relatively low fluence. The fluence up to 3×10^9 cm⁻² is measurable with the blue component. For EBT2 films, the available fluence range was two orders of magnitude lower. Similarly, it was found that, for 10-MeV H and 490-MeV Xe, the measurable fluence ranges of HD-810 films are 10^{10} ~ 10^{11} cm⁻² and 10^7 ~ 10^8 cm⁻², respectively. Note that the present result does not always guarantee the absolute values of the fluence against the optical density since it is not easy to keep film's environmental conditions, such as the fluence rate, elapsed time from irradiation to scanning, lot-to-lot variation, etc. However, we have experimentally confirmed that the response curve of the optical densities is reproducible within a tolerable level. It is, thus, possible to measure the relative intensity distribution of various ion beams at practical fluence ranges. As an example, the relative intensity distribution of an octupole-focused beam measured using the HD-810 film is shown in Fig. 2. A uniform region as large as 9 cm × 9 cm was formed with an rms uniformity of ±5%.

References

- 1) Y. Yuri et al., Nucl. Instrum. Meth. Phys. Res. A **642** (2011) 10.
- 2) T. Yuyama et al., Proc. 8th Annu. Meet. Part. Accel. Soc. Jpn. (2011) MOPS072 [in Japanese].
- 3) T. Agematsu et al., Radioisotopes **57** (2008) 87 [in Japanese].

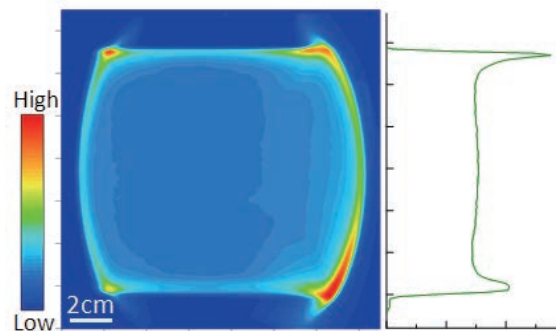


Fig. 2 Relative intensity distributions measured by a Gafchromic film HD-810. A 10-MeV H⁺ beam was focused by octupole magnets.

4 - 42 Detection Method for Dose Distribution of Focused Proton Beam by Using Common Polymer Film

M. Omichi^{a, b)}, K. Takano^{a)}, T. Satoh^{c)}, T. Kamiya^{c)}, Y. Ishii^{c)}, T. Ohkubo^{c)}, M. Koka^{c)}, W. Kada^{c)}, M. Sugimoto^{c)}, H. Nishikawa^{d)} and S. Seki^{a)}

^{a)}Department of Applied Chemistry, Graduate School of Engineering, Osaka University, ^{b)}Anan National College of Technology, ^{c)}Department of Advanced Radiation Technology, TARRI, JAEA, ^{d)}Department of Electrical Engineering, Shibaura Institute of Technology

High energy particles have also been a powerful tool to fabricate the material into nm-sized level, and the relatively high momentum of the individual particles secure their tracking in the materials, leading to precise pattern fabrication with ultra-high aspect ratio^{1,2)}. Focusing the beam into nm spaces is the key factor to determine the precision of the pattern fabricated, and rapid quantitative analysis of focused beam size were often realized by correcting the images of secondary electrons knocked out from the well-defined fine patterns. The averaged size of the focusing is statistically and simply examined by the technique, however the shape and precise structure of the single beam spot are hard to visualize despite being key parameter to control quality of the pattern fabricated. Here, we report a detection method for dose distribution of focused proton beam (FPB) coupled with atomic force microscopy (AFM) analysis using a common polymer and cross-linker, polyacrylic acid (PAA) -*N,N'*-methylene bisacrylamide (MBAAm), blend films as the 'proton beam-sensitive' polymer film.

PAA-MBAAm blend films on a silicon wafer were prepared by drop-casting with 1 wt% PAA of various MBAAm contents (PAA/MBAAm = 100/0, 95/5, 90/10, 80/20) in ethanol. The thickness of the films was adjusted to be 2 μm and confirmed by a stylus surface profiler. Irradiation of the proton beam with the energy of 3 MeV was performed on the films with a light ion microbeam system connected to the 3 MV single-ended electrostatic accelerator at Takasaki Ion Accelerators for Advanced Radiation Application facility of JAEA/Takasaki. Line and space were patterned by shifting of the spot irradiation with changing the fluence from 0.5×10^5 to 6.2×10^5 ions/μm² by controlling an exposure time, fixed the beam current to be 3.5 pA.

The writing traces were observed on the film surface over 10 wt% MBAAm content of the blend films by optical microscope, while the traces were almost invisible under 5 wt% MBAAm content. To examine the morphology of writing traces on the film surfaces at sub micro-meter scale, the film surfaces of 10 and 20 wt% MBAAm contents were observed by AFM (Fig. 1a). Figure 1b is a relation of the irradiation fluence and the height of swelling, estimated from AFM, for 10 and 20 wt% MBAAm content films. The height increased with increasing the fluence, and reached a maximum for both 10 and 20 wt%. There is a little difference between 10 and 20 wt% in the maximum

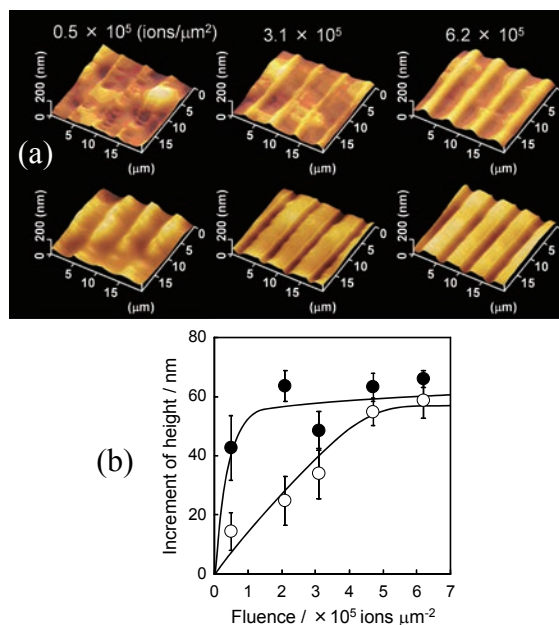


Fig. 1 (a) AFM images of line and space patterns patterned by 3 MeV proton beam at the fluence of 0.5×10^5 , 3.1×10^5 , 6.2×10^5 ions/μm² on the PAA-MBAAm films of 10 (upper) and 20 wt% (lower) MBAAm content. (b) Relationship between increment of height and fluence for PAA-MBAAm films of 10 (○) and 20 wt% (●) MBAAm content.

height. Increase in the height of swelling stopped. This would be attributable to lack of PAA as reactant. In the case of 10 wt%, the value of fluence can be estimated from the height using the proportional range. These results clearly indicated that the PAA-MBAAm film can be used to evaluate dose distribution of FPB irradiation at sub micro-meter scale.

In conclusion, we developed a simple and sensitive visualization method for the dose distribution of focused proton beam at sub micro-meter scale. The combination of common polymer and cross-linker is effective as the proton beam-sensitive polymer film to evaluate rapidly dose distribution on FPB irradiation at sub micro-meter scale³⁾.

References

- 1) A. van Kan et al., Phys. Lett. 83 (2003) 1629.
- 2) T. Kamiya et al., Nucl. Instrum. Meth. Phys. Res. B 267 (2009) 2317.
- 3) M. Omichi et al., J. Nanosci. Nanotechnol. accepted.

4 - 43

Development of Visible Light Measurement Techniques for Detention of Single-ion Hit

A. Yokoyama^{a)}, W. Kada^{a)}, T. Satoh^{a)}, M. Koka^{a)}, S. Yamamoto^{b)},
T. Kamiya^{a)} and W. Yokota^{a)}

^{a)}Department of Advanced Radiation Technology, TARRI, JAEA,
^{b)}Environment and Industrial Materials Research Division, QuBS, JAEA

Introduction

Single-ion hit for the microscopic irradiation experiments is used with spatial accuracy of a few micrometers by means of heavy ion microbeam of more than hundreds MeV at the TIARA cyclotron for the studies of irradiation effects on biological cells and semiconductor devices. Detection of single-ion hit position is essential in these experiments.

A film of CR-39 is generally used as a position detector of single-ion hit. The ion tracks are observed off-line after chemical etching and this procedure takes more than an hour and limits efficiency of experiment. Therefore, real-time single-ion hit detection is strongly required, and various scintillators are examined to detect hit position. But they don't have strong scintillation intensity or spatial resolution of 1 μm . It is taken notice of photostimulated luminescence (PSL) of $\text{Al}_2\text{O}_3:\text{C}$ in this study, which has a dose sensitive range of 0.1 μGy - 10 Gy. Photostimulable samples with high light efficiency are possible to be prepared with implantation of C by the TIARA ion implanter optimizing parameters such as implantation density and annealing temperature.

The following four subjects were carried out in the 2011 fiscal year, which is the first year of this study. (1) Assemble of a light detection system consisting of a long working distance objective lens, a lens tube with zoom, an image intensifier and an electron multiplying CCD camera, (2) Preparation of $\text{Al}_2\text{O}_3:\text{Eu}$ sample by means of Eu implantation into Al_2O_3 for the sensitivity test of the detection system because PSL measurement system was under development, (3) Sensitivity test of the system using $\text{Al}_2\text{O}_3:\text{Eu}$, (4) Measurement of ion beam induced luminescence (IBIL) spectra of the samples to ensure the light from Eu center by means of the wavelength-dispersive IBIL analysis system¹⁾. In next fiscal year, subjects (2), (3), (4) will be proceeded for $\text{Al}_2\text{O}_3:\text{C}$ and a PSL measurement system will be developed. The paper describes on subjects (2), (3) and (4) as follows.

Sample preparation

It was investigated how the luminescence intensity depends on implantation density, depth, multiplicity of irradiation layers and annealing temperature. Implantation density of Eu were changed from 1.0×10^{13} to $1.0 \times 10^{16} \text{ cm}^{-2}$ in ten time steps referring to semiconductor production. Implantation depth for each layer was controlled by changing energy of Eu beam; single-layer (350 keV, 70 nm), double-layer (350, 250 keV, 70~50 nm) and triple-layer (350, 250, 150 keV, 70 ~ 30 nm).

After implantation, samples were annealed to diffuse Eu for an hour and annealing temperature was changed from 500 °C to 1,000 °C in 100 °C steps. Photoluminescence (PL) measurement was carried out using a continuous excitation light of He-Cd laser line of 325 nm. The highest PL peak intensity was observed at around 600 nm from the triple-layer $\text{Al}_2\text{O}_3:\text{Eu}$ with density of $1.0 \times 10^{16} \text{ cm}^{-2}$ and annealing temperature of 600 °C. This sample was used in the sensitivity test.

Sensitivity test

Ion of 15 MeV- O^{4+} was selected for the sensitivity test of single-ion hit detection system at the TIARA tandem accelerator, so that the linear energy transfer of it is equivalent to that of 260 MeV- Ne^{7+} , in the sample. The system detected scintillation from the triple-layer $\text{Al}_2\text{O}_3:\text{Eu}$ at a hit rate of two hundreds ions per second. On the other hand, it detected scintillation from $\text{ZnS}:\text{Ag}$ which was thick enough to stop ions in it at a hit rate of an ion per second. This result indicates that it is necessary to enhance the sensitivity by 200 times both improving the light emission efficiency and replacing the objective lens to that with a larger numerical aperture to collect more scintillation.

Measurement by IBIL system

The IBIL spectra were obtained from single crystal Al_2O_3 and prepared $\text{Al}_2\text{O}_3:\text{Eu}$ by means of 3 MeV- H^+ microbeam from the TIARA single-ended accelerator. Peaks appeared at 325 nm and 415 nm corresponding to color centers of the Al_2O_3 for both samples. A specific peak for $\text{Al}_2\text{O}_3:\text{Eu}$ was at 690 nm of Eu color center appeared for the Eu implanted sample. Detecting scintillation along trajectory of diffracted ion by scattering worsens spatial resolution. A bandpass filter is necessary to avoid detecting scintillation only from the Eu implanted layer between 30 nm to 70 nm from the surface of the $\text{Al}_2\text{O}_3:\text{Eu}$. The IBIL intensity of $\text{Al}_2\text{O}_3:\text{Eu}$ annealed at 600 °C is higher than those at 700 °C and this is similar in trend to PL intensity. It suggests that the prepared samples for IBIL with optimum implantation density and annealing temperature would have good luminescence intensity for PL and PSL.

Acknowledgment

We would like to gratefully thank Dr. Miura in Graduate School of Engineering, Gunma University for PL measurement. This work was supported by KAKENHI, Grant-in-Aid for Young Scientists (B) 23760837.

Reference

1) W. Kada et al., Int. J. PIXE. 21(2011) 1-11.

4 - 44 Development of Transmission Thin Diamond Sensors for the Single Hit Detection of High-energy Ions

W. Kada^{a)}, T. Kamiya^{a)}, N. Iwamoto^{b)}, S. Onoda^{b)}, V. Grilj^{c)}, N. Skukan^{c)}, T. Makino^{b)}, M. Koka^{a)}, T. Satoh^{a)}, M. Jakšić^{c)} and T. Ohshima^{b)}

^{a)} Department of Advanced Radiation Technology, TARRI, JAEA, ^{b)} Environment and Industrial Materials Research Division, QuBS, JAEA, ^{c)} Rudjer Boskovic Institute, Croatia

Diamond is one of the most excellent candidate materials for futuristic high-energetic particle detector with advantages in the radiation-hardness and little influence of electrical and thermal noises. For the time-resolved detection of single-ions with several hundred MeV, a transmission detector using thin film CVD diamond is now under investigation for the futuristic utilization as replacing the window to extract ion beams to irradiate the sample in the atmosphere at the microbeam line of the AVF cyclotron of TIARA facility¹⁾. For this purpose, sufficiently high Charge Collection Efficiency (CCE) and radiation hardness are expected for a diamond detector, however, those characteristics have not yet been fully clarified in the case that focused ion microbeams are introduced into the transmission detectors fabricated from CVD diamond film.

Two kinds of diamond detectors using Poly-Crystalline (PC) and Single-Crystalline (SC) CVD diamond films with thickness around 50 μm and fabricated with ohmic-contact type electrodes were tested in this work. Figure 1 shows a part of SC detector. To obtain the energy- and timing response of the detectors to the ionized particles, single ion hit experiment was executed on microbeam lines of both tandem accelerators at TIARA and also at Rudjer Boskovic Institute (RBI) in Croatia. It was experimentally examined the response to the single ions through CCE and transient pulse signals. Pulse signals caused by the irradiation of each single hit of MeV ions were successfully obtained for the both detectors with the bias voltage of up to ±50 V.

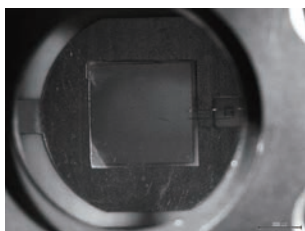


Fig. 1 Single crystalline (SC) CVD diamond film detector.

Uniformity of the response of the detector was obtained by scanning of 4.5 MeV proton microbeam and IBIC analysis at RBI. As shown in Fig. 2, PC CVD diamond detector showed totally different response to the irradiation with the microbeam from SC, which showed high and uniform intensity of pulse signals in the two dimensional area of ranged from 0 to 50 μm in both vertical and horizontal axis.

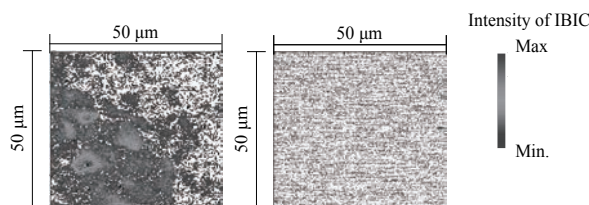


Fig. 2 IBIC images of left) PC and right) SC CVD diamond film detectors at 4.5 MeV proton microbeam. The beam scanning area was 50 × 50 μm.

Also transient current response of the detector was evaluated using an analysis system²⁾ processing signals at the irradiation of 15 MeV oxygen single ion hitting on the microbeam line at TIARA. Figure 3 shows an example of pulse response of transient current signals induced in the SC CVD diamond. The transient current pulses with the width of around 5 ns or less were directly observed by both 3 GHz and 15 GHz digital oscilloscope, respectively. These seemed to have enough time resolution to trigger the signal processing of single MeV heavy ion irradiation experiments.

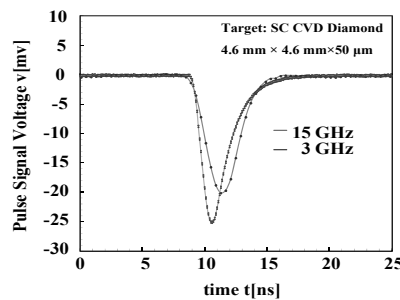


Fig. 3 Pulse shape of ion-beam-induced transient current caused by single ion hit of 15 MeV O⁴⁺.

This work is included in "Development of high-energy ion microbeam technology for novel applications of diamond" that has been supported by Strategic Japanese-Croatian Cooperative Program on Materials Science of Japan Science and Technology Agency (JST) the Ministry of Science, Education and Sports of the Republic of Croatia (MSES).

References

- 1) T. Kamiya, et al., Nucl. Instrum. Meth. B 269 (2011) 2184-87.
- 2) J. S. Laird, et al., Nucl. Instrum. Meth. B 181 (2001) 87-94.

4 - 45

Quantitative Evaluation of Charge State for Internuclear Distance of Constituent Ions Dissociated from C_2^+ Ion Moving in a Solid

A. Chiba^{a)}, Y. Saitoh^{a)}, K. Narumi^{a)}, K. Yamada^{a)} and T. Kaneko^{b)}

^{a)}Department of Advanced Radiation Technology, TARRI, JAEA,

^{b)}Department of Applied Physics, Okayama University of Science

Irradiation effects induced by the swift cluster ion bombardments are being studied actively in TIARA. Although fundamental researches for the applied use of cluster ion beams make advance, there is not still complete understanding of mechanisms of the cluster irradiation effects. We have so far investigated several characteristic phenomena exposed in interactions of the cluster ions with a solid. For example, it is known that an average charge of the constituent ions resulting from the foil-induced dissociation of cluster ions is smaller than that of monatomic ions at the same speed. This charge-reduction effect had been described by a few theoretical models^{1,2)}. In any models, a dominant cause on this effect was explained as due to an enhancement of the binding energy of outer-shell electrons by the Coulomb interaction between constituent ions. This means that the internuclear distance of the constituent ions moving in the solid is the most important parameter for understanding the mechanism of the charge-reduction effect. However, there are a few reports in which average charges of the constituent ions had been quantitatively evaluated in terms of their internuclear distance increased by the screened Coulomb repulsion.

In this report the relationship between the average charge and the internuclear distance of the constituent ions were quantitatively evaluated by analyzing their divergence angles after the foil penetration, using 6-MeV C_2^+ ions accelerated by 3-MV Tandem accelerator at TIARA.

The internuclear distance of cluster ions usually varies according to the molecular vibration in some electronic states. The divergence angle of the constituent ions which passed through a foil depends on their charges. If their charge states are varied according to their internuclear distance, r_0 of C_2^+ ion at the instant of dissociation of it, a distribution of the divergence angle, which was observed in a measurement, would be shaped in response to each specific distribution of the distance r_0 , as well as their charge states. In a previous report³⁾, we showed certainly that there are individual different distributions of r_0 for each divergence angle distribution classified according to the product of charges. Figure 1 shows distributions of the internuclear distance of the constituent ions after the foil penetration, which were respectively calculated based on the most appropriate distributions of r_0 being able to reproduce the divergence angle distribution of each product of charges. This figure just indicates the charge fraction of the constituent ions for the internuclear distance. By analyzing this charge fraction, as shown in Fig. 2, we demonstrated

that the charge-reduction effect can be described as a function of internuclear distance. Furthermore, a theoretical value indicated in a solid curve in this figure, calculated by the model considering the cluster effect on average charge¹⁾, is well consistent with our experimental value. This method allows us to quantitatively evaluate the internuclear distance of the cluster constituent ions moving in the medium, and these data will make a significant contribution to the further progress of studies on the interaction between swift cluster ions and solids.

References

- 1) T. Kaneko, Phys. Rev. A 66 (2002) 052901.
- 2) S. Heredia, et al., Euro. Phys. Lett. 56 (2001) 729.
- 3) A. Chiba, et al., Nucl. Instrum. Meth. Phys. Res. B 269 (2011) 824.

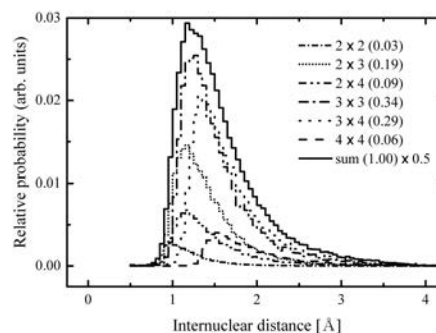


Fig. 1 Distributions of the internuclear distance of the constituent ions at the rear-surface of the foil, calculated on the basis of the measured divergence angle distributions. The abundance ratio of each product of charges is indicated in parentheses.

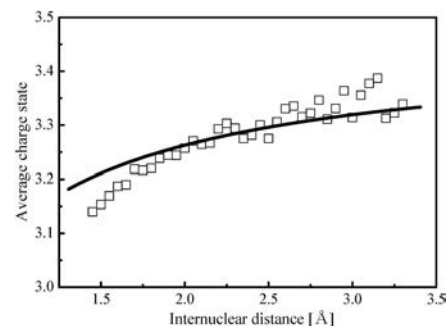


Fig. 2 Average charge state of the constituent ions of 3-MeV/atom C_2^+ ions moving in a carbon foil, as a function of internuclear distance. The solid curve indicates a calculated result using the cluster average charge theory reviewed in Ref. 1).

4 - 46 Ion Induced Luminescence from Sapphire Irradiated with Swift Cluster Ion Beams - Cluster Ion Size and Energy Dependences -

H. Shibata ^{a)}, Y. Saitoh ^{b)}, A. Chiba ^{b)}, K. Yamada ^{b)}, K. Narumi ^{b)} and M. Taguchi ^{c)}

^{a)} Graduate School of Engineering, Kyoto University,

^{b)} Department of Advanced Radiation Technology, TARRI, JAEA,

^{c)} Environment and Industrial Materials Research Division, QuBS, JAEA

The interaction of swift cluster ions with matter has attracted an attention in these years, because cluster ions bombard a very small area of a solid surface with many energetic atoms simultaneously and release large energy in the time range around pico-second. These situations cause non-linear effects or synergetic effects, which are not normally caused by a single atom collision with solid targets.

Our purpose of this study is to elucidate the characteristics of the interaction between energetic cluster ions and solids by means of measuring luminescence from solid surfaces irradiated with cluster ions. We report present results of luminescence measurement from sapphire target irradiated with carbon cluster ions.

Luminescent spectra from sapphire ($\alpha\text{-Al}_2\text{O}_3$) induced by 0.25 ~ 3.0 MeV/atom (21 ~ 252 keV/u) $\text{C}_1^+ \sim \text{C}_8^+$ ion irradiation were measured in the wavelength range of 250~800 nm as a function of ion fluence at room temperature. Cluster ion beams accelerated by the TIARA 3 MV tandem accelerator were used for this study. Beam intensities were typically 2.5 nA for C_1^+ and 50 pA for C_8^+ ions at 0.5 MeV/atom. The luminescence measurement has been carried out by using an optical multichannel analyzer (Hamamatsu Photonics PMA11). Cluster ion size and energy dependences of incident cluster ion beams on luminescence yield have been measured. Ion induced luminescent spectra peaked at 326 and 411 nm were observed. Luminescence of 326 nm was identified as F^+ center, whose intensity grew up and decayed gradually with irradiation. Luminescence of 411 nm was F center, whose intensity grew up rapidly and decayed faster than F^+ center luminescence with irradiation ¹⁾. Intensities of luminescence reached peaks with less fluence as the cluster size increased.

The incident cluster ion size dependence on the yield of the F^+ center luminescence from sapphire target is shown in Fig. 1. The incident energy dependence is also shown in this figure. In this study the maximum intensity of luminescence was set as the luminescence yield, since the intensity of luminescence was dependent on the ion fluence. Each yield was compare to the yield for C_1^+ ion irradiation. Ratios R_n of luminescence yields from sapphire target irradiated with 0.5, 1.0 and 1.5 MeV/atom $\text{C}_2^+ \sim \text{C}_6^+$ incident cluster ions to that for C_1^+ ion are described as $R_n = I(n) / nI(1)$, where n is number of cluster ion, $I(n)$ is the yield for

C_n^+ cluster ion and $I(1)$ is the yield for C_1^+ ion. The luminescence yields increase as the cluster sizes increase for every incident energy range, but the ratios R_n become less than unity except for the case of 1.5 MeV/atom. The ratio is unity if the yield increases linearly as the cluster size increases. This non-linearity also appears in the theoretical calculation of the stopping power ($S = -dE/dx$) for the united atom limit of cluster ions ²⁾. The ratio R_n of stopping power of cluster ion to that of single atom ion describes as $R_n = S(n) / nS(1)$. This value is independent to kinds of targets and depends on incident velocity only. The experimental results exist between unity and the calculated value for the united atom of the cluster ion. This suggests that luminescence caused by irradiation defects directly relates the stopping power of incident cluster ion.

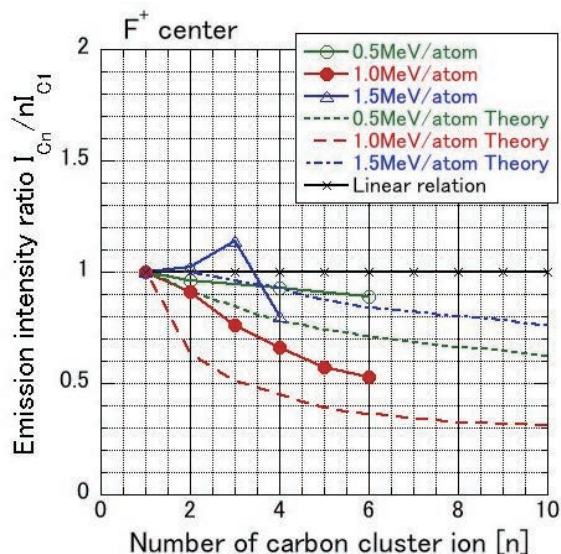


Fig. 1 The ratios of yields of luminescence from F^+ center of sapphire target irradiated with 0.5 ~ 1.5 MeV/atom $\text{C}_2^+ \sim \text{C}_6^+$ projectiles to that for C_1^+ ions in each energy indicate with continuous lines. Dashed and dotted lines show the theoretical stopping power calculation for the united atom of projectile.

References

- 1) Y. Aoki et al., Nucl. Instrum. Meth. Phys. Res. B 114 (1996) 276-80.
- 2) P. Sigmund et al., Nucl. Instrum. Meth. Phys. Res. B 112 (1996) 1-12.

4 - 47 Visualization of a Single Cluster Particle Track in Polystyrene Films

A. Asano^{a)}, K. Takano^{a)}, A. Chiba^{b)}, Y. Saitoh^{b)}, H. Marui^{a)}, M. Omichi^{a, c)},
Y. Maeyoshi^{a)}, Y. Honsho^{a)}, A. Saeki^{a)}, K. Yamada^{b)}, K. Narumi^{b)} and S. Seki^{a)}

^{a)} Division of Applied Chemistry, Graduate School of Engineering, Osaka University,

^{b)} Department of Advanced Radiation Technology, TARRI, JAEA,

^{c)} Department of Material Engineering, Anan National College of Technology

In our previous report, Single Particle Nanofabrication Technique (SPNT) with polycarbosilane (PCS) succeed in the visualization of a single cluster particle track on ion beam irradiations with carbon cluster ion, C_n^+ ($n=3-9$)¹⁾. As the results, the observed nanowire sizes were slightly lower values compared with the estimated ones from the formulation based on the single particle interaction with the polymeric materials²⁾. A fragmentation of the cluster particle during penetration in the polymer film was suggested to give a significant decrease in the radial dose distribution inside a particle tracks. On the other hand, it was found that polystyrene derivatives give well-controlled nanostructures, in the length, the radius, and the number density by the SPNT. And the radiation-induced cross-linking efficiency, G-value, of polystyrene derivatives (PSES) was estimated to be over $2.7 (100 \text{ eV})^{-1}$, larger than that of PCS³⁾. In this study, a visualization of the tracks from the fragmentation was tried by using polystyrene derivatives with higher sensitivity for the ion beam irradiation. And then the results was compared to the case of ion beam consisted single ion, considering the feature of cluster beam irradiation.

The polystyrene derivatives were synthesized from poly[styrene-co-4-(trimethylsilyl)ethynylstyrene] and poly(styrene-co-4-ethynylstyrene) by nitroxide-mediated radical polymerization. The molecular weight of average number, M_n , and polydispersity index were 18,200 g/mol and 1.32, respectively. The polystyrene derivatives films as the target were over coated by drop-cast method on Si substrate after an adequate surface treatment. The irradiations of swift ion beams were performed at TC beam-line connected to Tandem accelerator at Takasaki Advanced Radiation Research Institute, JAEA. The ion species were selected to be $^{12}C_4^+$ and $^{48}Ti^+$. The energies of both ions were adjusted to be 5.8 MeV. In the 5.8 MeV $^{48}Ti^+$ beam irradiation, the particle velocity and particle mass are the same to those of the 5.8 MeV $^{12}C_4^+$ beam irradiation. But, the LET of the 5.8 MeV $^{48}Ti^+$ is two thirds of that of 5.8 MeV $^{12}C_4^+$ calculated as the sum of atomic LET¹⁾. The ion fluence of these beams was adjusted to be $3 \times 10^9 \text{ ions/cm}^2$. After the irradiations, the samples were developed with tetrahydrofuran. The fabricated nanostructures were observed by atomic force microscope (AFM).

As the results, it was confirmed that polystyrene nanostructures were formed on the substrate by the 5.8 MeV $^{12}C_4^+$ beam and 5.8 MeV $^{48}Ti^+$ beam irradiation, as shown in

Fig. 1. All structures collapsed and lay down on the substrate due to the development. The density of the structures at the $^{48}Ti^+$ beam irradiation is almost the same to the ion fluence. However, the density at the $^{12}C_4^+$ irradiation was much less than the ion fluence. It was supposed that many cluster particles were fragmented during penetration in the polymer film. When the fragmentation was happened, the radial dose distribution inside a particle tracks was decreased, and then the cross-linking reaction was induced insufficiently. Therefore, the formed structures along the fragmented ion track were solved or swelled in the tetrahydrofuran. The adhesion between the substrate surface and the foot of the structures was also supposed to became weak so as to be flown away from the substrate at the development. In the case of the cross-linking reaction induced by non-fragmentized $^{12}C_4^+$, the adhesion was kept during the development. The radius of the structures formed by the non-fragmentized $^{12}C_4^+$ was 7.2 nm calculated with the ellipse model⁴⁾. The value was larger than that at the $^{48}Ti^+$ beam irradiation. This result was consistent in the estimation with the formulation. In order to visualize fragmented $^{12}C_4^+$ tracks, using the PSES with larger G-value, applying a post-exposure treatment to promote the cross-linking reaction, or optimization of the development condition is required.

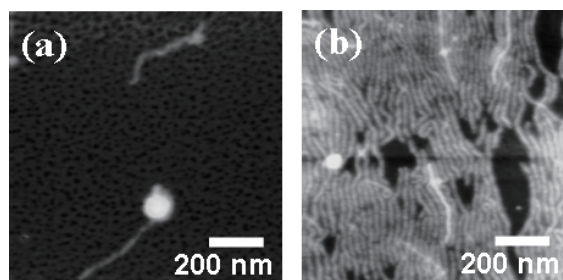


Fig. 1 AFM images of polystyrene nanostructures formed by the SPNT with 5.8 MeV $^{12}C_4^+$ (a), 5.8 MeV $^{48}Ti^+$ (b). The ion fluence was $3 \times 10^9 \text{ ions/cm}^2$.

References

- 1) S. Seki et al., JAEA Takasaki Annu. Rep. 2008 (2009) 159.
- 2) S. Seki et al., Phys. Rev. B 70 (2004) 144203.
- 3) S. Seki et al., JAEA Takasaki Annu. Rep. 2010 (2012) 120.
- 4) S. Tsukuda et al., Surf. Coatings Tech. 201 (2007) 8526.

4 - 48 Electronic Stopping Power Connected with Average Charge Reduction for Swift Carbon Cluster Ions in Carbon

T. Kaneko ^{a)}, K. Ihara ^{a)}, M. Kohno ^{a)}, Y. Saitoh ^{b)}, A. Chiba ^{b)} and K. Narumi ^{b)}

^{a)} Department of Applied Physics, Okayama University of Science,

^{b)} Department of Advanced Radiation Technology, TARRI, JAEA

Cluster-ion-solid interaction has attracted attention in that the irradiation effects are different from that expected in single-ion irradiation. The cluster effect, which is classified by the sub-linear and super-linear dependences on the number of constituent ions, has been found in the average charge ¹⁾, energy-loss ¹⁾, and secondary electron emission ²⁾ under MeV carbon cluster impacts. Especially, charge states of impinging ions play a significant role in those phenomena induced in a bulk. Regarding the average charge, Chiba et al. ³⁾ first reported the structure-dependent reduction effect in the cluster average charge using 3 MeV C₃ cluster impact on a carbon foil. Cluster impact electron excitation and related phenomena are closely connected with charge states and their spatial structure of constituent ions. To our knowledge, however, ample information on the above quantities has not been published yet. The aim of this study is to present as a basic quantity the electronic stopping power for swift carbon clusters, by taking into account of the charge reduction effect, in order to promote attention of experimental researches and to contribute to collection of cluster-impact electronic excitation data.

This theoretical research is composed of estimating the reduced average charges of constituent ions in a cluster and evaluating the electronic stopping power for a cluster, using the reduced average charges. The theoretical basis in the present study is to describe the incident cluster as an ensemble of partially stripped ions, where their charges are determined by the self-consistent cluster average-charge theory, and their spatial charge distribution is described in a statistical manner. The excitation of target electrons is treated in an electron gas model. In a case of carbon target, four electrons per atom are assumed to participate in electron gas and the rest two electrons are in the 1s state. The detail description was given in reference 1.

Figure 1 shows the average charge per ion, $\langle Q \rangle$, for C_n⁺ incidence (n=2, 3, 4, 6) in a linear-chain structure with equal separation of 2.4 a₀ (a₀ is the Bohr radius), as a function of ion speed in units of the Bohr speed v₀. Solid line refers to the average charge of a single carbon. The dotted line, the dot-dashed line, the dashed line, and the dot-dot-dashed line refer to C₂, C₃, C₄, and C₆ ion, respectively. From this figure, one finds that at the same speed the average charge per ion decreases with increasing the number of constituent ions in a cluster. This tendency can be understood by the theoretical model ¹⁾, which leads us to a conclusion that increase of the surrounding ions implies enhancement of the binding force on ionized electrons, resulting in less degree of ionization. Another feature is

that the average charge monotonously approaches the maximum charge value with increasing ion speed. We add a comment that even at a case of highest speed the influence of the surrounding ions still remains. This is because we do not take into account coulomb explosion.

Figure 2 shows the electronic stopping cross section per ion of carbon target for a C_n⁺ (n=1-4, 6) cluster ion as a function of ion speed in units of the Bohr speed v₀. Legend is the same as in Fig. 1. Roughly speaking, in the region of lower speed, the stopping values are almost the same values, though in an exact sense the negative cluster effect appears. In this region, single electron excitation is dominant. On the other hand, in the region of the higher speed, the positive cluster effect will clearly appear and it is a large contrast to the case of the lower speeds. Here, the collective excitation contributes significantly. This excitation mode becomes dominant for swift larger clusters.

References

- 1) T. Kaneko, Phys. Rev. A66 (2002) 052901.
- 2) S. Tomita et al., Phys. Rev. A73 (2006) 060901(R).
- 3) A. Chiba et al., Phys. Rev. A76 (2007) 063201.

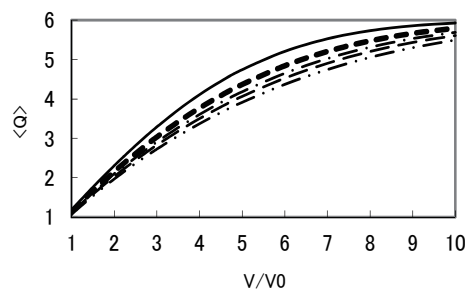


Fig. 1 Average charge per ion $\langle Q \rangle$ as a function of speed for C_n⁺ (n=1-4, 6). See text for a legend.

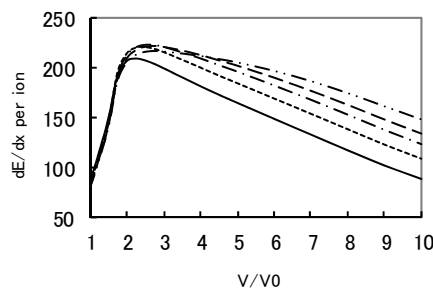


Fig. 2 Electronic stopping power per ion (in units of 10^{-15} eV cm²/atom) of carbon for C_n⁺ (n=1-4, 6) as a function of speed. Legend is the same as Fig. 1.

4 - 49 Reduction of Charging Effects on Negative Secondary Ion TOF Mass Spectra of PMMA Using Cluster Ion Impacts

K. Hirata^{a)}, Y. Saitoh^{b)}, A. Chiba^{b)}, K. Yamada^{b)}, K. Narumi^{b)} and T. Kamiya^{b)}

^{a)}National Institute of Advanced Industrial Science and Technology (AIST),

^{b)}Department of Advanced Radiation Technology, TARRI, JAEA

Secondary ion (SI) mass spectrometry, based on the phenomenon that primary ion impacts on a target produce SIs originating from the target, is one of the most powerful tools for surface analysis. One of the difficulties in SI mass measurements of insulating targets is to stabilize the surface potential during the measurements, because ion impacts on insulating targets usually lead to an increase in the potential caused by the difference between the injected and emitted charges. The increase of the potential would change the emission energy of SIs and thus make their precise mass analysis difficult, especially for negative SI (N-SI) mass analysis. We have found that use of C_{60} primary ions considerably reduces the charging effects on the N-SI TOF mass spectra of organic insulators even without charge compensation¹⁾. In this paper, we report comparison of time-sequential variations of N-SI TOF mass spectra of a thin poly(methyl methacrylate) (PMMA) film target for 0.5 MeV/atom C_1^+ and C_8^+ impacts to study difference in charging effects on N-SI mass spectra of insulating targets between monoatomic and cluster ions with the same incident energy per atom.

A 3 MV tandem accelerator of the Japan Atomic Energy Agency (JAEA)/Takasaki, as described elsewhere^{2,3)}, was used for this experiment. Briefly, pulsed primary ion beam was produced by chopping direct current ion beam with electrostatic deflection plates triggered by a pulse generator and a series of collimators before injecting into the target. The pulsed ion beam was incident on the target at an angle of 45° to the target surface. N-SIs produced by primary ion impacts were accelerated between the target and a TOF drift tube before hitting a microchannel plate (MCP). The start and stop signals for TOF measurements were provided by the pulse generator used for pulsing the incident ion beam and a constant fraction discriminator (CFD) connected with the MCP output via a pre-amplifier, respectively. A SI counting system of the spectrometer was improved using a fast digital storage oscilloscope in order to obtain more accurate TOF SI mass spectra⁴⁾.

Figure 1 shows time-sequential variation of the N-SI TOF spectra around m/z (mass to charge ratio) = 85 of PMMA for (a) 0.5 MeV/atom C_1^+ , and (b) 0.5 MeV/atom C_8^+ impacts, respectively. All SI mass spectra were obtained without intentional charge compensation. The spectra were time-sequentially numbered from spectrum 1 (the first spectrum) to 7 (the last). The acquisition time for each spectrum was 100 s. The total number of detected SIs integrated from spectrum 1 to 7 for 0.5 MeV/atom C_8^+ was estimated to be 2 times higher than that for 0.5 MeV/atom C_1^+ .

For C_1^+ impacts, the peak shift to longer flight time and

SI intensity reduction are observed as the spectrum number increases (Fig. 1(a)). The peak shift shows the surface potential of the target increases with the spectrum number and the increase of the potential results in a reduction of the fraction of N-SIs emitting from the target surface by overcoming the potential as the charge accumulation proceeds. Therefore, the peak shift and SI intensity reduction can be ascribed to the increase of the potential due to positive charge accumulation. In contrast to the C_1^+ impacts, the N-SI TOF mass spectra for C_8^+ do not show the peak shift and SI intensity reduction, which shows that the surface potential is stable during the C_8^+ bombardment (Fig. 1(b)). The results demonstrate that N-SI TOF mass measurement of the insulating thin film target is available using cluster ions as a primary ion without charge compensation.

In conclusion, even without charge compensation, cluster ion impacts prevent the N-SI peak intensity reduction and peak shift due to charge accumulation on the target during TOF measurements.

References

- 1) K. Hirata et al., *Appl. Phys. Express* **4** (2012) 116202.
- 2) Y. Saitoh et al., *Nucl. Instrum. Meth. B* **245** (2000) 61.
- 3) K. Hirata et al., *Appl. Phys. Lett.* **83** (2003) 4872.
- 4) K. Hirata et al., *Rev. Sci. Instrum.* **82** (2011) 033101.

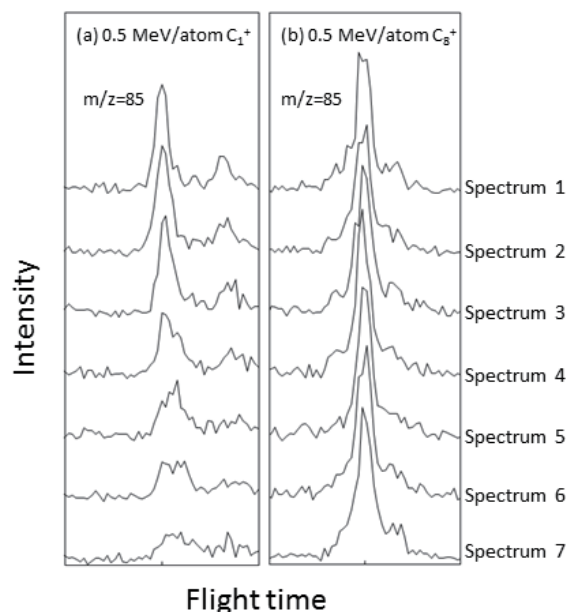


Fig. 1 Time-sequential variation of negative secondary ion TOF mass spectra of PMMA for 0.5 MeV/atom C_1^+ , and (b) 0.5 MeV/atom C_8^+ .

4 - 50 Cluster Effect on Damage Accumulation in a Si Crystal Bombarded with 10-540-keV C₆₀ Ions

K. Narumi^{a)}, H. Naramoto^{b)}, K. Yamada^{a)}, A. Chiba^{a)}, Y. Saitoh^{a)} and Y. Maeda^{b, c)}

^{a)} Department of Advanced Radiation Technology, TARRI, JAEA, ^{b)} Advanced Science Research Center, JAEA, ^{c)} Department of Energy Science and Technology, Kyoto University

When a solid target is bombarded with a molecular/cluster ion in the velocity region where nuclear collisions are dominant, cluster effect on sputtering, displacement of target atoms, *etc.* is observed^{1), 2)}. The effect on displacement of lattice atoms by molecular-ion bombardment has been reported by many groups: most of them investigated the effect in connection with nonlinear effect on the collision cascade or spike effect. Impact of large cluster such as C₆₀ would lead to huge cluster effect. On the other hand, the recent development of application studies using keV C₆₀-ion bombardment such as surface-sensitive analyses and secondary-ion mass spectroscopy of high-polymer materials and/or biomaterial has been based on the belief that little damage in the target is induced by its bombardment. However, there have been few studies on the damage accumulation by C₆₀ impact. In this study we have investigated damage accumulation in bombardment of a Si crystal with 10-540-keV C₆₀ ions.

Pieces of Si(100) wafer treated with an RCA method³⁾ were irradiated with 10-540-keV C₆₀ ions at room temperature. The areal density of displaced lattice atoms was determined from the area of a surface damage peak of backscattering yields of 2-MeV He⁺ ions for <100> axial alignment of a Si crystal. Fluence dependence of the areal density of displaced Si atoms can be well described by assuming a cylindrical volume affected by single-C₆₀-ion bombardment. The number of displaced Si atoms per C₆₀

ion, N_{D60} , has been derived from the fluence dependence of the areal density of displaced Si atoms. Figure 1 shows the result as a function of the energy of C₆₀ ions. Compared to that by monatomic-C-ion bombardment calculated with SRIM2008, N_{D1} , the energy dependence is different. Figure 2 shows the number ratio of displaced Si atoms per C atom $N_{D60}/(60 \times N_{D1})$ which demonstrates the magnitude of the cluster effect. The effect has been found to be huge and to have the maximum around 100 keV. The energy dependence of the ratio can be explained qualitatively by nuclear stopping powers S_n and increase of internuclear distances between C atoms in the target as follows: In the lower energy than 80 keV, S_n increases with increasing energy, which leads to a denser collision cascade; thus the nonlinear effect increases with increasing energy. In the higher energy than 200 keV, on the other hand, S_n has the maximum at deeper place in the target with increasing energy. In such a situation, internuclear distances between C atoms are larger at the place where S_n has the maximum. Therefore, a collision cascade is less dense, and the nonlinear effect decreases as the energy increases.

References

- 1) H. H. Andersen and H. L. Bay, Radiat. Eff. 19 (1973) 139.
- 2) J. A. Davies et al., Phys. Rev. Lett. 34 (1975) 1441.
- 3) W. Kern and D. A. Puotinen, RCA Review 31 (1970) 187.

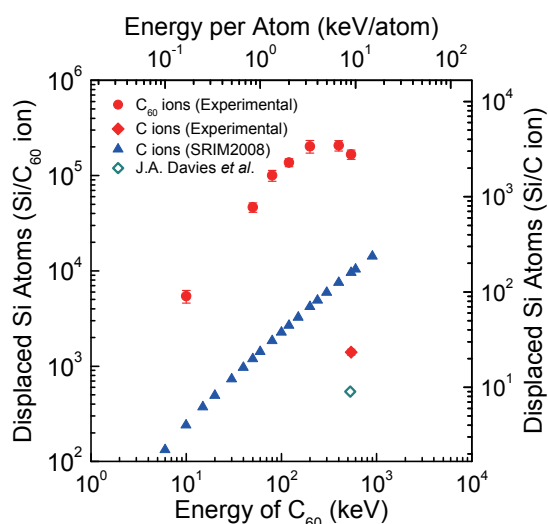


Fig. 1 Energy dependence of the number of displaced Si atoms per C₆₀ ion. For comparison, those by a monatomic C ion calculated with SRIM2008 and measured in the present study and the literature are shown.

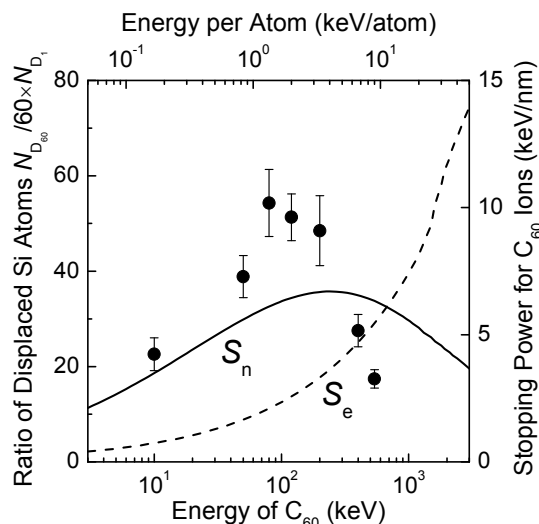


Fig. 2 Energy dependence of the number ratio of displaced Si atoms per C atom, which is derived from the results shown in Fig. 1. Solid and broken lines show 60 times as much as nuclear and electronic stopping powers of Si for C ions, respectively.

4 - 51 Cluster Effect on Projected Range of 30-keV C₆₀⁺ in Silicon

Y. Morita^{a)}, K. Nakajima^{a)}, M. Suzuki^{a)}, K. Narumi^{b)}, Y. Saitoh^{b)} and K. Kimura^{a)}

^{a)}Department of Micro Engineering, Kyoto University,

^{b)}Department of Advanced Radiation Technology, TARRI, JAEA

When cluster ions impinge on solids, pronounced non-linear behavior is expected which is called cluster effect. Many simulations have shown rather strong enhancement of the projected range for low-energy cluster ions of heavy elements in light materials ($M_1 > M_2$). The mechanism of the enhancement of the range was first proposed by Sigmund for $M_1 > M_2$ ¹⁾ and called “clearing-the-way” effect, i.e., the leading ions clear away the target atoms for the trailing ions. So far, both experimental and simulation studies concentrated on the case of $M_1 > M_2$. It is generally believed that the cluster effect on the range is rather small for $M_1 < M_2$ because the clearing-the-way effect is basically effective only for $M_1 > M_2$ ¹⁾. From a practical point of view, the cluster effect on the range is important particularly in semiconductor industries, because the cluster-ion implantation is employed mainly in the boron implantation to form ultra-shallow junctions. In the present study the range distributions of 30-keV C₆₀⁺ ions in Si have been measured with high-resolution Rutherford-backscattering spectrometry (HRBS) to see whether the range of the cluster ion is also enhanced in the case of $M_1 < M_2$.

Two Si(001) wafers were preamorphized by 3-keV As⁺ ions at a fluence of 1×10^{14} ions/cm² to prevent channeling effects in the C⁺ and C₆₀⁺ implantation. One of the wafers was implanted with 0.5-keV C⁺ ions at a fluence of 2×10^{15} ions/cm²; the other was implanted with 30-keV C₆₀⁺ ions at a fluence of 4×10^{13} ions/cm² using the 400-kV ion implanter of TIARA. Both implantations were performed at room temperature. Distributions of the implanted carbon atoms were measured with HRBS using 400-keV He⁺ ions at Kyoto University.

Figure 1 shows examples of the HRBS spectra. The carbon peak in the C₆₀⁺-implanted sample has a much longer tail in the low-energy side than that in the C⁺-implanted sample, suggesting the cluster effect on the projected range.

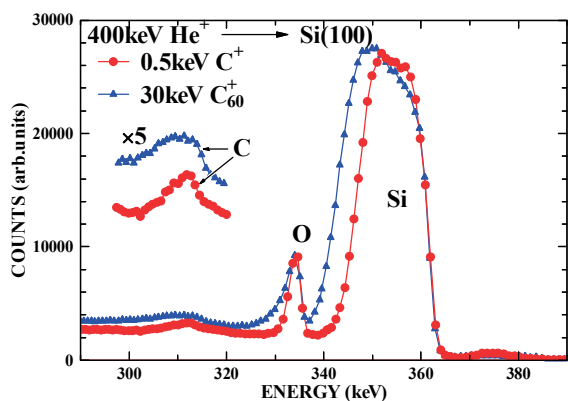


Fig. 1 HRBS spectra of samples implanted with 0.5-keV C⁺ ions and 30-keV C₆₀⁺ ions.

Figure 2 shows the carbon profiles derived from the observed HRBS spectra shown in Fig. 1. The profile for the C⁺ implantation has a peak at ~3 nm and extends up to ~8 nm. An implanted-C profile was calculated using the TRIM code²⁾ and the result is shown by a solid line in Fig. 2. The agreement between the measurements and simulations is rather good. The carbon profile for the C₆₀⁺ implantation is much broader than that for the C⁺ implantation and extends up to 14 nm. The average range was calculated to be 5.8 nm from the observed profile. This value is remarkably larger than that for the C⁺ implantation, which is 3.9 nm. By correcting the effects of the sputtering and the radiation-induced diffusion by the C₆₀⁺ irradiation on the carbon profile, the average range of 30-keV C₆₀⁺ is estimated to be 6.1 nm, which is about 50% larger than the observed range of 0.5-keV C⁺ (4.0 nm). This is a very large cluster effect which has not been observed so far.

Yamamura and Muramoto showed that the average range of Al_n in Ag is 0.98, 1.15 and 1.26 nm for $n = 1, 50$ and 100 at 0.4 keV/atom, respectively³⁾. Their result indicates that there is a notable cluster effect even in the case of $M_1 < M_2$. Because the clearing-the-way effect is effective only for $M_1 > M_2$, however, there is another mechanism to increase the projected range of the cluster ions: A possible mechanism is a so-called acceleration effect³⁾. Further theoretic and/or simulation studies are highly desirable to fully understand the mechanism not only from the fundamental but also from the practical points of view.

References

- 1) P. Sigmund, J. Phys. 50 (C2) (1989) 175.
- 2) J. F. Ziegler et al., The Stopping and Range of Ions in Solids, Pergamon Press, New York, (1985).
- 3) Y. Yamamura, T. Muramoto, Phys. Rev. Lett. 69 (1992) 1463.

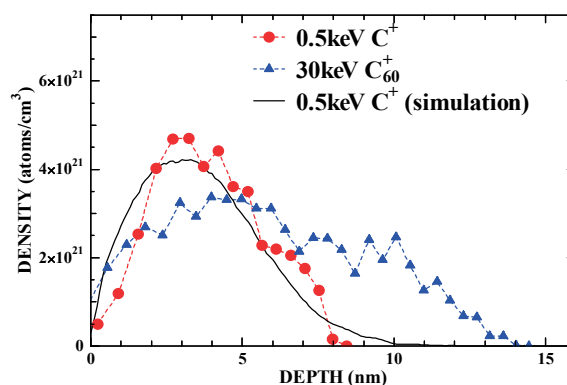


Fig. 2 Depth profiles of implanted C of the both samples and calculated by TRIM simulation.

This is a blank page.

5. Present Status of Irradiation Facilities 2011

5-01	Feature in FY2011, Utilization Status and Beam Time Proportion at TIARA Facility	171
	K. Mizuhashi, H. Takizawa, M. Hosono, Y. Nakamura, S. Kaneya, S. Mochizuki, T. Asai, M. Kawabata and K. Daikubara	
5-02	Operation of the AVF Cyclotron	172
	S. Okumura, I. Ishibori, S. Kurashima, K. Yoshida, T. Yuyama, T. Ishizaka, N. Miyawaki, H. Kashiwagi, Y. Yuri, T. Nara, K. Akaiwa, To. Yoshida, S. Ishiro, Tu. Yoshida, S. Kanou, A. Ihara, K. Takano and H. Saitoh	
5-03	Operation of Electrostatic Accelerators	173
	S. Uno, A. Chiba, K. Yamada, A. Yokoyama, Y. Saitoh, Y. Ishii, T. Satoh, T. Ohkubo, T. Nara, T. Kitano, T. Takayama, S. Kanai, T. Orimo, Y. Aoki and N. Yamada	
5-04	Operation of the Electron Accelerator and the Gamma-ray Irradiation Facilities	174
	T. Agematsu, Y. Haruyama, H. Hanaya, R. Yamagata, H. Seito, Y. Nagao, H. Kaneko, T. Yamaguchi, N. Yagi, M. Takagi, I. Kawashima and S. Matsuzaki	
5-05	Utilization of the Electron Accelerator and the Gamma-ray Irradiation Facilities	175
	Y. Haruyama, T. Agematsu, H. Hanaya, R. Yamagata, H. Seito, Y. Nagao, H. Kaneko, T. Yamaguchi, N. Yagi, M. Takagi, I. Kawashima and S. Matsuzaki	
5-06	Radiation Control in TIARA	176
	Safety Section	
5-07	Radioactive Waste Management in TIARA	177
	T. Ishibashi and T. Hosoi	
5-08	FACILITY USE PROGRAM in Takasaki Advanced Radiation Research Institute	178
	Y. Fukuta, H. Yoshida, D. Nogami and K. Watanabe	

This is a blank page.

5 - 01 Feature in FY2011, Utilization Status and Beam Time Proportion at TIARA Facility

K. Mizuhashi, H. Takizawa, M. Hosono,
Y. Nakamura, S. Kaneya, S. Mochizuki, T. Asai, M. Kawabata and K. Daikubara

Department of Advanced Radiation Technology, TARRI, JAEA

1. Feature in FY 2011

Fiscal year 2011 was significantly influenced by the East Japan Great Earthquake (March 11, 2011). The operation of the TIARA facility which was being planned from April started from the middle of May. Lost beam-time of the experiment due to the great earthquake was compensated with operations on Saturday biweekly. The number of Saturdays on which the accelerators were operated was 12. And it was obliged to re-examine the operation plan during the period of electric power reduction in July, August, and September. The demanded reduction rate of electric power in daytime for summer season was 15% as compared with 2010. The limited value in daytime was 3,600 kW. Therefore, the experiment in daytime was conducted with light ions (H, D with <20 MeV) only by the AVF Cyclotron. Since there were no electricity usage restrictions during the night, the experiment with heavy ions was conducted in night time. On the other hand, the electrostatic accelerators were operated according to prearranged plan at summer, because these accelerators have small amounts of electric power consumption as compared with the cyclotron. As mentioned above, the electric power in the daytime of summer did not exceed 3,200 kW. Moreover, the beam time as an ordinary year was secured.

2. Influence of the Fukushima nuclear power plant disaster

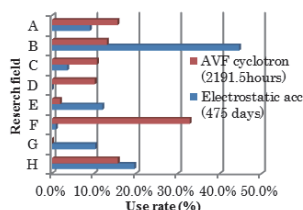
Hydrogen explosions occurred at No.1, No.3 and No.4 units of Fukushima nuclear power plant on March 12, 14 and 15 in 2011, respectively. Four sets of environmental radiation monitors at Takasaki research institute showed the high values at March 15, 2011. Their values were 0.638, 0.637, 0.629 and 0.735 $\mu\text{Sv/h}$, respectively. These proximate causes were ^{131}I from the Fukushima nuclear power plant. Because the half-time of ^{131}I is 8 day, the radiation level was stabilized after 2~3 weeks. Contamination monitoring in a control area for radiation was carried out. After checking that it is pollution-free, preparation of accelerators operation was started. The following managements were carried out before going into a radiation controlled area for three months after a nuclear power plant disaster so that the inside of a radiation control area might not be polluted, (1) Restrict entering (Photo. 1), (2) Wash a hand, (3) Sole cleaning, (4) Contamination monitoring.



Photo. 1 Restriction of entering the radiation controlled area.

3. Beam Time Proportion

Four accelerators were used for various research subjects according to operation plan in fiscal year 2011. The



A: Common use/Promotion use
B: Basic technology
C: Organic material/Radiation chemistry
D: RI production/Nuclear science
E: Inorganic material
F: Medical/Biotechnological application
G: Material for nuclear
H: Material for space

Fig. 1 Proportion of the beam time used for the research fields.

proportion of the beam time used in the fields of research is shown in Fig. 1. The total of utilization time of the AVF cyclotron and three electrostatic accelerators in fiscal year 2011 (2010) was 2,191.5 (2,491.5) hours and 475 (482) days, respectively which were offered to the experiments. The number of Saturdays on which experiment were made about 15. The highest of proportion at the cyclotron was for the field of Medical/Biotechnological application, 32.8%. At the electrostatic accelerators, the highest of proportion was for the field of the Basic technology, 44.6%. The total proportion of “the common use” and “the promotion use” was 15.6% at cyclotron and 9.0% at electrostatic accelerator, respectively. These values were within 20% of the total beam time which is provided as “the common use” and “the promotion use” at the TIARA facility.

About the proportion of the beam time used in the forms of use, the total proportion of “JAEA independent research use” and “the joint research use” was 81.8% at cyclotron and 69.9% at electrostatic accelerator, respectively.

4. Repair of the TIARA building

The number of the repair parts in the 2011 fiscal year was six in all. The articles of main repair were as follows.

1. The cracked parts considered to have influenced from the great earthquake were repaired. Photograph 2 shows the situation of repair of the crack occurred in the maze of the third target room.
2. The leakage of water which occurred during the heavy rain by the No.12 typhoon (September 2, 2011). Photograph 3 shows the repair of water leakage from the circumference of piping which penetrates a building.



Photo. 2 Repair of a wall crack in the third target room.



Photo. 3 Repair of the penetration part of a subterranean wall.

5 - 02

Operation of the AVF Cyclotron

S. Okumura^{a)}, I. Ishibori^{a)}, S. Kurashima^{a)}, K. Yoshida^{a)}, T. Yuyama^{a)}, T. Ishizaka^{a)},
 N. Miyawaki^{a)}, H. Kashiwagi^{a)}, Y. Yuri^{a)}, T. Nara^{a)}, K. Akaiwa^{b)}, To. Yoshida^{b)},
 S. Ishiro^{b)}, Tu. Yoshida^{b)}, S. Kanou^{b)}, A. Ihara^{b)}, K. Takano^{b)} and H. Saitoh^{b)}

^{a)} Department of Advanced Radiation Technology, TARRI, JAEA, ^{b)} Beam Operation Service, Co., Ltd.

Operation

The AVF cyclotron was operated from May 9th in fiscal 2011 and all the planned experiments on April were cancelled due to scheduled blackouts originated from the Great East Japan Earthquake. The cumulative operation time was 65,916.7 hours and the total number of experiments was 9,241 from the first beam extraction in 1991 to March 2012.

Table 1 shows the statistics of the cyclotron operation of fiscal 2011. The total operation time amounted to 3,038.4 hours, and monthly operation times are shown in Fig. 1. The percentages of operation time of the year used for regular experiments, facility use program, the promotion of shared use program, beam tuning, and beam development are 66.5%, 10.7%, 22.0%, and 0.8%, respectively. The extended operation from Friday evening to Saturday evening was carried out eight times in order to supply the cancellation on April.

Table 1 Statistics for cyclotron operation.

Beam service time	2343.6 h
Machine tuning	669.9 h
Beam development	24.9 h
Total operation time	3038.4 h
Change of particle and/or energy	223 times
Change of beam course	274 times
Change of harmonic number	69 times
The number of experiments	522
Experiment cancelled due to machine trouble	0

Table 2 shows the operation time of the multi-cusp ion source for H⁺ and D⁺ production and two ECR ion sources for heavier ions. The ECR ion sources are used alternatively. Fractional distribution of major ions used for experiments is shown in Fig. 2. The tendencies of the statistics are similar to those of the past years.

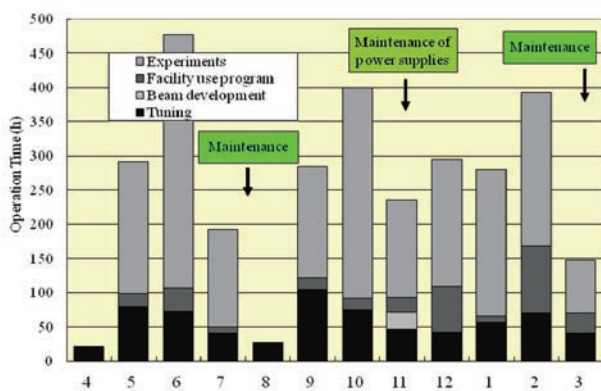


Fig. 1 Monthly operation time.

Table 2 Operation times of ion sources.

Ion source	Operation time (h)	Ratio(%)
Multi-cusp	957.2	27.5
ECR (OCTOPUS)	1249.2	35.8
ECR(HYPERNANOGAN)	1278.7	36.7

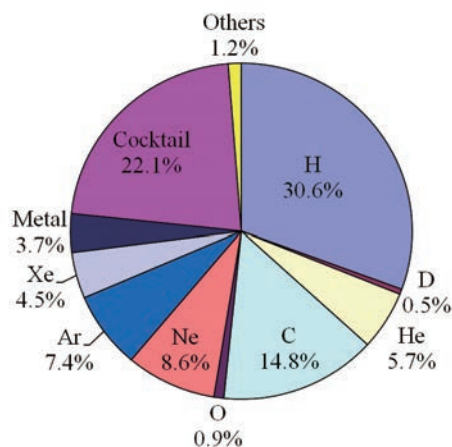


Fig. 2 Ion species used for experiments.

Measure for Power Shortage

In the daytime (9:00-20:00) on July and September, the cyclotron was operated at the condition of 10 or 20 MeV H⁺ beam only, to meet the requirement of reduction of electric power consumption.

Maintenance

The regular yearly overhaul and maintenance were carried out. The major items were as follows: 1) Exchange of circuit elements of the RF system and readjustment of the circuit. 2) Replacement of the cryogenic pumps in the injection system. 3) Exchange of cooling fans for power supplies. 4) Inspection of chilling machines for ion sources and the cyclotron. 5) Routine maintenance of the power supplies.

Technical Development

A new beam acceleration test was carried out for cocktail beam of M/Q (mass to charge ratio)=6.4 (210 MeV ⁸⁴Kr¹³⁺, 324 MeV ¹²⁹Xe²⁰⁺, and 490 MeV ¹⁹²Os³⁰⁺) and they are ready for use in experiments.

Additional vacuum pumps were installed in the LB experimental chamber for the large-area uniform irradiation in order to increase the evacuation capacity.

In order to reduce the tuning time, scaling method has been introduced to change the ion species having various mass to charge ratios (M/Q) in a short-time. The detail is described elsewhere in this annual report.

5 - 03

Operation of Electrostatic Accelerators

S. Uno ^{a)}, A. Chiba ^{a)}, K. Yamada ^{a)}, A. Yokoyama ^{a)}, Y. Saitoh ^{a)}, Y. Ishii ^{a)},
 T. Satoh ^{a)}, T. Ohkubo ^{a)}, T. Nara ^{a)}, T. Kitano ^{b)}, T. Takayama ^{b)}, S. Kanai ^{b)},
 T. Orimo ^{b)}, Y. Aoki ^{b)} and N. Yamada ^{b)}

^{a)} Department of Advanced Radiation Technology, TARRI, JAEA,
^{b)} Beam Operation Service, Co., Ltd

1. Operations and Status

Fortunately, the three electrostatic accelerators at the TIARA had no mechanical damage when the Tohoku earthquake happened on March 11, 2011. However, they could not be operated during April, due to the influence of planned power outage by Tokyo Electric Power Company. These electrostatic accelerators were operated on Saturday for twelve days in order to compensate for the lost experimental time. As a result, the yearly operation time of the 3 MV tandem accelerator, the 400 kV ion implanter and the 3 MV single-ended accelerator had kept the same level as the ordinary one, whose operation time amounted to about 2,000, 1,900 and 2,500 hours, respectively. The tandem accelerator had no trouble in this year, while the ion implanter and the single-ended accelerator stopped for troubles of two days and one day, respectively. The total operation time of each accelerator were 36,598, 32,457 and 41,674 hours, since the operations started. The monthly operation time of three electrostatic accelerators is shown in Fig. 1.

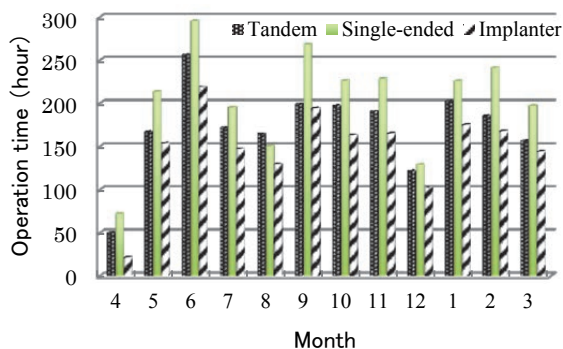


Fig. 1 Monthly operation time in FY 2011.

2. New Beams

The ion beam of erbium(Er) with 11.7 MeV was accelerated by the tandem accelerator, whose intensity was 20 nA at charge state of 3+, because of the request from a user.

The users of the ion implanter required the sequential irradiation by fullerene ions of C₆₀ and C₇₀ to study the irradiation effect of their ions. A mixed powder method has been developed for the requirement. These fullerene ions were generated without replacing the Freeman type ion source with another one. The generation of each fullerene ion could be controlled only by the temperature of the oven in the Freeman type ion source.



Fig. 2 Rectangular type gasket for the tandem.

3. Maintenance and Development

SF₆ gas is used as an insulator of internal devices for numerous electrostatic accelerators, although it is a global warming gas. In Addition, its warming coefficient has 23,900 times as large as CO₂ gas. The SF₆ gas of 90 kg leaked from the Viton gasket on the tank base flange for the tandem accelerator in the last fiscal year. The Viton gasket for the sealed in the gas was changed from a round shape type to a rectangular cross section type, because the leak of the SF₆ gas was found in the gasket whose diameter was 1,200 mm. The photograph of the new gasket attached on the tank base of the tandem is shown in Fig. 2.

The thermal mechanical leak valve adjusting gas for the RF ion source in the single-ended accelerator was replaced, because it reached to the operation time of over 3,000 hours.

The new beam line with the chamber was developed for experiments using cluster beam connected to the ion implanter in the No.2 target room. Additionally, the switching magnet was replaced with new one to serve a beam to the chamber, and the installation of apparatus was completed by the end of 2011. All the beam lines connected to the ion implanter are shown in Fig. 3.

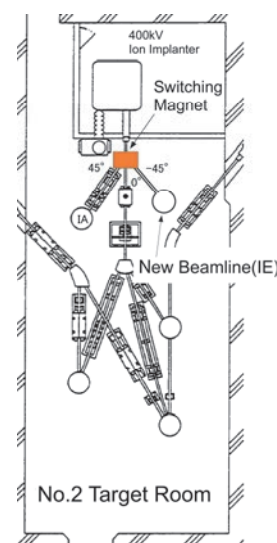


Fig. 3 All the beam lines of the implanter.

5 - 04 Operation of the Electron Accelerator and the Gamma-ray Irradiation Facilities

T. Agematsu^{a)}, Y. Haruyama^{a)}, H. Hanaya^{a)}, R. Yamagata^{a)}, H. Seito^{a)}, Y. Nagao^{a)}, H. Kaneko^{a)}, T. Yamaguchi^{b)}, N. Yagi^{b)}, M. Takagi^{b)}, I. Kawashima^{b)} and S. Matsuzaki^{b)}

^{a)} Department of Advanced Radiation Technology, TARRI, JAEA,

^{b)} Takasaki Establishment, Radiation Application Development Association (RADA)

1. Operation

The electron accelerator and the gamma-ray irradiation facilities were stopped by the influence of the earthquake that happened on March 11, 2011. Afterward, each irradiation facility was resumed on April 4, 2011, after the check mainly on an interlock system. The electron accelerator and the gamma-ray irradiation facilities have been operated without serious trouble.

1.1 Electron accelerator

The electron accelerator was on service as scheduled in 9:00~17:30 on Monday and Friday, and in 8:30~23:00 from Tuesday to Thursday, to satisfy user's demand for operation time. The annual operation time of the electron accelerator in FY 2011 is 1,059 h similarly in FY 2010, as shown in Fig. 1.

1.2 Gamma-ray irradiation facilities

The ⁶⁰Co gamma-ray irradiation facilities consisting of three buildings with eight irradiation rooms cover a wide dose-rate range from 10⁻¹ to 10⁴ Gy/h. The annual operation times for the first, the second cobalt irradiation facilities and food irradiation facility are 18,722 h, 9,976 h and 7,427 h, respectively, as shown in Fig. 2.

2. Maintenance

2.1 Electron accelerator

The operation of the accelerator was stopped three times. The first time was for repairs on the inside of the accelerator vessel with mechanical trouble for 4 days in April. This trouble was the post-influence of the earthquake. The second time was for 9 days in June by two troubles of the

beam control circuit inside the accelerator vessel and isolation trouble by mixing of air into SF₆ gas. However, the operation was continued using a temporary beam control circuit and keeping isolation by putting fine SF₆ gas. The third time was 11 days for repairs in September and October. The optical link control circuit for beam control was repaired, and SF₆ gas was refined using the low-purity SF₆ refining system of Taiyo Nippon Sanso Higashikanto Corporation after repair of the SF₆ gas withdrawal system.

2.2 Gamma-ray irradiation facilities

The periodical maintenance check on a mechanical system for radiation source transportation has been mainly performed every three years among three gamma-ray irradiation facilities one by one. The maintenance check of the second irradiation facility was done in July 2011, with 19 days interruption.

The ⁶⁰Co sources were purchased and loaded to the irradiation room No. 6 in the second irradiation facility to increase wide and homogeneous irradiation area with high dose rate in this room. Forty five pencil sources of ⁶⁰Co with length of 30 cm each, eight coin sources of ⁶⁰Co and the gamma-ray radiographic apparatus with a ⁶⁰Co source were disposed to JRIA (Japan Radioisotope Association).

The water-repellent sheet of the roof on the second irradiation facility building was re-covered. The PLC, which was the controller of the water purification system of the first and the second cobalt irradiation facilities, was renewed. The manipulator of the irradiation room No. 2 in the food irradiation facility was removed to avoid irradiation damage during non-use.

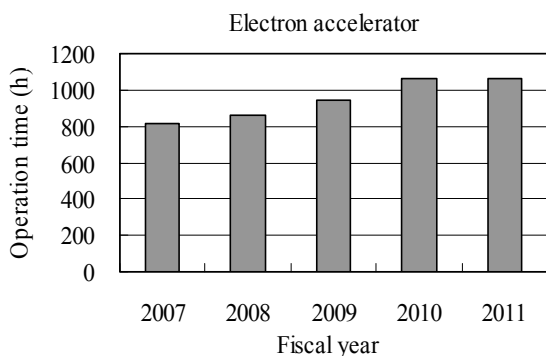


Fig. 1 Annual operation time of the electron accelerator.

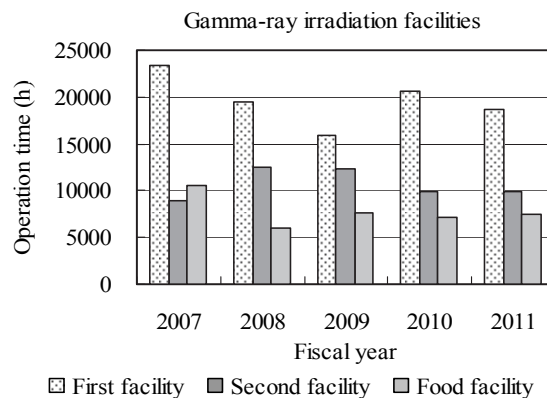


Fig. 2 Annual operation time of the ⁶⁰Co gamma-ray irradiation facilities.

5 - 05 Utilization of the Electron Accelerator and the Gamma-ray Irradiation Facilities

Y. Haruyama ^{a)}, T. Agematsu ^{a)}, H. Hanaya ^{a)}, R. Yamagata ^{a)}, H. Seito ^{a)}, Y. Nagao ^{a)}, H. Kaneko ^{a)}, T. Yamaguchi ^{b)}, N. Yagi ^{b)}, M. Takagi ^{b)}, I. Kawashima ^{b)} and S. Matsuzaki ^{b)}

^{a)}Department of Advanced Radiation Technology, TARRI, JAEA,

^{b)}Takasaki Establishment, Radiation Application Development Association (RADA)

The electron accelerator and the three gamma-ray irradiation facilities were operated for various research subjects according to the operation plan in FY 2011 without serious trouble.

The irradiation time and the number of research subjects for each facility in FY 2011 are shown in Table 1. The accelerator mainly served for graft-polymerization for new material development, radiation effect study on semiconductors and various experiments of visiting users. The first cobalt irradiation facility mainly served for radiation-resistance testing of cables used in nuclear power plants and nuclear reactor facilities with a long irradiation period. The second cobalt irradiation facility, involving the irradiation room No. 6 operated on an hourly schedule, mainly served for development of new functional materials and other research subjects of visiting users. The food irradiation facility mainly served for development of detection method for irradiated foods and radiation resistance testing at lower dose rates.

Figure 1 shows the number of research subjects in each research field at each facility in FY 2007-2011. The number of research subjects at the electron accelerator increased in the research fields of nuclear facilities and resources & biotechnology, and decreased in the fields of material processing and material for space. The number of research subjects at the gamma-ray irradiation facilities

increased in the fields of material for space and material processing, and decreased in the fields of nuclear facilities and resources & biotechnology.

Of all these research subjects, 15 ones at the electron accelerator and 94 ones at the gamma-ray irradiation facilities were relevant to the Fukushima Daiichi nuclear disaster.

Table 1 The irradiation time and the number of research subjects for each facility in FY 2011.

Research fields	Electron accelerator		Gamma-ray irradiation facilities	
	Irradiation time (h)	Research subject	Irradiation time (h)	Research subject
Material processing	174.0	195	4866.0	297
Heat-resist material	133.3	34	22.0	1
Material for space	431.1	91	3012.5	37
Nuclear facilities	37.4	5	17106.6	41
Environment	4.2	4	2516.9	74
Basic technology	117.5	12	202.3	24
Resources & Biotechnology	0.9	3	251.6	142
Joint use	160.8	24	32144.4	180
Total	1059.2	368	60122.3	796

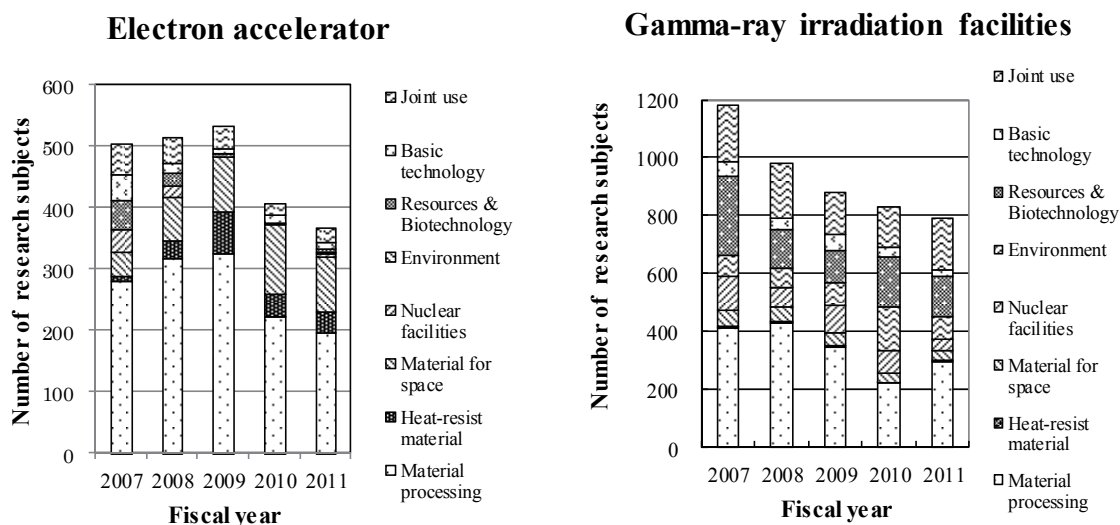


Fig. 1 The number of research subjects (FY 2007-2011).

5 - 06

Radiation Control in TIARA

Safety Section

Department of Administrative Services, TARRI, JAEA

1. Individual monitoring

(1) Individual monitoring for the radiation workers

Table 1 shows a distribution of effective dose of the radiation workers in FY 2011. The effective dose values of almost all radiation workers were below the detection limit (0.1 mSv).

The maximum dose was 0.2 mSv/y due to the overhaul of the TIARA AVF cyclotron.

Table 1 Distributions of the effective dose of the radiation workers in FY 2011.

Items	persons	Number of persons in each periods				Total *2
		1st quarter	2nd quarter	3rd quarter	4th quarter	
Distribution range of effective dose	HE < 0.1	573	606	605	634	713
	0.1 ≤ HE ≤ 1.0	0	3	1	0	4
	1.0 < HE ≤ 5.0	0	0	0	0	0
HE:Effective dose (mSv) *1	5.0 < HE ≤ 15.0	0	0	0	0	0
	15.0 < HE	0	0	0	0	0
Number of persons under radiation control (A)		573	609	606	634	717
Exposure above 1mSv	Number of persons (B)	0	0	0	0	0
	(B)/(A)×100(%)	0	0	0	0	0
Mass effective dose (Person·mSv)		0.0	0.4	0.1	0.0	0.5
Mean dose (mSv)		0.00	0.00	0.00	0.00	0.00
Maximum dose (mSv)		0	0.2	0.1	0	0.2

*1 The dose by the internal exposure was not detected.
*2 Net number.

(2) Individual monitoring for the visitors and others

Table 2 shows the number of persons who temporarily entered the radiation controlled areas. The effective dose of all persons was less than 0.1 mSv.

Table 2 The number of persons who temporary entered the radiation controlled areas in FY 2011.

Periods	1st quarter	2nd quarter	3rd quarter	4th quarter	Total
Number of persons	777	953	1116	1536	4382

2. Monitoring of radioactive gas and dust

Table 3 shows the maximum radioactive concentrations and total activities for radioactive gases released from the stack of TIARA, during each quarter of FY 2011.

Small amount of ⁴¹Ar, ¹¹C, ¹³N and ⁷⁶Br were detected for some time during operation of the cyclotron or experiment, but the pulverized substances (⁶⁵Zn, etc.) were not detected.

Table 3 Monitoring results of released radioactive gases and dust in FY 2011.

Nuclide	Items	1st quarter	2nd quarter	3rd quarter	4th quarter	Total
		⁴¹ Ar	Maximum concentration	<1.4×10 ⁻⁴	<1.4×10 ⁻⁴	
	Activity	0	0	0	7.6×10 ⁷	7.6×10 ⁷
¹¹ C	Maximum concentration	<1.4×10 ⁻⁴	<1.4×10 ⁻⁴	<1.4×10 ⁻⁴	<1.4×10 ⁻⁴	
	Activity	9.5×10 ⁷	7.5×10 ⁷	1.2×10 ⁸	1.4×10 ⁸	4.3×10 ⁸
¹³ N	Maximum concentration	<1.4×10 ⁻⁴	—	<1.4×10 ⁻⁴	<1.4×10 ⁻⁴	
	Activity	4.0×10 ⁸	—	9.8×10 ⁷	2.7×10 ⁸	7.7×10 ⁸
⁷⁶ Br	Maximum concentration	—	—	<1.4×10 ⁻⁴	—	
	Activity	—	—	1.8×10 ⁷	—	1.8×10 ⁷
⁶⁵ Zn	Maximum concentration	<6.1×10 ⁻¹⁰	<6.6×10 ⁻¹⁰	<5.9×10 ⁻¹⁰	<5.9×10 ⁻¹⁰	
	Activity	0	0	0	0	0

Unit : Bq/cm³ for Maximum concentration, Bq for Activity.

3. Monitoring for external radiation and surface contamination

External radiation monitoring was routinely carried out in/around the radiation controlled areas and surface contamination monitoring was also carried out. Neither unusual value of dose equivalent rate nor surface contamination was detected.

Figure 1 shows a typical example of distribution of the dose equivalent rate in the radiation controlled area of the cyclotron building.

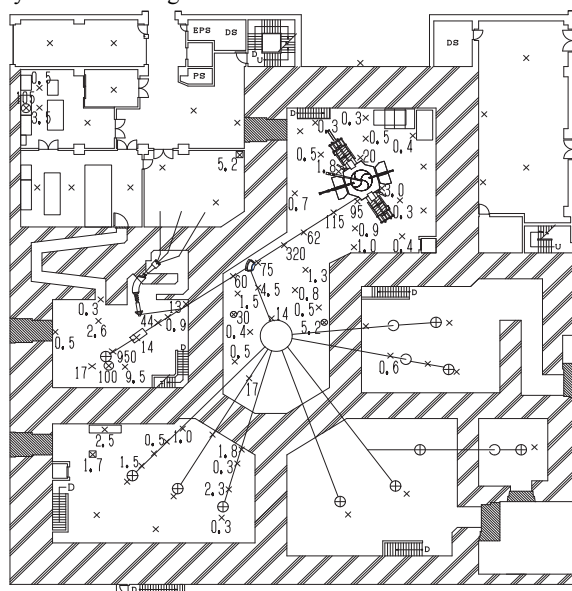


Fig. 1 Dose equivalent rate distribution in the radiation controlled area of the cyclotron building.

Measurement date : 26th, 27th and 30th March 2012,
Measuring position : indicated with × 1 m above floor,
Unit : μSv/h.

(The values are not indicated if they are less than 0.2 μSv/h.)

5 - 07

Radioactive Waste Management in TIARA

T. Ishibashi and T. Hosoi

Department of Administrative Services, TARRI, JAEA

1. The radioactive wastes management

The radioactive wastes generated in TIARA are managed by Utilities and Maintenance Section. The main radioactive wastes are the solid wastes generated from the research experiment and the maintenance of the cyclotron. Other radioactive wastes are the liquid wastes such as inorganic waste fluids generated from the research experiment and the air-conditioning machines in radiation controlled area. These wastes are managed according to their properties.

2. Solid radioactive waste

Table 1 shows the amounts of solid wastes at various properties and kinds generated in each quarter of FY 2011. The main solid waste is generated from the research experiment and the maintenance of the cyclotron.

Combustible wastes are rubber gloves, paper, and clothes, etc. Incombustible wastes are metal pieces, the glasses, and contaminated parts.

3. Liquid radioactive waste

Table 2 shows the amounts of liquid wastes generated in each quarter of FY 2011. Most of liquid waste was inorganic waste water generated from chemical experiments and condensed water from operation of air conditioning units installed in each room of the first class radiation controlled area. The largest quantity of waste water in summer season (2nd quarter) is mainly due to condensed water. After the treatment by evaporation, inorganic water is reused in the controlled area. Only small amounts of concentrated liquid are generated from the evaporation.

Table 1 Radioactive solid wastes generated in FY 2011.

Items	Amounts	Amounts of Solid wastes in each period (m ³)					Number of packages /drum
		1st quarter	2nd quarter	3rd quarter	4th quarter	Total	
Category A*		0.36	0.86	0.26	0.30	1.78	
1) Combustible		0.32	0.28	0.22	0.20	1.02	6**
2) Incombustible		0.04	0.58	0.04	0.10	0.76	0
Compressible		0.04	0.06	0.04	0.10	0.24	1**
Filters		0	0.52	0	0	0.52	0
Incompressible		0	0	0	0	0	0
Ion exchange resin		0	0	0	0	0	0
Category B*		0	0	0	0	0	0

* Defined by dose at the outer surface of container : (A) < 2 mSv/h ≤ (B),

** 200-liter drum.

Table 2 Radioactive liquid waste generated in FY 2011.

Items	Amounts	Amounts of generation in each period (m ³)					Number of packages /drum
		1st quarter	2nd quarter	3rd quarter	4th quarter	Total	
Category A*		11.03	33.04	3.07	3.09	50.23	
1) Inorganic		10.93	33.04	3.07	2.89	49.93	treatment
2) Organic		0	0	0	0	0	0
Organic		0	0	0	0	0	0
Oil		0	0	0	0	0	0
3) Sludge		0	0	0	0.1	0.1	1
4) Evaporation residue		0.1	0	0	0.1	0.2	2
Category B*		0	0	0	0	0	0

* Defined by concentrations in Bq/cm³ (β, γ) : (A) < 3.7 × 10 ≤ (B) < 3.7 × 10⁴.

5 - 08 FACILITY USE PROGRAM in Takasaki Advanced Radiation Research Institute

Y. Fukuta, H. Yoshida, D. Nogami and K. Watanabe

Department of Advanced Radiation Technology, TARRI, JAEA

1. Introduction

The facilities of JAEA are widely opened to users in universities, public institutes, and industries, etc. Taking over the former system, FACILITY USE PROGRAM started in 2006, which is the system of facility use for the user's service on fee-charging basis. The open used facilities in Takasaki are Co-60 Gamma-ray Irradiation Facilities, Electron Accelerator, TIARA (Takasaki Ion Accelerators for Advanced Radiation Application), and some of the off-line analysis instruments.

In this program, the Research Proposals are examined carefully every half year from the standpoint of the availability and the validity of the experimental plan by the special committee. The facility usage fee has revised in FY2011. The details of the fee consist of handling fees, the irradiation fee, the expendables fee, radioactive waste disposal expenses and the additional charge. In case of Non-proprietary research, the users, who are exempted from the irradiation fee, should report the experimental results to JAEA. And JAEA opens the reports to the public. Universities can also apply through another facility use program operated by The University of Tokyo. Such applications are accepted as priority case. Table 1 shows main classification of FACILITY USE PROGRAM.

Table 1 Main Classification of FACILITY USE PROGRAM.

Purpose	Research and Development		Except R&D
	General	Priority case	
Classification			Commercial
Result	Non-proprietary	Proprietary	
Referee	Yes	No	
Charge*	A	B	C

*A = handling fees + the expendables fee + radioactive waste disposal expenses,

B = handling fees + the irradiation fee,

C = handling fees + the irradiation fee + depreciation.

2. Use in FY2011

There were 12 applications of Research Proposals in FY2010 at Takasaki Institute, and 10 of them were as Non-proprietary use. Including the users from priority case and others, 250 applications from 81 users are accepted. Table 2 and Fig. 1 show user's classification for each facility and distribution of classification for FACILITY USE PROGRAM.

Table 2 User's classification for each facility.

Facility	User	University	Public Institute	Industry and others	Total
TIARA	AVF cyclotron	5	1	7	13
	3MV tandem accelerator	2	1	1	4
	3MV single-ended accelerator	2	0	0	2
	400kV ion implanter	4	0	0	4
Co-60 gamma-ray irradiation facilities		14	7	27	48
Electron accelerator		4	1	5	10
Total for each classification		31	10	40	81

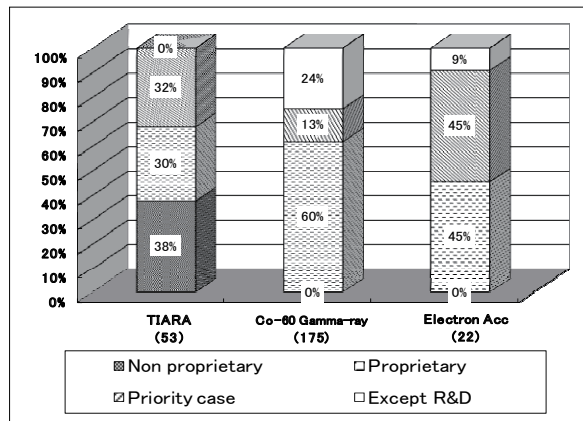


Fig. 1 Distribution of classification for FACILITY USE PROGRAM. The number of theme for each facility is shown in parentheses.

3. Public Relations

The information, such as an outline of this system, guidelines for applicants, format download etc. can be found on JAEA website as follows:

<http://sangaku.jaea.go.jp/3-facility/01-intro/index-02.html>.

The "Project for Promotion of Shared Use of High Technology Research Institute", which is one of the subsidiary project of Ministry of Education, Culture, Sports, Science and Technology (MEXT) has been cooperated from FY2009. This project intends that industrial users promote shared use of facilities, which accelerates the whole activity of science technology from basic research to innovation creation.

An outline of this project can be seen on website as follows: <http://www.taka.jaea.go.jp/innovation/index.html>.

Appendix

Appendix 1 List of Publication	181
A1.1 Publication in Journal	181
A1.2 Publication in Proceedings	193
Appendix 2 List of Related Patents	202
Appendix 3 List of Related Press-Release and Television Broadcasting	204
Symbol used in the Appendix 1 to 3	205
Appendix 4 Type of Research Collaboration and Facilities Used for Research ..	206
Appendix 5 Examples of Typical Abbreviation Name for Organizations	
in Japan Atomic Energy Agency (JAEA)	208

This is a blank page.

Appendix 1. List of Publication

A 1.1 Publications in Journal

11J001 1-01 E

C. Morioka, K. Shimazaki, S. Kawakita,
M. Imaizumi, H. Yamaguchi, T. Takamoto,
S. Sato, T. Ohshima, Y. Nakamura,
K. Hirako and M. Takahashi
“First Flight Demonstration of Film-Laminated
InGaP/GaAs and CIGS Thin-Film Solar Cells by
JAXA’s Small Satellite in LEO”
Prog. Photovolt: Res. Appl. 19 (2011) 825-33.

11J002 1-02 C, T, S, I

S. Sato, H. Sai, T. Ohshima, M. Imaizumi,
K. Shimazaki and M. Kondo
“Temporal Donor Generation in Undoped
Hydrogenated Amorphous Silicon Induced by
Proton Bombardment”
Appl. Phys. Express 4 (2011) 061401.

11J003 1-02 C, T, S, I

S. Sato, H. Sai, T. Ohshima, M. Imaizumi,
K. Shimazaki and M. Kondo
“Anomalous Enhancement in Radiation Induced
Conductivity of Hydrogenated Amorphous Silicon
Semiconductors”
Nucl. Instrum. Meth. Phys. Res. B, in press.

11J004 1-02 C, T, S, I

S. Sato, H. Sai, T. Ohshima, M. Imaizumi,
K. Shimazaki and M. Kondo
“Temporal Electric Conductivity Variations of
Hydrogenated Amorphous Silicon Due to High
Energy Protons”
J. Non-Cryst. Sol., in press.

11J005 1-03 C

S. Kuboyama, A. Maru, H. Shindou, N. Ikeda,
T. Hirao, H. Abe and T. Tamura
“Single-Event Damages Caused by Heavy Ions
Observed in AlGaIn/GaN HEMTs”
IEEE Trans. Nucl. Sci., Vol. 58, Issue 6 (2011)
2734-38.

11J006 1-09 C

S. Onoda, T. Yamamoto, T. Ohshima, J. Isoya,
T. Teraji and K. Watanabe
“Diamonds Utilized in the Development of Single
Ion Detector with High Spatial Resolution”
Trans. Mater. Res. Soc. Jpn., in press.

11J007 1-09 C, T

S. Onoda, T. Makino, S. Ono, S. Katakami,
M. Arai and T. Ohshima
“Spatial, LET and Range Dependence of Enhanced
Charge Collection by Single Ion Strike in 4H-SiC
MESFETs”
IEEE Trans. Nucl. Sci., in press.

11J008 1-10 E

K. Kubo, C. Grezes, A. Drewes, T. Umeda,
J. Isoya, H. Sumiya, N. Morishita, H. Abe,
S. Onoda, T. Ohshima, V. Jacques, A. Dréau,
J.-F. Roch, I. Diniz, A. Auffeves, D. Vion,
D. Esteve and P. Bertet
“Hybrid quantum circuit with a superconducting
qubit coupled to a spin ensemble”
Phys. Rev. Lett. 107 (2011) 220501(1-5).

11J009 1-12 I

H. Okada, A. Abderrahmane, S. Koide,
H. Takahashi, S. Sato, T. Ohshima and A. Sandhu
“Effects of Proton Irradiation on the
Magnetoelectric Properties of 2DEG AlGa_N/Ga_N
Micro-Hall Sensors”
J. Phys.: Conf. Series 352 (2012) 012010.

11J010 1-17 G

R. Yamada, Y. Kumagai and R. Nagaishi
“Effect of Alumina on the Enhancement of
Hydrogen Production and the Reduction of
Hydrogen Peroxide in the γ -Radiolysis of Pure
Water and 0.4 M H₂SO₄ Aqueous Solution”
Int. J. Hydrogen Energy, 36 (2011) 11646-53.

11J011 1-17 G

熊谷 友多、永石 隆二、木村 敦、田口 光正、
西原 健司、山岸 功、小川 徹
“放射性汚染水処理に関わるゼオライト系吸着剤と
海水との混合物からの水素発生量の測定と評価”
日本原子力学会 和文論文誌, 10(4) (2011) 235-39.

11J012 1-17 G

永石 隆二
“ゼオライトによる放射性汚染水処理における放射
線効果の検討”
放射線化学, 92 (2011) 15-21.

11J013 1-22 T, S, I

I. Ioka, Y. Ishijima, K. Usami, N. Sakuraba,
Y. Kato and K. Kiuchi
“Radiation Hardening and IASCC Susceptibility of
Extra High Purity Austenitic Stainless Steel”
J. Nucl. Mater. 417 (2011) 887.

11J014 1-27 G

J. Chen, D. Li, H. Koshikawa,
M. Asano and Y. Maekawa
“Crosslinking and grafting of polyetheretherketone
film by radiation techniques for application in fuel
cells”
J. Membr. Sci. 362 (2010) 488-94.

11J015 1-31 C

T. Yamaki, N. Nuryanthi, H. Koshikawa,
M. Asano, S. Sawada, S. Hasegawa, Y. Maekawa,
K.-O. Voss, C. Trautmann and R. Neumann
“Conductometric Analysis for the Formation of
Poly(vinylidene fluoride) -Based Ion Track
Membranes”
ECS Trans. 35 (2012) 1-12.

11J016 1-31 C

T. Yamaki, N. Nuryanthi, H. Koshikawa,
M. Asano, S. Sawada, S. Hasegawa, Y. Maekawa,
K.-O. Voss, C. Trautmann and R. Neumann
“Investigation of Nanopore Evolution in
Track-Etched Poly(vinylidene fluoride) Membranes”
Trans. Mater. Res. Soc. Jpn. (2012) in press.

11J017 1-31 C

T. Yamaki, M. Asano, H. Koshikawa,
Y. Maekawa, D. Severin,
T. Seidl and C. Trautmann
“In-Situ Analysis of Ion-Beam-Induced
Degradation and Post-Irradiation Oxidation in
Poly(vinylidene fluoride)”
GSI Sci. Rep. 2011 (2012) in press.

11J018 1-32 G

N. Tanaka, T. Yamaki, M. Asano, Y. Maekawa,
T. Terai and K. Onuki

“Effect of Temperature on Electro-Electrodialysis of HI-I₂-H₂O Mixture Using Ion Exchange Membranes”
J. Membr. Sci. (2012) in press.

11J019 1-33 C, I

八巻 徹也

“量子ビームを利用した燃料電池用高分子電解質膜の創製に関する研究”
膜 (MEMBRANE) 36 (2011) 240-47.

11J020 2-01 E

Y. Ueki, N.C.Dafader, H. Hoshina,
 N. Seko and M. Tamada

“Study and Optimization on Graft Polymerization under Normal Pressure and Air Atmospheric Conditions, and its Application to Metal Adsorbent”
Radiat. Phys. Chem., in press.

11J021 2-02 G

A. Iwanade, N. Kasai, H. Hoshina, Y. Ueki,
 S. Saiki and N. Seko

“Hybrid grafted ion exchanger for decontamination of radioactive cesium in Fukushima Prefecture and other contaminated areas”
J. Radioanal. Nucl. Chem., in press. (Published online: 10 March 2012).

11J022 2-04 G

H. Hoshina, N. Kasai, T. Shibata, Y. Aketagawa,
 M. Takahashi, A. Yoshii, Y. Tsunoda and N. Seko
 “Synthesis of arsenic graft adsorbent in pilot scale”
Radiat. Phys. Chem., in press.

11J023 2-06 O

S. Okubo, T. Takahashi, T. Gowa, T. Sasaki,
 N. Nagasawa, M. Tamada, A. Oshima,
 S. Tagawa and M. Washio

“Micro-fabrication of Biodegradable Polymers Using Focused Ion Beam”

J. Photopolym. Sci. Tech., 23 [3], (2010) 393-97.

11J024 2-06 E

S. Okubo, N. Nagasawa, A. Kobayashi, T. Gowa
 Oyama, M. Taguchi, A. Oshima,
 S. Tagawa and M. Washio

“Micro-/Nanofabrication of crosslinked poly(L-lactic acid) using electron beam nanoimprint lithography”
Appl. Phys. Express, 5 (2012) 027303.

11J025 2-09 G

T. M. Quynh, M. Yoneyama, Y. Maki,
 N. Nagasawa and T. Dobashi

“Thermosensitive micelles composed of poly(lactide)-g-poly(NIPAM-co-HEMA) graft copolymers”
Key Eng. Mater., 459 (2011) 51-56.

11J026 2-10 E, G

A. Kimura, M. Osawa and M. Taguchi

“Decomposition of persistent pharmaceuticals in wastewater by ionizing radiation”
Radiat. Phys. Chem., in press.

11J027 3-02 C, T

T. Ushigome, N. Shikazono, K. Fujii,
 R. Watanabe, M. Suzuki, C. Tsuruoka,
 H. Tauchi and A. Yokoya

“Yield of Single- and Double-Strand Breaks and Nucleobase Lesions in Fully Hydrated Plasmid DNA Films Irradiated with High-LET Charged Particles”
Radiat. Res. (2012) in press.

11J028 3-05 C

H. Matsumoto, M. Tomita, K. Otsuka,
M. Hatashita and N. Hamada.
“Nitric oxide is a key molecule serving as a bridge
between radiation-induced bystander and adaptive
responses”
Curr. Mol. Pharmacol. 4 (2011) 126-34.

11J029 3-10 C

A. Tanaka, Y. Nakatani, N. Hamada,
A. Jinno-Oue, N. Shimizu, S. Wada, T. Funayama,
T. Mori, S. Islam, S. A. Hoque, M. Shinagawa,
T. Ohtsuki, Y. Kobayashi and H. Hoshino
“Ionising irradiation alters the dynamics of human
long interspersed nuclear elements 1 (LINE1)
retrotransposon”
Mutagenesis (2012) in press.

11J030 3-12 C

Y. Kodama, A. Noda, C. Booth, D. Breault, T. Suda,
J. Hendry, T. Shinohara, C. Rube, EK. Nishimura,
H. Mitani, N. Nakamura and O. Niwa
“International workshop: Radiation effects on
mutation in somatic and germline stem cells”
Int. J. Radiat. Biol. (2012) in press.

11J031 3-13 C

A. Musha, Y. Yoshida, T. Takahashi, K. Ando,
T. Funayama, Y. Kobayashi, A. Negishi,
S. Yokoo and T. Nakano
“Synergistic effect of heat shock protein 90 inhibitor,
17-allylamino-17-demethoxygeldanamycin and
X-rays, but not carbon-ion beams, on lethality in
human oral squamous cell carcinoma cells”
J. Radiat. Res. (2012) in press.

11J032 3-13 C

Y. Yoshida, Y. Suzuki, WS. Al-Jahadari,
N. Hamada, T. Funayama, K. Shirai, H. Katoh,
T. Sakashita, Y. Kobayashi and T Nakano
“Evaluation of the relative biological effectiveness
of carbon ion beams in the cerebellum using the rat
organotypic slice culture system”
J. Radiat. Res. 53 (2012) 87-92.

11J033 3-16 C

Y. Mutou-Yoshihara, T. Funayama,
Y. Yokota and Y. Kobayashi
“Involvement of bystander effect in suppression of
the cytokine production induced by heavy-ion
broad beams”
Int. J. Radiat. Biol. 88 (2012) 258-66.

11J034 3-19 G

亀谷 宏美、鵜飼 光子
“殺菌処理された香辛料の成分変化の ESR による
解析”
日本調理科学会誌 44 (2011) 49-54.

11J035 3-19 G

鵜飼 光子
“解説 放射線照射香辛料の ESR 法による分析”
ぶんせき 3 (2011) 132-36.

11J036 3-19 G

H. Kameya, H. Nakamura,
M. Ukai and Y. Shimoyama
“Electron Spin Resonance Spectroscopy of
Gamma-Irradiated Glucose Polymers”
Appl. Magn. Reson. 40 (2011) 395-404.

11J037 3-18, 3-19 G

菊地 正博、下山 雄平、鵜飼 光子、小林 泰彦

“照射された生鮮果実パパイアの迅速 ESR 検知法”
Radioisotopes 60 (2011) 163-71.

11J038 3-19 G

亀谷 宏美、鵜飼 光子
 “国内の市販唐辛子と放射線処理唐辛子の ESR
 によるラジカルの解析”
Radioisotopes 60 (2011) 173-80.

11J039 3-18, 3-19 G

M. Kikuchi, Y. Shimoyama,
 M. Ukai and Y. Kobayashi
 “ESR detection procedure of irradiated papaya
 containing high water content”
Radiat. Phys. Chem. 80 (2011) 664-67.

11J040 3-19, 3-18 E, G

貝森 良彦、坂本 侑輝、菊地 正博、亀谷 宏美、
 中村 秀夫、下山 雄平、小林 泰彦、鵜飼 光子
 “照射食品に誘導されるラジカルの減衰挙動”
食品照射 46 (2011) 13-18.

11J041 3-19, 3-18 G

H. Kameya, M. Kikuchi, H. Hara, M. Furuta,
 S. Todoriki, Y. Kobayashi,
 M. Ukai and Y. Shimoyama
 “Relaxation Behaviors of Free Radicals from
 γ -Irradiated Black Pepper Using Pulsed EPR
 Spectroscopy”
Appl. Magn. Reson. 42 (2012) 153-59.

11J042 3-20 S

T. Satoh, M. Koka, W. Kada, A. Yokoyama,
 T. Ohkubo, A. Yamazaki, Y. Ishii and T. Kamiya
 “Effectiveness of a Combination of ML-EM and
 STIM-CT in PIXE-CT for Biological Specimen”
Int. J. PIXE (accepted).

11J043 3-20 S

K. Ishii, Y. Kikuchi, K. Takahashi, K. Nakamura,
 S. Matsuyama, A. Terakawa,
 H. Yamazaki and K. Hitomi
 “Development of a new two-dimensional
 position-sensitive detection based on resistive
 charge division and using CdTe detectors for a
 high-resolution semiconductor-based PET
 scanning”
Nucl. Instrum. Meth. Phys. Res. A 631 (2011) 138-43.

11J044 3-20 S

S. Matsuyama, G. Catella, K. Ishii, A. Terakawa,
 Y. Kikuchi, Y. Kawamura, S. Ohkura,
 M. Fujikawa, N. Hamada, K. Fujiki, Y. Hatori,
 Y. Ito, H. Yamazaki, Y. Hashimoto, M. Zitnik,
 P. Pelicon and N. Grilj
 “Microbeam analysis of individual particles in
 indoor working environment”
X-Ray Spectrometry 40 (2011) 172-75.

11J045 3-20 S

S. Ohkura, K. Ishii, S. Matsuyama, A. Terakawa,
 Y. Kikuchi, Y. Kawamura, G. Catella
 Y. Hashimoto, M. Fujiwara, N. Hamada,
 K. Fujiki, E. Hatori and H. Yamazaki
 “In vivo 3D imaging of *Drosophila melanogaster*
 using PIXE-micron-CT”
X-Ray Spectrometry 40 (2011) 191-93.

11J046 3-20 S

A. Terawaka, K. Ishii, H. Yamazaki,
 S. Matsuyama, Y. Kikuchi, Y. Ito, A. Tagawa,
 S. Yasunaga, T. Kawamura, Y. Takahashi,
 Y. Hatori, N. Hamada, K. Fujiki, N. Ito, S. Wada,
 Y. Funaki and K. Sera
 “PIXE analysis of a murine solid tumor treated

with proton therapy combined with cisplatin”
X-Ray Spectrometry 40 (2011) 198-201.

11J047 3-21 S

H. Komatsu, H. Yamamoto, Y. Matsuda,
T. Kijimura, M. Kinugawa, K. Okuyama,
M. Nomachi, K. Yasuda, T. Satoh and S. Oikawa
“Fluorine analysis of human enamel around
fluoride-containing materials under different
pH-cycling by μ -PIGE/PIXE system”
Nucl. Instrum. Meth. Phys. Res. B 269 (2011)
2274-77.

11J048 3-21 S

K. Okuyama, H. Komatsu, H. Yamamoto,
P.N.R. Pereira, A.K. Bedran-Russo,
M. Nomachi, T. Sato and H. Sano
“Fluorine analysis of human dentin surrounding
resin composite after fluoride application by
 μ -PIGE/PIXE analysis”
Nucl. Instrum. Meth. Phys. Res. B 269: (2011)
2269-73.

11J049 3-24 S

Y. Shimizu, S. Matsuzaki, T. Satoh, M. Koka,
A. Yokoyama, T. Ohkubo, Y. Ishii, T. Kamiya,
M. Fueki, M. Mori and K. Dobashi
“In-air microparticle induced X-ray emission
analysis of particles in interstitial pneumonia lung
tissue obtained by transbronchial biopsy”
J. Clin. Biochem. Nutr. 49(2) (2011) 125-30.
(Epub 2011).

11J050 3-24 S

Y. Shimizu, S. Matsuzaki, K. Dobashi,
N. Yanagitani, T. Satoh, M. Koka, A. Yokoyama,
T. Ohkubo, Y. Ishii, T. Kamiya and M. Mori

“Elemental analysis of lung tissue particles and
intracellular iron content of alveolar macro phages
in pulmonary alveolar proteinosis”
Respir. Res. 12 (2011) 88.

11J051 3-24 S

Y. Shimizu, S. Matsuzaki, T. Satoh, T. Ohkubo,
A. Yokoyama, Y. Ishii, T. Kamiya, K. Arakawa,
K. Shimizu, S. Tanaka, M. Mori and K. Dobashi
“Influence of tissue particles on Fas expression in
idiopathic interstitial pneumonia”
Front Biosci. (Elite Ed). 3 (2011) 65-73.

11J052 3-26 S

S. Harada, S. Ehara, K. Ishii, A. Tanaka, T. Satoh,
S. Matsuyama, H. Yamazaki, T. Kamiya, T. Sakai,
K. Arakawa, M. Saitoh, S. Oikawa and K. Sera
“Increasing antitumor effects of chemoradiotherapy
by drug efflux inhibition with encapsulated
RLIP-76”
Int. J. PIXE 21 (2011) 30-36.

11J053 3-28 C

K. Yamada, S. Watanabe, Y. Ohshima,
H. Hanaoka, N. Tsukui, C. Takano,
A. Yamaguchi, H. Oku and N. S. Ishioka
“Synthesis and In vivo Evaluation of
Radiohalogen-Labeled Antitumor Cyclic Peptides”
Peptide Sci. 2011 (2012) 287-90.

11J054 3-29 C

Y. Ohshima, H. Hanaoka, Sh. Watanabe, Y. Sugo,
Sa. Watanabe, H. Tominaga, N. Oriuchi,
K. Endo and N. S. Ishioka
“Preparation and biological evaluation of
3-[⁷⁶Br]bromo-a-methyl-L-tyrosine, a novel
tyrosine analog for PET imaging of tumors”

Nucl. Med. Biol. 38 (2011) 857-65.

11J055 3-31 C

S. Ishikawa, N. Suzui, S. Ito-Tanabata, S. Ishii, M. Igura, Tadashi Abe, M. Kuramata, N. Kawachi and S. Fujimaki
 “Real-Time Imaging and Analysis of Differences in Cadmium Dynamics in Rice Cultivars (*Oryza sativa*) using Positron-Emitting ¹⁰⁷Cd Tracer”
 BMC Plant Biol. 11 (2011) 172.

11J056 3-33 C

N. Kawachi, N. Suzui, S. Ishii, S. Ito, N.S. Ishioka, H. Yamazaki, A. H. Iwasaki, K. Ogawa and S. Fujimaki
 “Real-time whole-plant imaging of ¹¹C translocation using positron-emitting tracer imaging”
 Nucl. Instrum. Meth. Phys. Res. A 648 (2011) 317-20.

11J057 3-35 C

S. Arase, Y. Hase, J. Abe, M. Kasai, T. Yamada, K. Kitamura, I. Narumi, A. Tanaka and A. Kanazawa
 “Optimization of ion-beam irradiation for mutagenesis in soybean: effects on plant growth and production of visibly altered mutants”
 Plant Biotechnol. 28 (2011) 323-29.

11J058 3-38 C

長谷 純宏
 “イオンビーム育種研究の最前線”
 放射線と産業 130 号 (2011) 24-28.

11J059 3-38 C

Y. Hase, R. Yoshihara, S. Nozawa and I. Narumi
 “Mutagenic effects of carbon ions near the range

end in plants”

Mutat. Res. 731 (2012) 41-47.

11J060 3-45 C

K. Shimizu, Y. Matuo, Y. Izumi and T. Ikeda
 “Fundamental Study of the Radiation Monitoring System Based on Evaluation of DNA Lesions”
 Radiat. Protect. Dosim. 146 (2011) 62-64.

11J061 3-52 G

K. Tejima, K. Satoh, K. Takeda, T. Yokoyama and I. Narumi
 “The Effect of γ -sterilization of Carrier Materials Made with Different Types of Soils on the Shelf Life of Biofertilizer Containing *Bradyrhizobium japonicum* Strain USDA110”
 Radioisotopes 61 (2012) 161-71.

11J062 4-01 S

K. Kawaguchi, M. Saito, K. Takahiro, S. Yamamoto and M. Yoshikawa
 “Blueshift and narrowing of localized surface plasmon resonance of silver nanoparticles exposed to plasma”
 Plasmonics 6 (2012) 535-39.

11J063 4-05 S

K. Yoshimura, T. Hakoda, S. Yamamoto and M. Yoshikawa
 “Optical detection of organic hydrides with platinum-loaded tungsten trioxide”
 J. Phys. Chem. Solids 73 (2012) 696-98.

11J064 4-03 C

S. Tsukuda, S. Seki, M. Sugimoto, A. Idesaki and S.-I. Tanaka
 “Direct formation of sol-gel hybrid nanowires

using single particle nano-fabrication technique”
Surf. Coat. Technol., 206 (2011) 825-28.

11J065 4-05 E

五十住 幸大、箱田 照幸、山本 春也、有谷 博文、
吉川 正人
“低エネルギー電子線を用いた白金ナノ粒子の生
成と触媒反応への応用”
Radioisotopes, in press.

11J066 4-10 S

K. Miura, Y. Machida, M. Uehara, H. Kiryu,
Y. Ozawa, T. Sasaki, O. Hanaizumi, T. Satoh,
Y. Ishii, M. Kohka, K. Takano, T. Ohkubo,
A. Yamazaki, W. Kada, A. Yokoyama,
T. Kamiya and H. Nishikawa
“Fabrication of polymer optical waveguides for the
1.5-mm band using focused proton beam”
Key Eng. Mater. 497 (2012) 147-50.

11J067 4-11 I

Y. Yoneda and H. Abe
“Growth of Bi-Ti-O particles by ion implantation”
Trans. Mater. Res. Soc. Jpn., 33[1] (2011) 23.

11J068 4-11 I

H. Abe, S. Aone, R. Morimoto,
H. Uchida and T. Ohshima
“Improvement of Hydrogen Absorption
Characteristics of Pd Using Irradiation of Heavy
Ions”
Trans. Mater. Res. Soc. Jpn., 33[1] (2011) 133.

11J069 4-12 S

A. Kitamura (Ogawa), T. Satoh, M. Koka,
T. Kamiya and T. Kobayashi
“Morphological change of PTFE by ion micro

beam irradiation”
Trans. Mater. Res. Soc. Jpn., in press.

11J070 4-13 S

Y. Tanabe, H. Nishikawa, Y. Seki, T. Satoh,
Y. Ishii, T. Kamiya, T. Watanabe and A. Sekiguchi
“Electroforming of Ni mold for imprint lithography
using high-aspect-ratio PMMA microstructures
fabricated by proton beam writing”
Microelectron. Eng., Vol. 88, Issue 8 (2011) 2145-48.

11J071 4-14 I

Y. Chen, X. Feng, Y. Kasukabe, S. Yamamoto,
M. Yoshikawa and Y. Fujino
“Epitaxial Transformation of hcp-fcc Ti sublattices
during Nitriding Processes of Evaporated-Ti Thin
Films due to Nitrogen-Implantation”
J. Alloy Comp., in press.

11J072 4-16 S

Y. Maeda, K. Narumi, S. Sakai, Y. Terai,
K. Hamaya, T. Sadoh and M. Miyao
“Ion Channeling Study of Iron Based Heusler
Alloy Epitaxial Films on Ge(111)”
Thin Solid Films 519 (2011) 8461-67.

11J073 4-16 S

Y. Maeda, T. Ichikawa, T. Jonishi and M. Narumi
“Determination of Silicon Vacancy in Ion-Beam
Synthesized β -FeSi₂”
Phys. Procedia 11 (2011) 83-86.

11J074 4-17 T

K. Aikoh, A. Tohki, T. Matsui, A. Iwase,
T. Satoh, K. Takano, M. Kohka, Y. Saitoh,
T. Kamiya, T. Ohkochi, M. Kotsugi,
T. Nakamura and T. Kinoshita

- “MFM and PEEM observation of micrometre-sized magnetic dot arrays fabricated by ion-microbeam irradiation in FeRh thin films”
J. Synchrotron Rad. 19 (2012) 223-26.
- 11J075 4-17 T**
 S. Kosugi, Nao Fujita, T. Matsui, F. Hori, Y. Saitoh, N. Ishikawa, Y. Okamoto and A. Iwase
 “Effect of high temperature annealing on ferromagnetism induced by energetic ion irradiation in FeRh alloy”
Nucl. Instrum. Meth. Phys. Res. B 269 (9) (2011) 869-72.
- 11J076 4-17 T**
 T. Mitsuda, I. Kobayashi, S. Kosugi, N. Fujita, Y. Saitoh, F. Hori, S. Semboshi, Y. Kaneno, K. Nishida, N. Soneda and A. Iwase
 “Hardening of Al-Cu-Mg alloy by energetic ion irradiation”
J. Nucl. Mater. 408 (2011) 201-04.
- 11J077 4-17 T**
 S. Kosugi, N. Ishikawa, Y. Saitoh, F. Hori and A. Iwase
 “Determination of threshold energies for displacements of Fe and Rh atoms in Fe-50 at.%Rh intermetallic compound by using energetic electron irradiation at low temperatures”
J. Nucl. Mater. 411 (2011) 171-73.
- 11J078 4-19 T**
 K. Motohashi, Y. Saitoh and S. Kitazawa
 “Optical emission spectroscopy by Ar³⁺ ion sputtering of Ti surface under O₂ environment”
Appl. Surf. Sci. 257 (2011) 5789-92.
- 11J079 4-20 T**
 M. Kayama, H. Nishido, S. Toyoda, K. Komuro and K. Ninagawa
 “Radiation effects on cathodoluminescence of albite”
American Mineralogist, 96 (2011) 1238-47.
- 11J080 4-20 T**
 A. Gucsik, H. Nishido, A. Tsuchiyama and K. Ninagawa
 “In-situ Planetary Cathodoluminescence Microscopy and Spectroscopy for the Robotic Missions on Mars”
Advances in ESR Applications, 28 (2011) 4-8.
- 11J081 4-20 T**
 A. Gucsik, T. Okumura, H. Nishido, K. Ninagawa, S. Toyoda, M. Kayama, P. Rózsa and K. Mihályi
 “Planar Deformation Features in Quartz from the Ries Impact Crater, Advanced by Micro-Raman Spectroscopy”
Spectros. Lett. 44 (2011) 469-73.
- 11J082 4-20 T**
 M. Kayama, H. Nishido, S. Toyoda, K. Komuro and K. Ninagawa
 “A Combined Cathodoluminescence and Micro-Raman Study of He⁺-Ion-Implanted Albite”
Spectros. Lett. 44 (2011) 526-29.
- 11J083 4-20 T**
 T. Endo and H. Nishido
 “Mineral chemistry of CVoxB chondrite”
Bulletin of Research Institute of Natural Sciences, Okayama University of Science, 37 (2011) 51-69.

11J084 4-20 T

河野 俊夫、中野 聡志、牧野 州明、鹿山 雅裕、
西戸 裕嗣

“CCD 分光器を用いたアルカリ長石の蛍光スペクトル”

岩石鉱物科学, 40 (2011) 195-98.

11J085 4-22 C

A. Kawasuso, M. Maekawa, Y. Fukaya.

A. Yabuuchi and I. Mochizuki

“Doppler broadening of annihilation radiation measurements on 3d and 4f ferromagnets using polarized positrons”

Phys. Rev. B 85 (2012) 024417 (6).

11J086 4-22 C

A. Kawasuso, M. Maekawa, Y. Fukaya.

A. Yabuuchi and I. Mochizuki

“Spin-polarized positron annihilation measurements on polycrystalline Fe, Co, Ni and Gd based on Doppler broadening of annihilation radiation”

Phys. Rev. B 83 (2011) 100406(R).

11J087 4-23 E

A. Yabuuchi, M. Maekawa and A. Kawasuso

“Vacancy defects in a stress-corrosion-cracked Type 304 stainless steel investigated by positron annihilation spectroscopy”

J. Nucl. Mater. 419 (2011) 9-14.

11J088 4-25 O

Y. Fukaya, I. Matsuda, M. Hashimoto, K. Kubo,

T. Hirahara, S. Yamazaki, W. H. Choi,

H. W. Yeom, S. Hasegawa,

A. Kawasuso and A. Ichimiya

“Atomic structure of two-dimensional binary

surface alloy: Si(111)- $\sqrt{21} \times \sqrt{21}$ superstructure”
Surf. Sci. 606 (2012) 919-23.

11J089 4-26 O

I. Mochizuki, Y. Fukaya, A. Kawasuso, K. Wada,
T. Hyodo, K. Yaji, A. Harasawa and I. Matsuda

“Atomic configuration and phase transition of Pt-induced nanowire on Ge(001) surface studied by scanning tunneling microscopy, reflection high-energy positron diffraction and angle resolved photo-emission spectroscopy”

submitted to Phys. Rev. B (2012).

11J090 4-27 C

T. Maeyama, S. Yamashita, G. Baldacchino,
M. Taguchi, A. Kimura,

T. Murakami and Y. Katsumura

“Production of a fluorescence probe in ion-beam radiolysis of aqueous coumarin-3-carboxylic acid solution—1: Beam quality and concentration dependences”

Radiat. Phys. Chem. 80 (2011) 535-39.

11J091 4-27 C

K. Iwamatsu, M. Taguchi, Y. Sugo,

S. Kurashima and Y. Katsumura

“Concentration and Incident Energy Dependences of Transient Species in Water by H⁺ Ion Irradiation”

Trans. Mater. Res. Soc. Jpn., 36(2) (2011) 329-32.

11J092 4-27 C

T. Maeyama, S. Yamashita, M. Taguchi,

G. Baldacchino, L. Sihver,

T. Murakami and Y. Katsumura

“Production of a fluorescence probe in ion-beam radiolysis of aqueous coumarin-3-carboxylic acid

solution-2: Effects of nuclear fragmentation and its simulation with PHITS”
Radiat. Phys. Chem. 80 (2011) 1352-57.

11J093 4-28 C

T. Kondoh, J. Yang, K. Norizawa, K. Kan,
 T. Kozawa, A. Ogata, S. Tagawa and Y. Yoshida
 “Femtosecond pulse radiolysis study of geminate ion recombination in biphenyl-dodecane solution”
Radiat. Phys. Chem., in press.

11J094 4-29, 4-27 C

S. Nakagawa, M. Taguchi and A. Kimura
 “LET and Dose Rate Effect on Radiation Induced Copolymerization of Maleimide with Styrene in 2-propanol Solution”
Radiat. Phys. Chem. 80 (2011) 1199-202.

11J095 4-32, 4-31 C

M. Hagiwara, T. Sanami, K. Masumoto,
 Y. Iwamoto, N. Matsuda, Y. Sakamoto,
 Y. Nakane, H. Nakashima and Y. Uwamino
 “Spectrum Measurement of Neutrons and Gamma-rays from Thick H₂¹⁸O Target Bombarded with 18 MeV Protons”
J. Korean Phys. Soc. 59 (2011) 2035-38.

11J096 4-36 E

M. Chiba, T. Kamijo, F. Yabuki, O. Yasuda,
 H. Akiyama, Y. Chikashige, H. Kataoka,
 T. Kon, Y. Shimizu, Y. Taniuchi,
 M. Utsumi and M. Fujii
 “Radar for detection of ultra-high-energy neutrinos reacting in a rock salt dome”
Nucl. Instrum. Meth. Phys. Res. A 662 Supple. 1 (2012) S222-25.

11J097 4-37 G

Y. Nagao, H. Seito, Y. Momoki, H. Kaneko,
 K. Nakagawa and T. Kojima
 “The Effect of Temperature on the Response of Alanine Dosimeters under Low Dose and Long Time Irradiation”
Radioisotopes. 61 (2012) 173-77.

11J098 4-41 C

Y. Yuri, T. Ishizaka, T. Yuyama, I. Ishibori,
 S. Okumura and K. Yoshida
 “Formation of a Large-Area Uniform Ion Beam Using Multipole Magnets in the TIARA Cyclotron”
Nucl. Instrum. Meth. Phys. Res. A 642 (2011) 10-17.

11J099 4-42, 3-20 S

M. Omichi, K. Takano, T. Satoh, T. Kamiya,
 Y. Ishii, T. Ohkubo, M. Koka, W. Kada,
 M. Sugimoto, H. Nishikawa and S. Seki
 “Visualization Method for Dose Distribution of Focused Proton Beam Coupled with Atomic Force Microscopy Using Common Polymer Film”
J. Nanosci. Nanotechnol. Accepted.

11J100 4-45, 4-48 T

A. Chiba, Y. Saitoh, K. Narumi, Y. Takahashi,
 K. Yamada and T. Kaneko
 “Measurement of divergence angles classified by charge-state combination of C₂⁺ constituents passing through a thin carbon foil”
Nucl. Instrum. Meth. Phys. Res. B 269 (2011) 824-28.

11J101 4-49, 4-45 I

K. Hirata, Y. Saitoh, A. Chiba,
 K. Yamada and K. Narumi
 “Surface-sensitive chemical analysis of organic

insulating thin films using negative secondary ions
induced by medium energy C₆₀ impacts”
Appl. Phys. Express 4 (2012) 116202.

11J102 4-51 I

Y. Morita, K. Nakajima, M. Suzuki, K. Narumi,
Y. Saitoh, W. Vandervorst and K. Kimura
“Cluster effect on projected range of 30 keV C₆₀⁺ in
silicon”
Nucl. Instrum. Meth. Phys. Res. B 269 (2011) 2080.

A 1.2 Publication in Proceedings

11C001 1-01 C, T, I, E

M. Imaizumi, K. Shimazaki, Y. Kobayashi, M. Takahashi, K. Nakamura, T. Takamoto, S. Sato and T. Ohshima
 “Progress of a Qualified Space Solar Sheet with InGaP/GaAs Dual-Junction Thin Film Solar Cells”
 Proc. 9th Eur. Space Power Conf.
 [St Rafael, France] (2011) CD.

11C002 1-01 I, E

Y. Kobayashi, T. Okumura, S. Kawakita, M. Imaizumi and M. Takahashi
 “Development of Automatic Solar Array Inspection System Through Image Analysis of PL and EL”
 Proc. 9th Eur. Space Power Conf.
 [St Rafael, France] (2011) CD.

11C003 1-01 T, E

A. Kukita, M. Takahashi, K. Shimazaki, H. Toyota, M. Imaizumi, Y. Kobayashi, T. Takamoto, M. Uno and T. Shimada
 “On-Orbit Demonstration of Thin-Film Multi-Junction Solar Cells and Lithium-Ion Capacitors as Bus Components”
 Proc. 9th Eur. Space Power Conf.
 [St Rafael, France] (2011) CD.

11C004 1-01 I

M. Imaizumi, C. Morioka, T. Sumita, T. Ohshima and S. Okuda
 “Radiation Degradation and Damage Coefficients of InGaP/GaAs/Ge Triple-Junction Solar Cell by Low-Energy Electrons”
 Proc. 37th IEEE Photovoltaic Specialists Conf.
 [Seattle, USA] (2011) CD.

11C005 1-01 T, I, E

S. Kawakita, M. Imaizumi and M. Takahashi
 “Space Experiments of Cu(In,Ga)Se₂ Thin-Film Solar Cells by Japanese Small Satellites”
 Proc. 26th Eur. Photovoltaic Solar Energy Conf. Exhib.
 [Hamburg, Germany] (2011) CD.

11C006 1-01 T, I, E

M. Sugai, M. Imaizumi, Y. Takeda and M. Saito
 “Anomalous External Quantum Efficiency of Germanium Subcell in Multi-Junction Cells”
 Tech. Digest 21st Photovoltaic Sci. Eng. Conf.
 [Fukuoka, Japan] (2011) CD.

11C007 1-01 I, E

Y. Kobayashi, M. Imaizumi, S. Kawakita and M. Takahashi
 “PL/EL Image Analysis of Radiation Degradation in Triple-Junctions Solar Cells”
 Tech. Digest 21st Photovoltaic Sci. Eng. Conf.
 [Fukuoka, Japan] (2011) CD.

11C008 1-01 C, T, I, E

M. Imaizumi, M. Takahashi, T. Takamoto and T. Ohshima
 “Technological Trends and JAXA’s Activities on Space Solar Cells”
 Tech. Digest 21st Photovoltaic Sci. Eng. Conf.
 [Fukuoka, Japan] (2011) CD.

11C009 1-02 C, T, S, I

S. Sato, H. Sai, T. Ohshima, M. Imaizumi, K. Shimazaki and M. Kondo
 “Electron and Proton Irradiation Effects on

Substrate-Type Amorphous Silicon Solar Cells”
Proc. 37th IEEE Photovoltaic Specialists Conf.
[Seattle, USA] (2011) in Press.

11C010 1-03 C

S. Kuboyama, N. Ikeda, E. Mizuta, H. Abe,
T. Hirao and T. Tamura

“Rediscovery of Single-Event Gate Rupture
Mechanism in power MOSFETs”

Radiation and Its Effects on Components and
Systems (RADECS) (2011).

11C011 1-06 C, T

岡崎 勇志、小倉 俊太、高橋 芳浩、平尾 敏雄、
小野田 忍、牧野 高紘、大島 武

“SOI デバイスの重イオン照射誘起電流の抑制に
関する検討”

応用物理学会学術講演会, 2p-J-5 (2011) 13-028.

11C012 1-06 C, T

小倉 俊太、岡崎 勇志、小宮山 隆洋、
佐藤 江里子、高橋 芳浩

“SOI-MOSFET の重イオン照射誘起電流に関す
る検討(照射位置依存性)”

日大理工学術講演会, M-26 (2011/11) 1141-42.

11C013 1-06 C, T

岡崎 勇志、小倉 俊太、小宮山 隆洋、
佐藤江里子、高橋 芳浩

“SOI 基板上に作製した MOSFET の重イオン照
射誘起電流”

日大理工学術講演会, M-27 (2011/11) 1143-44.

11C014 1-06 C, T

高橋 芳浩

“半導体デバイスの宇宙放射線効果基礎”

第 1 回半導体デバイスの放射線照射効果研究会

(2012/02) 1.

11C015 1-07 C, T

牧野 高紘、大島 武、岩本 直也、小野田 忍、
野崎 眞次、児島 一聡

“SiC MOS キャパシタのイオン誘起電流”

第 58 回応用物理学関係連合講演会 (2011/03)

11C016 1-13 G

A. Shimada, H. Kudoh, A. Idesaki, M. Sugimoto,
M. Yoshikawa, K. Tamura and T. Seguchi

“The effect of antioxidants on degradation
mechanism of cable insulation material for nuclear
power plant”

Proc. RadTech Asia 2011 [Yokohama, Japan]
(2011/06).

11C017 1-13 G

T. Hirade, T. Oka, N. Morishita,

A. Idesaki and A. Shimada

“Positron annihilation lifetime of irradiated
polyimide”

10th Int. Workshop on Positron and Positronium
Chemistry (2011).

11C018 1-13 G

島田 明彦、工藤 久明、瀬口 忠男、田村 清俊、
杉本 雅樹、出崎 亮、吉川 正人

“原子力施設環境におけるケーブル絶縁材料の
劣化メカニズム”

第 54 回放射線化学討論会 [茨木] (2011/09).

11C019 1-13 G

平出 哲也、岡 壽崇、森下 憲雄、出崎 亮、
島田 明彦

“被照射ポリイミドの自由陽電子寿命による評価”

第 54 回放射線化学討論会 [茨木] (2011/09).

11C020 1-17 G

Y. Kumagai, R. Nagaishi, A. Kimura, M. Taguchi, K. Nishihara, I. Yamagishi and T. Ogawa
 “Hydrogen Production in Radiolysis of the Mixture of Mordenite and Seawater”
 14th Int. Cong. Radiat. Res.
 [Warsaw, Poland] (2011) 176.

11C021 1-17 G

Y. Kumagai, R. Nagaishi, A. Kimura, M. Taguchi, K. Nishihara and I. Yamagishi
 “Hydrogen Production in Radiolysis of the Mixture of Mordenite and Seawater”
 2nd Int. Workshop Radiat. Effects Nucl. Tech.,
 [The University of Tokyo, Tokyo] (2012) 17.

11C022 1-17 G

R. Nagaishi, T. Kondoh, N. Aoyagi, M. Taguchi, J. Yang and Y. Yoshida
 “Pulse Radiolysis Studies of Mixed Ionic Liquids containing Thiocyanate Ion”
 2nd Int. Workshop Radiat. Effects Nucl. Tech.,
 [The University of Tokyo, Tokyo] (2012) 21.

11C023 1-23 T, S, I

G. H. Kim, K. Shiba, T. Sawai, I. Ioka and K. Kiuchi
 “Irradiation Behavior of Precipitation Hardened Ni-base Superalloy With EHP Grade under Multi-ion Irradiation”
 Mater. Res. Soc. Proc. 2011 (2011) 1298
 mrsf10-1298-q06-08.

11C024 1-27 G

H. Koshikawa, T. Yamaki, M. Asano, Y. Maekawa, S. Yamaguchi, K. Yamamoto, K. Asazawa, K. Yamada and H. Tanaka
 “Preparation of anion-exchange membranes for

fuel cell applications by γ -ray pre-irradiation grafting”
 Proc.12th Int. Conf. Radiat. Curing in Asia, (2011)
 240-41.

11C025 1-28 G

T. T. Duy, S. Sawada, S. Hasegawa, A. Putra, D. Yamaguchi, Y. Oba, S. Koizumi, M. Onuma, Y. Maekawa and Y. Katsumura
 “Structural analysis of ETFE-based graft-type polymer electrolyte membranes by small angle X-ray/neutron scattering method”
 日本化学会第5回関東支部大会
 [Tokyo University of Agriculture and Technology, Japan] (2011).

11C026 1-28

T. T. Duy, S. Sawada, S. Hasegawa, Y. Oba, M. Onuma, Y. Katsumura and Y. Maekawa
 “Analysis of hierarchical structure of ETFE-based graft-type polymer electrolyte membranes by small angle X-ray scattering”
 第54回放射線化学討論会 (Jpn. Soc. Radiat. Chem.) [Osaka University, Japan] (2011).

11C027 1-28 G

T. T. Duy, S. Sawada, S. Hasegawa, K. Yoshimura, Y. Oba, M. Onuma, Y. Katsumura and Y. Maekawa
 “Analysis of the hierarchical structure - property relationship of ETFE-based graft-type polymer electrolyte membranes”
 2nd Int. Workshop Radiat. Effects Nucl. Tech.
 [The University of Tokyo, Japan] (2012).

11C028 1-28 G

T. T. Duy, S. Sawada, S. Hasegawa, K. Yoshimura, Y. Oba, M. Onuma, Y. Katsumura and Y. Maekawa

“Hierarchical structure / property analysis of ETFE-based graft-type polymer electrolyte membranes”

92nd Annu. Meeting Chem. Soc. Jpn.
[Keio University, Japan] (2012).

11C029 1-29 G

S. Hasegawa, J. Chen, H. Koshikawa, H. Iwase, S. Kosizumi, M. Ohnuma and Y. Maekawa
“Development of grafted type poly(ether ether ketone) electrolyte membranes. Morphology of PEEK substrate and radiation-induced graft polymerization”

Proc. Radtech Asia 2011 [Yokohama, Japan] (2011/06).

11C030 1-30 G

S. Sawada, Y. Iwai, T. Yamanishi and Y. Maekawa
“Radiation Degradation of Graft-Type Polymer Electrolyte Membranes”

Proc. RadTech Asia 2011 [Yokohama, Japan] (2011/06).

11C031 1-30 G

S. Sawada, D. Yamaguchi, A. Putra, S. Koizumi and Y. Maekawa
“Nano-meso Scale Structures on Radiation-Grafted Polymer Electrolyte Membranes Investigated by Small Angle Neutron Scattering Technique”

18th Int. Conf. Solid State Ionics [Warsaw, Poland] (2011).

11C032 1-30 G

S. Sawada and Y. Maekawa
“Proton Conduction Characteristics in Radiation-Grafted Polymer Electrolyte

Membranes Based on Perfluorinated and Aromatic Hydrocarbon Polymers”

220th Electrochem. Soc. Meeting [Boston, USA] (2011).

11C033 2-06 O

S. Okubo, T. Takahashi, T. Gowa, N. Nagasawa, M. Taguchi, A. Oshima, S. Tagawa and M. Washio
“Micro-fabrication of Biodegradable Polymers Using Focused Ion Beams”

Proc. RadTech Asia 2011 [Yokohama, Japan] (2011/06).

11C034 2-07 G, E

S. Yamashita, A. Hiroki, N. Nagasawa, M. Taguchi and T. Murakami
“Dose Response of a Natural-Polymer-Based Gel Dosimeter: Effects of Composition on White Turbidity Increase after Irradiations”

Inter. Workshop Radiat. Effects Nucl. Tech. (RENT-2012) [Tokyo, Japan] (2012/02).

11C035 2-07 G, E

山下 真一、廣木 章博、長澤 尚胤、田口 光正
“セルロース誘導体を母材とするゲル線量計の照射に伴う白濁化”

日本放射線影響学会第 54 回大会, [神戸] (2011/11) 17-19.

11C036 2-07 G, E

山下 真一、廣木 章博、長澤 尚胤、田口 光正
“ヒドロキシプロピルセルロースを母材とするゲル線量計の開発～ γ 線照射での白濁化に対する検出剤組成の影響～”

第 54 回 放射線化学討論会, [茨木] (2011/09).

11C037 3-25 S

菊地 弘記、時田 佳治、長嶺 竹明、佐藤 隆博、
神谷 富裕

“大気 micro-PIXE を用いた透析患者の赤血球
分析”

第 27 回 PIXE シンポジウム、[宇治] (2010/11).

11C038 3-35 C

種石 始弘、前島 慎一郎、片井 秀幸、大場 誠司、
山田 栄成、大橋 弘和、長谷 純宏、田中 淳

“イオンビームを用いた突然変異育種による温室
メロン‘静系 1 号’の育成”

園芸学会平成 23 年度秋季大会.

園芸学研究第 10 巻 別冊 2 (2011) 178

11C039 3-35 C

佐藤 悠輔、前田 智雄、本多 和茂、嵯峨 孝一、
石川 隆二、秋田 祐介、吉原 亮平、野澤 樹、
鳴海 一成

“イオンビーム照射を行った‘弘前在来’トウガラシ
の照射次代における変異の発現”

園芸学会平成 23 年度秋季大会.

園芸学研究第 10 巻 別冊 2 (2011) 421

11C040 3-35 C

岡田 智行、飯塚 正英、長谷 純宏、野澤 樹、
鳴海 一成、関口 政行

“イオンビームによる段階的変異形質付与を利用
したオステオスペルマム実用品種の開発”

園芸学会平成 24 年度春季大会.

園芸学研究第 11 巻 別冊 1 (2012) 185

11C041 3-38 C

長谷 純宏、吉原 亮平、野澤 樹、鳴海 一成

“シロイヌナズナ GL1 遺伝子座に生じる大規模
欠失変異頻度の LET 依存性”

日本放射線影響学会第 54 回大会講演要旨集

(2011) 146.

11C042 3-45 C

K. Shimizu, Y. Matuo, N. Sato and T. Yamamoto

“Development of the Radiation Monitoring
System Based on Evaluation of DNA Lesions”

7th Int. Workshop Individual Monitoring Ionizing
Radiat., [Oarai, Japan] (2011/12).

11C043 3-45 C

Y. Matuo, Y. Izumi, N. Sato,

T. Yamamoto and K. Shimizu

“Evaluation of the DNA Lesions Caused by

High-LET Radiation Using the Polymerase Chain
Reaction”

7th Int. Workshop Individual Monitoring Ionizing
Radiat., [Oarai, Japan] (2011/12).

11C044 4-03 C

S. Tsukuda, A. Asano, M. Sugimoto, A. Idesaki,

S. Seki and S. Tanaka

“Formation of Hybrid Nanowires by Single
Particle Nano-fabrication Technique”

Proc. Baltic Boat Conf. 2011, [Sweden] (2011/06).

11C045 4-03 C

S. Tsukuda, A. Asano, M. Sugimoto, A. Idesaki,

M. Yoshikawa, S. Seki and S. Tanaka

“Fabrication of Poly(vinylphenol)-TiO Hybrid
Nanowires by Single Particle Nanofabrication
Technique”

Proc. 12th Conf. Eur. Ceram. Soc.,

[Stochholm, Sweden] (2011/06).

11C046 4-07 S, I

T. Nakajima, T. Ichikawa,

B. Matsukura and Y. Maeda

“Photoluminescence Properties of Ion-Beam-Synthesized β -FeSi₂ Nanocrystals in Si”
Proc. Asian School-Conf. Phys. Tech. Nanostructured Mater. (ASCO-NANOMAT 2011), [Vladivostok, Russia] (2011/08).

11C047 4-07 S, I

Y. Maeda, T. Nakajima, K. Nisimura, B. Matsukura, K. Akasaka, K. Narumi, S. Sakai and Y. Terai
“Ion Beam Synthesis of Carbon Doped β -FeSi₂ Nanocrystals Embedded in Si and Their Photoluminescence Enhancement”
Proc. Int. Conf. Thin Films (ICTF 15) [Kyoto, Japan] (2011/11).

11C048 4-08 I

T. Tanaka, K. M. Yu, A. X. Levander, O. D. Dubon, L. A. Reichertz, N. Lopez, M. Nishio and W. Walukiewicz
“Optical Characterization of ZnTeO Intermediate Band Solar Cells”
Proc. 26th Eur. Photovoltaic Solar Energy Conf. Exhib. (26th EU PVSEC), [Hamburg, Germany] (2011/09).

11C049 4-08 I

草場 修平、田中 徹、斉藤 勝彦、郭 其新、西尾 光弘、Kin Man Yu、Wladek Walukiewicz
“酸素イオン注入により作製した ZnTeO 薄膜の評価”
平成 23 年度応用物理学会九州支部学術講演会 予稿集, [鹿児島] (2011/11) 26Dp-4.

11C050 4-10 S

K. Miura, T. Satoh, Y. Ishii, M. Kohka, Y. Machida, M. Uehara, H. Kiryu, K. Takano, T. Ohkubo, A. Yamazaki, W. Kada, A. Yokoyama, T. Kamiya, H. Nishikawa, T. Sasaki and O. Hanaizumi

“Fabrication of PMMA film waveguides utilizing proton beam writing”
16th Optoelectron. Comm. Conf. [Kaohsiung, Taiwan] (2011) 6E1_3.

11C051 4-10 I

S. Kikuchi, A. V. Umenyi, K. Inada, A. Kawashima, K. Noguchi, T. Sasaki, K. Miura, O. Hanaizumi, S. Yamamoto, K. Kawaguchi and M. Yoshikawa
“Fabrication and evaluation of light-emitting SiO₂ substrate co-implanted with Si and C ions”
3rd Int. Conf. Adv. Micro-Device Eng. [Kiryu, Japan] (2011) 60.

11C052 4-10 S

H. Kiryu, Y. Ozawa, K. Noguchi, T. Sasaki, K. Miura, O. Hanaizumi, T. Satoh, Y. Ishii, M. Kohka, K. Takano, T. Ohkubo, A. Yamazaki, W. Kada, A. Yokoyama and T. Kamiya
“Fabrication of optical waveguides by proton beam writing to photorefractive polysilane films”
3rd Int. Conf. Adv. Micro-Device Eng. [Kiryu, Japan] (2011) 61.

11C053 4-10 S

Y. Ozawa, H. Kiryu, K. Miura, O. Hanaizumi, T. Sasaki, K. Noguchi, T. Satoh, Y. Ishii, M. Kohka, K. Takano, T. Ohkubo, A. Yamazaki, W. Kada, A. Yokoyama and T. Kamiya
“Mach-Zehnder type waveguides for the 1550-nm band fabricated by proton beam writing”
3rd Int. Conf. Adv. Micro-Device Eng. [Kiryu, Japan] (2011) 64.

11C054 4-13 S

寺島 大貴、椎根 康晴、西川 宏之、小池 義和、佐藤 隆博、石井 保行、神谷 富裕、神 孝之、

浅井 千尋、内田 諭

“プロトンビーム描画による高アスペクト比ピラー配列の試作と誘電泳動特性”

第 72 回応用物理学学会学術講演会 [山形大学]
1a-ZG-3 (2011/09).

11C055 4-16 S

B. Matsukura, Y. Hiraiwa, T. Nakajima,

K. Narumi, S. Sakai, T. Sadoh,

M. Miyao and Y. Maeda

“Self Organization of FeGe/FeSi/FeGe Layered Structures on Ge and Their Electrical Conduction Properties”

Proc. Asian School-Conf. Phys. Tech. Nanostructured Mater. (ASCO-NANOMAT 2011), [Vladivostok, Russia] (2011/08).

11C056 4-16 S

Y. Maeda, B. Matsukura, K. Narumi, S. Sakai,

K. Hamaya and M. Miyao

“Thermal Stability of Fe₂MnSi/Ge(111) Heteroepitaxial Interfaces”

Proc. Int. Conf. Thin Films (ICTF 15) [Kyoto, Japan] (2011/11).

11C057 4-27 C

M. Taguchi, K. Iwamatsu, Y. Sugo, S. Kurashima, M. Yamaguchi and Y. Katsumura

“Pulse radiolysis of water by energetic heavy ions”

12th Tihany Symp. Radiat. Chem., [Zalakaros, Hungary] (2011/08-09) 2.

11C058 4-28 G

T. Kondoh, J. Yang, Y. Yoshida, R. Nagaishi,

M. Taguchi, K. Takahashi and R. Katohh

“Femtosecond Pulse Radiolysis Study of Excess Electron in Ionic Liquids”

2nd Int. Workshop Radiat. Effects Nucl. Tech., [The University of Tokyo, Tokyo] (2012) 20.

11C059 4-28 G

近藤 孝文、楊 金峰、吉田 陽一、永石 隆二、田口 光正、高橋 憲司、加藤 隆二

“フェムト秒パルスラジオリシスによるイオン液体中の溶媒和電子・溶媒和前電子と捕捉剤の反応の研究”

大阪大学産業科学研究所 附属量子ビーム科学研究施設 平成 23 年度報告書 (2012) 65-66.

11C060 4-28 C

T. Kondoh, J. Yang, K. Norizawa, K. Kan,

T. Kozawa, A. Ogata, S. Tagawa and Y. Yoshida

“Time-dependent behavior of electron in n-dodecane studied by femtosecond pulse radiolysis”

12th Tihany Symp. Radiat. Chem., [Zalakaros, Hungary] (2011/08-09) 89.

11C061 4-28 C

Y. Yoshida, J. Yang, T. Kondoh, K. Norizawa,

K. Kan, T. Kozawa, H. Kobayashi,

A. Ogata and S. Tagawa

“Femtosecond pulse radiolysis using a photocathode RF gun linac”

Proc. 8th Annu. Meeting Part. Accel. Soc. Jpn. 2011, [Tsukuba, Japan] (2011/08) 157.

11C062 4-28 C

T. Kondoh, J. Yang, K. Norizawa, K. Kan,

T. Kozawa, A. Ogata and Y. Yoshida

“The study of time dependent behavior of electron in dodecane by near infrared femtosecond pulse radiolysis using photocathode RF gun linac”

Proc. 8th Annu. Meeting Part. Accel. Soc. Jpn.

2011, [Tsukuba, Japan] (2011/08)160.

11C063 4-28 C

T. Kondoh, J. Yang, K. Norizawa, K. Kan,
T. Kozawa, T. Toigawa, A. Ogata, H. Kobayashi,
S. Tagawa and Y. Yoshida

“Time-dependent behavior of short lived active species in polymer model compound studied by femtosecond pulse radiolysis for advanced nano-fabrication”

7th Handai Nanosci. Nanotech. Int. Symp.,
[Osaka, Japan] (2011/11) 88.

11C064 4-28 C

T. Kondoh, J. Yang, K. Norizawa, K. Kan ,
T. Toigawa, A. Ogata, H. Kobayashi,
S. Tagawa and Y. Yoshida

“Electron capture in polymer model compound studied by femtosecond pulse radiolysis for advanced nano-fabrication”

15th SANKEN Int. Symp., 10th SANKEN
Nanotech. Symp., [Osaka, Japan] (2012/01) 111.

11C065 4-28 C

T. Kondoh, K. Kan, J. Yang, Y. Yoshida,
H. Kobayashi, T. Toigawa,
K. Norizawa and A. Ogata

“Progress of the equivalent velocity spectroscopy method for femtosecond pulse radiolysis by pulse rotation and pulse compression”

[New Orleans, USA], THPPR059 (2012/05).

11C066 4-29 C, T

S. Nakagawa, M. Taguchi and A. Kimura

“LET and dose rate effect on radiation induced polymerization”

Proc. 54th Annu. Meeting Jpn. Soc. Radiat. Chem.

[Osaka, Japan] (2011/09).

11C067 4-29 C, T

S. Nakagawa, M. Taguchi and A. Kimura

“Solvent effect on radiation induced polymerization”

Proc. 92nd Spring Meeting Chem. Soc. Jpn.

[Yokohama, Japan] (2012/03).

11C068 4-32 C

M. Hagiwara, T. Sanami, Y. Iwamoto, N. Matsuda,
Y. Sakamoto, Y. Nakane, H. Nakashima,
K. Masumoto and Y. Uwamino

“Systematic Measurement of Neutron and Gamma-ray Yields on Thick Targets Bombarded with 18 MeV Protons”

Proc. 2010 Symp.Nucl. Data, JAEA-Conf 2011-002,
[Kyushu University, Kasuga, Japan] (2010/11) 119.

11C069 4-39 C, S, T, I

K. Yamada, T. Nara, I. Ishibori, S. Kurashima,
K. Yoshida, T. Yuyama, T. Ishizaka, T. Agematsu,
S. Uno, A. Chiba, A. Yokoyama, S. Okumura,
N. Miyawaki, H. Kashiwagi, Y. Yuri, Y. Saitoh,
Y. Ishii, T. Satoh, T. Ohkubo and W. Yokota

“Status of TIARA Facility”

Proc. 8th Annu. Meeting Part. Accel. Soc. Jpn.

[Tsukuba, Japan] (2011/08) MOPS012.

11C070 4-41 C

T. Yuyama, Y. Yuri, T. Ishizaka,
I. Ishibori and S. Okumura

“Development of the Real-Time Beam Profile System for Uniform Beam Formation using Multipole Magnets”

Proc. 8th Annu. Meeting Part. Accel. Soc. Jpn.

[Tsukuba, Japan] (2011/08) in press.

11C071 4-44 S

W. Kada, A. Yokoyama, M. Koka, K. Takano,
T. Satoh and T. Kamiya
“Ion-Beam-Induced Luminescence Analysis as
Diagnostic Tool for Microstructure Patterning on
Diamond by Proton Beam Writing”
Proc. 24th Int. Microprocesses Nanotech. Conf.
[Kyoto, Japan] (2011) To be issued.

11C072 4-44 S

W. Kada, A. Yokoyama, M. Koka,
T. Satoh and T. Kamiya
“Development of Wavelength-Dispersive
Micro-IBIL for the Chemical Structure Analysis of
Micrometer-sized Particles”
Proc. 7th Int. Symp. Bio-PIXE
[Sendai, Japan] (2011) To be issued.

11C073 4-44 S

W. Kada, A. Yokoyama, M. Koka, K. Takano,
T. Satoh and T. Kamiya
“Development of an Ion Beam-Induced
Luminescence (IBIL) Analysis System for
Observation of Chemical-structures in
Micro-meter-sized targets”
Proc. 1st Int. Symp. Tech. Sustainability
[Bangkok, Thailand] (2011) 517-20.

11C074 4-44 T

W. Kada, T. Satoh, V. Grilj, N. Skukan,
T. Makino, S. Onoda, M. Koka, M. Jaksic,
T. Ohshima and T. Kamiya
“Transmission Charged-Particle Detectors of
Thin-film CVD Diamond for the Single Ion Hit
Measurement”
Proc. Workshop “Radiation Detectors and their
Uses“ [Tsukuba, Japan] (2012) To be issued.

11C075 4-45 T

千葉 敦也、齋藤 勇一、鳴海 一雅、山田 圭介、
金子 敏明
“薄膜を透過した C_2^+ 構成イオンの空間配置と電
荷の相関”
第 24 回「タンデム加速器およびその周辺技術の
研究会」報告集 [奈良] (2011/07) 121.

11C076 5-03 T, S, I

宇野 定則、千葉 敦也、山田 圭介、横山 彰人、
上松 敬、北野 敏彦、高山 輝充、織茂 貴雄、
金井 信二、青木 勇希、山田 尚人、齋藤 勇一、
石井 保行、佐藤 隆博、大久保 猛
“TIARA 静電加速器の現状”
第 24 回「タンデム加速器及びその周辺技術研究
会」報告集 [奈良] (2011/07) 125.

Appendix 2

List of Related Patents

11PAT001 1-03

“Single event effect tolerant SOI-based Inverter, NAND element, NOR element, semiconductor memory device and data latch circuit”

US patent No. US 7,504,850 B2.

(SOI-ASIC, HR5000S に適用)

11PAT002 1-03

“Single event effect tolerant latch circuit and flip-flop circuit,”

US patent No. US 7,576,583 B2.

(SOI-ASIC, SOI-FPGA, HR5000S に適用)

11PAT003 1-03

「シングルイベント耐性のラッチ回路」

公開番号:2009-105967 号.

(SOI-ASIC, SOI-FPGA, HR5000S に適用)

11PAT004 1-26

吉村 公男、越川 博、八巻 徹也、浅野 雅春、前川 康成(原子力機構・量子ビーム)、山本 和矢、猪谷 秀幸、朝澤 浩一郎、山口 進、田中 裕久(ダイハツ工業㈱)

「アニオン伝導電解質膜およびその製造方法」

出願番号:特願 2012-049960 号

11PAT005 1-27

古山 了、森山 順一、長井 陽三(日東電工㈱)、百合 庸介、石堀 郁夫、湯山 貴裕、石坂 知久、奥村 進(原子力機構・高崎研)、前川 康成、越川 博、八巻 徹也、浅野 雅春(原子力機構・量子ビーム)

「多孔性高分子フィルム」の製造方法および多孔

性高分子フィルム」

出願番号:特願 2012-081758 号

11PAT006 2-01

瀬古 典明、植木 悠二(原子力機構・量子ビーム)、片貝 秋雄、四元 俊郎、高橋 明男(㈱クリーンテック)

「重合性モノマーがグラフト重合されたグラフト重合高分子繊維の製造方法」

出願番号:特願 2011-079665 号

11PAT007 2-01

瀬古 典明、植木 悠二(原子力機構・量子ビーム)、片貝 秋雄、四元 俊郎、高橋 明男(㈱クリーンテック)

「重合性モノマーがグラフト重合されたグラフト重合高分子繊維の製造方法、機能性材料、並びに金属捕集材」

出願番号:特願 2012-077842 号

11PAT008 2-04

岩撫 暁生、瀬古 典明、保科 宏行、植木 悠二、佐伯 誠一(原子力機構・量子ビーム)

「布状の放射性物質吸着材及びその製造方法」

出願番号:特願 2011-136558 号,

出願日:平成 23 年 6 月 20 日

11PAT009 2-06

長澤 尚胤(原子力機構・量子ビーム)、大島 明博、田川 精一(大阪大)、鷲尾 方一、大久保 聡(早稲田大)、玉田 正男(原子力機構・量子ビーム)

「高分子材料の微細構造形成方法、微細構造

体」

出願番号:特願 2010-053172 号,

出願日:平成 22 年 3 月 10 日

11PAT010 2-06

大島 明博、田川 精一(大阪大)、鷲尾 方一、
大山 智子、大久保 聡、小林 亜暢(早稲田大)、
長澤 尚胤、田口 光正(原子力機構・量子ビーム)

「微細部材とその製造方法」

出願番号:特願 2011-52359 号,

出願日:平成 23 年 3 月 10 日

11PAT011 3-35

品種登録 サルビア・コクシネア品種“TL585”

品種登録出願:第 26831 号

出願日:平成 24 年 3 月 13 日

11PAT012 4-01

山本 春也、箱田 照幸、吉川 正人(原子力機
構・量子ビーム)

「光学的水素ガス検知素子」

出願番号:特願 2011-273058 号

11PAT013 4-04

杉本 雅樹、吉川 正人(原子力機構・量子ビーム)、
関 修平、佃 諭志、田川 精一(大阪大)

「高分子多段ナノワイヤー及びスターバースト型
ナノ粒子とそれらの製造法」

特許番号:第 4877806 号

11PAT014 4-05

吉村 公男、箱田 照幸、山本 春也、宮下 敦巳、
杉本 雅樹、吉川 正人(原子力機構・量子ビーム)

「有機ハイドロライトの検知部材及び有機ハイドロ
ライトの存在を検知する方法」

出願番号:特願 2011-095782 号

11PAT015 4-05

箱田 照幸、山本 春也、吉川 正人(原子力機
構・量子ビーム)

「属粒子膜、貴金属粒子膜構成材及び検知素
子、並びにその製造方法」

出願番号:特願 2011-056087 号

11PAT016 4-11

織茂 聡、阿部 浩之(原子力機構・量子ビーム)、
大道 博行(原子力機構・敦賀本部レーザー共同
研究所)、内田 裕久(東海大・工)

「水素吸蔵材の製造方法、水素吸蔵材」

公開番号:2011-236446 号

出願番号:特願 2010-106216 号

11PAT017 5-03

宇野 定則(原子力機構・高崎研)、

長岡 洋之(㈱日本ファインケム)

「高耐久型高抵抗器」

特許番号:第 4836070 号

Appendix 3

List of Related Press-Release and Television Broadcasting

11NP001 3-35

平成 24 年 2 月 1 日プレス発表「オステオスペルマムの新品種「ヴィエントラビオス(仮称)」を品種登録出願」

上毛新聞、産経新聞に掲載。FMぐんまで紹介。
(群馬県が単独で発表した共同研究成果)

Symbol used in the Appendix 1 to 3

An example of symbol expression is written as following.

11 **J** **0102** **4-51** **I**
 ① ② ③ ④-⑤ ⑥

- ① Number of last two orders in fiscal year
- ② Kind of publication
 - J** : Publication in Journal
 - C** : Publication as Proceedings
 - NP** : Press-Release (Newspaper)
 - TV** : Television Broadcasting
 - PA** : Patent
- ③ Consecutive numbers for the kind of publication
- ④-⑤ Paper number
- ④ Classification number of research field
 - 1** : Space, nuclear and energy engineering
 - 2** : Environment conservation and resource exploitation
 - 3** : Medical and biotechnological application
 - 4** : Advanced materials, analysis and novel technology
- ⑤ Consecutive number every research field
- ⑥ Accelerators or irradiation facilities utilized for the research
 - C** : AVF Cyclotron
 - T** : 3 MV Tandem Electrostatic Accelerator
 - S** : 3 MV Single-ended Electrostatic Accelerator
 - I** : 400 kV Ion Implanter
 - E** : 2 MV Electron Accelerator
 - G** : Co-60 Gamma-ray Irradiation Facilities
 - O** : Off-line (Research without the utilization of irradiation facilities)

Appendix 4 Type of Research Collaboration and Facilities Used for Research

Paper No.	Type of Research Collaboration* ¹					Irradiation Facilities* ²						Paper No.	Type of Research Collaboration* ¹					Irradiation Facilities* ²					
	Joint Res.	Entr. Res.	Coop. Res.	JAEA Inter.	Com. Use	C	T	S	I	E	G		Joint Res.	Entr. Res.	Coop. Res.	JAEA Inter.	Com. Use	C	T	S	I	E	G
1-01	●					⊙	⊙		⊙			2-12	●									⊙	⊙
1-02				●		⊙	⊙	⊙	⊙			2-13				●			⊙				
1-03	●					⊙						2-14				●			⊙				
1-04					●	⊙																	
1-05	●						⊙	⊙				3-01				●		⊙					
1-06	●					⊙	⊙					3-02				●		⊙					
1-07				●		⊙	⊙					3-03				●		⊙					
1-08				●OL								3-04	●					⊙					
1-09				●		⊙						3-05				●		⊙					⊙
1-10	●						⊙					3-06	●					⊙					
1-11					●		⊙				⊙	3-07	●					⊙					
1-12	●								⊙			3-08	●					⊙					
1-13				●						⊙		3-09	●					⊙					
1-14				●						⊙		3-10	●					⊙					
1-15				●						⊙		3-11	●					⊙					
1-16				●						⊙		3-12	●					⊙					
1-17				●					⊙	⊙		3-13	●					⊙					
1-18				●						⊙		3-14	●					⊙					
1-19				●						⊙		3-15	●					⊙					⊙
1-20			●				⊙	⊙	⊙			3-16				●		⊙					
1-21				●			⊙					3-17				●		⊙					
1-22				●			⊙	⊙	⊙			3-18	●										⊙
1-23				●			⊙	⊙	⊙			3-19	●								⊙	⊙	
1-24				●			⊙	⊙	⊙			3-20			●				⊙				
1-25					●					⊙		3-21			●				⊙				
1-26				●						⊙		3-22			●				⊙				
1-27	●									⊙		3-23			●				⊙				
1-28				●						⊙		3-24			●				⊙				
1-29				●					⊙	⊙		3-25			●				⊙				
1-30	●									⊙		3-26			●				⊙				
1-31				●		⊙						3-27			●				⊙				
1-32				●						⊙		3-28	●					⊙					
1-33	●					⊙			⊙			3-29				●			⊙				
												3-30	●						⊙				
2-01				●						⊙		3-31	●					⊙					
2-02				●						⊙		3-32				●			⊙				
2-03	●									⊙		3-33		●					⊙				
2-04		●								⊙		3-34				●			⊙				
2-05	●									⊙		3-35	●						⊙				
2-06	●						⊙	⊙				3-36	●						⊙				
2-07				●						⊙	⊙	3-37				●			⊙				
2-08	●									⊙		3-38				●			⊙				⊙
2-09	●									⊙		3-39		●					⊙				
2-10				●						⊙		3-40				●			⊙				
2-11	●									⊙		3-41	●						⊙				⊙

Paper No.	Type of Research Collaboration *1					Irradiation Facilities *2						Paper No.	Type of Research Collaboration *1					Irradiation Facilities *2					
	Joint Res.	Entr. Res.	Coop. Res.	JAEA Inter.	Com. Use	C	T	S	I	E	G		Joint Res.	Entr. Res.	Coop. Res.	JAEA Inter.	Com. Use	C	T	S	I	E	G
3-42					●	◎						4-27				●							◎
3-43				●		◎					◎	4-28	●										◎
3-44				●							◎	4-29	●										◎
3-45	●					◎						4-30	●										◎
3-46	●					◎						4-31	●										◎
3-47	●					◎						4-32				●							◎
3-48	●					◎						4-33				●							◎
3-49	●					◎					◎	4-34				●				◎			
3-50	●					◎						4-35				●							◎
3-51	●					◎						4-36					●						◎
3-52				●							◎	4-37	●										◎ ◎
												4-38				●							◎
4-01				●				◎	◎			4-39				●			◎	◎	◎		
4-02					●	◎						4-40				●				◎			
4-03					●	◎						4-41				●				◎			
4-04	●					◎						4-42				●				◎			
4-05				●						◎		4-43				●			◎	◎	◎		
4-06				●						◎		4-44	●							◎			
4-07					●			◎	◎			4-45				●				◎			
4-08					●				◎			4-46				●				◎			
4-09	●							◎	◎			4-47				●				◎			
4-10	●							◎	◎			4-48				●				◎			
4-11	●								◎			4-49				●				◎		◎	
4-12				●				◎				4-50				●				◎	◎		
4-13	●							◎	◎			4-51	●									◎	
4-14					●				◎														
4-15					●					◎		5-01								◎	◎	◎	◎
4-16	●							◎				5-02								◎			
4-17	●							◎				5-03								◎	◎	◎	
4-18	●							◎				5-04										◎	◎
4-19	●							◎				5-05										◎	◎
4-20					●	◎						5-06								◎	◎	◎	◎
4-21					●					◎		5-07								◎	◎	◎	◎
4-22				●		◎						5-08								◎	◎	◎	◎
4-23				●						◎													
4-24				●		◎																	
4-25				●OL																			
4-26				●OL																			
												Total	58	3	15	60	14	69	30	35	26	19	37
<p>*1 Type of Research Collaboration Joint Res. : Joint research with external users Entr. Res. : Research entrusted to JAEA Coop. Res. : Cooperative research with plural universities through The University of Tokyo JAEA Inter. : JAEA internal use Com. Use : Common use based on "JAEA-facility-use" OL : Off line (Research without the use of irradiation facilities)</p>												<p>*2 Utilization of Irradiation Facilities C : AVF Cyclotron System T : 3 MV Tandem Electrostatic Accelerator S : 3 MV Single-ended Electrostatic Accelerator I : 400 kV Ion Implanter E : 2 MV Electron Accelerator G : Co-60 Gamma-ray Irradiation Facilities</p>											

Appendix 5 Examples of Typical Abbreviation Name for Organizations in Japan Atomic Energy Agency (JAEA)

◆ Directorate, Center, Institute, etc.

QuBS (量子ビーム応用研究部門): Quantum Beam Science Directorate

NSED (原子力基礎工学研究部門): Nuclear Science and Engineering Directorate

FRDD (核融合研究開発部門): Fusion Research and Development Directorate

GIRDD (地層処分研究開発部門): Geological Isolation Research and
Development Directorate

ANSRD (次世代原子力システム研究開発部門): Advanced Nuclear System Research
and Development Directorate

NCBD (バックエンド推進部門): Nuclear Cycle Backend Directorate

NSRC (安全研究センター): Nuclear Safety Research Center

NFCEL (核燃料サイクル工学研究所): Nuclear Fuel Cycle Engineering Laboratories

NERCC (原子力エネルギー基盤連携センター): Nuclear Engineering Research
Collaboration Center

NHARC (原子力水素・熱利用研究センター): Nuclear Hydrogen and Heat Application
Research Center

J-PARC (J-PARC センター): J-PARC Center

TARRI (高崎量子応用研究所): Takasaki Advanced Radiation Research Institute

NSRI (原子力科学研究所): Nuclear Science Research Institute

ORDC (大洗研究開発センター): Oarai Research and Development Center

KPSI (関西光科学研究所): Kansai Photon Science Institute

◆ Division, Unit, Department, etc.

- ・ 量子ビーム応用研究部門、環境・産業応用量子ビーム技術研究ユニット
⇒ Environment and Industrial Materials Research Division, QuBS, JAEA
- ・ 量子ビーム応用研究部門、医療・バイオ応用量子ビーム技術研究ユニット
⇒ Medical and Biotechnological Application Division, QuBS, JAEA
- ・ 量子ビーム応用研究部門、量子ビーム材料評価・構造制御技術研究ユニット
⇒ Materials Science Research Division, QuBS, JAEA
- ・ 量子ビーム応用研究部門、レーザー応用技術研究ユニット
⇒ Laser Application Technology Division, QuBS, JAEA
- ・ 原子力基礎工学研究部門、環境・放射線工学ユニット
⇒ Division of Environment and Radiation Sciences, NSED, JAEA
- ・ 原子力基礎工学研究部門、燃料・材料工学ユニット
⇒ Division of Fuels and Materials Engineering, NSED, JAEA

- ・核融合研究開発部門、ITER プロジェクトユニット
⇒ Division of ITER Project, FRDD, JAEA
- ・核融合研究開発部門、核融合エネルギー工学研究開発ユニット
⇒ Division of Fusion Energy Technology, FRDD, JAEA
- ・先端基礎研究センター
⇒ Advanced Science Research Center, JAEA
- ・原子力科学研究所、放射線管理部
⇒ Department of Radiation Protection, NSRI, JAEA
- ・大洗研究開発センター、高速実験炉部
⇒ Experimental Fast Reactor Department, ORDC, JAEA
- ・高崎量子応用研究所、放射線高度利用施設部
⇒ Department of Advanced Radiation Technology, TARRI, JAEA
- ・J-PARC センター、加速器ディビジョン
⇒ Accelerator Division, J-PARC, JAEA
- ・J-PARC センター、安全ディビジョン
⇒ Safety Division, J-PARC, JAEA
- ・安全研究センター、軽水炉長期化対応研究ユニット
⇒ LWR Long-term Reliability Research Unit, NSRC, JAEA
- ・地層処分研究開発部門、地層処分基盤研究開発ユニット
⇒ Geological Isolation Research Unit, GIRDD, JAEA
- ・核燃料サイクル工学研究所、サイクル工学試験部
⇒ Nuclear Cycle Engineering Department, NFCEL, JAEA
- ・核燃料サイクル工学研究所、プルトニウム燃料技術開発センター
⇒ Plutonium Fuel Development Center, NFCEL, JAEA
- ・核燃料サイクル工学研究所、再処理技術開発センター
⇒ Tokai Reprocessing Technology Development Center, NFCEL, JAEA
- ・次世代原子力システム研究開発部門、再処理技術開発計画室
⇒ Reprocessing Technology Development Planning Office, ANSRD, JAEA
- ・バックエンド推進部門、バックエンド技術開発ユニット
⇒ Nuclear Cycle Backend Technology Development Unit, NCBBD, JAEA
- ・産学連携推進部
⇒ Industrial Collaboration Promotion Department, JAEA

This is a blank page.

国際単位系 (SI)

表1. SI基本単位

基本量	SI基本単位	
	名称	記号
長さ	メートル	m
質量	キログラム	kg
時間	秒	s
電流	アンペア	A
熱力学温度	ケルビン	K
物質	モル	mol
光	カンデラ	cd

表2. 基本単位を用いて表されるSI組立単位の例

組立量	SI基本単位	
	名称	記号
面積	平方メートル	m ²
体積	立方メートル	m ³
速度	メートル毎秒	m/s
加速度	メートル毎秒毎秒	m/s ²
波数	数メートル	m ⁻¹
密度, 質量密度	キログラム毎立方メートル	kg/m ³
面積密度	キログラム毎平方メートル	kg/m ²
比体積	立方メートル毎キログラム	m ³ /kg
電流密度	アンペア毎平方メートル	A/m ²
磁界の強さ	アンペア毎メートル	A/m
量濃度 ^(a) , 濃度	モル毎立方メートル	mol/m ³
質量濃度	キログラム毎立方メートル	kg/m ³
輝度	カンデラ毎平方メートル	cd/m ²
屈折率 ^(b)	(数字の) 1	1
比透磁率 ^(b)	(数字の) 1	1

(a) 量濃度 (amount concentration) は臨床化学の分野では物質濃度 (substance concentration) ともよばれる。
 (b) これらは無次元量あるいは次元1をもつ量であるが、そのことを表す単位記号である数字の1は通常は表記しない。

表3. 固有の名称と記号で表されるSI組立単位

組立量	SI組立単位			
	名称	記号	他のSI単位による表し方	SI基本単位による表し方
平面角	ラジアン ^(b)	rad	1 ^(b)	m/m
立体角	ステラジアン ^(b)	sr ^(c)	1 ^(b)	m ² /m ²
周波数	ヘルツ ^(d)	Hz	1	s ⁻¹
力	ニュートン	N		m kg s ⁻²
圧力, 応力	パスカル	Pa	N/m ²	m ⁻¹ kg s ⁻²
エネルギー, 仕事, 熱量	ジュール	J	N m	m ² kg s ⁻²
仕事率, 工率, 放射	ワット	W	J/s	m ² kg s ⁻³
電荷, 電気量	クーロン	C		s A
電位差 (電圧), 起電力	ボルト	V	W/A	m ² kg s ⁻³ A ⁻¹
静電容量	ファラド	F	C/V	m ⁻² kg ⁻¹ s ⁴ A ²
電気抵抗	オーム	Ω	V/A	m ² kg s ⁻³ A ⁻²
コンダクタンス	ジーメンズ	S	A/V	m ⁻² kg ⁻¹ s ³ A ²
磁束密度	ウェーバ	Wb	Vs	m ² kg s ⁻² A ⁻¹
磁束	テスラ	T	Wb/m ²	kg s ⁻² A ⁻¹
インダクタンス	ヘンリー	H	Wb/A	m ² kg s ⁻² A ⁻²
セルシウス温度	セルシウス度 ^(e)	°C		K
光照射度	ルーメン	lm		cd sr ^(c)
放射線核種の放射能 ^(f)	ベクレル ^(d)	Bq		s ⁻¹
吸収線量, 比エネルギー分与, カーマ	グレイ	Gy	J/kg	m ² s ⁻²
線量当量, 周辺線量当量, 方向性線量当量, 個人線量当量	シーベルト ^(g)	Sv	J/kg	m ² s ⁻²
酸素活性	カタール	kat		s ⁻¹ mol

(a) SI接頭語は固有の名称と記号を持つ組立単位と組み合わせても使用できる。しかし接頭語を付した単位はもはやコヒーレントではない。
 (b) ラジアンとステラジアンは数字の1に対する単位の特別な名称で、量についての情報をつたえるために使われる。実際には、使用する時には記号rad及びsrが用いられるが、習慣として組立単位としての記号である数字の1は明示されない。
 (c) 測光学ではステラジアンという名称と記号srを単位の表し方の中に、そのまま維持している。
 (d) ヘルツは周期現象についてのみ、ベクレルは放射性核種の統計的過程についてのみに使用される。
 (e) セルシウス度はケルビンの特別な名称で、セルシウス温度を表すために使用される。セルシウス度とケルビンの単位の大きさは同一である。したがって、温度差や温度間隔を表す数値はどちらの単位で表しても同じである。
 (f) 放射性核種の放射能 (activity referred to a radionuclide) は、しばしば誤った用語で"radioactivity"と記される。
 (g) 単位シーベルト (PV,2002,70,205) についてはCIPM勧告2 (CF-2002) を参照。

表4. 単位の中に固有の名称と記号を含むSI組立単位の例

組立量	SI組立単位		
	名称	記号	SI基本単位による表し方
粘着力のモーメント	ニュートンメートル	N m	m ² kg s ⁻²
表面張力	ニュートン毎メートル	N/m	kg s ⁻²
角速度	ラジアン毎秒	rad/s	m m ⁻¹ s ⁻¹ =s ⁻¹
角加速度	ラジアン毎秒毎秒	rad/s ²	m m ⁻¹ s ⁻² =s ⁻²
熱流密度, 放射照度	ワット毎平方メートル	W/m ²	kg s ⁻³
熱容量, エントロピー	ジュール毎ケルビン	J/K	m ² kg s ⁻² K ⁻¹
比熱容量, 比エントロピー	ジュール毎キログラム毎ケルビン	J/(kg K)	m ² s ⁻² K ⁻¹
比エントロピー	ジュール毎キログラム	J/kg	m ² s ⁻²
熱伝導率	ワット毎メートル毎ケルビン	W/(m K)	m kg s ⁻³ K ⁻¹
体積エネルギー	ジュール毎立方メートル	J/m ³	m ⁻¹ kg s ⁻²
電界の強さ	ボルト毎メートル	V/m	m kg s ⁻³ A ⁻¹
電荷密度	クーロン毎立方メートル	C/m ³	m ⁻³ s A
電表面積電荷	クーロン毎平方メートル	C/m ²	m ⁻² s A
電束密度, 電気変位	クーロン毎平方メートル	C/m ²	m ⁻² s A
誘電率	ファラド毎メートル	F/m	m ⁻² kg ⁻¹ s ⁴ A ²
透磁率	ヘンリー毎メートル	H/m	m kg s ⁻² A ⁻²
モルエネルギー	ジュール毎モル	J/mol	m ² kg s ⁻² mol ⁻¹
モルエントロピー, モル熱容量	ジュール毎モル毎ケルビン	J/(mol K)	m ² kg s ⁻² K ⁻¹ mol ⁻¹
照射線量 (X線及びγ線)	クーロン毎キログラム	C/kg	kg ⁻¹ s A
吸収線量	グレイ毎秒	Gy/s	m ² s ⁻³
放射強度	ワット毎ステラジアン	W/sr	m ³ m ⁻² kg s ⁻³ =m ² kg s ⁻³
放射輝度	ワット毎平方メートル毎ステラジアン	W/(m ² sr)	m ² m ⁻² kg s ⁻³ =kg s ⁻³
酵素活性濃度	カタール毎立方メートル	kat/m ³	m ⁻³ s ⁻¹ mol

表5. SI接頭語

乗数	接頭語	記号	乗数	接頭語	記号
10 ²⁴	ヨタ	Y	10 ¹	デシ	d
10 ²¹	ゼタ	Z	10 ²	センチ	c
10 ¹⁸	エクサ	E	10 ³	ミリ	m
10 ¹⁵	ペタ	P	10 ⁶	マイクロ	μ
10 ¹²	テラ	T	10 ⁹	ナノ	n
10 ⁹	ギガ	G	10 ¹²	ピコ	p
10 ⁶	メガ	M	10 ¹⁵	フェムト	f
10 ³	キロ	k	10 ¹⁸	アト	a
10 ²	ヘクト	h	10 ²¹	ゼプト	z
10 ¹	デカ	da	10 ²⁴	ヨクト	y

表6. SIに属さないが、SIと併用される単位

名称	記号	SI単位による値
分	min	1 min=60s
時	h	1 h=60 min=3600 s
日	d	1 d=24 h=86 400 s
度	°	1°=(π/180) rad
分	'	1'=(1/60)°=(π/10800) rad
秒	"	1"=(1/60)'=(π/648000) rad
ヘクタール	ha	1ha=1hm ² =10 ⁴ m ²
リットル	L, l	1L=11=1dm ³ =10 ³ cm ³ =10 ⁻³ m ³
トン	t	1t=10 ³ kg

表7. SIに属さないが、SIと併用される単位で、SI単位で表される数値が実験的に得られるもの

名称	記号	SI単位で表される数値
電子ボルト	eV	1eV=1.602 176 53(14)×10 ⁻¹⁹ J
ダルトン	Da	1Da=1.660 538 86(28)×10 ⁻²⁷ kg
統一原子質量単位	u	1u=1 Da
天文単位	ua	1ua=1.495 978 706 91(6)×10 ¹¹ m

表8. SIに属さないが、SIと併用されるその他の単位

名称	記号	SI単位で表される数値
バール	bar	1 bar=0.1MPa=100kPa=10 ⁵ Pa
水銀柱ミリメートル	mmHg	1mmHg=133.322Pa
オングストローム	Å	1 Å=0.1nm=100pm=10 ⁻¹⁰ m
海里	M	1 M=1852m
バイン	b	1 b=100fm ² =(10 ⁻¹² cm) ² =10 ⁻²⁸ m ²
ノット	kn	1 kn=(1852/3600)m/s
ネーパ	Np	SI単位との数値的な関係は、 対数量の定義に依存。
ベベル	B	
デジベル	dB	

表9. 固有の名称をもつCGS組立単位

名称	記号	SI単位で表される数値
エルグ	erg	1 erg=10 ⁻⁷ J
ダイン	dyn	1 dyn=10 ⁻⁵ N
ポアズ	P	1 P=1 dyn s cm ⁻² =0.1Pa s
ストークス	St	1 St=1cm ² s ⁻¹ =10 ⁻⁴ m ² s ⁻¹
ストルブ	sb	1 sb=1cd cm ⁻² =10 ⁻⁴ cd m ⁻²
フォト	ph	1 ph=1cd sr cm ⁻² 10 ⁴ lx
ガリ	Gal	1 Gal=1cm s ⁻² =10 ⁻² ms ⁻²
マクスウェル	Mx	1 Mx=1G cm ² =10 ⁸ Wb
ガウス	G	1 G=1Mx cm ⁻² =10 ⁴ T
エルステッド ^(c)	Oe	1 Oe ≡ (10 ³ /4π)A m ⁻¹

(c) 3元系のCGS単位系とSIでは直接比較できないため、等号「≡」は対応関係を示すものである。

表10. SIに属さないその他の単位の例

名称	記号	SI単位で表される数値
キュリー	Ci	1 Ci=3.7×10 ¹⁰ Bq
レントゲン	R	1 R=2.58×10 ⁻⁴ C/kg
ラド	rad	1 rad=1cGy=10 ⁻² Gy
レム	rem	1 rem=1cSv=10 ⁻² Sv
ガンマ	γ	1 γ=1 nT=10 ⁻⁹ T
フェルミ	fm	1 fm=10 ⁻¹⁵ m
メートル系カラット		1メートル系カラット=200 mg=2×10 ⁻⁴ kg
トル	Torr	1 Torr=(101 325/760) Pa
標準大気圧	atm	1 atm=101 325 Pa
カロリ	cal	1cal=4.1858J (「15°C」カロリ), 4.1868J (「IT」カロリ), 4.184J (「熱化学」カロリ)
マイクロン	μ	1 μ=1μm=10 ⁻⁶ m

